The influence of aggregate fracture on the shear strength of reinforced concrete beams

by

Juan Sagaseta Albajar

A thesis submitted to the Department of Civil & Environmental Engineering of the University of London in partial fulfilment of requirements for the degree of Doctor of Philosophy and Diploma of Membership of Imperial College London

Department of Civil & Environmental Engineering
Imperial College London
London SW7 2AZ, United Kingdom

September 2008

A mis padres Marta y César

y hermanos Pablo y Luis

Abstract

High-strength (HS) and light-weight aggregate (LWA) concretes are generally used to reduce member sizes and self-weight. The bond between the aggregate particles and the cement paste can be strong enough in HSC and LWAC to cause the aggregate to fracture at cracks which in turn reduces the shear stress which can be transferred across cracks by means of aggregate interlock. The contribution of aggregate interlock to the shear strength of reinforced concrete beams is uncertain and depends on parameters such as the amount of shear reinforcement and the contribution of arching action for loads applied close to the support. These aspects can influence the crack pattern and relative crack displacements, which in turn affects the contribution of aggregate interlock to shear strength. Previous tests on slender reinforced concrete beams without shear reinforcement have shown that shear strength is reduced by aggregate fracture. There is a lack of similar test data for members with stirrups and for members with varying shear span to effective depth ratios. This thesis describes a set of 22 beam tests carried out by the author, on short span beams and simply supported slender beams all with and without stirrups. Tests also include continuous beams with stirrups. Two different types of aggregate were used (gravel and limestone) to investigate the effect of aggregate fracture on shear strength. The cracks tended to pass around the gravel aggregate and through the limestone aggregate. Shear stresses were estimated at critical shear cracks from constitutive relationships derived from the author's push-off tests. The shear strengths of the 22 beams tested are compared with strengths calculated in accordance with the design provisions in EC2, BS8110 and CSA design codes, in which aggregate fracture is not explicitly considered. Strut-and-tie models for short span beams with and without stirrups are also presented. A discrete crack slip model is also developed for shear panels, short span and continuous beams, in which the behaviour is assumed to be governed by shear stresses along cracks. The analytical and finite element models developed can be used to assess the influence of crack roughness on the shear strength of reinforced concrete beams.

Acknowledgements

After spending almost four year of one's life working towards one specific target such as a PhD, one would think this a very lonely process, especially if this involves moving to a foreign country. However, when I came to write my thesis acknowledgements I realized that the list of people that guided me through my PhD was surprisingly long. I would like to thank all those people that helped me make my PhD a pleasant journey.

Firstly, I would like to thank my supervisor Dr. Robert Vollum for all the knowledge he has managed to transfer to me along all these years. I would like to thank him for his guidance and large amount of time invested in me, which has included endless meetings, long days in the structures lab and an infinite number of emails. I am very grateful for all this, which has helped me to keep my motivation up from first to last day at Imperial College.

The work carried out during the last two year had been possible thanks to the scholarship for international postgraduate studies awarded by *Fundación Caja Madrid* (Spain). I would like to acknowledge this financial support since it allowed me to pay tuition fees and living expenses for the last two year of this research project. Me gustaría agradecer a Caja Madrid y en concreto a la gente de la Fundación y Club Alumni, por haber organizado estupendos actos de entregas, cenas y reuniones de navidad entre becarios.

Another especial mention should be made to staff members of the Heavy Structures Laboratory at Imperial College, London. In particular, I am very grateful to Les Clark for his great work on the experimental part of this research project. I can not think of carrying this work without his valuable help. Thanks Les for sharing with me enthusiasm and long hours in the lab. Also I would like to thank Stef, Ken, Bob, Trevor, Ron and Gordon for their help casting the 22 beams.

I wish to thank those people in the concrete structures section at Imperial College who had helped me during these years, in particular to Dr. Sunday Popo-ola and Dr. Andy Pullen for their interesting comments regarding instrumentation and other testing related issues. I am also very grateful to Dr. Neil Tsang for letting me use his digital photogrammetric programme and showing me how to apply it to our beam tests. I wish to thank Miguel Castro (FEUP) and Luis Albajar (ETSICCP Madrid) for helping me so many times in finding useful references for my thesis.

During these years I have had the chance to work in collaboration with many experts in the field of structural concrete. I specially enjoyed working along with Dr. Bukhari Imran on CFRP strengthened members failing in shear. I would like to thank collie Mario Pimentel from Porto University for the big help provided in NLFEA using DIANA. Also, I would like to thank Wijtze Pieter from TNO DIANA, for the technical support provided, as well as DIANA Users Association and Ane de Boer in particular, for their interesting comments and promoting workshops and events that I had attended. I would like to thank Professor Muttoni, Professor Walraven and Dr. Evan Bentz for the interest shown in this project at international conferences and for their interesting comments.

In the next few lines I would like to thank all my friends from Imperial College, with whom I have shared living experiences and PhD anecdotes during all these years. Muchas gracias a Veronica, Marie, Elle, Ian, Kostas, Despoina, Anna, Amy, Rodrigo, Mike, Jeannette, Ana, Jason, Echat, Daesuke, Tassos, Olympia, Katherine y en especial a mi compañero de piso Olli. Thanks also to the Clayponds community in general for those fantastic barbeques, football games, film nights and Christmas parties.

También me gustaría agradecer a mis amigos de toda la vida de Santander, Blanca, Javi, Paula, Silvia, Natalia, David, Carmen, Vanesa, Sergio y Antonio, por todos los ánimos recibidos. A mis amigos "camineros" Carlos, Javi, Elena, Pablo, Carol, Quique, Marta, Fernando, Antonio, Almudena, Tama y Noelia por compartir conmigo momentos especiales y por acordarse de mi aún desde la distancia. Por último gracias por las visitas recibidas de antiguos compañeros de Proes, en especial a Gonzalo, Estela y César.

For her words of support over these years I would like to thank my girlfriend Dr. Michaela Pollock. Thank you, for listening to my "exciting" concrete beam stories, for checking my English grammar and for showing me the best Indian restaurants in London. Although I have thanked you already by cooking delicious quesadas, I would like to thank you once again for always being there.

Por último, quiero agradecer a mis padres y hermanos por su apoyo incondicional durante estos años. A mis padres, les agradezco el ejemplo que me han dado y el cariño que me han transmitido. Muchas gracias por animarme en todo momento y por cuidar de mí, en especial durante los últimos meses que pasé escribiendo la tesis. A mis hermanos y respectivas, gracias por sus palabras de aliento y por soportar mi sentido del humor inglés durante el verano en Santander.

Table of Contents

List of Figures

List of Tables

List of Symbols

a = Shear span measured between centrelines of bearing plates; Aggregate size

a_v = Clear shear span measured between inner edges of bearing plates

a_{eff} = Effective aggregate size assume in calculations

A_{sw} = Cross-sectional area of shear reinforcement

A_{sl} = Cross-sectional area of longitudinal reinforcement

b, b_w = Member width

b_f = Member width at the flange

c = Cohesion; Distance from bottom of the beam to centroid of flexural reinforcement

d = Effective depth

DP = Demerit point classification mark

D_T = Overall shear stiffness of discrete crack interface

D_{dw} = Dowel action stiffness contribution to D_T

D_{ai} = Shear stiffness after cracking provided to interface elements due to pure aggregate interlock action

E_c = Concrete Young's modulus

f_{cd} = Design concrete strength

$f_c' = f_{ck}$ = Cylinder concrete strength

f_{cu} = Cube strength, also refered to as f_{cc}

f_{ct} = Concrete tensile strength

f_1 = Principal tensile stress (MCFT)

f_2 = Principal compressive stress (MCFT)

f_{c2} = Principal compressive stress in concrete (MCFT)

f_{cr} = Stress in concrete at cracking (MCFT)

f_{cnt} = Effective concrete strength at the top node in STM

f_{cnb} = Effective concrete strength at the bottom node in STM

f_{cst} = Effective concrete strength of compression strut at top in STM

f_{csb} = Effective concrete strength of compression strut at bottom in STM

f_y = Yield strength of reinforcement steel

f_{ywd} = Design yield strength of the shear reinforcement

FOS = Overall factor of safety, including material and load factors

G_c = Fracture energy in compression

G_f = Fracture energy in tension

h = Member height; Crack bandwidth

h_f = Flange thickness

k = Aggregate interlock shear stiffness coefficient; Shear lever arm factor ($z=kd$)

k_n = Normal stiffness of interface element

k_t = Tangential stiffness of interface element

l_b, l_t = Length of bottom, top bearing plates

l_{fr} = Free-length parameter

n = Number of stirrups within the effective shear span (short span beams)

n_{lp} = Number of loading points (1 or 2)

P = Total load applied

P_{cr} = Total load applied at which first shear crack formed

P_{ult}, P_{test} = Total load applied at failure

P_d = Design shear force, including material and load factors of safety

r = Ratio between steel stress capacities in the x and y direction ($\rho_x f_{xy}/\rho_y f_{yy} \geq 1$)

s = Crack sliding or slip; Spacing of the stirrups

SG = Strain gauge

SI = Stirrup index: for short span beams $SI=nA_{sw}f_y/(bhf_c')$

for slender beams $SI=\rho f_y/(vf_c')$

s_θ = Diagonal crack spacing

s_{ze} = Effective crack spacing

s_{mx}, s_{my} = Crack control parameters in the x, y directions according to MC90

T = Tensile force transferred to the bottom node in strut-and-tie model

T_{si} = Tensile force carried by each stirrup

T_d = Tensile force transferred to the bottom node by direct strut

T_i = Tensile force transferred to the flexural reinforcement by indirect strut II

T_i' = Tensile force transferred to the bottom node by indirect strut III

V = Shear force

V_c = Shear concrete component

V_s = Stirrup contribution to shear

$V_{Rd,s}$ = Shear resistance to yielding of the shear reinforcement

$V_{Rd,max}$ = Maximum shear resistance limited by crushing of the compression struts

$V_{Rd,web}$ = Shear resistance provided by the web

V_{fd} = Vertical component of friction shear forces according to truss with friction model

v = Constant shear stress at cross section (V/bz)

v_n = Normalized shear stress (v/vf_c')

v_{ci} = Shear stress on crack surface (MCFT)

w = Crack opening or crack width

z = Effective level arm (for shear $z=jd=0.9d$, unless stated)

α = Inclination of shear crack (also refered as β_r); Threshold angle in multi-fix model

β = Shear retention factor; Compression softening factor of the concrete strength (MCFT); Fraction of total tensile force transferred by direct strut to bottom node in strut-and-tie model for short span beams with stirrups; Angle between the strut and the crack plane; Interpolation factor applied to V_c (EHE)

δ = Vertical deflection

ε_c' = Strain in concrete cylinder at peak stress f_c'

ε_e = Elastic strains

ε_{cr} = Crack strains

ε_1 = Principal tensile strain (MCFT)

ε_2 = Principal compressive strain (MCFT)

ε_x = Strain in the x-direction

ε_y = Strain in the y-direction

ε_{rcr}, ε_{dcr} = Strain in the r, d directions in the crack element

ε_{xcr}, ε_{ycr} = Strain in the x, y directions in the crack element

ϕ = Friction angle

ϕ_c, ϕ_s = Capacity reduction factors (CSA)

γ_{xy} = Shear strain relative to x, y axes

γ_c, γ_s = Partial factors for concrete and steel

λ = Proportion of load carried by direct strut in strut-and-tie model for short span beam

μ = Friction parameter

ν = Strength reduction factor for concrete cracked in shear; $\nu=0.6[1-f_c'/250]$ (EC2); Poisson ratio (NLFEA)

θ = Inclination of compression stress field (strut)

ρ_{sx}, ρ_{sy} = Reinforcement ratios for steel in x, y directions (MCFT)

ρ_l = Flexural reinforcement ratio

ρ_v = Shear reinforcement ratio

σ_{ncr} = Normal stresses at the crack

τ_{xy} = Shear stress at the element

τ_{cr} = Shear stress at the crack

ψ = Dilatancy angle

CHAPTER 1 – Introduction

1.1 Motivation and challenges

This work is primarily concerned with the influence of aggregate interlock on the shear strength of reinforced concrete beams. The bond between the aggregate particles and the cement paste can be strong enough in high-strength concretes (HSC) to cause the aggregate to fracture at cracks which in turn reduces the shear stress which can be transferred across cracks by means of aggregate interlock. A similar situation can arise in light-weight aggregate concretes (LWAC). The contribution of aggregate interlock to the shear strength of reinforced concrete beams is uncertain and depends on parameters such as the amount of shear reinforcement and the contribution of arching action for loads applied close to the support. These aspects can influence the crack pattern and relative crack displacements, which in turn affects the contribution of aggregate interlock to shear strength.

Taylor's [1, 2] pioneering experimental and analytical work on slender beams without shear reinforcement indicated that aggregate interlock could contribute up to 50% of the shear strength. Regan [3, 4] recently carried out a series of tests on beams without stirrups which showed that shear strength was reduced if the coarse aggregate fractured at cracks. This work led to the maximum design concrete strength being limited to 60MPa in the UK National Annex to Eurocode 2. Regan was unable to establish the influence of aggregate fracture on the shear strength of beams with stirrups due to the failure of many investigators to report the type of aggregate used in their tests. A key aim of the current work is investigate the influence of aggregate fracture on shear strength in beams with stirrups.

A significant limitation in the design methods for shear given in codes such as BS8110 [5], MC90 [6], or EC2 [7] is that they do not, with the exception of LWAC, take into consideration the type of aggregate used. In general, the potential reduction in shear strength due to smoother cracks is only considered by means of the concrete compressive strength and not by the type of aggregate. For example, UK National Annex to EC2 limits the concrete strength to 60MPa in shear calculations to account for fracturing of the course aggregate, unless further experimental evidence is provided. On the other hand, Canadian design equations, which are based on the well known Modified Compression Field Theory (Vecchio & Collins [8]), aggregate fracture can be considered by reducing the effective size of the aggregate in the calculations. However, this is generally done according to the concrete strength and not to the type of aggregate. Moreover, the allowance of changing the aggregate size in the simple approach suggested in the Canadian code seems to be only recommended for cases of members without shear reinforcement.

Concerns about aggregate fracture have been raised by authors including Walraven et al. [9, 10]. These concerns led to them testing several series of simply supported slender beams using HSC and LWAC. These tests did not show any significant reduction in shear strength due to aggregate fracture. However, to the author's knowledge, no tests have been carried out using different aggregate types in identical beams with similar concrete strengths and different shear span to effective depth ratios, including cases with and without shear reinforcement. Moreover, little experimental evidence is available on continuous beams with stirrups.

Shear in structures becomes more critical in zones near the supports or applied loads, where the stress distribution is not uniform. In these discontinuity regions, standard theory is not applicable and more recent approaches such as the strut-and-tie method (STM) have been developed in order to detail the reinforcement layout at these regions. Although the STM is transparent, several assumptions are required in terms of strength and geometry of truss elements (strut, nodes and ties). Again, the influence of aggregate fracture is not taken into account directly since cracking and transverse strains are only considered by means of "effectiveness" concrete strength factors. In particular, EC2 allows the STM to be used for designing short span beams as an alternative method to simple design formulas. However, the predictions of these formulae and STM can vary considerably. It is questionable which method is more realistic since aspects such as size

effects and the influence of the position of critical shear cracks on strength of the strut are neglected in many of these approaches. The inconsistencies between the predictions of simple design formulae, NLFEA and strut-and-tie models have intrigued the author since his early days as a structural engineer in a consultancy office in Madrid.

1.2 Objectives

The main objectives of this work are highlighted below.

1. The assessment of normal and shear stresses transmitted along cracks in which the aggregate particles had fractured completely for different shear reinforcement ratios.
2. The modelling of in-plane shear stress states by means of smeared and discrete crack approaches.
3. The development of an experimental programme in order to assess the influence of aggregate fracture on shear behaviour for different beam slenderness ratios (short span and slender beams), including cases with and without shear reinforcement.
4. To investigate the accuracy of the design equations for shear in RC short span and slender beams which are available in codes of practice. This study includes a close examination of critical parameters and assumptions made by each method, especially those related to aggregate interlock action.
5. The provision of general recommendations to improve shear strength predictions when using either design formulae or more elaborate smeared/discrete crack approaches, in particular for cases where the aggregate particles split at the crack surface.

1.3 Outline of Thesis

This thesis consists of nine chapters. The introductory chapter is followed by chapters 2 and 3 in which the different approaches for modelling shear in reinforced concrete members used in practice are reviewed. **Chapter 2** focuses on the different analytical methods which form the base for most of shear equations suggested in design codes such as EC2 or BS8110. Although most of these methods are grounded on the truss analogy concept, smeared and discrete crack approaches are also discussed.

In **chapter 3**, several approaches for modelling cracking in reinforced concrete members by means of the Finite Element Method are presented. The advantages and shortcomings of each approach are discussed, as well as recommended values for the different parameters required for non-linear finite element analysis.

Aggregate interlock action is studied in **chapter 4**, in which experimental push-off test data obtained in this work is presented. The results are also discussed in view of the predictions from analytical models described in previous chapters. Subsequently shear panel test results available in the literature are examined in **chapter 5**. A simple discrete crack slip approach is presented and validated using existing experimental data. This approach applies crack dilatancy relationships, which had been previously validated in chapter 4.

The experimental results and test procedures for a series of 22 beam tests carried by the author at the Heavy Structures Laboratory at Imperial College London is presented in **chapter 6**. The results obtained from the short span beams are analysed in **chapter 7**. In addition, a strut-and-tie model is proposed, which is consistent with EC2 recommendations for STM. The predictions of a large data base of short span beams using the proposed STM model are compared with those obtained from design methods suggested in EC2 and BS8110. In **chapter 8**, the slender beam tests presented in chapter 6 are analysed. Similarly as in chapter 7, the accuracy of the predictions from the different design equations is discussed. Estimations of shear stresses along critical cracks are shown in chapters 7 and 8, which were obtained by either interpolation of push-off test data or analytical models that had been previously studied in chapters 4 and 5.

Finally, in **chapter 9** the main conclusions drawn from this work are outlined as well as recommendations for future work.

CHAPTER 2 – Literature Review

2.1 Introduction

Shear design in structural concrete has been a topic of research for many years. The large number of factors influencing shear behaviour such as aggregate interlock, dowel action or size effect, makes the study of shear in reinforced concrete a challenging subject. This is evidenced by the large number of research groups that are currently carrying out experimental and analytical work in this area.

This great effort for improving shear design equations has been largely motivated by the shear failure of some existing structures, which were designed using early code formulations. Typical examples presented by Collins et al. [11, 12] include the collapse of roof beams in the Air Force warehouse in Ohio back in 1955 to the more recent collapse of Laval's bridge in Quebec (2006), which is shown in Figure 2.1. Both structural failures showed the importance of longitudinal reinforcement and size effects in shear design.

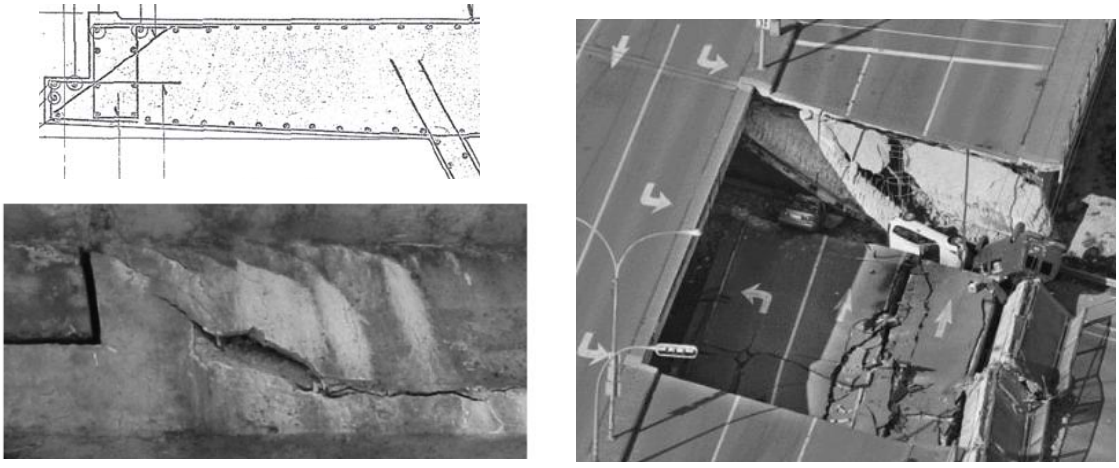

Figure 2.1: Shear failure of Laval's bridge, Quebec 2006 (adapted from [13]); *Left*- Photograph taken in road supervision hours before the collapse; *Right*- General view

Shear transfer in cracked reinforced concrete members is commonly described using the well known truss analogy, which was first proposed by Ritter [14] and Morsch [15] at the beginning of the Twentieth Century. Subsequently, many attempts have been made to improve the truss analogy.

In structural concrete, four major methods are commonly used to calculate shear strength:

1. Classical Method: based on the Truss Analogy ($\theta = 45^{\circ}$)
2. Variable Strut Angle Method: based on the Theory of Plasticity
3. Smeared Truss Models: Compression Field Theories
4. Discrete Crack Approaches

These four methods, which are the most commonly used in shear design/analysis, are reviewed in this chapter, which examines their assumptions, limitations and differences in in outcome. The role of aggregate interlock is presented, along with equations for several crack dilatancy models, which can be used in non-linear analytical procedures. The different approaches for studying shear, which are presented in this chapter, are also reviewed in terms of their capacity to model the potential reduction in shear strength resulting from the loss of aggregate interlock at smooth cracks passing throught the coarse aggregate. Some of these models are assessed in chapter 4 using experimental data from the author's push-off tests.

Shear in structures often becomes critical in zones near the supports or applied loads where the stress distribution is not uniform; these regions are commonly denoted as "Discontinuity regions" (D regions). The traditional assumption that plane sections remain plane no longer applies in D regions. The strut-and-tie method (STM) is widely recommended for the design and analysis of D regions. The STM has the advantage of being a relatively simple procedure but there are still significant uncertainties and questionable assumptions implicit in the method. Some of the most important aspects of strut-and-tie modelling are outlined in this chapter.

2.2 Classical and variable inclination strut methods

The truss analogy forms the basis of most design methods for shear. Traditionally the shear resistance is assumed to be given by $V=V_c+V_s$ where V_c is the shear resisted by a beam without stirrups and V_s is the contribution of the stirrups calculated using a truss system with struts inclined at 45˚. The concrete term "V_c" was introduced to improve the correlation between test results and strengths predicted with Morsch's truss. This term is estimated using empirical rules first appended in codes such as DIN1045 and SIA (Sociéte Suisse des Ingénieurs et des Architectes) as well as in the ACI 318.

Alternatively, in the plasticity approaches developed by Muttoni et al. [16], Nielsen [17] and Nielsen & Braestrup [18], shear is assumed to be completely resisted by the steel component V_s with no contribution of V_c. The plasticity methods form the basis of the variable strut inclination design method (VSI) given in EC2. In this design method, the inclination of the strut is freely selected within a prescribed range wich depends on the strength of the struts in the inclined stress field.

In practice, the lowest possible angle of inclination is usually adopted to minimise the area of stirrups. Codes provide different ranges for θ. For example, EC2 gives $2.5 \leq cot\theta \leq 1$ ($21.8^\circ \leq \theta \leq 45^\circ$) or MC90 gives $3 \leq cot\theta \leq 1$ ($18.4^\circ \leq \theta \leq 45^\circ$). From truss equilibrium the ultimate shear due to yielding of the stirrups is given by expression (2.1).

$$V_{Rd,s} = \frac{A_{sw}}{s} . f_{ywd} z \cot\theta \qquad \ldots (2.1)$$

where A_{sw} = area of the transverse reinforcement, s = stirrup spacing in the longitudinal direction, f_{ywd} = design yield strength of transverse reinforcement, z= inner lever arm taken as $0.9d$ in shear and θ = strut inclination.

Once the transverse reinforcement begins to yield, θ decreases to activate more stirrups. This strut rotation, which has been measured in tests by Walraven [9, 10] or Hamadi & Regan [19] amongst others, results in an increase of the compressive stress in the strut. The ultimate shear stress that causes crushing of the strut is given by equation (2.2):

$$V_{Rd,\max} = \nu f_{cd} . b_w z \sin\theta . \cos\theta = \nu f_{cd} b_w z / (\cot\theta + \tan\theta) \qquad \ldots (2.2)$$

where $\nu = 0.6(1-f_{ck}/250)$ according to EC2, f_{ck} = cylinder concrete strength, b_w = minimum width between tension and compression chords.

Figure 2.2 shows the variation in $V_{Rd,s}$ and $V_{Rd,max}$ with the strut angle. The minimum permissible value for θ is the greater of θ_{min} or the value calculated by equating the design shear force to the web crushing capacity ($V_{Rd,max}$), which is given by equation 2.2. On the other hand, if the ultimate shear strength is to be calculated for a given shear reinforcement ratio, θ must be obtained from equations (2.1) and (2.2), checking that $\theta_B \leq \theta \leq \theta_C$ as shown in Figure 2.2.

In the variable strut angle model the concrete strength has an "effective" strength factor ν that takes into account the biaxial compression-tension stress state and the influence of cracks running skew to the strut which reduce the effective area of the concrete in compression. The difference between the predictions given by the classical truss model and the variable strut angle method are shown in Figure 2.2. In the variable strut inclination method, the shear strength is generally taken not lower than the shear strength of equivalent beam without shear reinforcement (point A in Figure 2.2)

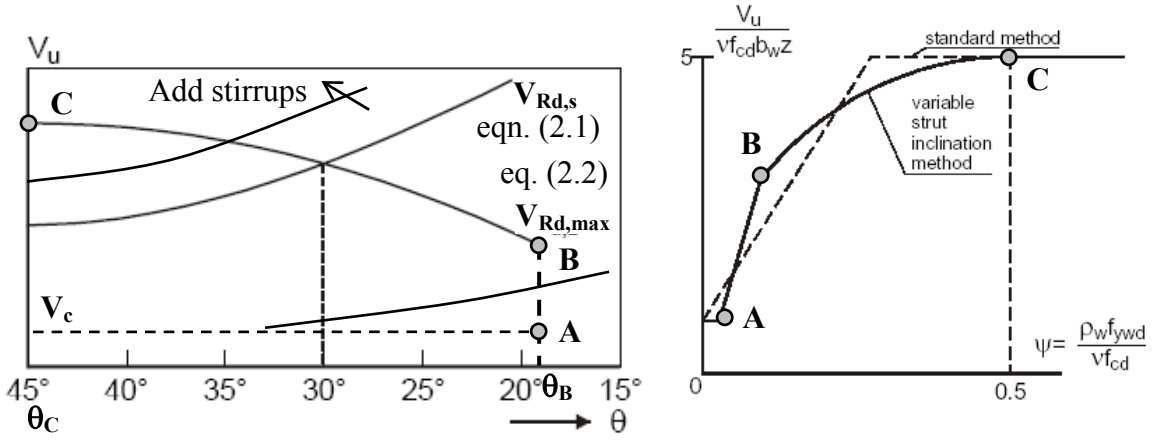

Figure 2.2: Variable strut inclination method

One of the advantages of using the variable strut inclination method is that since it is based on a pure truss, the contribution of concrete is more visible than with a simplified constant θ truss, where an empirical value for V_c must be added. As reported by Regan [20], the concrete term in the classical 45º truss approach, which is estimated as the strength of the equivalent beam without stirrups, can be physically misleading. This is due to the large difference in the ultimate load behaviour between members with and without shear reinforcement. Some authors like Reineck [21] suggest that the addition of this "artificial" concrete component in the 45˚ truss method can be explained as the contribution of concrete to shear strength due to friction forces along the failure cracks, (see section 2.4).

The Spanish code EHE [22] adopts a compromise solution between the classical 45º truss and the variable strut inclination method with regards to the concrete contribution. According to EHE, the total shear is given by the sum of βV_c and V_s, where β equals 1 if θ is 45º and 0 if θ is 26.6º ($cot\theta$=2). For intermediate values of β, EHE provides an interpolation relationship, which is a function of the assumed angle θ and the crack inclination, which is estimated from the elastic stresses at the level of the neutral axis. Once the angle of the strut is selected by the designer, similar checks are made as in the variable inclination strut method of EC2 (crushing of the strut, yielding of the stirrups and failure of the tensile chord). Although this method offers a transition between the extremes of the classical or variable strut inclination methods, it is possibly more misleading than either.

Another advantage of the VSI sectional method in EC2 worth mentioning is that it models the transition between regions of uniform stress fields and regions where trusses, fans and other strut-and-tie systems are used together. These regions can be modelled using a plasticity truss model, which considers the entire stress fields. The variable strut angle method seems more rational than the simple truss in such transition regions since it can be demonstrated clearly that all systems are in equilibrium (Walraven [23]).

A shortcoming in the variable strut inclination method is the assumption that the principal tensile stress is zero. In addition, the shear taken by the compression zone is neglected. The variable strut inclination angle method, which is justified with the lower bound theorem of plasticity, only considers the ULS. The plasticity truss model is effectively a rotating crack model in which the effect of previous cracks is neglected. No consideration is given to the effects of variations in aggregate interlock at cracks. The failure to consider shear transfer at cracks can lead to the shear strength being overestimated by the plasticity truss model if the minimum angle of the compressive stress field is governed by interface shear at the cracks. Aggregate fracture at the crack can only be taken into account in an indirect manner by limiting the effective concrete strength in the strut.

2.3 Modified Compression Theory

The Modified Compression Field Theory developed by Vecchio and Collins [8] is a further development of the Compression Field Theory. In the CFT it is assumed that the principal tensile stress f_1 is zero after the concrete has cracked while in the MCFT the effect of the residual tensile stress in the concrete between the cracks is taken into account. Tensile stresses across the diagonal struts increase from zero at the cracks to a maximum in the middle of the strut as shown in Figure 2.3 (left).

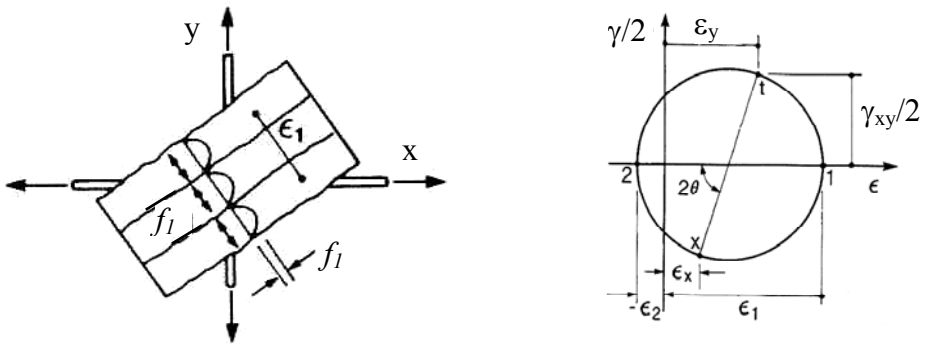

Figure 2.3: MCFT: *Left* – Tensile stresses along a cracked strut; *Right* – Mohr's circle for average strains (adapted from Collins & Mitchell [11])

The MCFT model consists of strain compatibility and equilibrium equations which can be used to predict the complete shear deformation response. All the compatibility equations are expressed in terms of "average" strains measured over base lengths long enough to include several cracks. The compatibility conditions for both CFT and MCFT are given in equations (2.3), (2.4) and (2.5), which are obtained from Mohr's circle shown in Figure 2.3 (right).

$$\gamma_{xy} = \frac{2(\varepsilon_x - \varepsilon_2)}{\tan\theta} \qquad \ldots (2.3)$$

$$\varepsilon_1 + \varepsilon_2 = \varepsilon_x + \varepsilon_y \qquad \ldots (2.4)$$

$$\tan^2\theta = \frac{\varepsilon_x - \varepsilon_2}{\varepsilon_y - \varepsilon_2} \qquad \ldots (2.5)$$

where γ_{xy}= shear strain, ε_x= strain in the x-direction, ε_y= strain in the y-direction, ε_1= principal tensile strain in concrete (positive value), ε_2= principal compressive strain in concrete (negative value).

The Mohr´s circle (Figure 2.4) can be used to derive an equation for relating the principal compressive stress f_2 and tensile stresses, see equation (2.6).

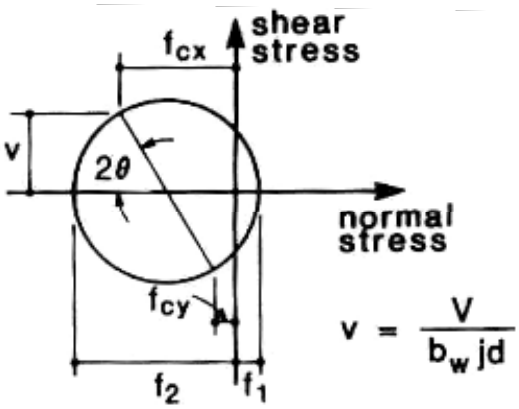

Figure 2.4: Mohr stress circle for average concrete.

$$f_2 = (\tan\theta + \cot\theta).v - f_1 \qquad \ldots (2.6)$$

where $v = V/(b_w jd)$.

The equilibrium conditions for a symmetrical cross section subjected to pure shear shown in Figure 2.5 can be expressed as

$$A_{sw} f_{ywd} = (f_2 \sin^2\theta - f_1 \cos^2\theta).b_w s \qquad \ldots (2.7)$$

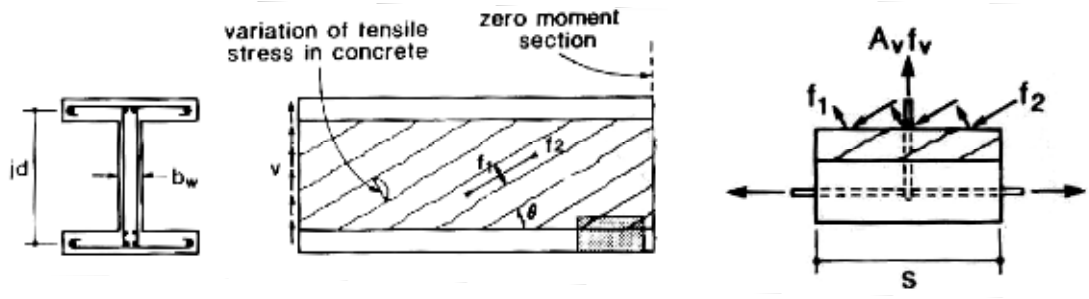

Figure 2.5: Cross section, principal stresses and tension in web reinforcement

Substituting equation (2.6) into (2.7) leads to the following expression

$$V = f_1 b_w jd \cot\theta + \frac{A_{sw} f_{ywd}}{s}.jd \cot\theta \qquad \ldots (2.8)$$

Collins & Mitchell [11] noted that equation (2.8) expresses shear resistance in terms of the sum of a concrete and steel contributions, as the traditional or classical method. The concrete contribution depends on the average tensile stresses in the concrete whilst the latter depends on the tensile stresses in the stirrups and the angle of the inclined stress field. It is important to highlight that although the approaches might seem similar, the concrete contribution suggested in the MCFT is not constant as assumed in the classical

truss method. Furthermore, V_c in the MCFT it is not equal to the shear strength of a similar member without shear reinforcement. As shown in this section, V_c according to the MCFT is a function primarily of the crack width. Increasing the number of stirrups reduces the crack spacing, which in turn decreases the crack width and hence increases the concrete contribution (Cladera [24]).

One of the most important features of the MCFT is the average strain-stress relationships derived from the tests of reinforced panels subjected to pure shear (Vecchio and Collins [8]). The concrete compressive strength is reduced to take into account softening due to transverse tensile strain (ε_1). Initially [8], a parabolic relationship for cracked concrete in compression subjected to high tensile strains in the direction normal to the compression was suggested, see equation (2.9).

$$f_{c2} = f_{c2\max}.\left[2.\left(\frac{\varepsilon_2}{\varepsilon_c'}\right) - \left(\frac{\varepsilon_2}{\varepsilon_c'}\right)^2\right] \qquad \ldots (2.9)$$

where

$$\beta(MCFT) = \frac{f_{c2\max}}{f_c'} = \frac{1}{0.8 - 0.34.\frac{\varepsilon_1}{\varepsilon_c'}} \leq 1.0 \qquad \ldots (2.10)$$

Later Vecchio & Collins [25] modified equations 2.9 and 2.10 in the light of the new experimental data. The compression curve used for concrete was changed to the Thorenfeldt asymmetric curve instead of the parabolic relationship used originally. Figure 2.6 shows that the new relationship given for concrete softening β(1993), which is referred to as Model B in [25], is not significantly different from the original one.

Alternative analytical relationships have been presented by different researchers to account for compression softening (Kollegger & Melhorn [26], Miyahara et al. [27], Belarbi & Hsu [28]). As recognized by Vecchio & Collins [25], there is a considerable variation between these models although the comparison is difficult for some of them since the equations were implemented in models which accounted for crack slip. As reported by Vecchio [29], compression softening is influenced by slippage on the cracks.

Equation (2.10) was derived for the MCFT in which the crack slip is not taken into account. On the other hand, if crack slip is to be considered in the model, the rate of softening must be reduced to account for the greater strains obtained in (2.10), which are

due to slippage (Vecchio [29]). Typical examples include the Disturbed Stress Field Model (DSFM) suggested by Vecchio [29], which is not discussed here, or in the Truss with Crack Friction model (see section 2.4). In both types of approaches, crack slip is considered. In the DSFM, the parameter C_s was introduced in the softening curve (2.10), as shown in Figure 2.6; a value of C_s=0.55 provided optimal predictions of shear panels investigated by Vecchio [29].

According to Vecchio & Collins [25], concrete strength can have also an influence in concrete softening; high-strength concretes tend to show a slightly larger softening than normal strength concretes. Moreover, size effects can also have an effect on β. Effective strengths used in plasticity approaches (see section 2.1), assume a constant reduction parameter ν, which is only a function of the concrete strength; for normal concrete strengths ν is around 0.5, which corresponds to similar levels of softening as in the MCFT for transverse strains of around $4\varepsilon_c'$ (see Figure 2.6).

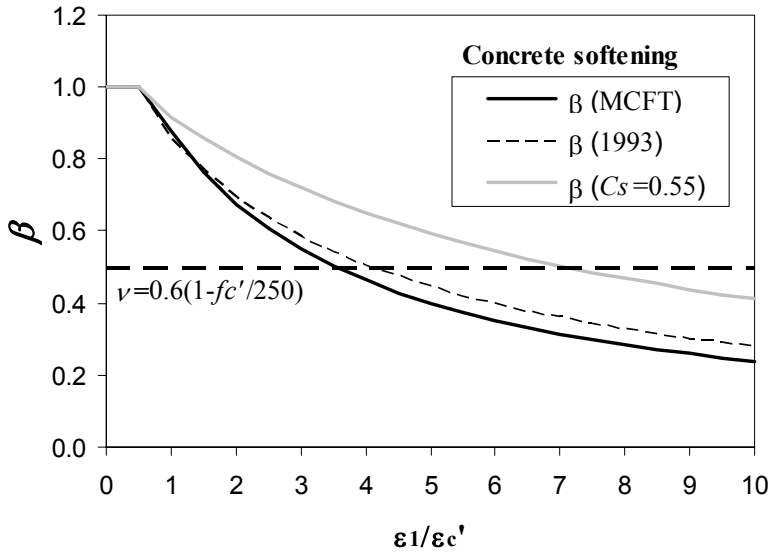

- *Vecchio & Collins* [8]

$$\beta(1993) = \frac{1}{1 + Cd.Cs} \leq 1.0$$

$$Cd = 0.27\left(\frac{\varepsilon_1}{\varepsilon_c'} - 0.37\right)$$

Cs = 1 (MCFT)

- *Vecchio* [29]

Cs = 0.55 (DSFM)

Figure 2.6: Concrete softening due to transverse strains according to Vecchio and Collins

For concrete in tension the curve proposed in Vecchio & Collins [8] is given by the following equations

$$\text{if } \varepsilon_1 \leq \varepsilon_{cr} \quad \text{then} \quad f_1 = E_c.\varepsilon_1 \qquad \ldots (2.11)$$

$$\text{if } \varepsilon_1 > \varepsilon_{cr} \quad \text{then} \quad f_1 = \frac{f_{cr}}{1 + \sqrt{200.\varepsilon_1}} \qquad \ldots (2.12)$$

Equation (2.12) was updated subsequently by Vecchio & Collins [25] to include two new parameters α_1 and α_2 that accounted for the bond characteristics of the reinforcement and the type of loading. The updated equation is as follows

$$f_1 = \frac{\alpha_1.\alpha_2.f_{cr}}{1+\sqrt{500.\varepsilon_1}} \quad \ldots (2.13)$$

where f_{cr} is usually taken as $0.33f_c^{1/2}$.

As mentioned earlier, the stress and strain formulations adopted in the MCFT, use average values and so local variations are not considered. In the method, a check must be done to ensure that reinforcement can take the increment in tensile stress at the crack. In order to make this check a value of the stress along the crack must be assumed. The shear transfer at the cracks by aggregate interlock action is estimated using relationship (2.14), which was derived from Walraven´s test data.

$$v_{ci} = 0.18.v_{ci\max} + 1.64.f_{ci} - 0.82.\frac{f_{ci}^2}{v_{ci\max}} \quad \ldots (2.14)$$

where

$$v_{ci\max} = \frac{\sqrt{f_c'}}{0.31+24.w/(a+16)} \quad \ldots (2.15)$$

In the expressions above, a is the maximum aggregate size in millimetres and w is the average crack width over the crack surface which is estimated as the product of the principal tensile strain (ε_1) and the crack spacing (s_θ). In order to account for aggregate fracture at the crack in high-strength concretes, an effective maximum aggregate size (a_{eff}) was suggested by Lubell et al. [30] and Angelakos et al. [31], which is a function of f_c' only. The maximum size of the aggregate used in equation (2.10) is reduced linearly as f_c' is increased from 60 to 70MPa. This approach does not make any allowance for the influence of aggregate type on crack roughness.

The spacing of the shear cracks is considered to be dependent on the crack spacing in the longitudinal and transverse reinforcement directions s_{mx} and s_{my}. The MCFT suggest expression (2.16) for s_θ. Values for s_{mx} and s_{my} can be estimated using MC90 equations for crack spacing which are dependent on the spacing between the reinforcement bars and the bond strength.

$$s_\theta = \frac{1}{\left(\frac{\sin\theta}{s_{mx}} + \frac{\cos\theta}{s_{my}}\right)} \quad \ldots (2.16)$$

According to the Modified Compression Theory at low shear values, tension is transmitted across the crack by increases in reinforcement stresses until yielding occurs. After yielding of the reinforcement at the cracks, a shear stress v_{ci} is needed along the crack to maintain equilibrium. The calculated average stress state and the local stress state at the crack must be statically equivalent. From this condition equation (2.17), which limits the value for the tensile stress, can be derived. Consideration of equations (2.8) and (2.17) shows that the shear stress v_{ci} is required to maintain equilibrium in a member without shear rebars (ρ_{sy}=0).

$$f_1 = v_{ci}.\tan\theta + \rho_{sy}.(f_{yy} - f_{sy}) \quad \ldots (2.17)$$

The Modified Compression Field Theory can provide accurate predictions of shear strength and deformation as shown in chapter 4, despite the simplifications in the method. The first and most important assumption made in the MCFT is that of a rotating crack model in which previous cracks are assumed to be inactive. The MCFT assumes that the angles of the principal strains and stresses axes coincide (θ); in the literature this is referred to as the co-axiality principle. The crack in which all the checks are carried is assumed to be oriented at the same angle θ as the compressive stress field. Theoretically, no shear stresses should be expected in this plane so the physical meaning of v_{ci} is troublesome. The advantages and disadvantages of using a rotating crack model instead of a fixed crack model are discussed in section 3.2.1.

Another concern with the MCFT is that no check is made on interface shear at previous cracks which may be critical for shear transfer. Furthermore the tension stiffening effect of the reinforcement can be significantly overestimated since it is modelled by adjusting the stress strain response for cracked concrete rather than the response of the reinforcement. As described previously, the MCFT defines equilibrium and compatibility in terms of average stress and strains without any bond slip considerations of the reinforcement bars, so it seems reasonable that the prediction of the local stresses at the reinforcement bars is not entirely accurate.

Lastly, the MCFT has been often criticized from a practical perspective since it requires the use of a computer in order to solve the system of equations. To overcome this problem

Bentz & Collins provide free software packages RESPONSE 2000 and MEMBRANE 2000, to solve the equations. Bentz et al. [32] developed simplified versions of the MCFT, which can be used in order to predict the maximum shear capacity rather than the complete load-deformation response. These simplified equations are incorporated in the Canadian code CSA A23.3 [33]; see equations (2.18) to (2.20).

$$V_r = V_c + V_s \le 0.25\phi_c f_c^{'} b_w d \qquad \ldots (2.18)$$

$$V_r = \phi_c \beta \sqrt{f_c^{'}} b_w d + \phi_s \frac{A_{sw}}{s} f_y d \cot\theta \qquad \ldots (2.19)$$

where ϕ_c, ϕ_s = capacity reduction factors, b_w = web width, d = effective shear depth (d_v=0.9d), A_s = area of longitudinal reinforcement on the flexural tension side. The CSA standard limits the maximum value of $\sqrt{f_c^{'}}$ to 8MPa. Parameter β represents the shear retention factor i.e. ability of cracked concrete to transmit shear by means of aggregate interlock, while θ is the angle of inclination of the strut. Both β and θ are estimated in terms of the longitudinal strain at the mid-depth of the section using equations (2.20) and (2.21).

$$\beta = \frac{0.40}{(1+1500\varepsilon_x)} \cdot \frac{1300}{(1000+s_{ze})} \qquad \ldots (2.20) \qquad \theta = 29^{o}+7000\varepsilon_x \qquad \ldots (2.21)$$

where $\varepsilon_x = \dfrac{M_f / d + V_f}{2E_s A_{sl}}$; M_f and V_f are the factored moment and shear force at section.

The effective crack spacing (s_{ze}) is taken as 300mm for members with at least minimum stirrups and s_{ze}=35s_z/(15+a)≥0.85s_z for members without stirrups. The crack spacing parameter (s_z) is the longitudinal spacing between cracks, measured at mid-depth of the member; s_z is usually taken as d_v for members without horizontal reinforcement at the web. As highlighted by Collins et al. [34], parameter β consists of the product of a strain effect factor, which is given by ε_x, and a size effect factor governed by s_{ze}. Hence shear strength decreases as the longitudinal strain increases and for members without stirrups, as the member depth decreases. In addition, for members with stirrups, an increase in ε_x results in a decrease in the shear strength due to the lower stirrup contribution V_s. Yielding of the longitudinal reinforcement on the flexural tension side must be checked as in the classical and variable strut inclination methods.

2.4 Discrete crack models

The methods for shear design described so far are "smeared approaches" where the compression field is analysed independently of the crack pattern. In addition, the angle of the compression field is skewed to the crack pattern ($\beta_r=\theta$) as shown in Figure 2.7 (left). In reality shear failure is likely to be governed by equilibrium at the critical shear crack as shown in Figure 2.7 (right), which is related to the aggregate interlock.

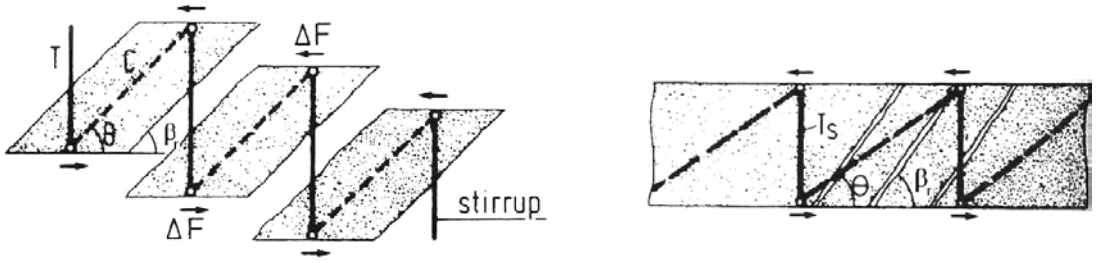

Figure 2.7: *Left*– Crack oriented as compression fields ($\theta=\beta_r$); *Right*– Strut crossed by cracks (adapted from Schlaich et al. [35])

As emphasized by Reineck [21], research should focus more on the so-called "failure mechanism approaches". In these methods the actual failure surface in a member or the critical crack and the localized crushing of the concrete in the compression zone are considered. Discrete crack approaches provide a more rational description of the shear behaviour, but are probably too complex for practical purposes since they usually require the solution of complicated analytical equations.

Truss Model with Crack Friction

An example of a discrete method for shear design is the Truss Model with Crack Friction proposed in 1996 FIP Recommendations [21]. These recommendations are based on previous work by Poli et al. [36, 37], Kirmair [38] and Kupfer [39]. The model considers the equilibrium of a free-body diagram of a separated element along a diagonal crack as it was done by Mörsch but also considers the friction force along the crack due to aggregate interlock.

The shear resisted by the web ($V_{Rd,web}$) is the total sum of the shear force component carried by the vertical stirrups ($V_{Rd,s}$), which is obtained using equation (2.1), and the vertical component of the friction forces at the crack (V_{fd}). The latter component represents the "concrete contribution" in the standard truss method. To calculate $V_{Rd,web}$, the inclination of the crack as well as the crack spacing must be assumed or estimated, for

example by performing a non-linear analysis. A constitutive law for the transfer of forces along the cracks by interface shear must be implemented. Several aggregate interlock models are available in the literature (see section 2.5), which relate crack opening and slip to shear and normal stresses at the crack.

According to the truss model with crack friction, strains must be determined in the chords and web in order to calculate V_{fd}, which depends on the crack width and slip. As pointed by Reineck [21], V_{fd} depends on the shear force, strain conditions in the member, on the longitudinal strain at mid-depth (ε_x) and crack spacing. However, for practical reasons and applicability of the method, a constant value of V_{fd} is generally assumed in the codes.

The 1996 FIP Recommendations give the following values:

- For members without axial forces:

$$V_{fd} = 0.07(b_w z f_{cd}) \quad \ldots (2.22)$$

$$\cot\beta_r = 1.20 \quad \ldots (2.23)$$

- with axial compression:

$$\cot\beta_r = 1.20 - 0.20\sigma_{xd} / f_{ctm} \quad \ldots (2.24)$$

$$V_{fd} = 0.10(1 - \cot\beta_r / 4).(b_w z f_{cd}) \geq 0 \quad \ldots (2.25)$$

- with axial tension:

$$\cot\beta_r = 1.20 - 0.90\sigma_{xd} / f_{ctm} \geq 0 \quad \ldots (2.26)$$

$$V_{fd} = 0.10(1 - 0.36 / \cot\beta_r).(b_w z f_{cd}) \geq 0 \quad \ldots (2.27)$$

A value for β_r of 40º is commonly used for members without axial tension force. However, as discussed in chapters 6, 7 and 8, the inclination of the critical shear crack can vary from 45º to 30º depending on the shear span to effective depth ratio (a/d) and type of loading. In beams with axial compression and tension the angle β_r is decreased and increased respectively. Equation (2.26) for members with axial tension can result in large amounts of transverse reinforcement (Reineck [21]).

Further improvements need to be implemented in the previous method for lightweight and high-strength concretes where the shear component resisted by friction at the interface

(V_{fd}) will be clearly overestimated using equations (2.22, 2.25 and 2.27). This is due to the fact that aggregate fracture at the crack is not taken into account.

One last important aspect that was highlighted by Reineck [21] refers to the strength assumed for the concrete struts between shear cracks. As mentioned in section 2.3 the concrete strength is decreased by transverse tensile strains in the struts, which are induced by stirrups and friction forces along cracks. Crack slip and shear transfer along cracks is taken into account in the truss model with crack friction and so the compression softening implemented in the model should be lower than normally used in the rotating crack approach, (see section 2.3). According to Reineck [40], a reduction factor of 0.85 is recommended, which is considerably larger than used in plasticity approaches, where ν is typically about 0.5. Reineck's recommendations for the strength reduction factor are based on work carried by Schlaich & Schäfer [41], Schäfer et al. [42], Eibl & Neuroth [43], Kollegger & Mehlhorn [26].

Other discrete crack models

Other examples of discrete cracking approaches, are the methods of Poli et al. [36, 37] and Prisco et al. [44]. All these approaches use a friction law to define the force transfer along the cracks. Opening and sliding of the crack are considered as well as non-coaxiality ($\beta_r > \theta$) in the orientation of the strut and the crack.

The method developed by Poli et al. [36, 37] used the Rough Crack Model described in detailed in section 2.5, to describe for the aggregate interlock at the crack. The contribution of V_f was studied by the authors for I thin-webbed beams basing their method on the plane truss proposed by Mörsch but with aggregate interlock considerations similarly as the truss with crack friction model. A system of non-linear equations was solved accounting for equilibrium, stirrups-to-concrete compatibility, friction law for aggregate interlock, solid concrete between shear cracks and crack spacing. Other aggregate interlock models were applied, such as the two-phase model (Walraven [45], see section 2.5), resulted in similar predictions.

In their initial method Poli et al. [36, 37] neglected any shear and bending stiffness of the diagonal struts as well as the beneficial effect of the dowel action. The ratio for transverse reinforcement was kept small in order to assure that shear failure would be governed by the yielding of the stirrups. Poli et al. [36, 37] made refinements to the model to take into consideration the shear and bending carrying capacity of the struts as well as bond-slip

between of the stirrups and concrete. These changes resulted in a decrease of the inclination of the compressive fields allowing for a more economical design compared to the original model.

Constant relative displacements along the crack were assumed in the original model. In later work done by Prisco & Gambarova [44] a non uniform law for the relative displacements along the crack (Figure 2.8) was implemented as well as plastic-strain accumulation in the stirrups and dowel action. The first two enhancements showed that the assumptions made initially were not on the safe side since they had a negative effect. The experimental values of the crack opening and slip obtained in the author's tests (see chapter 6), showed a more uniform distribution than that shown in Figure 2.8. This suggests that the variation of the crack displacements along the crack can be influenced by the depth of the member as well as the amount of longitudinal reinforcement.

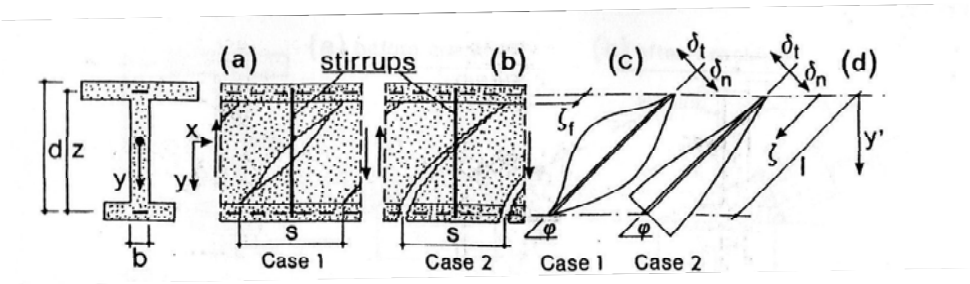

Figure 2.8: Analytical model proposed by Prisco & Gambarova [44]; a) Web-shear cracks; b) Flexure-shear cracks; c) & d) Assumed crack opening and slip distribution along crack (Case 1 & 2)

Another example of a truss model in which equilibrium at the crack was imposed in order to obtain the ultimate shear capacity was suggested by Hamadi & Regan [19]. In their model the inclination of the strut was obtained by minimising the total complementary energy of the internal structure. Although several simplifications were assumed, sensible predictions were obtained and most importantly the relevance of decreasing the stiffness of the aggregate interlock action could be assessed. An alternative approach reported by Regan [3], which seem to be adopted in DIN1045:2000, is to use the variable strut inclination method limiting the shear stress at the critical crack instead of using the plastic solution; this approach is discussed in further detail in section 8.3.3.

2.5 Aggregate interlock models

2.5.1 General aspects

The discrete crack approaches, described in section 2.4, consider failure along the actual critical crack surface and study the interface transfer of forces between the rough concrete crack faces, also known as "aggregate interlock action". Although this technique might seem to give a more physical meaning solution than smeared crack approaches, aggregate interlock must be implemented by means of analytical models. In this section, several aggregate interlock models available in the literature are reviewed. The performance of some of these models is further investigated in chapter 4 in view of the experimental results obtained from push-off test carried out in this work.

Numerous experiments have been performed in the past showing that the shear force transferred along the cracks is not related in a simple direct way to shear displacements. Crack width, slip, aggregate size and normal stresses are all interrelated. Hence it is extremely difficult to establish a precise analytical model to link them all together.

To understand the mechanical behaviour of aggregate interlock action concrete must be studied as a composite material consisting of two phases (see Figure 2.9). Phase I is composed of the aggregate particles that have high strength and stiffness and phase II is a matrix material consisting of hardened cement paste with fine sand, which has lower strength and stiffness. The interface between the aggregate and the matrix is the critical path that the crack is going to follow so that for normal concretes the crack intersects phase II but never phase I as shown in Figure 2.9 (left). However, there are other instances where the bond between the aggregate and the cement paste is strong enough to fracture the aggregate at the crack. This results in smooth cracks as shown in Figure 2.9 (right), which are commonly observed in lightweight and high-strength concretes.

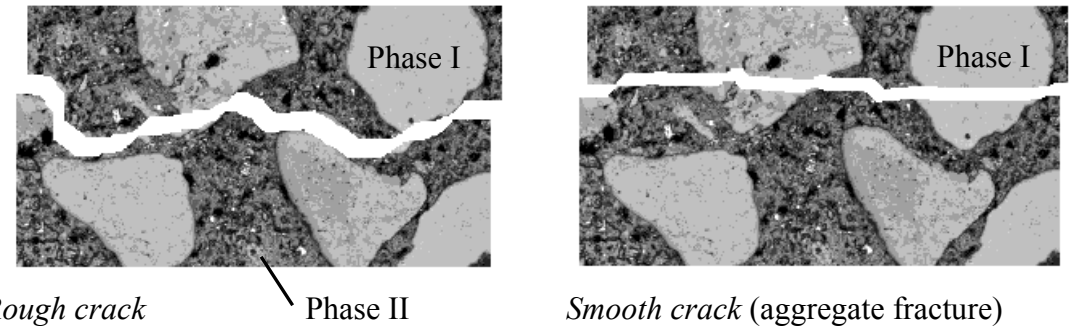

Phase I: aggregate particles; Phase II: Matrix (cement paste and sand particles)

Figure 2.9: Aggregate interlock; *Left*– Rough cracks; *Right*– Aggregate fracture (smooth cracks)

Experimental evidence shows that when crack faces are subjected to relative shear displacements a wedging action is initiated which generates normal stresses and activates the reinforcement that crosses the crack to maintain equilibrium. It is widely accepted that the crack width (w) has an important role in aggregate interlock action; higher values of w results in lower stiffness of the aggregate interlock. Different opinions exist about whether size and type of aggregate (rounded, crushed, lightweight) are crucial parameters. According to Taylor [1], the ratio between aggregate and matrix strengths is the most important parameter which influences the roughness of the crack. In practice, concrete strength is assumed to be the critical variable and only light-weight aggregate concrete is considered separately.

Hamadi & Regan [19] performed push-off experiments in order to study the influence of the aggregate type. These tests were carried using concretes with either lightweight or normal gravel aggregates. From their experimental results they concluded that stiffness at the crack was dependant on crack opening and type of aggregate but not on the normal stresses. On the contrary, the ultimate shear strength was found to be a function of the normal stresses and type of aggregate but not on the crack opening.

Similar tests were carried by Walraven and Reinhardt [46]. The variables to be studied in this case were the type of reinforcement (embedded and external reinforcement bars), the concrete strength (f_{cc}=13–60MPa), the type of concrete (sand gravel, lightweight concrete), the grading of the concrete, the scale of the concrete (D_{max}=16 and 32mm) and the initial crack width. An interesting aspect which was observed in these tests was the different behaviour of cracks with embedded or external reinforcement bars. A local concentration of stresses was observed near the embedded reinforcement bar, which was caused by the reduction of the crack width in this region. One consequence of this concentration of stresses is that the crack opening path (w–s relationship) is approximately linear for reinforced cracks independently of the reinforcement ratio, as shown in Figure 2.10.a. This was not the case for push-off tests with external reinforcement (Figure 2.10.b). Changes in bar diameter in reinforced cracks, while keeping ρ constant, showed no major influence on the response. Conclusions drawn for reinforced cracks were made for concretes with moderate strength (20–38MPa). However, in lightweight concrete specimens, the crack opening paths observed were much steeper with $\Delta s >> \Delta w$ as shown in Figure 2.10.c.

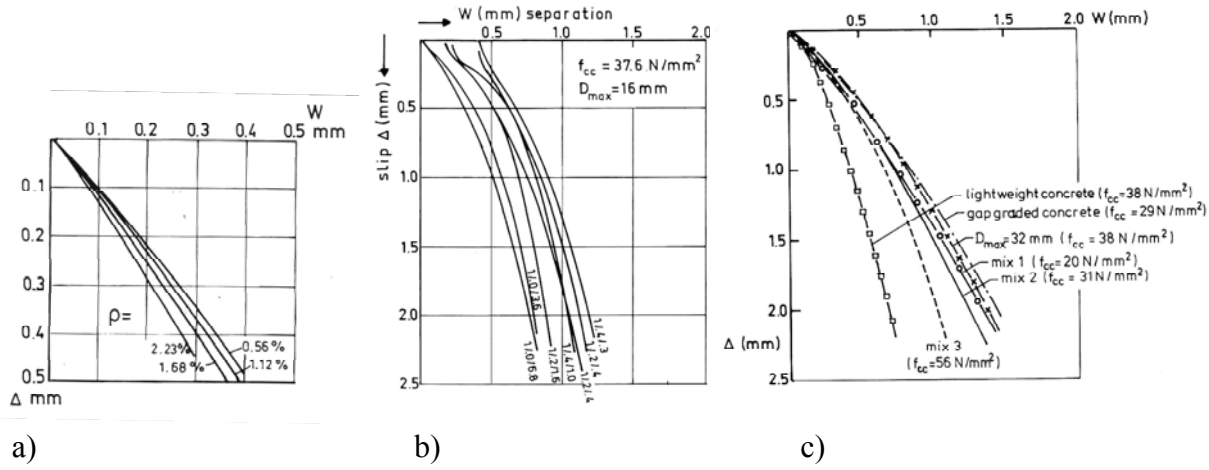

a) b) c)

Figure 2.10: Crack opening paths for a) Reinforced cracks; b) Unreinforced cracks; c) Reinforced cracks: lightweight and high-strength concretes (adapted from Walraven and Reinhardt [46])

Walraven & Reinhardt's [46] experiments showed that changing the grading of the aggregate in gravel concrete by increasing the size from 16 to 32mm or by removing all particles between 0.25 and 1.00mm had no significant influence. As expected, increasing the reinforcement ratio and concrete strength decreases the normal and shear displacements in reinforced cracks. Lastly, these tests showed similar results for specimens with external restraint bars and specimens with soft sleeves secured to both sides of the crack over a short length. The latter specimen configuration was used to avoid concentration of stresses around the embedded reinforcement bars.

2.5.2 Crack dilatancy models

To implement the aggregate interlock phenomena into the calculations crack dilatancy models can be used with constitutive laws that can be based on an empirical formulation (Hamadi & Regan [19], Walraven & Reinhardt [46]; Bazant & Gambarova [47]; Gambarova & Karakoç [48]) or an analytical rational formulation (Walraven [45]; Li, Maekawa & Okamura [49]). For most of the cases the formulation is based on a total deformation theory where normal and tangent stresses are expressed as functions of the relative displacements Δw and Δs.

The "Linear aggregate interlock" and" Crack rough" models

One of the most widely used friction laws is the linear aggregate interlock relation of Walraven & Reinhardt [46]. The method, which is a based on linear regression analysis of their experimental data, is simple and yet still achieves good accuracy. The model is given by equations (2.28) and (2.29) for normal gravel concrete. An interesting feature of this model is that a minimum value of the crack slip is required to mobilize the shear and

normal stresses; this value is larger for the normal stresses than for shear stresses as shown in Figure 2.11.a.

$$\sigma_{ncr} = -\frac{f_{cu}}{20} + \left[1.35.w^{-0.63} + \left(0.191.w^{-0.552} - 0.15\right).f_{cc}\right]\Delta s \qquad \ldots (2.28)$$

$$\tau_{cr} = -\frac{f_{cu}}{30} + \left[1.8.w^{-0.80} + \left(0.234.w^{-0.707} - 0.20\right).f_{cc}\right]\Delta s \qquad \ldots (2.29)$$

where σ_n and τ are greater than zero.

Expressions (2.28) and (2.29) are used for normal gravel concrete while the following expressions are suggested for a lightweight concrete.

$$\sigma_{ncr} = -\frac{f_{cu}}{40} + \left(1.928.w^{-0.87} - 1\right)\Delta s \qquad \ldots (2.30)$$

$$\tau_{cr} = -\frac{f_{cu}}{80} + \left(1.495.w^{-1.233} - 1\right)\Delta s \qquad \ldots (2.31)$$

An example of relations (2.28) and (2.29) is plotted in Figure 2.11.a for a concrete with a cube strength f_{cu} of 56.1 MPa. The stiffness of aggregate interlock given by the slope of these equations is considerably larger than for the lightweight concrete expressions (2.30) and (2.31).

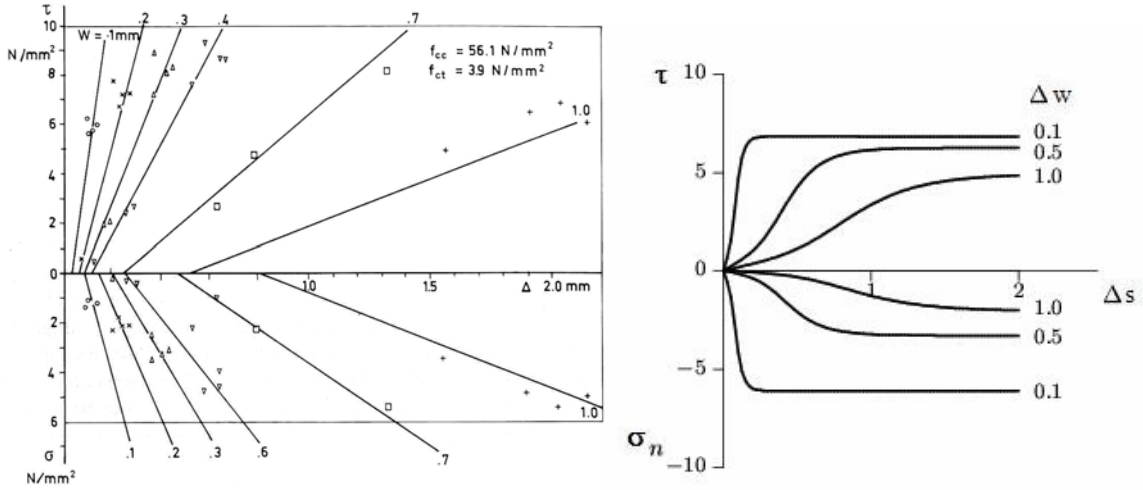

a) Linear aggregate model b) Rough crack model

Figure 2.11: Aggregate interlock models; a) Linear aggregate interlock model proposed by Walraven & Reinhardt [46]; b) Rough crack model proposed by Bazant & Gambarova [47]

The rough crack model proposed by Bazant & Gambarova [47] is also based on empirical results. In this case the constitutive model was obtained by optimising the fit of Paulay &

Loeber's [50] test results at constant crack width. The rough crack model considers the crack surface as a regular array of trapezoidal asperities.

One of the main features of this model is that shear stress is primarily dependant on the displacement ratio $r=\Delta s/\Delta w$. The curve has an asymptotic behaviour for large values of r, as shown in Figure 2.10.b, which is a consequence of microcracking and crushing of the matrix near the aggregate particles. For values of $\Delta w > D_{max}/2$ where D_{max} is the maximum aggregate size, the crack reaches the state of no contact.

The constitutive equations (2.32) and (2.33) are again functions of Δs, Δw and f_{cc} as in Walraven & Reinhardt's [46] model. However additional parameters D_{max} and tensile strength f_t are introduced.

$$\sigma_{ncr} = -\frac{a_1}{\Delta w}.\left(a_2.|f_t|\right)^p \qquad \ldots (2.32)$$

$$\tau_{cr} = \tau_u.r.\frac{a_3 + a_4.|r|^3}{1 + a_4.r^4} \qquad \ldots (2.33)$$

where

$$\begin{cases} p = 1.30.\left(1 - \dfrac{0.231}{1 + 0.185\Delta w + 5.63.(\Delta w)^2}\right) \\ r = \Delta s / \Delta w\,;\ \tau_u = \dfrac{\tau_0.a_0}{a_0 + (\Delta w)^2} \\ a_0 = 0.01.D_{\max}{}^2\,; \quad a_1 = 0.000534\,; \quad a_2 = 145.0\,; \quad a_3 = \dfrac{2.45}{\tau_0}\,; \quad a_4 = 2.44.\left(1 - \dfrac{4}{\tau_0}\right) \\ \tau_0 = 0.195.f_{cc} \end{cases}$$

Improvements to this model were proposed in later work by Gambarova & Karoç [48]. According to the authors a better formulation to the relation between normal traction and crack displacements was found. Daschner & Kupfer [51] tests were used to optimise the curve fitting because the confinement stress was kept constant. Expressions (2.32) and (2.33) were modified to:

$$\sigma_{ncr} = -a_1.a_2\sqrt{\Delta w}.\frac{r}{\left(1 + r^2\right)^{0.25}}.f_t \qquad \ldots (2.34)$$

$$\tau_{cr} = \tau_0.\left(1-\sqrt{\frac{2.\Delta w}{D_{\max}}}\right).r.\frac{a_3 + a_4.|r|^3}{1+a_4.r^4} \qquad \ldots (2.35)$$

where

$$a_1.a_2 = 0.62\ ;\ a_3 = \frac{2.45}{\tau_0}\ ;\ a_4 = 2.44.\left(1-\frac{4}{\tau_0}\right)\ ;\ \tau_0 = 0.2.f_{cc}$$

The "Two-phase" and" Contact density" models

Other attempts to model aggregate interlock action were done by developing a more theoretical approach such as the "Two-phase Model" proposed by Walraven [45] or the "Contact Density Model" introduced by Li et al. [49].

The two-phase model assumes that concrete consist of two ideal phases; spherical aggregate particles, which are perfectly stiff, and a perfectly plastic matrix, see Figure 2.12. As shown in Figure 2.12, shear stresses generate when the sphere particles intrude into the matrix.

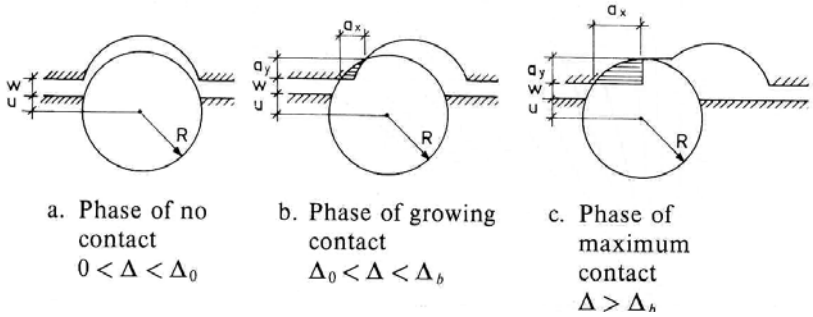

Figure 2.12: Different phases in aggregate interlock action assumed by the two-phase model (adapted from Walraven & Reinhardt [46])

The statistics of aggregate distribution are taken into account to estimate the active area between the inclusions and the matrix. The tangent stiffness is again a function of crack displacements (Δs, Δw) and aggregate distribution. The formulation is given by equations (2.36) and ((2.37).

$$\sigma_{ncr} = -\sigma_{pu}.\left(A_t - \mu.A_n\right) \qquad \ldots (2.36)$$

$$\tau_{cr} = \sigma_{pu}.(A_n + \mu.A_t) \qquad \ldots (2.37)$$

where σ_{pu} = matrix compressive strength; μ = friction coefficient between intrusion and matrix; A_t = tangent average contact area; A_n = normal average contact area.

The Contact Density Model developed by Li, Maekawa & Okamura [49] also deals with aggregate interlock using contact density probability functions. In this model the inclinations of the contact units or intrusions θ (within a range of -90º and 90º) is a stochastic variable described by its density probability function $\Omega(\theta)$. The direction of the contact stresses is proposed to be constant and normal to θ.

The mathematical formulation for this model is given by equations (2.38) and (2.39)

$$\sigma_{ncr} = \int_{-\pi/2}^{\pi/2} \sigma_{con}.K(\Delta w).A_t.\Omega(\theta).\cos\theta.d\theta \quad \ldots (2.38)$$

$$\tau_{cr} = \int_{-\pi/2}^{\pi/2} \sigma_{con}.K(\Delta w).A_t.\Omega(\theta).\sin\theta.d\theta \quad \ldots (2.39)$$

In expressions (2.38) and (2.39) Ω is assumed to be a trigonometric function independent of the size and grading of the aggregate as well as the strength and type of coarse aggregates. The effective ratio of contact area $K(\Delta w)$ expresses the contact stage along the crack when Δw is large compared with the roughness of the crack surface. The contact force (σ_{con}) is calculated using an elasto-perfectly plastic model. The surface area A_t is estimated as 1.27 times the area of the crack plane. This estimated value only applies for normal concretes with strengths not higher than 50MPa as will be discussed later on.

Considerations for smooth cracks

As mentioned earlier, cases where the aggregate fractures at the crack can lead to a reduction of the aggregate interlock action and so the crack dilatancy models described earlier need to be examined carefully.

The linear aggregate interlock model offers alternative equations (2.30) and (2.31) for lightweight aggregate, which seems to accounts for the lower stiffness due to smoother cracks. However, these equations do not always provide accurate results for normal concretes in which the aggregate splits at the crack, as it is shown in section 4.5. On the other hand, the two-phase model (Walraven [45]) is based on the assumption that the crack goes round the idealised sphere aggregate and the case of the crack going through the particle is not considered. The crack rough model, makes use of empirical parameters (a_0, a_1, a_2, a_3 and p) and so would seem necessary to perform a recalibration of these parameter in order to take into account for cases where aggregate breaks at the crack.

Although experimental work will be required, the enhancement of the latter method seems feasible, at least from a theoretical point of view.

The contact density model by Liu et al. [49], due to its rational derivation, can be oriented towards the assessment of flat surface cracks. Even though the background theory for this model is mostly applied to gravel aggregate concrete some innovations are being developed by Maekawa et al. [52] in recent publications in order to adapt the method to smooth fracture surfaces. As recognized by Maekawa et al. [52], the changes required to adapt the model to even cracks are not straightforward. First modification required would involved the density function $\Omega(\theta)$, which is generally assumed to be $0.5\cos\theta$. For smooth cracks this function can be substituted by a truncated normal distribution (Maekawa et al. [52]). The contact density function $\Omega(\theta)$ in this case will no longer be independent from the type of aggregate as it was assumed before. The other variable that would need to be modified is the effective ratio of contact $K(\Delta w)$ since the roughness is considerably small compared with Δw.

The formulas proposed by Maekawa et al. [52] for high-strength concrete are based on statistical analysis of histograms of directional crack distributions. For lightweight concrete where the aggregates are much softer the same formulas are suggested, but in order to avoid overestimating the stresses transferred at the crack a reduced contact yielding stress is recommended.

Simplified aggregate interlock models

Despite the extensive formulation and different alternatives among the crack dilatancy techniques some of the models described earlier can lead to extremely difficult and time-consuming calculations. In fact, crack dilatancy models as stated by Feenstra et al. [53] can result in asymmetrical tangential stiffness matrices, which generate numerical difficulties in solving the algebraic equations typically set for a non-linear finite element analysis.

In order to implement the crack dilatancy model into an interface finite element, the linear aggregate interlock model given by expressions (2.28) and (2.29) seems the simplest approach. The stability of mechanical systems with a non-symmetrical tangent-stiffness matrix K is satisfied if all the eigenvalues of the matrix $(K+K^t)$ are positive (Feenstra et al. [53]). This condition is derived from the fact that internal strain energy (U) must be positive for any kinematically admissible strain-rate vector in order to assure stability.

From Feenstra et al. [53] stability analysis, it was concluded that all the crack dilatancy models presented in this section showed cases with negative eigenvalues, where stability was lost before the maximum shear stress was attained. Only the contact density model showed a better stability, which was due to the fact that the stiffness matrix is less asymmetric than the remaining models.

This clearly justifies the use of simpler aggregate interlock models, which could be implemented in a simpler manner into shear design methods while keeping a certain level of accuracy. An example is shown in section 2.3 in the MCFT for the shear carried at the crack v_{ci} (see equations 2.14 and 2.15).

Another example of simplified formulation for aggregate interlock is equation (2.40) proposed by Hamadi & Regan [19], which was obtained from regression of the experimental data from push-off tests. The stiffness parameter k suggested by the authors was 5.4N/mm^2 and 2.7N/mm^2 for natural gravel and expanded clay aggregates respectively. According to equation (2.40) the aggregate interlock stiffness depends only on the type of aggregate and crack width. Hamadi & Regan [19] used a shear friction type of formula (2.41) to obtain the shear capacity (τ_{ult}), in which the cohesion (c) and friction (μ) parameters need to be estimated. Although this approach is commonly used in design codes, the influence of the crack width is neglected. This is inconsistent with other approaches such as the v_{cimax} value used in the MCFT (see equation 2.15). Further discussion regarding the shear friction formula is presented in section 4.4.

$$\tau_{cr} = \frac{k}{\Delta w}.\Delta s \qquad \ldots (2.40)$$

$$\tau_{ult} = c + \mu\sigma \qquad \ldots (2.41)$$

Li, Maekawa, Okamura & Soltani [49, 54] presented simplified equations (2.42) and (2.43), which were based on the contact density theory described earlier. Similarly as in the rough crack model, equations (2.42) and (2.43) are a function of the $\Delta s/\Delta w$ ratio.

$$\sigma_{ncr} = 3.83 f_c'^{1/3}\left[\frac{\pi}{2} - \cot^{-1}\psi - \frac{\psi}{1+\psi^2}\right] \qquad \ldots (2.42)$$

$$\tau_{cr} = 3.83 f_c'^{1/3}\frac{\psi}{1+\psi^2} \quad \text{where } \psi = \frac{\Delta s}{\Delta w} \qquad \ldots (2.43)$$

Lastly, MC90 provides design equations (2.44) and (2.45) for rough interfaces that can be used to assess the shear stresses mobilized for a certain value of crack sliding. This model assumes a linear relationship up to a crack slip of 0.1mm, as shown in Figure 2.13. The ultimate shear stress corresponds to a crack slip of approximately equal to 2mm and can be estimated using equation (2.46).

According to MC90, the crack slip is accompanied by a crack opening, which can be estimated as $w=0.6s^{2/3}$ (units in mm). These equations were presumably derived from push-off test data since the $\Delta s/\Delta w$ is similar to that shown in Figure 2.10.

- For s<0.1mm

$$\tau = 5\tau_{ult} s \quad \ldots (2.44)$$

- For s≥0.1mm

$$\left[\frac{\tau}{\tau_{ult}}\right]^4 - 0.5\left[\frac{\tau}{\tau_{ult}}\right]^3 = 0.3s - 0.03 \quad \ldots (2.45)$$

$$\text{where } \tau_{ult} = 0.4 f_c'^{2/3} \sigma^{1/3} \quad \ldots (2.46)$$

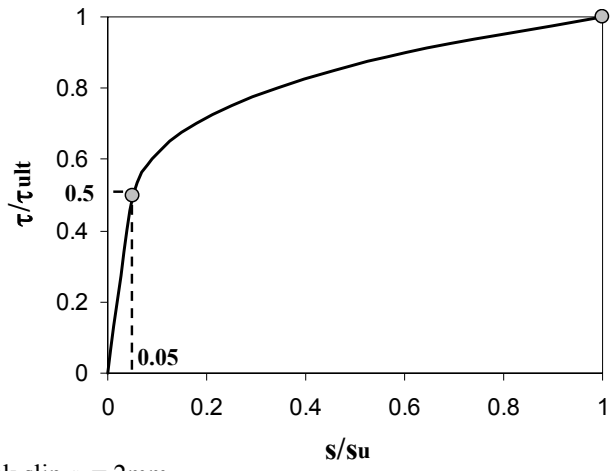

Note: Ultimate crack slip s_u = 2mm

Figure 2.13: MC90 predicted shear stress as a function of the crack slip

2.5.3 Aggregate interlock contribution to shear strength of RC beams

As shown in this chapter, the role of aggregate interlock action assumed by the different shear models available in the literature can be significantly different. The contribution of shear transfer along cracks must be considered either directly or indirectly in order to obtain reasonable predictions of shear strength in reinforced concrete beams. However, this contribution might vary depending on the amount of shear reinforcement provided, shear span to effective depth ratio, concrete strength or type of aggregate used.

Experimental data regarding aggregate interlock is mainly focused in members without shear reinforcement. Early estimates of the percentage of vertical shear carried across flexural cracks were provided by Fenwick & Paulay [55]. According to their experiments an approximate figure of 70% of the shear was taken by aggregate interlock, while the remaining 30% was carried by the compression zone and dowel action. Later work carried out by Taylor [1, 2] confirmed that the contribution of aggregate interlock was predominant, as shown in Figure 2.14. The percentages provided by Taylor [1, 2] for the contribution of aggregate interlock (35-50%), dowel force (15-25%) and shear contribution of the compression zone (20-40%) have been well documented in a great number of references found in the literature.

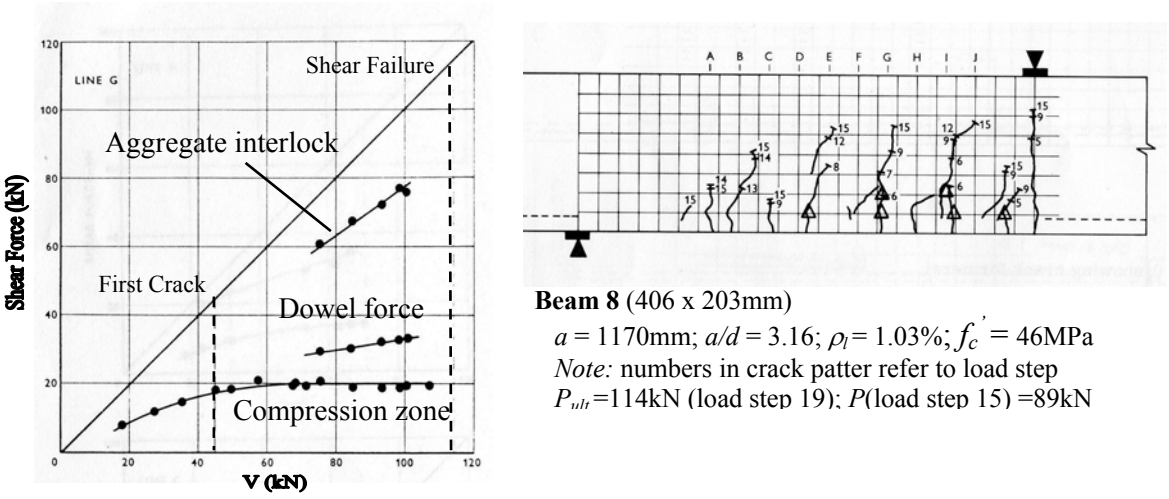

Figure 2.14: Components of shear resistance obtained experimentally by Taylor [1, 2] in members without shear reinforcement (adapted from Taylor [2])

According to these results, there seems little doubt that aggregate fracture in members without shear reinforcement can results in a reduction of shear strength due to the lower aggregate interlock capacity. As mentioned earlier, Taylor [1] supported the idea that the most critical parameter, which governs the crack roughness, is the ratio between the aggregate and matrix strengths. According to this, the influence of the type of course aggregate used in the concrete can be critical. Clear evidence regarding the effect of using different types of aggregates was provided by Regan et al. [4]. This work showed that beam tests using limestone aggregate, which generally fractures at the crack, had a lower shear resistance compared with beams made with granite or normal gravel aggregate concretes.

As highlighted by Regan [3], the type of aggregate used is generally not reported by researchers, which complicates the interpretation of the experimental databases. This is surprising, considering that experimental databases are being gathered using data from all continents, where presumably the type of aggregate used is completely different. Tests carried out in Canada generally used limestone aggregate (Collins [56]), which as recognized by Angelakos et al. [31] can result in a noticeable decrease of crack roughness with the concrete strength. In the UK, limestone aggregate is commonly used for high-strength concretes, while for normal strength concretes gravel aggregate is usually more common.

Although the contribution of aggregate interlock is more or less understood for members without stirrups, there is a lack of experimental data regarding aggregate interlock contribution for members with stirrups (Taylor [1, 2], Regan [4]). The shear design approaches described in this section rely upon the shear transfer across cracks and so it seems reasonable that aggregate fracture might also have an effect in this case. However, as mentioned by Regan et al. [4] this influence might be less than in members without stirrups since shear reinforcement provides a better control over the crack widths.

In this area, it is noticeable work carried by Walraven [9, 10] using either lightweight or high-strength concretes, in which the crack roughness was influenced by splitting of the aggregate. According to their experimental work of slender beams with stirrups, a reduction of the shear strength could not be observed. This was explained by the fact that shear forces could still be transmitted along the crack due to the irregular shape of the crack surfaces (roughness at a macrolevel) which allowed for additional contact areas to develop. However, it remains questionable whether this would apply to other load

arrangements and beam dimensions where these irregularities in the crack surface might not be attained. As reported by Regan et al. [4], experimental evidence provided by Motamed [57], seems to suggest that there might be a potential concern for lightly reinforced high-strength limestone aggregate members.

Design codes generally account for aggregate fracture indirectly by means of the concrete strength. UK National Annex to EC2 limits the concrete strength to 60MPa in shear design equations due to concerns about aggregate cracking. Similar approach is taken in other codes such as Spanish code (EHE). However, for both EC2 and EHE codes, this limitation is imposed for both cases of members with and without shear reinforcement, which might not be entirely accurate.

On the other hand, Canadian Code (see section 2.4) which is based on the MCFT, the aggregate size can be reduced in the calculations in order to account for aggregate fracture. As discussed previously, this is usually done according to the concrete strength only. Moreover, for members with stirrups the simplified equations in the Canadian Code, assumes a constant value for the crack spacing and so allowance for changing the size of the aggregate size is not made.

As shown, the design codes can be inconsistent regarding a potential reduction in shear strength due to aggregate fracture. Furthermore, the type of aggregate is completely neglected, except for lightweight aggregate concrete members. Therefore, it seems sensible that further research is carried out in order to assess these assumptions made by the different design codes.

2.6 Strut-and-tie modelling

General aspects

The Strut-and-Tie Method (STM) is an application of the lower bound theory of plasticity used in design for the ULS in regions where plane sections do not remain plane (D regions). In these areas called discontinuity regions, there is a statical or geometrical disturbance that causes non-uniformity of internal forces as shown in Figure 2.15.

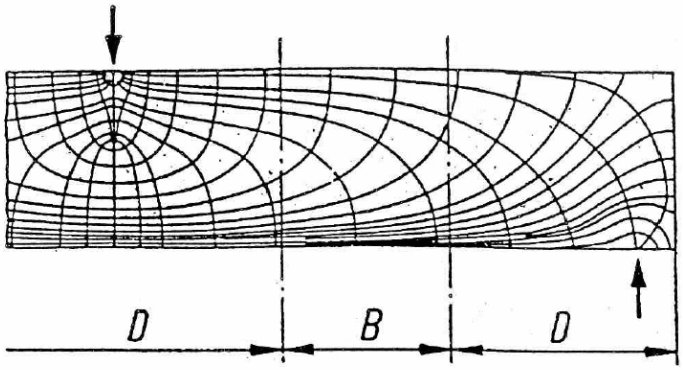

Figure 2.15: Stress lines in B and D regions for a concrete beam (adapted from Schlaich & Schafer. [58])

The load is assumed to be transferred from the loading points to the supports through a truss in which compression stress fields are resisted by concrete and tension stress fields by reinforcement (Figure 2.16). The main concept of STM is to solve a continuum concrete structure by calculating a truss structure (strut-and-tie system).

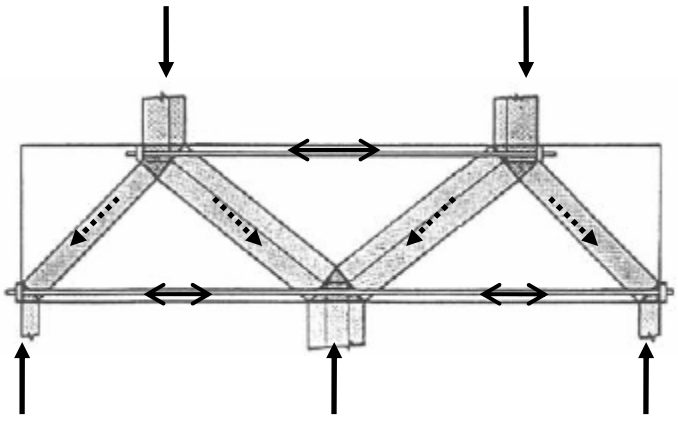

Figure 2.16: Example of a strut-and-tie model for a deep beam

The lower bound theory of plasticity states that for a given load case if there is a stress distribution that satisfies equilibrium with the boundary conditions and stresses everywhere are below a threshold value or strength defined by the codes, the structure

will carry those loads without collapsing. The theory does not require the actual stress state to be calculated since it is a lower bound theorem.

Although the method was originally based on Mörsch's truss analogy concept used to explain shear in a RC beam, it was not well established until 1987 when Schlaich, Shafer and Jennewein [35] defined the basis for this method and its applications for discontinuity regions. The Féderation Internationale du Béton (fib) enhanced this method helping STM make its way into codes of practice.

The following procedure is used to develop a strut-and-tie model.

1. Definition of the D-region; borders and forces within these boundaries.
2. Drawing a strut-and-tie model on the basis of assumed node geometry.
3. Solving for the truss member forces.
4. Calculate the reinforcement layout providing the required tie capacity and enough anchorage length for the bars to ensure the correct behaviour at the nodes.
5. Dimension nodes using truss member forces obtained previously.
6. Go back to new geometry (step 2) in order to find a converged solution.

Despite the didactic value of the STM and its many appealing applications the method is not always trouble-free and has many uncertainties. These difficulties are outlined here for general strut-and-tie modelling, although some of them are further discussed for the particular case of STM of short span beams shown in chapter 7. Regarding the steps listed, which are needed to develop a strut-and-tie model, steps number 1, 3, 4 and 6 are straightforward. On the contrary steps 2 and 5 are more problematic since the geometry of the strut-and-tie model changes not only with the load case but also with the magnitude of the load.

There are four major problems in developing strut-and-tie models. These are:

1. Uncertainties in obtaining dimensions, stiffness and effective strength of strut, ties and nodes for the truss models.
2. Need to select the optimal strut-and-tie model and iteratively adjust and refine the truss geometry.
3. Need to combine different load cases.
4. Uncertainties for statically indeterminate models.

Definition of nodes

In order to obtain the dimensions and shape of a node, the widths of the incoming strut and ties are needed. The widths of the elements are chosen so that stresses are below the code restrictions. One possible way of dimensioning a node is to assume that the stresses on all the sides of the node are equal which results in a hydrostatic biaxial state of stresses. This can be done by defining the boundaries of the nodes so that they are proportional and perpendicular to the forces acting on them. Defining the node in this manner guarantees that no shear is transmitted to the node face.

However, this procedure can be quite laborious for cases where more than three truss elements meet since the centrelines are unlikely to coincide. In addition, hydrostatic nodes are not always feasible due to geometrical constraints. An example of this is shown by Brown et al. [59], in Figure 2.17 (left). According to these limitations, non-hydrostatic nodes are usually recommended by the codes (AASHTO LRFD and ACI 318-05). Schlaich et al. [35] proposed a simplified method, where the centrelines coincide but the stresses on the sides of the node were different and constant. In this procedure a check to assure that these stresses were below the limit was needed. In addition, in order to limit the shear within the node it was recommended that the ratio of maximum to minimum principal stress be less than two.

A comprehensive study of modelling nodes in STM was presented by Schafer [60], which included general guidelines for dimensioning and checking bearing stresses for several types of nodes. These guidelines have been implemented in several design codes such as EC2. A typical example of compression-tension node (CT) is shown in Figure 2.17 (right), which is commonly used in STM of beams supported on bearing plates. The width of the incoming strut can be easily obtained from the length of the bearing plate (l_b) and distance from the bottom to the centroid of the reinforcement (c).

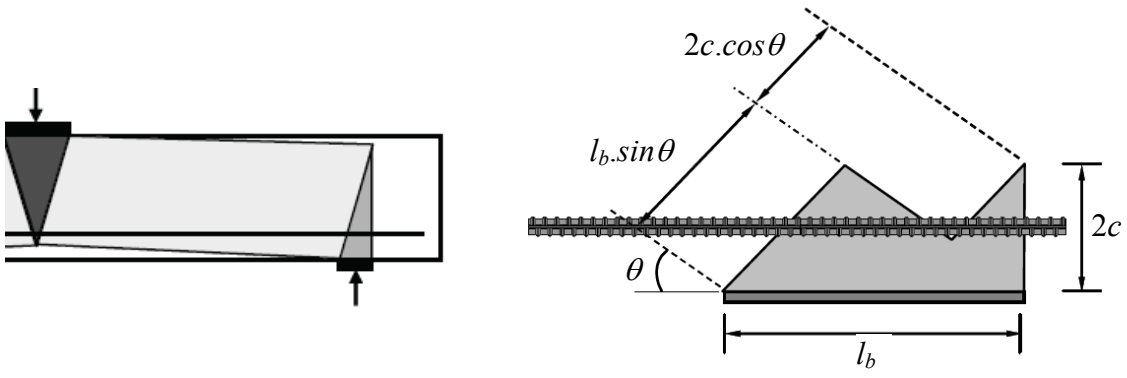

Figure 2.17: Types of nodes in STM (adapted from Brown et al. [59]); *Left*– Hydrostatic node at impractical case; *Right*– Non-hydrostatic CT node (estimation of strut width)

Statically indeterminate systems

Another problem faced by the STM is to estimate accurately the stiffness of struts and ties due to the presence of cracks. The truss systems to be solved in a strut-and-tie model must be simple so that all element forces can be obtained with only equilibrium conditions (i.e. statically determinate systems). Hence, in general cases the stiffness of both strut and ties are not required. However, if the stiffness of the truss elements could be estimated the member forces could then be calculated, even for statically indeterminate configurations. Moreover, if the load-deformation response of the struts and ties were known the equivalent deflection behaviour could be predicted for the evaluation of the serviceability limit state.

An example of a statically indeterminate system can be found in short span beams with stirrups (see chapter 7), in which the proportion of the load that is taken by the stirrups is not known. Several approaches can be applied to solve hyperstatic strut-and-tie systems. The simplest assumption is made by the classic plastic truss method, where the most loaded ties are assumed to yield. Another approach is the decomposing method proposed by Schaich & Schafer [61], in which the system is divided into several statically determinate systems. However, a reasonable estimation of the stiffness and the imposed-loading distribution of each model are needed in order to sum all these sub-models. Other authors such as Ameida [62], suggest an energetic technique in order to consider compatibility in the general model. Lastly, a stiffness analysis by strain compatibility can be carried out in a similar manner as the method applied for beam-column joints proposed by Vollum & Newman [63]. In any of these approaches, additional information from both laboratory testing and non-linear finite element analysis would be beneficial to validate the assumptions made in the strut-and-tie model.

Effective strength of struts

Another topic of debate in the strut-and-tie method is the effective strength assumed for the struts. Different design codes provide a wide range of reduction factors to apply to the cylinder compressive strength to estimate the capacity of the struts. EC2 applies no reduction for cases where the concrete strut is in a region with transverse compressive stress or no transverse stress, while ν is used to reduced f_c' for struts in cracked compression zones where ν=0.6(1-f_{ck}/250). This parameter is identical to the one suggested for the variable inclination strut method used for shear design (see section 2.1).

Other codes such as Model Code MC90 give different values depending on the constitutive laws used for concrete.

- For compression using a parabola-rectangle diagram

$$\sigma_{Rd,\max} = 0.85.f_{cd}.\left[2.(\varepsilon_c / \varepsilon_{cl}) - (\varepsilon_c / \varepsilon_{cl})^2\right] \quad \text{for} \quad \varepsilon_c \le \varepsilon_{cl}$$

$$\sigma_{Rd,\max} = 0.85.f_{cd} \quad \text{for} \quad \varepsilon_{cl} \le \varepsilon_c \le \varepsilon_{cu}$$

$$\sigma_{Rd,\max} = 0.00 \quad \text{for} \quad \varepsilon_{cu} \le \varepsilon_c$$

where ε_{cu}=0.002

- For a bi-linear stress-strain relationship

$$\sigma_{Rd,\max} = 0.85.f_{cd}.\left[1 - f_{ck} / 250\right] \quad \text{for uncracked areas}$$

$$\sigma_{Rd,\max} = 0.60.f_{cd}.\left[1 - f_{ck} / 250\right] \quad \text{for cracked areas}$$

There are six major factors influencing the strength of the concrete strut.

1. *Shape of the strut:* prismatic where the strength of the strut is closest to a concrete cylinder; fan and bottle-shaped where the strut spreads out as it moves from the ends causing splitting for smaller values than $f_c^{'}$.
2. *Disturbances in the strut:* initial cracks parallel or skewed with respect to the strut orientation. The influence of aggregate interlock is not taken into account in the codes. Another disturbance in the strut can be the tensile stresses or strains induced by a crossing tie such as the case of a stirrup in the truss analogy for shear in a RC beam.
3. *Distributed reinforcement:* well distributed reinforcement can control the spreading effect of the strut and increase the overall ductility.
4. *Confinement:* either by reinforcement or by mass surrounding the element the performance of the strut can be enhanced by confinement. This favourable effect had been studied thoroughly in the literature and has been implemented in most of the codes of practice.
5. *Angle of strut:* reduced angles between struts and ties should be avoided since it might violate strain compatibility at the nodes (Schafer [60]). Transverse strains induced by the ties into the strut will result in this extreme case in an excessive

reduction in strength of the strut. Collins & Mitchell [11] suggested a relationship (see Table 7.1) to obtain the effective strength in the strut in order to satisfy compatibility at the bottom node. The strength was written in terms of the strain at the tie and the angle between the strut and the tie.

6. *Size of strut:* STM generally do not make any allowance for size effects. However up to date, there is no general agreement on the influence of size effects in short span beam where strut-and-tie models are applied. This topic is discussed in further detailed in section 7.6, in view of experimental evidence available in the literature.

Uniqueness of strut-and-tie model and applicability to practical cases

In many instances, the STM can provide more than one possible truss that can satisfy equilibrium since the method is based on the lower bound theory. Optimal models will minimise the strain energy. The largest strains are concentrated in the most ductile elements, which are the steel ties. Hence a common rule is that models with shortest ties are optimal.

New procedures for topology optimisation are now being developed, for example evolutionary methods proposed by authors such as Qing Quan Liang et al. [64]. These techniques combine FEA with an optimisation algorithm, which systematically removes elements that have least contribution to stiffness. In this manner the optimal strut-and-tie model is defined gradually by the remaining elements. The element virtual strain energy is calculated for element removal and "Performance Index" is used to control the optimisation process. These techniques are found to be useful but quite hard to implement for cases of non-linearity.

In general, the calculations performed in a strut-and-tie analysis can be time-consuming since the truss must be iteratively adjusted. In addition, different truss models must be developed for each load case. As shown by the strut-and-tie models developed by the author (see chapter 7), an iterative scenario is generally required to solve these models, even for very simple geometrical cases. Computer-based graphical design programmes are being developed by research groups such as the Swiss Federal Institute of Technology (ETH), the University of Stuttgart, Purdue University or software programmes such as CAST developed by Tjhin and Kuchma [65] amongst others. The main objective of these aids is to provide the designer with powerful tools that can optimise the computations in a strut-and-tie design routine. Lastly, NLFEA can be carried out in addition, in order to asses the effect of crack pattern, although this process is not trouble-free (see chapter 3).

2.7 Conclusions

Shear design in structural concrete has been a challenging topic for many years. The truss analogy first proposed by Ritter [14] and then improved by Morsch [15] at the beginning of the Twentieth Century has been a powerful tool up to date in understanding the shear transfer mechanisms in a RC beam. However, progress has been made since those early truss models. Four different groups of approaches have been developed; classical 45º truss model, variable strut inclination method (plasticity trusses), smeared truss models (compression field theories) and discrete crack approaches.

Predictions of the shear strength provided by these approaches have improved considerably from early formulations, which were based only on empirical results. As reported by Collins et al. [12], early design equations for shear have been proven to be unsafe since the experimental data used in calibrating the models corresponded to rather small specimens. Nowadays it is a well know fact that aspects, which used to be considered secondary, such as size effect or amount of longitudinal reinforcement, can have a critical role in shear performance of RC members.

Analytical models for shear can be complex due to the large number of parameters that need to be taken into account. Aggregate interlock action has a significant contribution to shear strength. This contribution has been studied in depth for members without shear reinforcement (Taylor [1, 2], Regan [4]) but to a lower extent for shear reinforced members. Design methods for shear rely on the shear transfer across well-formed cracks in either a direct or indirect manner. Plasticity approaches, such as the variable inclination strut model for regions with uniform stress fields or the strut-and-tie models for discontinuity regions, make use of constant "effectiveness strength" factors to consider these aspects.

On the other hand, the modified compression field theory offers a rational approach in which the shear transmitted along the crack is limited according to the crack width and aggregate size. However, the MCFT is formulated in a smeared manner using average stresses and assuming coaxiality between strains and stresses. Discrete crack models using a truss with aggregate interlock models, offer an attractive alternative since failure is studied along the critical crack surface rather than a smeared crack element. Either smeared or discrete models can provide accurate predictions, although several simplifications are generally required in order to include them in design codes used in practice.

Strut-and-tie modelling, which was developed by Schaich et al. [35], is often claimed as a transparent method for designing and detailing discontinuity regions. It is shown that the method requires several simplifications regarding geometry assumed for the truss elements or the effective strength of the struts. In addition, several difficulties can be faced in developing a strut-and-tie model such as uniqueness of the model, combination with other load cases or dealing with statically indeterminate systems. Design provisions are available in the codes of practice for STM, which can be used in a regular basis for the design of D regions. In addition, solving strut-and-tie models generally require an iterative approach and so computational tools to optimise these calculations are being developed.

In order to produce an accurate strut-and-tie model in which some of the uncertainties mentioned above is critical, laboratory testing will be required. Additionally, the use of finite element modelling can also be helpful to generate strut-and-tie models, as recognized by Schaich & Schaffer [58]. Moreover, carrying a non-linear finite element analysis (NLFEA) can provide useful information of the crack pattern, which can be responsible for failure. However, as described in chapter 3 this analysis is not straightforward and often requires experimental data in order to calibrate the models used in the NLFEA.

CHAPTER 3 – Non-Linear Finite Element Analysis

3.1 Introduction

Finite element modelling has been applied on a regular basis by researchers and designers in order to predict shear behaviour of RC structures. In the past, non-linear finite element analysis (NLFEA) was restricted to few specific cases due to its difficult applicability. The considerable emerging number of user-friendly NLFEA software packages available has increased the number of cases where NLFEA are performed. However, two main difficulties have arisen. Firstly, NLFE predictions are highly dependent on the constitutive model applied and parameters assigned in the model. Due to the large amount of constitutive models available and considerable number of parameters required in each model, the calibration process of each parameter can be extremely time consuming. Secondly, mesh properties, solver configurations or boundary conditions can influence the numerical stability of the FE model. Numerical difficulties can be expected in the NLFE modelling of shear critical concrete structures due to their brittle behaviour. Additionally, NLFEA predictions may contradict in many instances existing design equations and irrational solutions can be obtained if the model has not been validated beforehand with existing experimental data.

The main objectives of the non-linear finite element models developed by the author were to support experimental data and validate proposed analytical methods. The FE models were developed using DIANA v.9 software package, which offers a large variety of state-of-the-art constitutive models for concrete. Several techniques to model cracking in reinforced concrete are investigated (smeared, discrete and combined). This chapter summarizes the main features of the constitutive models implemented in the NLFEA

presented in chapters 5, 7 and 8. In addition, values assumed for the parameters required in the NLFEA are contrasted with general recommendations from the literature. It must be noted that the performance of most of the constitutive models investigated for concrete, is case dependent. Hence the conclusions drawn in this chapter regarding NLFEA should be considered as a guideline only for similar models. The FE models presented here, assume plane stress conditions and in general shear behaviour was predominant over other types of failure.

3.2 Crack modelling in NLFEA

Two main techniques are commonly used to model cracking in NLFEA of reinforced concrete structures; namely smeared and discrete cracking methods. In the smeared crack approach, cracking is smeared within the element unlike the discrete approach where a gap is introduced into the mesh after cracking. The discrete crack approach is more realistic than the smeared crack formulation but it is far more complicated to implement in a finite element model since it requires the nodal connectivity to be changed on crack formation. Furthermore, the crack must follow the element edges. The smeared method idealises the cracked element as a continuum which can lead to "stress locking" effects near the crack. These local effects are usually unimportant and the general behaviour of the structure can be well predicted with smeared models. In case the stresses at the crack are to be estimated more accurately, the alternative method of combining smeared and discrete cracking elements seems more sensible, as shown in chapters 7 and 8. Other considerations related with smeared cracking models, which were investigated by authors such as Rots et al. [67-69], include "mesh-induced directional bias" and "numerical instabilities" due to bifurcations caused by closely spaced cracks. Some of these aspects are further discussed in section 3.5.

3.2.1 Smeared cracking models

Smeared cracking is commonly formulated based on either a total strain concept or in a strain-decomposition manner. The second approach offers several advantages since it divides the total strain into two components: strain of the concrete between cracks and strain at the crack itself ($\varepsilon=\varepsilon_{co}+\varepsilon_{cr}$). This division allows to combine different types models for concrete such as elastic, plastic or visco-elastic models. As reported by Rots and Blaauwendraad [66], the relevance of this approach has been documented in the past by several authors (Bazant & Gambarova [47], De Borst & Nauta [67], Rots et al. [68], Riggs & Powel [69]).

Independently of the decomposition of strains used, the inclination of the crack can be assumed to be totally fixed or fully rotating. An alternative hybrid approach, such as the multi-directional fixed crack technique (Rots and Blauuwendraad [66]), can incorporate the extreme cases of fully rotating and totally fixed cracks dependent on the choice of threshold angle (α) at which further cracking is permitted. The main features of these three approaches (fixed, fully rotating and hybrid) are reviewed in the next sections.

Fixed inclination crack models

The main advantage of using a fixed crack model, as opposed to a fully rotating approach, is that previous cracks are considered in the analysis. In addition, the fixed crack model enables the normal and shear actions to be considered separately (Maekawa et al. [52]). On the other hand, one of the main drawbacks of the totally fixed or multi-directional fixed models is that there are several uncertainties in the shear stiffness assumed after cracking. The reduction of shear strength once the crack has formed is defined by the shear retention factor (β), see Figure 3.1.

The shear retention factor, which is usually assumed constant, can have a significant effect on the rotation capacity of the struts crossing the cracks, due to shear friction along the crack. For simplicity β is generally assumed as 0.1 or 0.2, which was originally proposed by Suidan and Schnobrich [70]. These values of the shear retention are widely used in FE modelling, see TNO DIANA [71], Rots et al. [66, 68], Kotsovos & Pavlovic [72], Pimentel [73]. However, according to experimental evidence, shear stiffness after cracking is not constant and decreases as the crack gets wider. Authors such as Rots & Blaaunwendraad [66], Cervenka et al. [74], or Figueiras [75] presented more realistic models with a variable shear retention factor, which decreases as the normal strain at the crack (ε_{nn}) increases, see Figure 3.1. Rots and Blaaunwendraad's model applies to unreinforced cracks, while Cervenka and Figuiras' models were developed for cracks which are crossed by reinforcement bars. These models are given by equations (3.1, 3.2 and 3.3). The ultimate strain ($\varepsilon_{nn,ult}$) in equations (3.1) and (3.3) is dependent on the tension softening assumed in the model, the crack bandwidth (h), and the fracture energy (G_f).

- *Rots and Blaauwendraad* [66]

$$\beta = \left(1 - \frac{\varepsilon_{nn}}{\varepsilon_{nn,ult}}\right)^{k} \qquad \ldots (3.1)$$

where k is positive, usually taken as 1

- *Cervenka et al.* [74]

$$\beta = \frac{-c_3}{c_2}.\ln\left(\frac{1000.\varepsilon_{nn}}{c_1}\right) \qquad \ldots (3.2)$$

where c_1=7+333(p-0.005); c_2=10-167(p-0.005); c_3=1; $0 \leq p \leq 1$ (p is dependent on the reinforcement ratio)

- *Figueiras* [75]

$$\beta = \xi.\left(1 - \frac{\varepsilon_{nn}}{\varepsilon_{nn,ult}}\right) \quad \ldots (3.3)$$

where $\varepsilon_{nn,ult}$ = 0.0045and ξ=0.25/0.125 for single/double cracking

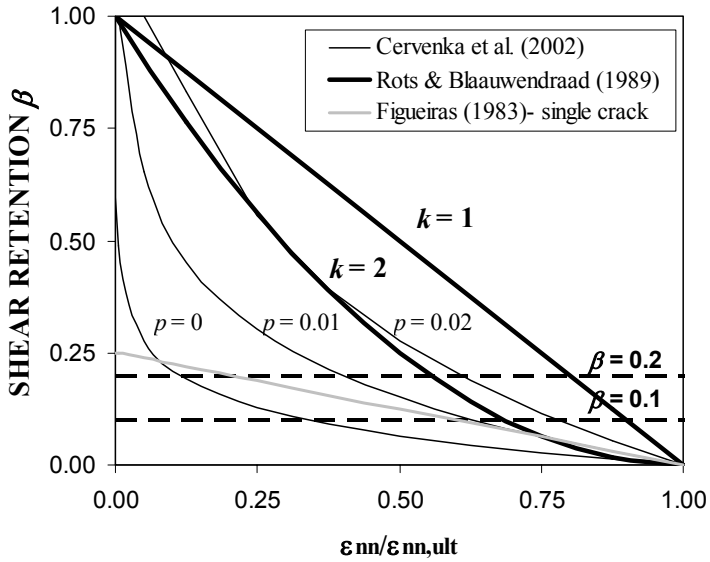

Figure 3.1: Shear retention factors according to different models

The models described above seem to be more realistic from a theoretical point of view than assuming a constant value of β. However, two main disadvantages can be highlighted. Firstly, the models given by equations (3.1 to 3.3) can produce shear retention factors well above 0.4 for low normal strains (Figure 3.1). As reported by Rots and Blaaunwendraad [66], assuming large values of β (>0.5) can result in extremely stiff responses due to overestimation of principle stress rotation after cracking. Secondly, these models assume that the shear stiffness of the aggregate interlock across macro-cracks is zero (β =0 for $\varepsilon_{nn} > \varepsilon_{nn,ult}$), which is inconsistent with experimental evidence, such as push-off tests data shown in chapter 4. In view of these limitations, a constant value of the shear retention factor was finally adopted in this work; conventional values of β (0.1-0.2) were used, although parametric studies were carried out for each model to assess the consequences of this assumption.

Rotating crack models

In the fully rotating models (threshold angle α=0), the stresses are computed along the axis of the principal strains (co-axiality principle). Hence shear transfer along the cracks and shear retention factors are not required. A typical example of fully rotating model is the Modified Compression Field Theory (MCFT) developed by Vecchio and Collins [8]. According to the authors of the MCFT, the co-axiality assumption seems to be valid for a large number of cases. However, as reported by Vecchio [29] or Maekawa et al. [52], the co-axiality principle does not apply for structural cases where shear slip and shear transfer along cracks is predominant. Experimental data shows a delay between the direction of the principal stresses and the principal strains (Vecchio [29]). According to Maekawa et al. [52] the co-axiality assumption would only seem reasonable for cases such as RC elements with no pre-cracks, a cracked RC element reinforced in both directions and cracked elements with small crack widths. As shown in short span beams modelled by the author (see section 7.4), similar predictions were obtained using totally fixed and fully rotating models. In this case this was due to the limited crack rotation within the shear span, and so the same did not apply for more slender beams. Another example of the performance of a fully rotational crack model can be seen in shear panels, which are investigated in chapter 4. As reported by Vecchio [29], one of the deficiencies in the MCFT, which is related with the co-axilality assumption, can be observed in shear panels which are lightly reinforced in one direction. In such cases, where there is a high strut rotation, the ultimate shear strength and stiffness is generally overestimated by the MCFT.

Hybrid fixed-rotating crack models

Several attempts have been made in order to improve fully rotational models to capture more realistically the influence of shear transfer along previous cracks. Hybrid models between fully rotating and fixed crack models have been developed. Although the predictions using these models are in many cases more accurate than the extreme rotating and fixed models, severe numerical difficulties can arise.

An example of hybrid formulation is the "Disturbed Stress Field Model" (DSFM) presented by Vecchio [29]. The main advantage of the DSFM compared to the MCFT is that co-axiality is no longer required since a crack slip relationship is introduced. Alternatively to the DSFM, other hybrid models such as the multi-directional fixed crack model (Rots et al. [68]) were developed. The multi-directional fixed crack model, which

is denoted as "multi-fix" in this work, is easily formulated for strain-decomposition models (see Rots et al. [68]). This model, which is implemented in DIANA, was adopted for the NLFEA shown in chapters 5, 7 and 8. The multi-fix model assumes that once the maximum tensile stress criterion is violated, a crack forms perpendicular to the principal tensile stress direction. The direction of the crack is kept fixed; hence the principal stress can rotate due to shear transfer along the crack. A new crack may form in a different direction if the maximum tensile stress criterion is again violated. Similarly as in the fixed model, a shear retention factor β must be assumed in the multi-fix model. However, the consequence of estimating β seems less relevant than in the fix model since in this case the orientation of the crack is updated to some extent.

Regarding the criteria for the formation of a new crack, four possible criteria are distinguished by Rots and Blaauwendraad [66]:

a) the principal tensile stress is violated

b) the angle between the principal tensile stress and the existing crack(s) exceed the value of the threshold angle (α)

c) both conditions (a) and (b) are violated

d) either conditions (a) or (b) is violated

As reported by Rots and Blaaunwendraad [66], condition (a) will not limit the number of cracks, which will lead to an inefficient algorithm especially when the stresses can rotate considerably (high values of β~0.5). Excessive number of cracks at a single point will result in ill conditioning of the stiffness matrix and numerical difficulties for cases of crack re-opening (Rots and Blaaunwendraad [66]). Similar problem as in case (a) will be faced if (d) is assumed. Condition (b) on its own would not be reasonable since the tensile stress would be completely ignored. Therefore, (c) seems to be the most suitable criteria from a numerical perspective and so was adopted in the FE models used in this work. It is important to note that this assumption can lead to extreme cases, as reported by Rots [68], where the principal tensile stress can reach up to three times the tensile strength while the threshold angle condition is still not violated. In order to avoid these situations a reasonable value of the threshold angle (α) needs to be chosen.

The default value of the threshold angle α assumed in DIANA is 60˚, which generally provided sensible results in FE models developed by the author. In most of the beams

analysed here, the value of α did not have a significant effect on the predictions. Furthermore, for beams with stirrups, the FE model was more stable assuming a value of α=60˚. However, in beams without shear reinforcement, where shear cracks crossed previous flexural cracks (see beams B0 in chapter 8), a value of α equal to 60˚ provided slightly higher values of the ultimate strength. In such cases, a value of α equals to 30˚ provided better predictions. Similar conclusion was obtained by Pimentel [73] in his analysis of slender beams without shear reinforcement, using the multi-fix model. Pimentel [73] justified this value of alpha from observation of the crack pattern obtained in the experiments. The value of α equals to 30˚ also agreed with earliest estimates given by Rots and Blaauwendraad [66], which was suggested as a balance between "computational cost and level of sophistication".

3.2.2 Discrete crack models

Discrete cracking is generally modelled by means of interface elements introduced in the FE mesh. In general, a previous analysis using smeared cracking elements only, is carried out in order to assess the exact position and geometry of the cracks. The formulation of constitutive model used in the interface elements are based on the total deformation theory, where normal and tangent stresses are expressed as functions of the crack relative displacements Δw and Δs, see Figure 3.2.

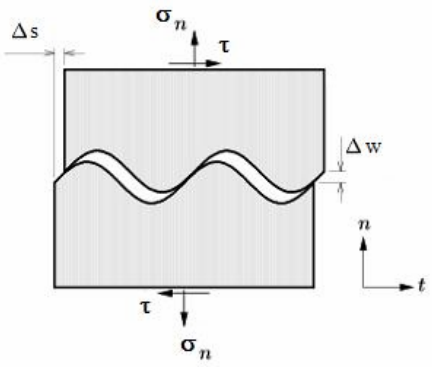

$$\sigma_n = f_1(\Delta w, \Delta s)$$
$$\tau = f_2(\Delta w, \Delta s)$$

$$\begin{cases} D_{11} = \dfrac{\partial \sigma_n}{\Delta w} \\ D_{12} = \dfrac{\partial \sigma_n}{\Delta s} \\ D_{21} = \dfrac{\partial \tau}{\Delta w} \\ D_{22} = \dfrac{\partial \tau}{\Delta s} \end{cases}$$

Figure 3.2: Relationships between normal/shear stresses and crack opening/slip displacements in interface elements (adapted from DIANA [71])

Two types of models, which are described in DIANA [71], were investigated:

a) Discrete crack model

b) Crack dilatancy models

Discrete crack model

The discrete crack model implemented in DIANA, is a simple formulation where the shear and normal stresses are uncoupled, hence $D_{ij} = 0$ ($i \neq j$) in Figure 3.2. The crack initiation is only governed by Mode I (tension) criteria. Once the tensile stress reaches the tensile strength a tension softening relation is applied for normal stresses while constant shear retention is assumed in shear. The model does not consider the reduction in shear stiffness due to crack widening nor the interaction between τ and σ. However, the numerical stability is guaranteed since the stiffness matrix remains symmetrical.

The main difficulty of this approach would be to provide a reasonable value for the shear stiffness (D_{22}) after cracking since this parameter has a direct effect on the sliding allowed at the crack. As reported by Feenstra et al. [53], if the discrete crack elements are aligned with the potential principal tensile stresses, D_{22} could be assumed as zero. Although this assumption might be reasonable up to a certain level of loading, it is questionable whether it would still apply at loads near failure, where strut realignments can be expected. According to the author, providing an estimate of $D_{22}>0$ would seem to be a more reasonable approach since it would allow for stress redistribution in some extent. As shown in sections 7.5.3 and 8.3.3, D_{22} can be estimated from either push-off test data or from analytical approximations. The aggregate interlock stiffness predicted by analytical models such as Hamadi and Regan's [19] formula or most of the crack dilatancy models discussed in section 2.5.2, is a function of the crack width. Therefore, an estimated of D_{22} can be obtained assuming a sensible value for the crack opening near failure. This initial estimated value of D_{22}, can be easily optimised if crack slip data from tests is available. Estimating the shear stiffness from crack openings at loads near failure should provide a lower bound of the shear stresses at early loading, since D_{22} is underestimated at these load stages.

Crack dilatancy models

Crack dilatancy models (CDM) can be applied to account for aggregate interlock in macro-cracks in a more realistic manner than the simple discrete crack model described above. As explained by Fenstra et al. [53], the crack dilatancy model is mobilized in the open-crack state, i.e. the tensile stress at the interface element reaches zero in the softening curve. Before the crack dilatancy model is mobilized, the initial linear-elastic and crack development (tensile softening) states are identical as in the simple discrete crack model described previously.

The main shortcoming of the CDM is that stiffness matrix $\underline{D}$ is non-symmetrical and so the stability of the analysis is compromised. From the author's experience using CDM, these difficulties can be partially overcome by reducing the load steps considerably or applying an adaptive type of loading. However, if failure is sudden, such as in beams without stirrups, an indirect displacement control such as the "Crack Mouth Opening Displacement" control (CMOD) seems necessary.

Another important aspect that must be highlighted is the relevance of the type of algorithm (see section 3.5.2) applied to solve the system of non-linear equations in the FEA, when using interface elements with CDM. In the NLFE models, the load stages at which the discrete crack started to open was critical in terms of numerical stability. Solvers such as the traditional Newton-Raphson or the Quasi-Newton (secant), described in section 3.5.2, provided a good performance. However, the constant and linear solvers, which apply the stiffness matrix obtained in previous load step, provided spurious results. These algorithms seemed to be inefficient to capture the sudden changes in stiffness produced at the crack initiation stage.

Several CDM relationships are implemented in DIANA:

- Linear aggregate-interlock model (Walraven & Reinhardt [46])
- Rough crack model (Bazant & Gambarova [47] or Gambarova & Karakoç [48])
- Two-phase model (Walraven [45])
- Contact density model (Li et al. [49])

These approaches, which are based on either empirical or analytical models, were presented in section 2.5.2. According to Feenstra et al. [53], the contact density model provided a better numerical stability compared with the rest of the models. The linear aggregate interlock relationship suggested by Walraven and Reinhardt [46] is also widely applied due to its simplicity. The performance of some of these models is investigated in section 4.5 using experimental data from the push-off tests carried out by the author.

In view of the numerical difficulties faced in some of the NLFEA performed in this work using CDM, it can be concluded that the use of CDM should be restricted to very limited cases, where the crack slip is significant compared with crack opening. As discussed in chapters 7 and 8 for the analysis of the beams tested, the simpler discrete crack model provided reasonable predictions when sensible estimates of D_{22} were applied.

3.3 Constitutive material models applied

In order to cover the main groups of smeared cracking techniques described in previous section, two types of material models were investigated.

1. Total Strain models: rotating and fixed crack model
2. Multi-directional fixed crack model

The first model is based on the total strain formulation and includes fully rotational and totally fixed alternatives. The second model used was a strain-decomposition, multi-directional smeared crack in tension with an elasto-plastic model in compression. The main features of these models are described in previous section. The constitutive equations for compression, tension and shear, as well as the parameters generally assumed in each model are described below. The expressions for the strain vectors and stiffness matrix assumed in each model are omitted; refer to Rots and Blaauwendraad [66] or DIANA's Users Manual [71] for detailed information regarding these equations.

Total Strain Models: fixed and rotating crack models

The equivalent stresses are calculated in terms of the strains in the crack directions, assuming a constant Poisson ratio. In the Total Strain fixed model this direction corresponds to the initial crack orientation, while in the rotating crack model the principal strain/stress direction is used. Unloading is modelled in both tension and compression through a straight secant strain-stress path, which passes through the zero point as shown in Figures 3.3 and 3.4.

After cracking, the shear stiffness is assumed constant in the fixed crack model (βG). In the rotating model, co-axiality is forced by introducing a tangential shear modulus (G_{12}, G_{23} and G_{31}) according to equation (3.4), derived by several researchers (Bazant [76], William et al. [77], Rots and Blaauwendraad [66]).

$$G_{ij} = \frac{\sigma_{ii} - \sigma_{jj}}{2.\left(\varepsilon_{ii} - \varepsilon_{jj}\right)} \qquad \ldots (3.4)$$

where $(i,j) = (1,2); (2,3); (3,1)$ for G_{12}, G_{23} and G_{31} respectively.

An important aspect that must be highlighted regarding the Total Strain models is that the Poisson ratio must be taken as zero. This assumption is not required in smeared models using a strain decomposition method, since the elastic strains in the concrete (ε_e) are independent of the strains in the crack (ε_{cr}). As described by Pimentel [73], the elastic

strains in the concrete reduce considerably right after cracking. This reduction of ε_e can only be captured in strain decomposition methods and not in the total strain models. If a conventional value of ν larger than zero is introduced in the Total Strain models, the transverse strains can be severely overestimated. The situation is more critical for cases with large crack openings, since the crack strains would be taken into account to obtain the transverse strains, which is not correct. As noted by Pimentel [73], these unrealistic transverse deformations can introduce large perturbations in the stress fields. Similar conclusions are obtained in the FE analysis carried outh by the author for shear panels tested by Vecchio & Collins [8], refer to chapter 5. This numerical analysis showed very low stiff predictions of the shear panels, if conventional values of ν=0.2 were used in the Total Strain models. Other researchers, such as Vecchio [78], have taken values of ν for the concrete after cracking equal to zero. This assumption seems to provide reasonable predictions in many structural cases. However, as pointed by Pimentel [73], this might not be the case in structures where the increase in concrete strength due to confinement is significant.

The tension softening relationships generally applied in the models developed in this work corresponded to either a linear relationship or a Hordyk [79] model (see Figure 3.3). Both models are defined by means of the fracture energy (G_f) and the crack bandwidth (h), which provides a certain degree of objectivity regarding mesh refinement, as discussed in section 3.5.1. The fracture energy was estimated from MC90 formula (3.5), which is dependent mainly on the tensile strength. In cases where the elements were heavily reinforced, G_f was increased in order to take into account tension stiffening.

$$G_f = G_{f0}.\left(\frac{f_{cm}}{f_{cm0}}\right)^{0.7} \qquad \ldots (3.5)$$

where f_{cm0}=10MPa and G_{f0} is a function of the aggregate size according to Table 3.1.

d_{max} [mm]	G_{f0} x 10^3 [N/mm]
8	25
16	30
32	58

Table 3.1: Coefficients required to obtain the fracture energy according to MC90

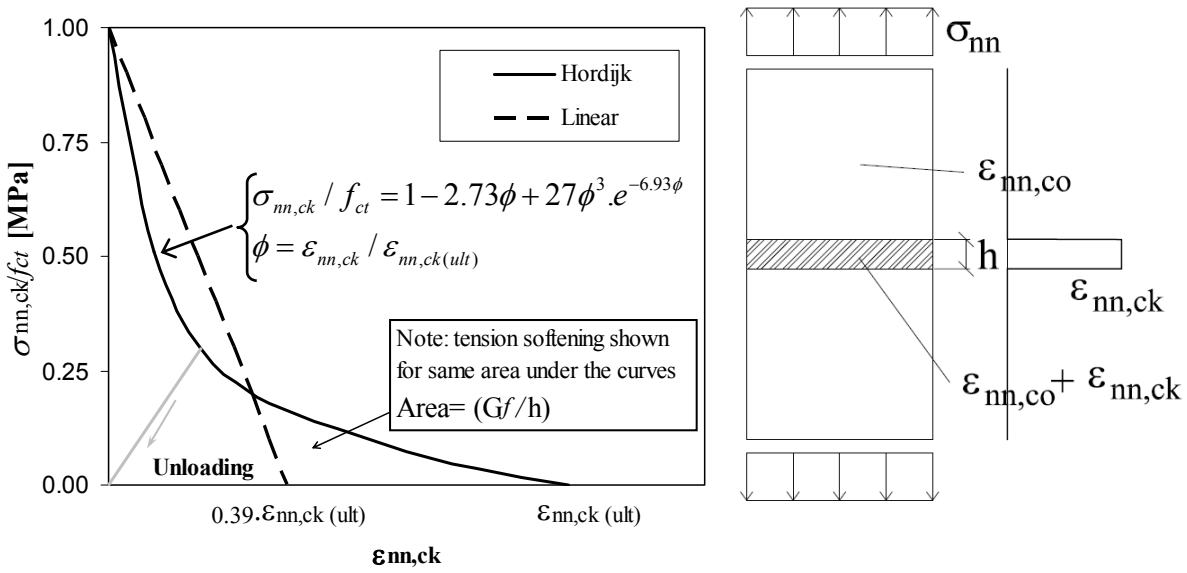

Notation: $\varepsilon_{nn,ck}$ (normal strains in the crack); $\varepsilon_{nn,co}$ (normal strains in the concrete)

Figure 3.3: Tension softening curves applied for loading and unloading (crack band concept)

As mentioned earlier, the crack bandwidth concept, which was originally introduced by Bazant & Oh [80], was used in the smeared crack models. This concept, which is generally used in non-linear fracture mechanics theory, assumes that the crack strains are concentrated along a strip or band of constant width (h) with a constant strain distribution as shown in Figure 3.3. In finite element modelling, the value assume for h depends on the element size and integration scheme. The crack bandwidth (h) was assumed in the models as the square root of the area of the element for bidimensional plane stress elements. More elaborate estimates of h for the plane stress elements would be rather problematic since the orientation of the cracks is not generally known a priori. On the other hand, for interface elements h was taken as the thickness of the element.

In compression, several relationships are commonly applied in practice (see Figure 3.4). Typical examples include symmetrical parabolic curve of Hognestad, Thorenfeldt curve or relationship proposed by *fib* [60, 81]. The asymmetric parabolic curve proposed by Feenstra [82] is adopted in this work. This strain-stress curve consists of three branches, which are limited by points O, A, B and D in Figure 3.4. An initial linear relationship is assumed until point A, while two parabolic curves are fitted for pre-peak and post-peak load branches; see equations in Figure 3.4. The residual compressive stress for large strains was limited to $0.2\sigma_c$, in order to avoid numerical difficulties.

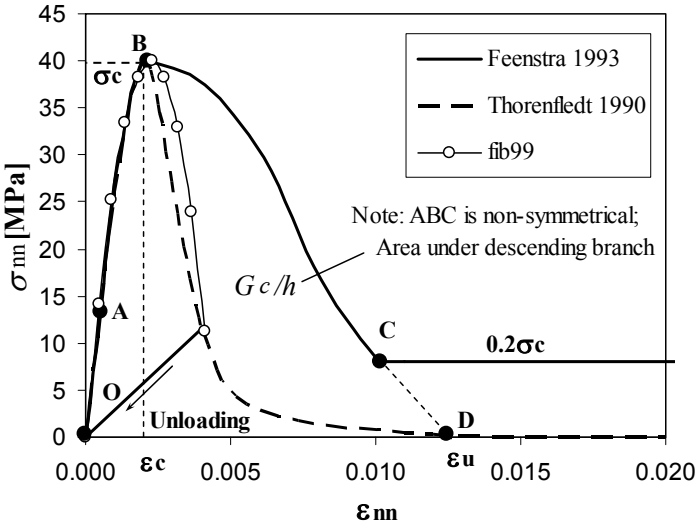

- *Asymmetric parabolic curve (Feenstra 1993)*:

$$A = \left(\frac{\sigma_c}{3E_c}, \frac{\sigma_c}{3} \right)$$

$$B = \left(\varepsilon_c = \frac{4\sigma_c}{3E_c}, \sigma_c \right)$$

$$D = \left(\varepsilon_u = \varepsilon_{nn,B} + \frac{3G_c}{2h\sigma_c}, 0 \right)$$

Figure 3.4: Strain-stress curves for concrete in compression

As shown in Figure 3.4, there is a good agreement between the different models in the ascending branch of the strain-stress curves for compression. However, this is not the case for the descending branch. Aspects such as the level of confinement or high strength compressive behaviour have a significant role on the post-peak strain-stress curve. An accurate definition of the post-peak branch is more relevant in the analysis of the load-deflections response of over-reinforced structures (Wong & Vecchio [83]), since a larger stress redistribution is expected after the critical region begins to crush.

The parabolic descending branch proposed by Feenstra [82], is defined by means of the compressive fracture energy G_c, although not much information is available in the literature about this parameter. In practice, G_c is generally estimated from the tensile fracture energy using an approximate value of $100G_f$ (Ožbolt & Reinhardt [84]). This estimated value of G_c was adopted in the FE models developed by the author. However, recent work from Pimentel [73] or Majewski et al. [85], shows that there is not a general agreement about this particular parameter. For example, Pimentel [73] applied estimates of G_c in his numerical models up to two times the reference value provided by Ožbolt and Reinhardt, obtaining equally accurate answers. On the other hand, in the NLFEA carried out by Majewski et al. [85], the conventional value of $100G_f$ produced a clear overestimation of the ductility of the specimen. In this case, values of G_c of around $50G_f$ provided more sensible answers (from personal communication).

These results support the idea that the influence of G_c on the numerical predictions is case dependent, which was otherwise expected. Pimentel [73] NLFEA involved slender beams failing in shear diagonal tension, while work carried by Majewski et al. [85] focused on columns failing in compression. It seems clear that the second case, the influence of G_c

would be much more relevant than in the former case. The NLFEA carried in this work, involved either cases where failure was due to shear in diagonal tension (slender beams without stirrups) and shear-compression (short span beams). Therefore, the influence of G_c on the predictions was expected to be different for either type of shear failures. In short span beams analysed in chapter 7, where the role of G_c would seemed to be more critical, only a small fraction of elements near the loading plate reached strains above the peak. Hence, the margin for stress redistribution was low and so changes in G_c in the NLFEA did not make much difference in the numerical predictions.

A more comprehensive model to consider the post-peak behaviour of concrete in compression was developed by Markeset and Hillerborg [86]; the Compression Damage Zone (CDZ) model. In their approach, energy is dissipated through a combination of smeared axial splitting and a localized deformation, as shown in Figure 3.5 (right). In the CDZ the axial splitting is related with the fracture energy in tension, while the localized deformation (w_c) depends on the crack surface; w_c can vary from 0.4mm to 0.7mm for normal density concrete or be less than 0.3mm if the aggregate fractures. Although CDZ offers a reasonable approach, there are large uncertainties in the material parameters required in the model. Furthermore, the values obtained for G_c using the CDZ, which had a good agreement with experimental data provided by Vonk [87], are not that different from the conventional value of $100G_f$, as shown in Figure 3.5 (left).

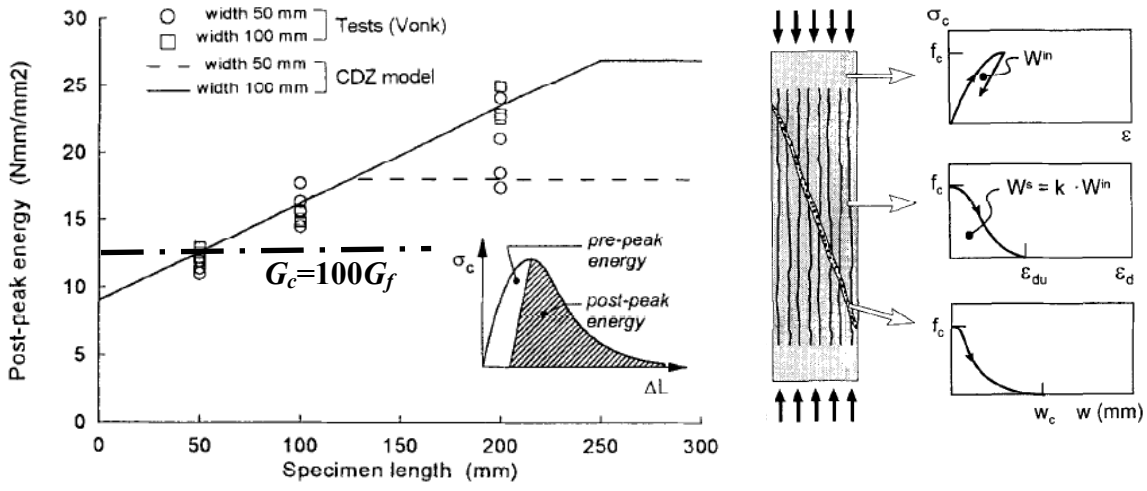

Note: values used in the CDZ model in the figure (G_f=0.12N/mm; f_c=45MPa; w_c=0.4mm)

Figure 3.5: Compression fracture energy according to CDZ (adapted from Markeset and Hillerborg [86]); *Left*- experimental and predicted values of G_c; *Right*- Fundamentals of CDZ

Finally, the reduction in compression strength of the concrete due to transverse strains was taken into consideration in the NLFEA by using predefined-function VC1993 implemented in DIANA, (see Figure 2.6). This algorithm, which is based on work carried by Vecchio and Collins [25], was applied in the Total Strain models. However, this might be questionable for the total strain fixed crack model, since concrete softening could be overestimated according to (Vecchio [29]). The performance of this softening curve is studied in chapter 5 in the analysis of shear panel tests.

Multi-directional fixed crack model

The multi-fixed model was applied using equivalent uniaxial strain-stress constitutive equations for tension and compression as in the Total Strain models described in previous section. A shear retention factor β is assumed since the model is based on a multi-directional fixed crack concept. Standard values of 0.1 and 0.2 are used, similarly as in the fixed crack models.

The multi-fix model combines smeared cracking with plasticity, since it is formulated based on strain decomposition concept (see section 3.2.1). Strains in the crack are modelled using a multi-directional fixed model, while plasticity theory is applied for the concrete strains. In order to deal with biaxial stress states (Figure 3.6), which often combines tension with compression, a constant (Rankine) cut-off was applied for tension and a Druker-Prager yield surface was adopted for compression, see equation (3.6).

$$f\left(\underline{\sigma}, c(k)\right) = \sqrt{\frac{1}{2}.\underline{\sigma}^T P \underline{\sigma}} + \alpha_f \underline{\pi}^T \underline{\sigma} - \beta_c c(k) \qquad \ldots (3.6)$$

where $\underline{P}$ / $\underline{\pi}$ are the projection matrix/vector respectively given by equations (3.7).

$$\underline{P} = \begin{bmatrix} 2 & -1 & -1 & 0 & 0 & 0 \\ -1 & 2 & -1 & 0 & 0 & 0 \\ -1 & -1 & 2 & 0 & 0 & 0 \\ 0 & 0 & 0 & 0 & 6 & 0 \\ 0 & 0 & 0 & 0 & 0 & 6 \end{bmatrix} \quad ; \quad \underline{\pi} = \{1 \quad 1 \quad 1 \quad 0 \quad 0 \quad 0\}^T \qquad \ldots (3.7)$$

parameters α_f and β_c are given by equations (3.8).

$$\alpha_f = \frac{2\sin\phi}{3-\sin\phi} \; ; \qquad \beta_c = \frac{6\cos\phi}{3-\sin\phi} \qquad \ldots (3.8)$$

The friction angle ϕ, which is generally assumed as 30˚ in other plasticity criteria, was taken as 10˚, in order to force equation (3.6) to go through points $A(0,0,-f_c)$ and $B(0,-1.16\ f_c,-1.16\ f_c)$ in Figure 3.6, which correspond to uniaxial and biaxial tests respectively. In a similar manner, the cohesion (c) must be equal to $0.42f_c$. According to DIANA [71], the dilatancy angle ψ is not essential for plane stress situations. Hence associative plasticity ($\psi = \phi$) is assumed for simplicity.

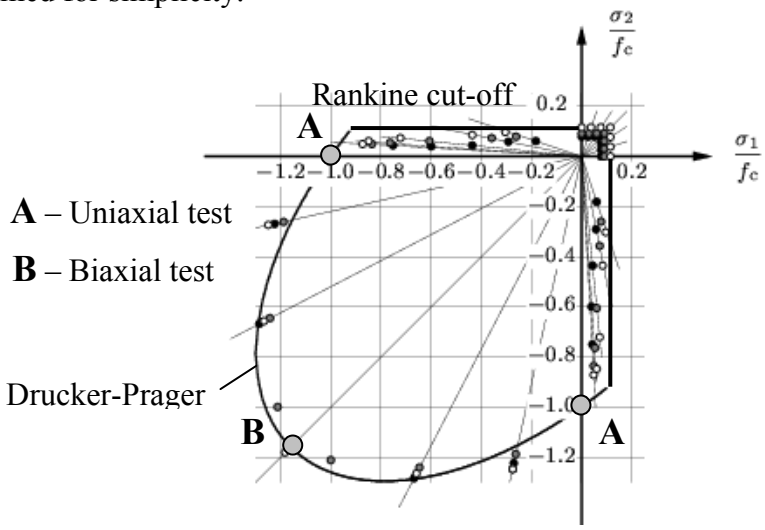

Figure 3.6: Biaxial stress state of concrete (adapted from Kupfer and Gerstle [88])

Strain hardening/softening c(k) is introduced in equation (3.6) by defining the uniaxial stress-strain parabolic relationship, which was previously described for the Total Strain models (see Figure 3.4). The only difference in the input of this relationship in DIANA is that the parabolic relationship is not pre-defined for plasticity models and so the points are introduced in a discrete manner in terms of stress-plastic strains. In order to assess the points, which define the descending parabolic branch, the crack bandwidth h is estimated manually from the average size of the elements in the mesh.

The compressive softening due to transverse strains is not taken into account directly in multi-fix model as in the Total Strain models. Instead, the concrete strength in elements, which are influenced by large transverse strains, is reduced to some extent. Shear panels examined by the author showed that the effectiveness factor ν suggested in EC2 could be applied as a reference value (see section 5.4). Alternatively, Pimentel [89] suggests a concrete strength of $0.85f_{cm}$, which is based on recommendations made by Reineck [40]. Concrete softening can be overestimated if same softening curves developed for rotating crack models are applied in models where the crack slip is taken into account (Vecchio [29]). As reported by Pimentel [89], this would be the case in the multi-fix model since the crack slip is considered in the model.

3.4 Modelling of reinforcement

Reinforcement bars are generally modelled in DIANA as "embedded elements" which add stiffness to the mother elements in which they are surrounded in. Alternatively, truss elements can be used, although the mesh must be adapted to the reinforcement in order to have perfect node connectivity. On the other hand, embedded elements provide no extra degrees of freedom to the model and strains are obtained from the displacement field of the mother elements. These assumptions imply perfect bonding between the concrete and the reinforcement bar. In order to introduce bond-slip relationships, truss elements must be then used in combination with interface elements that are placed between the reinforcement bar and the concrete. This compromises the mesh generation and the numerical stability of the model. Hence, perfect bonding was assumed in the models presented in this work. In addition, the material model applied for the reinforcement steel consists in a conventional perfect plasticity Von Misses yield criteria with no strain hardening. The reinforcement is defined in most of the models as discrete elements as opposed to continuous grids. The differences between both types of elements are discussed in next section. Reinforcement crossing interface elements required additional considerations which are further commented on section 3.4.2.

3.4.1 Grid and discrete embedded elements

Two main alternatives are commonly available to simulate reinforcement by means of embedded elements; namely discrete and smeared (grid) reinforcement. As discussed, the discrete embedded reinforcement can also be modelled by using truss elements with matching node connectivity to the mesh. The grid alternative is suitable for large areas where reinforcement is distributed evenly in two or one directions, such as two-way slabs or shear-reinforced beams respectively. However, the question may arise of whether to use discrete or smeared reinforcement when the spacing between reinforcement bars is significant. Aspects such as mesh density or type of material model used for concrete may have an influence in this decision since the decrease in stiffness in the system due to cracking might be more or less abrupt depending on these two variables.

In addition, the probability of having a significant number of finite elements with no reinforcement crossing them would be high if the spacing between discrete reinforcement elements is large. The situation may worsen if the FE mesh density is increased. The behaviour of plain concrete elements could vary depending on the type of constitutive model used.

In order to investigate the consequences of using either type of reinforcement elements, continuous beam BL1, described in chapter 6, was modelled using both discrete and grid reinforcements. The spacing between stirrups in BL1 is 150mm and the quadrilateral elements, which are used in the mesh, have an average side of 55mm. This mesh configuration leads to one column of finite elements located between stirrups, which are not crossed by any reinforcement, as shown in Figure 3.7. A second case was also investigated, which is denoted as BL1b, where the stirrup spacing was taken as 270mm resulting in three columns of finite elements between stirrups being un-reinforced. This last beam represents the worst case scenario in beams with shear reinforcement since the maximum spacing between stirrups is commonly taken as 300mm (BS8110).

The analysis of both BL1 and BL1b showed that the numerical predictions were very similar using either discrete or smeared embedded reinforcement elements. The load-deflection curves obtained (Figure 3.7) were identical for the multi-fix model, while for the total strain models only small deviations were observed at loads near failure. The overall performance of each model is discussed in further detail in chapters 5, 7 and 8.

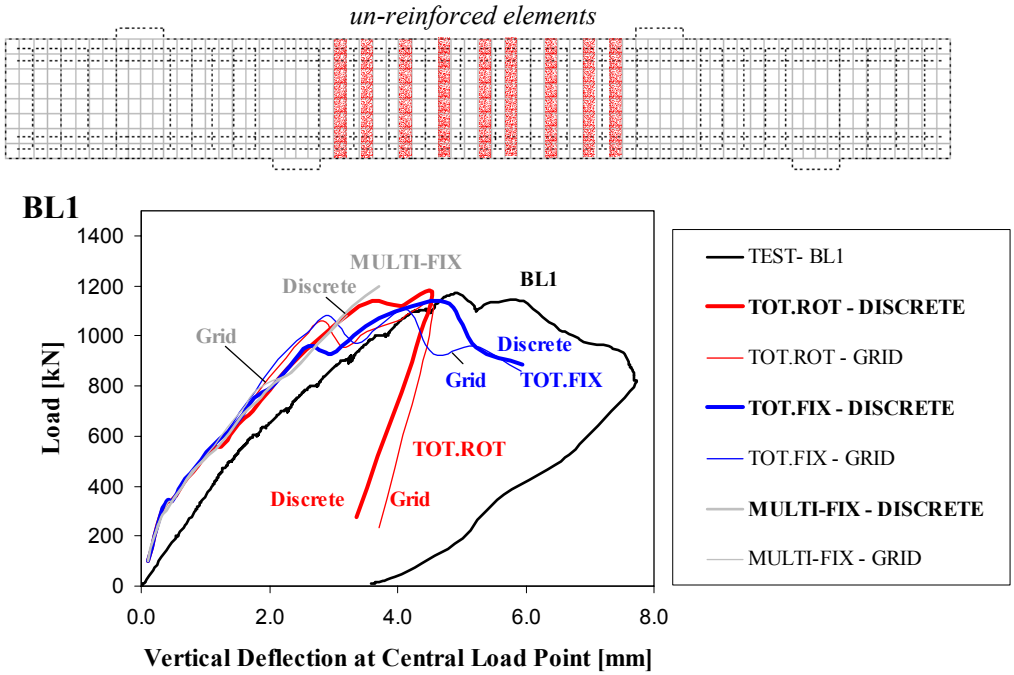

Note: Total Strain (ν=0, β=0.1 for Tot. Fix); Multi-fix (ν=0.2, α=60, β=0.1, fc was factored by 1.5 in elements near the plate); remaining material properties are given in chapter 8 for beams B

Figure 3.7: Load-deflection curves for beam BL1 using grid and discrete reinforcement

Although the aim of this analysis was to investigate the difference in using grid vs. discrete embedded reinforcement elements, two aspects must be highlighted in Figure 3.7. Firstly, the discrepancy for early load stages between numerical and experimental data, is

due to the fact that beam BL1 was pre-cracked, which is not considered in the NLFEA. Secondly, the ultimate load predicted in the multi-fix model in this case was highly influenced by the concrete strength assumed for the elements near the plate. This was not observed in the numerical predictions using Total Strain models. For the analysis shown in Figure 3.7 using the multi-fix model, the concrete strength of the elements near the plate was factored by 1.5. This approach, which is further discussed in section 3.5.3, was needed in some of the models developed to avoid premature failure of these elements. This allowed to assess stresses and crack patterns at loads near experimental failure loads.

Lastly, the only significant difference observed between predictions using grid or discrete reinforcement embedded elements was regarding the geometry of the cracks. In the FE models with grid shear reinforcement the cracks had a slightly curved path (Figure 3.8.b.1), which is due to the smearing of the tensile stresses provided by the grid. This curved crack path predicted was more noticeable in the total strain models, especially for intermediate loading, when higher realignment of principal stresses took place. Using discrete reinforcement elements eliminates this problem since the stirrups are positioned at discrete intervals rather than being smeared within the elements. Hence a polygonal type of crack path is predicted, which agrees better with experimental evidence (Figure 3.8.a). Furthermore, the exact location of the crack becomes clearer as shown in Figure 3.8.c.

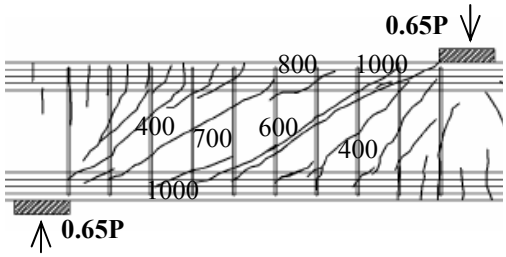

a) Experimental (BL1)

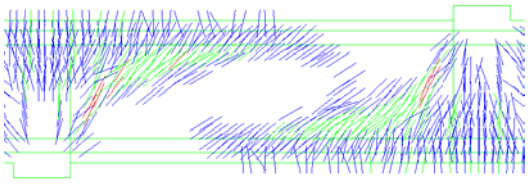

b.1) Grid (P=750kN)

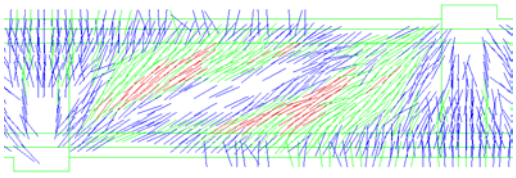

b.2) Grid (P=850kN)

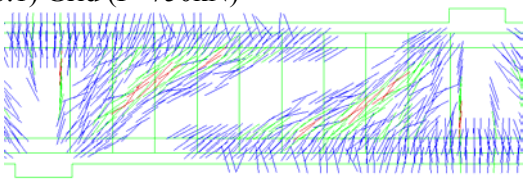

c.1) Discrete (P=750kN)

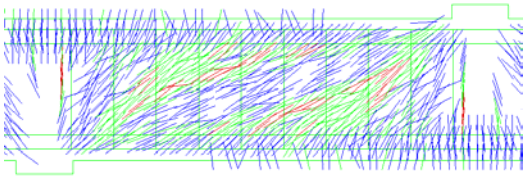

c.2) Discrete (P=850kN)

Figure 3.8: Predictions of crack pattern for multi-fix model using grid and discrete reinforcement

It can be concluded from the previous analysis that both smeared and discrete types of reinforcement elements can be used to model beams failing in shear, as long as the stirrup spacing complies with design standards. However, the second option (discrete elements) tended to give in general more realistic crack pattern for intermediate loadings. Therefore, the discrete reinforcement was preferred over the grid option for the models developed in this work.

3.4.2 Reinforcement bars crossing interface elements

So far, reinforcement elements have been assumed to be embedded in plane stress mother elements only. Additional considerations regarding the normal and shear stiffness must be made if the reinforcement is embedded in interface elements. This situation arises at discrete cracks crossed by reinforcement bars. As described by Maekawa et al. [52] or Soltani et al. [90], several phenomena related to dowel action and bond-slip effects take place at the crack where it is crossed by reinforcement (Figure 3.9). Bond stresses are highly influenced by deterioration of the concrete surrounding the reinforcement bar due to splitting and crushing of the concrete. Furthermore, if the reinforcement is skewed with respect the shear plane, the deterioration length increases due to spalling of the concrete near the reinforcement bar at the crack (Soltani et al. [90]).

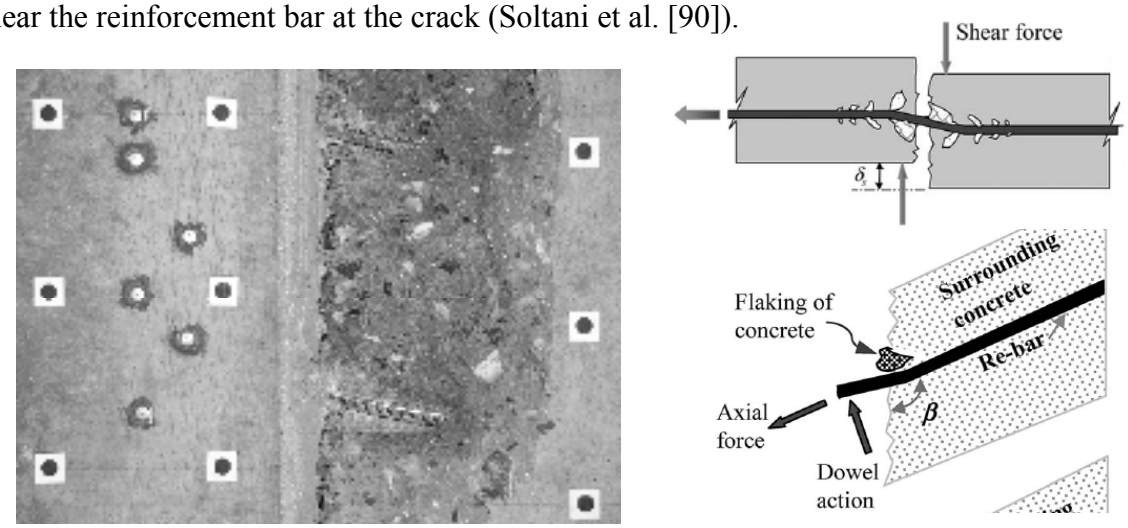

Figure 3.9: Local effects of reinforcement bars crossing cracks; *Left* – Push-off test PG3 tested by author; *Right* – Local effects according to Soltani et al [90].

As described by Walraven & Reinhardt [46], cracks crossed by embedded reinforcement have a different behaviour than when restrained by un-bonded or external reinforcement. This is due primarily to the reduced crack width immediately near the embedded reinforcement bar, which results in secondary diagonal cracking and an additional strut mechanism (Figure 3.10). On the other hand, externally reinforced cracks and un-bonded

(smooth bars) have a constant crack width, which results in shear forces to be transmitted by aggregate interlock action only since the diagonal strut is no longer present.

These different shear transmitting mechanisms that are present in cracks crossed by embedded reinforcement are difficult to take into account accurately in FE modelling. Several analytical models have been developed in order to simulate these mechanisms in a realistic manner. An example is the model proposed by Walraven and Reinhardt [46] (Figure 3.10.c).

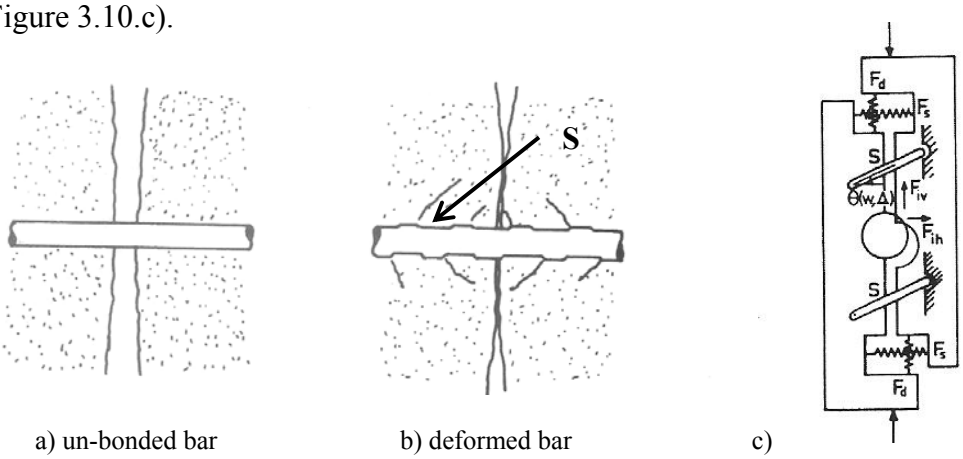

a) un-bonded bar b) deformed bar c)

Figure 3.10: Local mechanism at cracks with embedded reinforcement according to Walraven and Reinhardt [46]; a) constant crack widths for un-bonded reinforcement bars; b) secondary struts (*S*) with diagonal cracking in the vicinity of deformed reinforcement bars; c) shear transfer mechanisms along crack due to aggregate interlock (F_{iv}, F_{ih}), secondary struts (*S*), dowel action (F_d) and normal stiffness from reinforcement bars (F_s)

In DIANA, aggregate interlock action is modelled using interface constitutive relationships, which are described in section 3.2.2. The secondary strut mechanism illustrated in Figure 3.10.b, was not considered in the NLFEA carried out in this work. In DIANA, the normal and shear components introduced by the reinforcement bar, which refer to F_s and F_d in Figure 3.10.c, are estimated in terms of the free length (l_{fr}) parameter, according to Figure 3.11.

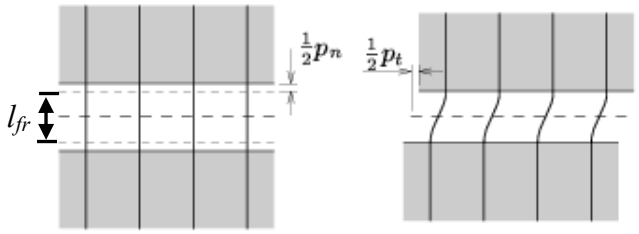

$$k_n = \frac{E_s}{l_{fr}} \quad ; \quad k_t = \frac{E_s}{2l_{fr}}$$

Note: the thickness of the interface element (*h*) does not have to be equal to l_{fr}

Figure 3.11: Estimation of stiffness per unit area in the normal and transverse direction of reinforcement element, which crosses an interface element (according to DIANA)

Additionally, reinforcement elements crossing interfaces are integrated in DIANA using a single Gauss point with normal and shear *dof* in the same directions as the interface elements and not along the reinforcement. The thickness of the interface elements is unimportant; in this work h=0.2mm. In order to estimate the free-length parameter, yielding of the stirrup reinforcement was assumed to occur at a crack opening of 0.4mm (l_{fr}=150mm). This assumption was based on experimental evidence shown in chapters 4 and 6.

Although the free-length parameter can be estimated from observed crack openings as shown above, the value assumed in DIANA for the dowel action stiffness (k_n) (Figure 3.11) seems highly questionable. To illustrate this, three different load-deformation models for dowel action were applied (Millard & Johnson [91], Walraven & Reinhardt [46], He & Kwan [92]), see Figure 3.12. These models, which are based on traditional beam over elastic foundation problem, provided very similar predictions for a single T8 stirrup bar (see parameters used in models in Figure 3.12). In addition, MC90 formula for dowel action was consistent with the previous three models; $P_{ult(MC90)}$=12.8kN.

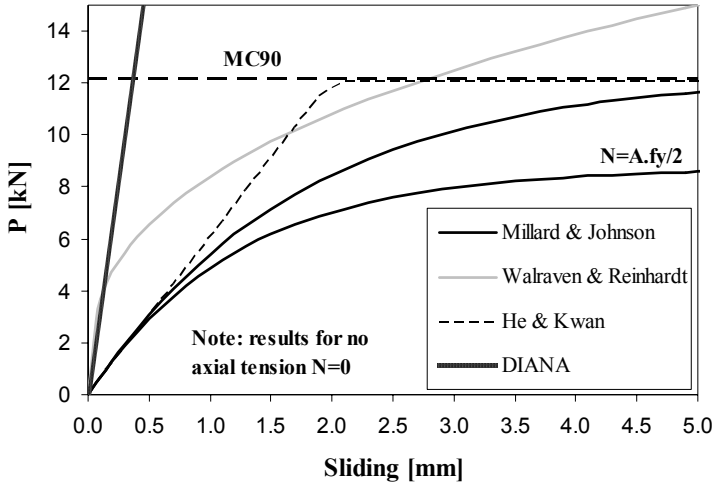

Parameters:
D =8mm (A=50.24mm^2)
E_s =200GP
f_{cc} =40MPa
f_y =550MPa
e =0.1mm (MC90)
α =1.3 (MC90)
β =1 (Millard & Johnson)
Results shown for no axial tension (N=0), unless stated

Figure 3.12: Load-deformation response of dowel according to different analytical models

A perfect-plastic behaviour is assumed in He & Kwan's model (Figure 3.12) based on experimental work carried by Dei Poli et al. [93], Dulacska [94] and Vintzeleou & Tassios [95]. On the other hand, Millard & Johnson's model assumes an elastic behaviour up to 40% of the ultimate load. The initial stiffness of the dowel action predicted by both models was identical and considerably lower than Walraven & Reinhardt's model, which appears to be too stiff. However, for slips greater than 0.1mm, the three models provided similar predictions. Results in Figure 3.11 are shown for no axial tension. However, experimental evidence provided by Eleiott [96] showed that the dowel stiffness can

considerably lower when axial tension is applied. This is shown for Millard & Johnson's model (Figure 3.11) for an axial stress of half the yielding capacity of the bar. Walraven & Reinhardt's model included a reduction factor to take into account for this, which provided similar answers as Millard & Johnson's curve.

According to these analytical models shown in Figure 3.12, the constant stiffness assumed in DIANA, which was estimated using the free-length parameter obtained from crack opening considerations (l_{fr} =150mm), seems excessive. According to these three models, which were applied for normal crack widths and reinforcement bar sizes used for stirrups, a more reasonable value for the k_t/k_n ratio would seem to be 1/10. Increasing parameter l_{fr} to optimise the dowel action stiffness would result in excessevily large normal deformations at the interface element.

Possible alternatives to embedded reinforcement elements could include using spring elements with user-supplied material constitutive equations (Eierle & Schikora [97]) or truss elements. Either option is not straight-forward since firstly, the mesh would have to be adapted to the shear reinforcement and secondly, constitutive equations would need to be developed for the element crossing the interface. This was not considered to be within the main scope of this project and so an alternative solution was adopted. As described in chapters 7 and 8, the value of the shear stiffness assigned to the interface elements due to pure aggregate interlock was decreased in order to account for the excess stiffness provided by the shear reinforcement. This compensation would have to be larger in beams with lower stirrup spacing. The aim was to provide overall shear stiffness that would be realistic in view of the experimental and analytical results from the push-off tests shown in chapter 4. This approach is less numerically demanding than using spring elements or truss elements with very short lengths.

3.5 Other aspects related to NLFEA

3.5.1 Mesh considerations

The finite element meshes generated in this work consisted of triangular and quadrilateral isoparametric plane stress elements with quadratic interpolation (6 and 8 nodes respectively); refer to Figure 3.13.a and b. Linear interpolation elements were avoided for the non-linear analysis, as recommended by DIANA [71]. A default Gauss integration of 2×2 for the quadrilateral elements and 3-point area integration schemes were adopted. On the other hand, in order to model discrete cracking, line interface elements with a 6-node and a 5-point Newton-Cotes integration were used (Figure 3.13.c). As reported by Feenstra et al. [53], numerical oscillations can occur in interface elements with small thicknesses unless a Newton-Cotes quadrature is used. Alternatively, lumped interface elements could be applied, although the stiffness matrix would be similar (Feenstra et al. [53]). Triangular plane stress elements were introduced in the meshes to provide a transition in the geometry from the quadrilateral elements to the inclined interface elements, see Figure 7.34.

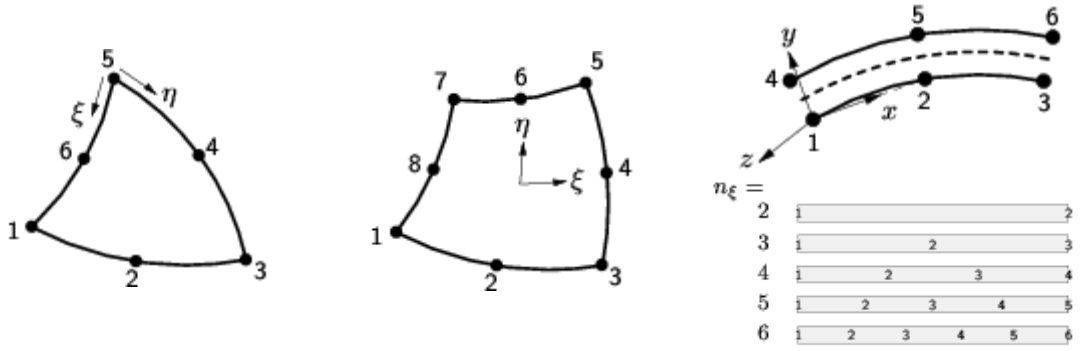

a) **b)** **c)**

Figure 3.13: Types of elements used in FE meshing (adapted from DIANA [71]); a) Triangular element (CT12M); b) Quadrilateral element (CQ16M); c) Line interface element (CL12I) with 5-point Newton-Cotes integration scheme

The FE meshes generally used in the models were uniform, as shown in Figure 3.7, with a number of divisions of around 10 for the height of the beam. This resulted in element sizes of around 50mm. This mesh density was of a similar magnitude as models developed by other authors (Vecchio & Shim [98], Kotsovos and Pavlovic [72], Pimentel [89] or Feenstra et al. [99]). In order to provide numerical results which are independent of the size of the elements, a regularization technique must be applied. As described in section 3.3, this is achieved in DIANA by using the crack bandwidth (h) concept. The constitutive models are formulated based on the fracture energy released in the element

after reaching the tensile strength, which guaranties the objectivity of the results as long as the total fracture energy is kept constant.

The main shortcoming of this approach occurs for coarse discretisations or large unreinforced concrete structures, where the values of h could be large enough to produce a snap-back in the constitutive model used for tension. This snap-back behaviour will occur if the maximum value of the tangent stiffness of the softening curve, which generally takes place at the start point of the curve, is greater than the Young's modulus of the material. According to softening curves shown in Figure 3.3, this limitation is more critical for the Hordyk's curve than for a linear relationship with the same G_f value. From the Hordyk's expression shown in Figure 3.3, the value of the ultimate strain ($\varepsilon_{nn,ck(ult)}$) can be written in terms of the fracture energy (G_f), crack bandwidth (h) and tensile strength (f_t), as shown in equation (3.9).

$$\varepsilon_{nn,ck(ult)} = 5.136.\frac{G_f}{hf_t} \qquad \ldots (3.9)$$

The minimum value of the ultimate strain ($\varepsilon_{nn,ck(ult)}|_{\min}$) for which the slope of the curve at the starting point becomes greater than E in the Hordijk's model is given by equation (3.10). Imposing $\varepsilon_{nn,ck(ult)} > \varepsilon_{nn,ck(ult)}|_{\min}$ yields to equation (3.11), which provides the maximum value of h_{max} for which snap-back behaviour will occur.

$$\varepsilon_{nn,ck(ult)}|_{\min} = 6.957.\frac{f_t}{E} \qquad \ldots (3.10)$$

$$h \le h_{\max} = 0.739\frac{EG_f}{f_t^2} \qquad \ldots (3.11)$$

If a linear softening curve was assumed, coefficients 5.136, 6.957 and 0.739 in equations (3.9) to (3.11) should be changed to 2, 1 and 2 respectively. Normal values used in this work include G_f=0.1N/mm, E=30000MPa and f_t=3.8MPa, which leads to values of h_{max} equals to 150mm and 400mm for the Hordijk and linear curves respectively. This clearly shows two important aspects of these models. Firstly, the Hordijk relationship is much more restrictive than a linear softening and secondly, element sizes assumed in the author's models were free of this snap-back behaviour (h~50mm). This work does not include cases where $h>h_{max}$, although in such situations, there are three possible alternatives. The first two would be decreasing either the effective tensile strength or the

value of *h*, in order to satisfy the energy balance in the system (Bazant and Oh [80]). Thirdly, the fracture energy could be increased.

Although the strain-stress relationships used in the models (section 3.3) were defined using fracture energy and crack bandwidth concept, which provide a level of objectivity of the results to mesh refinement, two additional comments can be made. Firstly, it is well documented that the predictions of the crack patterns are influenced by the type of mesh discretisation used, where cracks tend to form in the direction of the finite element sides. This "mesh-induced directional bias", which was investigated by authors such as Rots [100], Rots & Blaauwendraad [66] or Rots & Borst [101], can result in stiff predictions or convergence difficulties. This problem can be mitigated by refining the mesh, although as stated by Lie & Zimmerman [102], it cannot be fully overcome.

One last aspect with regards to the crack bandwidth concept, which was raised by Pimentel [73], refers to the implicit assumption of constant strains along the bandwidth. This assumption, which is shown in Figure 3.3, would seem consistent with strain fields found in finite elements with a linear interpolation and not in a quadratic interpolation element. In this other case, regularization techniques based on the non-local theory, in which the strains are assumed to change along the specimen, would seem more consistent than the crack band concept. Although these types of models can provide useful information of the strains at the fracture zone, the size of the elements required would be very small.

3.5.2 Solution procedures for non-linear systems

In order to solve the system of non-linear equations in the NLFEA, a conventional incremental-iterative procedure was applied. For the iterations a traditional Newton-Rapson was generally adopted. An energy norm was used for the converge criteria, with a tolerance value of 1% for the type of solver used, refer to Figure 3.14. The value assumed for the tolerance, which was obtained from Khwaounjoo et al. [103], seemed to be adequate for the cases investigated and the strength of beams analysed was not generally overestimated. On the contrary, divergence occurred in some cases at very low loads (around 30-50% of the ultimate load). These numerical difficulties seemed to be related more to the smeared cracking model and type of failure, rather than to the tolerance value assumed for the norm. This was confirmed by changing the tolerance in some of the analysis performed.

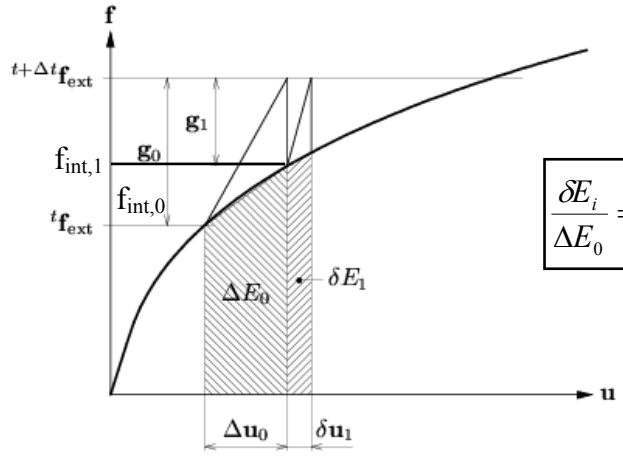

$$\frac{\delta E_i}{\Delta E_0} = \frac{\left|\delta u_i^T \left(f_{\text{int},i+1} + f_{\text{int},i}\right)\right|}{\Delta u_0^T \left(f_{\text{int},1} + f_{\text{int},0}\right)} \leq 0.01$$

Note: Δu (relative displacements), f_{int} (internal forces)

Figure 3.14: Energy norm converge criteria for iteration (adapted from DIANA [71])

As discussed in section 3.5.3, a large concentration of stresses around the edge of the loading plates seems to be responsible for the premature failure in some of the FE models shown in chapters 7 and 8. In other cases, a converged solution was obtained up to loads near the experimental failure load. In general, the total strain models had a more robust behaviour from a numerical perspective, although in some cases a spurious post-peak response was obtained. This is discussed further for each particular model in chapters 5, 7 and 8. In the multi-fix model, on the other hand, the iterative process diverged at loads near the failure load obtained experimentally. This problem has already been reported by Pimentel [73] in similar NLFEA using the multi-fix model. In the shear panels modelled in chapter 4 using plasticity models, this was overcome by changing the type of solver at load steps just before failure from Newton-Rapson to a Constant solver. The Constant solver uses the same stiffness matrix for each iteration, which is estimated from the previous increment. Although this method is very robust, it was not effective for more complex models such as beams, which had a larger number of elements.

Finite element models that included discrete cracking had an even more problematic numerical stability. As discussed in section 3.2.2, the load steps had to be reduced quite considerably when using interface elements. In models with smeared cracking only, the load/displacements increments generally used were around 10% of the ultimate load/displacement, while models with discrete cracking the steps had to be reduced down to 1-2% the ultimate load/displacement. Constant solver provided unrealistic answers in models with interface elements, especially if crack dilatancy models were applied, since the algorithm could not handle the asymmetry in the stiffness matrix.

For the incremental algorithm in the solver, both load and displacement controls were applied. The latter was faster and was generally used in the NLFEA of simply supported beams. Load control, which was applied to the analysis of continuous beams, can also be efficient, especially if an arc-length method is implemented. This algorithm adapts the steps size depending on the results in the current step, allowing to capture snap-back behaviour as good as in displacement control. Therefore, it was not surprising that the load control with arc-length method applied to the simply supported beams resulted in similar answers as using a displacement control. Finally, adaptive loading was also investigated for the analysis of some of the FE models, which faced numerical difficulties. This analysis was helpful in order to estimate a load step size, which balanced accuracy and numerical stability. However it did not overcome the numerical difficulties in those models with a high concentration of stresses near the edges of the loading plates. This concern is further discussed in next section.

3.5.3 Modelling of loading plates

Boundary considerations can have a significant effect on the numerical performance of FE models. Load can be applied in testing by means of different arrangements of loading platens, rollers or rockets. Depending on this arrangement vertical/horizontal displacements and rotation can be restrained at these points. In addition, load can be applied directly to the specimen as an edge load (point load in plane stress problems) or as a pressure load (bearing plate). However, it is frequent to see in FE modelling that loads are assumed to be point loads irrespective of the type of loading plate used. This assumption can be questionable in some cases, such as short span beams, where the size of the bearing plates can have a significant influence in the shear behaviour (see chapter 7). According to these considerations, it seems surprising the general lack of detailed information in the literature concerning the modelling of loading points in FEA.

A clear example of the importance of modelling loading plates accurately was seen in the international shear panel test contest (Collins et al. [104]) in which the winner entry was Dr. Vladimir Cervenska. As recognized by Cervenska (Walraven [105]), one of the key aspect in order to obtain accurate predictions using NLFEA, was to include in the model aspects related to how the load was transferred from the complex set of hydraulic jacks into to the panel.

In the NLFEA of beam tests carried in this work, loading plates were included in the FE mesh, assuming a perfect nodal connectivity (Figure 3.15) with the same thickness as the platens used in the test. In load control, a uniform pressure load was applied to the plate, which seemed consistent with the test arrangement shown in chapter 6. Similar results were obtained using displacement control. An equal value of the vertical displacement was forced to all the nodes at the top of the plate when using displacement control. However, for the relatively thick plates used in the analysis similar results were obtained by imposing vertical displacement at the central node only, see Figure 3.15. b (top). At the supports, pin rotation allowed by rollers was simulated by constraining vertical displacements at the central node of the plate, as shown in Figure 3.15.a.

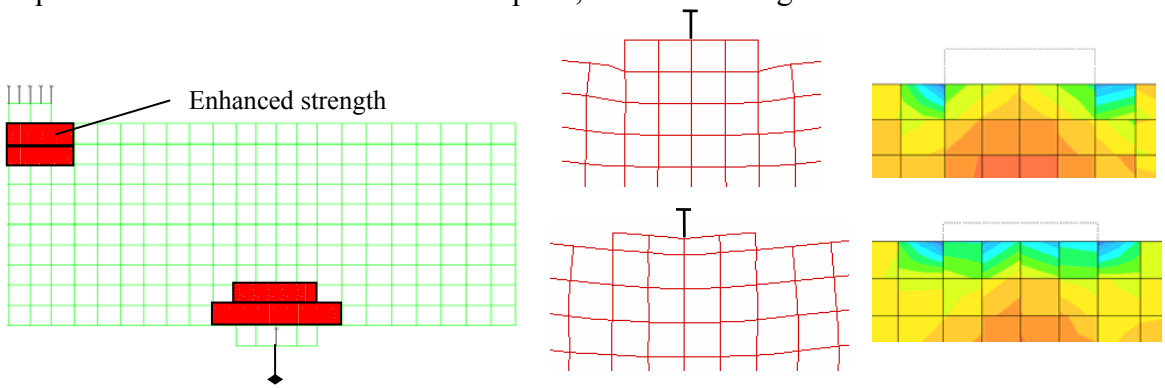

a) Pressure load b) Point load: (top) normal; (bottom) thin plate

Figure 3.15: Loading plates considerations in NLFEA; a) Pressure load; b) Point load (normal and thin loading plates)

Although this approach for modelling the loading plates seemed consistent with the experimental setup, a large concentration of stresses was generally obtained at the edge of the loading plate as shown in Figure 3.15.b (top). As discussed in previous section, this concentration of stresses resulted in a premature failure in some of FE models at loads of around 30-50% the ultimate failure load. In order to overcome this problem, the concrete strength of the elements in this region was increased (Figure 3.15.a). Although this approach was practical to assess deflection, strains, crack patterns and relative displacements at loads near failure, the ultimate load predicted was highly dependent on the values assumed for the enhanced concrete strength of these elements.

This concrete strength enhancement in elements near the loading plate could be justified based on the lateral confinement provided by the steel plates, which is not taken into account in the NLFEA (Vecchio & Shim [98]). However, this confinement seems rather difficult to consider using simple two-dimensional models; more refined 3D NLFEA

would be required. Alternatively, in the two-dimensional FE models developed by Vecchio & Shim [98], a small amount of "out-of-plane reinforcement" (ρ_z=5–2.5%) was introduced into the elements near the loading plate, similar to those shown in Figure 3.15.a. According to Vecchio & Shim [98], this allowed for some enhancement of both strength and most importantly ductility of these elements. Other alternatives, such as introducing an interface layer between the load plate and the concrete, would seem problematic since the friction at the interface would have to be estimated.

The local high stresses under the loading platen predicted by the FEA are influenced by the flexural stiffness of the plate. As shown in Figure 3.15.b, decreasing the thickness of the loading plate while concentrating the load to the central node, results in a more uniform stress distribution under the plate. In addition, the numerical sensitivity to this localization of stresses seemed to be different depending on the material model assumed for the concrete in the NLFEA. From the author's experience using Total Strain and Multi-fix smeared crack models, the latter tended to be more sensitive to the stress concentration around the edge of the plate than Total Strain models. The situation worsened when discrete cracks, which extended to the edge of the load plate, were introduced into the mesh.

To the author's knowledge up to date, experimental evidence is not available from beam tests regarding stress development at different points under loading plates. The NLFEA seem to suggest that stresses tend to localized at the edges while strut-and-tie modelling assume that the stresses are constant. In the beam tests carried by the author, cracks that form near the edge of the loading plates (see Figure 3.16) could have indicated a certain level of stress concentration in this region, although experimental data is not available.

Figure 3.16: Cracks at the edge of the loading plate observed in short span beam (Beams A, refer to section 6.3)

3.6 Conclusions

Several alternative approaches are available to model cracking in reinforced concrete structures using NLFEA. The most commonly used smeared and discrete crack models in NLFEA are reviewed in this chapter. Smeared cracking models offer a simpler approach than discrete crack models since mesh modifications are not required. Rotating crack models, such as the MCFT, can provide accurate predictions for large number of cases. However, the co-axiality principle assumed between strains and stresses does not apply to other cases where crack slip and shear transfer along the cracks is predominant (Vecchio [29], Maekawa [52]). In such cases, fixed crack models might seem more suitable, although shear retention factors, which are uncertain to evaluate, must be applied. Hybrid solutions between rotating and fixed crack models, such the multi-directional fixed crack model (Rots et al. [68]), can partially overcome these difficulties. Although the choice of crack inclination (rotating, fixed or hybrid) assumed in the NLFEA can have an influence on the accuracy of the predictions, more important to this seems to select consistent values for the parameters used for each model. This is the main shortcoming of NLFEA.

From a comprehensive study of the different models available, two smeared cracking models were finally adopted in this work; Total Strain (rotating and fixed crack) and Multi-directional fixed crack models. Tension softening and compression strain-stress relationships used in the FE models are given in terms of the fracture energy and crack bandwidth in order to guarantee mesh-independent results. Fracture energy in tension (G_f) was estimated from MC90 formulas, while for compression, an estimated value of $100G_f$ was assumed. For the descending branch in tension, either linear and Hordijk curves were used, while in compression, parabolic relationship proposed by Feenstra [82] was adopted. Compression softening due to transverse strains was taken into account in the total strain models using Vecchio & Collins [25] softening curve. This softening relationship was not applied in the multi-fix model, instead the concrete strength was decreased by a constant factor. The use of the softening curve [25] in the total strain model with a fixed crack is questionable since this relationship was originally derived for rotating crack models, where the slip is completely ignored. The performance of these models is further discussed for the analysis of shear panels and beam tests in chapters 5, 7 and 8.

Two discrete cracking models were reviewed. First model (Discrete Crack Model) assume both constant shear stiffness after cracking and uncoupled normal-shear stresses.

The second model included crack dilatancy relationships with a variable shear stiffness and normal/shear stresses interdependency. Although the later assumptions are more realistic for aggregate interlock behaviour (see chapter 4), comparable results can be obtained using both models, if proper calibration of the aggregate interlock stiffness is provided. Severe numerical instabilities can be obtained using crack dilatancy models, due to asymmetry in the stiffness matrix (Feenstra et al. [53]). Numerical solvers such as the "constant stiffness" algorithm seemed to be inefficient to handle these situations.

Steel reinforcement is usually modelled in FEA using discrete or smeared (grid) embedded elements. The NLFEA of a continuous beam in which the stirrup spacing was increased up to 300mm, showed that numerical predictions were very similar using either type of elements. Reinforcement elements crossing discrete cracks require additional considerations regarding normal and shear stiffness introduced to the interface mother element. Local phenomena related to bond-slip, dowel action or secondary diagonal struts can be difficult to implement in FE modelling. It has been shown that the simplified approach assumed in DIANA using normal values of the free-length parameter can lead to extremely stiff predictions of the dowel action. If using this method, the shear stiffness assigned to the interface elements should be reduced in order to account for the excess in dowel stiffness assumed.

Ultimately, numerical predictions from NLFEA can be influenced by other considerations such as mesh generation, numerical solvers used or modelling of the loading plates. Although these issues are not within the main scope of this work, the consequences of the assumptions made regarding these points were investigated. The numerical difficulties faced in the NLFEA of the shear critical reinforced concrete beams were expected, due to their brittle behaviour, especially for high-strength concretes and large depths. Moreover, the concentration of stresses around the elements near the loading plates resulted in a premature failure in some of the FE models shown in chapters 7 and 8. In order to overcome this problem, the concrete strength of these elements was enhanced. The selection of a proper numerical solver and incremental-iterative algorithm is also critical in obtaining converged solutions. Even so, in many of the NLFEA this was not possible and the iterative process diverged at loads near failure, especially when using the multi-fix smeared crack model. These numerical difficulties using smeared and discrete cracking models are well documented in the literature and clearly show the need of performing hand calculations in addition to NLFEA.

CHAPTER 4 – Push-off Tests

4.1 Introduction

Aggregate interlock at concrete cracks is a complex phenomenon since it involves several shear resisting mechanisms in which normal and shear stresses interact. As the crack slides, it tends to open due to overriding of the aggregates particles against each other, which is known as “crack dilatancy”. Normal stresses are introduced at the crack face, if the widening of the crack is constrained by embedded or external reinforcement. In addition, the shear stiffness decreases as the crack gets wider due to contact lost between crack faces.

Although the fundamentals of aggregate interlock may seem straightforward, the analytical solutions to model this behaviour are complex and often produce significant discrepancies with experimental results. As discussed in chapters 2 and 3, this is due to the large number of secondary aspects involved, which may not be considered in the model; typical examples are dowel action, localized stresses around embedded bars, tension stiffening of the concrete, normal stiffness introduced by the reinforcement or uncertainties in the crack roughness. Moreover, cracks that form in real concrete structures have additional uncertainties related to variable conditions of loading, creep and shrinkage, which introduce complex stress fields that are difficult to assess. Therefore, the attempt of estimating the normal and shear stresses directly at cracks that form in reinforced concrete structures seems unrealistic.

In order to have a better understanding of the stresses transmitted at the crack, a common approach is to isolate the crack in a simple test configuration so that a good control of the variables mentioned above is achieved. Push-off tests, such as the one shown in Figure

4.1, is a widely recognized procedure for assessing shear and normal stresses at reinforced cracks. In general, a push-off test consists of two stages; firstly, the specimen is pre-cracked and then the load is applied vertically (Figure 4.1) so that the entire shear force applied is transmitted along the crack plane.

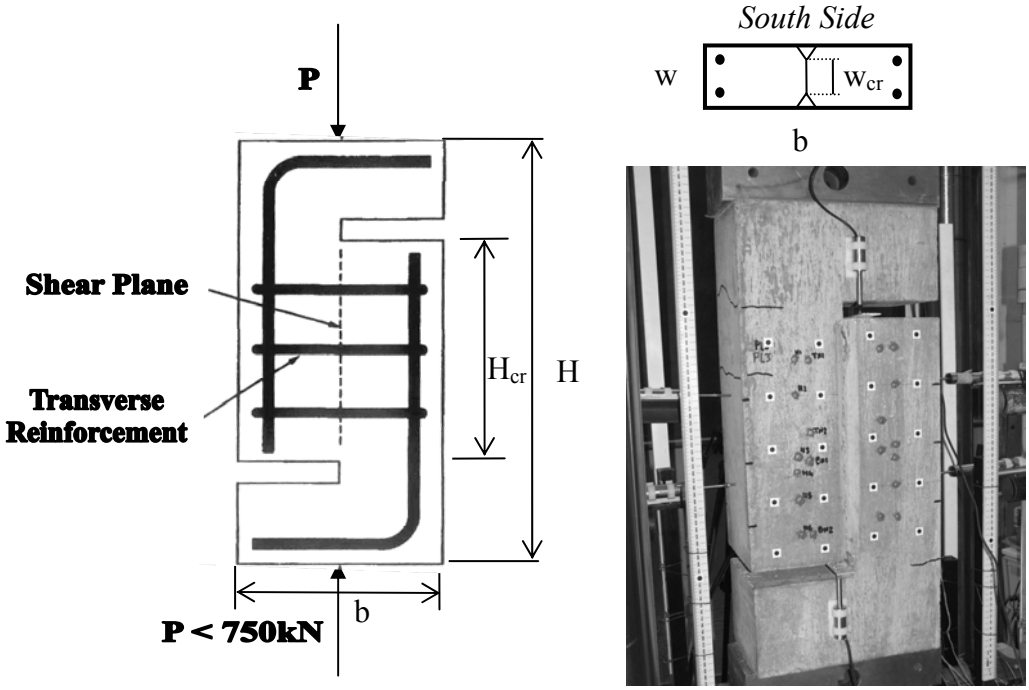

Figure 4.1: *Left*- Typical push-off test arrangement; *Right*- Test carried by the author

Many of the analytical models described in chapter 2, were developed using experimental data obtained from push-off tests similar to the one shown in Figure 4.1. Early experimental work by Mattock et al. [106], Walraven & Reinhardt [46] or Hamadi [107] was carried to validate shear friction equations, which were provided in the codes to design concrete joints or interfaces.

This chapter describes the experimental results of seven push-off tests carried out by the author. These tests were required in order to assess the magnitude of the normal and shear stresses carried at cracks of specimens where the aggregate had fractured in comparison with others where the crack went round the aggregate. In addition, the results obtained for shear stresses are interpolated for different values of crack opening and slip, in order to extrapolate the results to cracks measured in beam tests, which are described in chapters 6. Lastly, the experimental data is compared with different analytical models, which are used in chapters 7 and 8, to validate the values of the empirical parameters assumed in the models. These figures are also compared with traditional values recommended by the codes.

4.2 Experimental results

4.2.1 General aspects

A total of seven push-off tests were carried out by the author using the same concrete as in beams B described in chapter 6. The specimens were cast in two groups; one group made with limestone aggregate concrete (PL2, PL2b, PL3 and PL4) and another group made with normal gravel aggregate (PG2, PG3 and PG4). Similarly as in beams B, the limestone aggregate fractured completely at the crack unlike the gravel, where the crack went round the aggregate. The aim was to investigate the relationship between aggregate interlock and relative crack displacements (opening and sliding) in order to extrapolate the results to the beam tests. The crack area ($H_{cr} \times w_{cr}$, see Figure 4.1) was kept similar to that in beams A and B in order to correlate the results with both types of tests. In addition, the size of the specimens was designed to be similar to those used by other authors, as shown in Table 4.1, in order to facilitate the comparison between tests results.

[mm]	**Mattock** Ref. [106]	**Hamadi** Ref. [107]	**Walraven** Ref. [46]	**This work**
H	660.4	700	600	700
H_{cr}	304.8	350	300	350
b	355.6	300	400	300
w	177.8	150	120	165
w_{cr}	177.8	120	120	135

Note: For notation refer to Figure 4.1; Area of the crack = $H_{cr} \times w_{cr}$

Table 4.1: Specimen dimensions in push-off tests carried by different researchers

As explained in previous section, the specimens were pre-cracked by applying a lateral edge load. Once the crack had formed, the specimen was loaded vertically until failure along the crack plane (see Figure 4.1). The peak load was reached without much damage of the specimen; hence the specimen was un-loaded and re-loaded two more times. The two additional cycles provided useful information about the influence of changing the initial crack width on the aggregate interlock action.

The stirrups crossing the crack were embedded in the concrete in all specimens. Stirrups T8 were used, which had a yielding strength of 550MPa; see section 6.2.1 for further details. Specimens were labelled according to the number of stirrups crossing the crack plane as shown in Figure 4.2. The reinforcement layout provided showed to be sufficient to avoid local failure of the corbel in all specimens except for PG4. This undesired behaviour of specimen PG4 was due to the strength obtained in mix 4 used in specimens

PG, which was significantly lower to the concrete strength assumed in the design. Fortunately, failure of the corbel did not occur for the rest of specimens PG and so only data from PG4 was neglected. A replicate of specimen PL2 was made in order to test the loading rig and testing procedure; this specimen is denoted as PL2b.

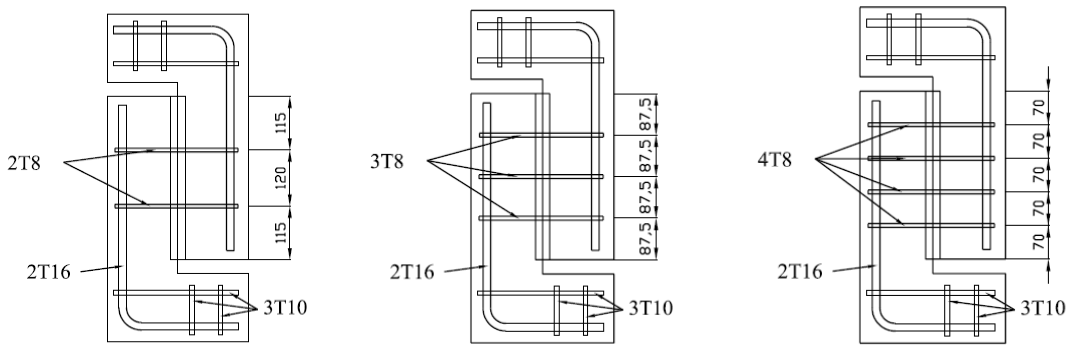

a) PG2, PL2 (ρ_v =0.42%) b) PG3, PL3 (ρ_v =0.64%) c) PG4, PL4 (ρ_v =0.85%)

Note: f_c' (PL)=53.11MPa and f_c'(PG)=31.7MPa; refer to mixes 3 and 4 (section 6.2.2)
Reinforcement steel: f_y(T8)=550MPa and f_y(T16)=600MPa

Figure 4.2: Reinforcement layout in push-off specimens (dimensions in mm)

The load was applied at the top through a loading plate and a spherical seating at the centre (Figure 4.3), which allowed for free rotation of the top half. A layer of grout was provided between the specimen and bearing plates. The lateral displacements were released by the use of mini-rollers placed between the plates at the support (Figure 4.3). The test was carried in displacement control with increment of 0.1mm for the first cycle and 0.2mm for the second and third cycles. The load rate was 0.1mm/min.

Figure 4.3: *Left* – Top loading plates and spherical seating; *Right* – Release of horizontal displacements at the bottom support by using mini-rollers

Splitting (pre-cracking) of specimens

In order to generate the crack along the plane of interest, the specimens were rested on one side and loaded with an edged load by using a steel wedge as shown in Figure 4.4. A spherical seating was used at the top plate to distribute the load. The initial crack widths obtained were around 0.1-0.3mm, as shown in Table 4.2 with small variations along the crack plane. The worst deviations in w_0 were found for specimens with lesser number of stirrups as shown in Table 4.2. These variations in the readings were found mainly between faces of the specimen and not between top and bottom of the crack plane. Nevertheless, this slight asymmetry in the crack plane tended to decrease as the specimen was loaded in the vertical direction. Soon after the vertical load was applied, readings of the crack opening at both sides became very similar.

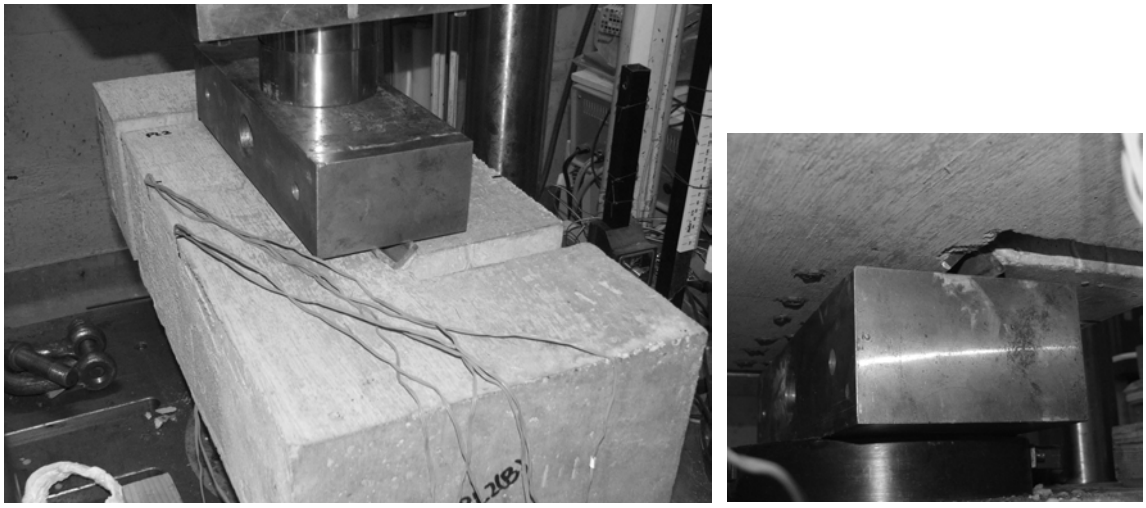

Figure 4.4: Pre-cracking of push-off specimens (*Left* – Top view; *Right* – Bottom view)

4.2.2 Manufacture and curing

The specimens were cast in wood moulds simultaneously to beams B, which are described in chapter 6. The concrete used for specimens PL and PG relate to mixes 3 and 4 respectively, which are fully described in section 6.2.2. The concrete was poured in the direction perpendicular to the crack plane in three batches to assure similar vibration conditions of the concrete near the crack plane. Good compaction of the concrete was achieved by casting the specimens on a vibrating table. Once the top surface was levelled, the specimens were covered with polythene sheets until stripping the moulds two days after casting. The curing conditions for the push-off specimens and their respective control cubes and cylinders were identical as beams B, refer to section 6.5.2.

4.2.3 Instrumentation

The load and total deflection were monitored by the load cell and displacement transducer incorporated in the loading rig. Six additional LVTDs displacement transducers (#1 to #6) were placed at different location (see Figure 4.5) to assess the general response of the specimen.

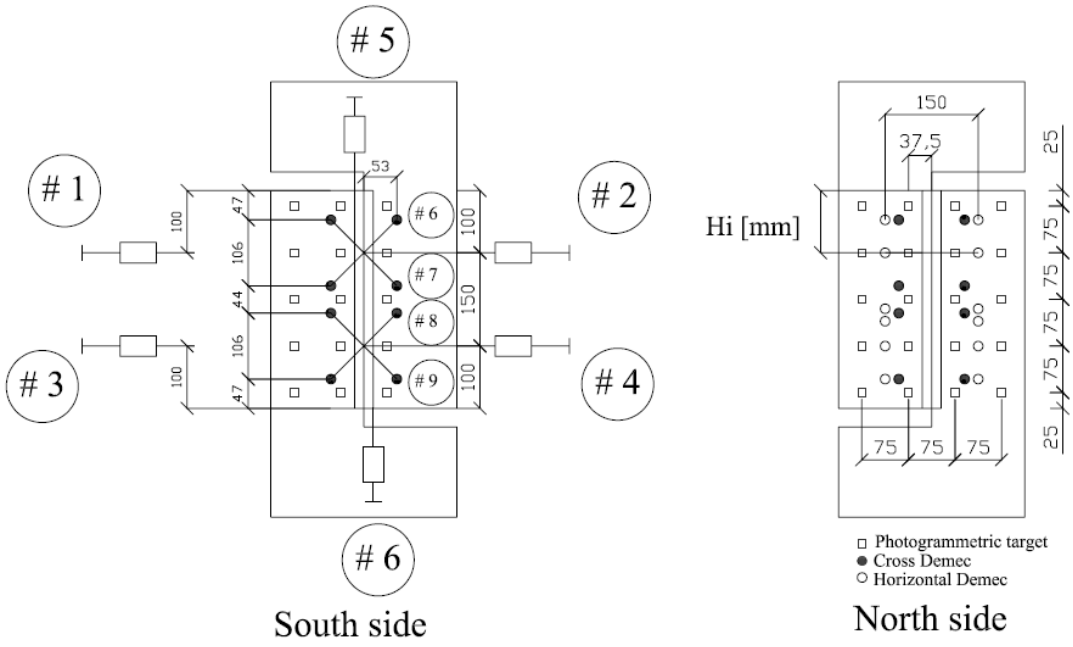

Figure 4.5: Instrumentation used in push-off tests

Digital photogrammetric surveying

Alternatively to traditional displacement measurements taken by LVTDs, digital photogrammetric surveying was carried out. This relatively new technique, which is based on image processing, allows to obtain information of displacements in the x-y directions at several points (targets) of the specimen. These readings were used to obtain the crack opening and sliding at four different heights of the crack. The computer software required to analyse the digital photographs was developed and calibrated by McCarthy & Tsang [108], from the Department of Environmental and Civil Engineering at Imperial College London. The programme was written in the LabVIEW platform. The results were compared with LVTD, Demec and strain gauge readings.

Digital photogrammetry is a recent method, although it has been applied in the past for testing beams, see Jauregui et al. [109], Ortlepp et al. [110] or Lee & Al-Mahaidi [111]. The level of accuracy depends on many factors, as explained by McCarthy and Tsang [108], which are related with the system setup: resolution, field of view, working distance, sensor and depth of field. Other factors such as contrast, perspective and

distortion optical effects can introduce errors in the image processing analysis. The maximum errors observed in this work using digital photogrammetry were around 0.03mm. Although this tolerance might be acceptable for displacements, it is not accurate enough to estimate strains.

The primary function of image processing is to track given patterns (targets) and assign them coordinates relative to fixed reference points. The targets consisted of dark circles of 7mm diameter, which were printed on a white background (13mm square) in order to provide sufficient contrast. For each camera it was necessary to provide four reference targets, which were fixed to plastic rulers located at the left and right ends of the picture, see Figure 4.1. The horizontal and vertical distances between these reference points were around 450mm and 370mm respectively. The moving targets were arranged in an orthogonal grid with 75mm spacing, as shown in Figure 4.5, which was placed at both north and south sides of the specimen. Two digital cameras were used, one at each side, in order to measure the crack opening and sliding at four different levels of the crack for each side. Digital pictures were taken manually at each load step. Adequate lighting was provided by two halogen lamps and the working distance between the camera and the specimen was around 500mm for both cameras.

Crack opening and sliding measurements

Several types of crosses were used (Figure 4.5) to measure the crack opening and sliding at different heights of the specimen. In this work three different monitoring systems were used in the cross; crosses of demec discs, LVTDs and photogrammetric targets. The gauge length of the Demec and LVTDs was 150mm, while the grid of photogrammetric targets was 75×75mm.

In order to calculate the crack opening and sliding, independently of the system used, cross readings were taken between two pair of points, which form a cross so that one point of each pair is on the same side of the crack (see Figure 4.6). This simple procedure has been applied in the past by authors such as Hamadi [107], which derived the following equations in order to obtain the crack opening (Δh) and sliding (Δv) from the cross readings.

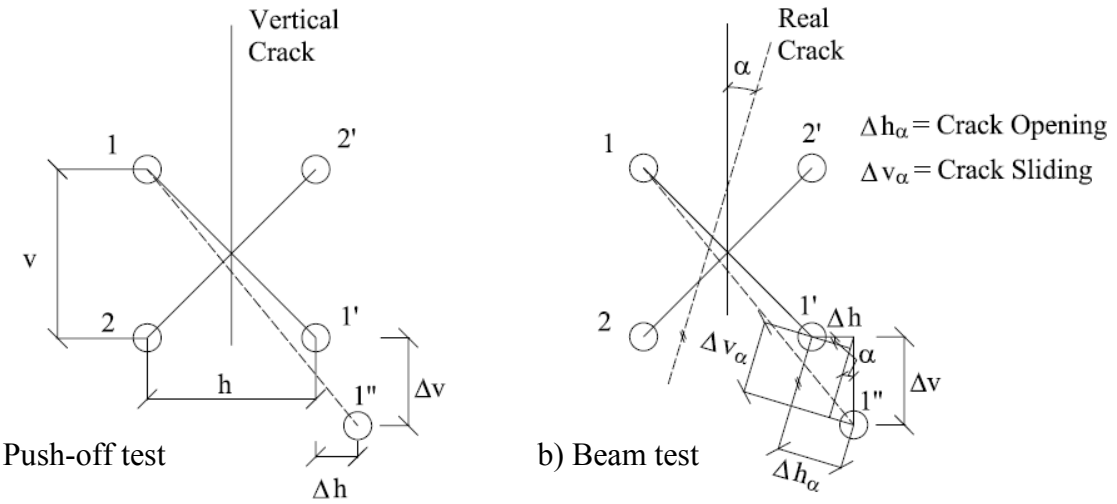

Figure 4.6: Obtaining relative crack displacements through cross Demec/LVTDs readings

From the geometry of the cross shown in Figure 4.6, the length between points 1-1' (l) can be written in equation (4.1). After deformation, points 1' and 2' move to 1'' and 2'' respectively. The length between 1-1'' can be written as in equation (4.2). Squaring both sides of equations (4.1) and (4.2) and subtracting the second one from the first one leads to equation (4.3). In the last step, second order terms are neglected. In the same manner for points 2-2', within a distance l', equation (4.4) can be obtained.

$$l = \sqrt{h^2 + v^2} \quad \ldots (4.1)$$

$$l + \Delta l = \sqrt{(h + \Delta h)^2 + (v + \Delta v)^2} \quad \ldots (4.2)$$

$$2l\Delta l = 2h\Delta h + 2v\Delta v \quad \ldots (4.3)$$

$$2l'\Delta l' = 2h\Delta h - 2v\Delta v \quad \ldots (4.4)$$

Finally, from equations (4.3) and (4.4) and assuming $l=l'$, the sliding and opening of the vertical crack can be obtained, see equation (4.5) and (4.6) respectively. In this work the crack opening and sliding are usually referred to as w and s respectively. However for equations (4.1) to (4.6), Δv and Δh have been used for consistency with Hamadi's notation.

$$\Delta v = \frac{l}{2v}(\Delta l - \Delta l') \quad \ldots (4.5)$$

$$\Delta h = \frac{l}{2v}(\Delta l + \Delta l') \quad \ldots (4.6)$$

In the push-off tests, the cross nails were placed with points 1 and 2 aligned vertically, as shown in Figure 4.6. However, shear cracks that were measured in beam tests presented

in chapter 6 were not vertical. In this case, cracks were generally oriented 45º with respect the horizontal line and therefore the cross was placed so that the line defined by 1-1' was vertical and line 2-2' horizontal. In cases where the crack orientation was exactly 45º, equations derived by Hamadi (4.5 and 4.6) still applied. However in many other cases where the crack was flatter than 45º, equations (4.5 and 4.6) were modified to take into account the deviation angle (α) with respect the 45º plane, refer to Figure 4.6.b. Equations (4.7) and (4.8) allow to obtain the crack opening (Δh_α) and sliding (Δv_α) along the actual plane of the crack. The deviation angle α is considered positive in the clockwise direction, in other words if the crack is flatter than 45º and 1-1' is vertical.

$$\Delta v_\alpha = \cos\alpha.\Delta v - \sin\alpha.\Delta h \quad \ldots (4.7)$$

$$\Delta h_\alpha = \sin\alpha.\Delta v + \cos\alpha.\Delta h \quad \ldots (4.8)$$

Only demec readings could be used to estimate the initial crack displacements due to the type of loading required for pre-cracking the specimen (see Figure 4.3). Once the specimen was uplifted in its final position before testing, demec discs on the south side were removed and replaced by nails, which were needed for the cross of LVTDs (transducers #6 to #9 in Figure 4.5). On the north side, the Demec discs were kept and used for taking readings during the test. Additional discs had been previously attached on the north side at six different heights (H_i), as shown in Figure 4.5, to obtain horizontal strain readings at the several levels, including at the reinforcement. These readings were compared with strain gauge readings described in next section

Strain gauges

Two strain gauges were placed in one leg (top and bottom) on each stirrup where the crack crossed the stirrup, see section 2.4.4. Two extra strain gauges were placed in specimens P2 and P3, at top and bottom of the stirrup leg, far from the crack plane. The aim was to assess the distribution of strains along the stirrups. Lastly, two additional strain gauges were attached in PL2, on the other leg of one of the stirrups, in order to study possible asymmetric behaviour between north and south sides.

4.2.4 Results

Summary of experimental results

Table 4.2 summarizes the experimental results obtained for the seven push-off tests. Results are shown for specimen PG4, although premature failure occurred at the corbel in this case, hence these results were neglected. The crack opening and sliding at the peak load (w_{peak}, s_{peak}) are given in Table 4.2 for each cycle; measurements were taken from the LVTD crosses placed on the south face. On the other hand, the initial crack width (w_0) was obtained from averaging readings from the four Demec crosses placed on the both sides of the specimen; the maximum standard deviation (S.D) obtained was 0.14mm (Table 4.2). For the second and third load cycles, the initial crack width was estimated from the two crosses placed on the north side.

Specimen	Cycle	w_0 [mm]	S.D [mm]	τ_{peak} [MPa]	w_{peak} [mm]	s_{peak} [mm]
PG2	**1**	0.273	0.148	3.67	0.65	0.93
	2	0.714	0.108	3.46	0.79	1.46
	3	0.877	0.043	3.31	0.92	2.02
PG3	**1**	0.081	0.039	4.91	0.51	0.60
	2	0.395	0.082	4.72	0.68	1.00
	3	0.628	0.080	4.45	0.92	1.64
PG4^{+}	**1**	0.237	0.088	5.14^{+}	0.47^{+}	0.46^{+}
	2	0.359	0.060	4.70^{+}	0.54^{+}	0.62^{+}
	3	0.386	0.232	4.09^{+}	0.65^{+}	0.82^{+}
PL2	**1**	0.132	0.051	4.85	0.36	0,29
	2	0.296	0.043	4.52	0.48	0.57
	3	0.705	0.091	3.85	0.93	1.61
PL2b	**1**	0.093	0.068	5.82	0.24	0.20
	2	0.491	0.098	4.76	0.57	0.67
	3	0.711	0.146	4.48	0.75	0.98
	4	0.804	0.169	4.40	0.85	1.15
PL3	**1**	0.123	0.043	5.55	0.37	0.40
	2	0.380	0.044	5.17	0.47	0.71
	3	0.545	0.066	4.76	0.61	1.16
PL4	**1**	0.120	0.024	7.10	0.38	0.50
	2	0.418	0.021	6.63	0.52	0.89
	3	0.766	0.090	6.03	0.85	1.77

Note: $^{+}$Specimen PG4 had a premature local failure, results are not taken into consideration

Table 4.2: Summary of push-off test results

Relative crack displacements

Figure 4.7 shows the crack opening and sliding history of the specimens during the three load cycles; results are shown for the top LVTD cross. The crack path (ΔW-ΔS) was very similar for gravel and limestone specimens with an average crack opening-sliding ratio ($\delta w/\delta s$) for the first two load cycles of around 0.5. These results are consistent with Walraven & Reinhardt's [46] tests using normal gravel aggregate. In addition, the crack dilatancy formula suggested in MC90 (w=0.6.$s^{2/3}$) is in excellent agreement with experimental data from PG and PL specimens, as shown in Figure 4.7. According to this analytical expression, the $\delta w/\delta s$ ratio is only dependent on the crack sliding; crack slips of 0.1, 0.5 and 4mm relate to $\delta w/\delta s$ ratios of 0.86, 0.5 and 0.25 respectively.

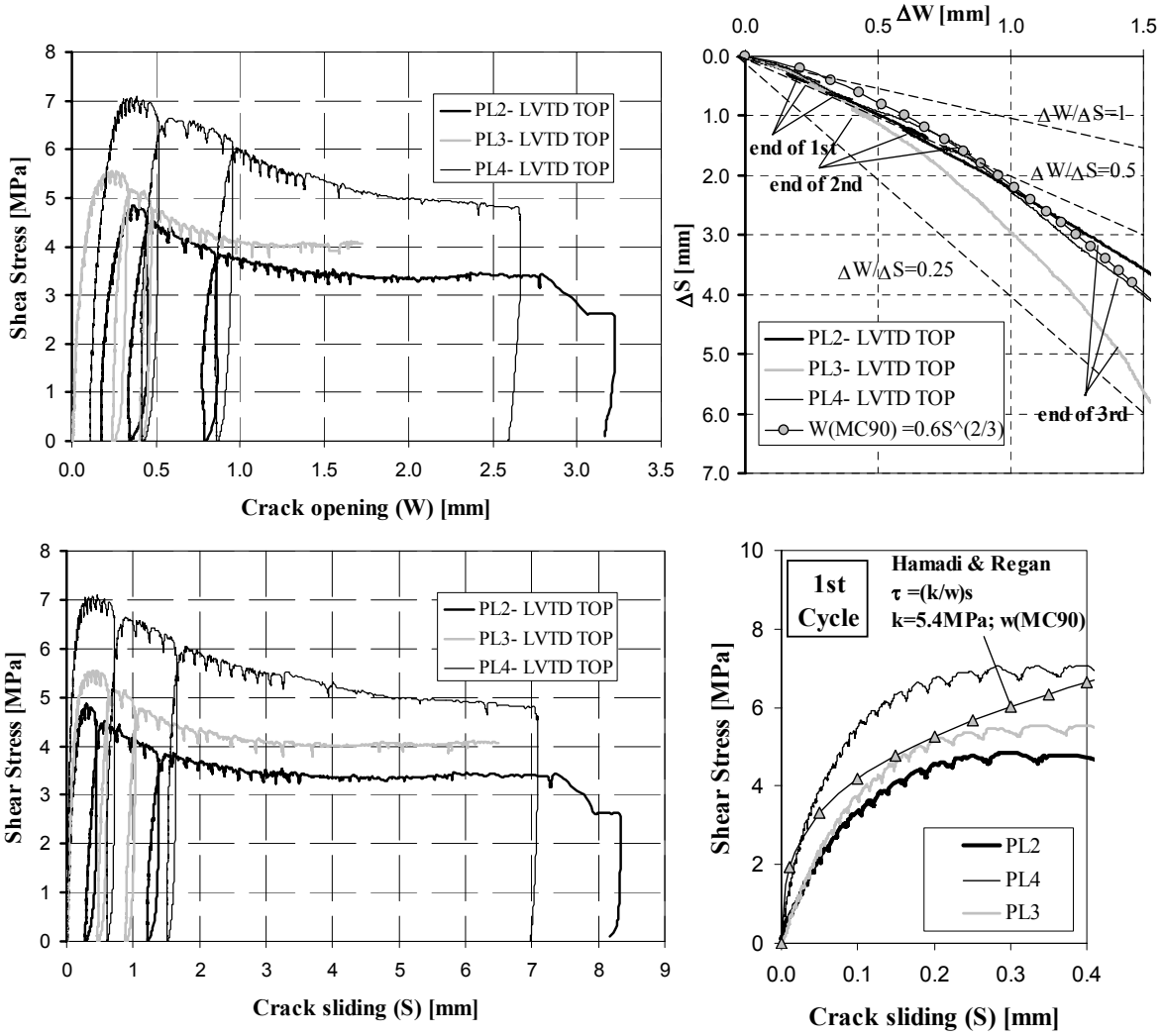

Note: for crack path diagram (ΔW-ΔS) the initial crack width is not considered

Figure 4.7: Relative crack displacements and shear stresses in push-off tests

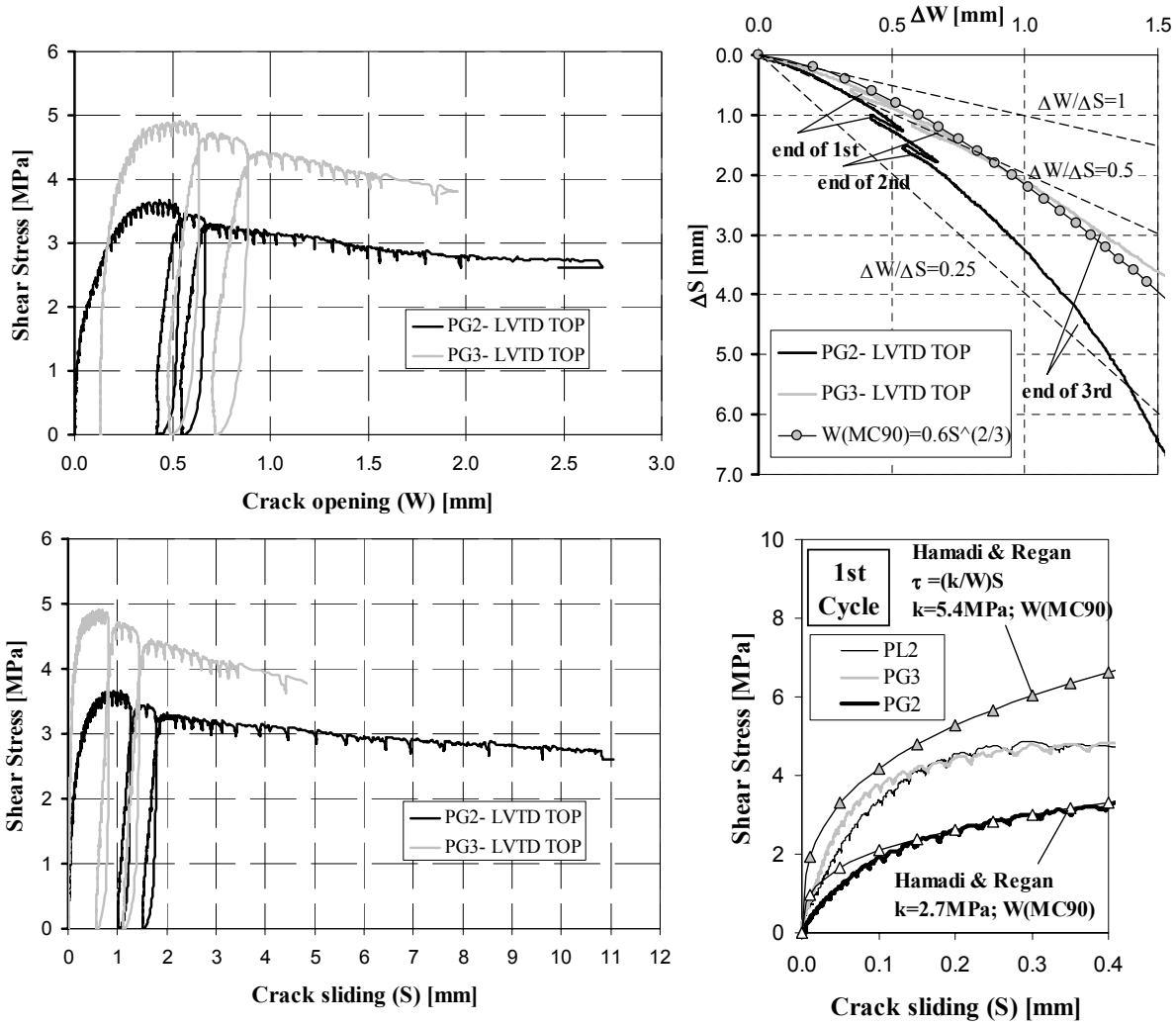

Note: for crack path diagram (ΔW-ΔS) the initial crack width is not considered

Figure 4.7 (Cont.): Relative crack displacements in push-off tests

The relative crack displacements required to obtain the maximum shear stress were larger for the gravel specimens than for the limestone ones, which had a more brittle behaviour. An interesting aspect that can be seen in Figure 4.7 is the post-peak behaviour of the specimens. In the tests, once the maximum value of the shear stress was reached, the load started decreasing down to around 70% of the peak value at around 7mm slip. This reduction was similar for both PG and PL tests. The peak values obtained at the different cycles followed the same load curve, similarly as in Walraven & Reinhardt's [46] tests, in which the time interval between cycles was as long as months.

Lastly, the shear stiffness at the crack during the first load cycle was similar for specimens PL2, PL3 and PG3, as shown in Figure 4.7. The shear-slip response was in good agreement with Hamadi & Regan's model (see section 2.5.2) using k=5.4N/mm^2 and w from MC90 formula. As shown in Figure 4.7, specimens PL4 and PG2 had different stiffness compared to the remaining specimens. The lower stiffness observed in

PG2 was probably due to the larger initial crack width obtained, see Table 4.2. However, the stiff response of specimen PL4 could not be explained by lower values of w_0. Hence it is questionable whether this was due to dowel action or influence of normal stresses in the shear sfiffness for highly reinforced cracks.

Crack opening and sliding variations along the height of the crack

In general, readings obtained from the LVTD, Demec and photogrammetric crosses had an excellent agreement with each other as shown in Figure 4.8. Only in particular cases, such as south face of specimen PL2 (see Figure 4.8), photogrammetric readings presented some oscillations; readings taken on the other side of the specimen did not presented such oscillations. Two important aspects were observed from these measurements. Firstly, the crack opening and sliding were fairly constant along the crack. Secondly, the difference in initial crack widths between north and south sides, which was obtained in the pre-cracking of the specimen, was mitigated during loading so that near failure these readings were almost equal.

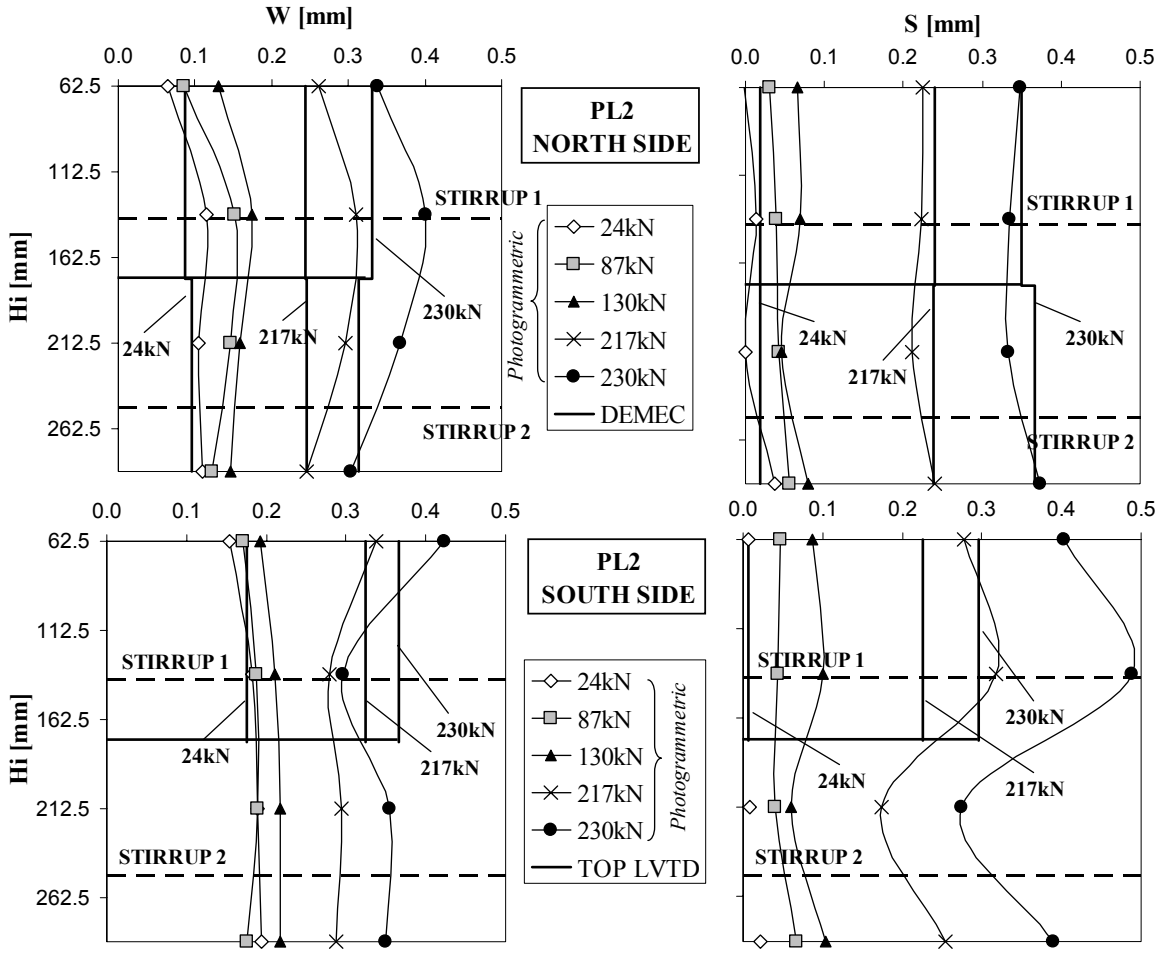

Note: bottom LVTD was faulty; Initial crack widths at both sides were estimated from demec readings

Figure 4.8: Crack opening and sliding measured at different heights (specimen PL2)

Global deflections and post-failure behaviour of specimens

As shown in previous section, both halves of the push-off specimen had a relative displacement with respect to each other due to opening and sliding at the critical crack. In addition, both halves had a joined global displacement due to bending of the corbels, as shown in Figure 4.9; measurements were taken from side transducers (#1-4) and photogrammetric targets (see Figure 4.5). Near failure, sliding at the crack became predominant and the overall rotation of the specimen due to bending of the corbels remained constant, which corresponds to sector A-B in Figure 4.9 (left).

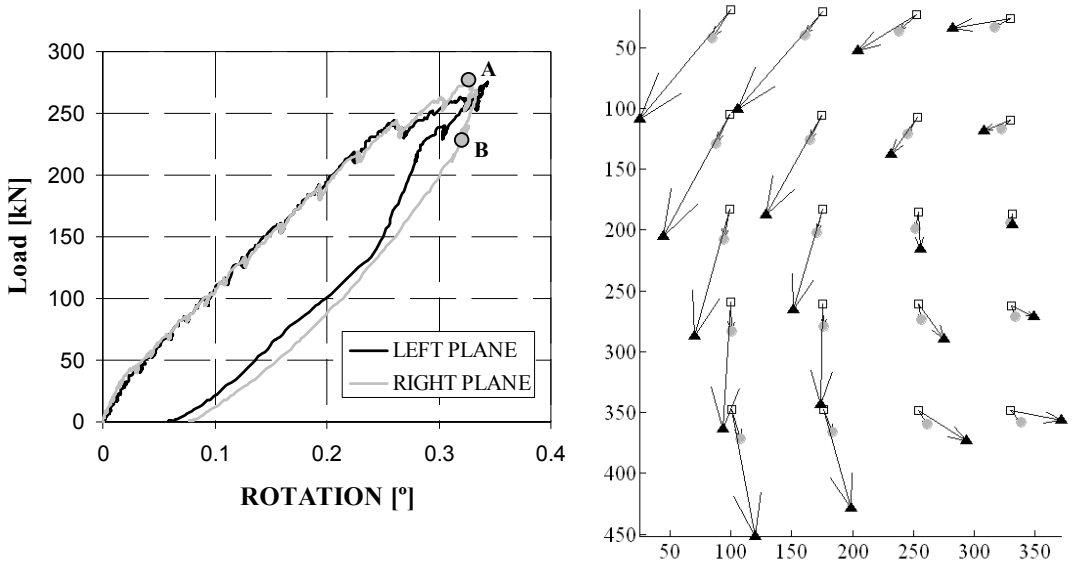

Note: rotation obtained from LVTDs #1-4, refer to Figure 4.5

Figure 4.9: Kinematics of specimen PL2b. *Left*- rotation of specimen; *Right*- global displacements (squares- 0kN, circles- 70kN, triangles- 250kN between A and B)

During the tests, only minor cracking occurred at the corbels. These small flexural cracks formed at around 100kN at symmetrical points as shown in Figure 4.1 (right). The width of these cracks was constant during the test and had no influence on the results, except in specimen PG4, where they became critical.

In the last cycle, specimens were subjected to very large crack displacements. The crack sliding was around 7 to 10mm. The type of failure obtained in this cycle was different for each specimen. In PL2 at a 6.7mm sliding, one of the stirrups fractured. On the other hand, spalling of the concrete cover around the crack occurred in specimen PG2. The concrete cover spalled out at the top or bottom of the strut in the limestone specimens PL3 and PL4 for crack slidings greater than 6mm.

Strains in stirrups

According to Demec and strain gauge readings at the level of the reinforcement shown in Figure 4.10, stirrups started to yield at the end of the first load cycle, when the crack opening was about 0.4mm (Table 4.2). In general Demec readings were similar to each other and had a good correlation with strain gauge data, which provide slightly larger strains. Strain gauges readings of the top stirrup in specimens PL2 and PL3 were significantly large, which could have been due to flexure at the corbel.

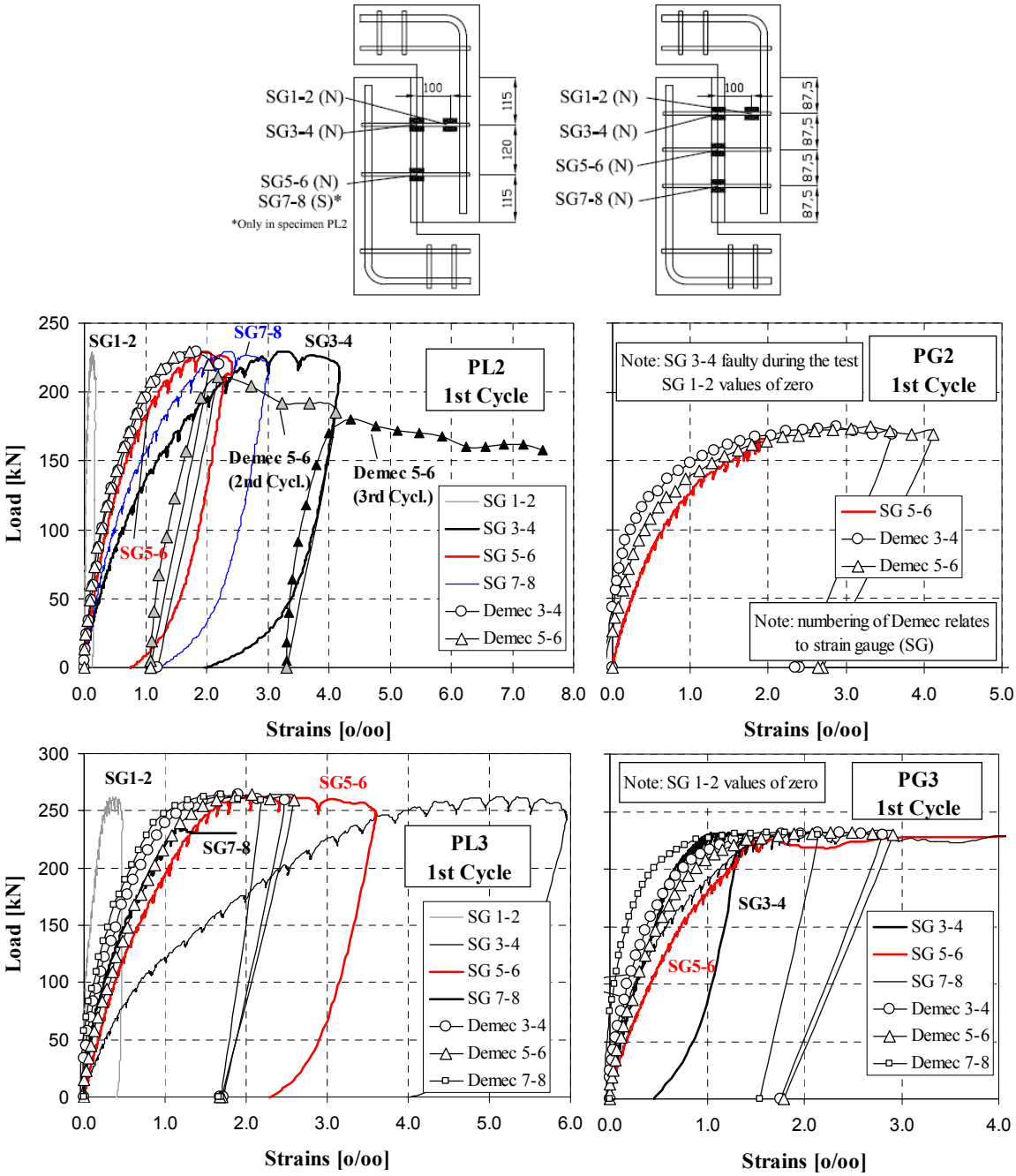

Note: Strain gauge numbering (Even - top; Odd - bottom); N/S refers to stirrup leg (north/south face)
Demec numbering refers to stirrup at which strain gauge with same number was placed

Figure 4.10: Strain at shear reinforcement of push-off specimens (1st Cycle)

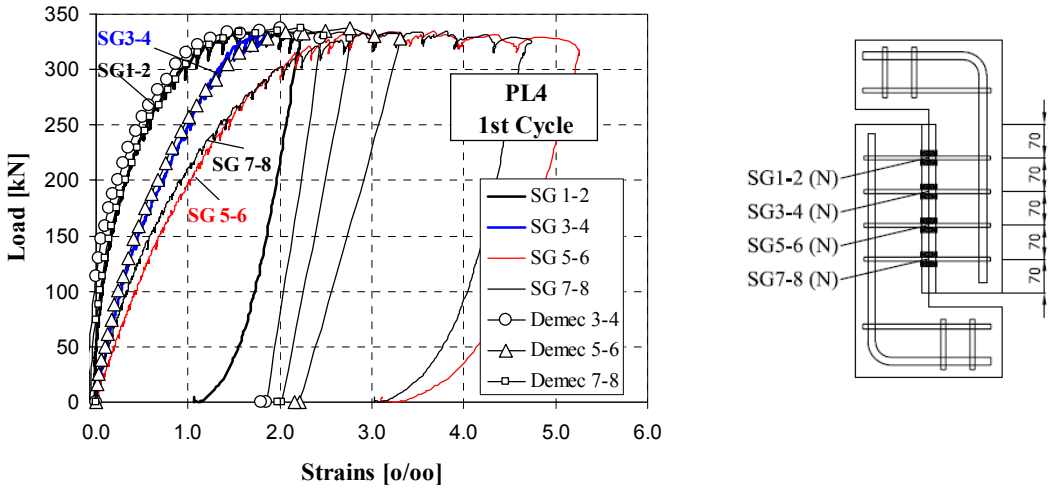

Note: Strain gauge numbering (Even - top; Odd - bottom); N/S refers to stirrup leg (north/south face)
Demec numbering refers to stirrup at which strain gauge with same number was placed

Figure 4.10 (Cont.): Strain at shear reinforcement of push-off specimens (1st Cycle)

In the second and third load cycles, the load-strain curve followed a similar path as in the first loading as shown in specimen PL2 (Figure 4.10). Once the peak load was reached, strains increased considerably reaching maximum values of around 7-10‰ at the end of the third load cycle. Strain gauges started to fail usually by the end of the second cycle.

In general, strains recorded at different stirrups of the same specimen were similar. Moreover, strains recorded at both legs of the stirrup in specimen PL2 (SG5-6 & SG7-8) were also similar.

Strain gauges placed 100mm away from the crack plane in specimens P2 and P3, provided values which were almost zero as shown in Figure 4.10. A relationship between strain gauge and demec readings can be estimated from compatibility conditions along the stirrup. The demec strain is an average measurement over a gauge length of 150mm. If the strain distribution along the stirrup is assumed to be parabolic from maximum at the crack to zero at 100mm from the crack, the ratio between the maximum strain (i.e. reading provided by strain gauge) and demec reading would be 1.12. If the strain distribution is assumed linear this ratio would be 1.5. These figures seem consistent with the differences between demec and strain gauge readings shown in Figure 4.10.

4.3 Interpolated shear stress curves for correlating push-off and beam test data

4.3.1 General aspects

In order to estimate the shear stresses transmitted along cracks in beams tested by the author (see chapters 7 and 8), the experimental results from the push-off tests described in section 4.2 are extrapolated. As mentioned earlier, this was possible due to three main aspects which were considered in the design of both types of tests. Firstly, same concrete was used for beam and push-off specimens. Secondly, the area of the crack and shear reinforcement ratio crossing it was similar. Thirdly, the crack openings measured in both types of tests were of similar magnitude.

On the other hand, two main drawbacks are found, which complicate the correlation between beam and push-off test data. The first difficulty faced is that the position of the stirrups is skewed with respect the crack plane in the beam tests while in a push-off test the stirrups are perpendicular to the crack plane. The efficiency of stirrups crossing the crack increases with decreasing the angle between the crack plane and the stirrup in the direction of the sliding, as shown in Figure 4.11 (Maekawa et al. [52]). This increase in the shear capacity has been observed in push-off tests carried by authors such as Walraven & Reinhard [46] or Maekawa et al [52].

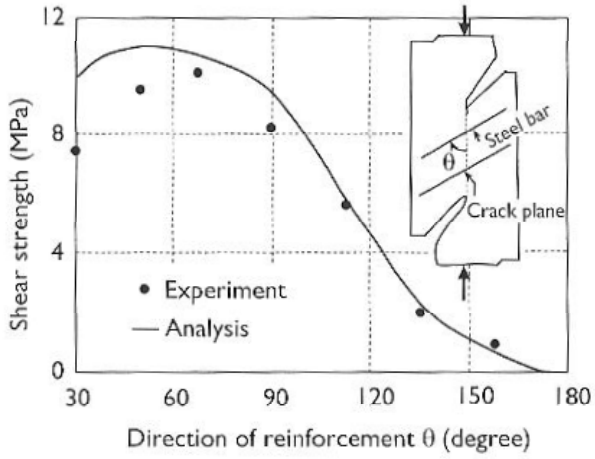

Figure 4.11: Influence of the angle of stirrups relative to crack plane in shear strength of push-off tests (adapted from Maekawa et al. [52])

In the beam tests performed in this work, the inclination of the stirrups relative to the crack plane varied from 60º for the flattest shear cracks to 45º. As an order of magnitude, the increase in strength from perpendicular to 45º orientated stirrups is around 30% according to tests carried by Walraven & Reinhardt [46]. In their tests, the $\delta w/\delta s$ ratio

was approximately equal to 1 and the shear reinforcement ratio was 0.56%, which is similar to specimens P2 and P3 tested in this work. The results obtained by Walraven & Reinhardt are broadly consistent with Maekawa's findings shown in Figure 4.11, despite the reinforcement ratio in these latter tests was almost double (1.27%).

The second drawback in correlating push-off and beam test data is related to the differences in loading and stress fields produced at each type of test. As discussed in chapters 7 and 8, the crack opening and sliding ratio $\delta w/\delta s$ in a push-off test ($\delta w/\delta s$~0.5, see section 4.2.4) is considerably lower than in a beam test, which can vary from 3 to 1.5 depending on the geometry and type of loading. According to Walraven & Reinhardt [46], the inclination of the stirrup in relation with the crack plane does not seem to have an important effect on the $\delta w/\delta s$. The difference in $\delta w/\delta s$ between both types of tests seems to be related more to the type of loading and to the fact that the crack in a push-off test can slide freely while in the beam tests this movement is restraint by the longitudinal reinforcement. The question could be raised of whether the crack opening and sliding in beams would be uniform as in a push-off test. The experimental results shown in chapter 6 showed that the crack opening and sliding measured in the beams tested did not change significantly along the crack and so shear stresses were extrapolated directly from the push-off test data.

4.3.2 Interpolated curves

The experimental data from the three load cycles was used in order to generate an interpolated 3D surface ($w-s-\tau$) for each push-off test, see example in Figure 4.12 for specimen PG2. The interpolated surfaces were used to estimate the shear stresses at cracks in the beams tested for the measured crack displacements (w, s), see chapter 7 and 8. The results from the three load cycles were treated separately, as shown in Figure 4.12, with the only difference that the initial crack width increased from one cycle to the next one. The crack slip was taken as zero at the end of each cycle, in order to measure relative crack slip values. The peak shear stresses relate to the 1st cycle. The different crack paths ($\delta w/\delta s$ ratio) obtained in push-off and beam tests, which were discussed earlier, are also illustrated in Figure 4.12.

The interpolated surfaces were generated using the built-in algorithm in MATLAB called "nearests", which is based on a Delaunay triangulation using Qhull joggle option (see Barber et al. [112]). These surfaces seem valid for values of w and s up to around 1.5mm,

above which more experimental data would be required. However, the values obtained of *w* and *s* in the beam tests were within this range and so additional test data does not seem necessary.

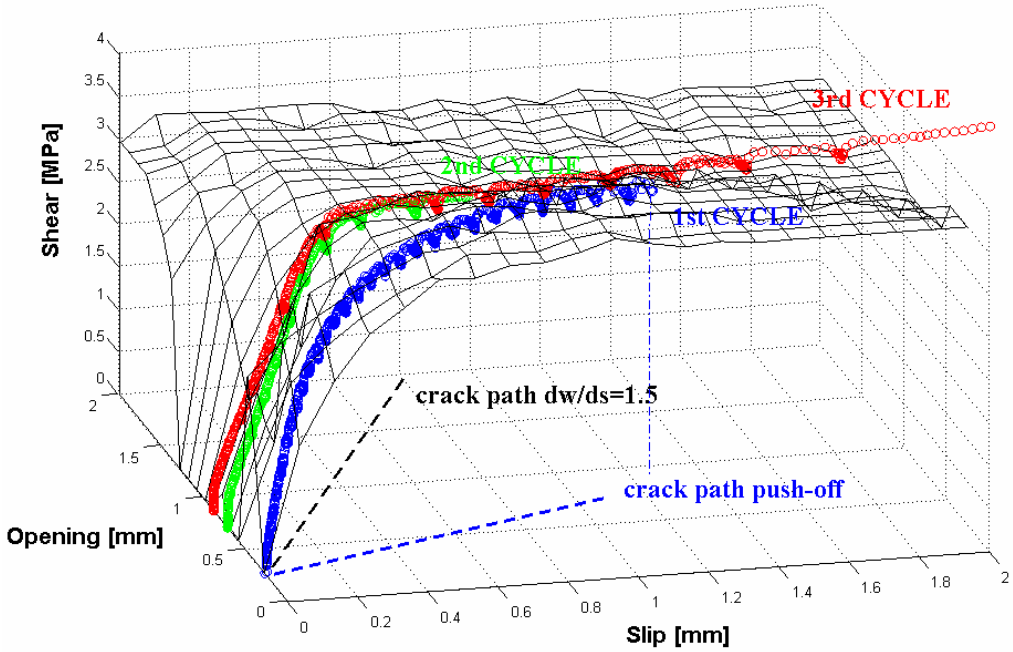

Figure 4.12: Example of interpolation surface for push-off test PG2

The results obtained for all the push-off tests are shown as contour plots in Figure 4.13 in which the contour lines relate to different crack openings. These curves are used in chapters 7 and 8 to estimate the shear stresses transmitted along cracks measured in the beams tested in shear.

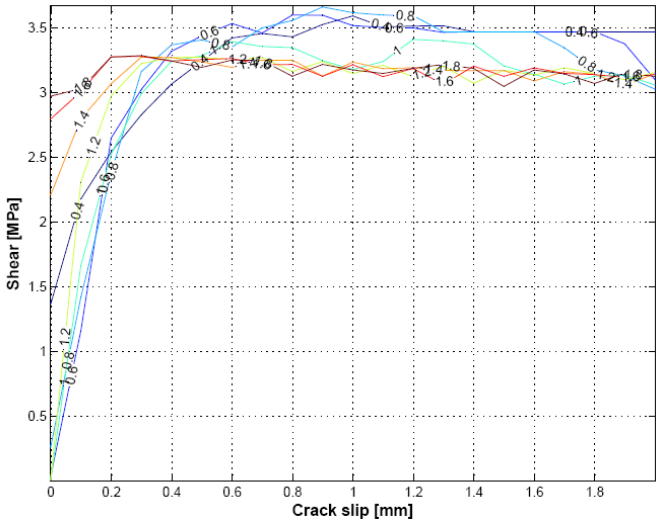

PG2 ($\rho f_y / v f_c'$ = 0.14) - used for beam BG1
Note: contour lines relate to different crack widths [mm]

Figure 4.13: Shear stresses for different crack widths derived from interpolated surfaces

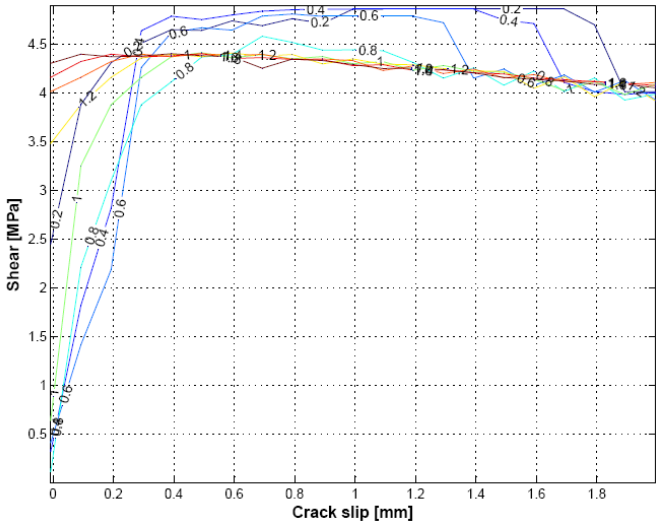

PG3 ($\rho f_y / v f_c'$ = 0.64) - used for beam BG2

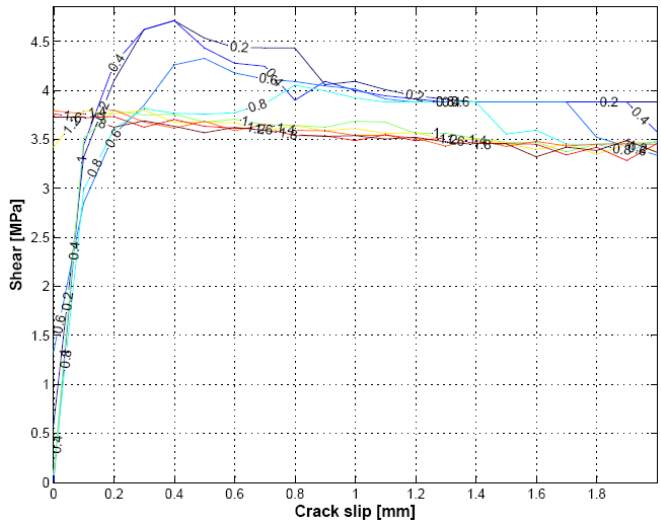

PL2 ($\rho f_y / v f_c'$ = 0.09) - used for beams BL2 & AL2

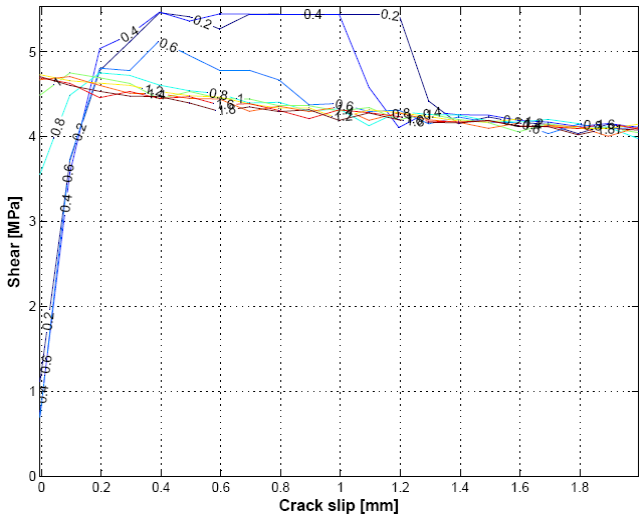

PL3 ($\rho f_y / v f_c'$ = 0.14) - used for beam BL2 & AL3/AL4

Note: contour lines relate to different crack widths [mm]

Figure 4.13 (Cont.): Shear stresses for different crack widths derived from interpolated surfaces

Contour plots, which are shown in Figure 4.13, seem sensible for crack slips greater than around 0.2mm for which shear stresses decreases as the crack width increases. For small values of crack sliding (s<0.2mm) and large crack openings (w>0.8mm) the interpolated surface is no longer representative of the experimental data, as shown in Figure 4.12. However, the crack slip obtained experimentally in beam tests were generally larger than 0.3mm, so curves shown in Figure 4.13 were still applicable.

4.4 Estimation of cohesion and friction parameters

Shear friction relationships, which are usually given in the form of Coulomb failure criteria ($\tau = C+\mu\sigma$), are used in design codes such as EC2 or ACI-318 to obtain the shear capacity of contact interfaces between two concrete surfaces. The cohesion factor (C) is generally given as a function of the tensile strength of the concrete and the friction (μ) depends exclusively on the roughness of the interface (see Table 4.3). Such equations are used in the design of construction joints, although it could also be extrapolated to crack interfaces in reinforced concrete beams. Although the formulation can be easily implemented in other methods, such as variable inclination strut method or strut-and-tie models (see chapters 7 and 8), the results are highly dependent on the values assumed for C and μ.

As shown in Table 4.3, there is a large inconsistency between the values of C and μ recommended by different design codes. In order to apply the shear friction formula in the analysis of reinforced concrete beams carried in chapters 7 and 8, parameters C and μ were estimated from the push-off test data. This was possible due to the similarities between cracks in push-off and beam tests carried by the author, which are discussed in further detailed in section 4.3. The values of C and μ obtained are shown in Table 4.3.

Reference	Surface	Cohesion (C)	Friction (μ)
EC2	Rough	$0.625 f_{ctk}^{**}$	0.70
	Smooth	$0.486 f_{ctk}^{**}$	0.60
	Very smooth	$0.347 f_{ctk}^{**}$	0.50
ACI-318 (for NW concrete)	Monolithically	2.75 MPa	1.4
	Rough	2.75 MPa	1.0
	Medium	-	0.6
Clímaco and Regan	Rough	$0.25(f_c')^{2/3}$	1.4
	Medium	$0.25(f_c')^{2/3}$	0.9
	Smooth	5 MPa	0.7
Hamadi and Regan	Natural gravel	$0.25(f_c')^{2/3}$	0.7
	Expanded Clay	$0.25(f_c')^{2/3}$	0.3
Interpolation of push-off tests	Gravel (PG) (f_c' = 31.7MPa)	1.20 MPa (~0.41 f_{ct})	1.06
	Limestone (PL) (f_c' = 53.1MPa)	2.50 MPa (~0.63 f_{ct})	0.95

Notes: $f_{ctk}^{**} = 0.21(f_c')^{2/3}$ for $f_{ck} \leq 50$MPa
$f_{ctk}^{**} = 1.48\ln[1+f_{cm}/10]$ for $90 \leq f_{ck} \leq 50$MPa

Table 4.3: Cohesion and friction parameters according to design codes and experimental work

Figure 4.14 shows the linear regression of the experimental data that was carried to estimate C and μ; results are presented for the ultimate loads obtained at the first cycle, where the crack widths at failure were between 0.4 and 0.6mm. The shear stresses were normalized by conventional factor $f_c'^{2/3}$.

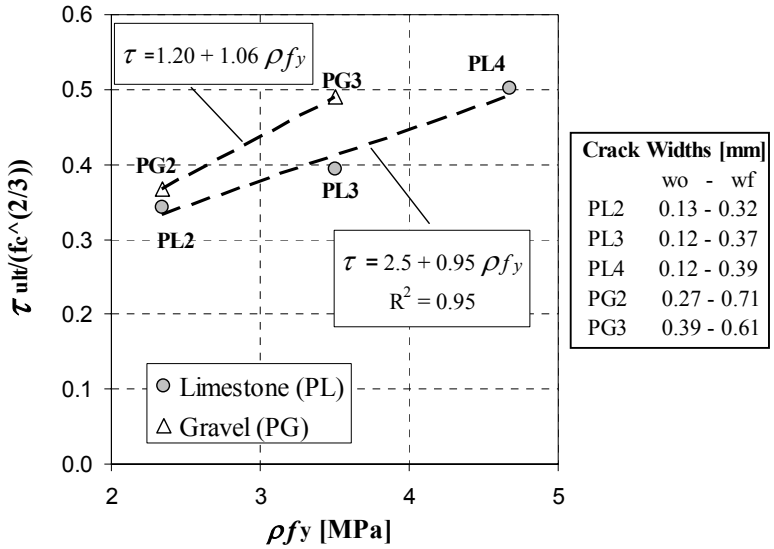

Figure 4.14: Estimation of cohesion and friction parameters from experimental data

It is important to note that the shear friction formulas described above assume that the shear strength is not influenced by the crack width. This assumption seems to agree with experimental data from Hamadi & Regan [19] of specimens with large normal stresses (greater than around 1MPa), which is the case of specimens PG and PL. In addition, work carried by these authors also showed that the initial crack widths required in order to obtain a significant reduction in the shear strength were very large (w_0~0.9mm) compared with values commonly seen in push-off tests. Similar conclusions can be drawn from interpolation curves derived in section 4.3 (Figure 4.13), where maximum values of the shear stresses remained almost constant for different values of w, up to crack openings of around 0.6mm. The initial crack widths measured at beams tests carried in this work were of similar magnitude as those obtained in the push-off tests, which were around 0.1-0.3mm. All of this supports the idea that the values of C and μ obtained from the push-off tests, which are shown in Table 4. 3 and Figure 4.14 are not highly influenced by this assumption made in the shear friction model.

The cohesion estimated from the linear regression was in good agreement with EC2 recommended values (Table 4.3). However, the friction factor obtained in PG and PL specimens were larger than the highest values suggested in EC2, which relate to rough

cracks. According to ACI-318 or Climaco & Regan's [113] classification, the friction estimated from the push-off tests corresponded to a medium-rough type of surface (μ = 0.9-1).

It is noteworthy that the friction of both limestone and gravel specimens was comparable, despite that in the former case the aggregate fractured completely at the crack. The large value obtained for μ in specimens PL was unexpected in view of previous test data of lightweight aggregate specimens where the friction was as low as 0.3 (see Hamadi and Regan [19]); ACI-318 provisions for light-weight aggregate recommends using a factor of 0.75 to be applied to μ. The interpolated values obtained for the gravel specimens are of course approximate, since only two data points were available. However, in the limestone specimens, the three data points seem to have a good correlation factor for the linear fit (R^2=0.95), as shown in Figure 4.14.

A possible explanation for the large value of μ obtained in the limestone specimens could be due to friction at a macro-level as shown in Figure 4.15 (right). Similar conclusions were obtained by Walraven & Al-Zubi [9] from their beam tests using lightweight aggregate, in which the aggregate particles fractured completely at the crack. The shear performance of their beams was similar to equivalent beams made of normal aggregate concrete.

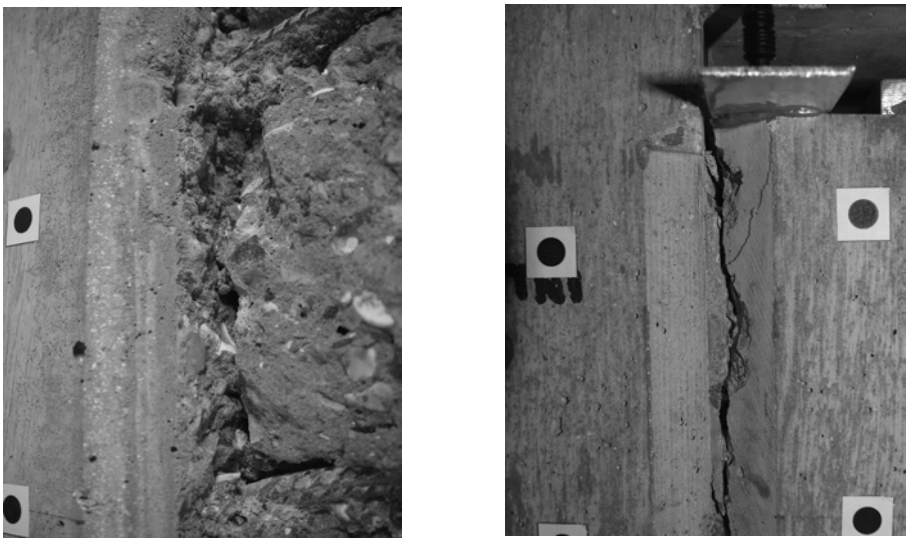

a) Gravel specimen (Crack level) b) Limestone specimen (Macro-level)

Figure 4.15: Crack roughness in gravel and limestone specimens

4.5 Comparison of experimental results with analytical models

In previous section, the experimental results were examined using the traditional shear friction formula, which can be used to estimate the ultimate shear load carried at the crack. As discussed in chapter 2, there are many other models, which can be used to assess the shear stress development at the crack as a function of the relative crack displacements. Four of these models, which are defined in section 2.5.2, were applied to investigate their performance using the experimental data presented in this chapter. The models which were investigated were originally proposed by Walraven & Reinhardt [46], Hamadi & Regan [19], Gambarova & Karakoç [48], and Li et al. [49]. In Figures 4.17 to 4.18 these models are denoted with the name of the first author.

The crack opening and sliding measured from the top cross of LVTDs were used in order to obtain the shear stresses (τ) at the crack shown in Figures 4.16 and 4.17, which relates to the first load cycle. The normal stresses (σ) were estimated from the mean strains measured in all stirrups measured at the crack plane, except for specimen PG3, where strain gauges failed at early load stages and so demec readings were used instead.

In order to apply the linear aggregate interlock model proposed by Walraven & Reinhardt [46], concrete cube strengths of 30.4MPa and 60.3MPa were used for the PG and PL specimens respectively. Cylinder strengths were used for the rest of the models (Figure 4.2). Modified equations for light-weight aggregate concrete propossed by Walraven & Reinhardt [46], were also investigated. The shear stresses were clearly underestimated using these modified equations, which are denoted as Walraven (LWT) in Figures 4.16 and 4.17.

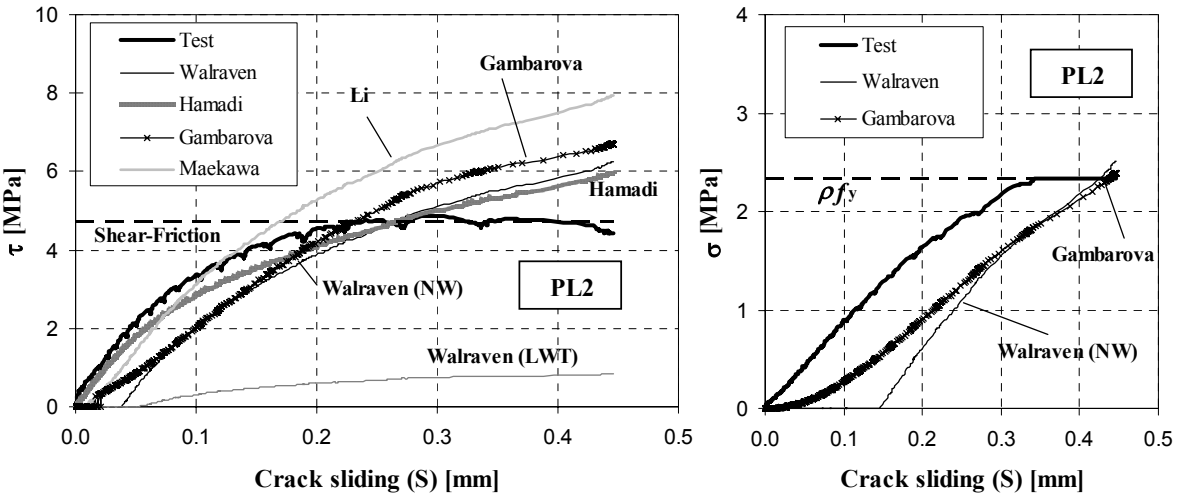

Figure 4.16: Experimental and predicted shear/normal stresses (specimens PL)

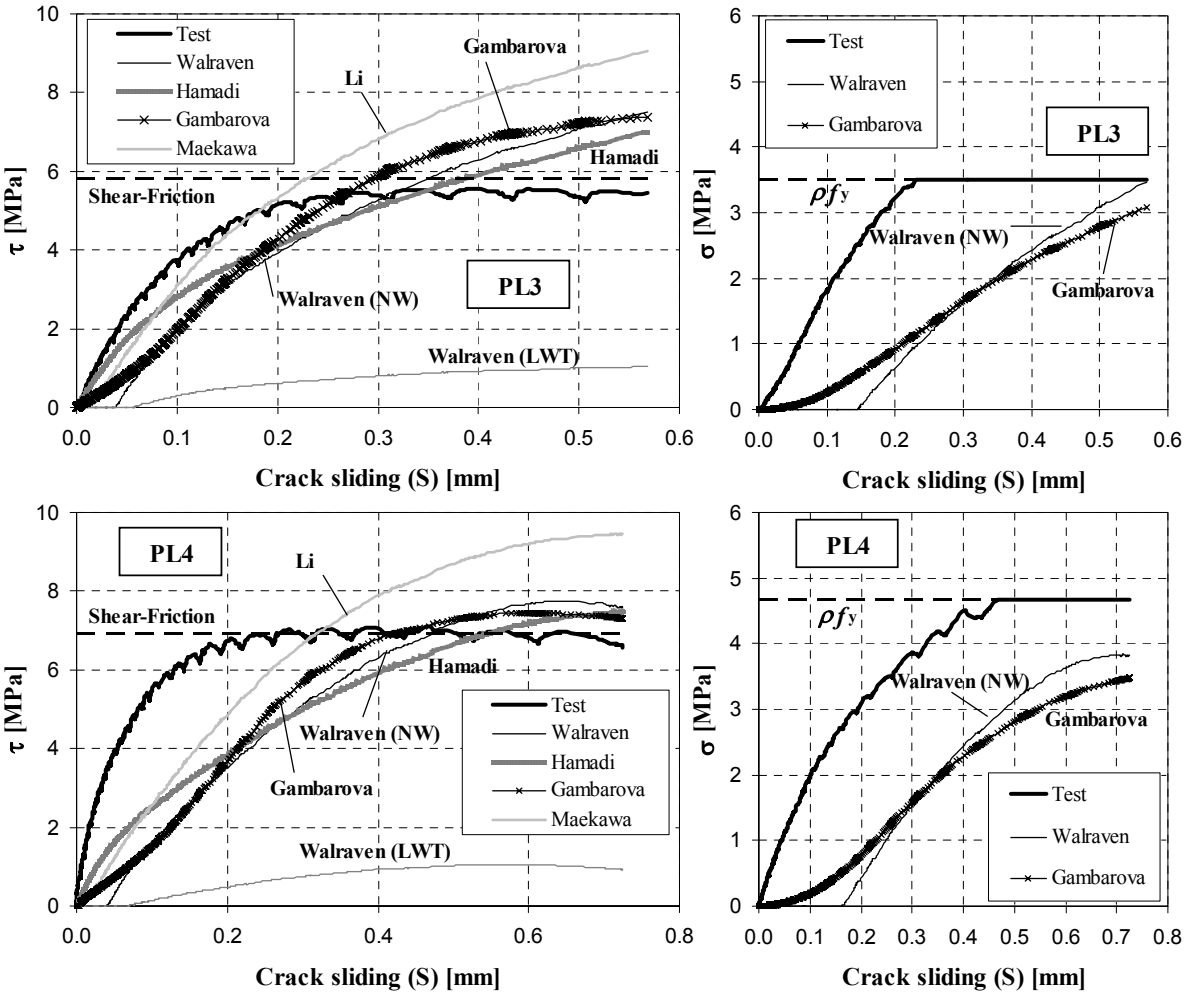

Figure 4.16 (Cont.): Experimental and predicted shear/normal stresses (specimens PL)

The shear friction model predictions shown in Figures 4.16 and 4.17, were obtained using optimal values for C and μ shown in Table 4.3. In Hamadi & Regan's [19] model, the aggregate interlock stiffness (k) was taken as 5.4MPa, as suggested by the authors for gravel concrete. The results obtained using this value of k were acceptable for the limestone specimens, although for specimens PG parameter k seemed to be overestimated (see Figures 4.16 and 4.17).

The different models provided similar answers for specimens PL. However this was not the case for specimens PG, where models proposed by Hamadi & Regan [19] or Li et al. [49] produced much higher shear stresses than the rest of the crack dilatancy models. In addition, the models tended to underestimate the shear stresses of the push-off specimens for crack slips lower than around 0.2-0.3mm. On the contrary, the shear stress was overestimated at the end of the first load cycle (s~0.5-0.7mm), especially using formula proposed by Li et al. [49] (see Table 4.4).

Despite the large differences in the formulations proposed by Gambarova & Karakoç [48] and Walraven & Reinhardt [46] discussed in chapter 2, the models produced very similar answers for the first cycle, see Figures 4.16-4.18. These two models produced reasonable predictions of the shear stresses at the end of the first cycle, as shown in Table 4.4. Normal stresses predicted by these two models, were again similar to each other. However, the normal stresses predicted were lower than the experimenta values (~25%); worse predictions were obtained for specimens PL3 and PL4 (~35%).

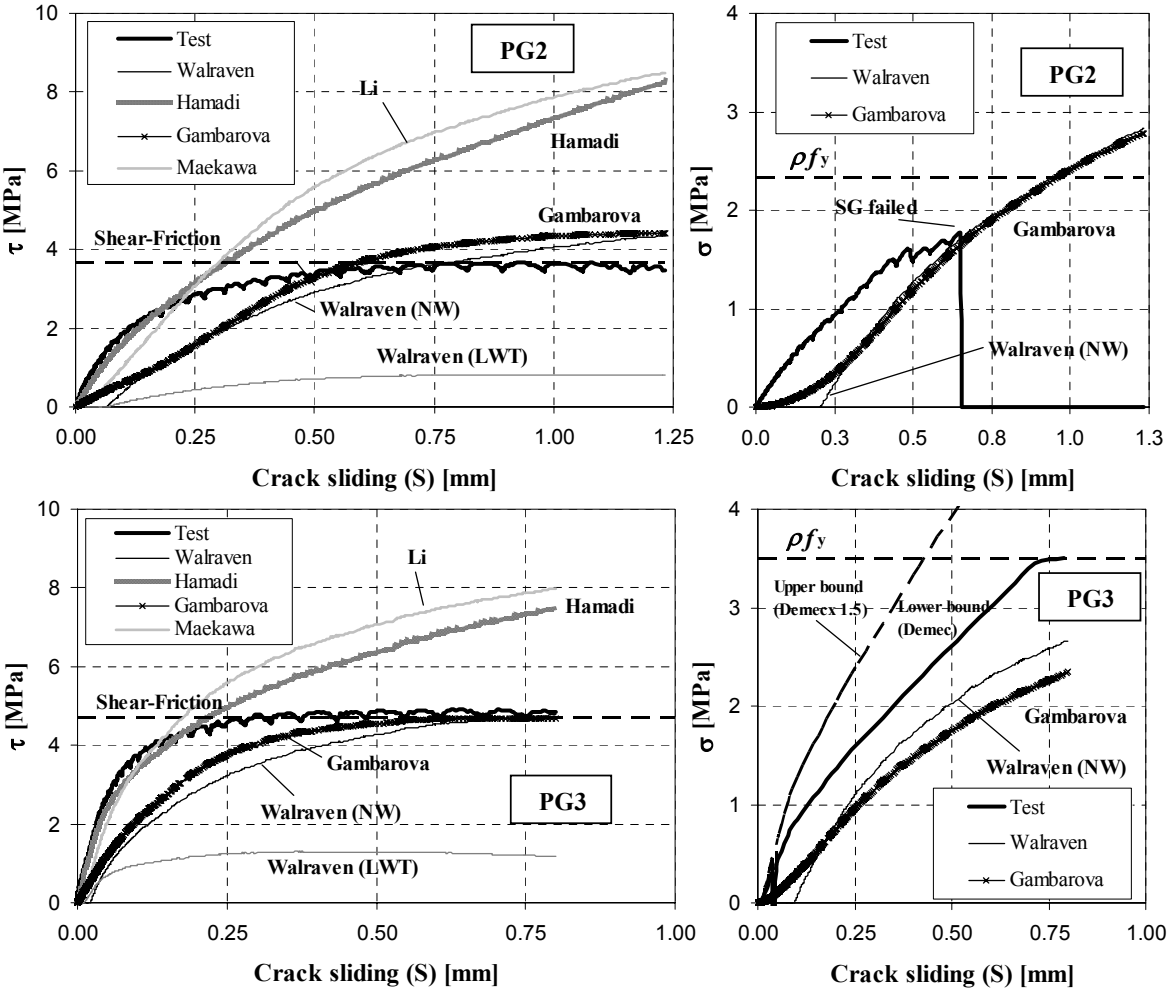

Note: Normal stresses obtained experimentally in PG3 are between lower and upper bound given by Demec readings (factors between 1 and 1.5, as discussed in section 4.2.4)

Figure 4.17: Experimental and predicted shear/normal stresses (specimens PG)

Lastly, aggregate interlock provisions from MC90 were also examined. As discussed in section 2.4.2, crack dilatancy formula (w=0.6.$s^{2/3}$) recommended in MC90 had an excellent agreement with experimental data obtained in this work. Equations for estimating the shear stress carried at the crack are also provided in MC90. These formulas assume that for crack slips (s) up to 0.1mm τ is proportional to the crack slip. This assumption seems reasonable, in view of the results shown in Figure 4.18. For values of s

greater than 0.1mm, τ is assumed to follow a polynomial relationship (fourth grade) up to 2mm, where the ultimate shear stress is predicted (refer to section 2.5.2). The shear stresses estimated with the MC90 formulae are compared with experimental data from the first load cycle in Figure 4.18. The predictions seem sensible, although shear stresses are slightly overestimated at the end of the first cycle. The τ_{calc}/τ_{peak} ratio obtained for each analytical method shown in Table 4.4, improved with increasing the number of stirrups. As shown in Table 4.4, MC90 along with Walraven & Reinhardt [46] and Gambarova & Karakoç's [48] methods provided the most accurate predictions.

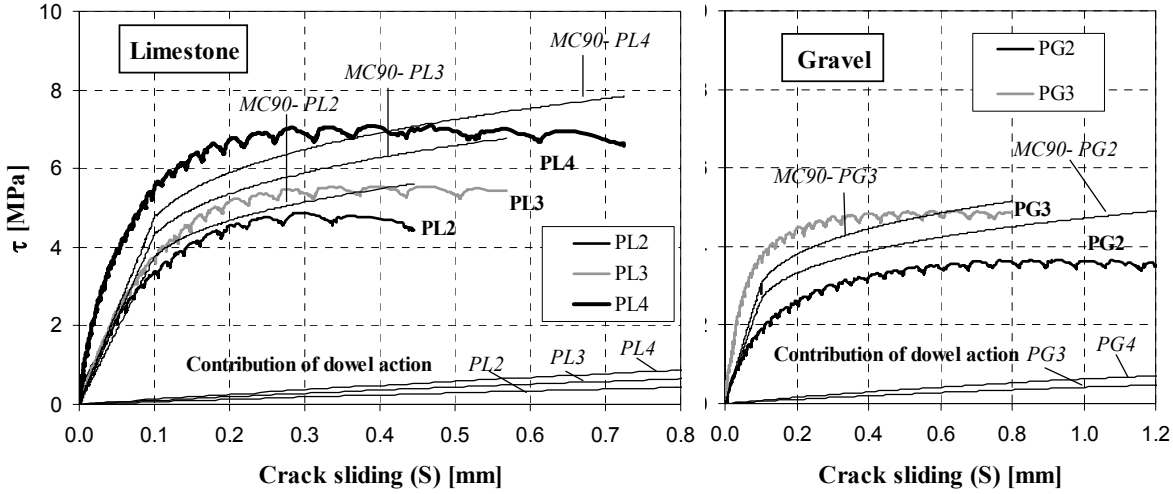

Figure 4.18: MC90 shear stress predictions compared with experimental data

Specimen	w_{peak} [mm]	s_{peak} [mm]	τ_{peak} [MPa]	τ_{calc}/τ_{peak} *Ref.1*	*Ref.2*	*Ref.3*	*Ref.4*	*MC90*
PG2	0.65	0.93	3.67	1.25	2.38	1.27	2.45	1.42
PG3	0.51	0.60	4.91	0.98	1.54	0.97	1.64	1.06
PL2	0.36	0,29	4.85	1.41	1.35	1.51	1.79	1.27
PL3	0.37	0.40	5.55	1.38	1.29	1.36	1.66	1.24
PL4	0.38	0.50	7.10	1.15	1.14	1.11	1.44	1.19
			Mean	1.23	1.54	1.24	1.80	1.24
			SD	0.18	0.49	0.21	0.39	0.13
			COV	14.3	31.9	17.0	21.5	10.6

Ref. 1- Walraven & Reinhardt
Ref. 2- Hamadi & Regan
Ref. 3- Gambarova & Karakoç
Ref. 4- Maekawa & Okamura

Table 4.4: Experimental and predicted values of the peak shear stress at the end of the first cycle

The predictions from the analytical models worsened for the second and third load cycles, where the relative crack displacements were larger. All the models showed a reduction in the stiffness due to crack widening from one cycle to the next one (see Figure 4.19). However, the predicted shear stiffness reduction seemed to be excessive compared with

the experimental data, especially for the models proposed by Walraven & Reinhardt [46] or Gambarova & Karakoç [48]. Regarding shear stress predictions, only model suggested by Gambarova & Karakoç's [48] seemed to provide reasonable answers for such large crack displacements (s>1mm), see Figure 4.19.

In view of these results, it seems questionable whether the analytical models are suitable for crack sliding greater than around 1mm. However, the maximum crack slip measured in the beams tested by the author, was around 0.5mm and so the use of these models in analysing beam test seems reasonable. According to the results shown in this section, for values of s lower than 0.2mm, Hamadi & Regan [19] and Li et al. [49] models provided accurate predictions. For crack sliding between 0.2 and 0.75mm, Walraven & Reinhardt [46] and Gambarova & Karakoç [48] seem to provide more realistic predictions. For simplicity, the linear aggregate interlock relationship proposed by Walraven & Reinhardt [46] and the model presented by Hamadi & Regan [19] were applied in this work for the analysis of the beam tests (see chapters 7 and 8).

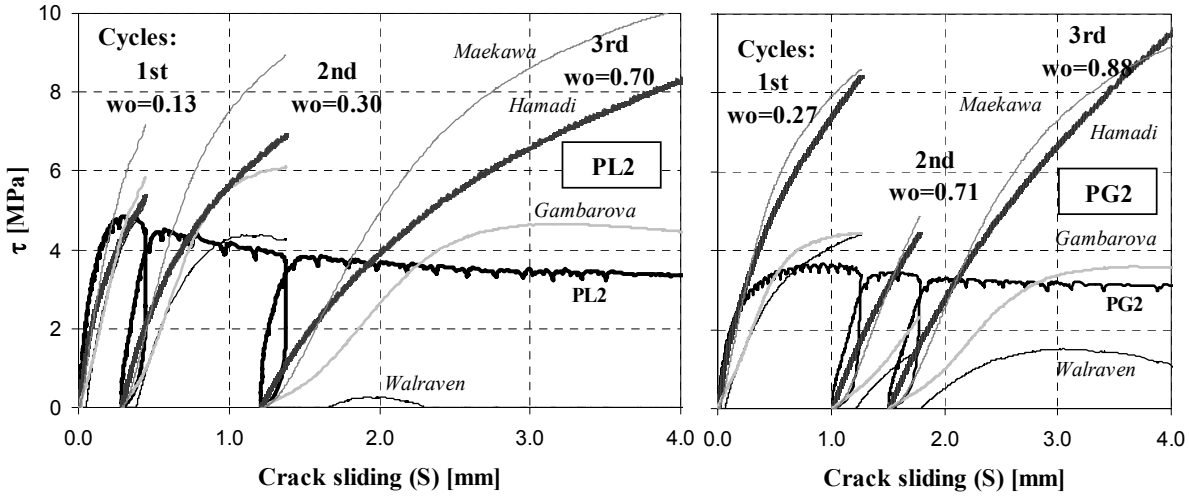

Figure 4.19: Experimental and predicted values of the shear stress at the three load cycles

Contribution of dowel action

The contribution of dowel action to the shear strength of the specimens was investigated using the Millard & Johnson's [91] model. This formula, which was applied in section 3.4.2, is based on a traditional solution of a beam resting on elastic foundation. The model gives slightly lower values compared to MC90 formulae in this case, although the difference in shear stresses is lower than around 30%. From this analysis, it was concluded that contribution of dowel action was negligible, as shown in Figure 4.18. Walraven & Reinhardt [46] reached a similar conclusion on the basis of their test results.

4.6 Conclusions

Push-off tests are commonly used in order to study the stresses transmitted along concrete cracks by means of aggregate interlock. This testing arrangement is practical since the entire load applied is transferred through a pre-cracked surface of which both geometry and amount of shear reinforcement crossing it is known. In addition, relative crack displacements (*w*-opening; *s*-sliding) can be monitored easily by using traditional measuring crosses. The experimental results presented in this chapter show a good agreement between relative crack displacements obtained using crosses of Demec, LVTDs and digital photogrametric targets. Readings were taken at different levels of the crack, showing similar values of *w* and *s* along the crack. The initial crack widths obtained after pre-cracking the specimens were somewhat different along the crack. However, the results seem not to be influenced by these small variations of the initial crack opening since at early load stages the values of *w* had levelled out considerably at both sides of the specimen. The contribution of dowel action to the shear strength of the specimens tested was negligible.

Push-off tests carried by the author using gravel and limestone aggregates showed that considerable shear stresses could be transmitted through the crack in the limestone specimens. This was surprising since the limestone aggregate had fractured completely at the crack in these specimens. In addition, the friction parameter μ estimated from linear regression of the experimental data according to the shear friction formula ($\tau = C+\mu\sigma$), was very similar between the gravel and limestone push-off tests ($\mu \sim 1.0$). The estimated value of the friction coefficient was considerably larger than those usually obtained experimentally for light-weight aggregate (μ = 0.3, Hamadi & Regan [19]) or those recommended in EC2 for very smooth surfaces ($\mu = 0.5$).

Finally, the crack path ($\delta w/\delta s$ ratio) was similar for both gravel and limestone specimens. The average $\delta w/\delta s$ was around 0.5 at the first cycle, at which the peak shear stress was obtained. This value is in good agreement with Walraven & Reinhardt [46] test data and MC90 crack dilatancy rule ($w=0.6.s^{2/3}$) in which the $\delta w/\delta s$ ratio decreases from 0.5 to 0.25 at crack slips of 0.5mm and 4mm respectively. Push-off tests carried by Walraven & Reinhardt [46] using light-weight aggregate showed a much lower value of $\delta w/\delta s$ of around 0.25 for the entire test. From these considerations, it can be concluded that limestone specimens had an unexpected level of "roughness" or friction considering that

the aggregate had fractured completely at the crack. This might have been due to friction at a macro-level.

The main drawbacks of extrapolating push-off test data for analysing cracks in beam tests have been investigated. The experimental data obtained from the Push-off tests has been used to generate interpolation curves, which were used to estimate the shear stresses at similar cracks formed at beams tested by the author. The peak shear stresses predicted by these curves seem to be independent of the crack width up to values of w of around 0.6mm. This is consistent with the assumption made in shear friction formulas, which seems reasonable according to experimental data provided by Hamadi & Regan [19] amongs others. The cohesion parameter used in the shear friction formula was obtained similarly as parameter μ. In this case, the estimated cohesion was in good agreement with EC2 recommended values. Both estimates of C and μ are used in chapters 7 and 8 for the analysis of the critical shear cracks in beam tests.

The shear and normal stress development at the crack, which was obtained experimentally, was compared with predictions from five different crack dilatancy models proposed by Walraven & Reinhardt [46], Hamadi & Regan [19], Gambarova & Karakoç [48], Li et al. [49] and MC90. The shear stresses were generally underestimated for low values of the crack slip (s<0.2mm). However, analytical models tended to overestimate the shear stress for values of the crack opening and sliding measured experimentally at the peak load. According to the experimental data provided, this was worse for the formula based in the contact density theory developed by Li et al. [49]. The rough crack model proposed by Gambarova & Karakoç [48] provided very similar predictions as the linear aggregate interlock relationship suggested by Walraven & Reinhardt [46]. Due to their simple formulation, the linear aggregate interlock relationship and model presented by Hamadi & Regan [19] were finally adopted for the analysis of shear cracks at the beam tests (chapters 7 and 8). The predictions of the shear stresses in the push-off tests using these two models seemed sensible for crack slips up to around 1mm. This was acceptable for the analysis of cracks at beam tests, since the crack slips measured in this case were usually lower than 0.5mm. Formulas included in MC90 had similar level of accuracy as the two models finally adopted in this work.

CHAPTER 5 – Analysis of Shear Panels

5.1 Introduction

The study of rectangular reinforced concrete membrane elements, which are subjected to in-plane shear and axial stresses, is commonly believed to be relevant to the prediction of the shear strength of beams. Considerable experimental data is available from previous tests on shear panels by investigators such as Vecchio & Collins [8] or Hsu [114]. As recognized by these researchers, shear panel tests are more difficult to carry out than regular beam tests, since they require a special rig that is capable to synchronize a large number of actuators as shown in Figure 5.1. On the other hand, the experimental data obtained from shear panel test is far easier to interpret than beam test data. This is due to the fact that the biaxial state of stresses in the panels shown in Figure 5.1 is totally isolated from other aspects such as bending stresses or dowel action of the flexural reinforcement that can occur in normal beam tests.

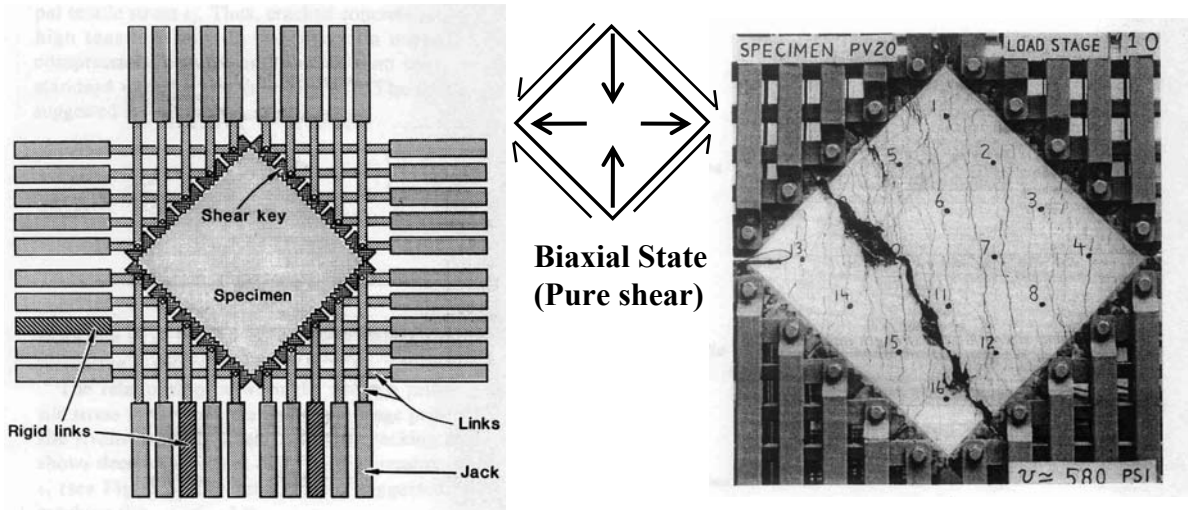

Figure 5.1: Shear panel tests (adapted from Vecchio & Collins [8])

In this chapter, two main concerns related to shear panel tests are investigated; namely compression softening and aggregate interlock action. Compression softening due to the presence of transverse strains to the main struts was first reported by Vecchio & Collins [115]. Aggregate interlock on the other hand, has been generally studied using pure shear tests such as push-off tests, which are described in chapter 4.

A group of 64 shear panel test were selected from an experimental database of 102 tests, which was gathered by Bentz et al. [32], in order to study these two parameters. The predictions of the ultimate failure load, deflection-load response and strut inclination using the Modified Compression Field Theory are compared with different non-linear finite element models, which include both fixed and rotating smeared crack approaches. These smeared crack models are described in chapter 3.

The ultimate failure load was also predicted using simple truss approaches, which are suggested in EC2. In addition, a simple analytical discrete crack approach is presented, which is referred to in this work as “crack slip model”. This approach was developed by the author and applies constitutive equations for aggregate interlock, which have been previously been validated against push-off test data shown in chapter 4. Subsecuently, the crack slip model is applied to continuous beams in chapter 8, in order to estimate relative crack displacements and shear stresses transmitted along shear cracks.

5.2 Database of experimental results

A large database of experimental results from shear panel tests have been gathered by Bentz et al. [32]. This database includes tests from five different testing machines in four different research laboratories, adding up to 102 tests. However, in this study only shear panels without axial load and with shear reinforcement in both orthogonal directions were investigated. In addition, specimens tested by Vecchio & Collins [8], which had an edge type of failure or were poorly cast were neglected since in some cases it is not clear whether this lead to a premature failure. These specimens are PV1, 5, 7, 8, 9, 14, 30.

Two cases for pure shear were investigated; shear panels equally reinforced in both directions ($r=\rho_x f_{xy}/\rho_y f_{yy}=1$) and panels with a predominant reinforced direction x ($r=\rho_x f_{xy}/\rho_y f_{yy}>1$), which are referred to as Case I and II respectively. Tables 5.1 and 5.2, summarise all the specimens considered, which add up to 32 panels for Case I & II respectively. The 64 panels examined were tested by eight different researchers (Vecchio & Collins [8], Yamaguchi et al. [116], Andre [117], Kirschner [118], Porasz & Beidermann [119], Vecchio et al. [120], Pang & Hsu [121], Zhang & Hsu [122]).

A distinction is made between cases I and II since both types of panels have a considerably different performance. As shown in Figure 5.1 (left), in Case I panels, the inclination of the strut θ remains constant and equal to 45º. In such cases only concrete softening due to transverse strains is expected. In addition, the shear along the 45º crack is zero and no crack slip will occur. On the other hand, in Case II panels, the compressive strut will rotate as shown in Figure 5.2 (right). Hence aggregate interlock will be mobilized in addition to compression softening. This strut realignment results on normal and shear stresses at the crack by means of aggregate interlock.

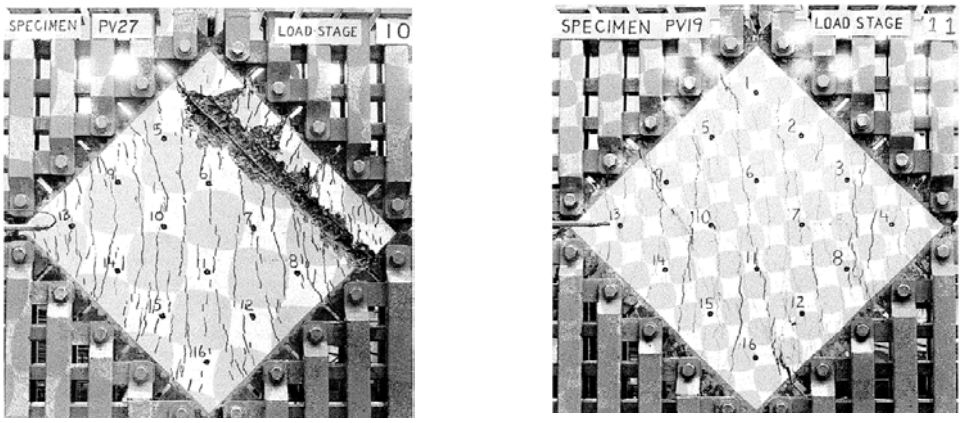

Figure 5.2: Crack pattern in shear panels; *Left*– Case I, PV27; *Right*– Case II, PV19 (adapted from Collins et al. [104])

CASE I (r=1)								τcalc/τtest	τcalc/τtest ¦ F.M	
Author	**Panel**	**a**	**fc' [MPa]**	**ρxfxy [MPa]**	**ρyfyy [MPa]**	**r**	**τtest [MPa]**	**1- MCFT**	**2- Truss EC2***	
Vecchio & Collins	PV2	6	23.5	0.77	0.77	1.0	1.15	0.68	0.67	yield
	PV3	6	26.6	3.18	3.18	1.0	3.06	1.05	1.04	yield
	PV4	6	26.6	2.49	2.49	1.0	2.90	0.89	0.86	yield
	PV6	6	29.8	4.76	4.76	1.0	4.56	1.05	1.04	yield
	PV16	6	21.7	1.89	1.89	1.0	2.15	0.89	0.88	yield
	PV27	6	20.5	7.91	7.91	1.0	6.36	1.04	0.89	crush
Yamaguchi et al.	S-21	20	19.0	16.18	16.18	1.0	6.46	1.12	0.82	crush
	S-31	20	30.2	16.18	16.18	1.0	8.46	1.25	0.94	crush
	S-32	20	30.8	12.88	12.88	1.0	8.62	1.15	0.94	crush
	S-33	20	31.4	10.11	10.11	1.0	8.16	1.16	1.01	crush
	S-34	20	34.6	7.98	7.98	1.0	7.27	1.10	1.10	yield
	S-35	20	34.6	4.92	4.92	1.0	5.64	0.87	0.87	yield
	S-41	20	38.7	17.51	17.51	1.0	12.00	1.05	0.82	crush
	S-42	20	38.7	17.51	17.51	1.0	12.77	0.98	0.77	crush
	S-43	20	41.0	17.51	17.51	1.0	11.89	1.10	0.86	crush
	S-44	20	41.0	17.51	17.51	1.0	12.30	1.06	0.84	crush
	S-61	20	60.7	17.51	17.51	1.0	15.18	1.11	0.91	crush
	S-62	20	60.7	17.51	17.51	1.0	15.78	1.10	0.87	crush
	S-81	20	79.7	17.51	17.51	1.0	15.94	1.09	1.02	crush
	S-82	20	79.7	17.51	17.51	1.0	15.94	1.09	1.02	crush
Andre	TP4	9	23.2	9.18	9.18	1.0	8.12	0.92	0.78	crush
	TP4A	9	24.9	9.18	9.18	1.0	8.72	0.88	0.77	crush
	KP4	20	23.0	8.77	8.77	1.0	6.90	1.06	0.91	crush
Kirschner & Collins	SE5	10	25.9	22.14	22.14	1.0	8.03	1.12	0.87	crush
Porasz & Beidermann	SE14	10	60.4	22.80	22.80	1.0	18.12	0.97	0.76	crush
Pang & Hsu	A2	19	41.3	5.51	5.53	1.0	5.62	0.99	0.98	yield
	A3	19	41.6	8.00	7.99	1.0	7.90	1.02	1.01	yield
	A4	19	42.5	14.01	14.03	1.0	11.90	1.03	0.89	crush
Zhang & Hsu	VA1	13	95.1	5.30	5.33	1.0	6.47	0.96	0.82	yield
	VA2	13	98.2	9.78	9.82	1.0	10.11	0.97	0.97	yield
	VA3	13	94.6	16.33	16.37	1.0	15.42	1.06	1.06	yield
	VA4	13	103.1	24.63	24.64	1.0	22.68	1.00	0.80	crush
Total	**32**							**1- MCFT**	**2- Truss EC2***	
	max value =	20	103.1	24.6	24.6		**Mean**	**1.03**	**0.90**	
	min value =	6	19.0	0.8	0.8		**SD**	**0.11**	**0.10**	
							COV %	**10.62**	**11.58**	

Note: a= maximum aggregate size; $r = \rho_x f_{xy} / \rho_y f_{yy}$

FM= predicted failure mode: "yield" = yielding of reinforcement in x and y directions

"crush" = strut crushing

*Truss EC2 = both rotating and fixed approaches provide identical answers (θ=45º)

Table 5.1: Experimental database of shear panels equally reinforced in both directions (Case I, r=1)

CASE II (r >1)								τcalc/τtest	τcalc/τtest ¦ F.M			
Author	**Panel**	**a**	**fc' [MPa]**	**ρxfxy [MPa]**	**ρyfyy [MPa]**	**r**	**τtest [MPa]**	**1- MCFT**	**2- Truss EC2 (rotating)**		**3- Truss EC2 (fixed)**	
Vecchio &	PV10	6	14.5	4.94	2.76	1.8	3.92	0.94	0.94	yield	0.98	yield
Collins	PV11	6	15.6	4.21	3.07	1.4	3.59	1.02	1.00	yield	1.01	yield
	PV12	6	16.0	8.40	1.20	7.0	3.14	0.92	0.97	crush	1.43	crush
	PV19	6	19.0	8.20	2.13	3.9	3.99	1.05	1.05	yield	1.29	yield
	PV20	6	19.6	8.23	2.63	3.1	4.31	1.08	1.08	crush	1.26	crush
	PV21	6	19.5	8.20	3.92	2.1	5.07	1.10	1.02	crush	1.06	crush
	PV22	6	19.6	8.20	6.41	1.3	6.08	1.02	0.88	crush	0.89	crush
	PV26	6	21.3	8.16	4.66	1.7	5.33	1.14	1.08	crush	1.10	crush
Andre	TP1	9	22.1	9.18	4.60	2.0	5.75	1.09	1.02	crush	1.05	crush
	TP1A	9	25.6	9.18	4.58	2.0	5.63	1.12	1.15	yield	1.22	yield
	KP1	20	25.2	8.77	4.38	2.0	5.54	1.12	1.12	yield	1.19	yield
Kirschner	SE1	10	42.5	14.37	4.68	3.1	6.76	1.11	1.21	yield	1.41	yield
& Collins	SE6	10	40.0	14.37	1.60	9.0	3.76	1.05	1.28	yield	2.12	yield
Porasz	SE11	10	70.8	14.01	4.46	3.1	6.58	1.20	1.20	yield	1.40	yield
& Beidermann	SE12	10	75.9	13.23	4.55	2.9	7.44	1.04	1.04	yield	1.20	yield
	SE13	10	80.5	32.53	9.26	3.5	11.99	1.22	1.23	crush	1.37	crush
Vecchio et al.	PA1	10	49.9	10.00	4.29	2.3	6.29	1.06	1.04	yield	1.14	yield
	PA2	10	43.0	10.06	4.30	2.3	6.24	1.06	1.05	yield	1.15	yield
	PHS2	10	66.1	19.70	2.18	9.0	6.15	0.88	1.07	yield	1.78	yield
	PHS3	10	58.4	19.70	4.32	4.6	8.18	1.01	1.13	yield	1.47	yield
	PHS8	10	55.9	19.70	6.43	3.1	10.79	0.98	1.04	crush	1.21	crush
	PC1	10	25.1	8.25	4.09	2.0	4.94	1.19	1.17	yield	1.25	yield
Pang & Hsu	B1	19	45.2	5.51	2.53	2.2	4.16	0.99	0.90	yield	0.97	yield
	B2	19	44.1	8.00	5.56	1.4	6.44	1.04	1.04	yield	1.05	yield
	B3	19	44.9	8.00	2.56	3.1	4.58	1.06	0.99	yield	1.15	yield
	B4	19	44.8	14.05	2.55	5.5	5.33	1.09	1.12	yield	1.56	yield
	B5	19	42.8	14.01	5.52	2.5	7.58	1.12	1.16	yield	1.29	yield
	B6	19	42.8	14.01	8.30	1.7	9.84	1.05	1.05	crush	1.08	crush
Zhang & Hsu	VB1	13	98.2	9.78	5.30	1.8	7.86	0.99	0.92	yield	0.96	yield
	VB2	13	97.6	16.33	5.27	3.1	9.47	1.05	0.98	yield	1.14	yield
	VB3	13	102.3	26.61	5.32	5.0	10.13	1.11	1.17	yield	1.58	yield
	VB4	13	96.9	8.14	2.62	3.1	5.04	1.03	0.92	yield	1.07	yield
Total	**32**							**1- MCFT**	**2- Truss EC2 (rotating)**		**3- Truss EC2 (fixed)**	
	max value =	20	102.3	32.53	9.26	9.0	**Mean**	**1.06**	**1.07**		**1.26**	
	min value =	6	14.5	4.21	1.20	1.3	**SD**	**0.09**	**0.10**		**0.27**	
							COV %	**8.14**	**9.59**		**21.76**	

Note: a= maximum aggregate size; $r = \rho_x f_{xy} / \rho_y f_{yy}$
FM= predicted failure mode: "yield" = yielding of reinforcement in x and y directions
"crush" = strut crushing while yielding in the y direction

Table 5.2: Experimental database of shear panels with a predominant reinforced direction x (Case II, r>1)

5.3 Analytical modelling of shear panel tests

As discussed in chapter 2, several analytical methods for predicting the shear response of reinforced concrete members subjected to two-dimensional stress states have been proposed. Some of these methods such as the Modified Compression Field Theory (Vecchio & Collins [8]) or the Unified Theory of Reinforced Concrete (Hsu [114]), were derived from experimental data provided by shear panel tests. These theories, which are either based on a rotating or fixed crack concept can provide predictions of the full load-deformation response. On the other hand, plasticity truss approaches, which are also discussed in chapter 2, can be used in order to predict the ultimate failure load of the shear panels. In this section, the predictions of the ultimate shear strength of shear panels shown in Tables 5.1 and 5.2 using the MCFT and truss approaches suggested in EC2 are compared. The basic assumptions made for each method are discussed in the following sections.

5.3.1 Modified Compression Field Theory

The fundamentals of the MCFT are described in detailed in section 2.3. The predictions of the shear strength using the MCFT shown in Tables 5.1 and 5.2, were obtained by Bentz et al. [32] using software Membrane 2000 in order to solve the full set of equations given in section 2.3. The equation applied for the softening of the concrete in compression relates to early formula provided in Vecchio & Collins [8], see equations (2.9, 2.10) . In tension, latest version given by equation 2.13 was used in Bentz et al. [32] analysis. The strain at which the concrete crushes is assumed to be 0.002 and the aggregate size (a) was taken as zero for concrete strengths greater than 70MPa, as discussed in section 2.3. As shown in Bentz et al. [32] the predictions using the full set of equation defined in the MCFT were similar to those using the simplified approach, which is suggested in the Canadian code.

A preliminary analysis was carried by the author using the MCFT for shear panels tested by Vecchio & Collins [8]. This analysis was carried out before Bentz et al. [32] results were available to the author and were obtained using a spreadsheet. In this analysis the actual crushing strain of the concrete was used and the softening curve for compression adopted was the β(1993). In addition, the tension softening used corresponded to early formula given in the MCFT. Despite these differences with respect Bentz et al. [32] analysis, identical results were obtained to those shown in Tables 5.1 and 5.2.

5.3.2 Simple truss approaches

A simple truss model can be used to predict the shear strength of the panels. Two different alternatives can be adopted: rotating or fixed crack approach. In neither of these two methods the contribution of the tensile stresses in the concrete is taken into account. In addition, the stresses at the crack are not limited, which can result in the shear capacity being overestimated.

Rotating crack truss

The rotating crack truss model can be derived by considering equilibrium of the panel shown in Figure 5.3, thus obtaining equations (5.1) and (5.2).

$$D = \sigma_c . \cos\theta \qquad \ldots (5.1)$$

$$\tau_{xy} = D . \sin\theta = \frac{\sigma_c}{\cot\theta + \tan\theta} \qquad \ldots (5.2)$$

where D = diagonal compression force; σ_c = normal strut stress; θ = strut inclination

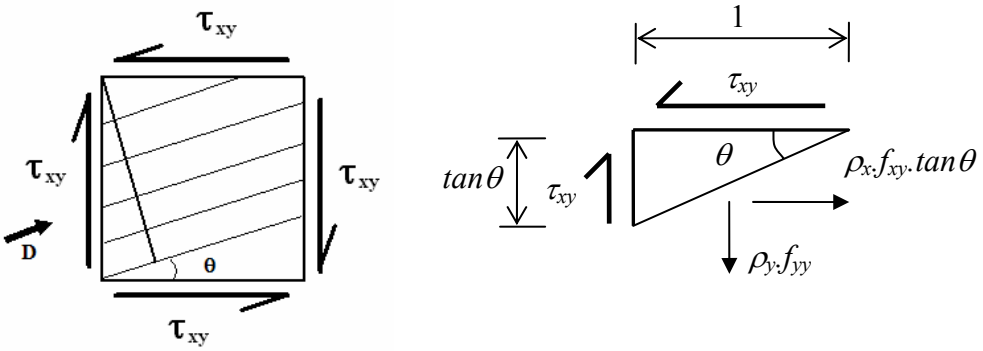

Figure 5.3: Rotating crack truss approach for shear panels; *Left*– Global forces; *Right*– Equilibrium of local stresses

The angle of the crack is assumed to be equal to θ in the rotating crack model and previous cracks are considered to be inactive. The crack is assumed to be stress-free as shown in Figure 5.3 (right).

Two types of failure modes are considered. Firstly, assuming that reinforcement bars in both x and y directions yield at failure, equilibrium conditions yield to equations (5.3) and (5.4).

$$\rho_x . f_{xy} . \tan\theta = \tau_{xy} \qquad \ldots (5.3)$$

$$\rho_y . f_{yy} = \tau_{xy} . \tan\theta \qquad \ldots (5.4)$$

Substituting (5.3) into (5.4), the inclination of the strut θ and the ultimate shear stress can be obtained as shown in equations (5.5) and (5.6) respectively.

$$\tan\theta = \sqrt{\frac{\rho_y . f_{yy}}{\rho_x . f_{xy}}} \quad \ldots (5.5)$$

$$\tau_{xy} = \sqrt{\rho_x . f_{xy} . \rho_y . f_{yy}} \quad \ldots (5.6)$$

For Case I where r=1 and θ=45º, equation (5.6) can be simplified to $\tau_{xy}=\rho f_y$ and $\sigma_c=2\tau_{xy}$.

The second failure mode considered is yielding in the weak direction y combined with concrete crushing. The ultimate shear stress and strut angle can be found for this failure mode by substituting equation (5.2) into (5.4) for σ_{cmax} and solving for θ and τ_{xy} hence obtaining equations (5.7) and (5.8). According to EC2, $\sigma_{cmax} = \nu f_c' = 0.6(1-f_c/250)f_c'$.

$$\tau_{xy} = \rho_y . f_{yy} . \cot\theta \quad \ldots (5.7)$$

$$\cot\theta = \sqrt{\frac{\sigma_{c\max} - \rho_y . f_{yy}}{\rho_y . f_{yy}}} \quad \ldots (5.8)$$

where $\rho_y f_{yy} \leq 0.5\sigma_c$

Fixed crack truss

An alternative approach is to adopt a fixed crack truss model in which the normal stresses on the crack equals zero at failure and that the shear retention factor β is constant. As shown in Figure 5.4, the fixed model needs shear stress (τ_{cr}) acting along the crack to maintain equilibrium, which does not limit the shear stress since β is assumed to be constant.

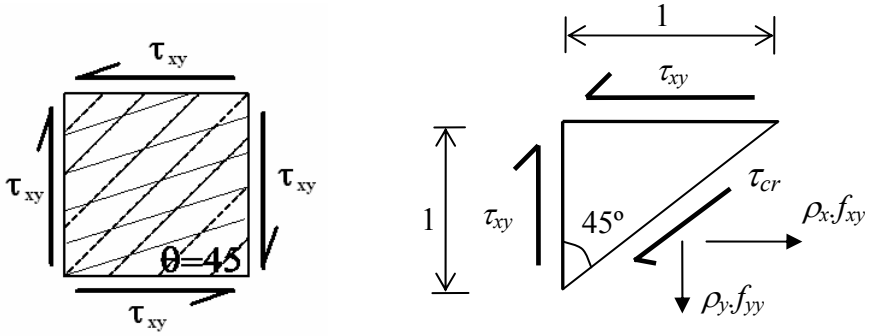

Figure 5.4: Fixed crack truss approach for shear panels; *Left*– Global forces; *Right*– Equilibrium of local stresses

The same failure modes were considered as in the rotating crack truss models. For a 45º initial crack shown in Figure 5.4 applying equilibrium conditions and assuming yielding of reinforcement in both directions, equations (5.9) and (5.10) are obtained for τ_{xy} and τ_{cr}.

$$\tau_{xy} = \frac{\rho_x . f_{xy} + \rho_y . f_{yy}}{2} \qquad \ldots(5.9)$$

$$\tau_{cr} = \frac{\sqrt{2}}{2} . \left(\rho_x . f_{xy} - \rho_y . f_{yy} \right) = \beta . \gamma_{cr} \qquad \ldots(5.10)$$

Failure mode which combines crushing of the strut while yielding of the reinforcement bars in the weak direction is again obtained from substituting equation (5.2) into (5.4) for θ=45º. This yields to equations (5.11) and (5.12).

$$\tau_{xy} = \frac{\sigma_{c\max}}{2} \qquad \ldots(5.11)$$

$$\tau_{cr} = \sqrt{2} . \left(\tau_{xy} - \rho_y . f_{yy} \right) \qquad \ldots(5.12)$$

where σ_{cmax}(EC2) = $\nu f_c'$ = 0.6(1-f_c/250)f_c'

It can be easily demonstrated that for panels equally reinforced in both directions, the rotating or fixed crack approaches provide identical solutions. In addition, the critical value of $\rho f_y / \nu f_c'$ which divides both failure modes investigated (rebar yielding and strut crushing) is 0.5 for panels in Case I (see Figure 5.5). This is in agreement with Bentz et al. [32], in which the shear stress in this type of panels is generally assumed to be equal to ρf_y until a ceiling value of $0.25 f_c'$ (~$0.5 \nu f_c'$). For panels with one predominant reinforcement direction the line that divides both types of failure according to the simple rotating truss model suggested in EC2 is defined by $\rho_x f_{xy} / (\nu f_c' - \rho_y f_{yy})$=1, as shown in Figure 5.6.

Typical examples of a crushing type of failure are shown in Figure 5.1 and 5.2 (left) for specimens PV20 and PV27 respectively. Figure 5.2 (right) shows the failure of panel PV19 due to yielding of reinforcement in both directions. As shown in Tables 5.1 and 5.2, both types of failure mode observed agreed with the predicted failure mode.

5.3.3 Results: MCFT vs. Simple truss approaches

The predictions of the shear strength using either the MCFT or simple truss approaches are summarised in Tables 5.1 and 5.2 for Cases I and II respectively. Despite secondary aspects such as potential slippage between loading platen and panel or bond-slip between reinforcement bars and concrete are neglected, accurate predictions were obtained using both MCFT and the simple truss approaches described in previous section.

For Case I panels, both rotating and fixed truss approaches provided identical results. In addition, MCFT and simple truss predictions for panels which failed due to yielding of the reinforcement were identical, as shown in Figure 5.5. However, panels which were predicted to be limited by crushing of the strut, the shear strength obtained experimentally lay between MCFT and truss predictions (Figure 5.5). This is in agreement with the model assumptions since the truss model neglects the tensile strength of the concrete. It is noteworthy that although the predictions from the simple truss approach were conservative, the results can be considered acceptable with a mean τ_{calc}/τ_{test} ratio of 0.90 and a coefficient of variation of 11.6% (see Table 5.1).

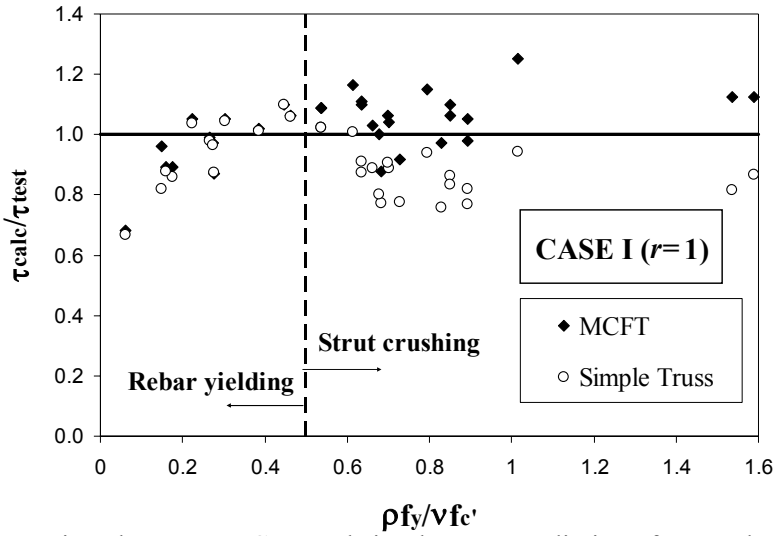

Figure 5.5: Comparison between MCFT and simple truss predictions for panels equally reinforced in both *x* and *y* directions (Case I)

As shown in Table 5.2 and Figure 5.6, the fixed crack approach overestimated the shear strength of the panels with predominant reinforcement in one direction (Case II). Worse predictions were obtained for panels with both low $\rho_y f_{yy}$ stresses (~2MPa) and large values of *r* (greater than 5). In these panels, the strut rotation would be highest. Hence, the fixed truss model becomes less accurate since it does not impose a limit on the shear transmitted at a crack. On the contrary, the MCFT limits the shear carried at the crack

depending on the crack opening and type of aggregate, which seem to provide more accurate predictions than the simple fixed crack truss model, as shown in Figure 5.6. The simple rotating truss model provided similar predictions to the MCFT as shown in Table 5.2 and Figure 5.6, regardless of the type of failure mode predicted. This is remarkable considering the large differences between the formulations.

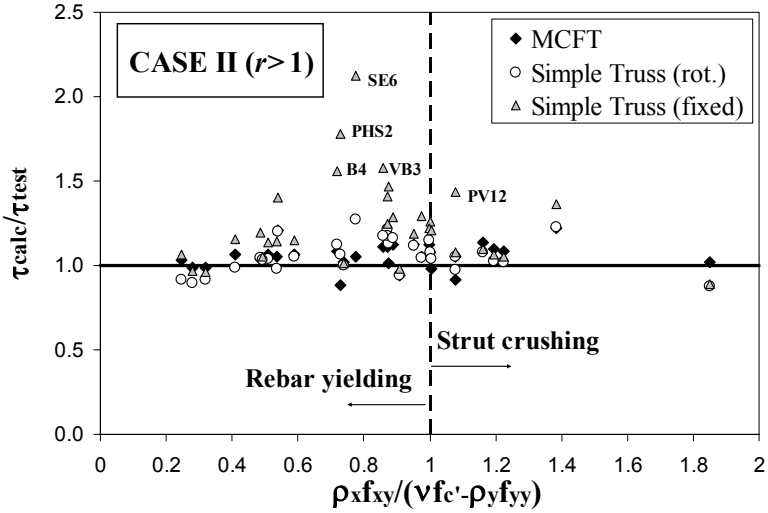

Figure 5.6: Predictions of ultimate shear strength of panels in Case I (r=1)

In panels where strut rotation was expected, the MCFT provided larger values of the angle θ than those predicted using the rotating truss model, as shown in Figure 5.7 for specimens PV12, PV18, PV19 and PV20. The reason behind this is that unlike the MCFT, truss models neglect the tensile strength of the concrete.

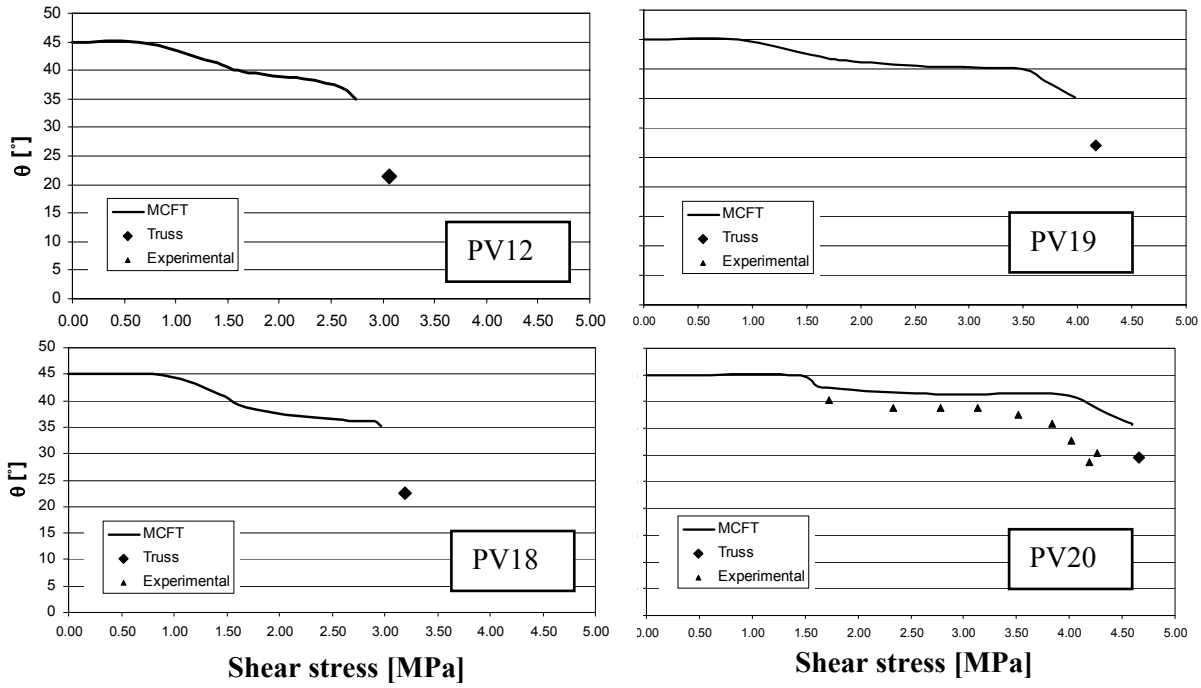

Figure 5.7: Development of strut inclination according to MCFT and truss approach

The influence of changing the aggregate size on the MCFT predictions was investigated in panels with a predominant reinforced direction. Four panels were selected from Table 5.2 (PHS2, SE12, SE13, VB3) which had concrete strengths from 66.1MPa to 102.3MPa. According to the MCFT the shear stress along the crack surface v_{ci} was governed by the threshold value v_{cimax} in these panels. As discussed in section 2.3, the value of v_{cimax} depends on the concrete strength, crack opening and aggregate size. The shear strain-stress curves for these panels are shown in Figure 5.8. Point A labelled in Figure 5.8, represents the load at which v_{ci} is limited to v_{cimax}.

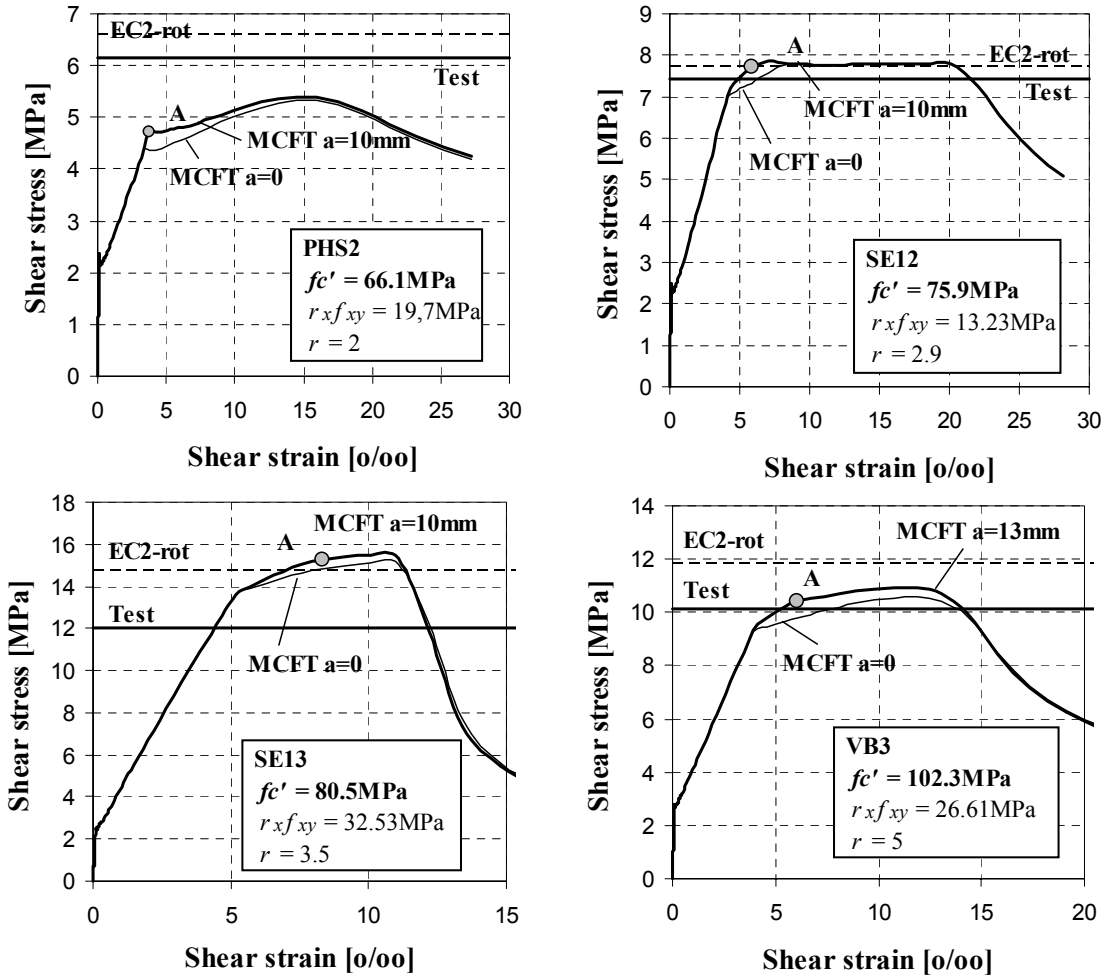

Figure 5.8: Predicted shear strain-stress curves for high-strength concrete panels with predominant reinforcement in the *x* direction; influence of aggregate size assumed

As shown in Figure 5.8, the influence of reducing the aggregate size using the MCFT was insignificant, although the prediction of panels with f_c' greater than 70MPa was slightly improved by taking *a* equal to zero. The ultimate strength reduced slightly when decreasing the aggregate size *a*, from the maximum diameter of the coarse aggregate to zero.

The types of failure predicted by the MCFT and rotating truss model were identical for panels SE12 and SE13. The former was predicted to fail by yielding of both reinforcement bars *x* and *y* since $\rho_x f_{xy}/(\nu f_c' - \rho_y f_{yy})$=0.48<1, while the latter was expected to failed by strut crushing combined with yielding of the reinforcement in the *y* direction, $\rho_x f_{xy}/(\nu f_c' - \rho_y f_{yy})$=1.38>1.

On the other hand, panels PHS2 and VB3, with intermediate values of $\rho_x f_{xy}/(\nu f_c' - \rho_y f_{yy})$ equal to 0.73 and 0.85 respectively, the predicted failure mode from the MCFT and rotating truss model were different. According to the MCFT, panel PHS2 would fail due to crushing of the strut while in VB3 yielding of both reinforcement bars would occur. The results shown in Figure 5.8 suggest that the MCFT failure mode prediction seems more sensible than the rotating crack approach for panel VB3 but not in panel PHS2, where the MCFT tends to underestimate the ultimate shear strength.

5.4 Non-linear finite element modelling of shear panels

5.4.1 General aspects

In this section, some of the smeared cracking models commonly used in non-linear finite element modelling, which are described in chapter 3, were used in order to predict the shear response of panels in pure shear. One of the aims of this analysis was to find whether similar predictions to the MCFT could be obtained using other types of smeared cracking models. Moreover, the analysis was used to validate these smeared crack models against simple shear stress state scenarios before implementing them into more complex FE models for the analysis of short span and slender beams (see chapters 7 and 8).

The NLFEA was carried out using DIANA with an incremental-iterative solution technique (fixed size increment steps and Newton-Raphson solver for the iterations). Similarly as Vecchio [123], shear panels were modelled using a single 4 noded element (Figure 5.9) since both stress and material conditions were homogeneous throughout the member. The accuracy of the predictions was comparable to that obtained by authors such as Broo et al. [124], in which a more complex mesh was adopted. Point loads were applied at the nodes (Figure 5.9) to simulate the constant shear stress state at the panel.

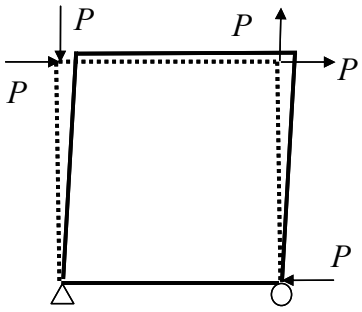

Concrete strain-stress curves for NLFEA (refer to section 3.3)

- Compression:
  Symmetrical parabola (Hognestad)
- Compression softening:
  β(1993) or constant reduction factor
- Tension:
  Equation 2.13

Figure 5.9: Finite element mesh of shear panels in pure shear (4 noded element with linear interpolation and Gauss integration) and concrete strain-stress curves assumed in the NLFEA

The steel reinforcement was modelled using an embedded smeared grid, although discrete embedded reinforcement elements provided identical results in this case. A perfect plastic Von Misses constitutive law was adopted for steel. Two types of smeared crack models were investigated for concrete: total strain (rotating and fixed crack) and multi-directional fixed crack model; for full detail of these models refer to section 3.3.

In order to obtain comparable results with the MCFT, equivalent constitutive equations (see Figure 5.9) and parameters were provided for each procedure. Therefore similar

solutions were expected from this analysis. To consider compression softening due to transverse strains, Vecchio & Collins [25] formula (see Figure 2.6) was applied in the total strain models via the built-in algorithm (VC1993) included in DIANA. In the multi-fix model different reduction factors were applied to study this effect. In general, the shear retention in the total strain fixed and multi-fix models was taken as 0.1.

5.4.2 Summary of results

Case I: Shear panels with equally reinforced directions

As mentioned in section 5.2, panels with equal amounts of reinforcement in both *x* and *y* directions are only subjected to compression softening due to transverse cracking. Two representative cases are shown here which relate to panels PV27 and PV6 (Vecchio & Collins [8]); crushing of the strut was critical for panel PV27 while yielding of the reinforcement was expected for panel PV6, as shown in Table 5.2.

The types of failure modes were satisfactory reproduced both FE models investigated as shown in Figures 5.10 and 5.11. However, important remarks regarding parameters assumed in the models must be made. Looking at panel PV27, in which the softening of concrete in compression governed the shear behaviour, it can be seen that neglecting this effect can lead in some cases to a clear overestimation of the shear strength. Moreover, it can result in the prediction of a different failure mode, as shown in Figure 5.10 (right). In Case I panels, total strain models using either a fixed or rotating approaches provided identical predictions. Another important aspect, which was discussed in section 3.3, is that the Poisson ratio (ν) must be taken as zero in the total strain models; otherwise the shear strains are clearly overestimated in the element, as shown in Figure 5.10 (right).

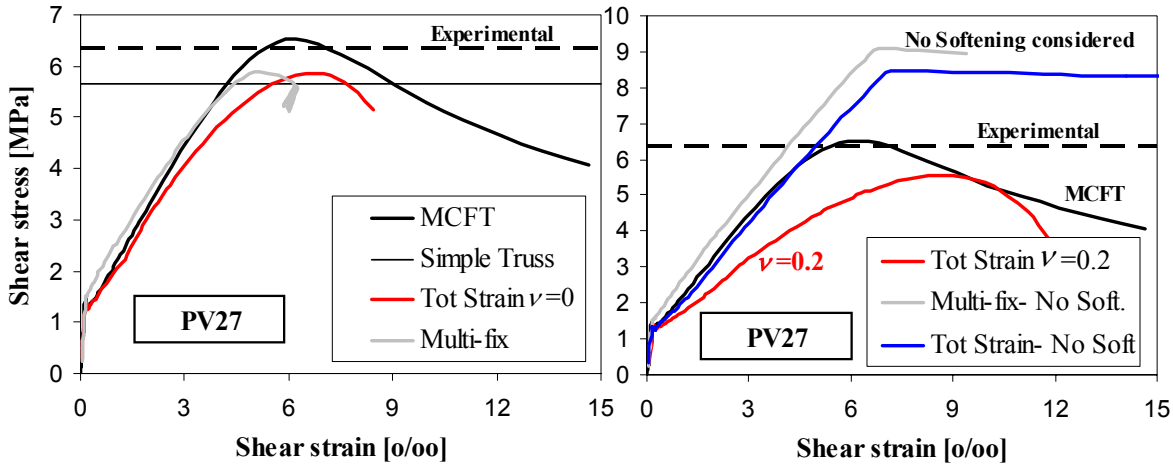

Note: Compression softening factors assumed (*left*) – multi-fix model $\nu f_c^{'}$; total strain $\beta(93)$ see Figure 2.6

Figure 5.10: FE predictions of panel PV27; *Left*– Valid models; *Right*– Incorrect assumptions

As shown in Figure 5.10, similar predictions were obtained using the multi-fix, total strain, MCFT and simple truss approaches. In the multi-fix approach, the strength of the concrete was reduced by conventional plasticity "effectiveness" factor $\nu = 0.6(1-f_c'/250)f_c'$ (EC2). As discussed in sections 2.3 & 3.3 this "effectiveness" value, which provided sensible predictions for this particular case, is considerably lower than the reduction factors proposed by authors such as Reineck [40]. It is questionable whether it is realistic to use the same concrete reducing factors for single elements in pure shear and elements found in dense meshes with more complex biaxial stress states since previous cracks can influence the strength of the struts.

Panel PV6 was predicted to fail due to yielding of the reinforcement, as shown by the strain-stress curve in Figure 5.11 (left). As reported by Hsu [125], in such types of panels NLFE models tend to overestimate the yield strength since the increment of stresses in the reinforcement at the crack is not considered. Similar problem is obtained in Case II panels in which failure is due to yielding of reinforcement bars in both directions, see Figure 5.11 (right). In this work, a sensible prediction of these shear panels was obtained by reducing the yield strength of the reinforcement bars by a factor of 0.75, as shown in Figure 5.11. MCFT or simple rotating truss models provided more accurate predictions than the NLFEA for panels governed by yielding of the reinforcement. An alternative method to reducing the yield strength of the reinforcement would be modifying the tension softening curve for concrete, although both approaches are approximate solutions.

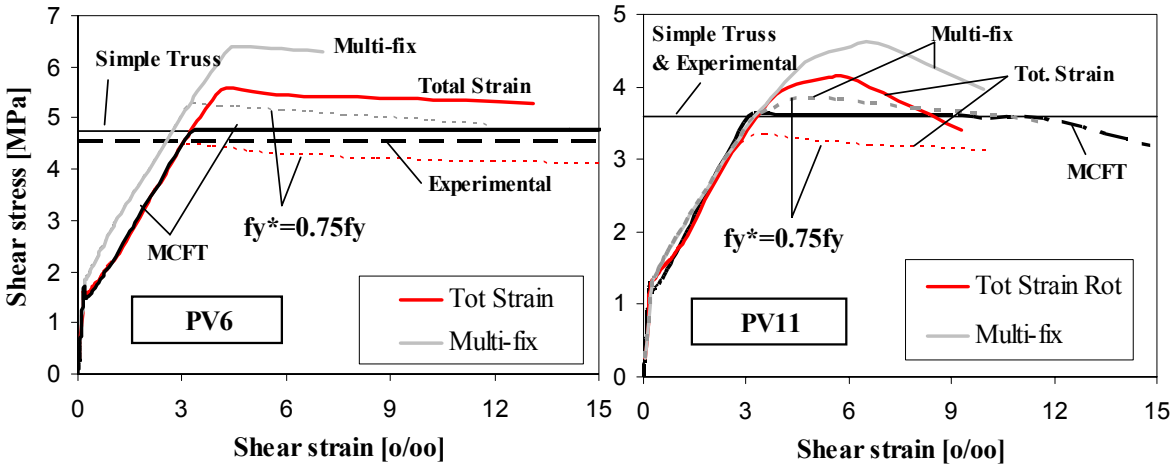

Note: Total strain rotating and fixed models provided identical predictions for both panels

Figure 5.11: FE predictions of shear panels in which yielding of reinforcement was critical; *Left*– Panel PV6 (Case I); *Right*– Panel PV11 (Case II); refer to Table 5.1 and 5.2 respectively

Case II: Shear panels with predominant reinforcement in the x direction

The predictions for the Case II panels, which were governed by crushing of the strut while yielding of the reinforcement in the weak direction, were similar using either NLFE total strain models or MCFT (Figure 5.12). On the other hand, multi-directional fixed crack model tended to overestimate the ultimate strength if same reduction factor $\nu = 0.6(1-f_c'/250)f_c'$ used for Case I panels was applied. This seemed to worsen for panels with larger strut rotation, such as PV12 (r =7). The results using this model are referred to as "Multi-fix" in Figure 5.12.

The considerably larger level of softening adopted by the MCFT, which had a reduction strength factor of around 0.45, provided more accurate predictions for these panels compared to using the effectiveness factor $\nu = 0.6(1-f_c'/250)f_c'$. As shown in Figure 5.12, the predictions of the multi-fix model can be improved for these panels by assuming this reduction factor of 0.45 for f_c' in combination to reducing f_{yy} by 0.75, as discussed in previous section; the results are denoted as "Multi-fix (modified)" in Figure 5.12.

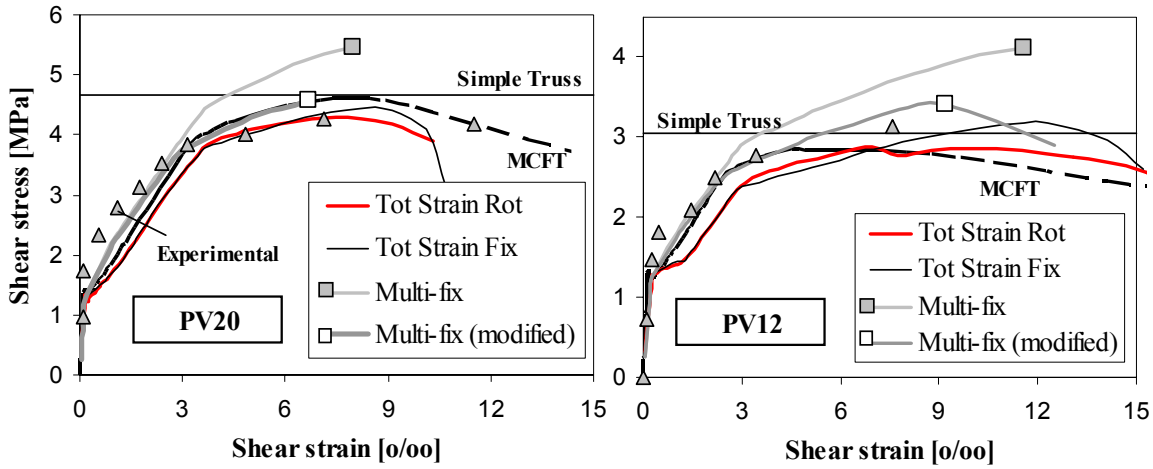

Note: Reduction of concrete strength in "Multi-fix" model of $\nu f_c'$
In Multi-fix (modified) concrete strength and yield strength of y-reinforcement has been factored by 0.45 and 0.75 respectively

Figure 5.12: FE predictions of Case II panels failing due to crushing of the strut while yielding of the reinforcement in the y direction; *Left*– Panel PV20 (r =3.1); *Right*– Panel PV12 (r =7)

In view of these results it seems that total strain models are more suitable to simulate shear panels with large reorientation of stress fields than the multi-directional fixed crack approach. Surprisingly, both rotating and fixed total strain models provided comparable results. However, this was not the case if the shear retention factor in the total strain fixed crack model was increased from 0.1, which was the initial value adopted in the NLFEA. Figure 5.13 shows the increase in the ultimate strength due to increasing shear retention

factor β in the total strain fixed models. The increase seems to be larger for panel PV12 since larger strut realignment took place. The value of β equal to 0.1, which is commonly adopted in the NLFE models developed in this work, provided optimal predictions as illustrated in Figure 5.13.

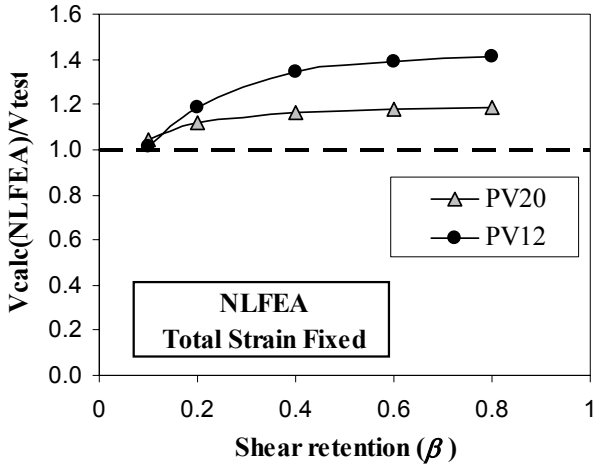

Figure 5.13: Influence of shear retention factor assumed in NLFEA using total strains fixed crack model (panels PV20 and PV12)

5.5 Discrete crack approach: Crack slip model

In order to assess the influence of neglecting the stresses at previous cracks, a discrete approach using a crack slip model has been derived by the author. The model assumes that the shear strength can be limited by shear transfer across cracks. As recognized by Vecchio [29], models such as the Disturbed Stress Field Model (DSFM, [29]), in which the crack slip is taken into account directly, are numerically demanding. Hence, several simplifications were adopted in the discrete model presented in this section to keep the analytical model practical. Whilst simple, the approach seems rational and can provide sensible predictions. Moreover, the crack slip model can be implemented with few modifications to study the development of crack displacements and stresses in continuous beams as shown in section 8.3.3.

5.5.1 General assumptions

The crack slip model is a discrete approach in which strains are obtained in terms of relative crack displacements i.e. slip (s) and opening (w), neglecting deformation within the concrete for a first estimation. A single square element is isolated from the crack with a size of $L=S_\theta/(2sin\theta)$, as shown in Figure 5.14. The furthest point of the element from the crack corresponds with the location of the maximum tensile stress i.e. midpoint between two consecutive cracks.

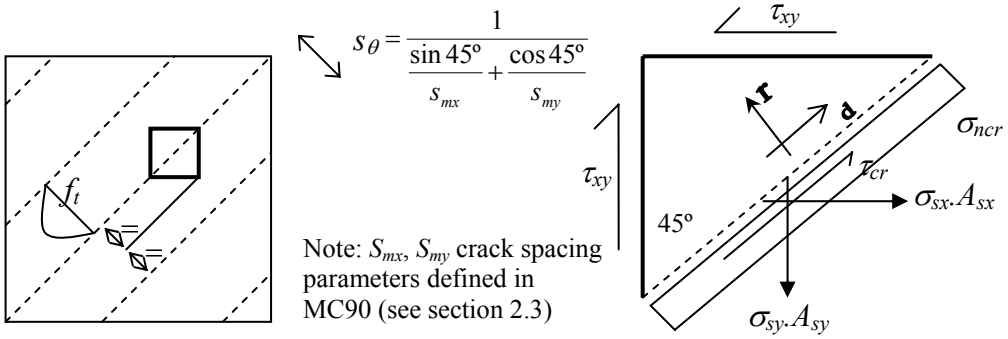

Figure 5.14: Crack slip model; Left– Isolated element; Right– Equilibrium at the crack

Only pure shear conditions are considered, without axial tension nor compression. In this section, the formulas are derived by imposing compatibility and equilibrium conditions at cracks, which have an inclination of 45º (Figure 5.14). This is the general case of cracks that form at early load stages in a shear panel or in the web of a simply supported beam. In section 8.3.3, these formulas are generalized for different crack inclinations, in order to apply them to continuous beams, where the shear cracks were considerably flatter than 45º.

5.5.2 Equilibrium and compatibility conditions

The strains generated in the element for a given relative displacement w (crack opening) in the local r-direction, see Figure 5.15 (left), are given by equations (5.13) to (5.15).

$$\varepsilon_{rcr} = \frac{w}{\sqrt{2}.L} \text{ and } \varepsilon_{dcr} = 0 \quad \ldots (5.13)$$

$$\gamma_{cr} = \varepsilon_{rcr} - \varepsilon_{dcr} = \varepsilon_{rcr} \quad \ldots (5.14)$$

$$\varepsilon_{xcr} = \frac{w}{\sqrt{2}.L} \text{ and } \varepsilon_{ycr} = \frac{w}{\sqrt{2}.L} \quad \ldots (5.15)$$

where r-d are local crack directions, $L=S_\theta/\sqrt{2}$, w = crack opening, s = crack slip, and tension is considered positive. Crack spacing S_θ is estimated as shown in Figure 5.14, assuming that crack parameters s_{mx} and s_{my} are 1.5 times the maximum distance between reinforcement bars (Vecchio & Collins [8]).

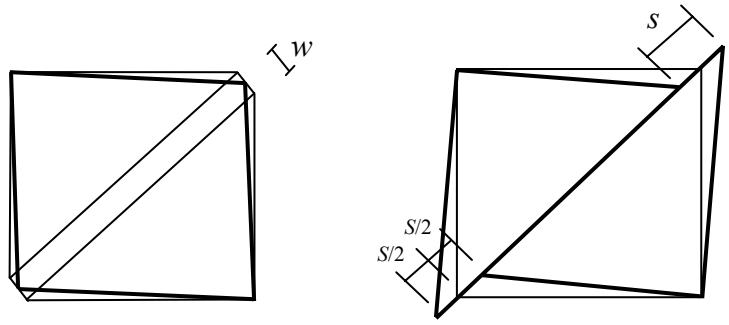

Figure 5.15: Strains generated due to normal and shear relative crack displacements; *Left*– Opening relative displacement (w); *Right*– Slip relative displacement (s)

In the same manner for a relative displacement s in the d-direction, see Figure 5.15 (right), the strains obtained for this case are given by equations (5.16) and (5.17).

$$\varepsilon_{rcr} = \varepsilon_{dcr} = \gamma_{cr} = 0 \quad \ldots (5.16)$$

$$\varepsilon_{xcr} = \frac{s}{\sqrt{2}.L} \text{ and } \varepsilon_{ycr} = \frac{-s}{\sqrt{2}.L} \quad \ldots (5.17)$$

Unlike the simple truss approaches, which are described in section 5.3.2, the crack is no longer stress free. The shear and normal stresses can be calculated by considering equilibrium in the element (Figure 5.14), which yields to the following expressions:

$$\sigma_{ncr} + \tau_{xy} = \tau_{cr} + \sigma_{sx}.\rho_x \quad \ldots (5.18)$$

$$\sigma_{ncr} + \tau_{xy} = \sigma_{sy}.\rho_y - \tau_{cr} \quad \ldots (5.19)$$

The normal and shear stresses at the crack (σ_{ncr}, τ_{cr}) in equations (5.18) and (5.19), can be written in terms of the crack opening and slip, using any of the formulations based on the deformation theory, which are described in chapter 2 (section 2.5.2). Five of these models were validated in section 4.5, using push-off test data obtained in this work. In view of the results presented in chapter 4, the linear aggregate interlock relationship (Walraven & Reinhardt [46]) was finally adopted for the crack slip model. This constitutive equation for aggregate interlock has also been adopted in other discrete crack approaches, such as the already mentioned DSFM (Vecchio [29]).

In equations (5.18) and (5.19), the steel stresses σ_{sx} and σ_{sy} can also be written in terms of the crack slip and opening, as shown in equations (5.20) and (5.21). Term E_{sm} in equations (5.20) and (5.21) is the enhanced value of the Young's modulus for steel, which takes into account the contribution of cracked concrete to steel strength (tension stiffening). In order to estimate E_{sm}, approach proposed by Hsu [114] for embedded reinforcement could be used or alternatively a derived value for E_{sm} from the MCFT. For simplicity, an approximate value of 1.5 times E_s was finally adopted, where E_s =200000MPa.

$$\sigma_{sx} = \min\left[f_{xy}, E_{sm}\left(\frac{w}{\sqrt{2}.L} + \frac{s}{\sqrt{2}.L} \right) \right] \quad \ldots (5.20)$$

$$\sigma_{sy} = \min\left[f_{yy}, E_{sm}\left(\frac{w}{\sqrt{2}.L} - \frac{s}{\sqrt{2}.L} \right) \right] \quad \ldots (5.21)$$

where E_{sm} = enhanced value of Young's modulus (=1.5E_s), f_{xy}–f_{yy} = yield strength of reinforcement bars in the x–y direction

The crack opening and sliding can be solved numerically implementing equations (5.13) to (5.21) into a spreadsheet. The inclination of the principal compression stress θ can be calculated from Mohr's circle knowing points A($\sigma_{sx}\rho_x$, τ_{xy}) and B($\sigma_{sy}\rho_y$, -τ_{xy}), as shown in equation (5.22).

$$\cot\theta = \frac{1}{2}\left[\frac{\sigma_y - \sigma_x}{\tau_{xy}} + \sqrt{\left(\frac{\sigma_y - \sigma_x}{\tau_{xy}} \right)^2 + 4} \right] \quad \ldots (5.22)$$

where $\sigma_x = \sigma_{sx}\rho_x$ and $\sigma_y = \sigma_{sy}\rho_y$

5.5.3 Crack slip model predictions of shear panel tests

The discrete crack slip model described in previous section was applied to estimate the shear response of panels tested by Vecchio & Collins [8], see Table 5.2. Despite the initial assumptions made, the results are quite favourable, especially for panel PV20, where the predictions of the shear strains seem even better than those given by MCFT, as shown in Figure 5.16.

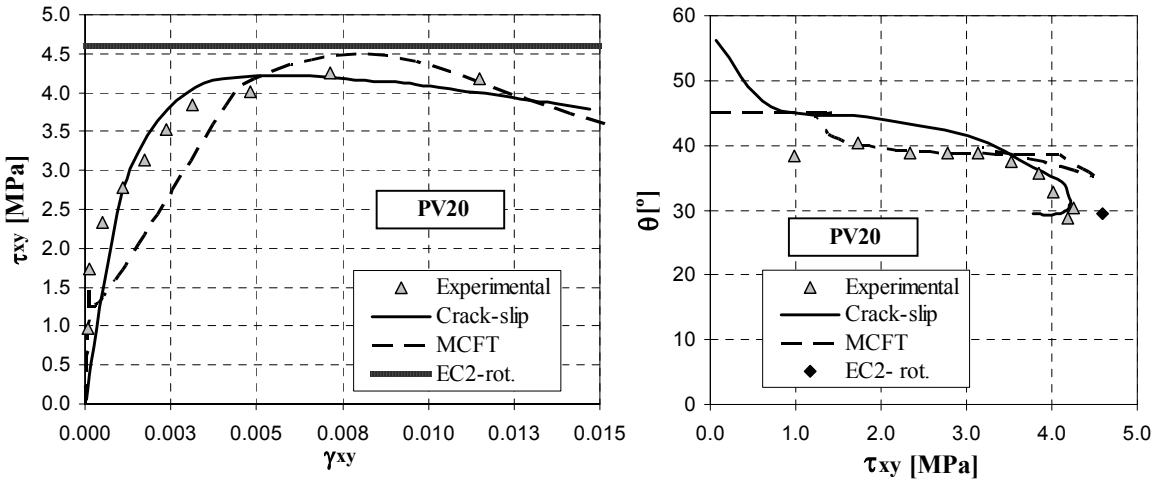

Figure 5.16: Predictions for shear response of panel PV20; MCFT, Crack slip and Truss models

The predictions of the ultimate strength obtained using the crack slip model were reasonable for the eight panels investigated, as shown in Figure 5.17. However a slightly larger coefficient of variation was obtained (11.8%) compared with MCFT and simple truss rotating model, which had a COV of around 7%. The results for ultimate loads, crack displacements and inclination of strut at failure are also shown in Figure 5.17.

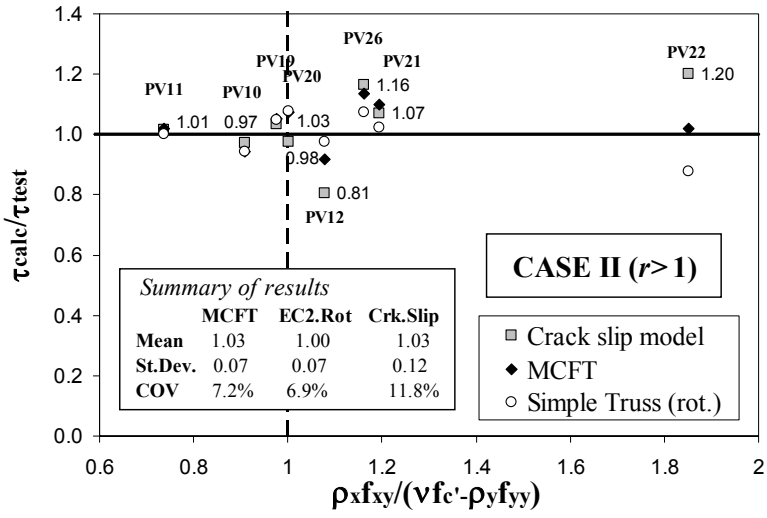

Panel	Sθ [mm]	Wult [mm]	Sult [mm]	θ [°]
PV11	49	0.10	0.04	40.60
PV10	49	0.15	0.08	37.02
PV19	72	0.30	0.21	32.12
PV20	49	0.18	0.25	31.53
PV12	78	0.30	0.22	26.06
PV26	49	0.15	0.08	37.27
PV21	49	0.25	0.17	34.93
PV22	49	0.07	0.15	41.45

Note: w_{ult}, s_{ult} = crack opening and slip at peak load

Figure 5.17: Crack slip model predictions of shear panels tested by Vecchio & Collins [8]

The shear strain-stress curves of panels PV19 and PV12 are shown in Figure 5.18. These panels have considerably less reinforcement in the *y* direction than panel PV20 shown in Figure 2.16. The shear strength of panel PV12 was underestimated using the crack slip model or MCFT. As mentioned in section 5.4.1, this panel had a significantly greater value of $r = \rho_x f_{xy} / \rho_y f_{yy} = 7$ compared with the remaining panels, in which *r* ranged from 1.5 to 4. The larger strut rotation expected in this panel was in agreement with the lower strut angle θ shown in Figure 5.17 for PV12.

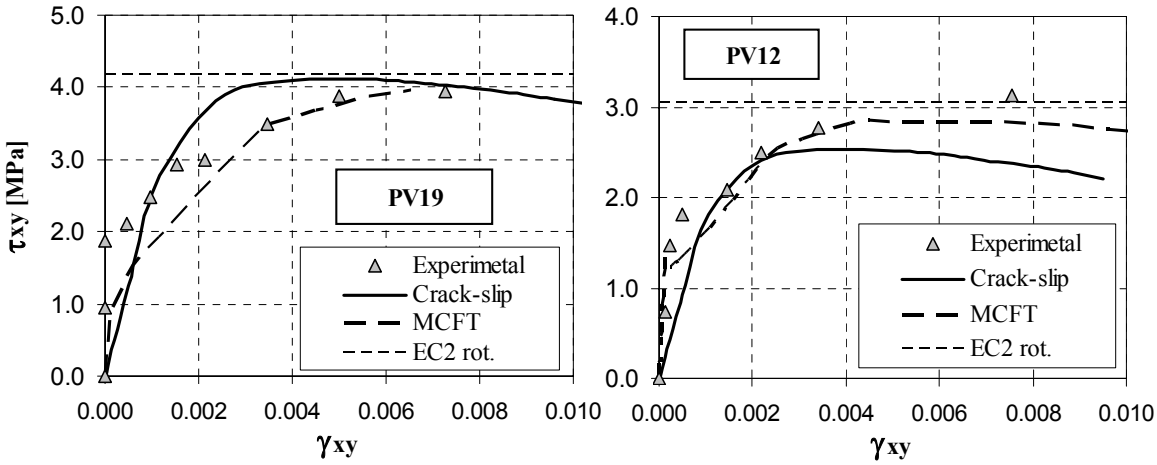

Figure 5.18: Shear strain-stress predictions using MCFT and crack slip model (PV19 and PV12)

The predictions of the shear response using the crack slip model are not realistic for early load stages as shown in Figures 5.16 and 5.18. This is due to the fact that in the crack slip model the un-cracked state was not taken into consideration. As discussed in chapter 8, this assumption is equivalent to assuming that the specimen is pre-cracked in shear.

5.6 Conclusions

Although shear panel tests are complex in terms of execution, the experimental data obtained is considerably easier to interpret than results gathered from traditional beam tests. A pure shear stress state in the concrete member can be attained in these panel tests, which can be helpful to obtain a better understanding in the contribution to shear behaviour of aggregate interlock and compression softening due to transverse cracking.

The extensive database gathered by Bentz et al. [32] of experimental results from several researchers, shows that MCFT can predict accurately the response of shear panels in pure shear. Moreover, the simplified MCFT formulas proposed by Bentz. et al. [32] can also be used in order to assess the ultimate strength by simple hand calculations. The alternative simple truss models presented in this chapter, which are based on either a rotating or fixed crack concept, can provide equally accurate strength predictions for panels with the same reinforcement in each orthogonal direction. On the other hand, panels with one predominant reinforced direction (Case II) only the simple rotating truss approach provided accurate predictions, which are comparable to those obtained using the MCFT. The inclination of the strut was found to be steeper using the MCFT than the rotating truss model in the panels investigated.

Two types of failure modes were usually observed, which referred to yielding of the reinforcement or crushing of the strut. In Case II panels, the crushing of the strut occurs in combination with yielding of the reinforcement in the weak direction, which is followed by a stress fields rotation and mobilization of the aggregate interlock action. In general, the predicted failure mode was identical for MCFT and simple truss approaches, which was in agreement with experimental evidence.

The influence of changing the aggregate size (a) in the MCFT predictions of the shear panels constructed with high-strength concrete was insignificant. Nevertheless, reducing a from the maximum diameter of the course aggregate to zero for concretes with f_c' greater than 70MPa, as recommended in the Canadian code, gave a slight improvement in the predictions. However, no information regarding the type of aggregate used or whether it had fractured at the crack was available for the panels studied.

It has been shown that the response of shear panels can also be predicted carrying a NLFEA using a single element mesh, in which some of the smeared crack approaches described in chapter 3 were adopted (Total strains and Multi-directional fixed crack

models). Despite the different formulations applied in each of these smeared crack approaches (fixed/rotating, total strain/strain decomposition with plasticity), comparable predictions can be obtained to MCFT, if equivalent parameters and constitutive strain-stress relationships are provided. The NLFEA showed the importance of adopting consistent values for the different parameter required in the models, such as the Poisson ratio (ν) or shear retention factor (β). Optimal predictions using the total strain fixed crack model were obtained using values of ν=0 and β=0.1.

The results from the NLFEA of shear panels indicated that compression softening due to transverse strains must be taken into account in order to obtain reasonable predictions. The predictions of Case II panels, in which failing was governed by concrete crushing, were in general more accurate using total strain models, which are formulated in a similar fashion as the MCFT, than the multi-fix model. The strength of these panels was slightly overestimated using the multi-fix model which was surprising since a considerably low reduction factor for the concrete strength was applied ($\nu f_c'$). However, the same "effectiveness" factor applied to similar panels with equal amounts of reinforcement in both orthogonal directions, showed to be adequate using the multi-fix model. It remains questionable whether this low constant factor is suitable for this case only or it can be applied to more advanced stress state conditions. The strength of panels failing due to yielding of the reinforcement was overestimated by the NLFE models. This was expected since the increase of stresses in the reinforcement at cracks is not considered; a reduction factor for the yield strength of 0.75 was found to provide reasonable predictions. An alternative method would be to modify the tension softening behaviour of the concrete.

Lastly, the discrete crack slip model presented in this chapter shows a simple whilst rational approach to assess the limit case where the behaviour is governed by shear stresses along cracks. More sophisticated models such as the DSFM [29], have been developed, in which the crack slip is also taken into account. Despite the large number of simplifications adopted in the model presented here, reasonable predictions of the shear strain-stress response were obtained for the panels investigated. The ultimate shear strengths were similar to those obtained using both MCFT and simple truss approaches, although a slightly larger COV was observed. Once the model had been validated for the particular case of shear panels in pure shear, the model was adapted for estimating stresses and displacement at critical shear cracks at webs of continuous beams (section 8.3.3.).

CHAPTER 6 – Beam Tests

6.1 Introduction

This chapter summarises the experimental results and testing methodology of 22 beam tests carried out by the author in the Heavy Structures Laboratory at Imperial College London. The experimental results are discussed in further detail and compared with analytical/numerical predictions in chapters 7 and 8. The main goal of these tests was to investigate the influence of aggregate fracture on shear strength of reinforced concrete beams for different types of loading. Tests included beams with and without shear reinforcement. Shear span to effective depth ratios (*a/d*) of 1.5 and 3.5 were investigated, which relate to short span and slender beams respectively. The different tests series are summarised in Table 6.1. Previous experimental data was available in the literature regarding slender beams without shear reinforcement focusing on the type of aggregate (see Regan [4]); hence this type of test was chosen as the starting point of the experimental programme. Beams B0 were designed using a similar geometry and load configuration as tests carried out by Regan [4], which included beams with different types of aggregate.

Beams	*a/d*	Stirrups?	Type of Loading
AG0; AL0	1.50	no	Simply supported
AG2, AG3, AG4; AL2, AL3, AL4	1.50	yes	Simply supported
BG01, BG02; BL01, BL02	3.46	no	Simply supported
BG1, BG2; BL1, BL2	3.52	yes	Continuous beam
CB1, CB2; CA1, CA2	3.52	yes	Continuous beam
DB1; DA1	3.68	yes	Simply supported

Note: Beams A and B- prefix “G” stands for gravel and “L” limestone aggregate concretes
Beams C and D- (gravel aggregate concrete); prefixes “A” and “B” stands for steel class (stirrups)

Table 6.1: Summary of experimental work (beam tests)

Beams A and B were constructed in pairs using two types of aggregate (gravel and limestone); which are denoted as "G" and "L" respectively. The crack surfaces in the limestone specimens were smooth due to splitting of the course aggregate at the crack. The main parameters investigated in beams C-D, which were cast using normal gravel aggregate, were the amount of shear reinforcement and the class of steel used in the stirrups. Beams B-C were loaded with a point of contra-flexure while the remaining beams were simply supported. Beams C-D were not included in the original test programme. However, the undesired concrete strength variations obtained in beams B and the interest of studying the effects of the type of loading, motivated testing beams C-D.

6.2 Material properties

6.2.1 Reinforcement

The reinforcement used for manufacturing beams A and B was hot-rolled round deformed high yield steel bars (T). Two samples of each bar diameter (8mm and 25mm) were tested to calculate the yielding strength. The yield strength, which was obtained using the 0.2% offset rule, was found to be different for the T8 bars and T25 bars, 550MPa and 580MPa respectively. The stress-strain diagrams are plotted in Figure 6.1.

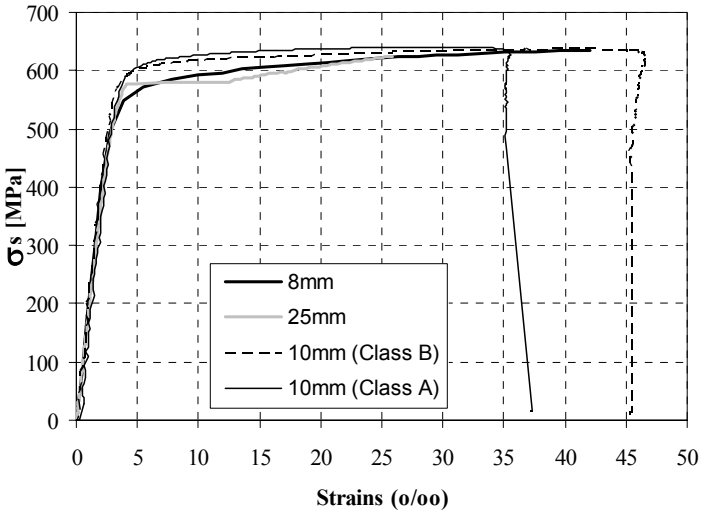

Figure 6.1: Stress-strain diagrams for T8 and T25 reinforcement bars

Beams C and D were constructed using 10mm diameter stirrups, with either class A or B steel, according to EC2 classification. Both types of steel had similar yield strength (f_y=600MPa) but class A had a more brittle behaviour (Figure 6.1).

The amount of reinforcement provided in the beams was designed using EC2 and BS8110 to avoid flexural and local failures. The design was verified by performing a non-linear finite element analysis, which corroborated that longitudinal reinforcement, would not

yield for the design concrete strength assumed. Sufficient anchorage length was provided with straight bars adding in each end four extra stirrups spaced 120mm.

6.2.2 Concrete

Beams A and B were designed for a cylinder concrete strength of 60MPa, although several deviations from this target were obtained due to errors from the Readymix suppliers. Beams C and D were designed for a cylinder concrete strength of 40MPa. Two types of course aggregate were used for beams A and B; namely normal gravel and limestone aggregates. The "normal gravel" referred to in this work corresponds to marine pebbles or bench gravel, which has a siliceous nature. This type of aggregate is obtained from natural gravel pits, which are commonly found in Southern England. On the other hand, limestone aggregate is a crushed stone from a carbonated rock.

Special attention was paid when designing the concrete mixes to optimise the concrete strength at which the limestone aggregate would fracture at the crack while in the gravel specimens the crack went round the aggregate. Several trial mixes were tested in the lab before casting the definite specimens in order to assess the concrete strength at which only the limestone aggregate would fracture completely. A slump test of 180mm was set as target due to the high workability required for the short span beams with stirrups, which were cast vertically. Brazilian splitting test showed that for the limestone concrete with cylinder strengths as low as 50MPa the limestone aggregate fractured. In the gravel aggregate concrete, only a small fraction (~30%) of the aggregate fractured, which in general corresponded to sandstone particles (white aggregates in Figure 6.2 left).

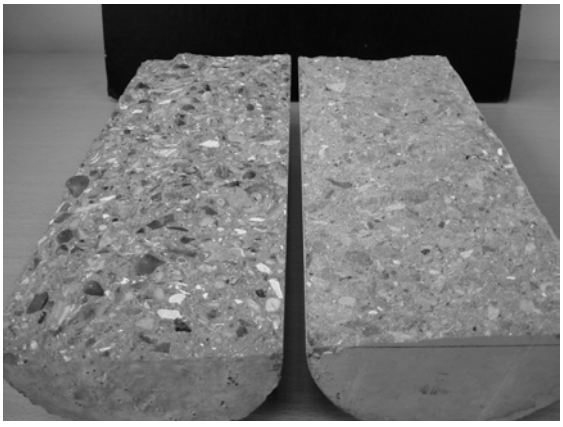

Figure 6.2: Crack surfaces of cylinders after Brazilian test (*Left*- gravel; *Right*- limestone)

The final mix designs are summarised in Table 6.2. Although the mix design was identical for mixes 1 and 3, the concrete strength was slightly different for both mixes, as

shown in Figure 6.3. In addition, the concrete strength varied considerably for mixes 3 and 4, even though the only difference between the mixes was the type of coarse aggregate. The low strength observed in mix 4 might have been due to insufficient water content required in the mix for hydration.

Mix constituents and proportions (kg/m^3)	**Mix 1 [06/03/07]**	**Mix 2 [22/03/07]**	**Mix 3 [01/08/07]**	**Mix 4 [08/08/07]**	**Mix 5 [08/05/08]**
CEM I 42,5 R	400	350	400	400	390
GGBS - Slag	100	87.5	100	100	-
Coarse aggregate	limestone	gravel	limestone	gravel	gravel
10mm gravel	-	1051	-	1051	940
10mm limestone	1051	-	1051	-	-
Marine sand	610	670	610	610	750
CSP313 RMC	4.32	2.6	4.32	4.32	2.34
Microsilica$^+$	40	35	40	40	-
Water	140	138	140	140	200

Notes: Proportions given in **dry aggregate**
Mixes 1 and 2 = Short span beams (beams A) + Slender beams without stirrups (beams B0)
Mixes 3 and 4 = Slender beams with stirrups (beams B) + Push-off tests
Mix 5 = Slender beams with stirrups (beams C and D)
+ Microsilica is given in proportions of dry weight

Table 6.2: Mix designs used for beam and push-off specimens

The concrete strength was obtained by crushing cubes (100mm) and cylinders (4" diameter and 10" height), which were cured in under two different conditions: water (20˚) and air exposed with same temperature and moisture conditions as the test specimens. The compressive strength development over time was also monitored as shown in Figure 6.3. Compressive strengths adopted in the analysis (chapter 7 and 8) related to cylinders which were cured in water and crushed around the day of the test. The tensile strength of the concrete was obtained by splitting cylinders (6" diameter and 9" height) in a standard Brazilian test arrangement.

Table 6.3 summarises the results of all the control specimens for mixes 1 to 5. In all cases, the specimens were tested well after 28 days, where the strength had reached the plateau shown in Figure 6.3. Mixes 1 and 2 were used for casting the short span beams and slender beams with no stirrups while 3 and 4 were used in slender beams with stirrups as well as the push-off test. Lastly, mix 5 was used in beams C and D

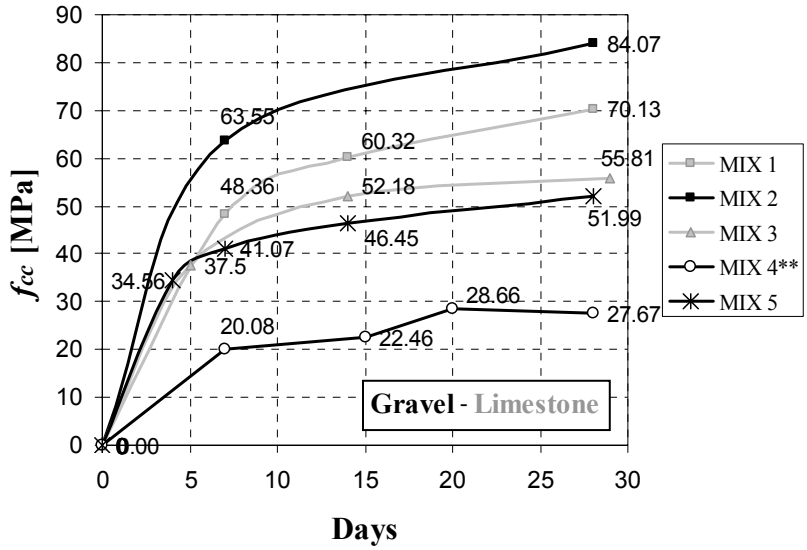

Note: Mix 4** - cube strength was excessively low (cylinder strengths seemed more realistic)

Figure 6.3: Cube strength development (f_{cc}) over time (Mixes 1 to 5)

		Mix 1 (Limestone)			**Mix 2 (Gravel)**		
Avg. Surf. Dried Density		2352 kg/m^3			2302 kg/m^3		
Compression	*Curing*	*Num.*	f_c^+ *[MPa]*		*Num.*	f_c^{++} *[MPa]*	
Cube [100mm]	air	3	65.27		3	90.76	
	water	2	78.56		3	90.38	
Cylinder [4″ x 10″]	air	3	54.43		3	84.67	
	water	3	68.44		3	80.20	
Tension	*Curing*	*Num.*	f_{ct}^+ *[MPa]*		*Num.*	f_{ct}^{++} *[MPa]*	
Cylinder [6″ x 9″]	air	3	3.72		3	4.16	
	water	3	4.86		3	5.67	
E-value	*Curing*	*Num.*	E_c *[GPa]*	ν	*Num.*	E_c *[GPa]*	ν
Cylinder [4″ x 10″]	air	1	34.97	0.20	1	42.61	0.16
Comp. over time	*Curing*	*Num.*	*Day*	f_c	*Num.*	*Day*	f_c
Cube [100mm]	water	1	7	48.36	1	7	63.55
	water	1	14	60.32	-	-	-
	water	1	28	70.13	1	28	84.07
	water	2	87	77.47	1	68	90.22

Notes: $^+$Mix 1: values relate to day 133 after casting (testing of beams AL)
BL01-BL02 were tested on the 87 and 89 day respectively
$^{++}$Mix 2: values relate to day 104 after casting (testing of beams AG)
BG01-BG02 were tested on the 68 and 70 day respectively

Table 6.3: Material properties obtained from control specimens

		Mix 3 (Limestone)			Mix 4 (Gravel)		
Avg. Surf. Dried Density		2330.70 kg/m^3			2059.24 kg/m^3		
Compression	*Curing*	*Num.*	f_c^+ *[MPa]*		*Num.*	f_c^{++} *[MPa]*	
Cube [100mm]	air	2	60.21		2	31.70	
	water	3	60.30		3	30.37	
	poorly*	2	41.64		2	23.22	
Cylinder [4″ x 10″]	air	3	49.66		3	32.50	
	water	3	53.11		3	31.70	
Tension	*Curing*	*Num.*	f_{ct}^+ *[MPa]*		*Num.*	f_{ct}^{++} *[MPa]*	
Cylinder [6″ x 9″]	air	3	3.48		3	2.53	
	water	3	3.79		3	2.80	
E-value	*Curing*	*Num.*	E_c *[GPa]*	ν	*Num.*	E_c *[GPa]*	ν
Cylinder [4″ x 10″]	air	-	-	-	1	27.21	0.17
Comp. over time	*Curing*	*Num.*	*Day*	f_c	*Num.*	*Day*	f_c
Cube [100mm]	water	1	5	37.5	1	7	20.08
	water	1	14	52.18	1	15	22.46
	water	2	29	55.81	1	28	27.67
	air	2	120	59.68	2	126	31.69
	water	3	120	61.21	3	126	32.27
Cylinder [4″ x 10″]	water	3	120	55.05	3	126	33.66
Cylinder [6″ x 9″]	water	3	120	55.13	3	126	27.04

Notes: $^+$Mix 3: values relate to day 57 after casting (testing of beams BL)
PL specimens were tested around 120 days after casting
$^{++}$Mix 4: values relate to day 64 after casting (testing of beams BG)
PG specimens were tested around 126 days after casting

		Mix 5 (Gravel)		
Avg. Surf. Dried Density		2331.09 kg/m^3		
Compression	*Curing*	*Num.*	f_c^+ *[MPa]*	
Cube [100mm]	air	3	56.15	
	water	2	55.55	
Cylinder [4″ x 10″]	air	3	46.82	
	water	3	49.35	
Tension	*Curing*	*Num.*	f_{ct}^+ *[MPa]*	
Cylinder [6″ x 9″]	water	3	3.16	
Comp. over time	*Curing*	*Num.*	*Day*	f_c
Cube [100mm]	water	1	4	34.56
	water	1	7	41.07
	water	2	14	46.45
	water	2	28	51.99
	water	2	62^{++}	57.84

Notes: $^+$Mix 5: values relate to day 50 after casting (testing of beams C)
$^{++}$Mix 5: beams D were tested around 60 days after casting

Table 6.3(Cont.): Material properties obtained from control specimens

The ratio between cube and cylinder strength (f_c'/f_{cc}) was different for each mix and varied between 0.83 and 0.95. This variation justified testing cylinders in addition to cubes. EC2 and BS8110 apply cylinder and cube strengths respectively, so this approach seemed more accurate than using a constant conversion factor. The need of testing cylinder and cube control specimens for high strength concretes has been raised by authors such as Larrard et al. [126].

Mix 4 had significant anomalies regarding cube strengths with a f_c'/f_{cc} ratio of 1. This mix had reduced density (11% lower than the rest) due to air entrapment. The Poisson ratio was similar for all mixes (ν = 0.20-0.18). Low values of ν could have explained the higher value for f_c'/f_{cc} ratio according to Larrard et al. [126], but ν in mix 4 was similar to the other mixes. In order to obtain further information about the real uniaxial strength of mix 4, cylinders with a different size (6" by 9"), which are usually used for Brazilian tests, were crushed in compression. The results are shown in Table 6.3 and had a good correlation with the 4" diameter cylinder strengths. Hence, cube strengths for mix 4 were neglected in the analysis of specimens made with mix 4.

Another important aspect that was observed while testing the control specimens was the influence of proper curing of cube specimens. Air cured cube specimens for mix 1 had a significantly lower strength (15%) in comparison with the water cured ones, as shown in Table 6.3. This was not consistent with the rest of the mixes, where air and water cured specimens had similar strengths. The reason for this discrepancy in cube strengths in mix 1, was most likely due to poor curing during first days. Additional cubes were tested for mixes 3 and 4 that were intentionally poorly cured under normal room conditions without keeping good moisture levels. The results for these poorly cured cubes (see Table 6.3) showed strength reductions up to 30%, which is even larger than those observed for mix 1.

6.3 Short span beams (Beams A)

6.3.1 General aspects

A total of 8 short span beams (beams A) were tested, which were 3m long and had a shear span to effective depth of 1.5. The beams were simply supported and were loaded monotonically at midspan. The clear shear span to effective depth ratios (a_v/d) in all the specimens were 1.12 and 1.04 for the left and right spans respectively, since different plate sizes were used for each support; plates were 125mm and 200mm as shown in Figure 6.4. The aim of using different plate sizes was to study the influence of the bottom node geometry on the strength. In addition, failure was encouraged in the span with larger a_v/d ratio, which had more instrumentation.

Four cases of transverse reinforcement were tested, see Figures 6.4 and 6.5:

1. Specimens AG0, AL0: no web reinforcement ($\rho_v = 0\%$)
2. Specimens AG2, AL2: four T8 stirrups ($\rho_v = 0.22\%$)
3. Specimens AG3, AL3: six T8 stirrups ($\rho_v = 0.34\%$)
4. Specimens AG4, AL4: eight T8 stirrups ($\rho_v = 0.45\%$)

The beams had a central span of 1320mm, measured between centrelines of the supports. Rollers were placed under the bearing plates to allow horizontal displacements and pinned rotation. The thickness of the bearing plates were 75mm for the left plate, 65mm for the right plate and 30mm for the loading plate in order to assure an uniform stress distribution under the plate.

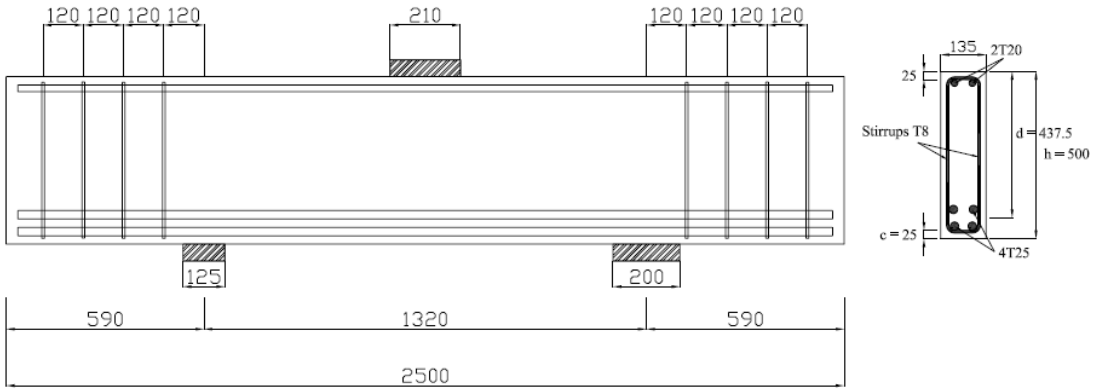

Figure 6.4: General dimensions of short span beams (Beams AG0 and AL0)

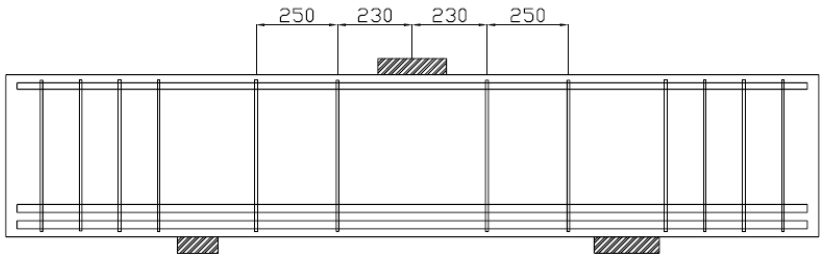

Beams AG2 and AL2

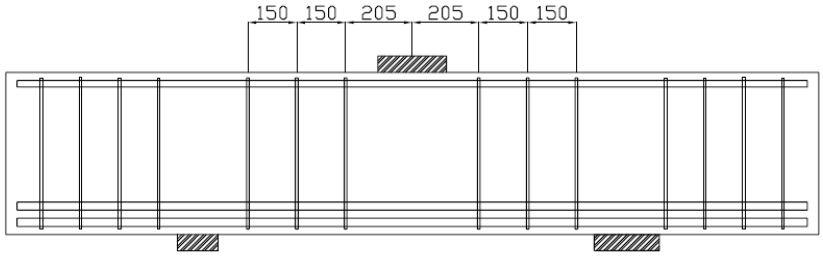

Beams AG3 and AL3

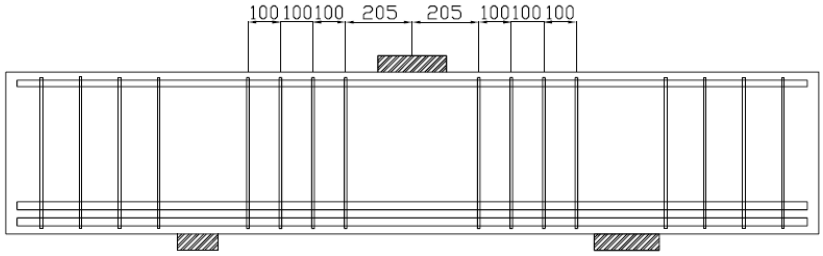

Beams AG4 and AL4

Figure 6.5: Position of stirrups in beams AG2 to AG4 and AL2 to AL4

The longitudinal reinforcement consisted of two layers of two T25 each (ρ_l = 3.32%) in order to avoid flexural failure. Two T20 bars were placed on the top to hang the stirrups as shown in Figure 6.5. Four extra stirrups were placed every 120mm at the ends of the beams to provide adequate anchorage. Four beams (AL0-AL4) were cast using mix 2 with limestone aggregate concrete (see section 6.2.2). Mix 1, which had gravel aggregate, was used for the remaining beams (AG0 to AG4).

6.3.2 Manufacture and curing

The beams were cast vertically in wood moulds in groups of four (AG0-AG4 and AL0-AL4), see Figure 6.6. Two internal vibrators were used to compact the concrete. The control cubes and cylinders were vibrated on a standard vibrating table. All specimens were covered with polythene sheets until stripping of the moulds as shown in Figure 6.7.

The control specimens were taken out of the moulds the following day while the beams were stripped two days after casting. The beams were then covered with wet Hessian and polythene sheets, which were watered weekly to keep adequate moisture levels for proper curing. The control cubes and cylinders were cured as described in section 6.2.2.

Figure 6.6: *Left* - Moulds for beams AL4 to AL0 (left to right); *Right* - Casting of gravel beams

Figure 6.7: Gravel aggregate concrete beams before stripping (AG0-AG4; B0L1-B0L2)

6.3.3 Instrumentation

A 2500kN capacity load cell was allocated under the hydraulic jack, see Figure 6.8, to record the total load and another one (1000kN capacity) was placed under the right support to assess any possible asymmetries in the rig. Deflections, strains and relative crack displacements were monitored in the beams using:

1. Linear variable displacement transducers (LVTDs)
2. Demec readings (150mm and 250mm Demec gauges)
3. Strain gauges at the reinforcement bars (transverse and longitudinal)

Global displacements

A total of 7 LVTDs were placed at the beam to monitor global deflections as shown in Figure 6.8. Transducers #1 and #2 recorded the vertical deflection at the centre point relative to the supports and floor respectively. Out-of-plane deflections were measured with LVTD #3. Transducers #4 and #5, which were placed at 480mm from the centre in both spans, were used to record vertical deflections near the plate relative to the ground, see Figure 6.8. Finally, the beam rotation at the support was measured by LVTDs #6 and #7 placed at the left end of the beam.

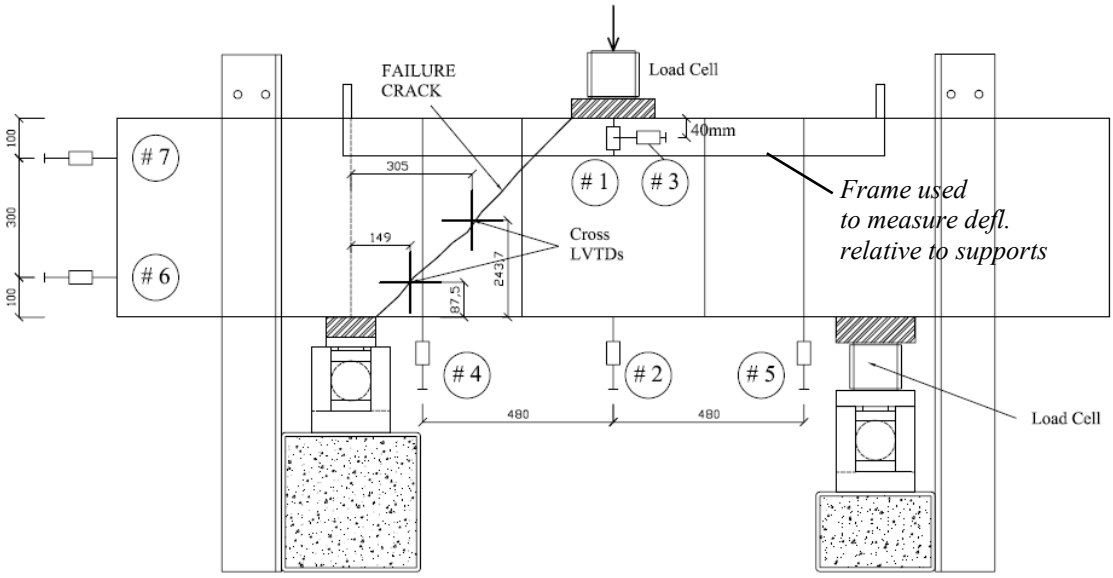

Figure 6.8: Position of LVTDs in the short span beam tests

Strains at the centre section and direct strut

The horizontal strains at the central section were obtained at six points using Demec gauges. Two of these points corresponded with the longitudinal reinforcement as shown in Figure 6.9.a.

One grid of 150mm Demec targets was placed with the purpose of monitoring longitudinal and transverse strains along the direct strut of the left span (a_v/d of 1.12). In order to make direct comparisons between different specimens, the grid shown in Figure 6.9.a for the direct strut (line AB), which was obtained from the strut-and-tie model of the beam without stirrups, was kept constant for all the beams.

Strains in the reinforcement bars

In addition, Demec targets were placed to control strains at every stirrup, see Figure 6.9.b. The strains of the longitudinal reinforcement were also recorded, (Figure 6.9.a). The readings from the Demec gauges could be compared in some specimens with readings from strain gauges located at the same position as the centroid between two Demec targets.

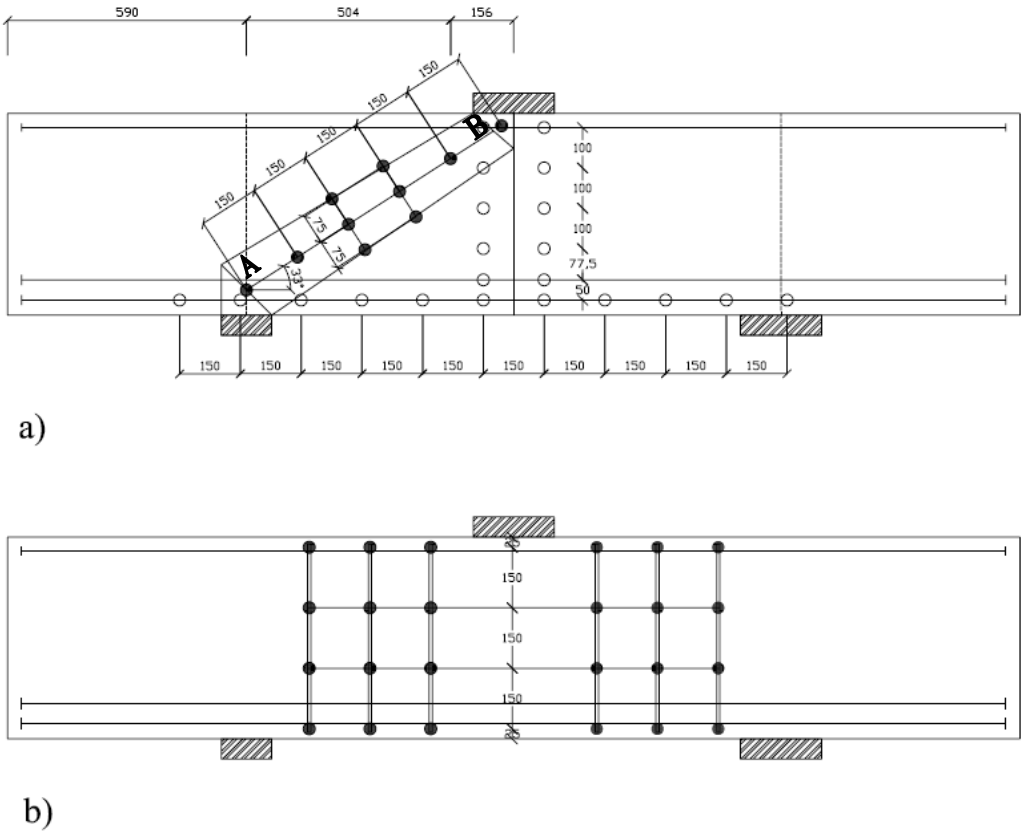

Figure 6.9: a) Demec grid used to obtain strains at the central section (hollow marks) and direct strut (filled marks); b) Demec grid used to obtain strains in the stirrups

Beams AG0, AL0, AG3 and AL3 were instrumented with strain gauges as shown in Figure 6.10. Strain gauges 1 to 10 were placed in pairs at bottom and top of the same reinforcement bar to take flexure into account. The main objective of these measurements was to assess the strain distribution along the longitudinal reinforcement, verified Demec

readings and detect any potential yielding of the reinforcement steel. Strain gauges 11 to 16 were only placed on one side of the stirrup. Readings 11, 13 and 16 corresponded to points near the critical crack while points 12, 14 and 15 were far from this crack.

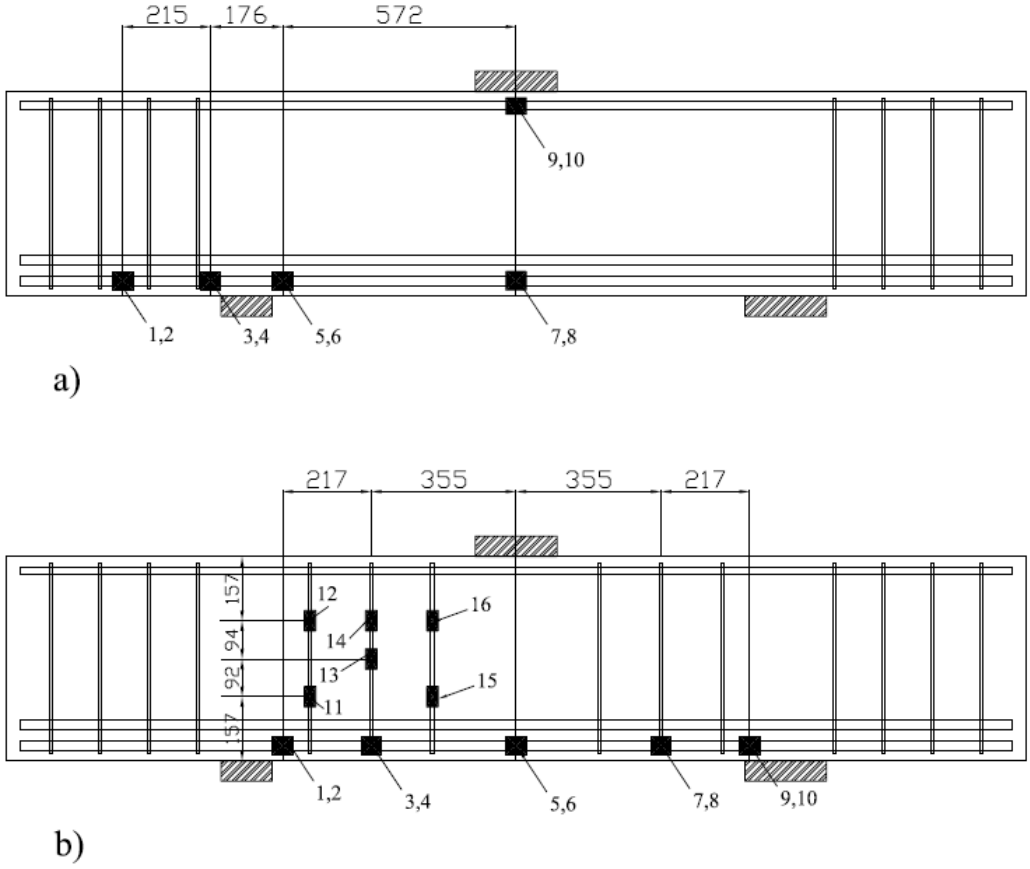

Figure 6.10: a) Strain gauges for beams AG0 and AL0; b) Strain gauges for beams AG3 and AL3

Relative crack displacements

The predominant crack was studied in terms of its relative displacements: opening and sliding. Three methods were applied:

1. Grid of Cross Demec gauges
2. Cross LVTDs
3. Microscopic ruler (crack opening only)

The first two methods were also used in the push-off tests presented in this work; see section 4.2.3. Additionally, the measurements obtained from the crosses were compared with simple visual readings using a microscopic ruler with a precision of 1/26mm. In general, readings using Demec, LVTDs and visual methods were in very good agreement. Although the cross LVTDs seems the most optimal procedure, since it provides

continuous readings, the other methods were also found very useful due to their simplicity and reliability.

The cross Demec targets (250mm gauge) were placed before testing to cover the area where the main crack was most likely to appear, see Figure 6.11, which is along the line that connects the inner edges of the loading and support plates. On the other side of the beam, two LVTDs crosses (150mm length) were placed on the critical shear span as shown in Figures 6.8 and 6.12.

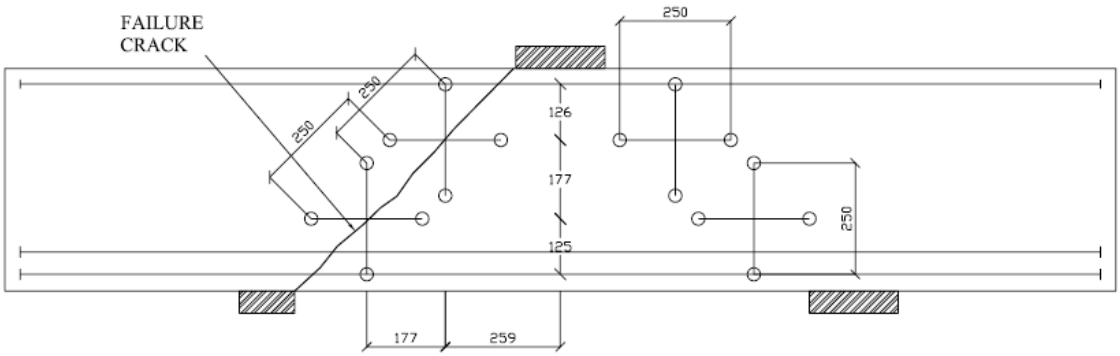

Figure 6.11: Grid of cross Demec (250mm gauge) used to obtain relative crack displacements

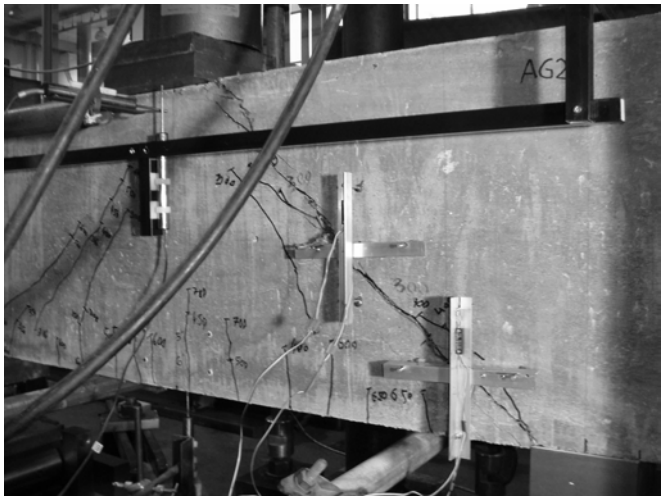

Figure 6.12: Cross LVTDs used on one side of the beam

6.3.4 Results

Summary of experimental results

Table 6.4 summarises the experimental results obtained for the short span beams. With the exception of beams AG4 & AL2, failure occurred on the span with higher a_v/d ratio. In addition, the ultimate load for beam AL2 exceeded the one for AL3, which was not expected. In Table 6.4, δ_{ctr} is the measured deflection at failure under the loading plate relative to the supports; P_{cr} and P_{ult} are the loads at which the critical shear crack appeared and at failure respectively.

Beam	f_c' [MPa]	f_s [MPa]	stirrups	a_v/d (critical)	δ_{ctr} [mm]	P_{cr} [kN]	P_{ult} [kN]	Failure
AG0	80.20	550	0	1.12	2.37	250	651.53	Sh. Prop
AG2	80.20	550	2T8	1.12	3.84	300	1126.05	Sh. Comp.
AG3	80.20	550	3T8	1.12	4.37	200	1309.21	Sh. Comp*
AG4	80.20	550	4T8	1.04	4.57	300	1414.20	Sh. Comp*
AL0	68.44	550	0	1.12	2.87	230	731.01	Sh. Comp.
AL2	68.44	550	2T8	1.04	3.95	400	1063.79	Sh. Comp.
AL3	68.44	550	3T8	1.12	3.68	173	961.46	Sh. Prop.
AL4	68.44	550	4T8	1.12	4.21	270	1204.39	Sh. Comp.

Note: Failure: Sh. Prop. – Shear Proper; Sh. Comp. – Shear Compression; Sh. Comp* - Shear Compression and longitudinal reinforcement near yielding

Table 6.4: Summary of experimental results of short span beams (Beams A)

Type of Failure and Crack pattern

All beams failed in shear, although the type of failure was slightly different for each specimen. Beams AG0 and AL3 had shear proper type of failure with the main diagonal crack crossing the direct strut from early load stages. This crack connected the inner edges of loading and support plates. On the other hand, beams that failed in shear compression, the diagonal crack was slightly flatter and did not extend to the ends until near failure, where the concrete under loading plate crushed completely. In beams AG3 and AG4, the longitudinal reinforcement started to yield near failure, which was due to crushing of the direct strut (shear compression failure).

Cracks were measured in each span at both sides (North and South) showing symmetrical results. Several parallel cracks to the main diagonal crack were observed, especially as the number of stirrups was increased. Angles between the main diagonal crack with respect to the longitudinal reinforcement were steeper for the shear span with smaller a_v/d as expected.

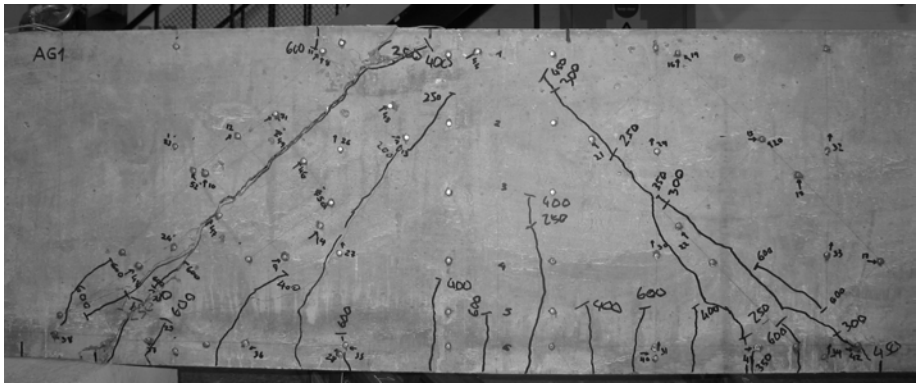

AG0

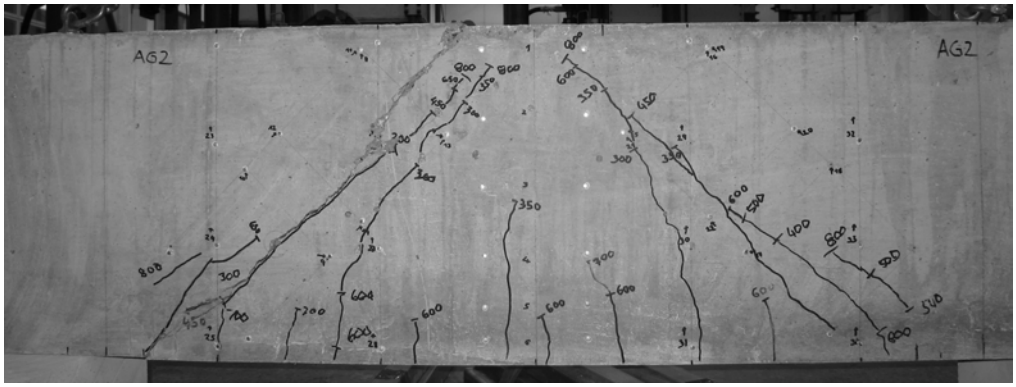

AG2

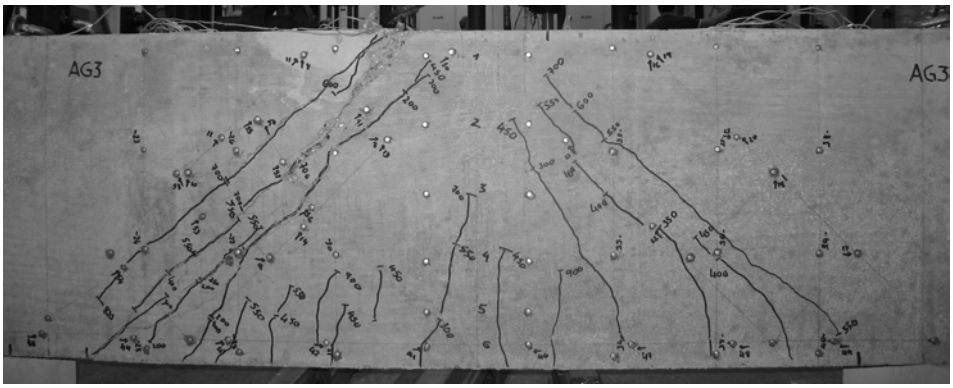

AG3

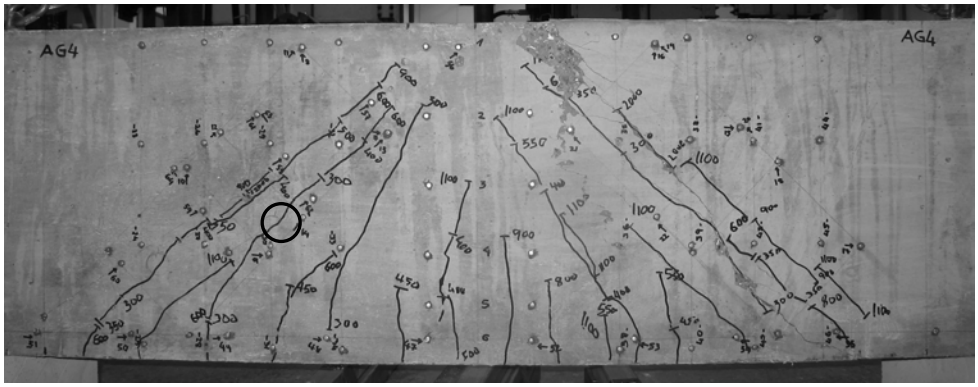

AG4

Figure 6.13: Crack pattern in the gravel short span beams (North side)

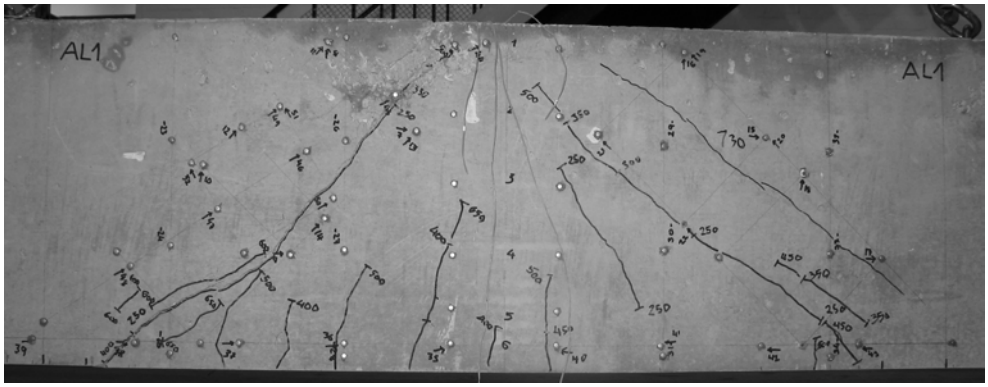

AL0

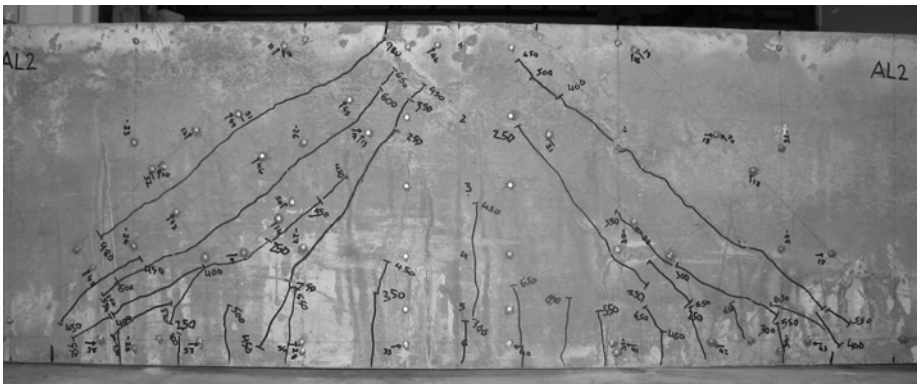

AL2

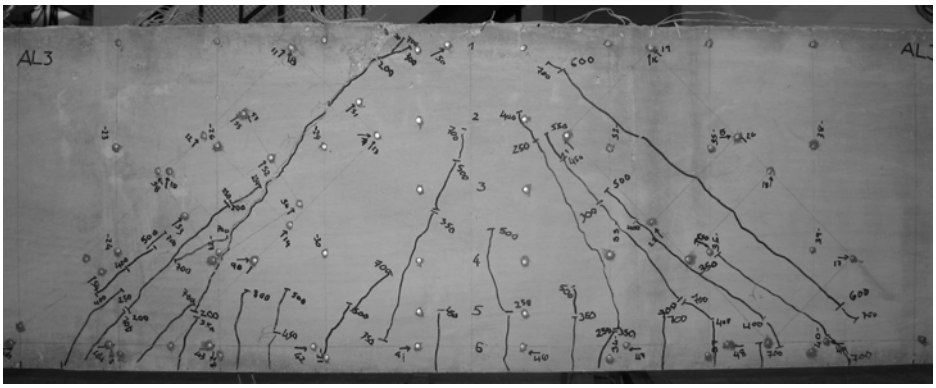

AL3

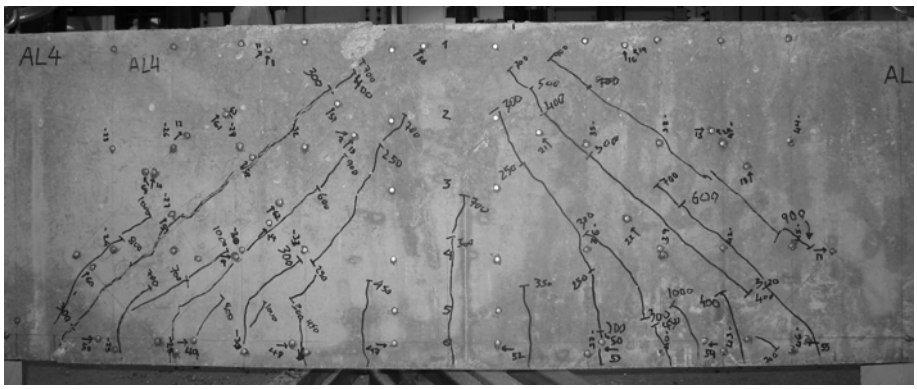

AL4

Figure 6.14: Crack pattern in the limestone short span beams (North side)

Secondary shear cracks (see circle mark in beam AG4, Figure 6.13), which ran parallel and below the main diagonal crack, originated almost simultaneously to the formation of the main diagonal crack. These cracks, which extended to the bottom into flexural cracks, relate to the indirect strut that fans out from the top node to the bottom of the stirrups. Flexural cracks formed in all cases after the shear cracks had developed. In general two stages were observed; one first stage around 400kN where first flexural cracks formed, and one second stage around 600kN where old flexural cracks propagated to the top and new flexural cracks originated. In all cases the main diagonal crack was independent from these flexural cracks.

Load-deflection curves

Vertical deflections were very small, between 2 and 5mm. Figure 6.15 shows the load-deflection curves for beams AG and AL, taken from transducer 1 (Figure 6.8). The out-of-plane deformations measured were negligible (<0.1mm). This confirmed that the loading was applied correctly without no-eccentricity in the out-of-plane direction.

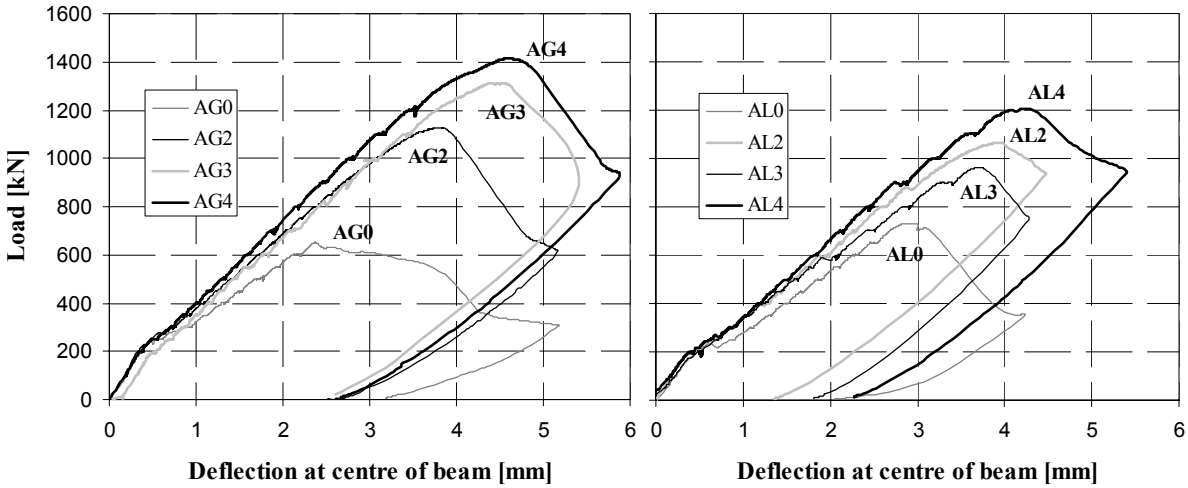

Note: deflections given at the centre of the beam, measured relative to frame

Figure 6.15: Load-deflection curves for short span beams

The horizontal displacement and rotation of the beam were monitored at the end of the shear span (a_v/d of 1.12) using transducers #6 (top) and #7 (bottom), refer to Figure 6.8. Figure 6.16 shows the global displacements with respect to the middle height fibre of the beam. The horizontal displacement is considered positive outwards the centre of the beam and rotation of the plane is positive for sagging and negative for hogging. An interesting aspect that can be highlighted from end displacements shown in Figure 6.16, is the different behaviour in beams AG4 and AL2 after reaching the ultimate load in comparison with the rest of the specimens. The horizontal displacement and the rotation

measured in AG4 and AL2 kept increasing after reaching the ultimate load, which is opposite to the rest of the beams where the displacements changed direction. This trend confirms that failure occurred in the shear span with a_v/d of 1.04 in beams AG4 and AL2 and agrees with general kinematics described in Figure 6.17.

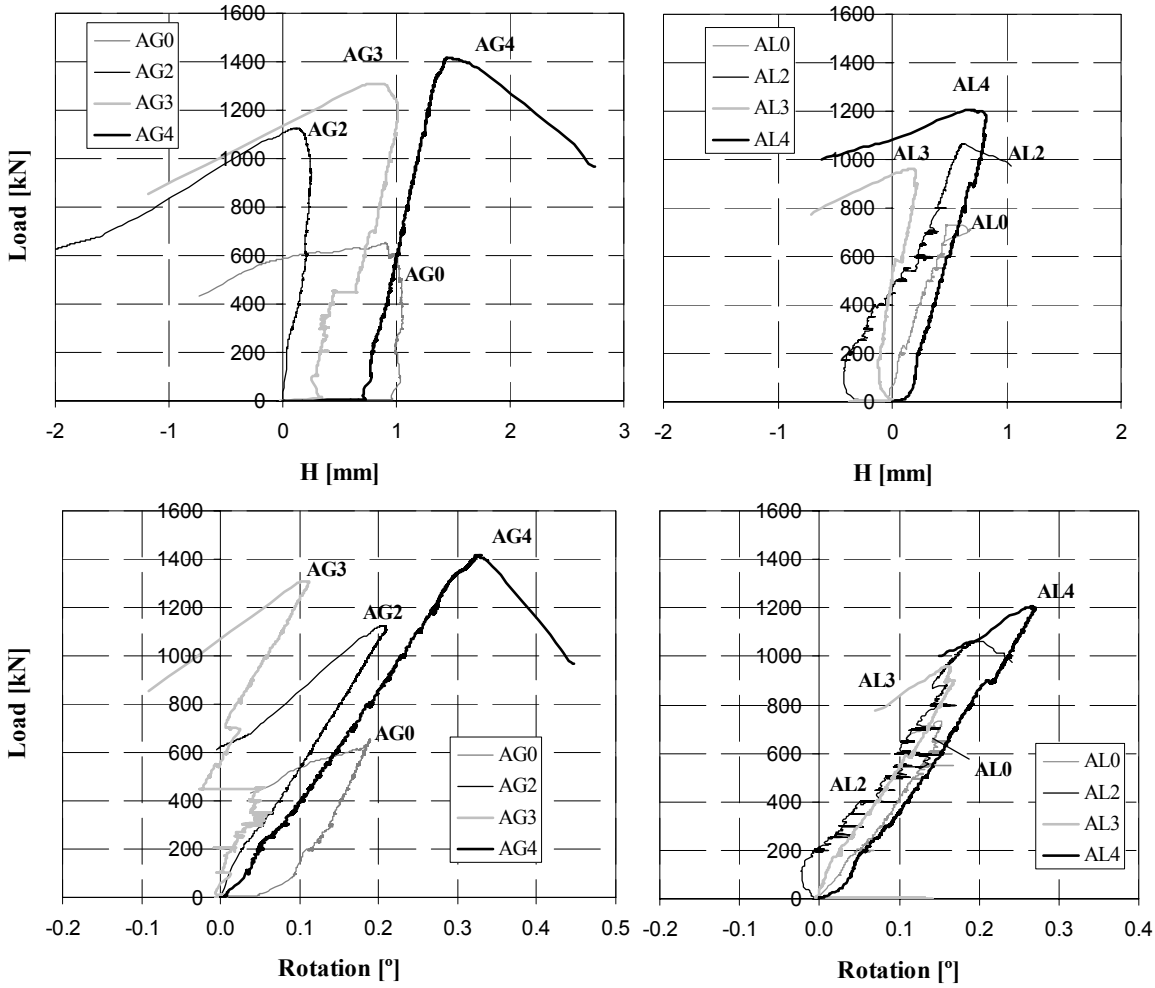

Note: Horizontal displacement (H) and rotation (see Figure 6.17 for sign criteria)

Figure 6.16: End movements of beams AG and AB

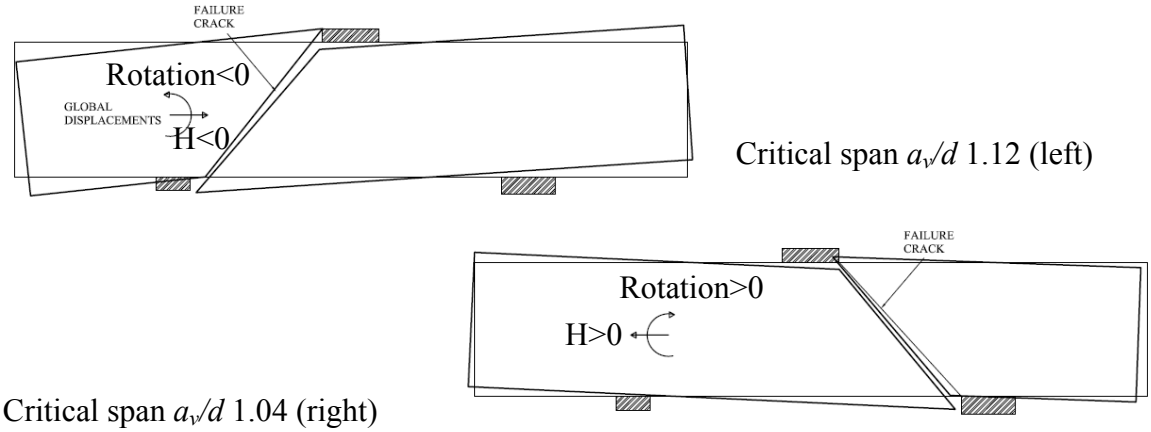

Critical span a_v/d 1.12 (left)

Critical span a_v/d 1.04 (right)

Figure 6.17: General kinematics of short span beams after failure

Strains at central section

The strains at the central section of the beam, which were measured with the Demec gauges, are shown in Figure 6.18 for AG and AL beams. The measurements are compared with readings from the strain gauges 7-8 and 5-6 for beams A0 and A3 (Figure 6.10). In general, the readings from the Demec gauge were slightly larger (10%) than those obtained from strain gauges, which could be due to bond-slip between the concrete and reinforcement. However, in beam AG0 Demec and strain gauge readings are almost identical (Figure 6.18). The oscillations of strains along the height obtained with the Demec gauge, especially at the bottom of AG3 and at 150mm from the bottom in AL3, were due to crack bypassing the Demec gauge, as shown in Figure 6.13 and 6.14.

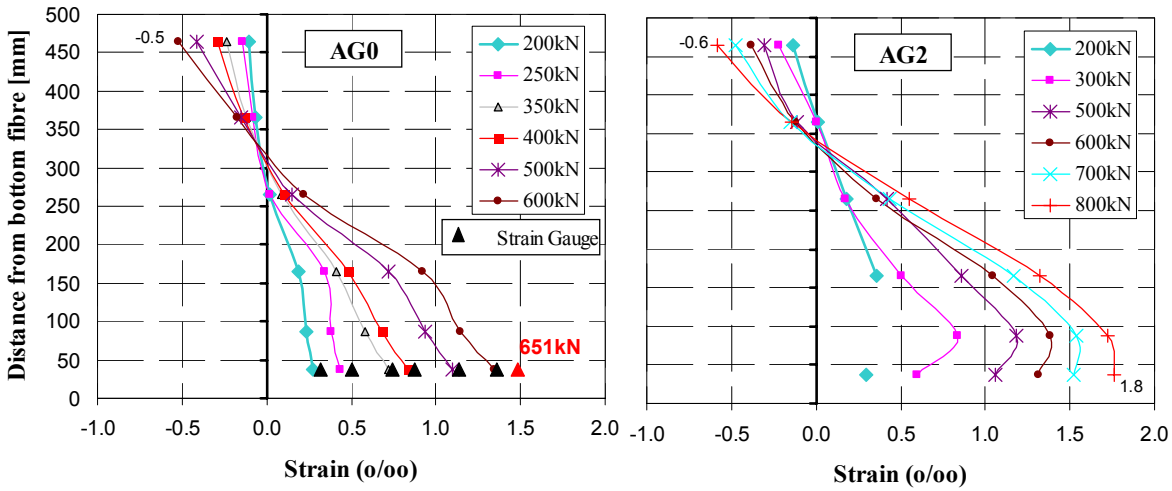

a) Beam AG0 b) Beam AG2

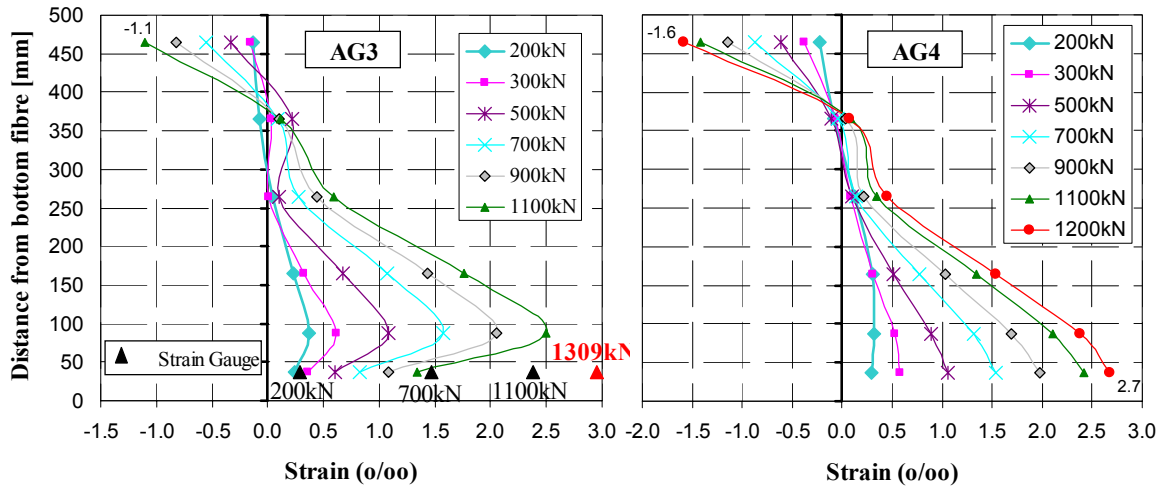

c) Beam AG3 d) Beam AG4

Figure 6.18: Strains at the central section of the beam AG and AL

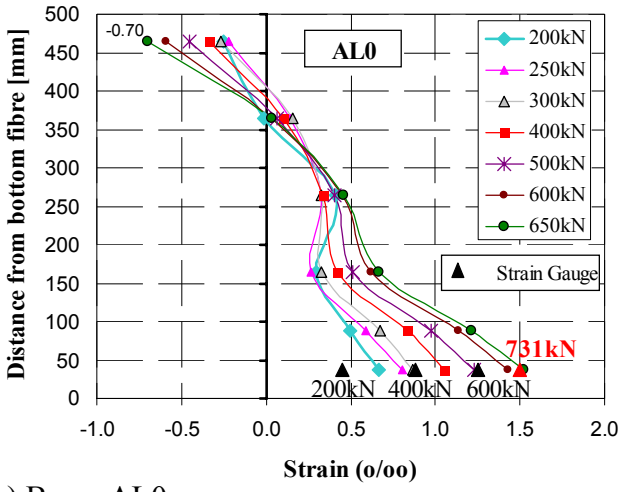

e) Beam AL0

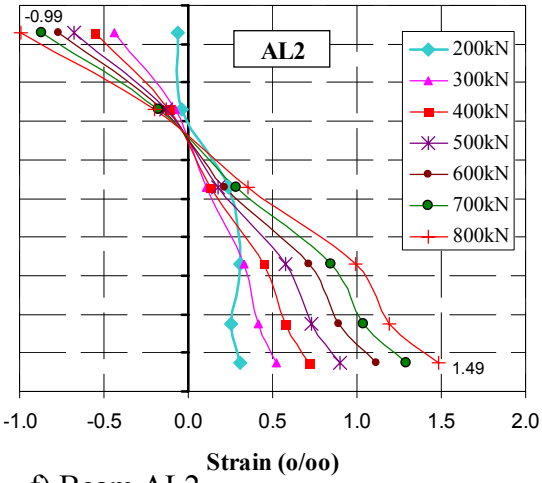

f) Beam AL2

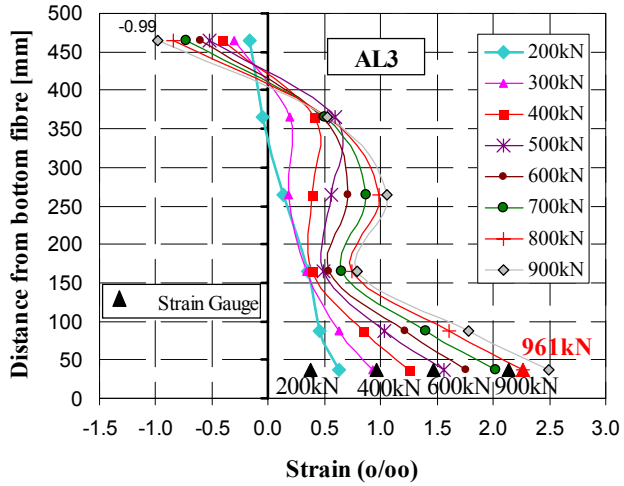

g) Beam AL3

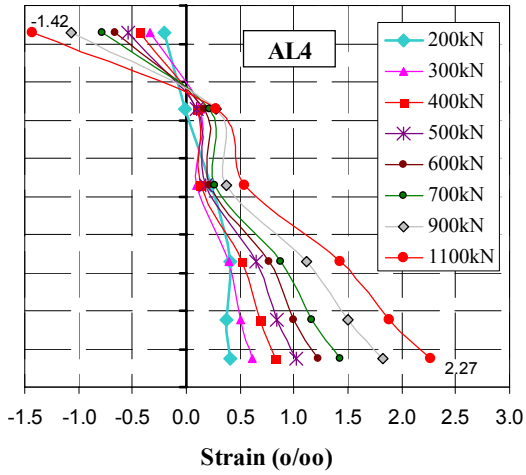

h) Beam AL4

Figure 6.18 (Cont.): Strains at the central section of the beam AG and AL

Strains in stirrups

The stirrups yielded (ε_y=2.75‰) before failure as shown in Figure 6.19. The Demec gauge readings shown in Figure 6.19 are average values in the sector where the main diagonal crack crossed the stirrup and therefore where strains reached their maximum value. The strains in the stirrups increased more rapidly after the main diagonal had originated. The readings recorded at sectors of the stirrup that were not crossed by the main diagonal crack were negligible. This was confirmed by strain gauges 12 and 15 (Figure 6.10), which were placed at the stirrup away from the diagonal crack. In general the strains were slightly larger in stirrups at middle shear span than nearer the supports. The stirrups of the right span (a_v/d=1.04), which are drawn as dashed lines in Figure 6.19, did not yield except for AG4 and AL2, where this span was critical. In general, Demec readings were consistent with the data obtained from the strain gauges.

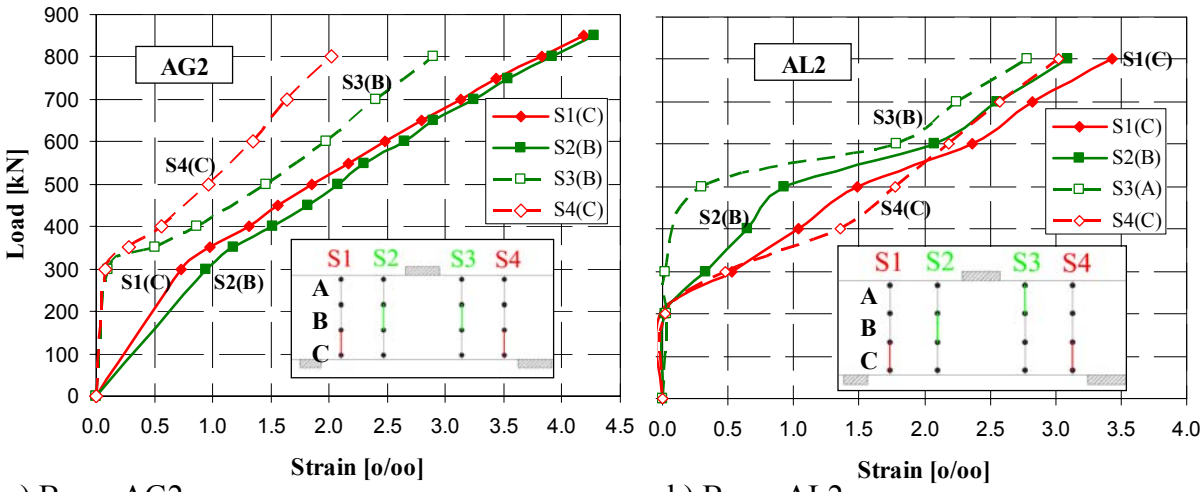

a) Beam AG2 b) Beam AL2

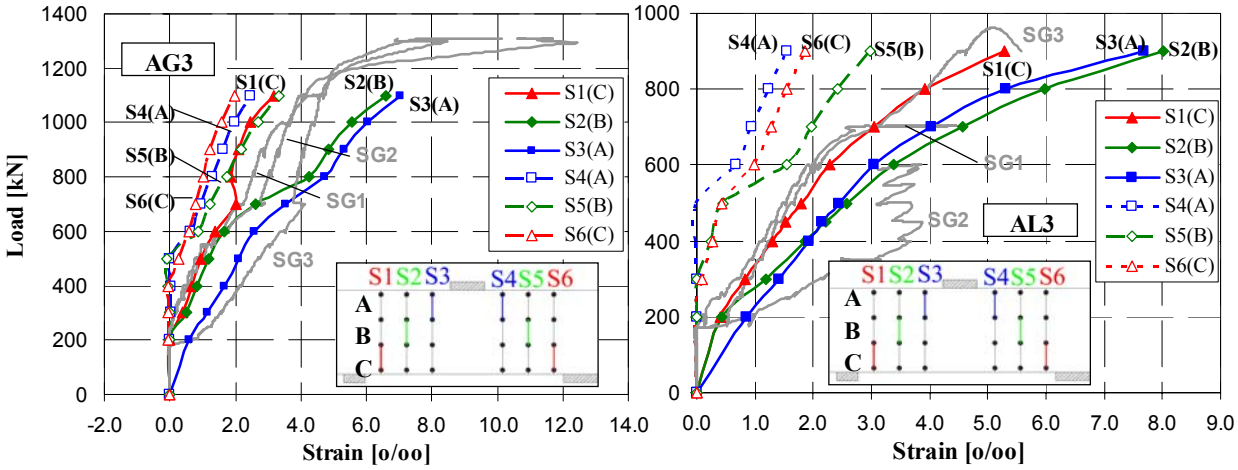

c) Beam AG3 d) Beam AL3

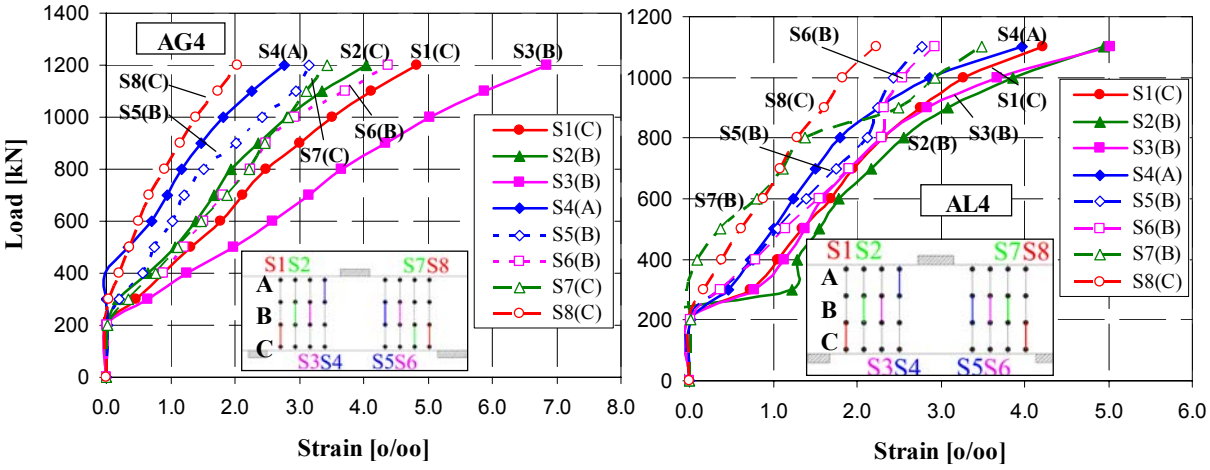

e) Beam AG4 f) Beam AL4

Note: SG#- strain gauge at stirrup # (stirrups are labelled from left to right):
Refer to strain gauges 11, 13 and 16 (Figure 6.10)

Figure 6.19: Strains at critical section of stirrups for AG and AL beams

Strains in the longitudinal reinforcement

The tensile strains in the longitudinal reinforcement bars are shown in Figure 6.20. The experimental data suggest that the longitudinal steel started to yield (ε_y=2.90‰) at failure only in beams AG3 and AG4. The readings from the strain gauges, which are available for beams A1 and A3, show a more uniform profile than the Demec gauge readings (Figure 6.20). However in several points both readings were very similar. The variations in the Demec readings seem to be related with flexural cracks crossing the Demec gauge. The relatively low strains obtained with the Demec gauge at the central section of AG3 were not consistent with Demec readings in adjacent sectors. This suggests that strain gauge readings seem more realistic than the Demec readings for the central section of beam AG3.

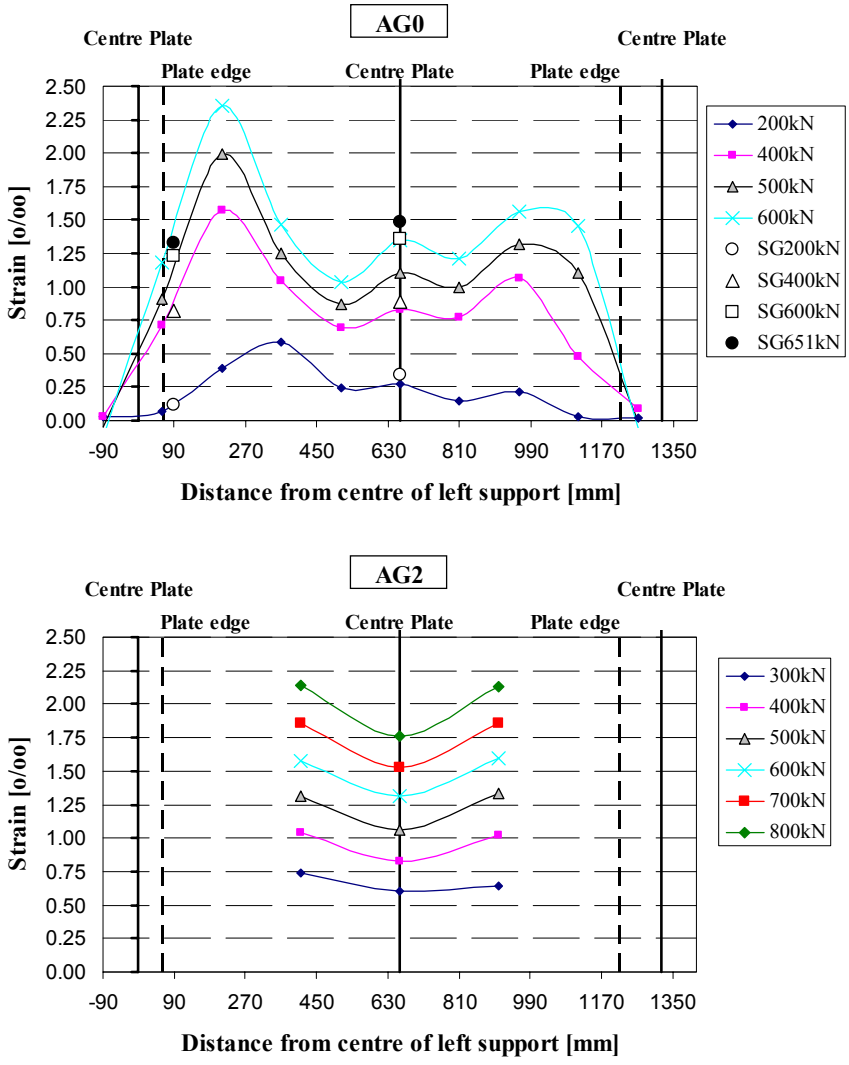

Notation: SG# – strain gauge at load # (kN)

Figure 6.20: Strains of longitudinal reinforcement in beams AG and AL

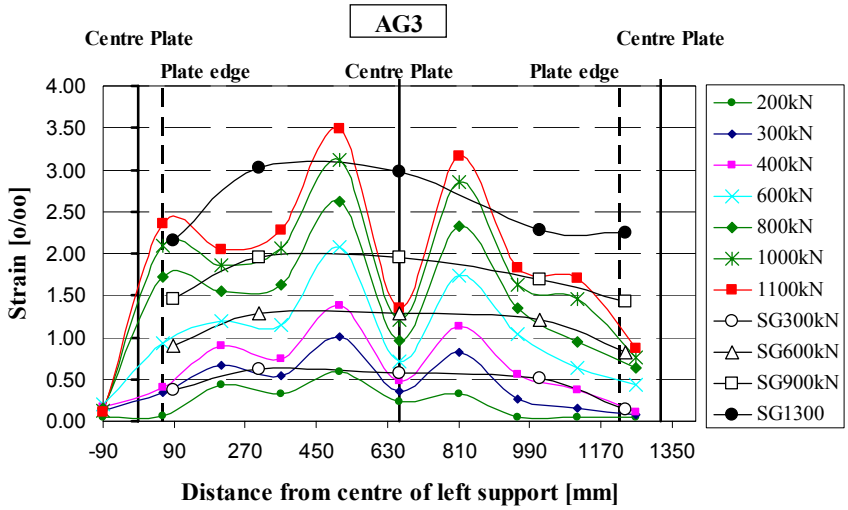

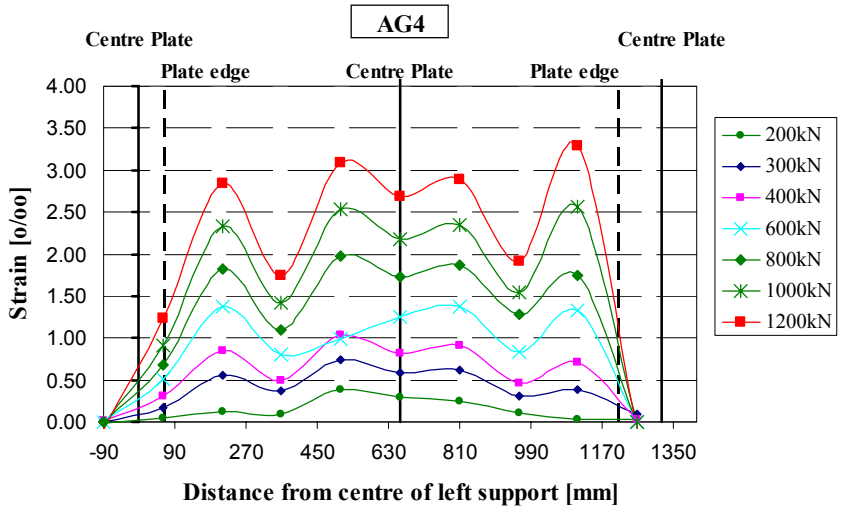

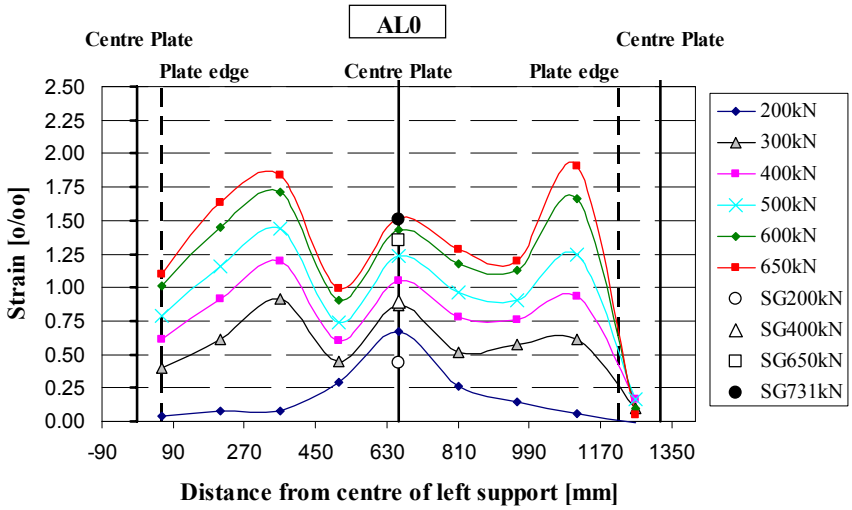

Notation: SG# – strain gauge at load # (kN)

Figure 6.20 (Cont.): Strains of longitudinal reinforcement in beams AG and AL

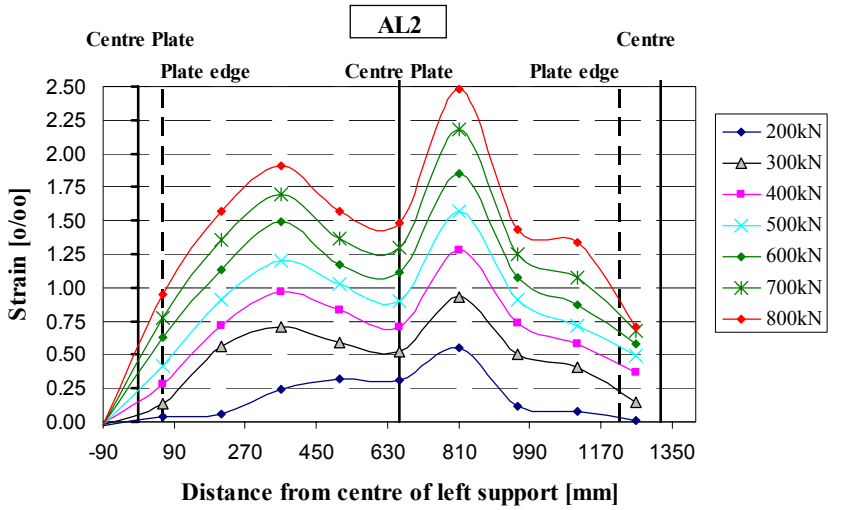

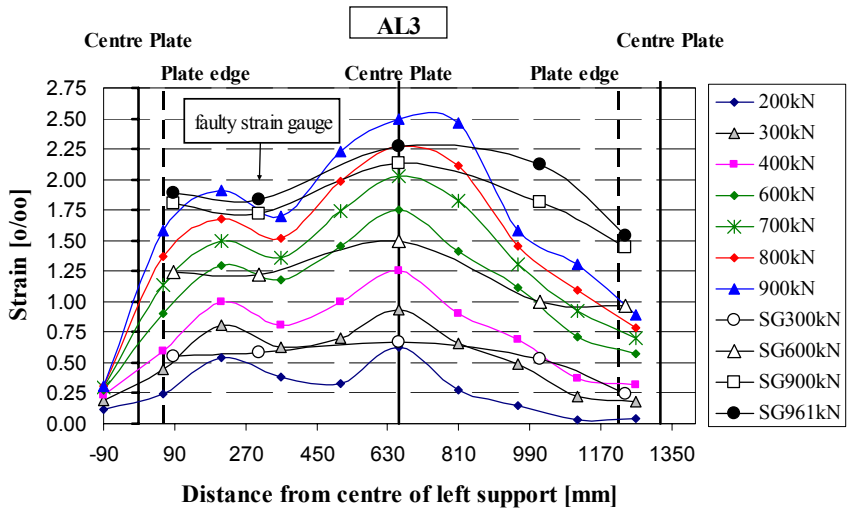

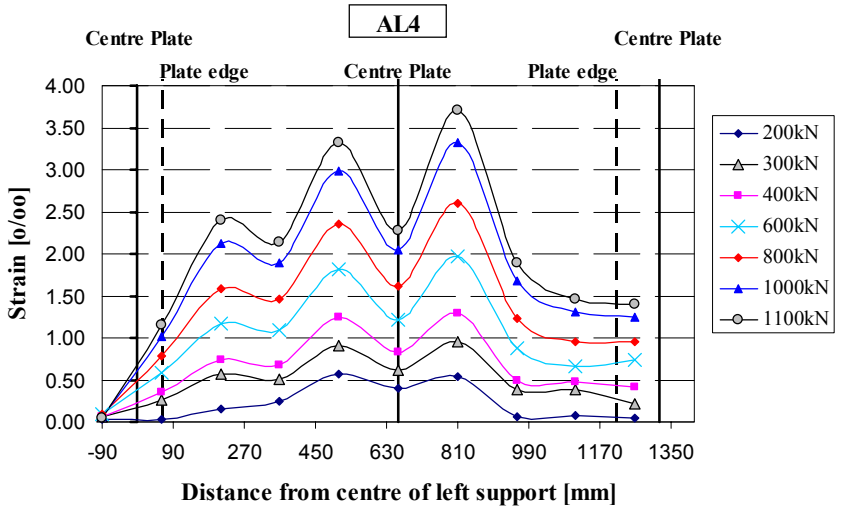

Notation: SG# – strain gauge at load # (kN)

Figure 6.20 (Cont.): Strains of longitudinal reinforcement in beams AG and AL

The strains obtained by the strain gauges in beams A0 were uniform along the longitudinal rebar and drop to zero on the outer side of the bearing plate (Figure 6.21). For beams with three stirrups the strains increased slightly at the first sector of the rebar near the inner edge of the plate but were constant for the rest of the rebar (Figure 6.20). In beam AG3, strain gauges 3/4 placed at the centre of the critical shear span recorded same readings as strain gauges 5/6 located at the centre of the beam. Unfortunately for beam AL3, the readings were influence by strain gauge 3, which was faulty during the test, and a direct comparison with AG3 could not be made.

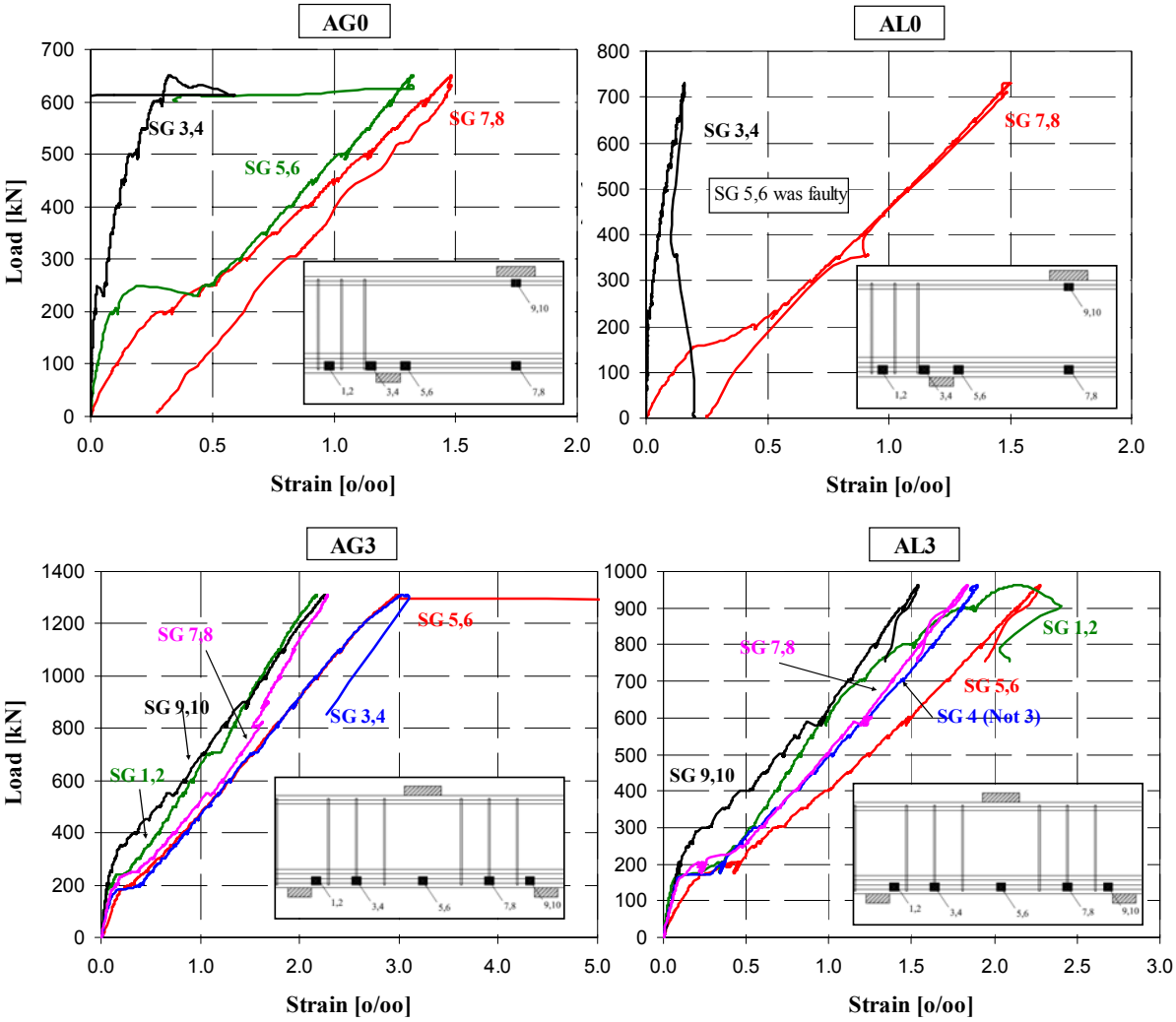

Note: A0- strain gauges 1,2 at the anchorage zone had values close to zero
A0- strain gauges 5,6 were faulty during test
AL3- strain gauge 3 was faulty during test (readings of strain gauge 4 are shown)

Figure 6.21: Strain readings from strain gauges at longitudinal reinforcement bars

Strains at direct strut (longitudinal and transverse)

Figure 6.22 shows the longitudinal and transverse profiles of the compressive strains of the direct strut according to the Demec grid described in Figure 6.9. The origin of the longitudinal section corresponds to the bottom node (point A, Figure 6.9) and the transverse section is measured at 375mm from this origin. The transverse profiles generally had the maximum value at the centre line of the direct strut. This is true for all beams except for AL0 and AL3 where the maximum was at the reading below the centre line. The reason behind this was that for beams AL0 and AL3, this sector was crossed by a shear crack (Figure 6.14).

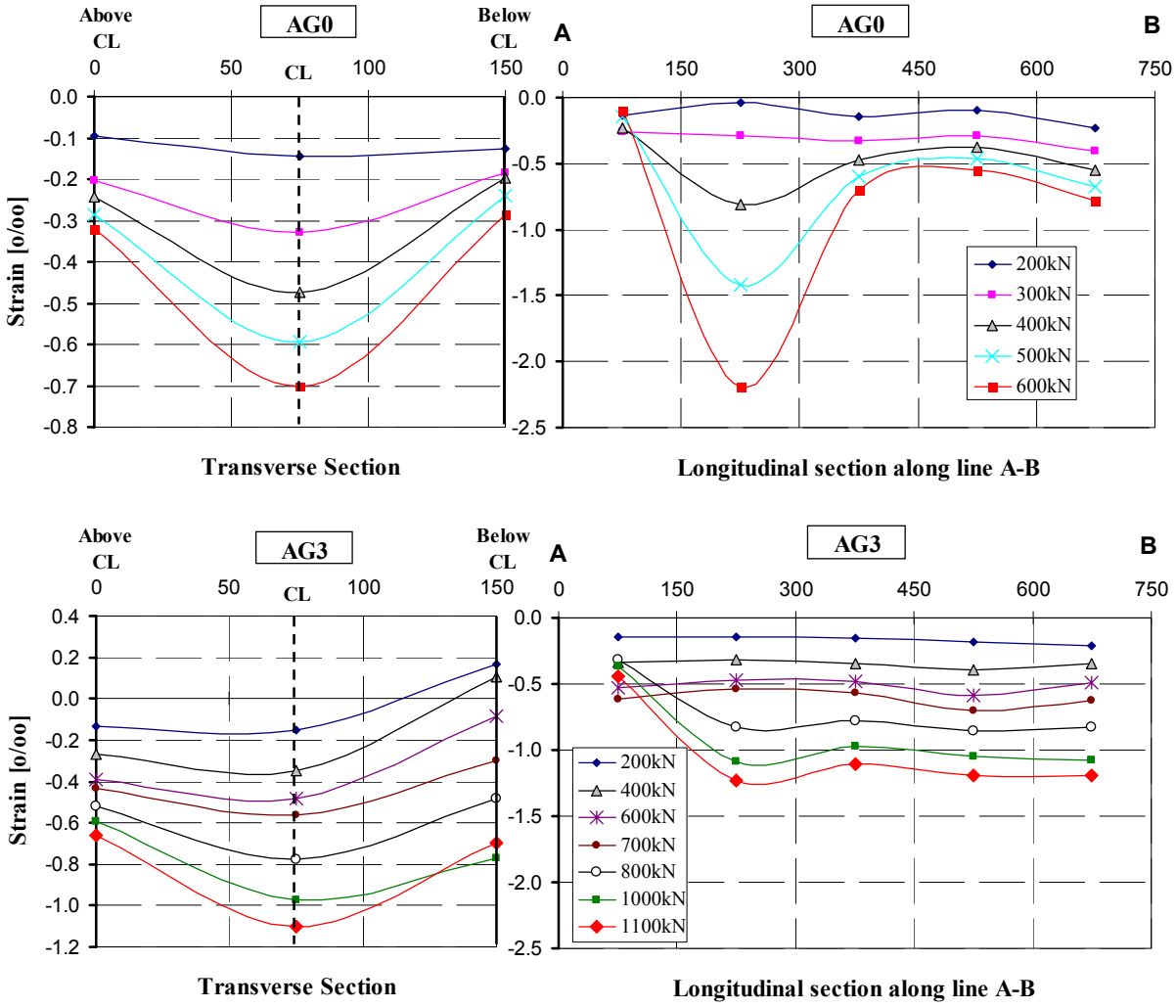

Note: Transverse section measured at the middle of the strut (350mm from point A), refer to Figure 6.9

Figure 6.22: Longitudinal strains along direct strut (transverse and longitudinal sections)

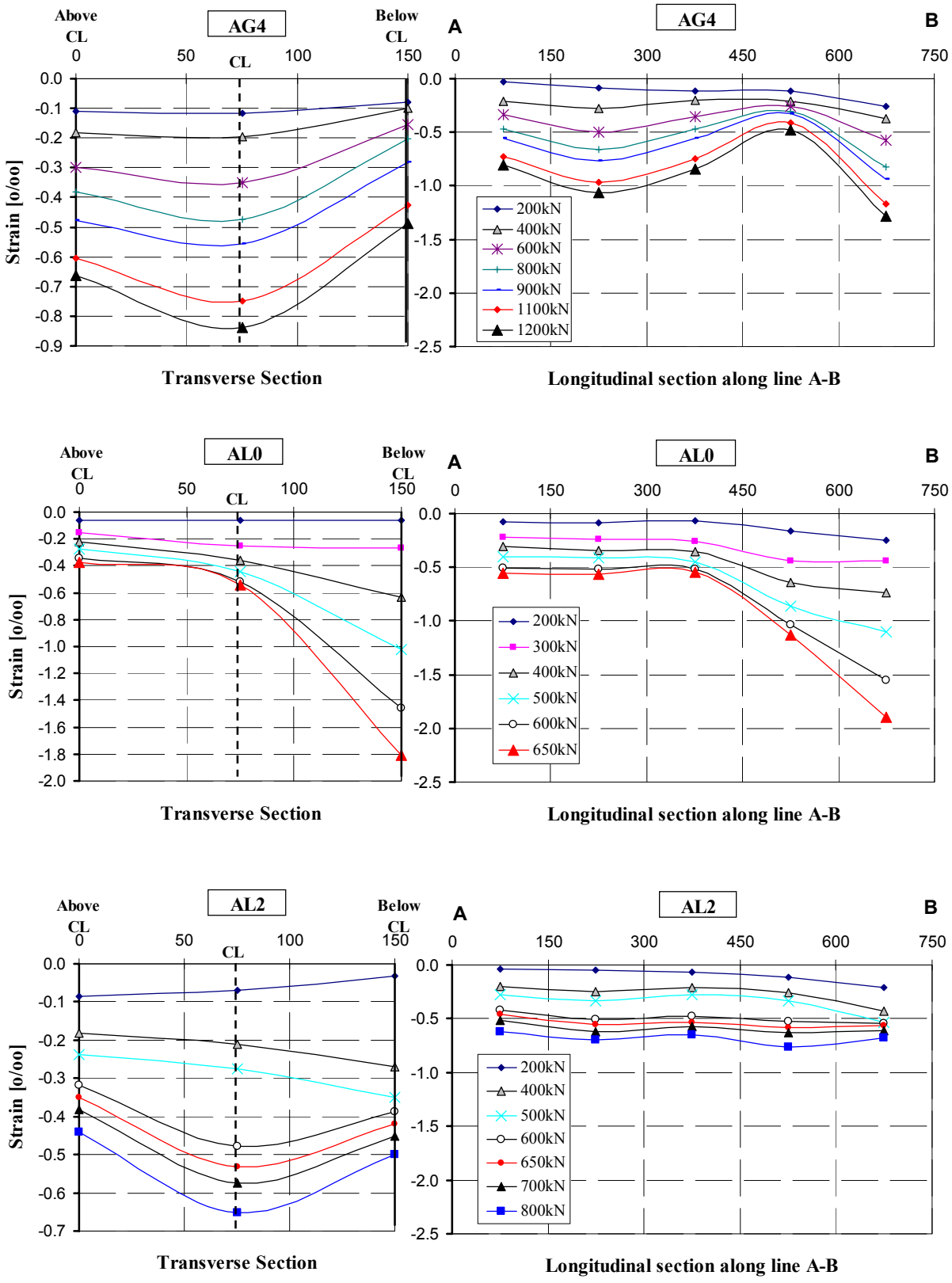

Note: Transverse section measured at the middle of the strut (350mm from point A), refer to Figure 6.9

Figure 6.22 (Cont.): Longitudinal strains along direct strut (transverse and longitudinal sections)

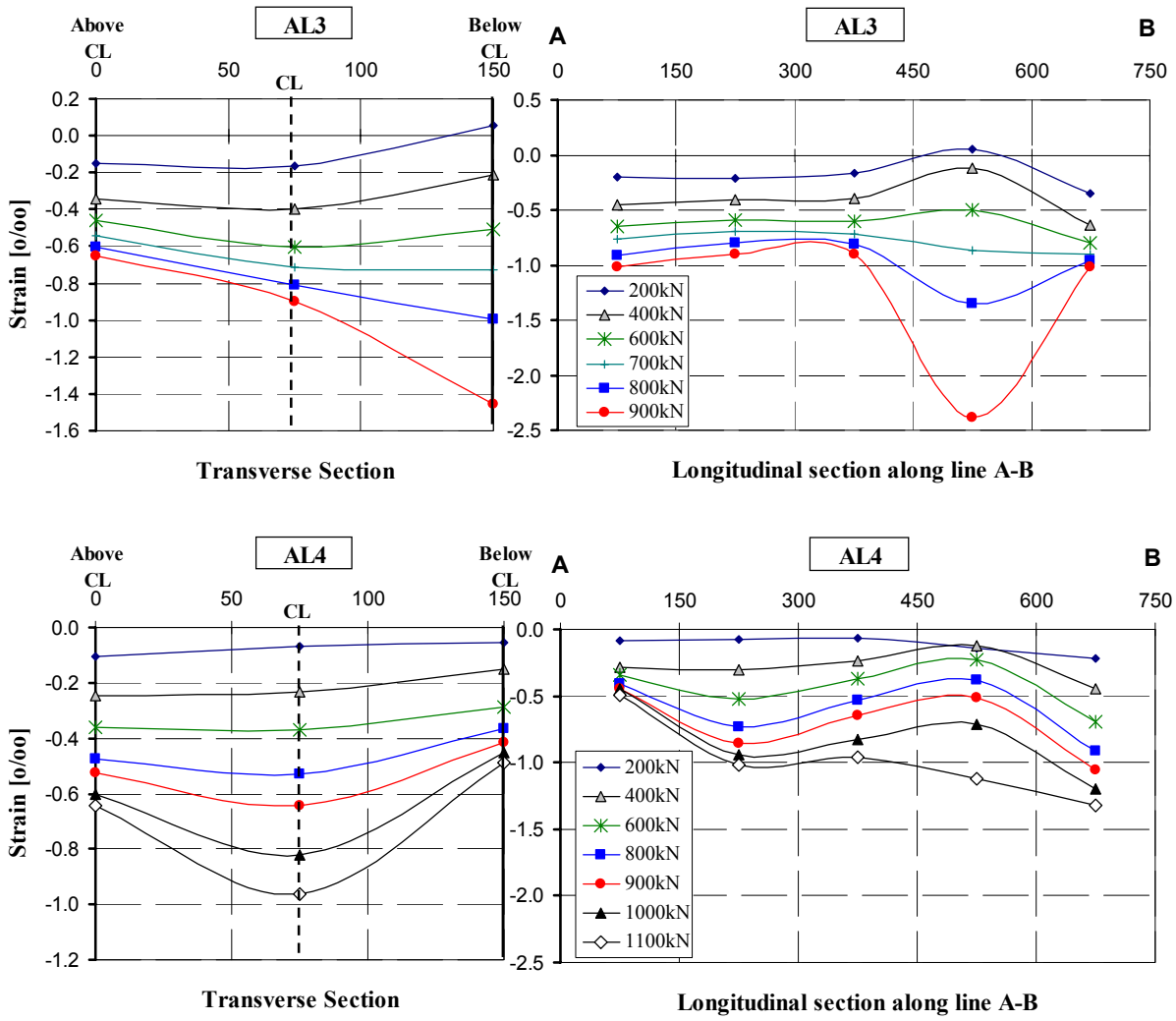

Note: Transverse section measured at the middle of the strut (350mm from point A), refer to Figure 6.9

Figure 6.22 (Cont.): Longitudinal strains along direct strut (transverse and longitudinal sections)

Relative crack displacements

The crack opening (w) and sliding (s) near failure are shown in Table 6.5 and Figure 6.23. These results refer to the shear span with a_v/d of 1.12, which was critical for all the beams except for AG4 and AL2. In some specimens the readings from the Demec/LVTD crosses were influenced by additional shear cracks that formed at later load stages. Table 6.5 summarises the number of cracks that went through each cross and the deviation α from the 45° reference plane with respect the longitudinal reinforcement. In Figure 6.23, measurements from crosses of targets, which were only crossed by one crack, are highlighted in red. Readings from crosses where three points of the cross of targets were at the same side of the crack were ignored.

As shown in Figure 6.23, crack opening was the predominant mode over crack sliding. The relative crack displacements were very similar for both gravel and limestone aggregate concrete beams. The $\delta w/\delta s$ ratio was almost linear and very similar for all beams, regardless the type of aggregate used. The average value for $\delta w/\delta s$ was around 3. Beams AG4 and AL2 had a larger $\delta w/\delta s$ ratio due to the fact that failure occurred on the other shear span (a_v/d of 1.04) hence crack sliding was not mobilized.

			(a) TOP DEMEC		**(b) BOT. DEMEC**		**(c) TOP LVTD**		**(d) BOT. LVTD**	
Distance from bottom			*339.33mm*		*162.5mm*		*243.72mm*		*87.5mm*	
Beam	$w_{failure}$ [mm]	$s_{failure}$ [mm]	Cracks	α [°]	Cracks	α [°]	Cracks	α [°]	Cracks	α [°]
AG0	1.22[(a)]	0.57[(a)]	1	3	2	8	1	8	2	6-17
AG2	1.40[(c)]	0.56[(c)]	1	4	2	2	1	2	-	3
AG3	1.22[(a)]	0.40[(a)]	1[xx]	2	3[+]	6	1[+]	4	2[+]	17
AG4	1.03[(c)]	0.12[(c)]	2	0	2[+]	8	1	3	2	2
AL0	1.15[(a)]	0.41[(a)]	1	11	1[+]	16	0	-	2[+]	15
AL2	1.35[(c)]	0.28[(c)]	3	5	2	23	1	4	1	11
AL3	1.30[(a)]	0.45[(a)]	1	7	2	1	2	6	2[+]	11
AL4	0.94[(c)]	0.31[(c)]	1	6	3	5	1	5	2	7

Note- [+] Three points on one side of the crack (readings are neglected)
[xx] In beam AG3 only one crack went through the cross until load 730kN
- Beam AG2 had a faulty transducer at the bottom cross
α>0 for cracks flatter than 45°

Table 6.5: Summary of relative crack displacements near failure, number of cracks going through the Demec/LVTD crosses and deviation α with respect the 45° plane

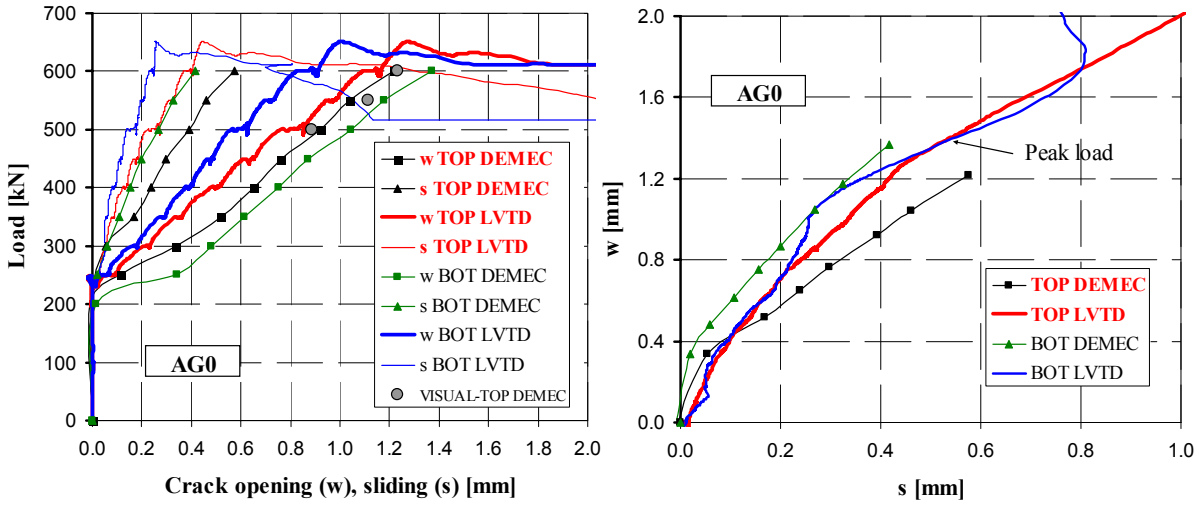

a) Beam AG0 (P_{ult} = 651.53kN)

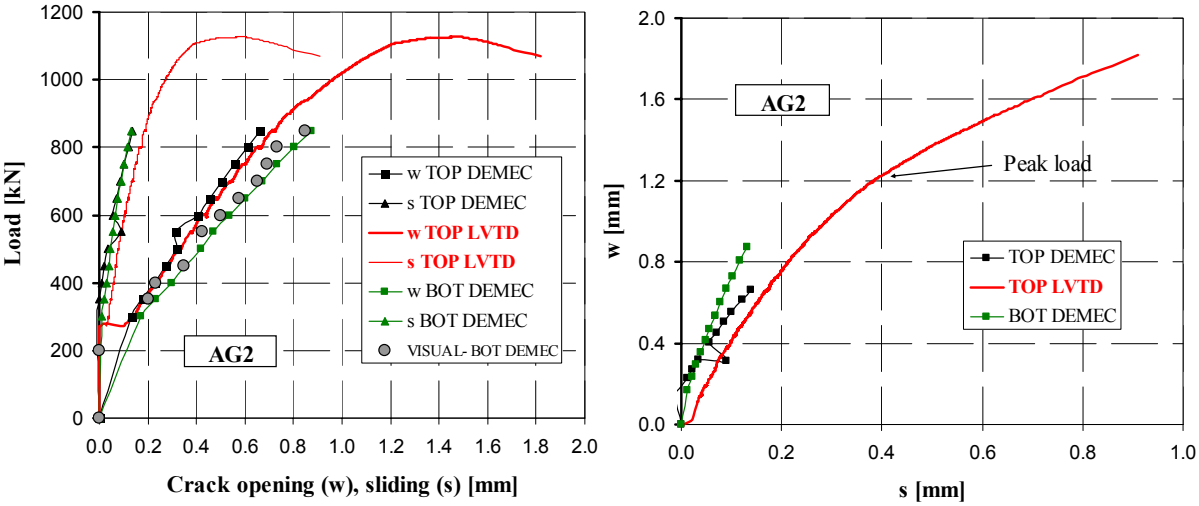

b) Beam AG2 (P_{ult} = 1126.05kN)

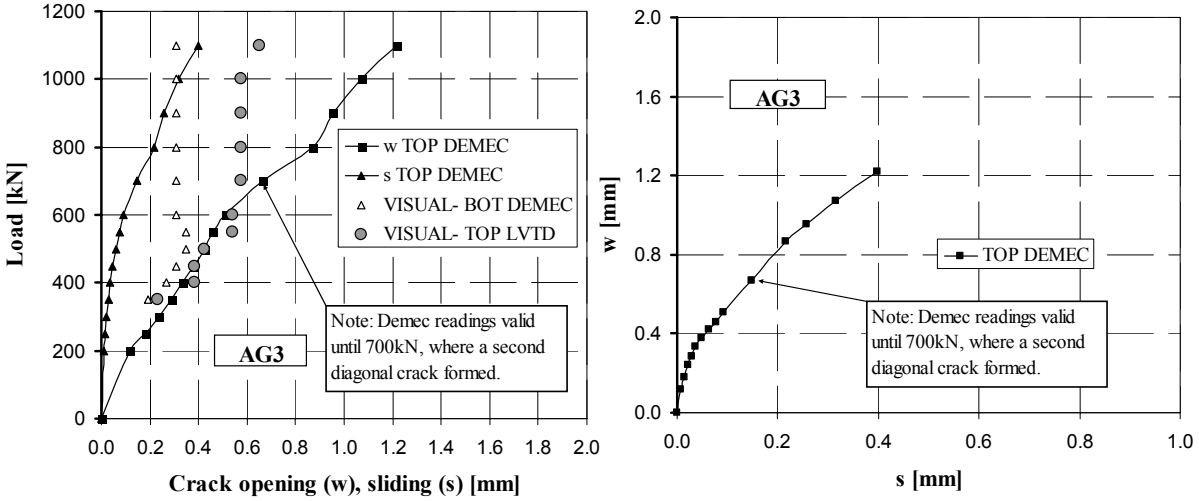

c) Beam AG3 (P_{ult} = 1309.21kN)

Figure 6.23: Crack opening (w) and sliding (s) in beams A

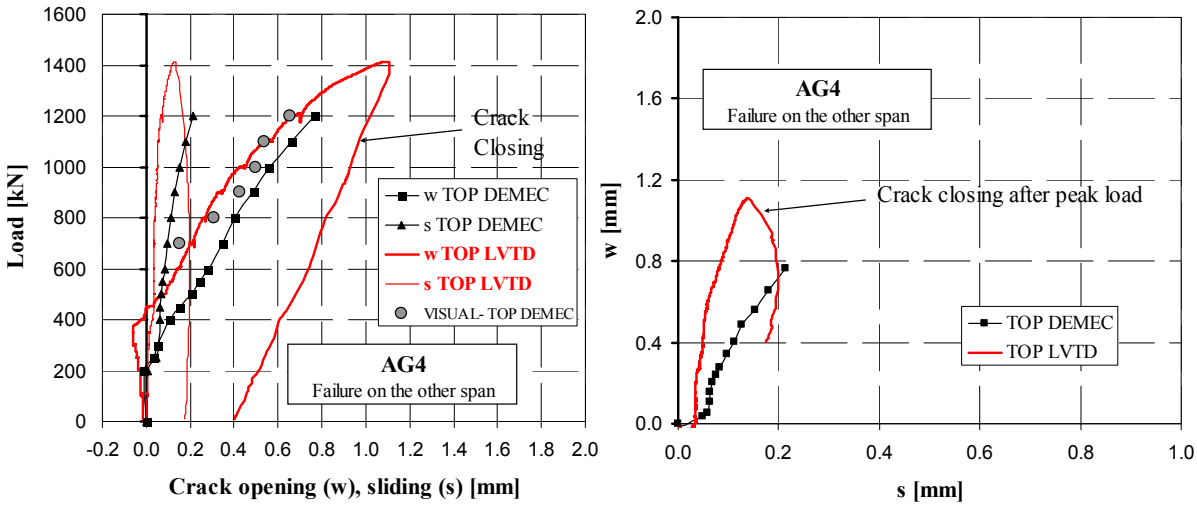

d) Beam AG4 (P_{ult} =1414.20kN)

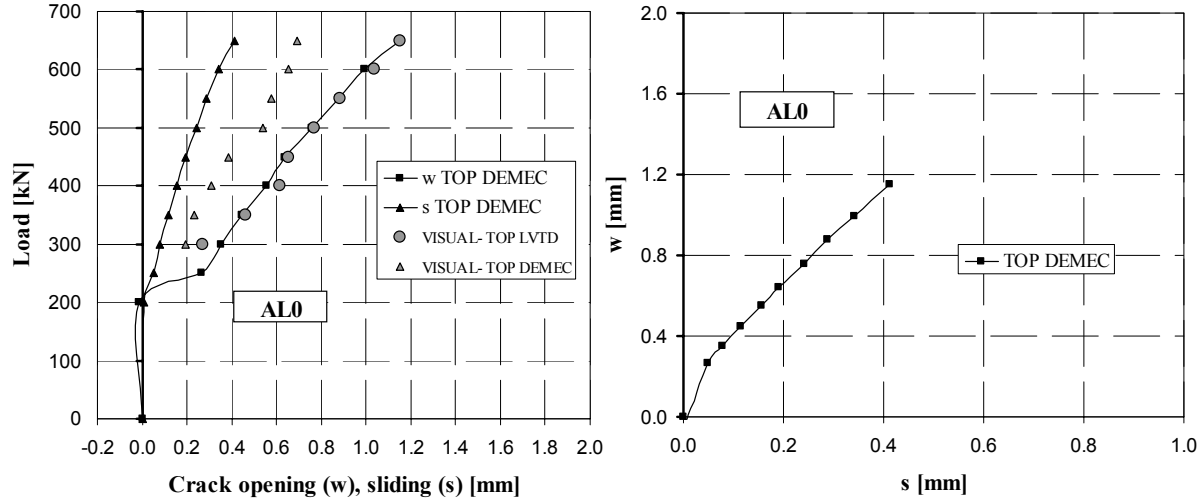

e) Beam AL0 (P_{ult} = 731.01kN)

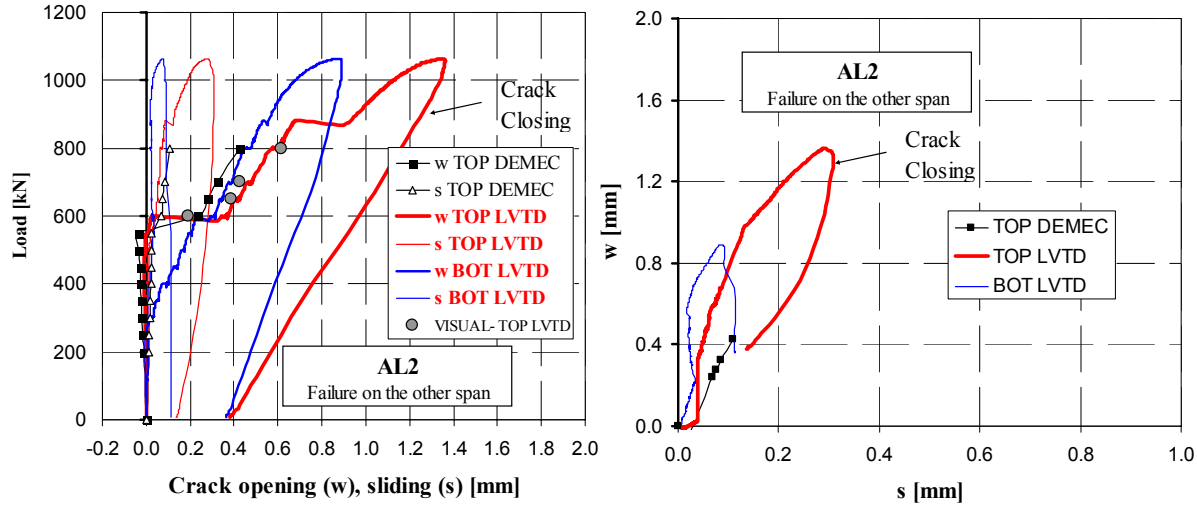

f) Beam AL2 (P_{ult} = 1063.79kN)

Figure 6.23 (Cont.): Crack opening (w) and sliding (s) in beams A

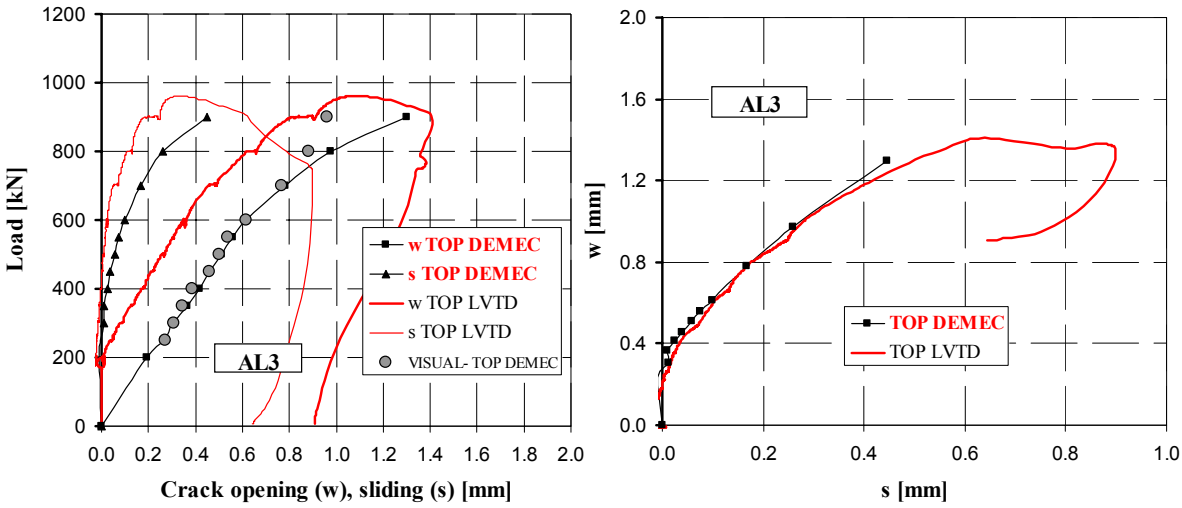

g) Beam AL3 (P_{ult} = 961.46kN)

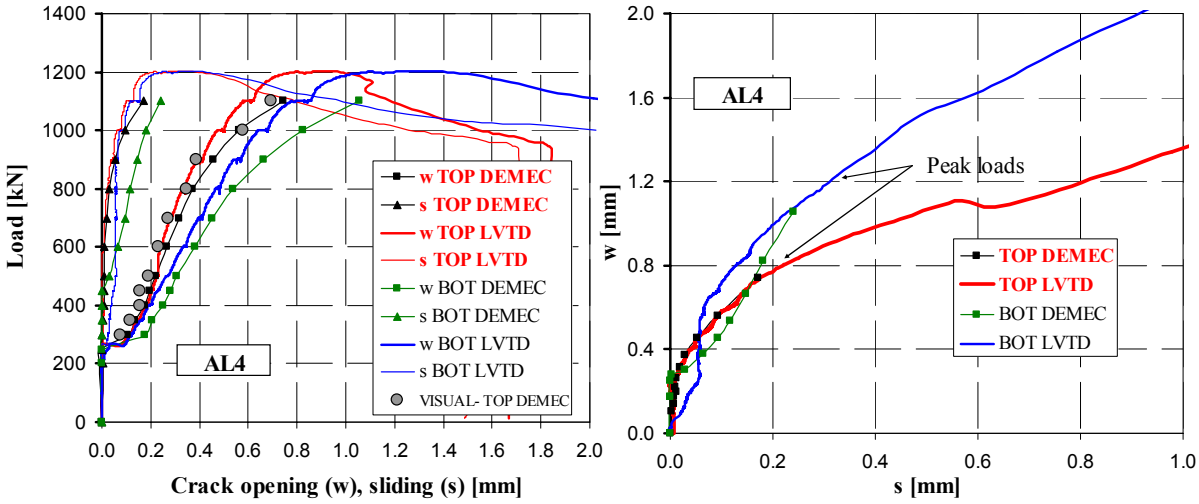

h) Beam AL4 (P_{ult} = 1204.39kN)

Figure 6.23 (Cont.): Crack opening (w) and sliding (s) measured in beams A

The crack opening of AG4 and AL2 was similar than the rest of the beams, although the diagonal crack at the shear span of a_v/d=1.12 closed after reaching the peak load (Figure 6.23). In the shear span with an a_v/d ratio of 1.04 the relative crack displacements were monitored only with two Demec crosses. The values recorded for w and s (refer to Figure 6.24) were approximately half of those obtained at the other shear span with a w/s ratio equal to 3, which is similar to the other shear span. The main diagonal crack in the shear span with a_v/d of 1.04 was steeper, with values of α generally lower than in the other shear span.

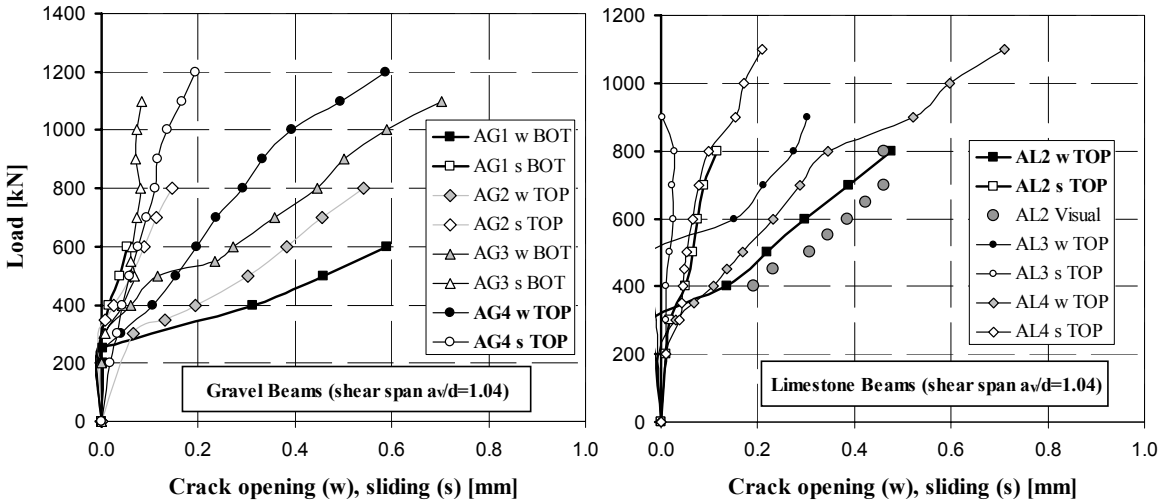

a) Gravel beams b) Limestone beams

Figure 6.24: Crack opening and sliding in the a_v/d 1.04 shear span of beams A

In general there was a good agreement between Demec and LVTD readings, as shown in Figure 6.23. Crack openings were validated by visual readings, marked as circles in Figures 6.23 and 6.24, which were in excellent agreement with the other types of measurements. In beam AG3 (Figure 6.23.c), the visual readings agreed with the values obtained from the Demec gauges until a load of 700kN. At this load, a new diagonal crack formed, which caused the previous crack to remain with a constant *w* as the new crack got wider. This explains the difference between the values of *w* measured by the Demec gauge and optical ruler in beam AG3, since the former included both cracks while the later only included the original crack.

Visual local readings of the main diagonal crack of beam AL4 at different points, showed that the crack opening was constant through the height of the beam (Figure 6.25). The readings were in good agreement with the results provided by the top LVTD and Demec crosses, as shown in Figure 6.23. Only visual reading 3, located at the stirrup, provided lower values of *w*. Closer examination of the crack showed that the reading in point 3 were influenced by a secondary crack that had formed near the stirrup, see Figure 6.25. Similar secondary cracks to the one shown in Figure 6.25, were found in other beams at points where the stirrups crossed the shear cracks. Visual readings of the crack opening should be avoided in such local points.

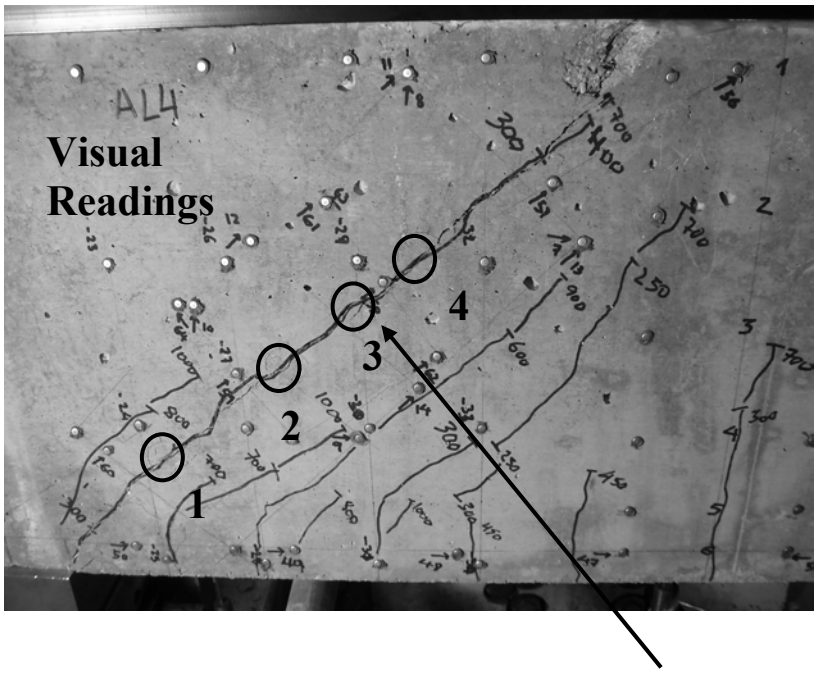

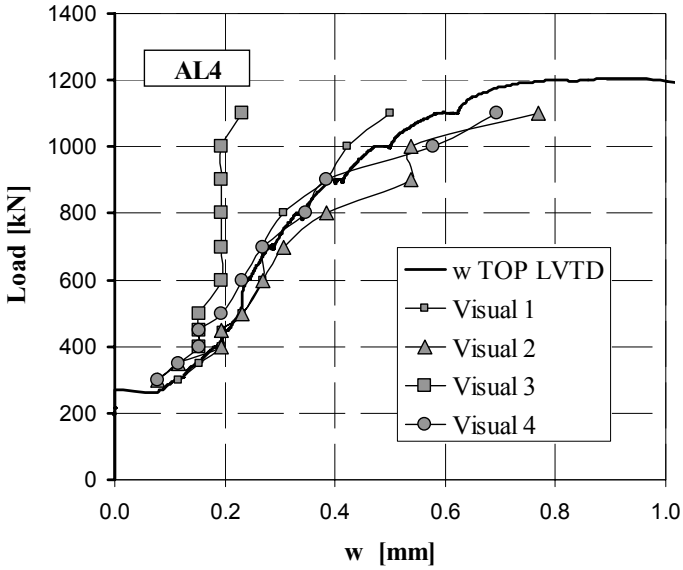

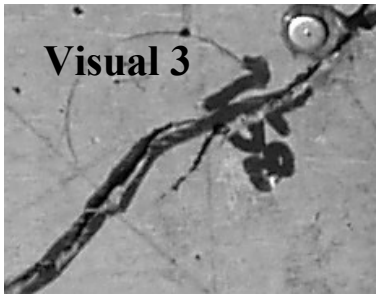

Note: TOP LVTD placed on the South side of the beam at similar position as visual point 3

Figure 6.25: Crack opening of main diagonal crack of AL4 at different beam heights (North Side)

6.4 Slender beams without stirrups (Beams B0)

6.4.1 General aspects

Four slender beams without transverse reinforcement, which are denoted as beams B0, were designed and tested by the author to fail in shear. Two of these beams (BG01 and BG02), were cast using normal aggregate concrete. The remaining two beams (BL01 and BL02) were made of limestone aggregate concrete. The beams were cast using the same concretes as for the short span beams, i.e. mix 1 for BG0 beams and mix 2 for BL0 beams, see section 6.2.2 for further details.

Beams B0 were all identical and were loaded at the centre span as shown in Figure 6.26. The cross section was the same as for the short span beams except for the longitudinal reinforcement, which consisted of 2T20 bars (ρ_l = 1%), see Figure 6.26. The amount of longitudinal reinforcement provided was sufficient in order to avoid flexural failure. The shear span to effective depth ratio *a/d* was 3.46 to avoid any shear strength contribution due to arching action.

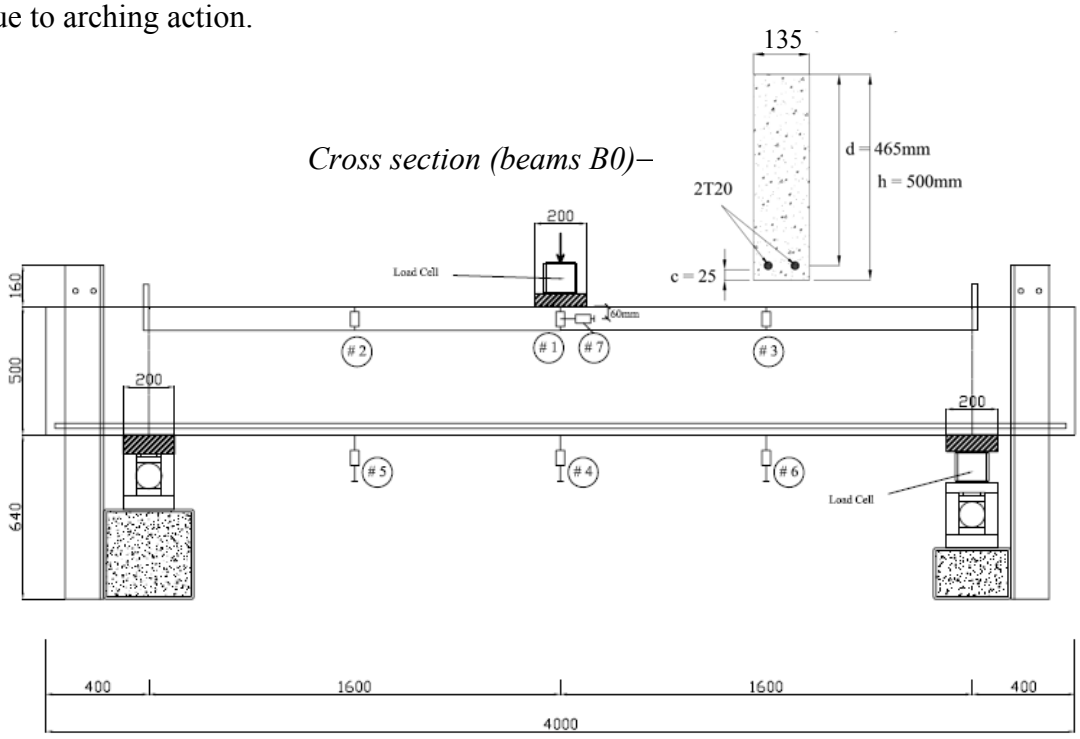

Figure 6.26: Slender beams without stirrups (Beams B0)

The central span was 3200mm long, measured between centrelines of the supports. The same rollers supports as for the short span beams were placed under the bearing plates to allow horizontal displacements and pinned rotation. The thickness of the bearing plates were 75mm for the left plate, 65mm for the right plate and 30mm for the loading plate.

6.4.2 Manufacture and curing

The beams were cast at the same time as the short span beams. The same procedure described in section 6.3.2 applies for the manufacture and curing of the slender beams without stirrups.

6.4.3 Instrumentation

The instrumentation consisted of two load cells (1000kN), one placed under the hydraulic jack and the other located under one support, in order to assess any potential asymmetries in the rig. Vertical and side displacements were monitored using LVTDs transducers.

A total of seven LVTDs transducers were applied, see Figure 6.26: six (#1-6) for measuring the vertical displacements along the beam and one (#7) to control side displacements at the centre. Transducers #1-3 measured deflections relative to the supports, while transducers #4-6 took measurements relative to the floor.

6.4.4 Results

Summary of experimental results

The type of failure was similar for all beams, regardless the type of aggregate used; all beams had a very brittle behaviour. Identical specimens BG01/BG02 and BL01/BL02 had very similar failure loads as shown in Table 6.6. Flexural cracks formed at early load stages of around 50% of the ultimate load. Failure occurred suddenly at P_{ult} when the diagonal shear crack developed from a previous flexural crack. The deflection under the loading plate (δ_{centre}) given in Table 6.6 was measured relative to the support.

Beam	f_c' [MPa]	f_{sl} [MPa]	ρ_l [%]	a/d	δ_{centre} [mm]	$P_{cr,flex}$ [kN]	P_{ult} [kN]	Failure
BG01	80.20	580	1	3.46	4.14	56.2	122.63	Diag. Tens
BG02	80.20	580	1	3.46	4.70	50.0	126.22	Diag. Tens
BL01	68.44	580	1	3.46	3.58	50.0	93.72	Diag. Tens
BL02	68.44	580	1	3.46	4.27	50.0	108.14	Diag. Tens

Table 6.6: Summary of experimental results of slender beams without shear reinforcement (Failure: Diagonal Tension)

Type of Failure and Crack pattern

The first flexural cracks that formed were completely vertical and reached in most cases the middle height of the beam. As the load was increased, the outer flexural cracks turned into flexural-shear cracks, which were inclined towards the centre of the beam at the top and were shorter than the central flexural cracks, see Figures 6.27 to 6.30.

The type of failure was the same for all the beams and corresponded to a typical brittle shear failure (diagonal tension failure) along the main shear crack. The critical crack initiated at a previous flexural-shear crack and propagated suddenly to the load and support plates (Figure 6.27). The main diagonal crack reached the support plate through a horizontal splitting crack, which formed due to the loss of bond and dowel action along the longitudinal reinforcement.

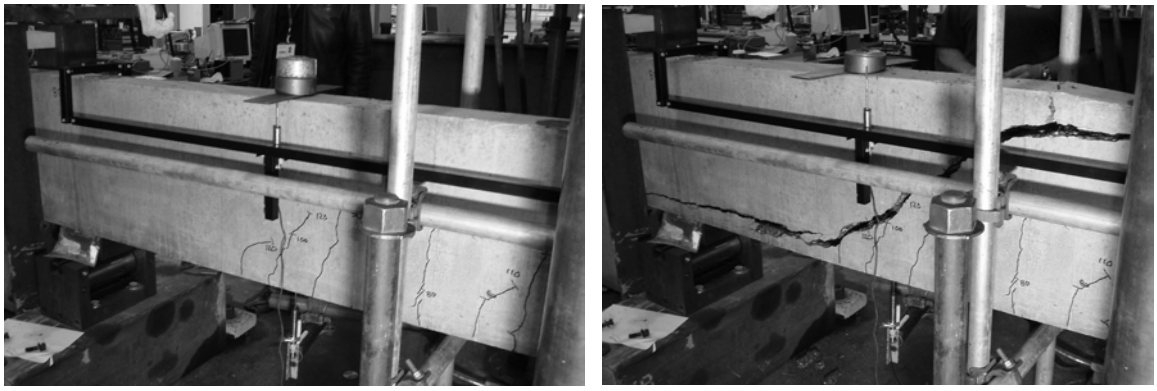

Figure 6.27: Diagonal tension failure along main shear crack (Beam BL01)

The beams failed in either shear span, BG01/BL01 on the right span and BG02/BL02 on the left span from north side, which showed a good symmetric arrangement in the loading rig. After removing the top halve of the beam the crack surfaces showed two different types of roughness (Figure 6.28). In the limestone concrete specimens the aggregate fracture while the crack only went through a fraction of the aggregate for the gravel specimens, as shown in Figure 6.28. An estimated figure of the percentage of the gravel aggregate that fractured at the crack surface is 30% (±5).

Figure 6.28: Crack surfaces: *Left*- Limestone aggregate beam; *Right*- Gravel aggregate beam

Despite the difference in roughness between the limestone aggregate and gravel aggregate surface cracks, the geometry of the main diagonal crack was similar for all the beams, as shown in Figures 6.28 and 6.29. The only minor difference between limestone and gravel specimens, which is illustrated in Figure 6.29, was that the angle between the longitudinal reinforcement and the first section of the main diagonal crack was larger for the limestone beams than for the gravel aggregate beams.

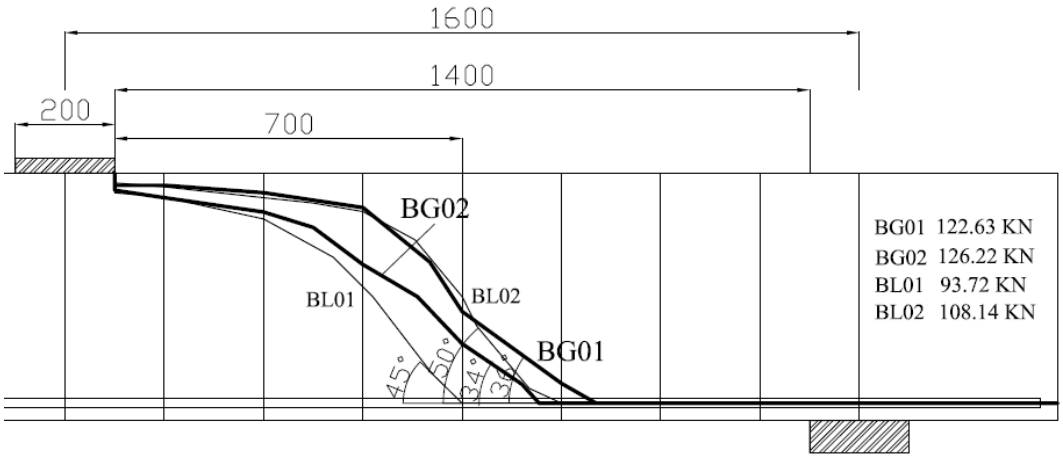

Figure 6.29: Relative position of main shear cracks (beams B0)

BG01 (North Side)

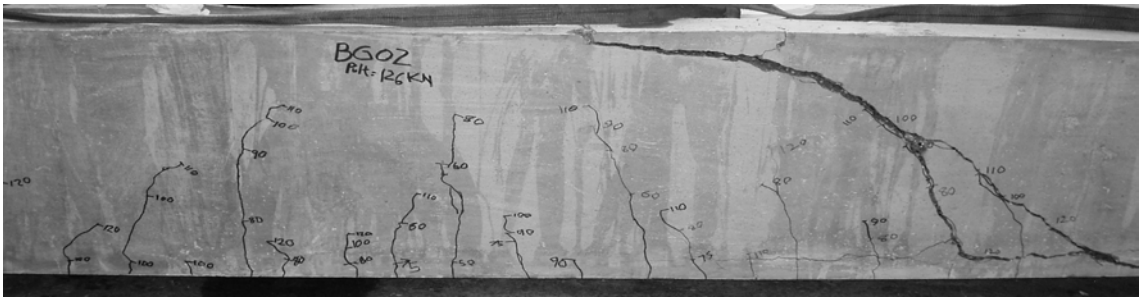

BG02 (South Side)

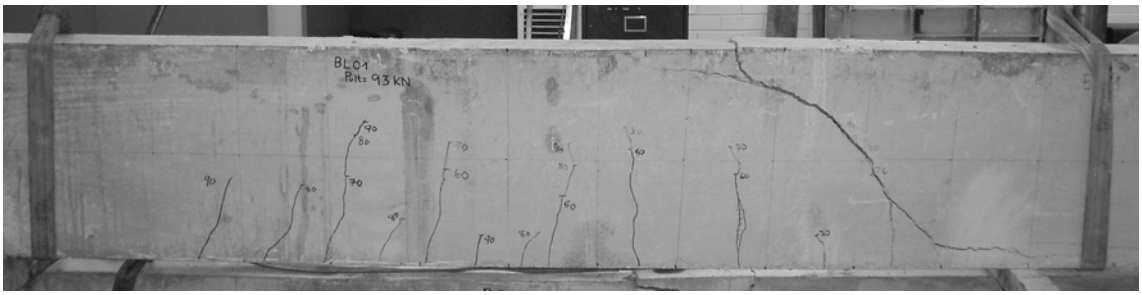

BL01 (North Side)

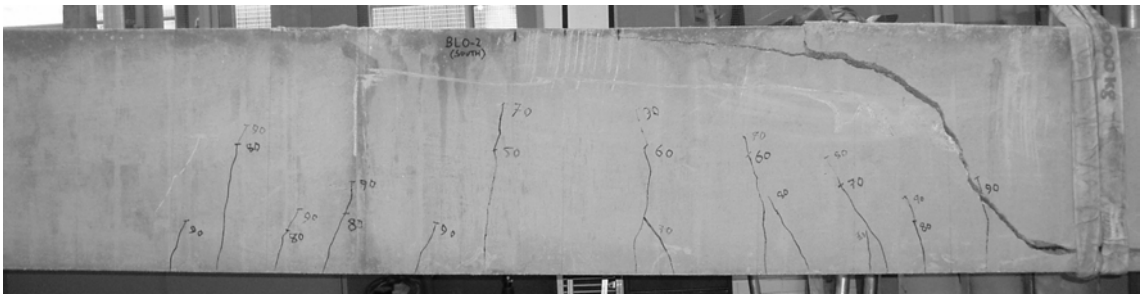

BL02 (South Side)

Figure 6.30: Crack pattern of slender beams without stirrups

Load-deflection curves

The deflections under the load plate relative to the supports were between 4 and 5mm at failure (Figure 6.31). All beams had similar stiffness until failure. The deflections measured by the LVTDs relative to the floor were slightly higher than those measured relative to the support, which indicated that a bedding in settlement occurred at early load stages. At failure the difference between readings taken relative to the supports and floor was around 20-30%.

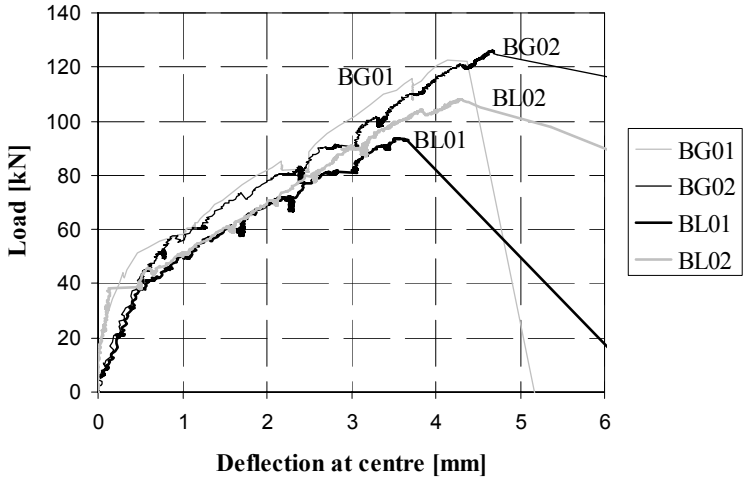

Figure 6.31: Deflections at the centre of the beam, relative to the support

The deflections at quarter points were approximately half as at the centre (Figure 6.32), with a symmetrical response with respect the centre line. Lateral deflection, monitored by transducer #7 (refer Figure 6.26) were negligible throughout the test.

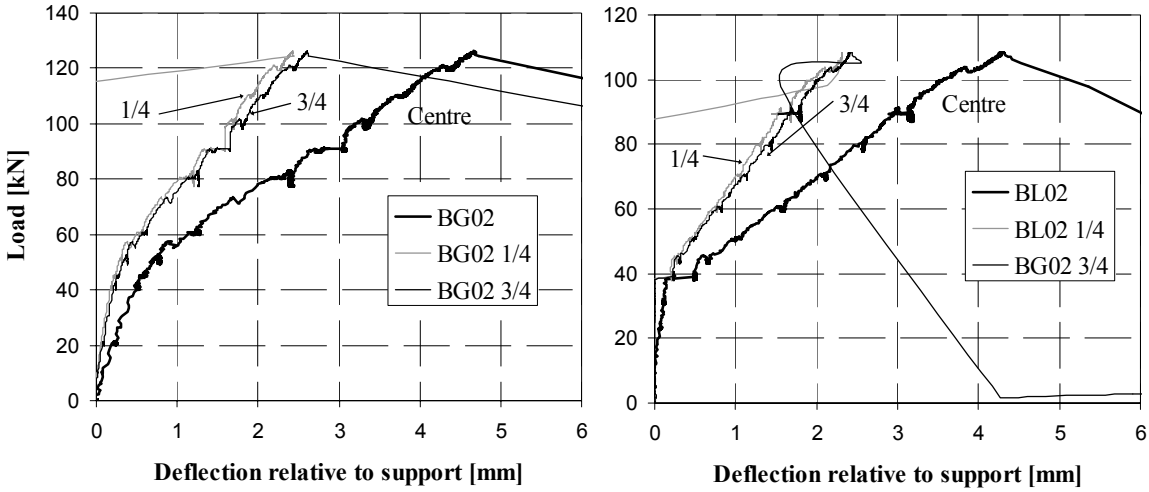

Figure 6.32: Vertical deflections relative to the supports at quarter points for BG02 & BL02

6.5 Slender continuous beams with stirrups (Beams B and C)

6.5.1 General aspects

A total of eight continuous beams (beams B and C) with a shear span over effective depth ratio *a/d* of 3.52 were tested (Table 6.7). The main parameter investigated in beams B was the type of aggregate used; "G" for gravel and "L" for limestone. In beams C, the width of the beam was increased from 135mm used for beams A and B to 160mm. The diameter of the stirrups was 10mm as opposed to 8mm, which was used in beams A and B.

Beam	Concrete Sect.6.2.2	f_c' [MPa]	f_{sl} [MPa]	f_s [MPa]	b [mm]	n stirrups	s [mm]	ρ_v [%]
BG1	Mix 3	31.70	580	550	135	10	T8@150	0.50
BG2	Mix 3	31.70	580	550	135	16	T8@90	0.83
BL1	Mix 4	53.11	580	550	135	10	T8@150	0.50
BL2	Mix 4	53.11	580	550	135	16	T8@90	0.83
CB1	Mix 5	49.35	580	600	160	5	10@300	0.33
CB2	Mix 5	49.35	580	600	160	7	10@200	0.49
CA1	Mix 5	49.35	580	600	160	5	10@300	0.33
CA2	Mix 5	49.35	580	600	160	7	10@200	0.49

Table 6.7: Material properties and shear reinforcement at the critical span

An identical two point loading arrangement was used in tests B and C, in order to obtain a point of contra-flexure within the shear span as shown in Figure 6.33.a. This load arrangement gives rise to the bending moment distribution shown in Figure 6.33.b. This load configuration produced high shear forces, and minimised the hogging and sagging bending moments at critical sections. Another advantage of introducing a point of contra-flexure was that the shear resisted by the compressive zone at the head of the shear crack was eliminated with the result that the beam was loaded in pure shear rather than flexural-shear as in a simply supported beam.

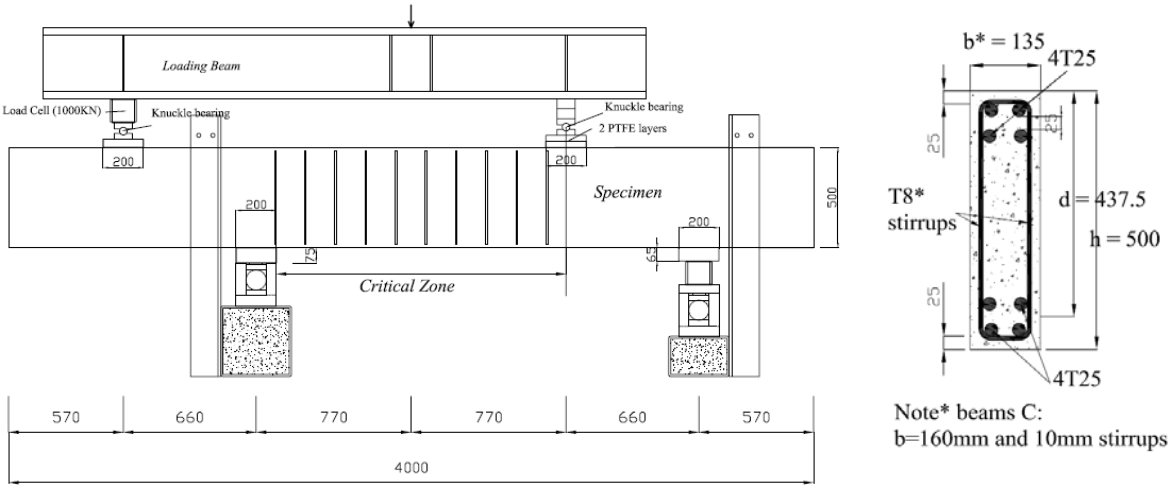

a) Testing rig and cross section of beams

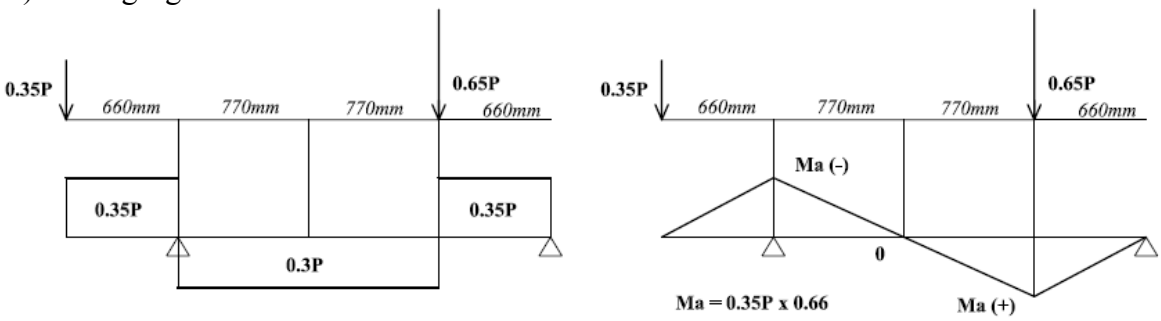

b) *Shear Force Diagram* *Bending Moment Diagram*

Note: Beams C were 4500mm long instead of 4000m shown in (a) for beams B. This leads to 820mm overhangs as opposed to 570mm in beams B shown in (a)

Figure 6.33: Loading arrangements: a) Testing rig and cross section of beams; b) Shear force and bending moment diagrams

The short shear spans had an a_v/d ratio of 1.05 and a shear force equal to 35% of the total load. However, they were not critical since they had larger shear reinforcement ratios plus strength was enhanced by arching action. The stirrups provided in the short spans in beams B were 2 leg stirrups of T8 every 90mm and 60mm for B1 and B2 beams respectively (Figure 6.34). An additional 2 stirrups for B1 and 3 stirrups for B2 were placed at the centre of each short shear span as shown in Figure 6.34, to strengthen these regions. In beams C, the spacing between stirrups in the short shear spans was half that in the critical span.

The arrangement of longitudinal reinforcement in beams B and C was similar to that used in Beams A except that two layers of two T25 each were placed at the top of the beam (Figure 6.33.a). This symmetrical arrangement of longitudinal reinforcement allowed the beam to resist the anti-symmetric bending moment distribution, shown in Figure 6.33.b, without yielding of the longitudinal reinforcement bars.

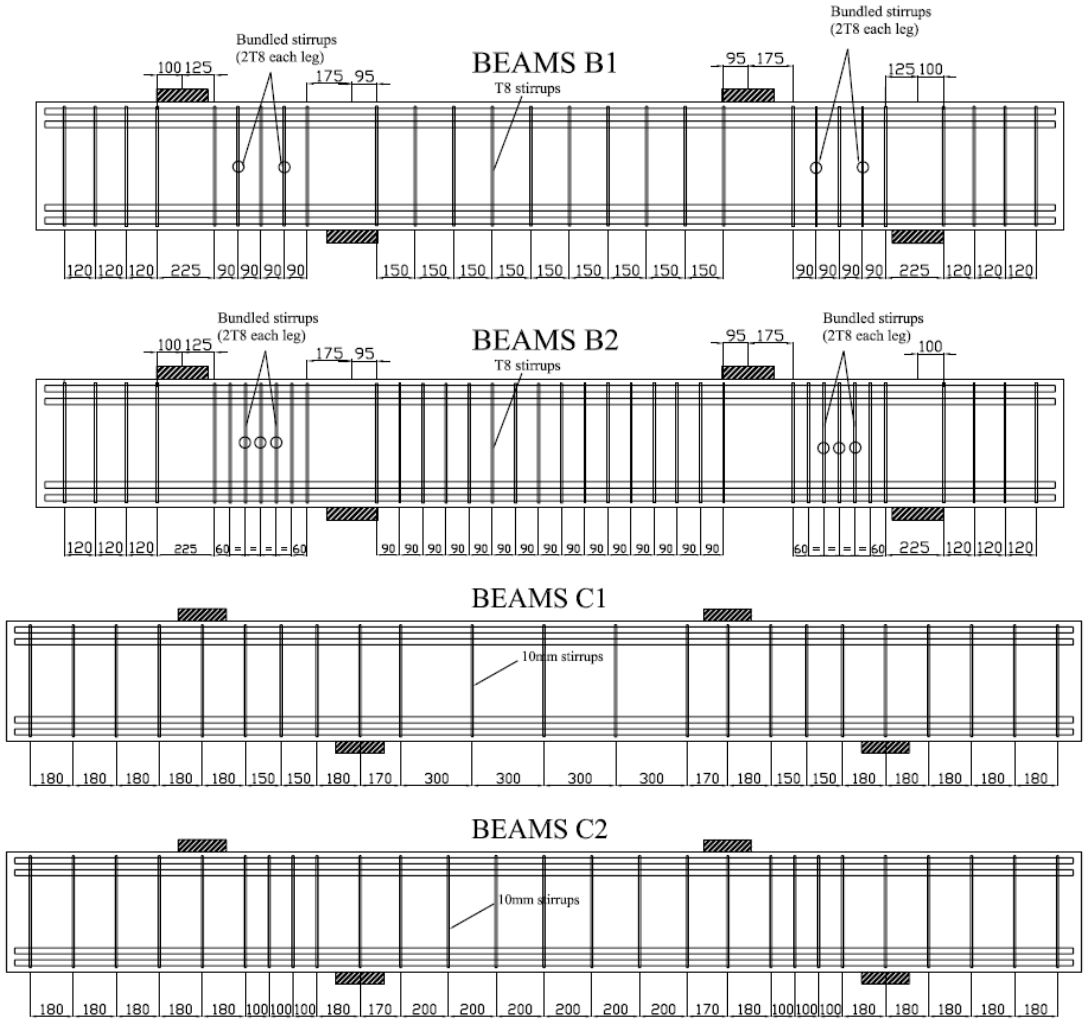

Figure 6.34: Spacing between stirrups in beams B and C

The specimens were supported on the rollers used for beams A and B0 that allowed rotation and horizontal displacements. The loads were applied through a loading beams. The concrete beam was restrained longitudinally at the cantilever loading point and released laterally at the other end using two PTFE layers under the central loading plate, see Figure 6.33.a. The forces were transmitted to the testing beam through knuckle bearings in order to allow rotation of the loading beam, although the deflection of the cantilever and centre load points were expected to be very similar. All the loading and support plates in contact with the testing beam were 200mm long.

The loading beam, which consisted of a universal column 305x305x240 (S355) had a total dead load of 720kg. The dead load of the loading beam was not transmitted to the supports of the testing beam evenly, due to the position of the loads. Instead, 80% of the self weight of the loading beam was taken by the support nearer the cantilever end. However, the dead load of the loading beam was negligible compared with the total load

applied and therefore the internal stresses is well represented by the diagrams shown in Figure 6.33.b. This was confirmed by the load readings from the load cells, which were set to zero after the loading beam was placed on top of the testing beam.

Beams B and C were pre-cracked and then loaded monotonically to failure, as opposed to beams B0 and A, which were taken directly to failure. Pre-cracking the specimen was necessary in order to place the instrumentation around the critical crack since the exact location of this crack was uncertain a priori.

6.5.2 Manufacture and curing

Due to the large amount of reinforcement provided in beams B, the specimens were cast horizontally, (Figure 6.35). Beams B were cast in two groups of two (BG1/BG2 and BL1/BL2) and vibrated with a standard 1" head vibrator. Beams C were cast vertically (Figure 6.35) along with beams D. The control cubes and cylinders were cast and cured in the same manner as for beams B0 and A, see section 6.2.2. Same methods were adopted for curing the specimens as for beams B0 and A.

Figure 6.35: Cast of beams B (left) and beams C-D (right)

6.5.3 Instrumentation

In order to control that the load was applied correctly, three load cells were used, as shown in Figure 6.33.a. First one, which had 2500kN capacity, was located under the hydraulic jack to monitor the total loading. The second and third load cells (1000kN capacity) were placed at the cantilever load point and right support; both readings should be equal to 35% of the total load.

In a similar manner as in the short span beams (beams A) deflections, strains and relative crack displacements were monitored using different methods:

1. Linear variable displacement transducers (LVTDs)
2. Demec readings (150mm Demec gauge)
3. Strain gauges at the reinforcement bars (only at longitudinal reinforcement bars)
4. Digital photogrammetric surveying

Digital photogrammetric surveying

Digital photogrammetric surveying, which is based on digital image processing, was introduced for beams B and C tests and provided useful information of global displacements. This monitoring technique was also used in the push-off tests, see section 4.2.3 for further details. The computer software required to analyse the digital photographs was developed and calibrated by McCarthy & Tsang [108]. Similarly as in the push-off tests, experimental results were compared with more conventional methods (LVTD, Demec and strain gauging).

The setup for the photogrammetric surveying consisted of four digital cameras, which were placed on the north face of the beam as shown in Figure 6.36. Cameras 2 and 3 (C2, C3) covered the critical shear span while C1 and C4 captured both extreme short shear spans. The working distances for each camera were 880mm, 750mm, 850mm and 915mm for C1, C2, C3 and C4 respectively. The height measured from floor to lens was 900mm. In beams C, only the critical shear span was monitored using photogrametric targets.

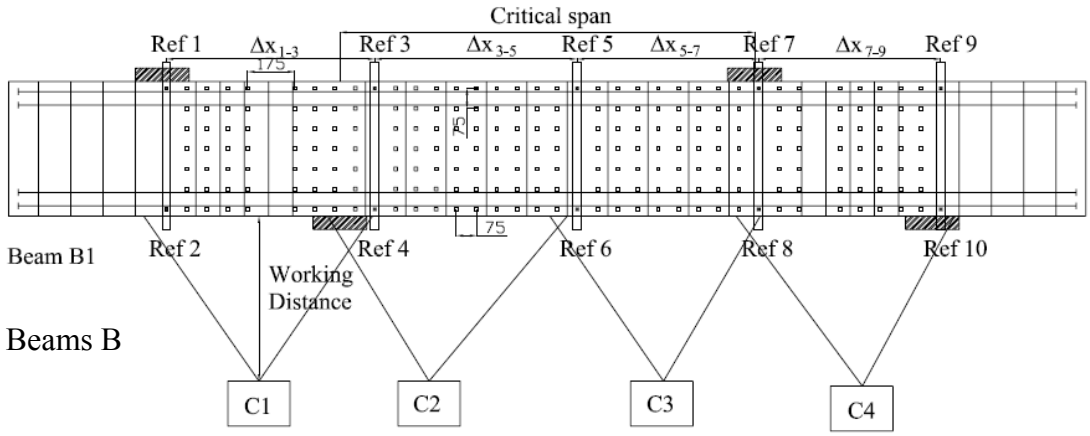

a) Beams B

Note- Cameras used: C1 – FujiFilm FinePix S5500 (4MG); C2 – Canon PowerShot S70 (7.1MG); C3 – Sony Cybershot DSC-F707 (5MG); C4 – Olympus mju 410 (4MG)

Figure 6.36: Test setup for digital photogrammetric surveying

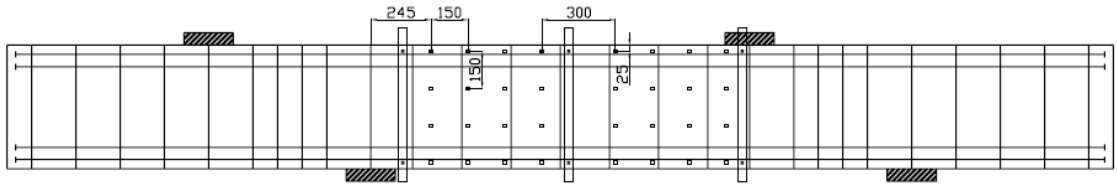

b) Beams C

Note-Cameras used: C2 – Canon PowerShot S70 (7.1MG); C3 – Sony Cybershot DSC-F707 (5MG)

Figure 6.36 (Cont.): Test setup for digital photogrammetric surveying

The grid of moving targets was an orthogonal regular grid throughout the entire beam with 75mm spacing for beams B and 150mm for beams C (with a 25mm cover), refer to Figure 6.36. The fixed referenced targets had horizontal spacings of 780-750-680-680mm for cameras C1 to C4 respectively, while the vertical distance between the reference points was around 450mm. Digital pictures were taken manually at each load step for both pre-crack and normal loading stages. Even though adequate lighting was provided by five halogen lamps, which produced uniform white light, the lighting conditions changed from one test to another due to unavoidable light variations in the laboratory.

Global displacements

The photogrammetric survey was complemented with traditional LVTDs measurements to monitor global displacements of the beams. A total of 7 LVTD transducers were placed in the beam, (Figure 6.37). Transducers #1 and #3 were placed under the central loading plate and measured vertical displacements relative to the supports and floor respectively. LVTD #7 measured relative vertical displacements to the supports at the central section of the critical shear span. Side deflections were controlled by transducer #2, which showed that the out-of-plane displacements were negligible. The vertical movement at the cantilever end was measured relative to the floor by transducer #4. Similar as in beams A, two transducers (#5,6) were place at simply supported end to calculate horizontal and end rotation movements.

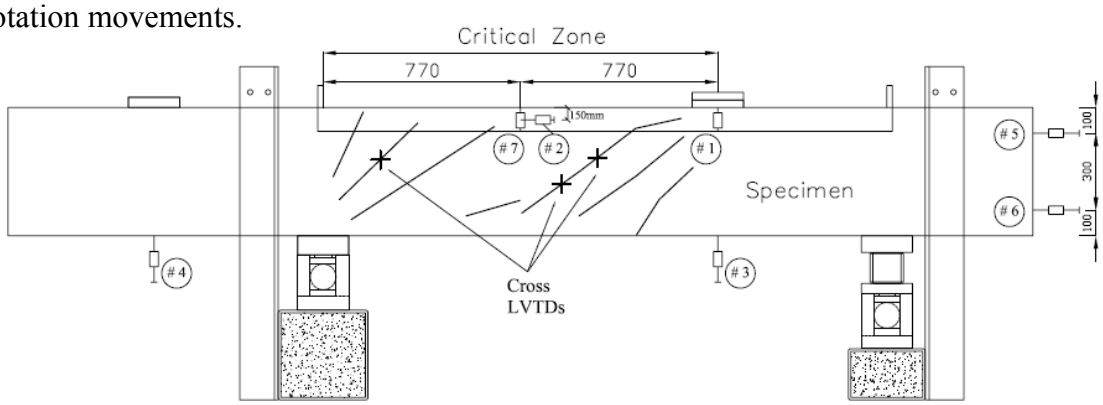

Figure 6.37: Position of LVTD transducers in beams B and C

Strains at sections of maximum bending moments and in the reinforcement bars

The horizontal strains were measured with a Demec gauge at sections of maximum bending moments at five different heights (Figure 6.38). The Demec grid located at the critical shear span, shown in Figure 6.38, allowed to measure the strains in the stirrups and longitudinal reinforcement. Although the centroid of the reinforcement did not coincide exactly with the position of the Demec targets in the longitudinal reinforcement (Figure 6.38), the distance between them was negligible. Similar happened with some stirrups in beams B2. The extreme short span beams were also instrumented with Demec targets in order to assess the strains along the outer longitudinal reinforcement and at two central stirrups.

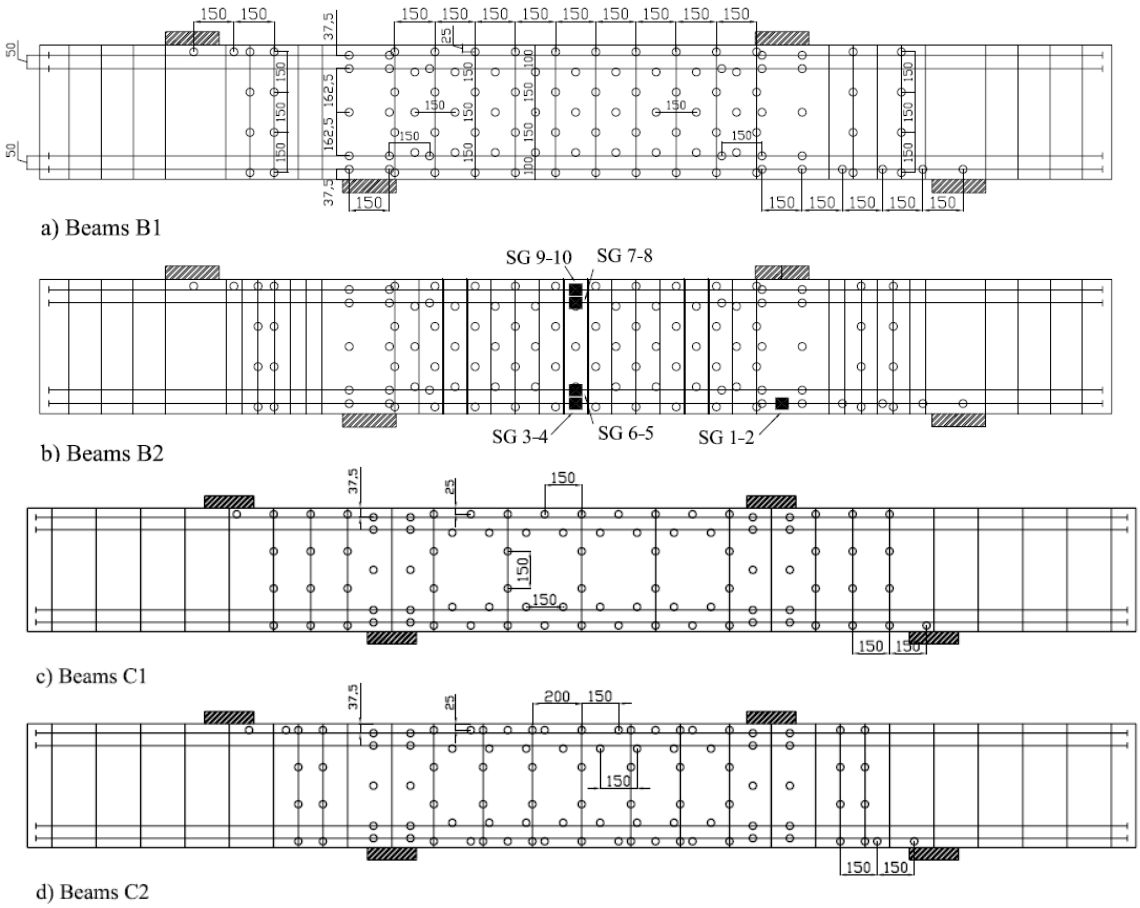

Figure 6.38: Demec grids- a) Beams B1; b) Beams B2 (strain gauges); c) Beams C1; d) Beams C2

In addition, 10 strain gauges were attached to the longitudinal reinforcement in beams B2, as illustrated in Figure 6.38.b. The purpose was to control the maximum tensile strains (strain gauges 1-2) and confirm readings at the centre of the critical shear span, where the bending moment is zero (strain gauges 3-10). The strain gauges were placed in pairs, one on top and the other on the bottom of the reinforcement bar, to take flexure into account.

Relative crack displacements

The crack opening and sliding were monitored using three different methods, similarly as in beams A (see section 6.3.3): crosses of Demec targets, crosses of LVTDs and crosses of photogrammetric targets. The first two methods were effective, while the photogrammetric approach only provided reliable answers in some specimens with large crack widths (beam BL1).

The dense demec grid shown in Figure 6.38.a and b for beams B allowed monitoring several of the initial and main shear cracks without knowing their location a priori. However, this process was time consuming and a simpler mesh was adopted for beams C (Figure 6.38.c and d); additional demec crosses were attached to beams C once the shear cracks had formed. On the other side of the beam (South side), three crosses of LVTDs (70mm gauge length) were placed after pre-cracking the specimen at different levels of the critical cracks and other shear cracks (Figure 6.39). Only two crosses of LVTDs were available for beams C.

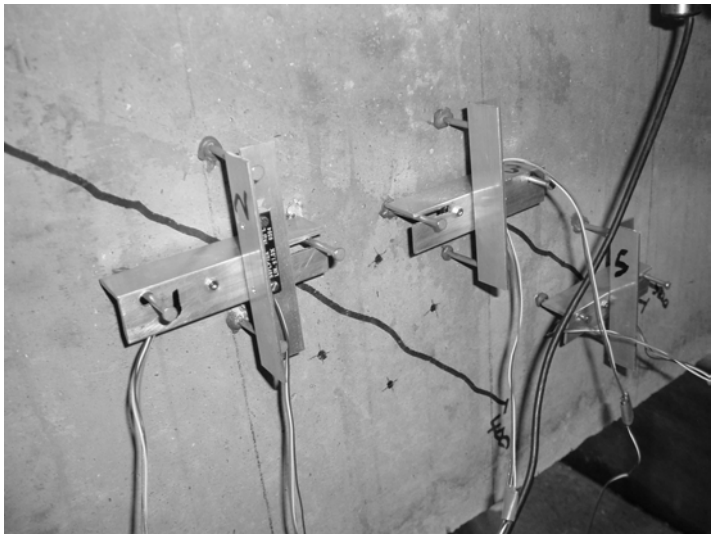

Figure 6.39: Cross of LVTDs placed after pre-cracking the beam (South Side, BG1)

6.5.4 Results

Summary of experimental results

Table 6.8 summarises the most important experimental values obtained for beams B and C. Beams failed in either strut crushing or excessive straining of the stirrups; the type of failure is described in further detailed in next section. In all the beams the stirrups yielded at failure. The longitudinal reinforcement remained in the elastic range and the overall asymmetrical behaviour (deflections and reactions) was satisfactory reproduced.

In Table 6.8, δ^*_{centre} is the vertical deflection measured relative to the floor, under the central load point at the ultimate load (P_{ult}). P_{cr} is the total load at which the first shear crack was observed and P_{unl} the load at which the beam was unloaded.

Beam	f_c' [MPa]	$\rho_v.f_{sv}$ [MPa]	δ^*_{centre} [mm]	P_{cr} [kN]	P_{unl} [kN]	P_{ult} [kN]	Shear Failure
BG1	31.70	2.73	5.29	300	550	950.63	Shear-comp.*
BG2	31.70	4.55	5.43	300	600	1074.13	Crack widening*
BL1	53.11	2.73	4.90	400	500	1169.09	Crack widening
BL2	53.11	4.55	6.02	300	700	1593.93	Shear-comp.
CB1	49.35	1.96	3.14	400	500	1029.34	Crack widening
CB2	49.35	2.94	5.99	450	900	1429.02	Crack widening
CA1	49.35	1.96	4.23	400	500	979.85	Crack widening
CA2	49.35	2.94	4.76	450	1000	1395.54	Crack widening

Note: * Failure of these beams was accompanied with bond cracking

Table 6.8: Summary of experimental results of Beams B and C

Crack pattern and type of failure

The crack pattern at early and middle stages of loading was similar for all beams and only the development of these cracks near failure was different. At early load stages (around 300kN) initial shear cracks formed, which were oriented 45º or steeper, and formed a clear fan shape from the loading points. These cracks are labelled as cracks 1 in Figure 6.40. At higher loads, pure flexural cracks started forming under the points of maximum bending moments (cracks 3 in Figure 6.40). Two main shear cracks (cracks 2), which were flatter than shear cracks 1 (around 35º), formed at intermediate loading. At this load stage, the beam was unloaded and instrumentation was placed around cracks 2. In beams with larger number of stirrups (beams B2), cracks 2 were smeared out into several closely spaced parallel cracks, see Figure 6.41 and 6.42. The crack pattern of the critical shear span of beams B and C is given in Figures 6.41, 6.42 and 6.49.

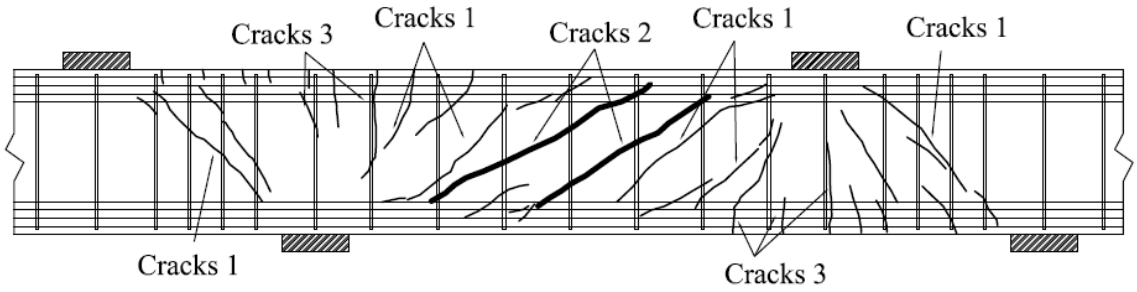

Figure 6.40: Typical crack pattern in beams B and C (beam CA2)

BL1

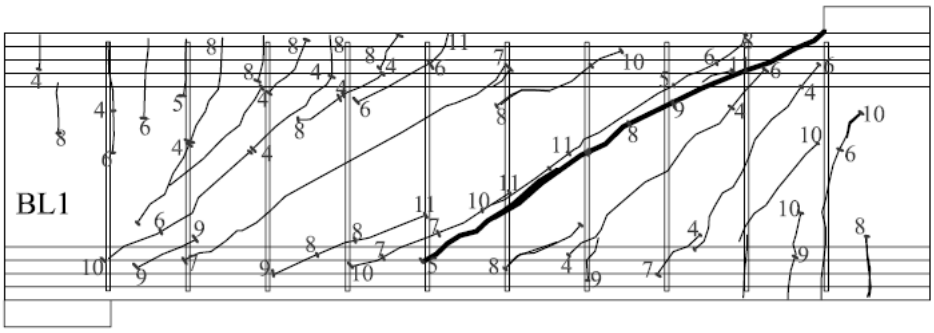

BG1

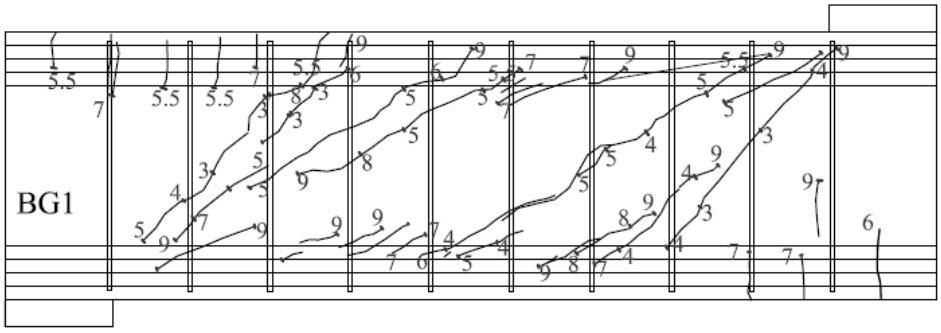

BL2

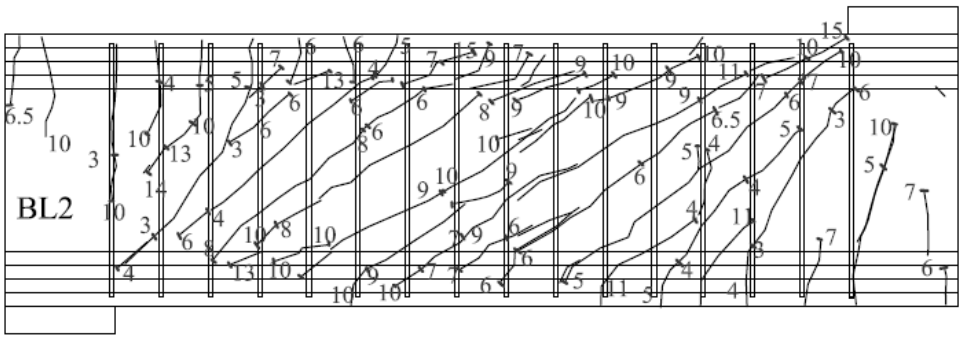

BG2

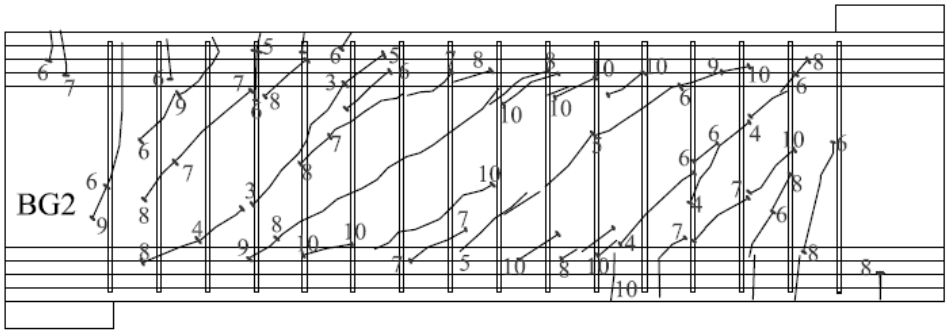

Note: numbers relate to load (x100kN) at which crack formed. Critical cracks are highlighted

Figure 6.41: Crack pattern of beams B at critical span

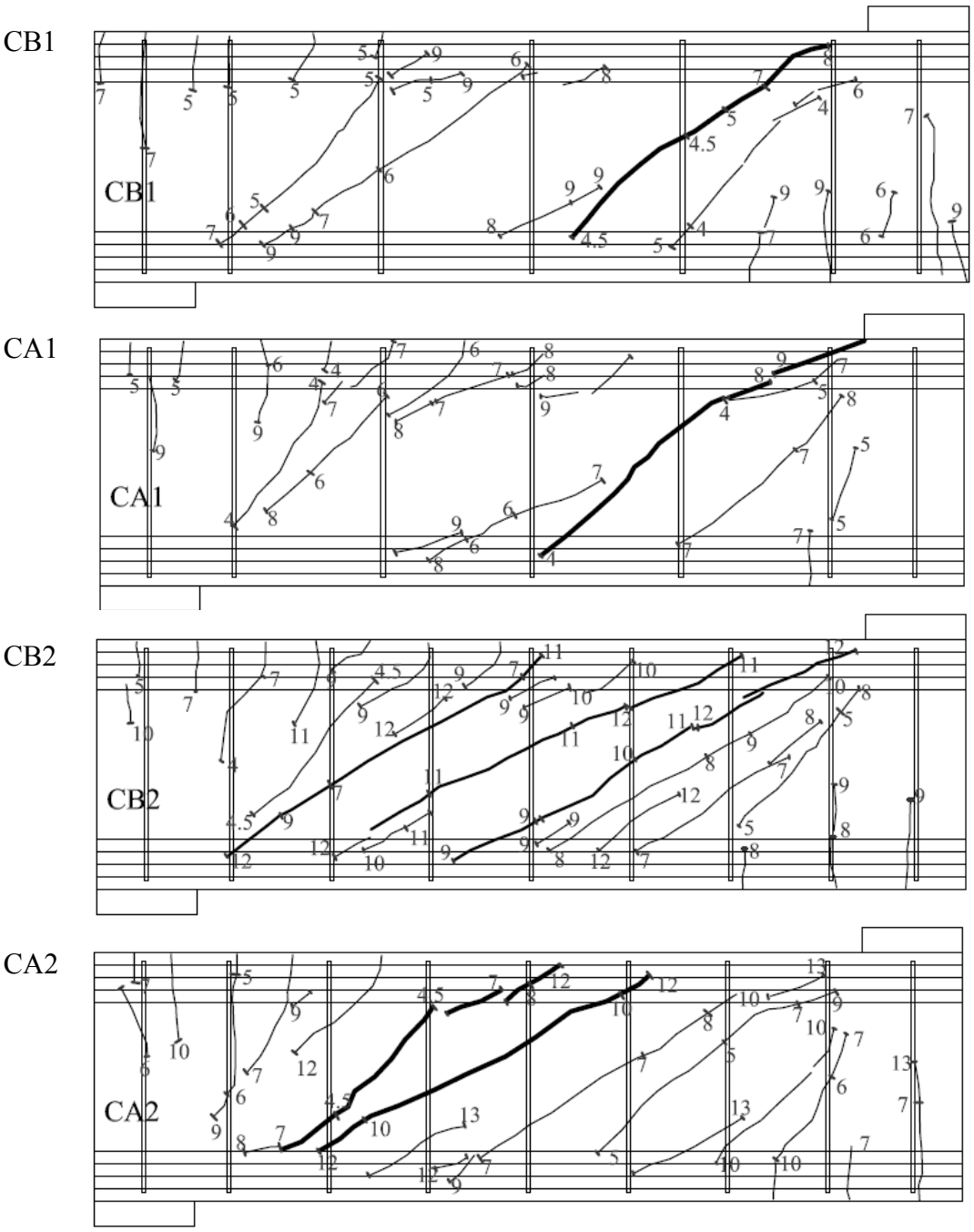

Note: numbers relate to load (x100kN) at which crack formed. Critical cracks are highlighted

Figure 6.42: Crack pattern of beams C at critical span

The crack pattern in the short shear spans was similar to those described in section 6.3.4 for the short span beams. However, these cracks did not become critical in beams B-C.

It is important to highlight that the inclination and position of the cracks were very similar in the limestone (BL) and gravel (BG) beams as shown in Figure 6.41. The only difference was that a larger amount of cracks appeared in the limestone beams compared with the gravel ones. At failure, beams BG had a splitting type of crack along the longitudinal reinforcement, which initiated at the start of the shear crack (around the point

of contra-flexure), see Figure 6.41. In the literature this is often denoted as “bond failure”, although this term is subjective since it can occur in combination with other types of shear failures.

In beams CA1, CB1 and BL1, which had the lowest stirrup indexes, failure was due to excessive straining of the stirrups crossed by the main diagonal crack, which is denoted as “crack widening” in Table 6.8. At failure, the diagonal crack extended to the loading point and started widening quite considerably. The load reached its peak value and remained constant for a short period of time as the crack got wider.

Beams CA2/CB2 had a similar behaviour but several shear cracks got wider simultaneously (Figure 6.42) as opposed to one in beams C1 and BL1. Well after reaching the failure load, new cracks formed at top and bottom of the beam along the flexural reinforcement and in many cases the concrete cover was push out. This was very explosive for beams CA1 and CA2 since many of the stirrups crossed by the critical crack fractured at this stage, see Figure 6.43. The concrete cover was pushed out in some cases due to failure of the anchorage length of the stirrups. The anchorage of the stirrups was staggered in order to avoid weak points but it remains questionable whether this could have had an influence on the ultimate load. It is noteworthy that the failure loads of beams CB were very similar to their equivalent beams CA.

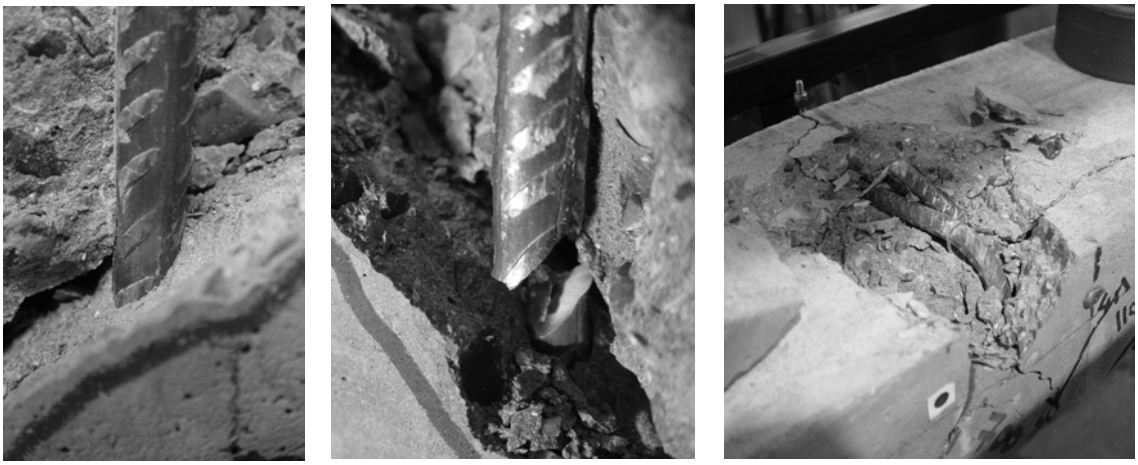

Figure 6.43: *Left*- necking of stirrups; *Centre*- fracture of stirrup; *Right*- spalling of concrete cover due to anchorage failure of stirrups

Beam BG2 and BL2 failed due to shear-compression. Once the ultimate load was reached in beam BL2, the diagonal strut split in the out-of-plane direction. This led to spalling of the concrete at the top and bottom and detaching of the lateral walls of the beam from the main core (Figure 6.44). On the other hand, beam BG2 the strut split at the level of the

reinforcement in a typical horizontal bond crack. This was confirmed by two additional cracks, which were observed at top and bottom faces of the beam (Figure 6.44). These cracks ran longitudinally at middle of the width of the beam and were located immediately above/below the horizontal bond cracks with similar length.

Figure 6.44: Post-failure cracks: *Left*- beam BL2; *Right*- beam BG2

Load-deflection curves

The maximum vertical deflections (~6mm) were registered under the two loading points, which were very similar to each other as expected. The deflections at the cantilever loading point were slightly lower (10-30%) than those measured at the central loading point, see Figure 6.45. The deflections shown in Figure 6.45 are given relative to the floor for beams B in order to compare the results with deflections at the cantilever loading point and photogrammetric targets.

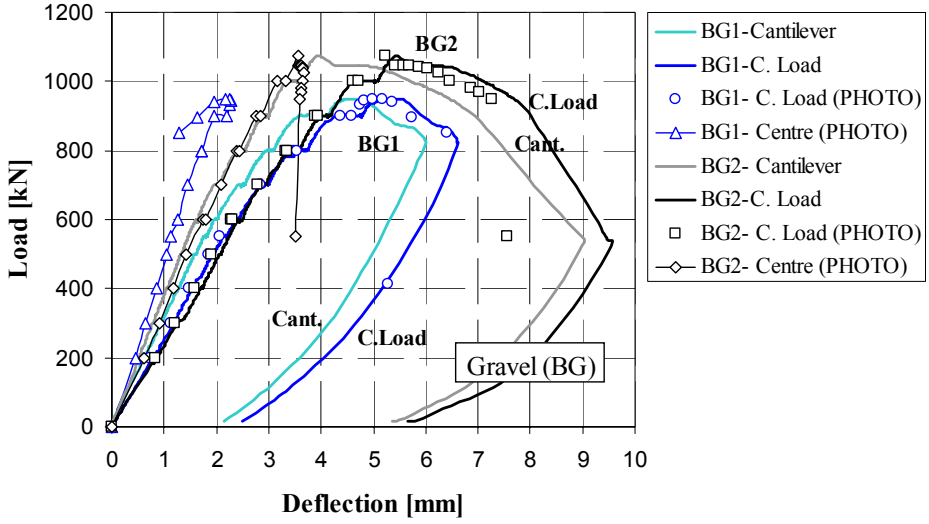

Note: deflections are measured relative to the floor

Figure 6.45: Vertical displacements of beams B at loading points and centre of critical span

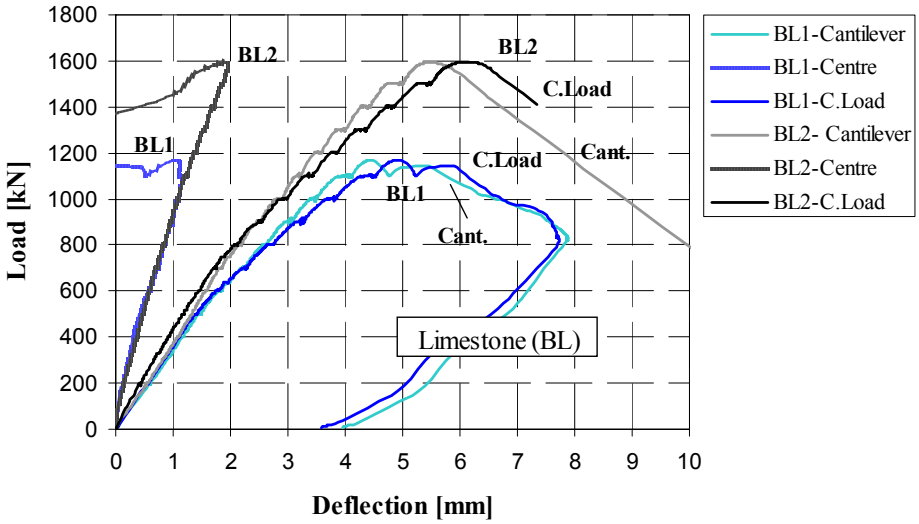

Figure 6.45 (Cont.): Vertical displacements of beams B at loading points and centre of critical span

It is important to highlight that the curves shown in Figures 6.45 and 6.46 correspond to loading once the beams had already been pre-cracked and therefore the change in stiffness at early load stages is not reflected. The LVTD readings were in good agreement with photogrammetric measurements, which are shown as dots in Figure 6.45. Deflections at the centre of the critical span were small in both beams B and C (see Figures 6.45 and 6.47), except for beam BG2 where they were similar to the ones at the cantilever end.

Beams with fewer amount of stirrups (beams C and BL1) had a load plateau near failure, as shown in Figures 6.45 and 6.46. Beams CB had a slightly higher ductility than beams CA, although the difference was not significant.

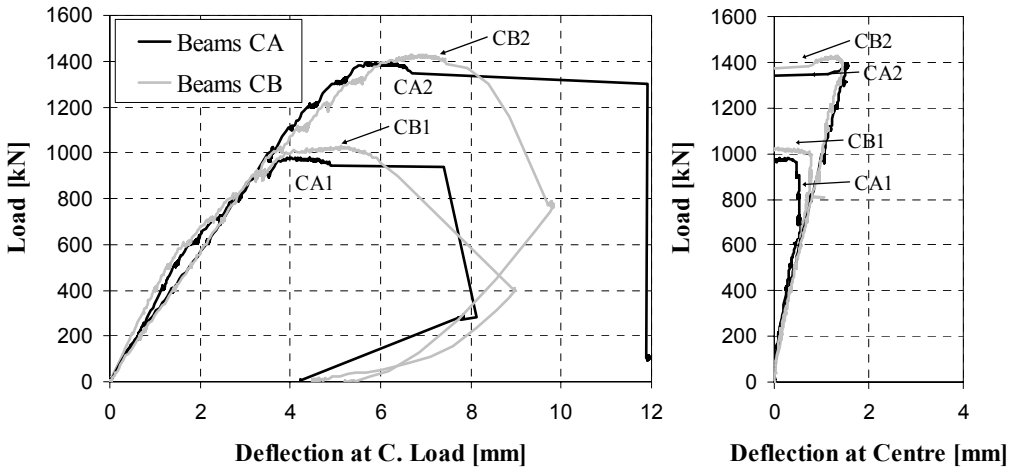

Note: deflections are measured relative to the frame

Figure 6.46: Vertical displacements of beams C at central loading point and centre of critical span

The overall kinematics of the beams can be clearly seen in Figure 6.47, which was obtained from the photogrammetric analysis. The horizontal and end rotation, given by transducers #5 and 6, confirmed the values shown in Figure 6.47 (deflected shape is scaled by 50). The horizontal displacement (*H*) and end rotation for beams B are shown in Figure 6.48. Results for beams C are not shown in Figure 6.48 for clarity, although the data followed the same path for *H* and end rotation and so can be easily extrapolated using their ultimate load. Lastly, the out-of-plane deformations, measured by transducer #2, were negligible (<0.1mm) as for beams A and B0.

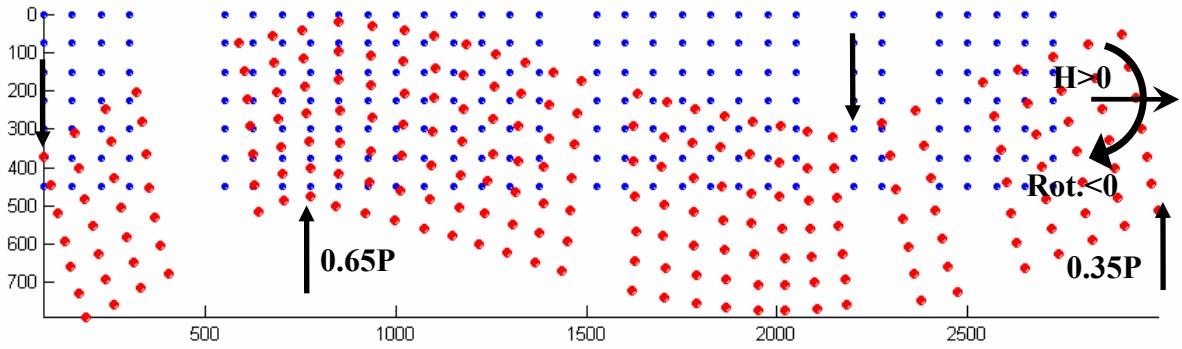

Distance from inner edge of cantilever load plate [mm]

Note: Scaled by 50

Figure 6.47: Global displacements of beam BL2 at failure (1500kN)

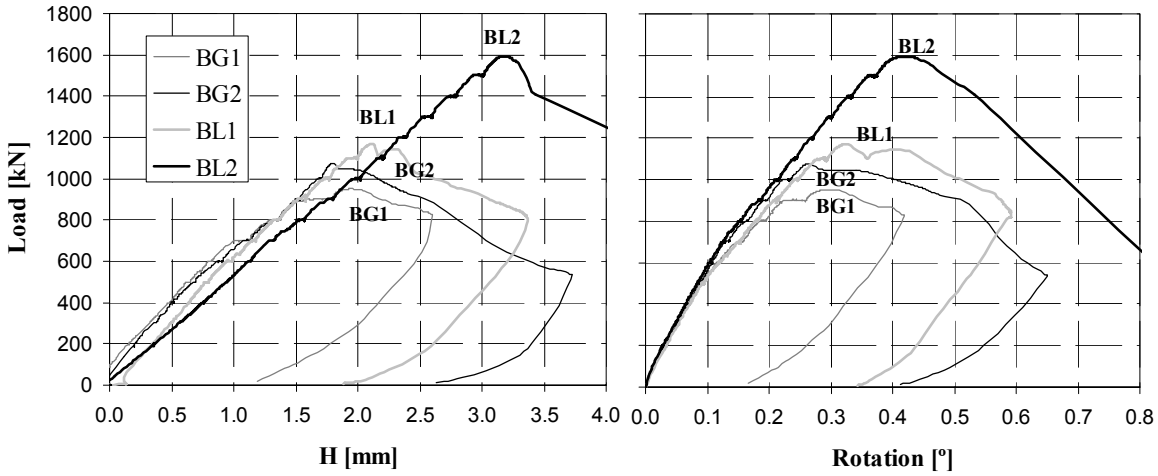

Note: Sign criteria: *H*>0 outwards and Rotation >0 for sagging (relative to mid-height fibre), see Figue 6.47
H and Rotation in beams C followed the same path as beams B, results can be extrapolated using the corresponding ultimate load

Figure 6.48: Horizontal displacement and rotation of simply supported end (beams B)

Figure 6.49 shows the photos taken from the beam test inmediatly before failure. As explain in next section the position of the cracks had an effect on Demec readings.

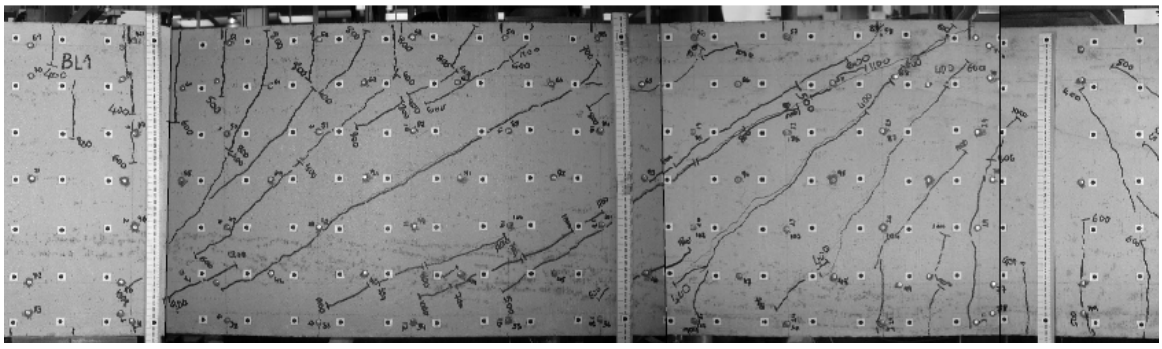

BL1

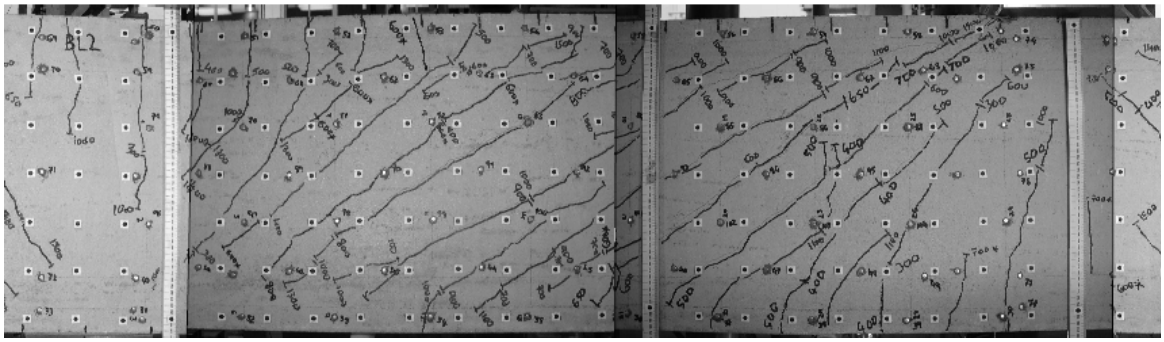

BL2

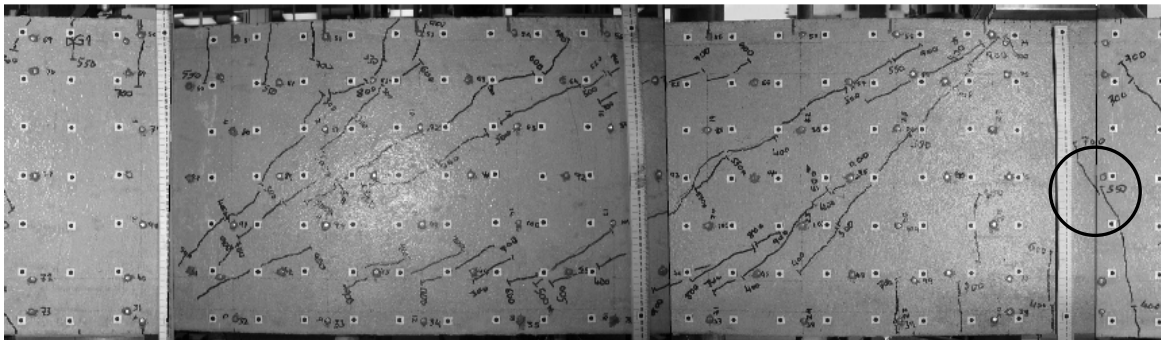

BG1

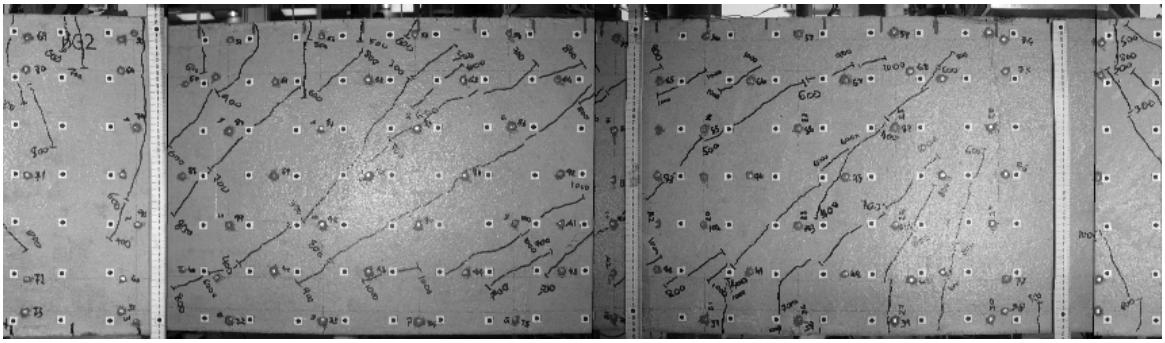

BG2

Figure 6.49: Photogrammetric monitoring in beams B and C

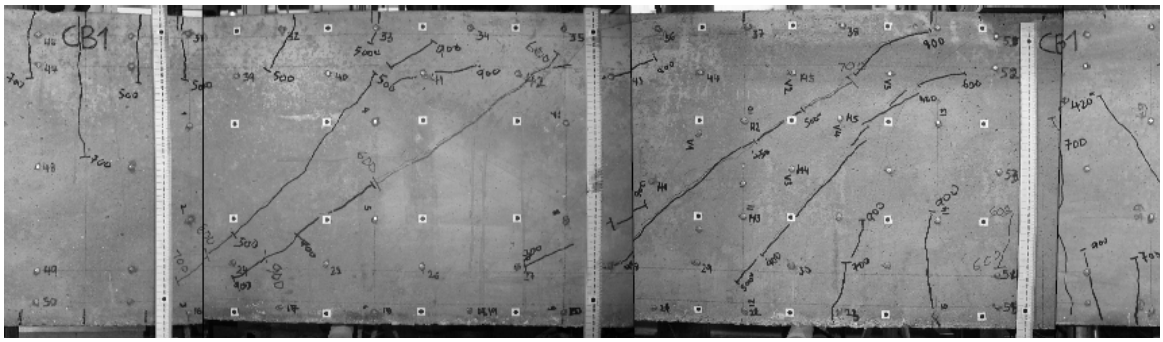

CB1

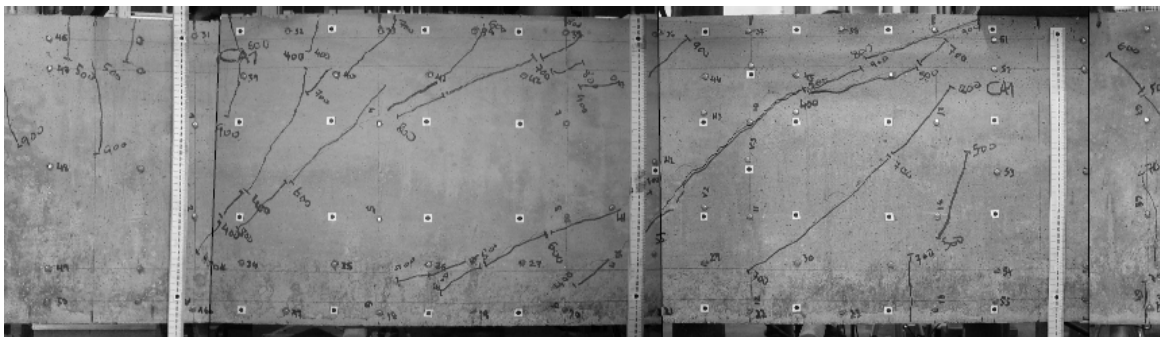

CA1

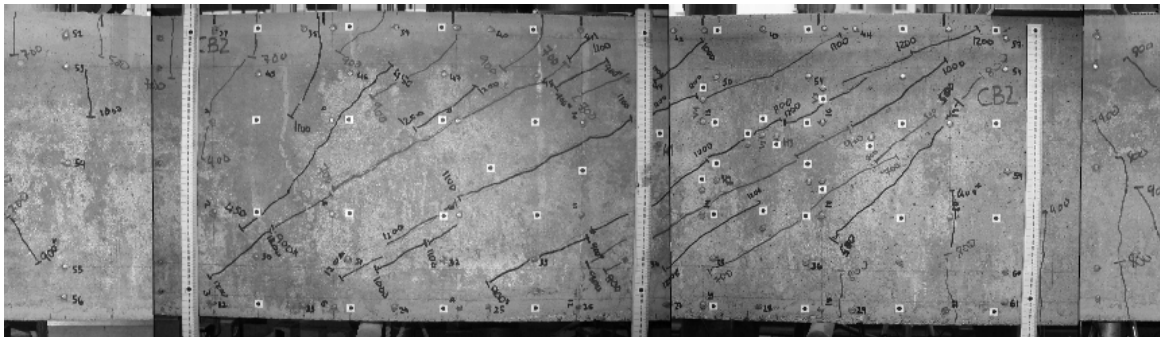

CB2

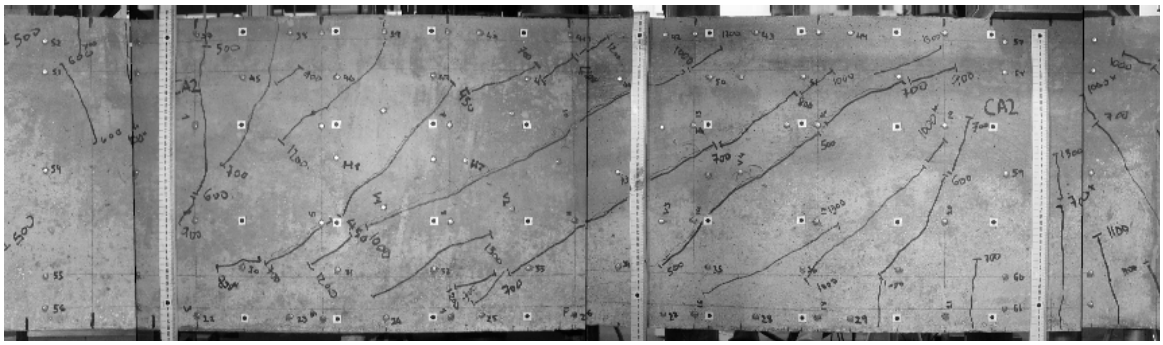

CA2

Figure 6.49: Photogrammetric monitoring in beams B and C

Strains at sections with maximum bending moments

The horizontal strains, which were measured with the Demec gauge, at points of maximum bending moments are shown in Figure 6.50 and 6.51 for beams B and C respectively. The experimental data showed that the longitudinal reinforcement did not yield in any of the beams. The maximum compression strain recorded was 1.5 ‰ in BL2. In many cases, the demec readings at the outer reinforcement were relatively low compared with the rest of the cross section. This was confirmed by strain gauges available in beams B2, which provided slightly higher values than the demec gauges. Similarly as in beams A, the oscillations in the strain profiles were due to crack bypassing the demec gauge readings; see circle mark in Figure 6.49 for beam BG1 and corresponding strain readings in Figure 6.50. Beams C showed more uniform strain profiles (Figure 6.50). According to the experimental data shown in Figure 6.51 the depth of the neutral fibre in beams C was around 150mm.

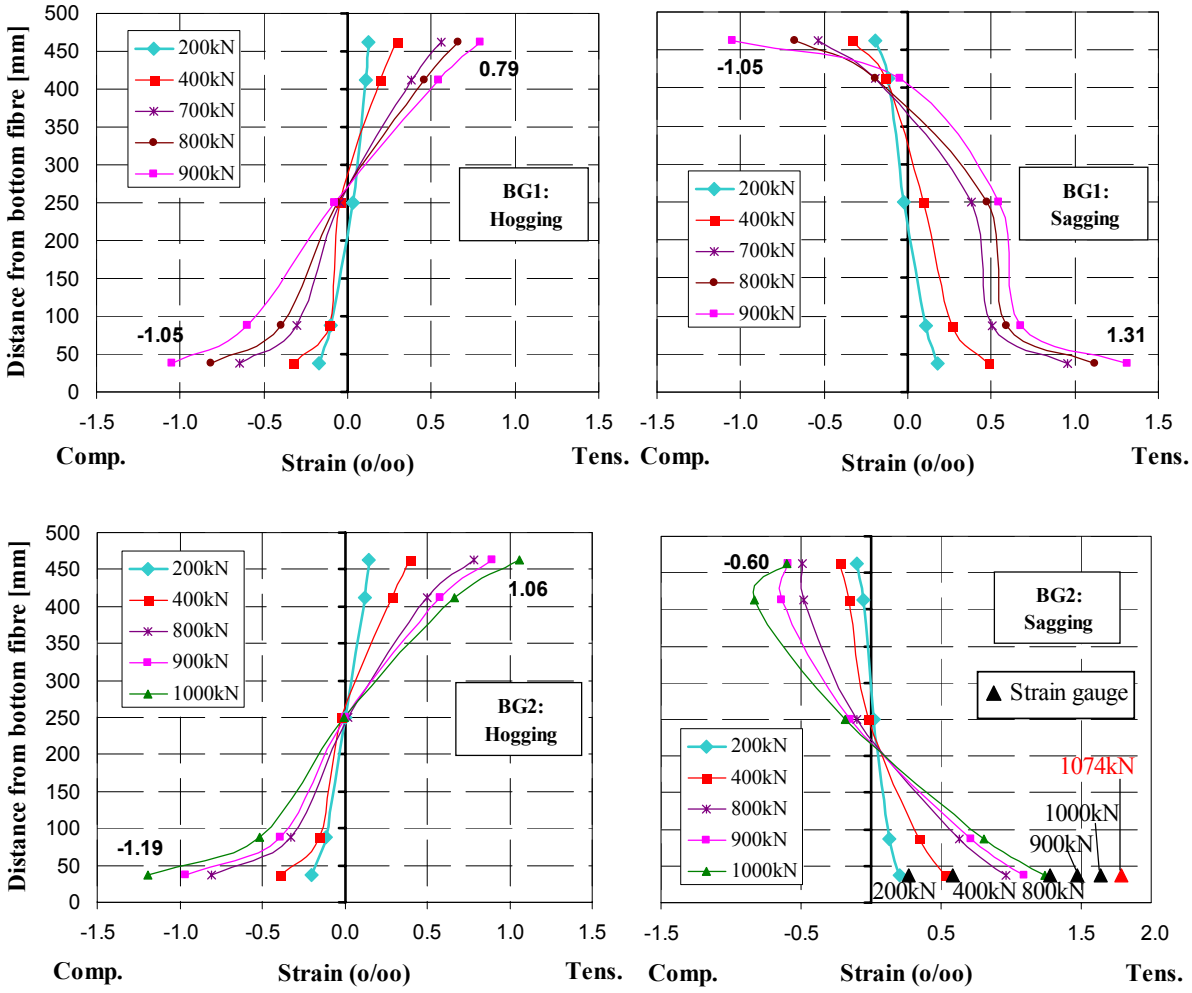

Note: strain gauge readings marked as black triangles in beams B2 (red at failure)

Figure 6.50: Horizontal strains at sections of maximum bending moments (beams B)

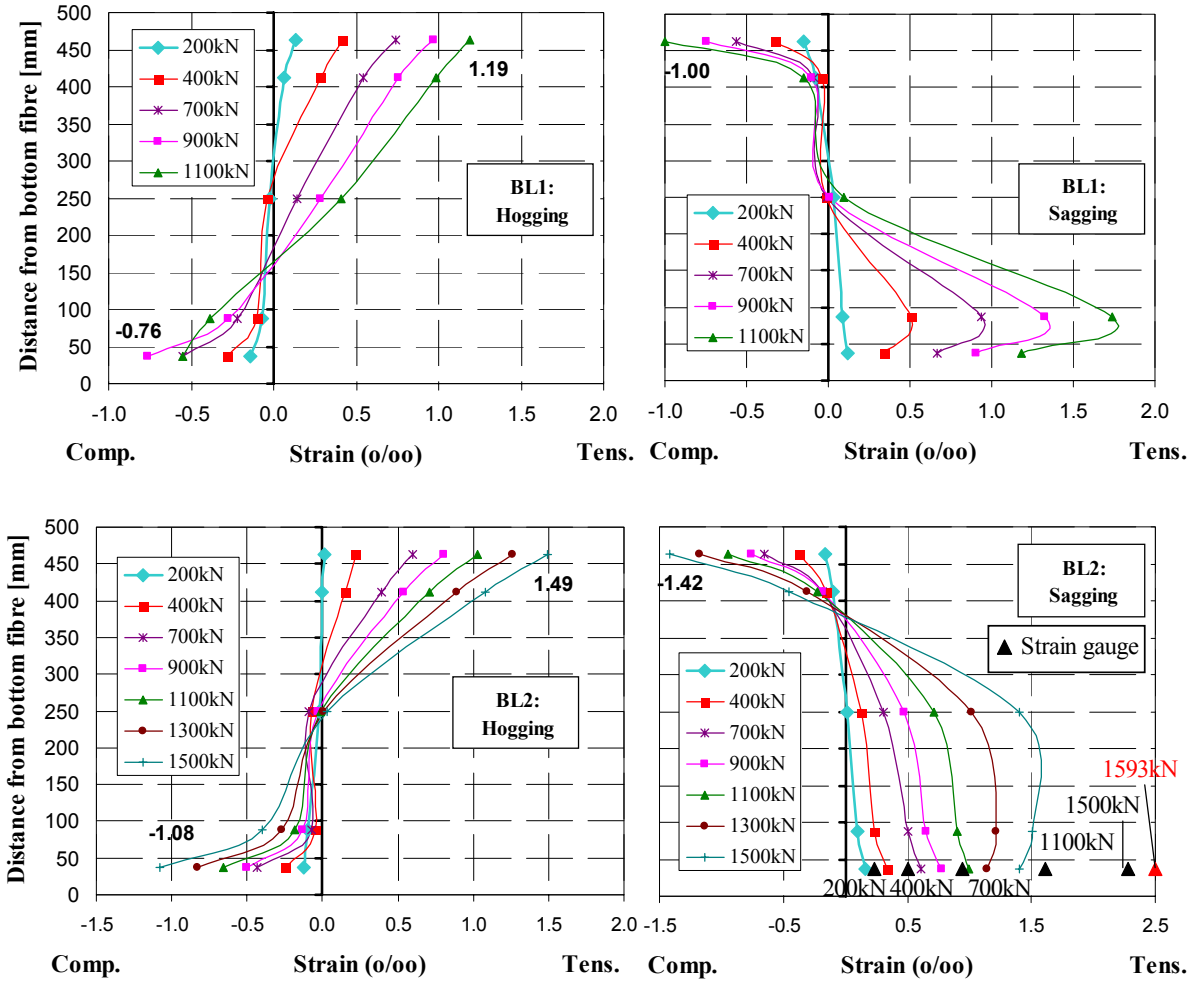

Note: strain gauge readings marked as black triangles in beams B2 (red at failure)

Figure 6.50 (Cont.): Horizontal strains at sections of maximum bending moments (beams B)

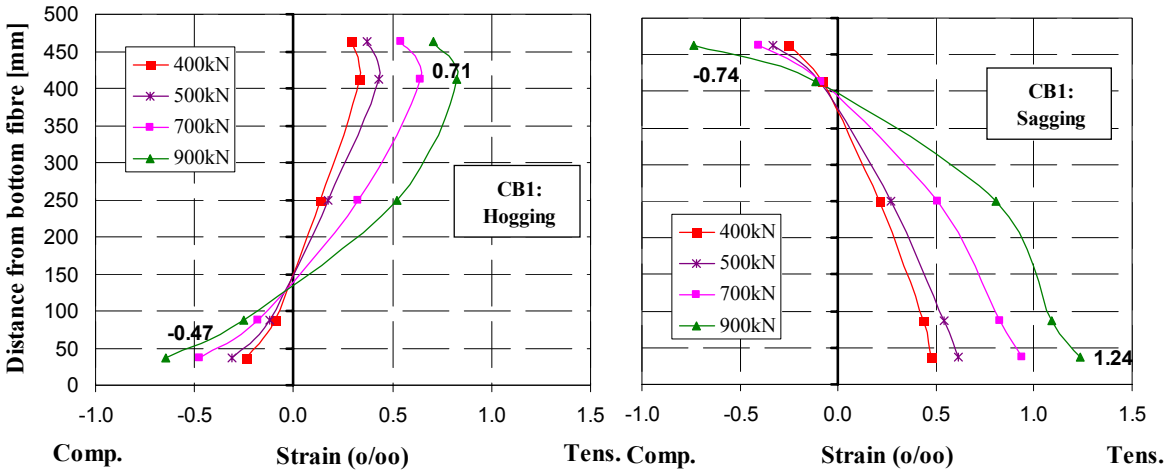

Figure 6.51: Horizontal strains at sections of maximum bending moments (beams C)

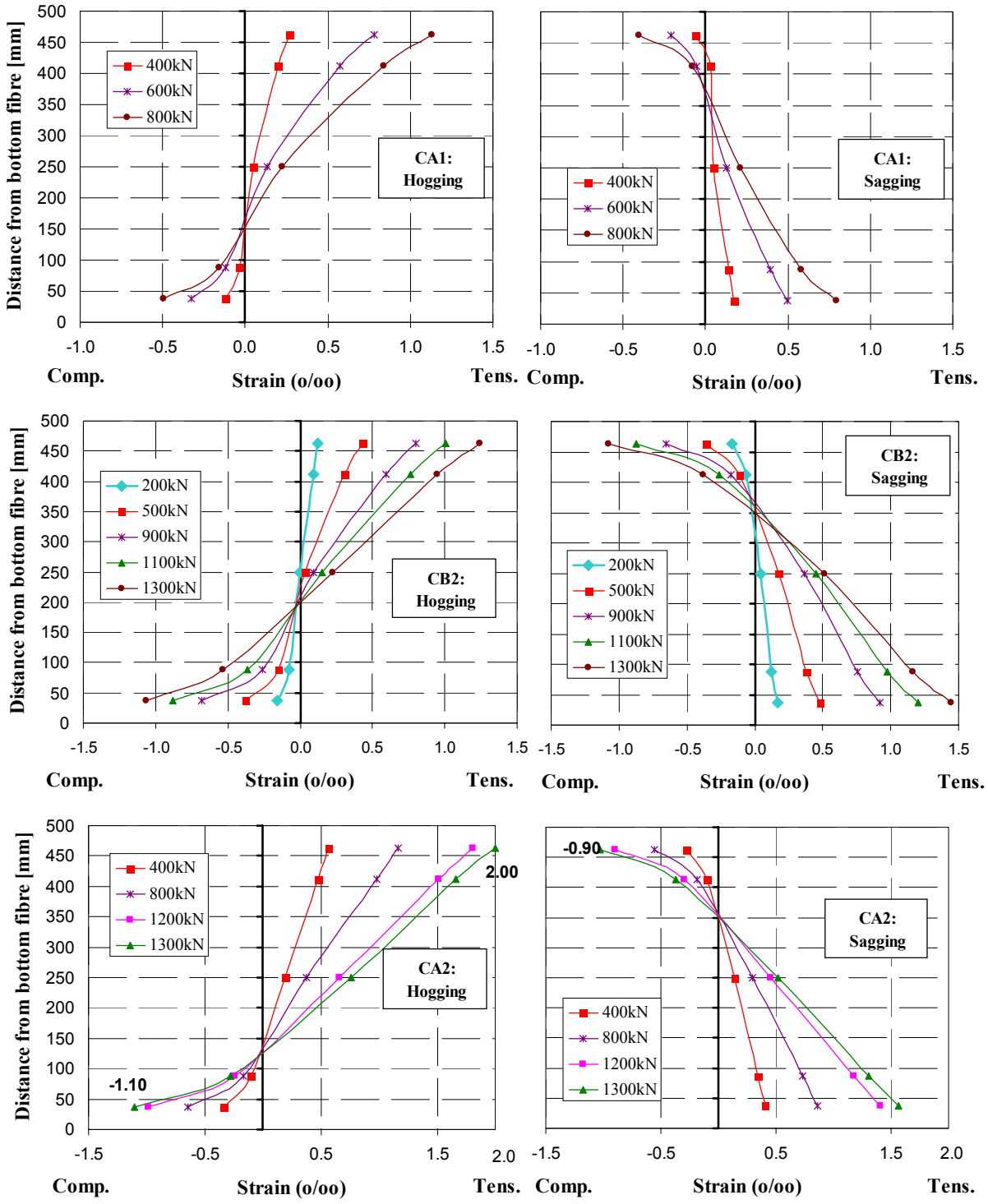

Figure 6.51 (Cont.): Horizontal strains at sections of maximum bending moments (beams C)

Strains in stirrups

According to the demec gauge readings, the stirrups had the maximum strains at the level where they were crossed by the main shear cracks (Figure 6.52). For beams B, refer to Figure 8.33. Three readings were taken per stirrup, which relate to sectors A to C (top to bottom); results are shown for the sector with highest strains, which is highlighted. All the central stirrups in beams B and C yielded at failure (Figures 6.52 and 8.33). However the strains were lower in beam BG2, which had the highest stirrup index. In BG2, only central stirrups S5, 6, 7 and 9 seemed to yield. The yielding strain of the stirrups was 2.75‰ and 3‰ for beams B and C respectively.

In all cases, the first stirrup in the shear span nearest to the loading plate was significantly less effective than the other stirrups in the shear span (Figure 6.52 and 8.33). This effect was most significant in beams B, where the outer stirrups were close to the supports. The stirrups in the short spans did not yield in any of the beams tested, with maximum strain values of 2.45 ‰, although this is an average value so the peak may have been greater.

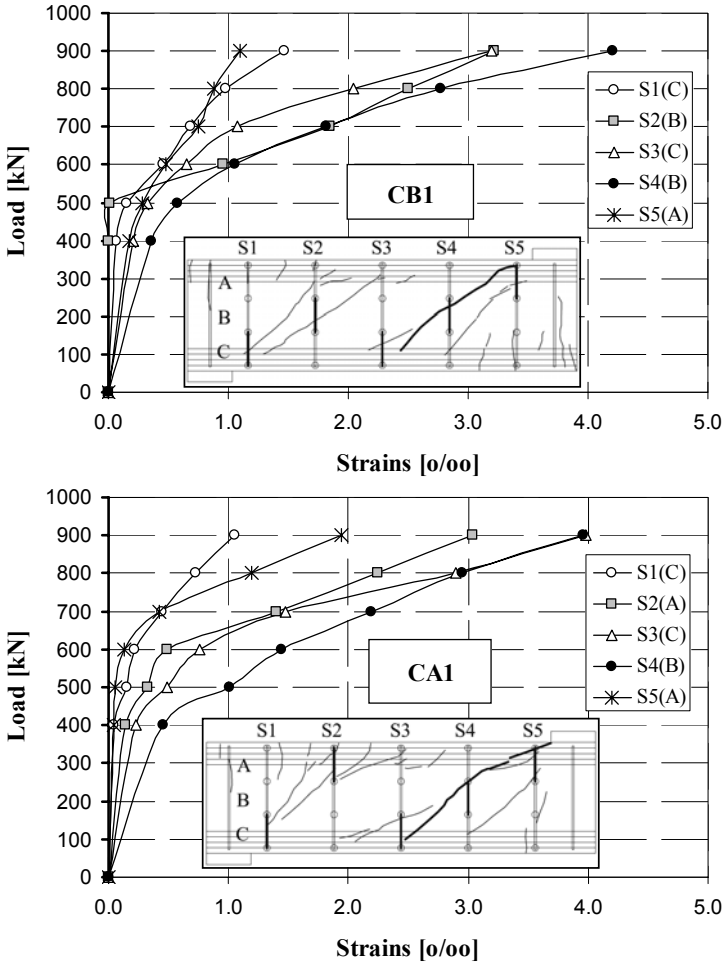

Figure 6.52: Maximum strains in stirrups in the critical shear span (beams C)

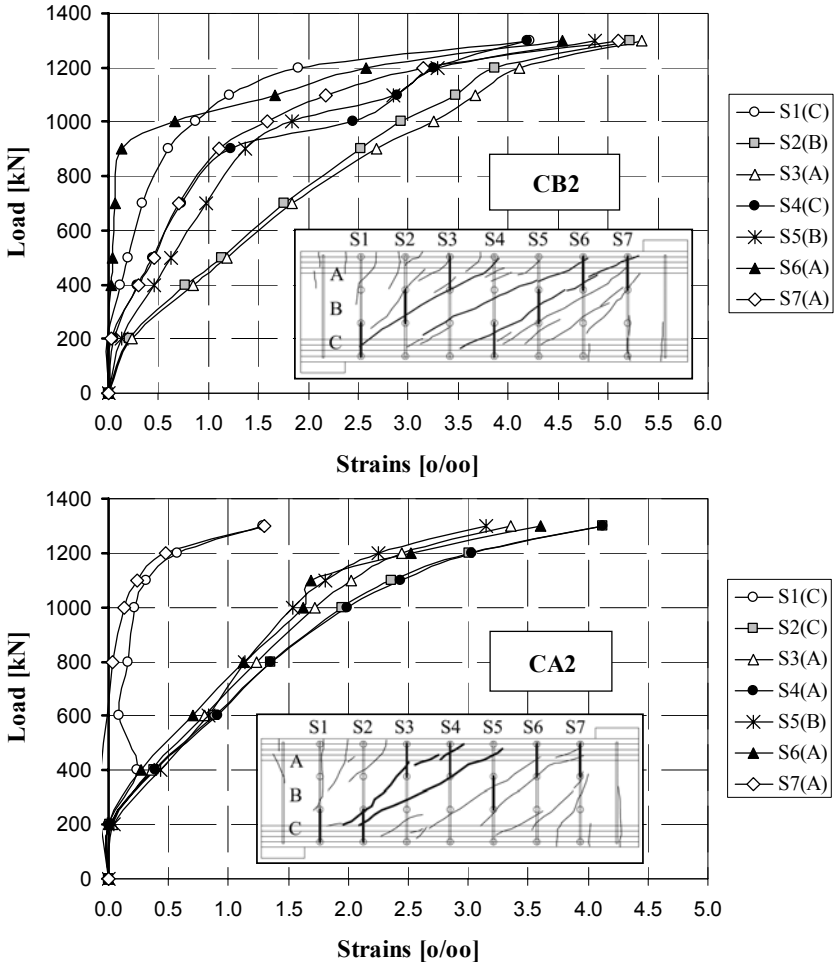

Figure 6.52 (Cont.): Maximum strains in stirrups in the critical shear span (beams C)

The variation of strain along the stirrup was dependant on the number of shear cracks crossing the stirrup. In beams with larger ρ_v ratios, stirrups at the centre of the critical span, which were crossed by at least three shear cracks, had an uniform strain distribution as shown in Figure 6.53. In stirrups closer to the supports, the strains began to localize more towards the compression head.

CB1 at 900kN

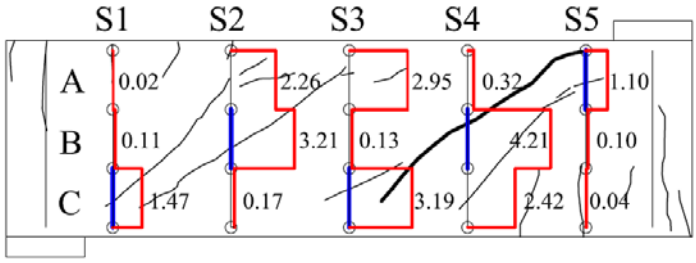

CB2 at 1300kN

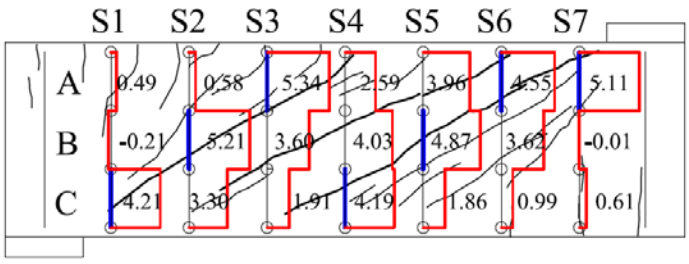

Figure 6.53: Strain distribution along stirrups in beams CB (strains in ‰)

Strains in the longitudinal reinforcement

Figure 6.54 shows the strain distribution along the longitudinal reinforcement, between centre lines of the bearing plates at the critical span, which was provided by the Demec gauge. The readings had high fluctuations along the reinforcement bar, especially near failure at the inner layers. Again, these oscillations were due to the presence of cracks crossing the Demec gauge.

In spite of the scatter in the Demec readings shown in Figure 6.54, the results were fairly symmetrical with respect to the top and bottom layers. According to experimental data shown in Figure 6.54, the longitudinal reinforcement working in tension extended a length of around 270mm from the point of contra-flexure (M=0 at 770mm from the centre line of the support, Figure 6.54). This length was consistent in all beams tested.

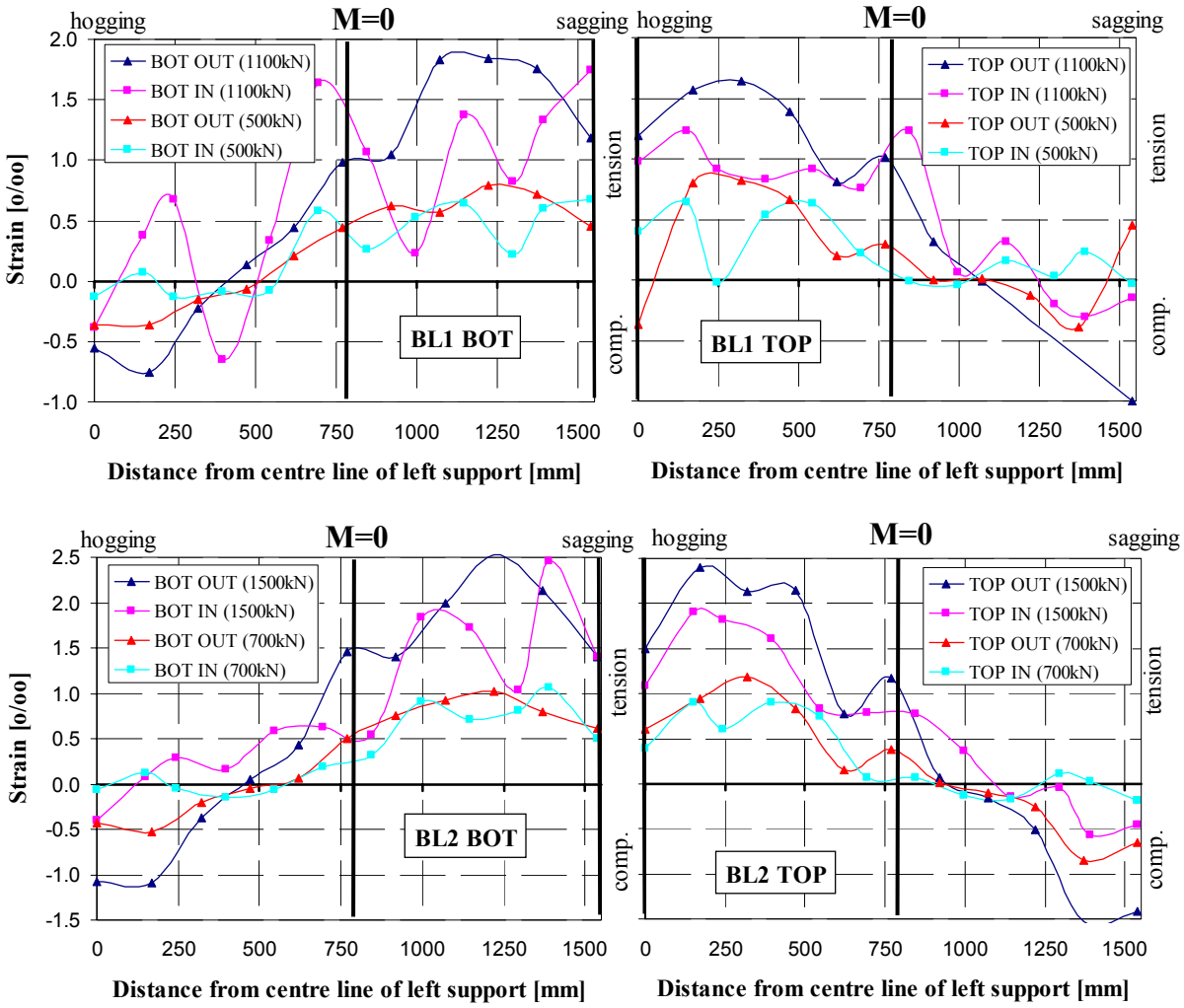

Figure 6.54: Strains in the longitudinal reinforcement (Demec gauge readings)

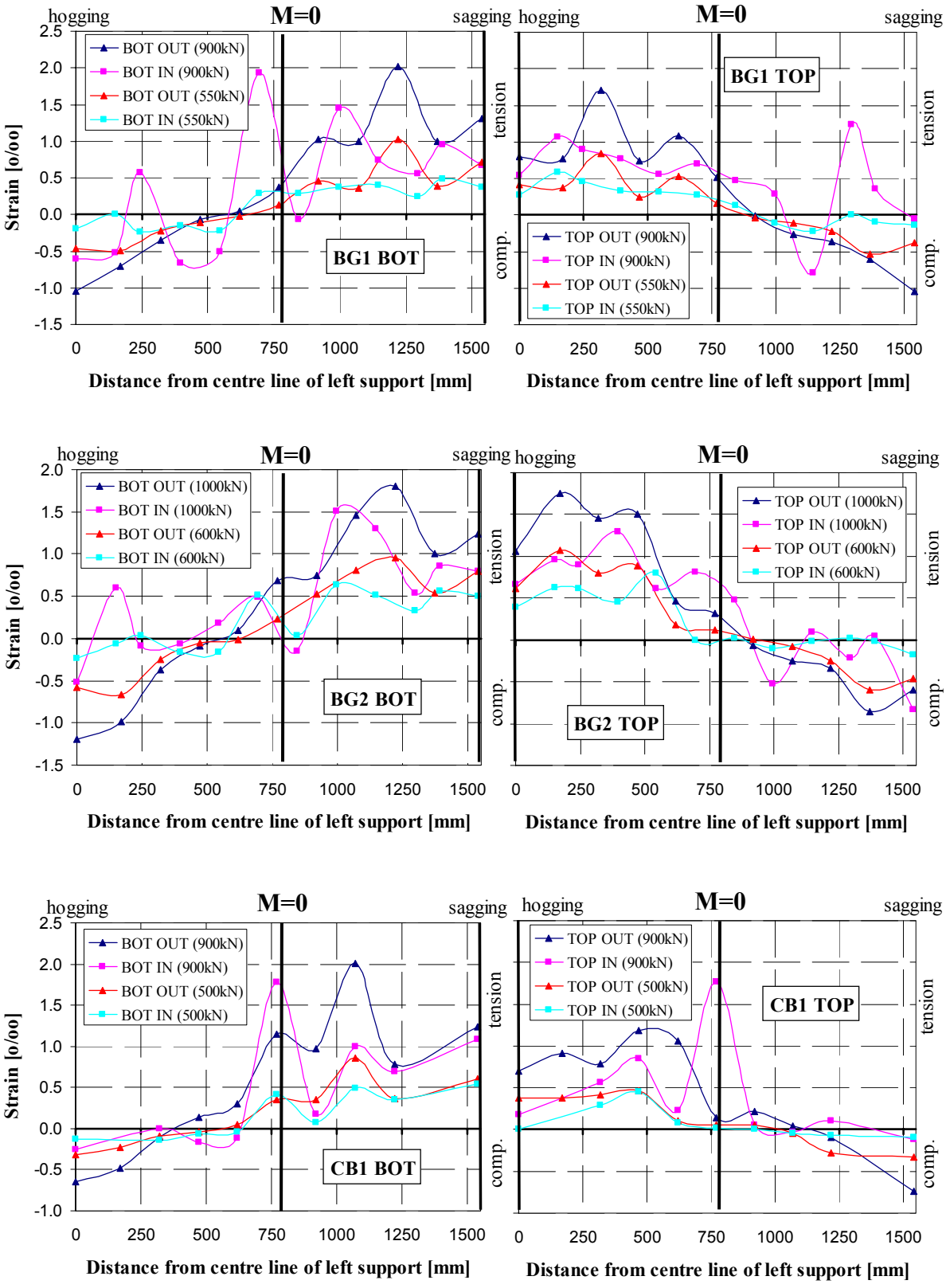

Figure 6.54 (Cont.): Strains in the longitudinal reinforcement (Demec gauge readings)

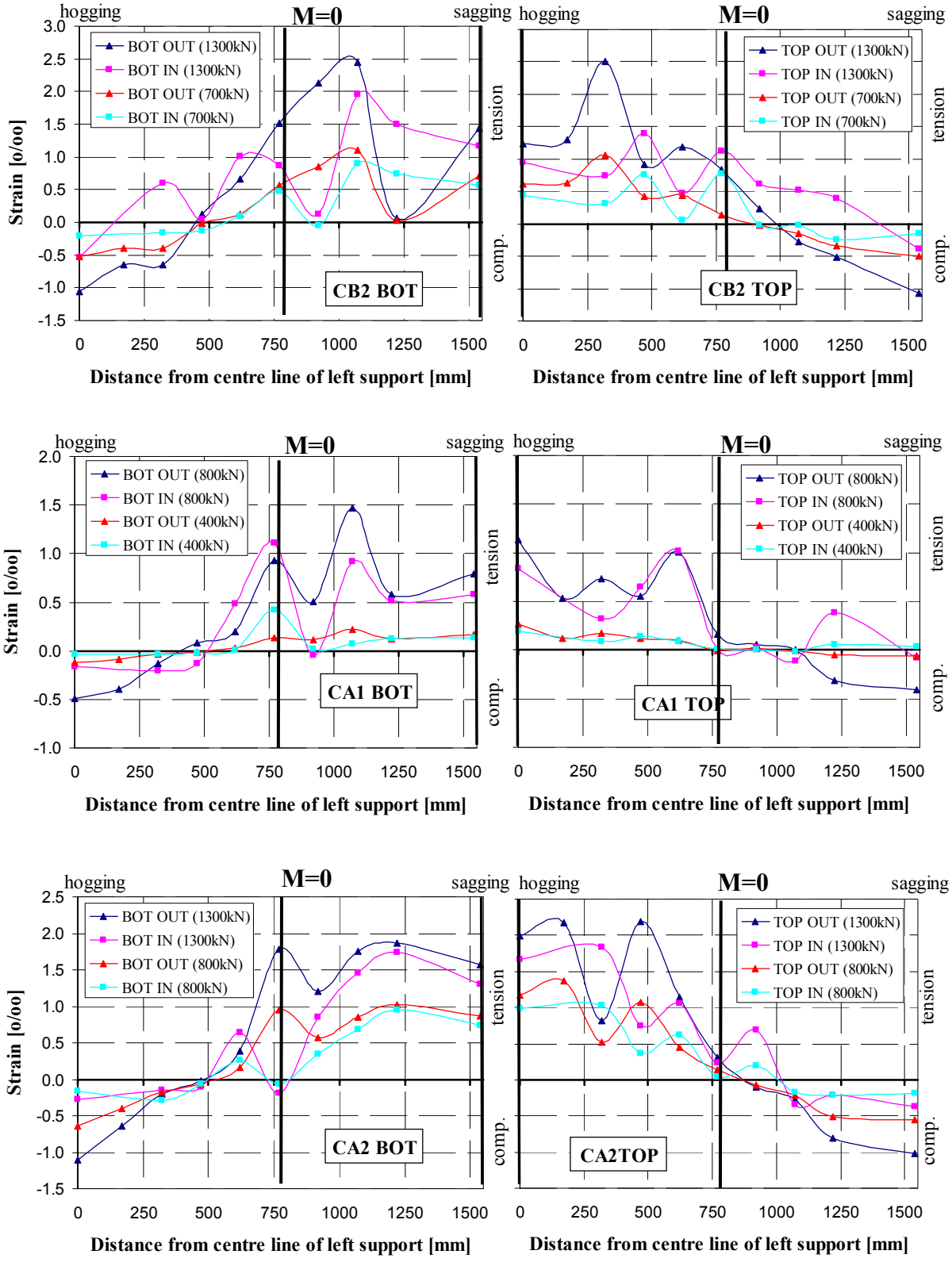

Figure 6.54 (Cont.): Strains in the longitudinal reinforcement (Demec gauge readings)

The experimental data from the strain gauges, which were placed in beams B2 (Figure 6.55), seemed to be more representative than readings from the Demec gauge. The values recorded by the strain gauges under the central loading point (SG 1-2) were around 40% larger than those obtained from the Demec gauge, as shown in Figure 6.55. However, the strains remained on the elastic range, even for the most heavily loaded beam BL2.

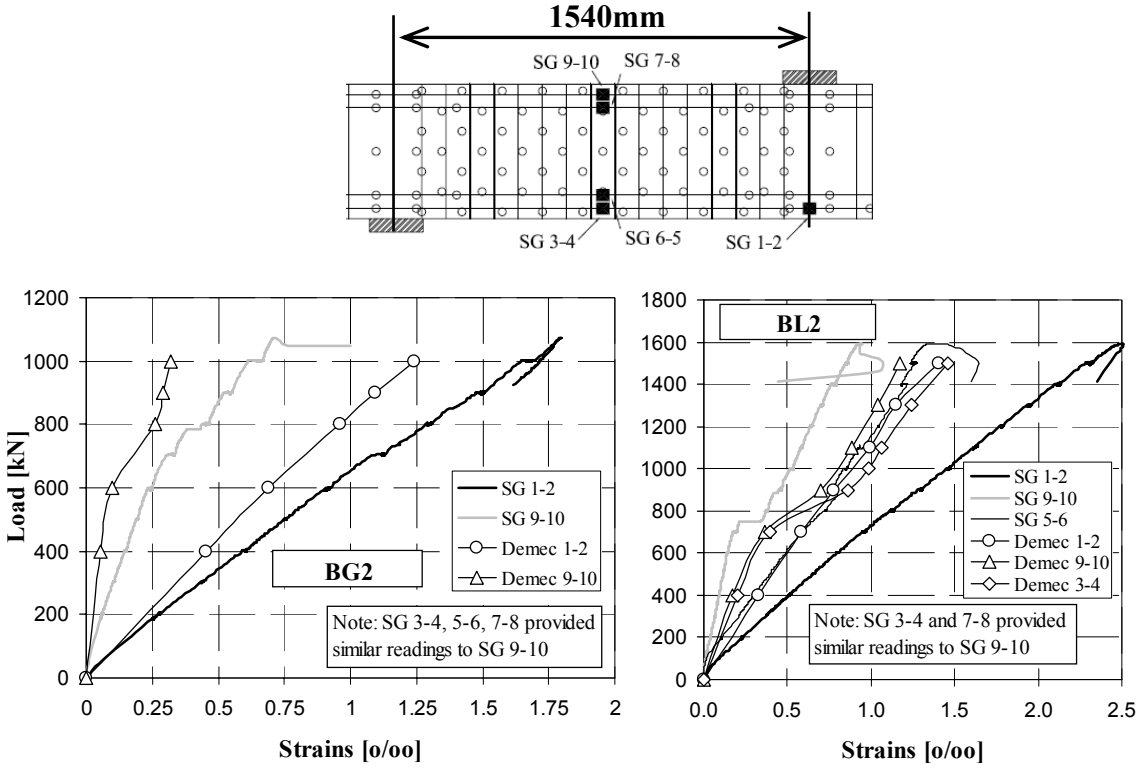

Figure 6.55: Strains in the longitudinal reinforcement in beam B2 (strain gauge readings)

Relative crack displacements

Figures 6.56 and 6.57 show the crack opening and sliding obtained experimentally for beams B and C respectively. The results, which relate to the loading after the beam had been pre-cracked, are divided into two groups according to the type of crack; namely crack 1 and 2 (refer to Figure 6.40). Crack 1 refer to the steeper cracks that formed at the extremes of the shear span, while cracks 2 corresponded to the flatter shear cracks that formed at later load stages. Only Demec readings with one crack going through the Demec cross were considered. Sliding is taken as positive when the block below the crack moved downwards with respect the block above.

The predominant mode (opening or sliding) of the cracks varied depending on the type of crack and loading stage. At early load stages, the cracks that formed at the pre-cracking stage reopened, hence the predominant mode was opening over sliding. The ratio ($\delta w/\delta s$) at this stage varied between 3 and 4, see Figures 6.56-6.57. Once the load reached the point at which the beam was unloaded at the pre-cracking stage, the $\delta w/\delta s$ ratio decreased. In the majority of the cases, the sliding increased significantly and the $\delta w/\delta s$ ratio became closer to 1.5. The largest crack widths at the critical crack were recorded in beams C (~1.25mm). In general, crack widths were around 0.75-1mm near failure. Measurements of crack opening and sliding showed fairly constant values along the cracks, as shown in Figures 6.56 and 6.57. These results, along with data from the Push-off tests, were applied in order to estimate the shear stresses transmitted at the cracks by means of aggregate interlock (see section 8.3.3).

In general, visual readings taken with the microscopic ruler had an excellent agreement with Demec and LVTD measurements, as shown in Figures 6.56 and 6.57. In addition, readings from the photogrammetric analysis were used to assess the crack opening and sliding. Although the results were reasonable in some beams (see BL1 in Figure 6.56), large oscillations of these measurements along cracks were obtained in many others. These results were unrealistic in many cases and were inconsistent with neither visual nor LVTD data, which showed much more uniform values. This inaccuracy in the photogrammetric measurements was not observed in the push-off tests shown in chapter 4. This suggests that errors were probably induced due an excessive working distance between the camera and the beam, which was required on the other hand in order to cover the entire shear span. Beam BL1, in which the results were acceptable, the grid of targets was dense (75mm) and the crack widths were considerably wide.

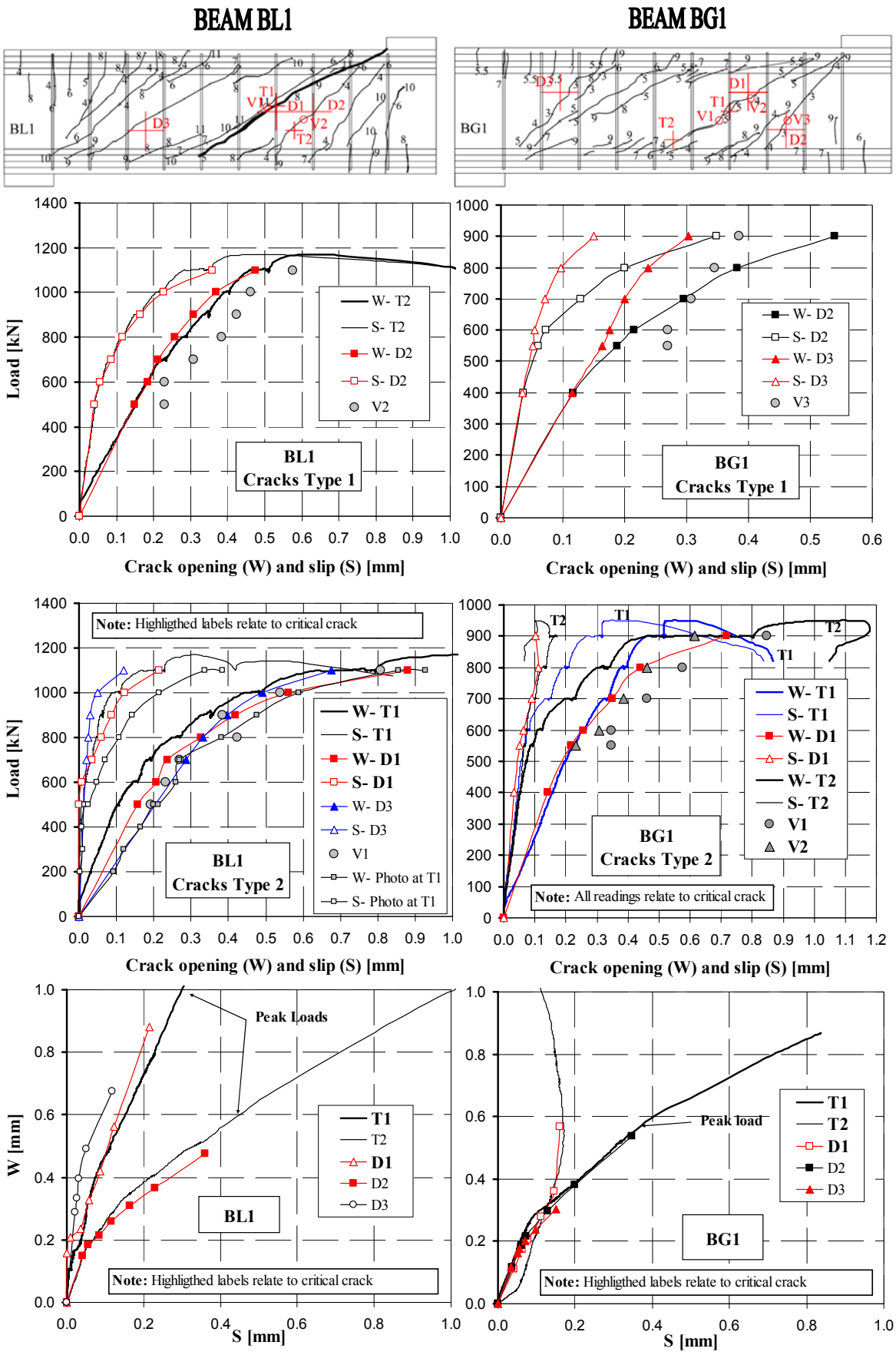

Notation: Cracks 1 are the first shear cracks to appear, which are steeper than cracks 2 (refer to Figure 6.40)
Types of readings: T- transducers (small cross); D- demec (large cross); V- visual (circle)

Figure 6.56: Crack opening and sliding in beams B

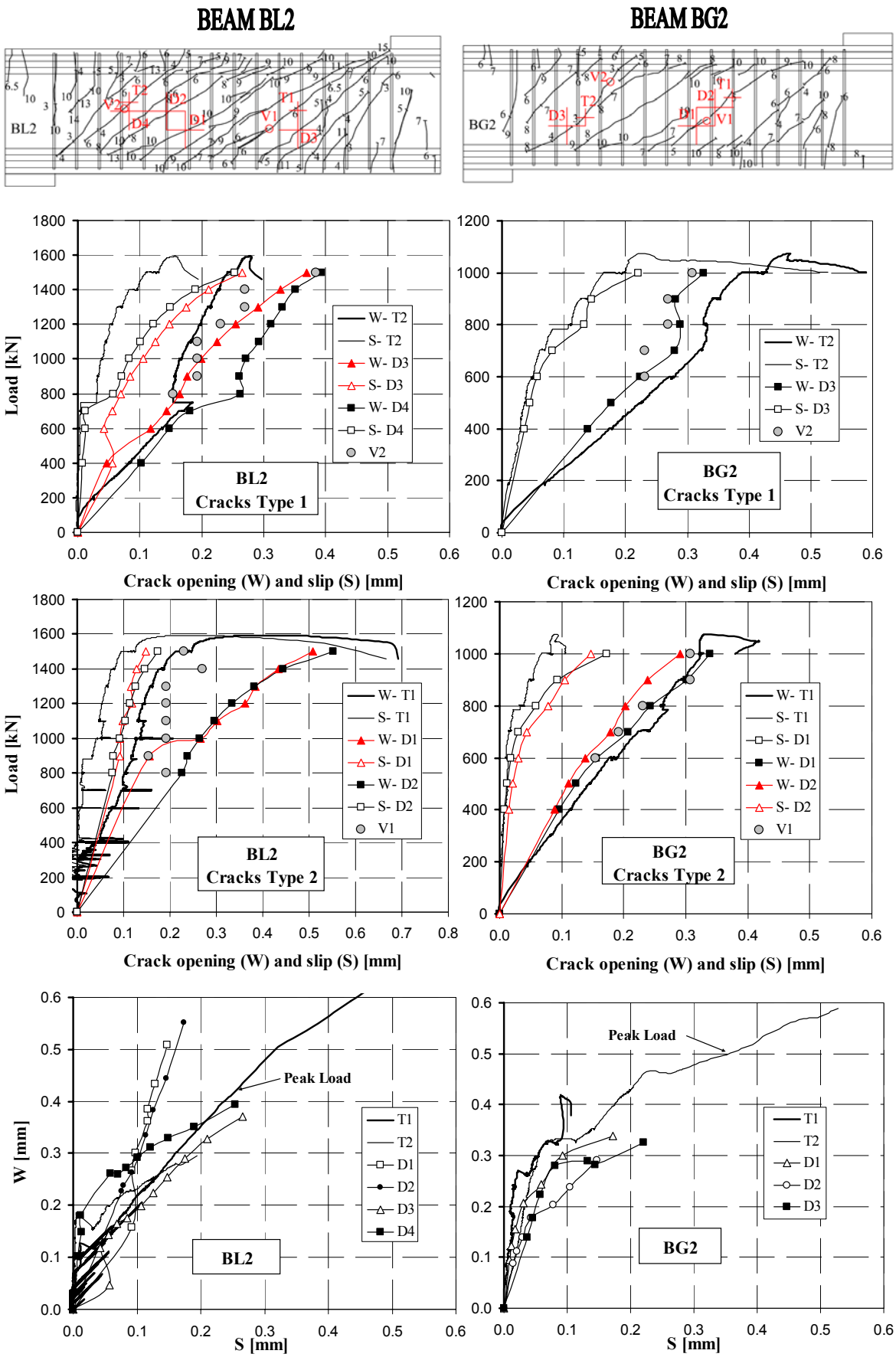

Notation: Cracks 1 are the first shear cracks to appear, which are steeper than cracks 2 (refer to Figure 6.40)
Types of readings: T- transducers (small cross); D- demec (large cross); V- visual (circle)

Figure 6.56 (Cont.): Crack opening and sliding in beams B

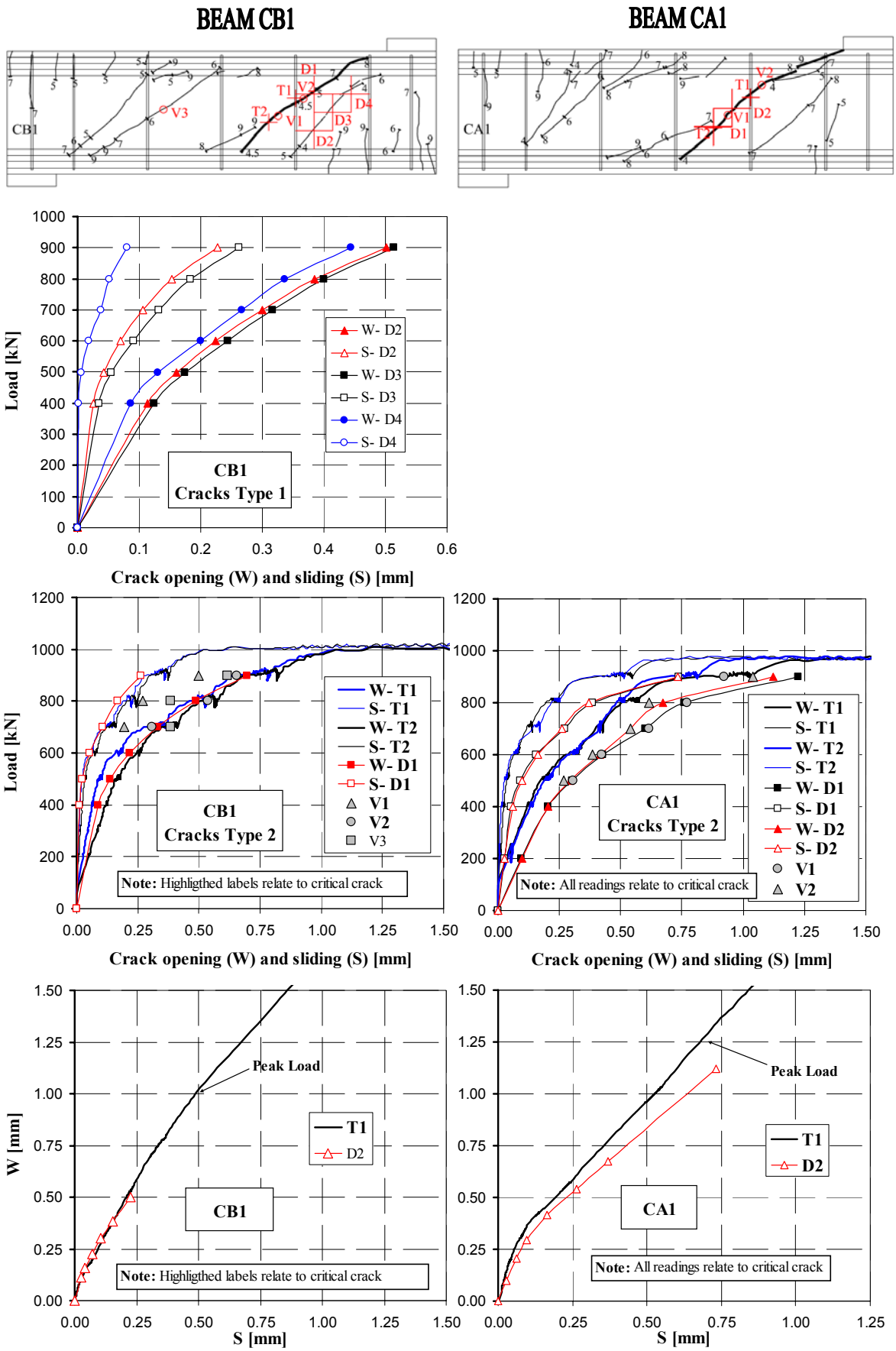

Notation: Cracks 1 are the first shear cracks to appear, which are steeper than cracks 2 (refer to Figure 6.40)
Types of readings: T- transducers (small cross); D- demec (large cross); V- visual (circle)

Figure 6.57: Crack opening and sliding in beams C

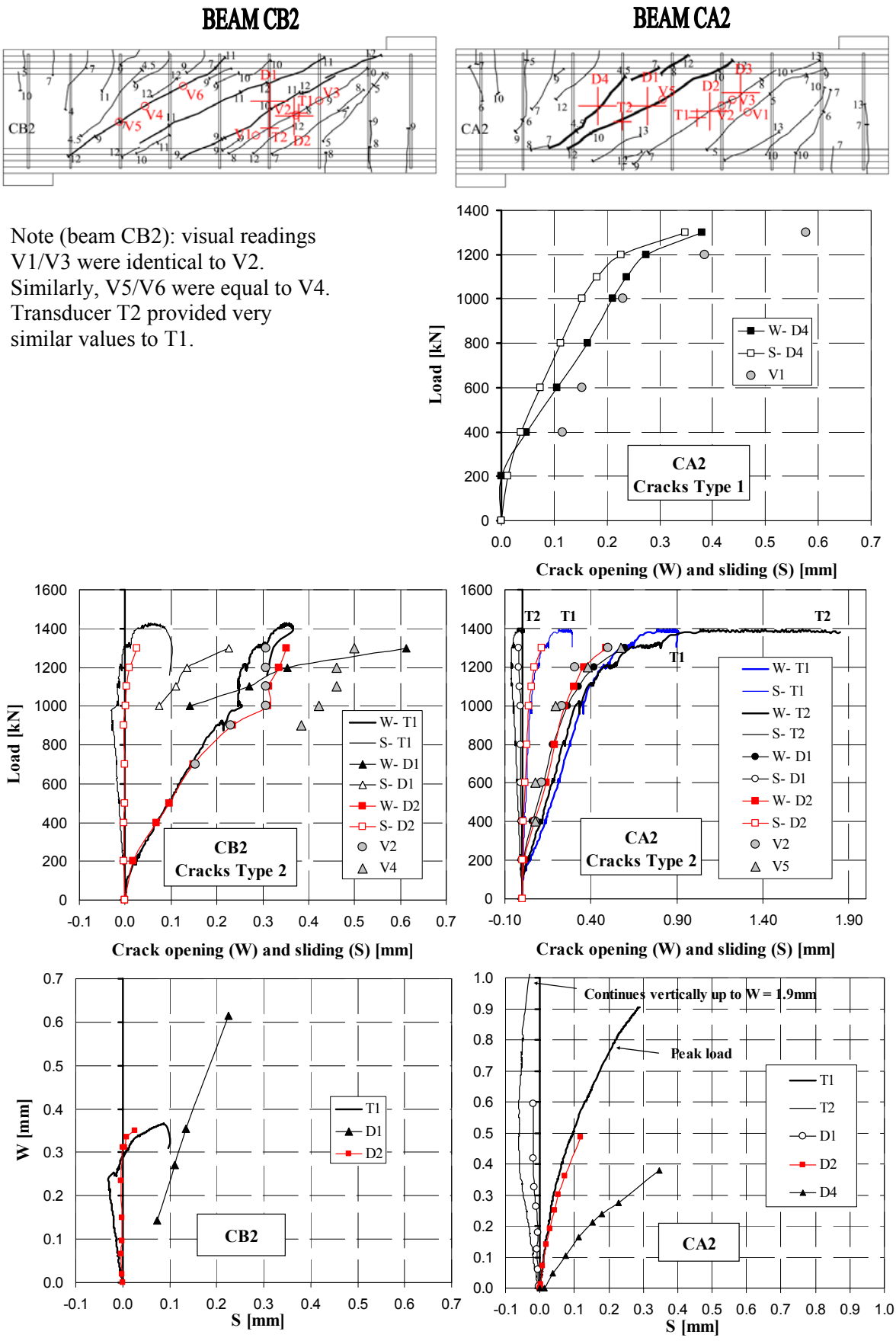

Notation: Cracks 1 are the first shear cracks to appear, which are steeper than cracks 2 (refer to Figure 6.40)
Types of readings: T- transducers (small cross); D- demec (large cross); V- visual (circle)

Figure 6.57 (Cont.): Crack opening and sliding in beams C

6.6 Slender beams with stirrups (Beams D)

6.6.1 General aspects

An additional two beams (beams DB1 and DA1), which contained same shear reinforcement ratio and type of stirrups as beams CB1 and CA1, were tested in order to assess the influence of the type of loading in the shear response. Beams D were simply supported, as beams B0, and so two additional T25 reinforcement bars at the bottom (refer to Figure 6.58) were required to avoid yielding of the flexural reinforcement. The central span was 3040mm long (a/d=3.68), measured between centrelines of the supports. The loading and support plates used were identical as for beams C.

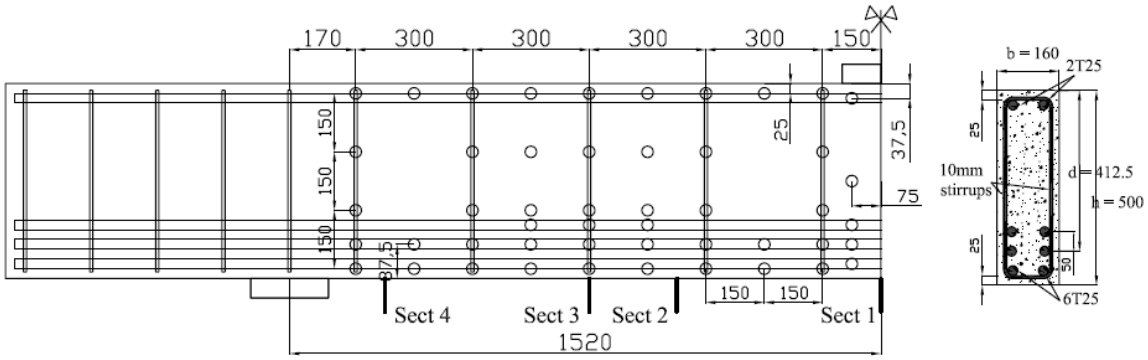

Note: Sect 2 is placed at a distance of 425mm (~d=412.5mm) from the edge of the loading plate
Sect 3 is placed at the centre of the shear span; Sect 4 is 245mm from the centre of the support

Figure 6.58: Slender beams with stirrups (Beams D)

Beams D were cast along with beams C using the same concrete, refer to mix 5 in section 6.2.2. The main geometrical/material properties and experimental results of beams D are summarised in Figure 6.58 and Table 6.9.

Beam	f_c' [MPa]	f_{sl} [MPa]	ρ_l [%]	$\rho_v f_{sv}$ [MPa]	δ_{centre} [mm]	P_{cr} [kN]	P_{unl} [kN]	P_{ult} [kN]
DA1	49.35	580	4.46	1.96	14.87	200	400	622.74
DB1	49.35	580	4.46	1.96	13.84	200	400	598.43

Note: deflection at peak load δ_{centre} is given relative to the floor

Table 6.9: Summary of experimental results of slender beams with shear reinforcement

6.6.2 Manufacture and curing

Same procedure described for beams C (see section 6.5.2) applies for the manufacture and curing of the slender beams with stirrups.

6.6.3 Instrumentation

Similarly as in beams B0, load was monitored by two load cells (1000kN), one placed under the hydraulic jack and the other located under one support. Vertical displacements were recorded at centre and quarter points of the length of the beam with respect the supports, using a similar frame as in beams B0 (see Figure 6.26). In addition, deflections at the centre of the beam were measured relative to the floor. Lastly, two transducers were placed at the end of the beam to measure horizontal displacements and rotation similarly as in beams A, B and C (see Figures 6.8 and 6.37).

A grid of Demec discs was used (see Figure 6.58) to measure horizontal strains at several levels of the beam. Measurements include several sections along the beam (refer to Figure 6.58); central section of the beam (Sect 1), section at a distance from the edge of the loading plate approximately equal to the effective depth (Sect 2), central section of the shear span (Sect 3) and section near the supports (Sect 4). Strains in the longitudinal reinforcement were also monitored with the Demec gauge. Crack opening and sliding were measured in a similar manner as in beams A, B and C; Demec and LVTD crosses were placed after pre-cracking the specimens (see Table 6.9 for load at which beam was unloaded P_{unl}).

6.6.4 Results

Type of failure and crack pattern

Equally as in beams C, the ultimate loads in beams DA and DB were very similar to each other (see Table 6.9). Failure in beams D was due to excessive straining of the stirrups crossed by the critical crack in a similar fashion as beams C. Stirrups fractured in both beams DA1 and DB1.

The crack patter was rather different in beams D compared with beams B or C, which was expected due to the interaction between bending and shear. The crack patterns of beams DA1 and DB1 are shown in Figure 6.59; thin lines represent cracks that formed after reaching the ultimate load. First shear cracks to appear (200-300kN), had an inclination with respect the longitudinal reinforcement of around 45º. At loads near failure (500-550kN) these steep cracks were either crossed by new flatter shear cracks or they extended towards the supports with a much flatter angle (Figure 6.59). The presence of flatter cracks crossing previous steeper cracks indicated a clear strut reorientation to mobilize more stirrups. It is well documented in beam tests found in the literature that

new cracks can cross previous shear cracks due to this strut reorientation. However this was not observed in any of other beam tests carried in this work (beams A, B and C).

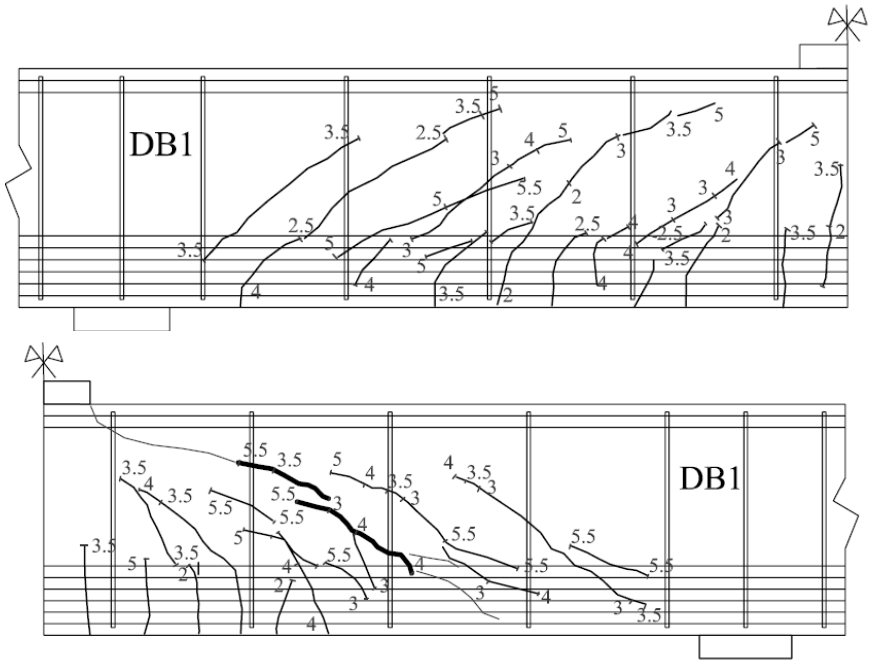

a) Beam DB1 (P_{ult}=598.43kN)

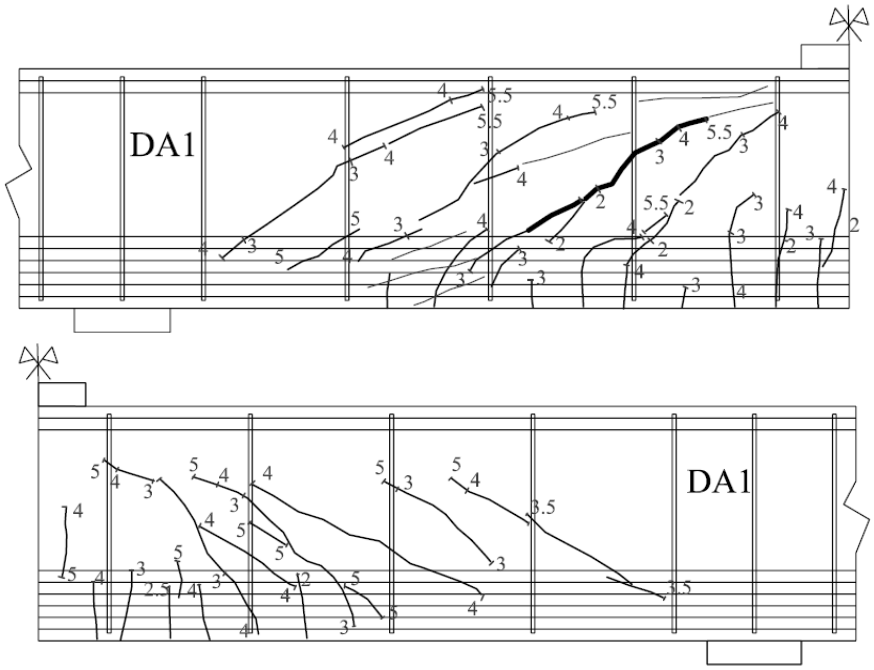

b) Beam DA1 (P_{ult}=622.74kN)

Note: numbers relate to load (x100kN) at which crack formed. Critical cracks are highlighted. Thin lines refer to cracks that formed at failure

Figure 6.59: Crack pattern in beams D

Load-deflection curves

The load-deflections curves shown in Figure 6.60, were almost identical for beam DA1 and DB1, reaching a maximum deflection at the centre of around 13mm. These values are around three times larger those obtained with similar shear forces in beam C1, which had a point of contra-flexure. The measurements taken relative to the floor in beams D were similar to those taken relative to the frame. Vertical deflections at quarter points were around half the values at the centre.

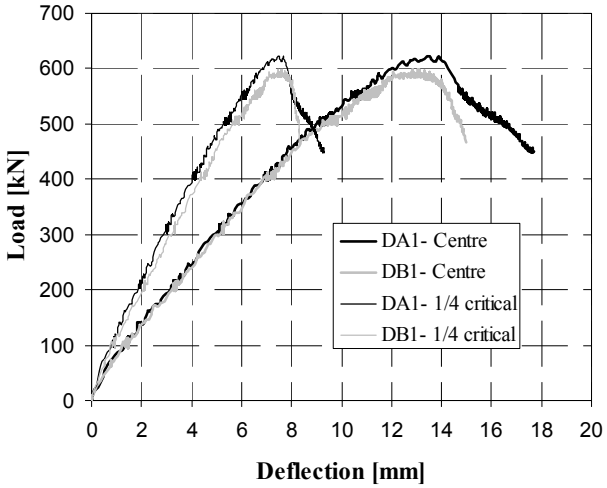

Note: deflections are measured relative to the frame

Figure 6.60: Vertical displacements of beams D (loading after pre-cracking the specimens)

Similarly as in beams A (see Figure 6.17), the end displacements (horizontal and rotation) measured experimentally, clearly showed which shear span was critical. Beam DB1 failed at the shear span where the transducers were placed, and so the horizontal displacements changed sign at failure. This indicated that once the beam started failing, the block above the critical crack started moving inwards, as opposed to outwards during normal loading.

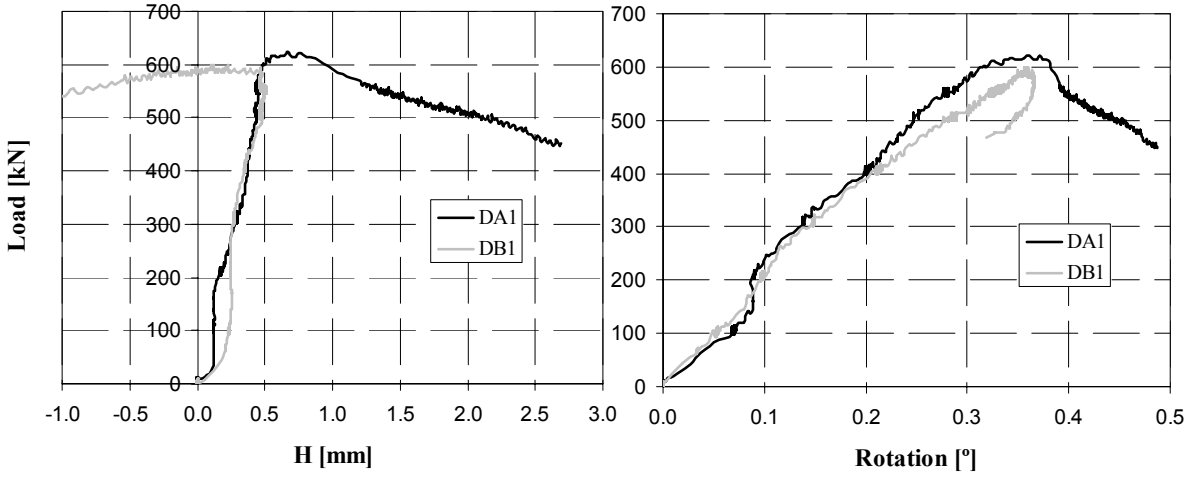

Figure 6.61: End displacements (horizontal and rotation) of beams D

Strains at different sections along the beam

The horizontal strains measured at different heights and sections of the beam were similar for beams DB1 and DA1, as shown in Figure 6.62. The results are shown at different sections of the critical shear span (Sect 1 to 4, according to Figure 6.58). The critical crack formed at a distance approximately equal to the effective depth of the beam, measured from the edge of the loading plate. The maximum compression strains registered at the centre of the beam were 2‰. In tension, the maximum strains obtained at the lower reinforcement layers were near the yielding point. The horizontal tensile strains at section of almost zero bending moments were around 0.75-1‰.

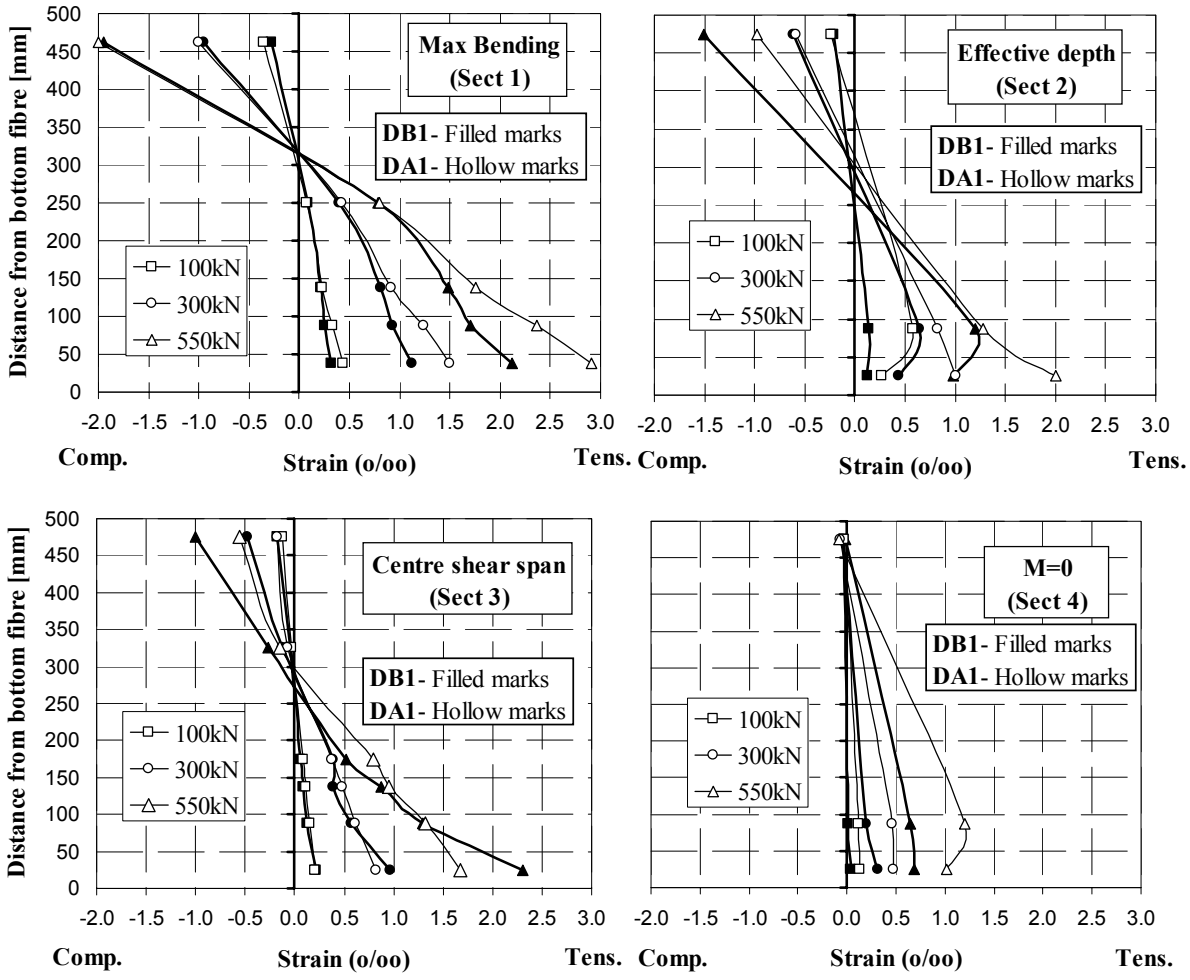

Note: Results are shown for different sections of the critical shear span: Max bending (Sect 1), Effective depth (Sect 2), Centre shear span (Sect 3) and M=0 (Sect 4); refer to Figure 6.58

Figure 6.62: Horizontal strains at different sections in beams D

Strains in stirrups

Stirrups at the centre of the shear span yielded at failure. In both beams DA1 and DB1 several stirrups that were crossed by the critical shear crack fractured; for example stirrup S8 in beam DB1 (see Figure 6.63). The strain readings from the Demec gauge at the critical shear span (Figure 6.63) indicated that the outer stirrups were less effective, similar as in beams A, B and C. The results are plotted for the sector of the stirrup that was crossed by the main shear crack and hence had the highest strains.

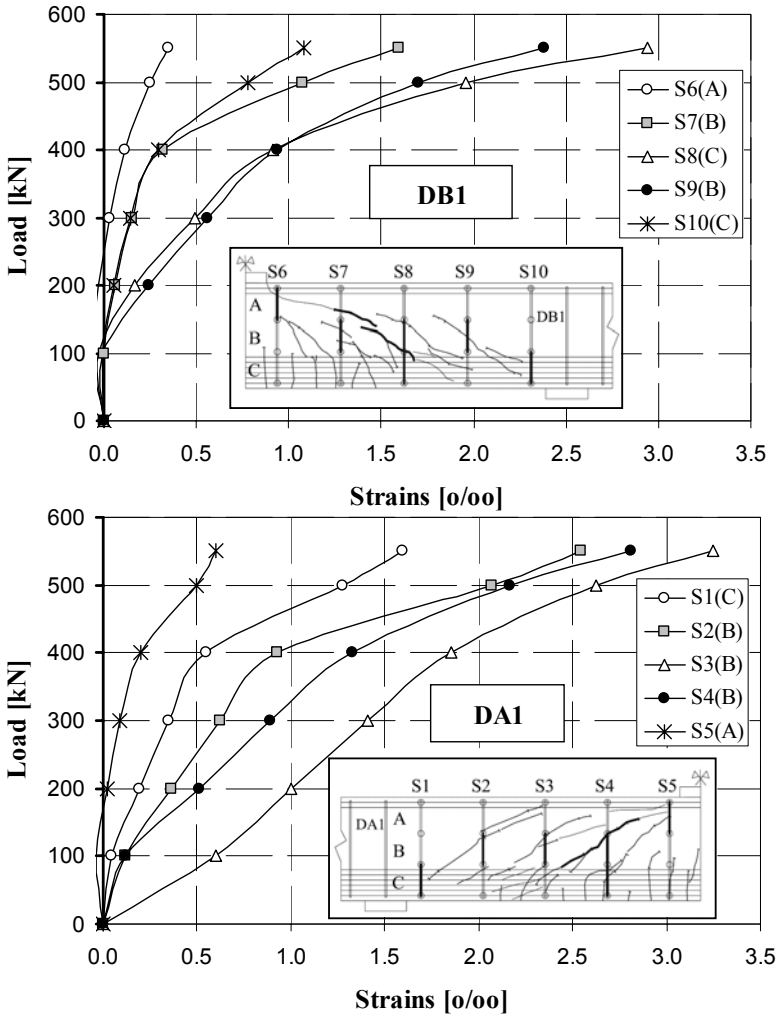

Figure 6.63: Maximum strains in stirrups in the critical shear span (beams D)

Strains in the longitudinal reinforcement

Again, strain readings along the longitudinal reinforcement taken with the Demec gauge had large oscillations especially at the centre of the shear span (see Figure 6.64). This was worse in beam DB1 than in beam DA1, where the results seemed more realistic. As mentioned earlier, the strains were near the yielding point at the centre of beam DA1.

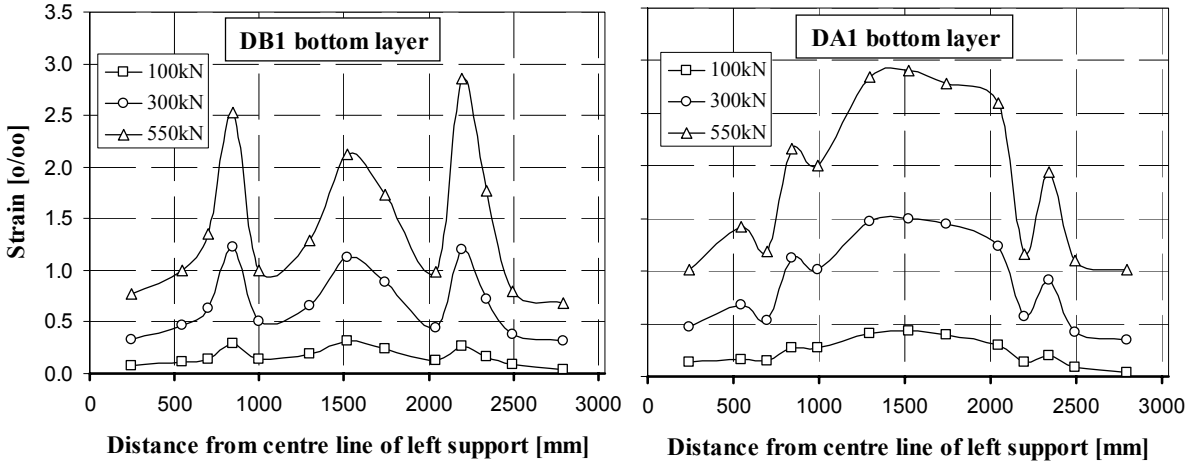

Figure 6.64: Strains in the longitudinal reinforcement (Demec gauge readings)

Relative crack displacements

The crack opening and sliding at different shear cracks are shown in Figure 6.65 for both shear spans. Only Demec readings with one crack going through the Demec cross were considered and again sliding was taken as positive when the block below the crack moved downwards with respect the block above.

Similarly as in beams B and C, the crack opened more rapidly at early load stages until the same load at which the beam was unloaded was reached. Again, the $\delta w/\delta s$ ratio after the pre-cracking load was reached was generally around 1.5 and decreased down to 1 at failure, as shown in Figure 6.66. The magnitude of the crack widths was similar as in beams C1 (0.75-1mm at failure). Measurements were validated by visual readings taken with the optical ruler.

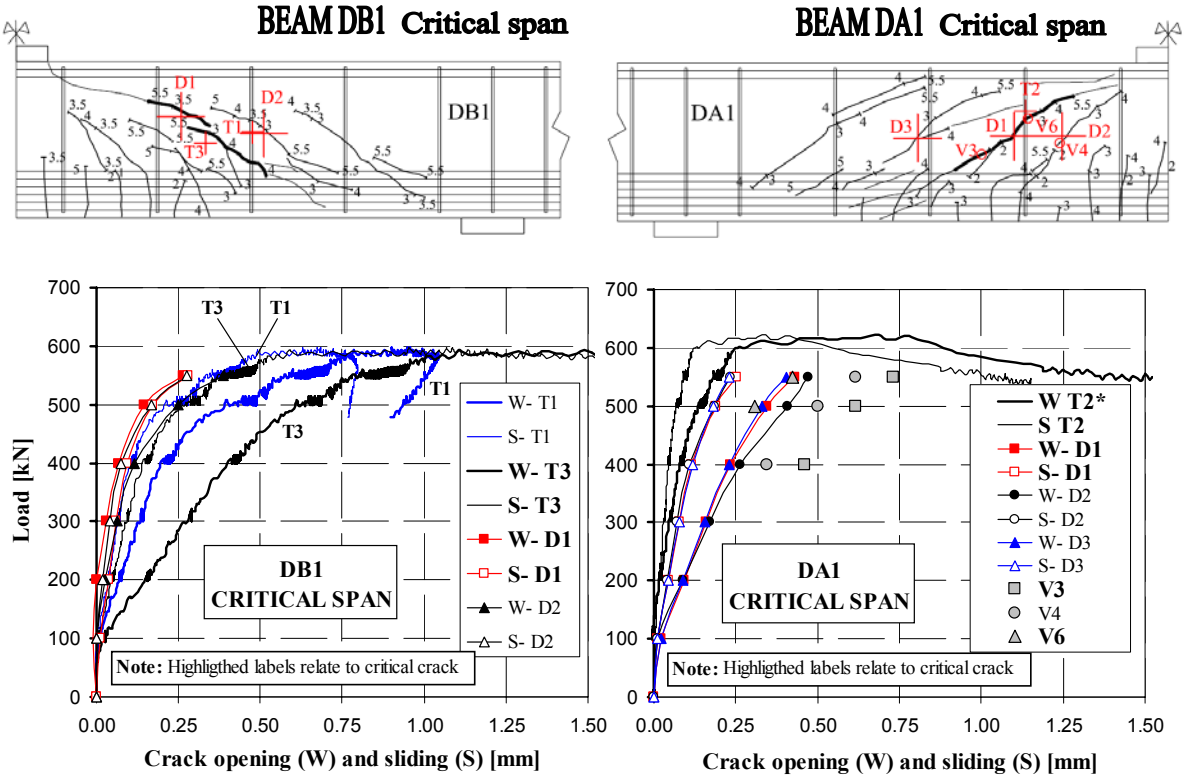

*Note (DA1): Readings from Transducer T2 are dubious due to the proximity of the crack to one end of the cross. Data from D1 seems more reliable.

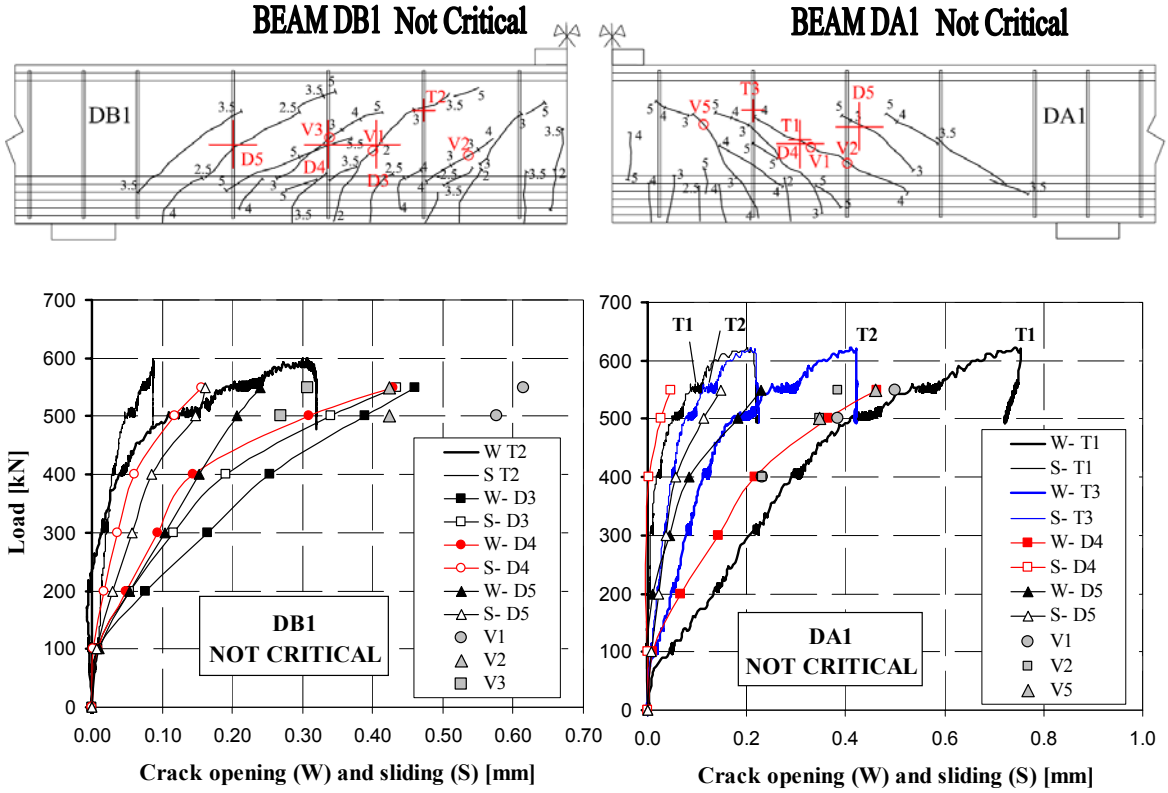

Notation: Types of readings: T- transducers (small cross); D- demec (large cross); V- visual (circle)

Figure 6.65: Crack opening and sliding in beams D at critical and not critical shear spans

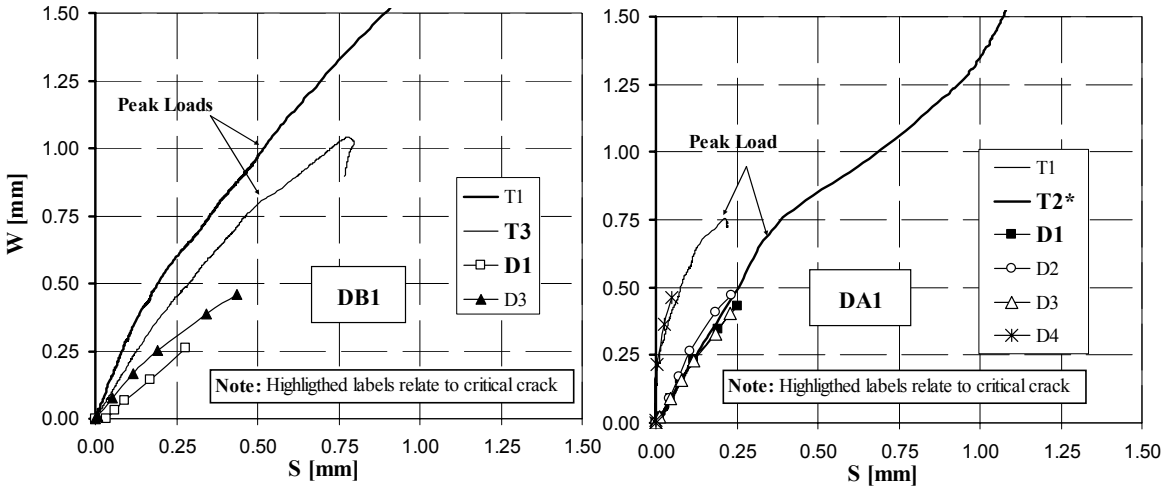

*Note (DA1): Readings from transducer T2 are dubious due to the proximity of the crack to one end of the cross. Data from D1 seems more reliable.

Notation: Types of readings: T- transducers (small cross); D- demec (large cross); V- visual (circle) Refer to Figure 6.65 for exact location at which measurements were taken

Figure 6.66: Crack opening and sliding variations in beams D

6.7 Conclusions

Valuable experimental data has been obtained from a total of 22 beam tests regarding ultimate loads, strains, crack patterns and opening/sliding of shear cracks. Tests consisted of several series which covered a wide range of shear reinforcement ratios, geometries and load arrangements; tests included short span and slender beams (with and without stirrups) and continuous beams with stirrups. Although all beams failed in shear, several types of shear failing mechanisms were observed depending on the beam slenderness, shear reinforcement ratio and concrete strength.

As expected, the crack pattern was significantly different between these beam series. The critical shear cracks in the short span beams and continuous beams remained independent from flexural cracks, which was not the case for the simply supported beams. Shear cracks that formed near failure crossed previous 45º shear cracks in the simply supported beams with stirrups. However, this did not occur in identical beams loaded with a point of contra-flexure. The critical shear crack remained stable until failure in all beams tested, except in the slender beams without stirrups, where failure occurred immediately after the main diagonal crack formed.

Geometrical aspects, such as the size of the bearing plates or exact location of the shear reinforcement, were found to be critical in many of the beam tests. These parameters, which are in many cases not reported by researchers, can have an influence on the ultimate load if they are not detailed properly. The relative position of the stirrups can be

critical since stirrups nearer the supports are less effective than those placed at the centre of the shear span, as shown by the strain readings obtained experimentally. On the other hand, the different size of the bearing plates used at the supports of the short span beams tested, showed that failure can be forced in one of the shear spans by increasing the size of one plate from 125 to 200mm. Lastly, the experimental results from the control specimens tested showed the relevance of testing cylinders in addition to cube specimens, since the transformation factor between them was not constant, as assumed in practice.

The type of aggregate used had a significant influence on the crack roughness. Aggregate fractured at cracks in beams made with limestone aggregate (f_c'=68MPa and 53MPa), which resulted on much smoother cracks than equivalent beams made with gravel (f_c'=80MPa and 31MPa), where the crack went round the aggregate. This occurred in beams independently of the load arrangement and amount of shear reinforcement used in the test. The consequences of aggregate fracture on the shear stresses transmitted along cracks in the beams, is studied in chapters 7 and 8 in light of data (crack opening and sliding) provided by the push-off and beam tests.

In general, crack opening (w) was predominant over crack sliding (s). However, the $\delta w/\delta s$ ratio was considerably larger in short span beams ($\delta w/\delta s$=3), independently of the type of aggregate used. In general the $\delta w/\delta s$ ratio in slender beams with stirrups was around 1.5. Crack opening readings at different heights of the beam indicated that the crack width was fairly uniform along its length, especially once the crack had fully developed.

Measurements taken in the tests were validated using different techniques, combining conventional with more innovative methods, such as digital photogrammetry. Strains were measured with either strain or Demec gauges. Both types of measurements were in good agreement in most of the cases. However, measurements along the flexural reinforcement were highly influenced by the presence of flexural cracks resulting in large oscillations in the Demec gauge data. Visual readings of the crack openings were consistent with the experimental data from either Demec or LVTDs crosses. Digital photogrammetry was found to be a useful tool since it allowed to measure deflections at several points of the beam. Measurements had an excellent agreement with traditional LVTDs placed along the beam. However, this method was not accurate enough in order to neither obtain reliable readings for strains nor relative crack displacements, due to the large working distance required. Although digital photogrammetry still has considerable margin for improvement, the results shown in this work look quite promising.

CHAPTER 7 - Analysis of Short Span Beams

7.1 Introduction

There are many instances, in the design of concrete structures, where loads are applied within *2d* of the supports. Typical examples include corbels, pile caps, hammerhead piers, deep beams and short span beams. Early experimental and analytical work by Kani [127], Zsutty [128] and Regan [129] showed that the shear strength of reinforced concrete beams is highly influenced by the location of the load with respect the support. It was observed that shear strength increases significantly due to arching action when loads are applied within approximately twice the beams effective depth of the support. Design codes such as BS8110 allow for arching action by increasing the basic shear strength of the concrete by a factor $1/\beta$ equal to $2d/a_v$, where a_v is the clear shear span and d is the effective depth as defined in Figure 7.1. EC2 adopts the alternative approach of reducing the component of shear force due to loads applied within *2d* of the support by the factor β.

Considerable experimental work has been carried out over the past 50 years into the shear behaviour of RC beams, with particular emphasis on slender beams with shear span to effective depth ratios (a_v/d) higher than 2 and on deep beams with a_v/d lower than 1. Short span beams with a_v/d ratios ranging from 1 to 2, have been studied to a lesser extent. Early work by Clark [130] and Zsutty [128] provided the first empirical formulations for short span beams, which failed in diagonal tension type of failure, that led to design equations used in the ACI codes.

The behaviour of short span beams is significantly different from normal and deep beams. In short span beams the diagonal crack forms independently of the flexural cracks and remains stable until failure. The diagonal crack typically runs in a straight line from the

inner edges of the loading plates (see Figure 7.1). Shear strength and ductility can be enhanced by adding transverse reinforcement. Vertical stirrups have been shown to be more efficient than horizontal links for a_v/d larger than 1 (Kong & Robins [131]). Design codes usually recommend that horizontal stirrups are used in beams with a_v/d less than 0.5. Vertical stirrups increase the shear strength if they cross the diagonal shear crack and are considered effective for design purposes if placed within the central three quarters of the clear shear span a_v.

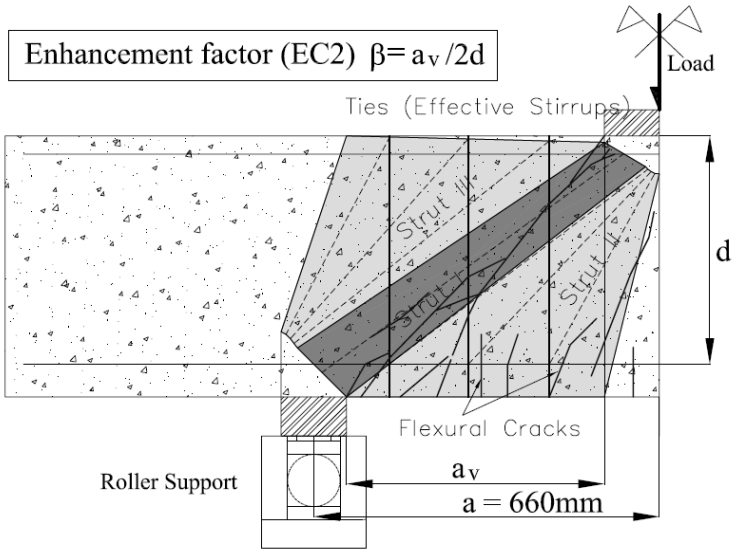

Figure 7.1: Typical crack pattern in short span beams (Beam AL3)

Two main load paths are commonly distinguished in short span beams with stirrups (see Figure 7.1) as discussed by Walraven & Lehwalter [132], Marti [133], Regan [129], Schlaich & Schaffer [35]. Firstly, a proportion of the load is transmitted directly from the loading plate to the support through a direct strut (Strut I). The second load path is the truss mechanism provided by the stirrups (Strut II–stirrups–Strut III). The main uncertainty is the percentage of load that is carried by each load path since the system is statically indeterminate. In addition, the influence of aggregate interlock and how the load is transmitted through the crack is unclear. The sensitivity of the shear strength predictions of short span beams to parameters such as the size of the bearing plates, concrete cover to the flexural reinforcement and anchorage length depends significantly on the method of analysis.

In this chapter, several design methods for short span beams with and without stirrups that are available in MC90, BS8110 and EC2 are investigated. A simple strut-and-tie model (STM) is presented to estimate the shear strength of short span beams which gives a good

correlation with experimental results. The STM model for short span beams is consistent with the EC2 recommendations for strut-and-tie models. The model is also shown to give reasonable predictions of the failure load of short span beams reinforced in shear with externally-bonded carbon fibre reinforced polymer sheets (CFRP). The influence of the crack development into the effective strength of the direct strut is investigated, along with the consequences of aggregate fracture. The analytical results from the STM models are compared with the experimental results of beams A and numerical predictions from the author's non-linear finite element models (NLFEA).

7.2 Short span beams without transverse reinforcement

Transverse reinforcement is often not required for strength in short span beams due to the enhanced shear strength provided by arching action. The entire load is transferred to the support in a direct strut as shown in Figure 7.2 in beams where stirrups are not provided. Despite the simplicity of the strut-and-tie model (STM) shown in Figure 7.2, there are several uncertainties in terms of load redistribution after the diagonal crack has formed. In addition, although the assumptions made in the strut-and-tie model in terms of geometry and effectiveness material strength factors are practical for design purposes, they are a stark representation of the real behaviour.

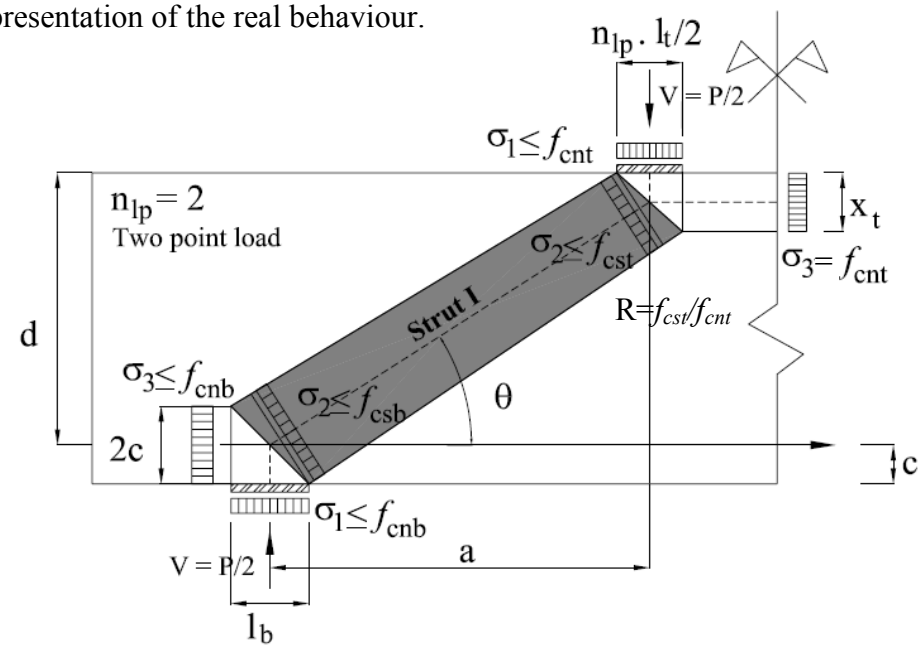

Figure 7.2: Strut-and-tie model for a short span beam without stirrups

According to Regan [129], two major types of failure can occur in short span beams:

1. *Shear-compression failure:* due to crushing of the diagonal strut over the inclined crack.
2. *Shear-proper failure:* the diagonal crack runs straight from the inner edges of the support to the loading plate, separating the beam into two parts.

Other types of failure are related to local effects such as bearing failure or loss of dowel action following the developments of a crack along the flexural reinforcement adjacent to the support. Local failures can be avoided by providing sufficient bearing length at the support/loading plates and sufficient anchorage length respectively.

7.2.1 Existing design methods

The design method suggested in EC2 and BS8110 for short span beams without transverse reinforcement is a sectional method based on empirical formulations. All shear resisting components such as shear at the compression zone, aggregate interlock and dowel action are assessed in one single term $V_{Rd,c}$, which represents the shear strength of the beam without transverse reinforcement. $V_{Rd,c}$ is given by the empirical equations (7.1) and (7.2) below in EC2 and BS8110 respectively. Equations (7.1) and (7.2) take into account size effects, dowel action, shear resisted in the compression zone and concrete strength.

$$V_{Rd,c}(EC2) = 0.18.(100.\rho_l f_{ck})^{1/3}.\left(1+\sqrt{200/d}\right)bd \quad \ldots (7.1)$$

$$V_{Rd,c}(BS8110) = 0.27.(100.\rho_l f_{cu})^{1/3}.(400/d)^{1/4}.bd \quad \ldots (7.2)$$

where $\rho_l = A_{sl}/(bd)$; f_{ck} = cylinder strength; f_{cu} = cube strength; d = effective strength; and b = width of the member.

BS8110 takes into account the increase in strength due to arching action by increasing $V_{Rd,c}$ by an "enhancement" factor equal to $2d/a_v$ where d is the effective depth and a_v is the clear shear span. EC2 adopts an alternative approach of reducing the design shear force by $\beta=a_v/2d$.

EC2 permits the use of the strut-and-tie method for designing short span beams as an alternative approach to its empirical formula. This raises the question whether to apply strut-and-tie provisions or $V_{enhanced}$ for design since both approaches can produce significantly different solutions.

7.2.2 Proposed Strut-and-Tie model

The simple strut-and-tie model shown in Figure 7.2, which is similar to that proposed by Vollum & Tay [134] amongst others, was used by the author to estimate the strength of short span beams without stirrups. The stresses in the nodes were assumed to be non-hydrostatic, hence the normal stresses at each face were different. The dimensions of the bottom node are defined by the bearing length l_b and the concrete cover c. In addition, the width of the direct strut was estimated from the geometry of the bottom node. The strut-and-tie model is applicable to beams with either one or two symmetrically placed concentrated loads.

In the strut-and-tie model shown in Figure 7.2, expression (7.3) is obtained from stating equilibrium at the top node.

$$P = 4 f_{cnt}.b \tan\theta.\frac{x_t}{2} \qquad \ldots (7.3)$$

where $\frac{x_t}{2} = d - a^*.\tan\theta$ and $a^* = a - \frac{l_t.(2 - n_{lp})}{4}$; n_{lp} = number of loading points (1 or 2).

The load P is the total load applied so the shear force V is equal to $P/2$ for both cases of one and two loading points. The notation f_{cnb} and f_{cnt} refers to the concrete strength at the bottom and top nodes while f_{csb} and f_{cst} correspond to the concrete strength of the strut at the top and bottom respectively (refer to Figure 7.2). These concrete strength values were taken from the latest EC2 draft and were compared with previous recommended values suggested in MC90 or Collins & Mitchell [11], see Table 7.1.

Method	**Uncracked (top)**	**Cracked (bottom)**
STM-MC90	$f_{cst} = f_{cnt} = 0.85(1\text{-}f_{ck}/250).f_{ck}$	$f_{csb} = f_{cnb} = 0.6(1\text{-}f_{ck}/250).f_{ck}$
STM-Collins*	$f_{cst} = f_{cnt} = f_{ck}$	$f_{csb} = f_{cnb} = f_{ck}/(0.8+170.\varepsilon_1$*)
STM-EC2	Strut without transv. tension $f_{cst} = f_{ck}$	Strut with transv. tension $f_{csb} = 0.6(1\text{-}f_{ck}/250).f_{ck}$
	Node (C-C) $f_{cnt} = (1\text{-}f_{ck}/250).f_{ck}$	Node (C-T) $f_{cnb} = 0.85(1\text{-}f_{ck}/250).f_{ck}$

Note: * $\varepsilon_1 = \varepsilon_L + (\varepsilon_L + 0.002).cot^2\theta$ where ε_L is the strain in the tie (Collins & Mitchell [11])

Table 7.1: Concrete strengths applied in the STM

In order to solve for P and θ in equation (7.3), an additional equation is needed. This relationship is obtained from the failure mode taken into account. Six different modes of failure were considered in order to obtain the shear strength. However, the critical failure mode was in most cases crushing in the strut (Mode 2). The failure modes examined are listed below:

Mode 1: Flexure.

$$P_1 = 2 A_{sl}.f_{yl}.\tan\theta \qquad \ldots (7.4)$$

Mode 2: Crushing in strut at bottom node.

$$P_2 = 2(l_b.\sin^2\theta + c.\sin 2\theta).f_{csb}.b \qquad \ldots (7.5)$$

Mode 3: Crushing at rear face at the bottom node.

$$P_3 = 4c.f_{cnb}.b.\tan\theta \quad \ldots (7.6)$$

Mode 4: Bearing failure at bottom node.

$$P_4 = 2f_{cnb}.l_b.b \quad \ldots (7.7)$$

Mode 5: Crushing in strut at top node.

$$P_5 = 2\left(\frac{n_{lp}.l_t}{2}.\sin^2\theta + \frac{x_t}{2}.\sin 2\theta\right).b.f_{cst} = \frac{n_{lp}.f_{cst}.l_t.b.\sin^2\theta}{1-\frac{f_{cst}}{f_{cnt}}.\cos^2\theta} \quad \ldots (7.8)$$

Mode 6: Bearing failure at top node.

$$P_6 = n_{lp}f_{cnt}.l_t.b \quad \ldots (7.9)$$

Iterating for different values of θ, a converged solution is found for each failure mode that satisfied both equation (7.3) and the corresponding mode of failure constraint (7.4 to 7.9). From the three references shown in Table 7.1, only EC2 distinguishes between an effective concrete strength for the strut and nodes. If the concrete strengths suggested by MC90 or Collins & Mitchell's [11] formula are applied, Mode 5 coincides with Mode 6. This can be seen clearly by taking $f_{cst} = f_{cnt}$ in equations 7.8 and 7.9. The proposal by Collins & Mitchell [11] relates the concrete strength of the strut to the tensile strain of the tie in order to satisfy compatibility of deformations at the bottom node. A converged solution similar to STM-MC90 prediction was obtained using the softening model suggested by Collins & Mitchell [11].

The critical failure mode predicted by the three methods investigated varied as shown in Tables 7.2 to 7.4. In general, the governing failure mode predicted by STM-EC2 was Mode 2, which corresponds to strut crushing at the bottom node. On the other hand, Mode 3 (failing of the rear face of the bottom node) was critical in STM-MC90 and STM-Collins approaches. This type of failure mode is generally neglected by the codes and no check is required as long as the reinforcement anchorage length is sufficient. Neglecting Mode 3 in the STM-MC90 approach results in identical results to STM-EC2 since Mode 2 becomes critical in both; on the other hand the STM-Collins predictions showed a slight improvement, as shown in the next section.

According to STM, failure is governed by the bottom node. As reported by Vollum & Tay [134], it is not clear whether this is consistent with experimental evidence since failure generally occurs by crushing of the concrete at the top node. In addition, it is debatable which value of the effective concrete strength should be used for the strut at the top node. No solution is generally found for Mode 5 (strut crushing at the top node) using EC2 concrete strengths shown in Table 7.1. This can be explained by solving analytically equations (7.3) and (7.8). A cubic relationship $F(tan\theta)$ is obtained, see equation (7.10), in which R is the ratio between f_{cst}/f_{cnt} assumed. The roots of equation (7.10) provide the solution to the problem; at least one root is a real number. However, depending on the coefficients of the cubic equation, the root can become negative. This is usually the case for R>1 using normal values of l_t, a^* and d (see Figure 7.3).

$$F(\tan\theta) = \tan^3\theta - \frac{d}{a^*}\tan^2\theta + \left(1 - R + \frac{n_{lp}.R.lt}{4a^*}\right).\tan\theta - \frac{d}{a^*}(1-R) \qquad \ldots (7.10)$$

As discussed earlier, for MC90 and Collins & Mitchell's [11] formulas, Mode 5 is equivalent to Mode 6 (bearing failure at top plate) since R=1. On the other hand, the value of R in EC2 according to Table 7.1 would be $1/\nu$ where ν=(1-f_{ck}/250); R values of 1.2 are obtained for concretes of 40MPa. As discussed earlier, these values of R can be problematic and only cases with very small load plates would lead to a solution in the STM (see Figure 7.3). In addition, it is debatable whether the same strut effective factor should be used for the top and bottom nodes (R=0.6). This alternative interpretation would generally leads to a solution as shown in Figure 7.3. Results using this alternative approach are discussed in next the section.

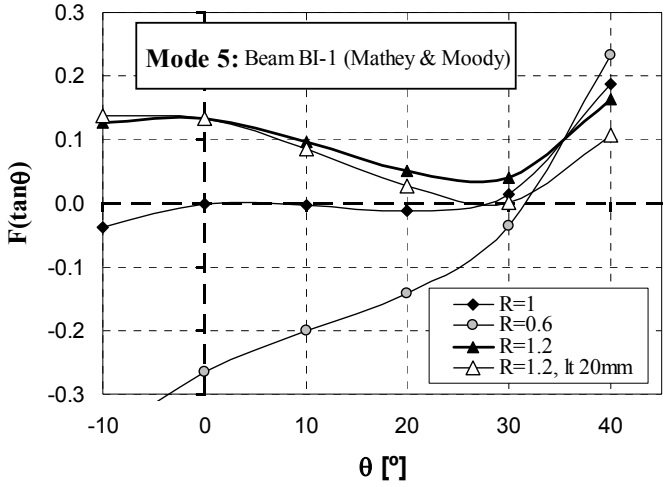

Note: Beam BI-1 tested by Mathey & Watsein [135] (l_b=l_t=89mm, a^*=610mm, f_{ck}=25.8MPa)

Figure 7.3: Converged solutions in STM for Mode 5 (strut crushing at the top node)

7.2.3 Performance of existing design methods compared to proposed strut-and-tie model (Experimental validation)

A total of 104 beams without stirrups, from fourteen different researchers [130-132, 134-146] including the authors (see Tables 7.2 to 7.4) were analysed using the design methods described in sections 7.2.1 and 7.2.2. The majority of the beams studied corresponded to short span beams (67) although 15 deep beams with a_v/d<1 and 9 more slender beams with a_v/d>2 were included in the analysis in order to verify the range of validity of the design methods. Results are summarized in Tables 7.2, 7.3 and 7.4 (γ_c=1).

The strut-and-tie methods (1-3 in Tables 7.2-7.4) were found to be more accurate than the sectional approaches described in section 7.2.1 (4-5 in Tables 7.2-7.4). In addition, the EC2 recommended values for the effective concrete strengths in the STM, provided better estimates of the ultimate strength than the MC90 and Collins & Mitchell [11] approaches, which gave more conservative results.

av/d <1								Pcalc/Ptest ¦ F.M						Pcalc/Ptest	
Author	Beam	av/d	d [mm]	b [mm]	fc' [MPa]	ρl [%]	Ptest [kN]	1- STM - EC2		2- STM - MC90		3- STM - Collins		4- EC2	5- BS8110
Walraven	V711	0.69	160	250	18	1.52	330	0.64	M6	0.76	M4	0.93	M2	0.77	0.78
& Lehwalter	V022	0.72	360	250	20	1.13	540	0.85	M6	0.87	M2	0.93	M2	0.82	0.78
	V511	0.73	560	250	20	1.12	700	0.90	M2	0.85	M2	0.97	M2	0.88	0.82
	V411	0.73	740	250	19	1.10	730	1.18	M2	1.12	M2	1.25	M2	1.05	0.96
	V211	0.73	930	250	20	1.08	1010	1.07	M2	1.01	M2	1.13	M2	0.92	0.83
Smith	0A0-44	0.67	305	102	20	1.93	280	0.78	M2	0.74	M3	0.83	M3	0.74	0.71
& Vantsiotis	0A0-48	0.67	305	102	21	1.93	272	0.82	M2	0.78	M3	0.87	M3	0.77	0.73
Tan et al	II-1/1.00	0.85	443	110	78	2.58	510	1.33	M2	1.28	M3	1.54	M3	0.73	0.75
Kong	S-10	0.83	216	76	23	1.75	220	0.56	M2	0.46	M3	-	-	0.44	0.42
	D-10	0.83	216	76	24	1.75	238	0.52	M1	0.44	M3	-	-	0.41	0.39
	S-15	0.52	343	76	28	1.10	416	0.45	M2	0.41	M4	-	-	0.48	0.45
	D-15	0.52	343	76	28	1.10	474	0.40	M2	0.36	M4	-	-	0.42	0.40
Oh	H4300	0.94	500	130	49	1.56	675	0.92	M1	0.80	M3	0.86	M2	0.51	0.48
& Shin	N4200	0.54	500	130	24	1.56	530	0.82	M2	0.82	M3	1.02	M2	0.89	0.83
	H4200	0.54	500	130	49	1.56	802	1.00	M2	0.99	M3	1.15	M1	0.75	0.70
Clark	D0-1	0.94	390	203	26	0.98	443	0.90	M1	0.88	M1	0.90	M1	0.69	0.65
	D0-3	0.94	390	203	26	0.98	446	0.89	M1	0.88	M1	0.90	M1	0.68	0.65
Tan & Lu	I-500/0.5	0.34	444	140	49	2.60	1700	0.48	M2	0.39	M4	0.81	M5	0.41	0.62
	I-500/0.75	0.62	444	140	43	2.60	1400	0.47	M2	0.42	M4	0.68	M3	0.38	0.39
	I-500/1.0	0.90	444	140	37	2.60	1140	0.45	M2	0.42	M3	0.49	M3	0.31	0.32
Zhan & Tan	2DB35	0.95	314	80	27	1.25	170	0.79	M2	0.72	M4	0.82	M2	0.66	0.63
	2DB50	0.93	459	80	32	1.15	271	0.73	M2	0.72	M2	0.77	M2	0.58	0.55
	2DB70	0.92	650	80	25	1.28	311	0.66	M2	0.66	M2	0.75	M2	0.65	0.60
	2DB100	0.92	926	80	31	1.26	483	0.74	M2	0.74	M2	0.82	M2	0.60	0.53
	3DB35b	0.95	314	80	27	1.25	170	0.79	M2	0.72	M4	0.82	M2	0.66	0.63
	3DB50b	0.94	454	115	28	1.28	334	0.80	M2	0.78	M4	0.85	M2	0.66	0.62
	3DB70b	0.93	642	160	29	1.22	721	0.69	M2	0.69	M2	0.75	M2	0.56	0.52
	3DB100b	0.94	904	230	29	1.20	1344	0.84	M2	0.80	M4	0.87	M2	0.57	0.51
Total =	**28**							**1- STM - EC2**		**2- STM - MC90**		**3- STM - Collins**		**4- EC2**	**5- BS8110**
	max value =	0.95	930	250	78	2.60	**Mean**	**0.77**		**0.73**		**0.90**		**0.64**	**0.62**
	min value =	0.34	160	76	18	0.98	**SD**	**0.23**		**0.23**		**0.21**		**0.18**	**0.16**
							COV %	**29.52**		**31.10**		**22.84**		**28.59**	**26.31**

Note: FM – Critical failure mode (M1- flexure, M2- crushing in strut at bottom node, M3- crushing at rear face at the bottom node, M4- bearing failure at bottom node, M5- crushing in strut at top node, M6- bearing failure at top node

Table 7.2: Summary of analysis of experimental data of beams without stirrups (a_v/d <1)

2 >av/d >1								Pcalc/Ptest ¦ F.M						Pcalc/Ptest	
Author	**Beam**	**av/d**	**d [mm]**	**b [mm]**	**fc' [MPa]**	**ρl [%]**	**Ptest [kN]**	**1- STM - EC2**		**2- STM - MC90**		**3- STM - Collins**		**4- EC2**	**5- BS8110**
Mathey	BI-1	1.29	403	203	26	3.05	626	0.64	M2	0.58	M3	0.55	M3	0.46	0.50
& Watsein	BI-2	1.29	403	203	23	3.05	621	0.59	M2	0.54	M3	0.50	M3	0.45	0.49
	BII-3	1.29	403	203	22	1.88	524	0.67	M2	0.61	M3	0.54	M3	0.51	0.49
	BII-4	1.29	403	203	27	1.88	626	0.67	M2	0.60	M3	0.53	M3	0.46	0.43
	BIII-5	1.29	403	203	26	1.85	577	0.70	M2	0.64	M3	0.56	M3	0.49	0.46
	BIII-6	1.29	403	203	26	1.85	581	0.70	M2	0.63	M3	0.55	M3	0.49	0.46
	BIV-7	1.29	403	203	25	1.86	582	0.66	M2	0.60	M3	0.53	M3	0.48	0.45
	BIV-8	1.29	403	203	25	1.86	608	0.65	M2	0.59	M3	0.52	M3	0.46	0.44
	BV-9	1.29	403	203	24	1.16	448	0.83	M2	0.75	M3	0.60	M3	0.52	0.49
	BV-10	1.29	403	203	27	1.16	537	0.79	M2	0.72	M3	0.57	M3	0.46	0.43
	BVI-11	1.29	403	203	26	1.17	448	0.90	M2	0.81	M3	0.65	M3	0.54	0.51
	BVI-12	1.29	403	203	26	1.17	537	0.75	M2	0.68	M3	0.55	M3	0.45	0.43
	BV-13	1.29	403	203	23	0.75	445	0.81	M2	0.73	M3	0.54	M3	0.45	0.43
	BV14	1.29	403	203	27	0.75	448	0.94	M2	0.85	M3	0.61	M3	0.47	0.45
	BVI-15	1.29	403	203	26	0.75	359	1.13	M2	1.02	M3	0.73	M3	0.58	0.55
	BVI-16	1.29	403	203	23	0.75	377	0.97	M2	0.88	M3	0.64	M3	0.53	0.51
Moodey et al	III-24a	1.14	533	178	18	2.72	592	0.71	M2	0.54	M3	0.50	M3	0.54	0.56
	III-24b	1.14	533	178	21	2.72	605	0.79	M2	0.61	M3	0.56	M3	0.55	0.57
	III-25a	1.14	533	178	25	3.46	534	1.05	M2	0.80	M3	0.76	M3	0.66	0.71
	III-25b	1.14	533	178	18	3.46	578	0.71	M2	0.54	M3	0.51	M3	0.54	0.58
	III-26a	1.14	533	178	22	4.25	841	0.60	M2	0.46	M3	0.44	M3	0.40	0.43
	III-26b	1.14	533	178	21	4.25	792	0.61	M2	0.46	M3	0.45	M3	0.42	0.45
	III-27a	1.14	533	178	22	2.72	694	0.72	M2	0.55	M3	0.50	M3	0.49	0.50
	III-27b	1.14	533	178	23	2.72	712	0.74	M2	0.57	M3	0.52	M3	0.49	0.50
	III-28a	1.14	533	178	24	3.46	605	0.89	M2	0.68	M3	0.64	M3	0.58	0.62
	III-28b	1.14	533	178	23	3.46	681	0.76	M2	0.58	M3	0.55	M3	0.51	0.54
	III-29a	1.14	533	178	22	4.25	778	0.65	M2	0.50	M3	0.48	M3	0.44	0.47
	III-29b	1.14	533	178	25	4.25	872	0.65	M2	0.50	M3	0.48	M3	0.41	0.44
Walraven	V311	1.25	930	250	16	1.69	735	0.76	M3	0.54	M3	0.53	M3	0.80	0.72
Lehwalter	V321	1.25	930	250	16	1.69	778	0.71	M3	0.51	M3	0.49	M3	0.75	0.67
	V322	1.25	930	250	14	1.69	752	0.66	M3	0.47	M3	0.46	M3	0.75	0.67
	V811	1.25	160	250	19	1.90	281	0.81	M2	0.73	M4	0.58	M4	0.54	0.55
Leonhardt et al.	2	1.10	270	190	21	2.07	531	0.52	M2	0.48	M3	0.42	M3	0.41	0.40
Placas	R4	1.99	272	152	34	1.46	302	0.51	M2	0.48	M3	0.28	M3	0.34	0.33
	R5	1.99	272	152	34	0.97	169	0.92	M2	0.86	M3	0.46	M3	0.53	0.51
	R6	1.99	272	152	34	1.46	249	0.63	M2	0.59	M3	0.34	M3	0.41	0.40
Vollum & Tay	1	1.14	180	100	44	2.23	137	1.05	M2	0.83	M3	0.95	M3	0.74	0.76
	2	1.14	180	100	44	2.23	201	0.71	M2	0.56	M3	0.65	M3	0.50	0.52
	3	1.14	180	100	44	1.26	145	0.99	M2	0.78	M3	0.79	M3	0.60	0.59
	4	1.28	160	100	44	2.51	161	1.19	M2	1.12	M3	0.88	M3	0.50	0.55
	7	1.14	180	100	25	2.23	135	0.66	M2	0.52	M3	0.61	M3	0.62	0.64
	8	1.14	180	100	25	2.23	165	0.54	M2	0.43	M3	0.50	M3	0.51	0.52
	9	1.14	180	100	25	2.23	178	0.50	M2	0.39	M3	0.46	M3	0.47	0.48
	10	1.21	180	100	25	2.23	180	0.39	M2	0.37	M4	0.38	M2	0.44	0.45
	11	1.21	180	100	25	2.23	134	0.52	M2	0.50	M4	0.51	M2	0.59	0.61
	12	1.21	180	100	25	2.23	133	0.53	M2	0.51	M4	0.51	M2	0.59	0.61
Reyer de Ortiz	1	1.10	363	150	51	1.80	560	0.82	M3	0.59	M3	0.54	M3	0.50	0.48
	2	1.24	363	150	36	1.80	440	0.75	M2	0.57	M3	0.52	M3	0.50	0.48
	3	1.38	326	150	32	2.06	310	0.89	M2	0.69	M3	0.56	M3	0.59	0.57
	3B	1.38	326	150	49	2.06	580	0.67	M2	0.52	M3	0.43	M3	0.36	0.35
	4	1.38	326	150	33	2.06	490	0.84	M2	0.78	M3	0.57	M3	0.38	0.36
Smith	0C0-50	1.16	305	102	21	1.93	232	0.69	M2	0.60	M3	0.52	M3	0.51	0.49
& Vantsiotis	0B0-49	1.16	305	102	22	1.93	298	0.56	M2	0.49	M3	0.42	M3	0.41	0.39
	0D0-47	1.75	305	102	20	1.93	148	0.75	M2	0.64	M3	0.41	M3	0.53	0.50
Chen et al	1-500/1.5	1.46	444	140	42	2.60	680	0.60	M2	0.52	M3	0.44	M3	0.33	0.34
	2-1000/1.5	1.53	884	140	39	2.60	940	0.78	M2	0.74	M3	0.61	M3	0.39	0.38
	3-1400/1.5	1.55	1243	140	44	2.60	1380	0.76	M2	0.75	M3	0.62	M4	0.36	0.35
	4-1750/1.5	1.56	1559	140	43	2.60	940	1.32	M2	1.22	M4	1.03	M4	0.64	0.60
Tan et al	III-1/1.50	1.41	443	110	78	2.58	370	1.34	M2	1.18	M3	1.05	M3	0.60	0.62
Clark	B0-1	1.72	390	203	24	0.98	242	0.98	M1	0.96	M1	0.71	M3	0.67	0.63
	B0-2	1.72	390	203	24	0.98	188	1.26	M1	1.24	M1	0.68	M3	0.86	0.82
	B0-3	1.72	390	203	24	0.98	256	0.92	M1	0.91	M1	0.77	M3	0.63	0.60
	C0-1	1.33	390	203	25	0.98	349	0.85	M1	0.84	M1	1.00	M3	0.61	0.58
	C0-3	1.33	390	203	24	0.98	334	0.89	M1	0.87	M1	0.72	M3	0.63	0.59
De Cossio et al.	L-1	1.41	252	152	21	3.36	232	0.90	M2	0.67	M3	0.47	M3	0.56	0.61
Sagaseta	AG0	1.12	438	135	80	3.33	652	1.27	M2	1.10	M3	1.21	M3	0.53	0.57
& Vollum	AL0	1.12	438	135	68	3.33	731	1.04	M2	0.90	M3	0.96	M3	0.45	0.49
Total =	**67**							**1- STM - EC2**		**2- STM - MC90**		**3- STM - Collins**		**4- EC2**	**5- BS8110**
	max value =	1.99	1559	250	80	4.25	**Mean**	**0.79**		**0.68**		**0.59**		**0.52**	**0.52**
	min value =	1.10	160	100	14	0.75	**SD**	**0.21**		**0.20**		**0.18**		**0.11**	**0.10**
							COV %	**26.08**		**29.85**		**29.98**		**20.83**	**19.83**

Table 7.3: Summary of analysis of experimental data of beams without stirrups (2> a_v/d >1)

av/d >2								Pcalc/Ptest ¦ F.M						Pcalc/Ptest	
Author	Beam	av/d	d [mm]	b [mm]	fc' [MPa]	ρl [%]	Ptest [kN]	1- STM - EC2		2- STM - MC90		3- STM - Collins		4- EC2	5- BS8110
Clark	A0-1	2.11	390	203	22	0.98	178	1.13	M1	1.11	M1	0.71	M3	0.72	0.72
	A0-2	2.11	390	203	26	0.98	216	0.94	M1	0.93	M1	0.68	M3	0.63	0.63
De Cossio	L-2	2.41	252	152	22	3.36	151	0.90	M2	0.70	M3	0.31	M3	0.61	0.67
& Siess	L-2a	2.41	252	152	37	3.36	160	1.28	M1	1.06	M3	0.47	M3	0.68	0.75
	L-3	3.42	252	152	28	3.36	107	1.17	M2	0.95	M3	0.28	M3	0.94	1.03
	L-4	4.43	252	152	26	3.36	102	0.88	M2	0.73	M3	0.15	M3	0.95	1.05
	L-5	5.43	252	152	28	3.36	102	0.78	M2	0.66	M3	0.10	M3	0.98	1.08
Sagaseta	BG0	3.01	465	135	80	1.00	124	1.66	M1	1.41	M3	0.55	M3	1.30	1.22
& Vollum	BL0	3.01	465	135	68	1.00	101	2.04	M1	1.59	M3	0.60	M3	1.52	1.43
Total =	**9**							**1- STM - EC2**		**2- STM - MC90**		**3- STM - Collins**		**4- EC2**	**5- BS8110**
	max value =	5.43	465	203	80	3.36	**Mean**	**1.20**		**1.02**		**0.43**		**0.93**	**0.95**
	min value =	2.11	252	135	22	0.98	**SD**	**0.41**		**0.32**		**0.23**		**0.31**	**0.27**
							COV %	**34.46**		**31.30**		**53.23**		**33.76**	**28.86**

Note: Results for beams BG0 and BL0 are averaged values from B0-1 and B0-2 beams

Table 7.4: Summary of analysis of experimental data of beams without stirrups (a_v/d >2), where STM is no longer valid

Mode 5 (crushing of the strut at the top node) was not considered for the predictions of STM-EC2 shown in Tables 7.2 to 7.4, since converged solutions were rarely found. As discussed in previous section, this was due to the assumed f_{cst}/f_{cnt} ratio (Table 7.1). The alternative option of taking same effective strength ($0.6\nu f_{ck}$) for the top and bottom of the strut, provided rather conservative predictions; mean value of P_{calc}/P_{test}=0.57 and a coefficient of variation (COV) of 16% for beams with a_v/d=1–2. This suggests that using the bottom node geometry in order to assess the strut width is sensible since it is simpler and provides better predictions than using the geometry of the top node, which is not totally defined from geometric considerations.

As discussed in previous section, Mode 3 (failure of the rear face of the bottom node) was only critical in STM-MC90 and STM-Collins approaches. If this mode is neglected, STM-MC90 provides identical solutions to STM-EC2. The predictions from the STM-Collins approach neglecting Mode 3, improved slightly from those shown in Tables 7.2 to 7.4; an average value of P_{calc}/P_{test} equal to 0.65 and a coefficient of variation of 28% was obtained for beams with a_v/d=1–2.

Even though the strut-and-tie predictions were in general more reasonable than those provided by empirical formulas (7.1) and (7.2), a large scatter was observed in the STM predictions of short span beams without stirrups. The average value for P_{calc}/P_{test} using the STM-EC2 for the 67 beams analysed was 0.79, although the coefficient of variation was 26.6% and the ultimate load was overestimated for several beams such as beam AG0 (see Table 7.3). The EC2 empirical method provided results which were more conservative than the STM (average P_{calc}/P_{test} = 0.52) but had a slightly lower COV equal to 21.1%.

Very similar results to the EC2 empirical formula were obtained using the BS8110 formula, although the cube strength had to be estimated in most of the cases from cylinder tests. Unless cube strengths were available a conversion cylinder-cube strength factor of 0.8 was assumed.

The main reason for the large scatter in the STM predictions was that the effective concrete strength assumed in the direct strut was most likely overestimated in some specimens. It appears that beams, which exhibited a particularly lower strength such as beam AG0 tested in this work, the strength of the direct strut was highly influenced by the position of the diagonal crack. Beams with a shear proper type of failure in which the diagonal crack crossed the direct strut completely can exhibit a reduced strength, see further discussion in section 7.5.2. An interesting example is shown for beams AG0 and AL0 in which the first specimen failed at a lower ultimate load than second one even though the concrete was 17% stronger. The position of the main diagonal crack in beam AL0 allowed the direct strut to sustain higher loads than AG0 in which the direct strut was crossed completely by the diagonal crack since early load stages. The development of the main diagonal shear crack depends on factors such as the initial state of stress (creep and shrinkage) or load history. These parameters that affect the crack development are difficult to have control over them and justify the use of empirical based formulas such as EC2 formula (7.1).

The previous analysis was carried out with a material factor of safety (γ_c) of 1.0. Despite the large scatter observed in the strut-and-tie models, predictions are considered to be safe for beams with a_v/d between 1 and 2 and concrete strengths up to 80MPa.

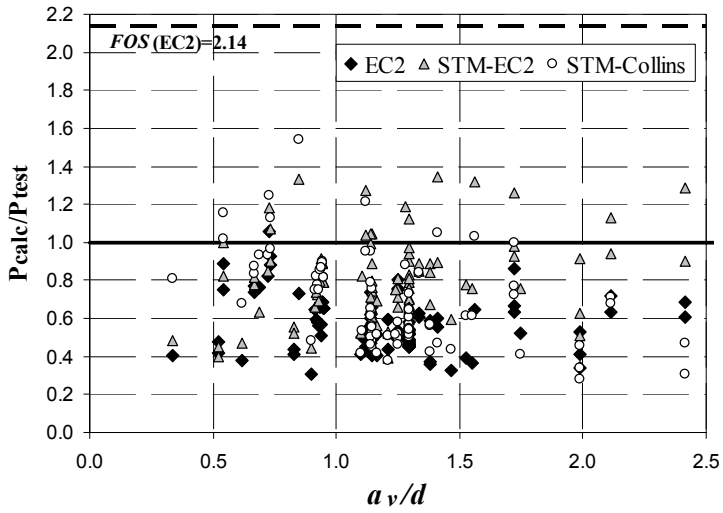

Figure 7.4: Performance of EC2 and STM methods for short span beams without stirrups ($1<a_v/d<2$)

The use of the material safety factors in the STM can compensate for the uncertainties in the effective concrete strength assumed as shown in Figure 7.4, leaving a reasonable margin for safety. The overall factor of safety (*FOS*) provided by EC2 can be estimated as 2.14, assuming dead load equal to live load (1.35+1.5)/2=1.42 and a material factor of safety for the concrete of 1.5. The *FOS* for ACI and CSA standards are 1.87 and 2.12 respectively (Collins et al. [12]). Using STM-EC2 approach in beams with a_v/d between 1 and 2, the maximum value for P_{calc}/P_{test} was 1.34, which still allows for a *FOS* of 1.58 according to EC2 provisions. Similar margins of safety were obtained using STM-Collins approach, although the predictions became more conservative with increasing a_v/d, as shown in Figure 7.4.

All the design methods that were examined, showed a very similar performance for the 15 deeper beams with $a_v/d<1$ than for beams with a_v/d between 1 and 2. This similar performance was unexpected since some of the beams had a_v/d ratios as low as 0.34. On the other hand, the results for more slender beams with $a_v/d>2$ using the STM-EC2 model were not satisfactory since an even larger scatter in the results was obtained than for beams with a_v/d between 1 and 2. In some cases such as beams B0 tested by the author, which had high concrete strength (80MPa) and depth of 462mm, the overall *FOS* obtained was almost zero when using STM-EC2 method (see Figure 7.5).

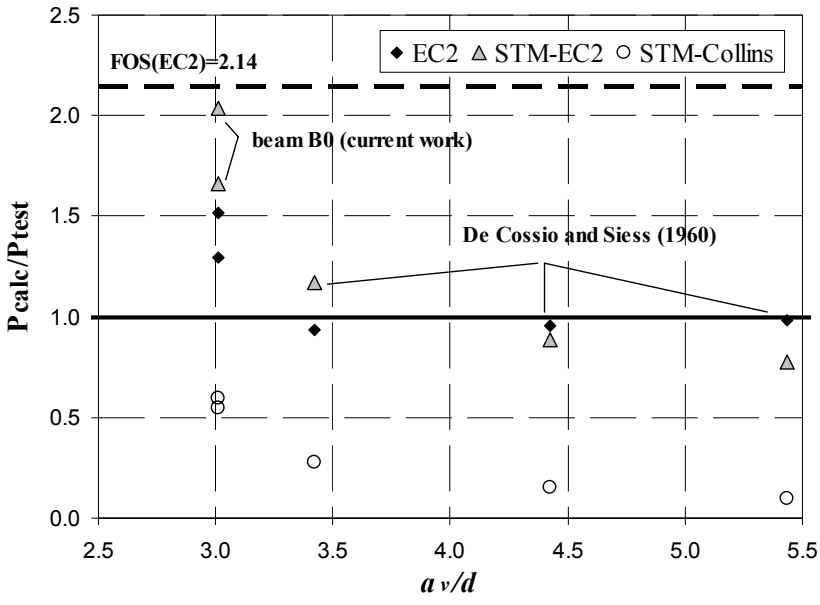

Figure 7.5: Shear strength predictions for slender beams with $a_v/d>2$ (refer to Table 7.4)

The poor performance of the STM for more slender beams was expected since the diagonal crack restricts quite considerably the formation of the direct strut for such

geometry (Muttoni & Schwartz [147]). It is widely accepted that for a/d>3.0, sectional approaches provide more accurate predictions than strut-and-tie models. Surprisingly, the predicted strength of some of the slender beams analysed with a_v/d up to 5.5 using STM-EC2 was near the experimental value (Figure 7.5). However, these beams, which were tested by De Cossio & Siess [146], had significantly low values of d and f_c. As shown in Table 7.4, the ultimate strength of the slender beams is generally overestimated using strut-and-tie models STM-EC2 and STM-MC90, as opposed to the STM-Collins approach, where the strength is clearly underestimated. The softening model suggested by Collins & Mitchell [11] seemed inadequate for such beams since the high transverse tensile strains induced in the strut by the tie result in an excessive reduction in concrete strength.

The empirical formulas provided more sensible results than STM models, which seems reasonable since equations (7.1) and (7.2) were originally calibrated for slender beams. The enhancement factor β was limited to 1 for beams with an a_v/d larger than 2 as specified in EC2. The accuracy of these empirical formulas regarding f_c, d and the type of aggregate, is discussed in more detail in chapter 8.

Demerit Point Classification

The different design methods investigated for short span beams with a_v/d between 1 and 2 were compared with each other using the "Demerit Point Classification" system proposed by Collins [148]. This simple approach is based on assigning marks (DP- Demerit Point) to each range of P_{test}/P_{calc}. This marking system has been used by other researchers, such as Cladera [24] amongst others, to compare shear design provisions given by different codes. The total demerit point score is obtained by summing the products of the percentage of specimens within each range of P_{test}/P_{calc} by the demerit point (DP) for that range, see Table 7.5. Predictions within the range of P_{test}/P_{calc}=0.85-1.30 are considered appropriate and so DP equals to zero. Predictions within the unsafe region are penalized more intensively than those on the conservative side (refer to Table 7.5).

The demerit point classification for the short span beams (a_v/d=1–2) without stirrups is shown in Table 7.5 and Figure 7.6. As expected, the strut-and-tie models had the lowest value of DP compared to EC2 and BS8110 approaches, which had a large number of specimens on the conservative side (see Table 7.5).

Ptest/Pcalc	**av/d: 1 - 2**	*DP*	**STM-EC2**	**STM-MC90**	**STM-Collins**	**EC2**	**BS8110**
<0.5	*Extremely dangerous*	*10*	0	0	0	0	0
0.5-0.65	*Dangerous*	*5*	0	0	0	0	0
0.65-0.85	*Low safety*	*2*	7	4	1	0	0
0.85-1.30	*Appropiate safety*	*0*	36	24	13	3	1
1.30-2.00	*Conservative*	*1*	54	55	58	52	52
>2.00	*Extremely conservative*	*2*	3	16	27	45	46
	TOTAL DP		**75**	**97**	**115**	**142**	**145**

Table 7.5: Demerit point classification for short span beams

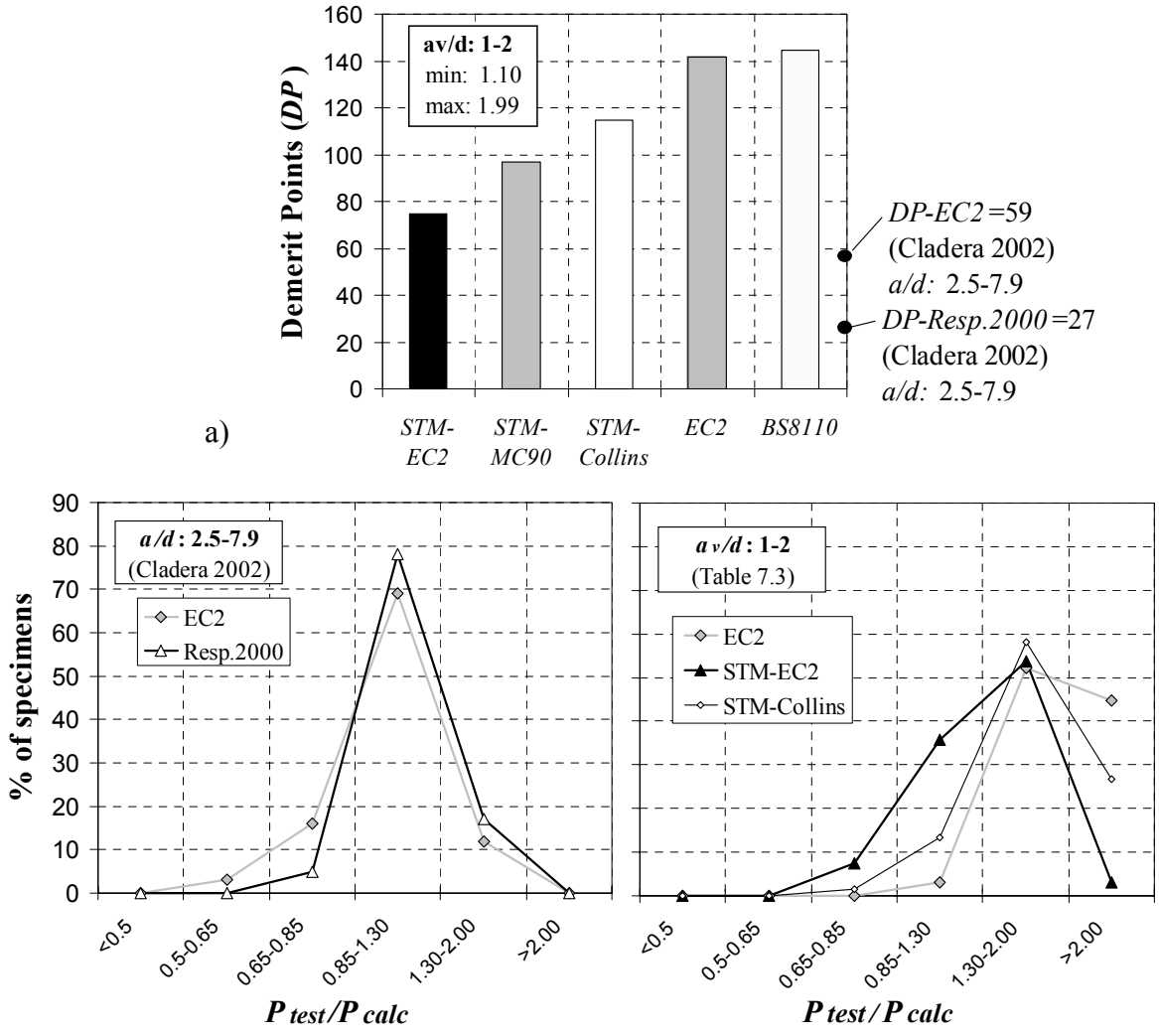

b) Results from Cladera [24] c) Refer to data in Table 7.3

Figure 7.6: Demerit point classification of beams without stirrups for different design methods: a) DP of beams with a_v/d =1-2; b) Results obtained by Cladera [24] for slender beams using EC2 and Response 2000; c) Results obtained in this work for short span beams using EC2 and STM approaches

It is of interest to compare the results with those obtained by Cladera [24] for more slender beams with *a/d* between 2.5 and 7.4, using EC2 and Response 2000. The total value of *DP* obtained by Cladera using EC2 was less than half the one obtained in this work for short span beams. This difference in the total value of DP reflects the excessive level of conservatism in EC2 method for short span beams, as shown in Figure 7.6. These results suggest that there is still some margin for improvement in the β factor used in EC2.

Although the Demerit Point Classification system proposed by Collins [148] is a practical approach to compare the performance of different design methods it can be argued that the approach does not reflect the differences in material and load factors used in the codes. According to the author this method seem suitable for comparing the accuracy of different design formulas, but it can be misleading if margins of safety are to be compared, since the P_{test}/P_{calc} ratio applied for the comparison does not consider any factors of safety. For example, the high *DP* mark obtained using the BS8110 method (see Table 7.5), which is due to an excessive level of conservatism, does not reflect that the material factor of safety used in BS8110 is considerably lower (γ_c=1.25) than the other codes examined (γ_c=1.5/1.54 for EC2/CSA codes). This difference might be compensated by lower load factors of safety but again this is not reflected in *DP* mark. A more rigorous comparison including safety factors is not always straightforward, as shown in sections 7.3.5 and 8.3.2, especially for beams with stirrups since partial factors of safety are applied to concrete and steel separately. As discussed in chapter 2, the assumptions made regarding V_c and V_s vary significantly according to the design method used.

A possible alternative is suggested by the author, which consists of modifying the Demerit Point Classification system proposed by Collins [148] by using parameter P_{test}/P_d instead of P_{test}/P_{calc}, where P_d is the design strength, including material and load factors. Table 7.6 shows a possible scoring scenario proposed by the author. The limits for the different ranges proposed shown in Table 7.6 seem reasonable, although they are open to discussion. These ranges of P_{test}/P_d were obtained from multlipying the original values of P_{test}/P_d suggested by Collins [148] by a constant factor of around 1.75, which was estimated from overall factors of safety used in CSA for slender beams with stirrups (see section 8.3.3). For members without stirrups the factor of 1.75 used to obtain the critical values of P_{test}/P_d shown in Table 7.6, could be increased since the material factors are

generally higher for such instances. For simplicity, same ranges of P_{test}/P_d were finally adopted for both cases of beams with and without shear reinforcement.

As shown in Table 7.6, the demerit mark obtained by the BS8110 method using the modified demerit point system becomes lower than for EC2, which results from the lower material factors of safety assumed, as discussed earlier. The results shown in Table 7.6 were obtained assuming γ_c equal to 1.5 and 1.25 for EC2 and BS8110 methods respectively. In addition, dead load was assumed to be equal to live load, which results on load factors of 1.42 and 1.5 for EC2 and BS8110 respectively. Results from the STM-Collins approach are not shown since the method combines formulas from two different codes, i.e. strength at the nodes from STM provisions according to EC2 and Collins & Mitchell [11] formula for the effective strength of the strut.

			STM	Sectional	
Ptest/Pd	**av/d: 1-2**	*DP*	**STM-EC2**	**EC2**	**BS8110**
<1.0	*Extremely dangerous*	*10*	0	0	0
1.0-1.15	*Dangerous*	*5*	0	0	0
1.15-1.5	*Low safety*	*2*	0	0	0
1.5-2.3	*Appropiate safety*	*0*	19	0	1
2.3-3.5	*Conservative*	*1*	63	16	39
>3.5	*Extremely conservative*	*2*	18	84	60
		TOTAL DP	**99**	**184**	**158**

Note: P_d design load using material and load factors (*DL=LL*; γ_{load}=1.42/1.5 and γ_c =1.5/1.25 for EC2/BS8110 design codes)

Table 7.6: Modified Demerit Point Classification by using overall factors of safety

7.3 Short span beams with transverse reinforcement

Transverse reinforcement should be provided in short span beams in cases when the applied shear force is greater than $V_{Rd,c}$. The shear strength and ductility of short span beam specimens is increased by vertical shear reinforcement. Design codes provide nominal shear reinforcement in order to assure ductile behaviour. EC2 defines a minimum shear reinforcement ratio of $\rho_{wmin} = 0.08 f_c^{0.5}/f_y$. On the other hand BS8110 requires a minimum design shear resistance provided by the links of 0.4N/mm^2 if the applied shear stress is larger than half of the shear resisted by the concrete ($v_c=V_{Rd,c}/bd$).

The load transfer mechanism in a short span beam with stirrups becomes statically indeterminate internally due to the additional load path provided by the transverse reinforcement. Following EC2 recommendations, only stirrups placed within the central three quarters of the clear shear span (a_v) were considered to contribute into the shear strength, which are denoted as "effective" stirrups. It is convenient to define the amount of transverse reinforcement in short span beams in terms of the stirrup index $SI=nA_{sw}f_y/(bh\,f_c')$, where n = number of effective stirrups, A_{sw} = area of steel provided by each stirrup, f_y = yield strength of steel, b = width, h = height, f_c' = cylinder strength of concrete.

7.3.1 Existing design methods

MC90

One of the earliest formulas for estimating the force carried by vertical stirrups for point loads near the supports was provided by Schlaich et al. [35] and was also included in the model code MC90. Expression (7.11), which also takes into account axial tension, is a linear interpolation of the shear carried by the stirrups (F_w), between the borderline cases $F_w = F$, for $a/z = 2$, and $F_w = 0$, for $a/z = 0.5$. If $a/z>2$ the beam is considered to be outside the short span beam behaviour range while in the other boundary case, $a/z>0.5$, the entire shear force is carried by the direct strut.

$$F_w = \frac{2.a/z - 1}{3 - N_{Sd}/F}.F \qquad \ldots (7.11)$$

where F_w is the shear carried by the stirrups, F is the total shear, a is the distance between centre load points, z is the lever arm which is taken as 0.9 times the effective depth and N_{Sd} is the axial tension (positive for tension).

It is noteworthy that equation (7.11) is only dependent on a/z and not the stirrup index SI, which is inconsistent with the experimental results presented in sections 7.3.5. Furthermore, the lever arm z is assumed constant in equation (7.11) and independent of SI, which seems to be unrealistic.

Standard Truss (BS8110 and first draft of EC2)

BS8110, as well as earlier drafts of EC2, proposes a design method for short span beams based on a traditional truss approach (V_c+V_s) with a concrete (V_c) and steel (V_s) components. The concrete component V_c, which is estimated from equations (7.1) or (7.2), is enhanced by factor $2d/a_v$ in order to take into account arching action. EC2 limits this factor to a maximum of 4, which corresponds to cases where a_v/d equals to 0.5. In short span beams, the stirrups contribution V_s is calculated as $nA_{sw}f_y$. For the analysis of the experimental database equation (7.1) is adopted in the calculations and referred to as (V_c+V_s) method.

An alternative approach to the standard truss method is to calculate the enhanced concrete component using a strut-and-tie model with no stirrups, instead of empirical equations (7.1-7.2) and then add the V_s term. In this work this is referred to as the $V_c(STM)+V_s$ method. The shear strength calculated in this manner is clearly overestimated, especially for higher values of SI, since the contribution of the direct strut, which is assumed constant and equal to $V_c(STM)$, appears to reduce as the SI increases.

EC2

The approach suggested in EC2 for designing short span beams consists of reducing the component of shear force due to loads applied within $2d$ of the support by a factor $\beta = a_v/2d$. This shear reduced value is limited by the yielding capacity of the stirrups located in the effective shear span. In the analysis of the experimental database of short span beams using EC2 approach presented in section 7.3.5, the strength of the beam was taken not lower than the strength of the beam without stirrups obtained from equation (7.1).

7.3.2 Proposed Strut-and-Tie model

Short span beams can be considered as a discontinuity region, thus EC2 allows short span beams to be designed using the strut-and-tie method (STM). The sensitivity of the predictions from the STM and the other design methods described in the previous section, to geometrical and material properties differ significantly. The STM is a transparent approach but various assumptions need to be made regarding the geometry of the nodes, the width of the struts and the concrete strength. The predictions of strut-and-tie models are dependent on these assumptions in addition to geometrical parameters such as the length of bearing plates and the concrete cover to the main tensile reinforcement.

The strut-and-tie model for short span beams presented in this section is consistent with the recommendations for STM made in EC2. The models are applicable to symmetrically loaded beams with either one or two point loads. The bearing stress under the loading and supporting plates were limited to νf_{cd} and $0.85\nu f_{cd}$ respectively as recommended in EC2 for compression-compression (CC) and compression-tension (CT) nodes in strut-and-tie models. The nodes were assumed to be non-hydrostatic and the bearing stress was considered constant under the plate. The previous assumptions are consistent with the strut-and-tie model suggested in section 7.2.2 for short span beams without shear reinforcement.

The load paths in the strut-and-tie model proposed for short span beams with stirrups consist of a direct strut (strut I) and a truss system (strut II-stirrups-strut III), as shown in Figure 7.1. In order to simplify the problem of internal statical indeterminacy, the stirrups were assumed to yield at failure. This assumption is justified by the experimental work of Clark [130], Regan [149], and the author amongst others for beams with a stirrup index (SI) up to at least 0.1.

The strength of strut I is affected by the diagonal crack and transverse tensile strains induced by the stirrups crossing it. Strut II, which is equilibrated by the stirrups, is affected by flexural cracks that decrease its strength. The third compressive stress field, strut III, is fan shaped like strut II, but the concrete in this region is essentially uncracked. The geometry of the strut-and-tie model is defined in Figure 7.7.

In the strut-and-tie model, λ is the fraction of the shear force taken by the direct strut (strut I) defined in equation (7.12). The remaining fraction of the load (1-λ) is taken by the stirrups $\sum_1^n T_{Si}$, where T_{Si} is tensile force carried by each stirrup assuming it has

yielded ($T_{Si}=A_{sw}f_y$) and n is the number of effective stirrups. In a similar manner, β is the fraction of the total tensile force T transmitted to the bottom node by the direct strut (T_d), see equation (7.13).

$$P = \frac{2}{(1-\lambda)}.\sum_{1}^{n} T_{Si} \quad \ldots (7.12)$$

$$T_d = \beta T \quad \ldots (7.13)$$

The geometry of the bottom node is defined once λ and β are known, since the other dimensions are given; namely length of the bearing plate (l_b) and $2c$ (see Figure 7.7).

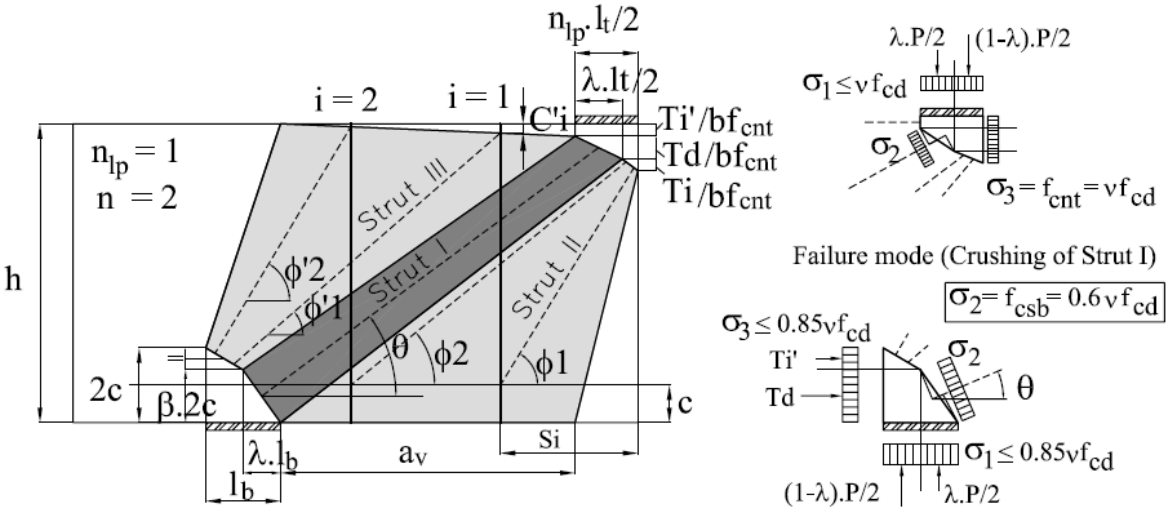

a) STM geometry b) Node stresses and failure mode

Figure 7.7: Strut-and-tie model definition for short span beams with vertical shear reinforcement (example for one point loading and two stirrups; n_{lp}=1 and n=2)

The tensile force in the reinforcement at the bottom node (T) can be divided into two components $T = T_i' + T_d$, where T_i' is the force transmitted by the indirect strut III and T_d is force transmitted by the direct strut. Both components are given by the equations (7.14) and (7.15). Equation (7.13) can be written in terms of T_i' and T_d, see equation (7.16).

$$T_i' = T_{Si}.\sum_{1}^{n} \cot\phi_i' \quad \ldots (7.14)$$

$$T_d = \frac{\lambda}{1-\lambda}.\cot\theta.\sum_{1}^{n} T_{Si} \quad \ldots (7.15)$$

$$\frac{T_d}{\beta} = \frac{T_i'}{1-\beta} \quad \ldots (7.16)$$

where $\phi_i^{'}$ = angles to the horizontal made by lines drawn from the top of each stirrup *i* to the bottom node as shown in Figure 7.7, and θ = angle of the centreline of the direct strut to the horizontal.

Stresses at the rear face of the top node are assumed to be plastic ($f_{cnt}=\nu f_{cd}$), which is consistent with the strut-and-tie model presented for beams without stirrups. Hence the inclinations of the struts θ and $\phi_i^{'}$ can be written in terms of the geometry, $T_i^{'}$ and T_d, as shown in equations (7.17) and (7.18).

$$\cot\theta = \frac{a_v + \frac{l_b\lambda}{2} + \frac{l_t\lambda}{4}.n_{lp}}{h - c\beta - \left(\frac{T_i^{'} + T_d/2}{bf_{cnt}}\right)} \qquad \ldots (7.17)$$

$$\cot\phi_i' = \frac{a_v + l_b - \frac{2(n-i)+1}{2n}.(1-\lambda).l_b - S_i + \frac{l_t}{2}.n_{lp}}{h - 2c + \frac{2(n-i)+1}{2n}.(1-\beta).2c - C_i^{'}} \qquad \ldots (7.18)$$

where a_v = clear shear span, n_{lp} = number of loading points at the top of the beam (1 or 2), l_b–l_t = length of bottom–top bearing plate, h = height, c = distance to centroid of longitudinal reinforcement, f_{cnt} = concrete stress at the top node, n = number of stirrups, b = width, i = stirrup number, S_i = distance from stirrup to rear face of the top node, $C_i^{'}$ = vertical distance from top of the beam to start of centreline of indirect strut III at stirrup *i*.

For simplicity, the top boundary of strut III was assumed to be linear in order to estimate $C_i^{'}$, see equation (7.19). This assumption has no significant effect on the angle $\phi_i^{'}$.

$$C_i^{'} = \frac{T_i^{'}}{bf_{cnt}}.\frac{a_v - S_i + l_t n_{lp}/2}{a_v} \qquad \ldots (7.19)$$

So far only geometric relationships and equilibrium at the nodes have been considered. Similarly as in the STM without stirrups, an additional condition must be considered from the mode of failure in order to obtain the ultimate load. Two failure modes were considered in the estimation of the ultimate load; namely crushing of the direct strut and failure at the bearing plates. The ultimate load was taken as the lowest value corresponding to these modes of failure. The critical failure mode in the majority of the beams studied was crushing of the direct strut. In addition, the tensile force T in the longitudinal reinforcement must be verified to be lower than the yielding capacity to avoid flexural failure.

The strength of the direct strut is governed by the product of its cross-sectional area and the effective concrete strength. In general good predictions were obtained using the effectiveness factor 0.6ν defined in EC2, where $\nu=(1-f_{ck}/250)$. The effectiveness factor accounts for the reduction in concrete compressive strength due to transverse tensile strain. Alternatively, as discussed for short span beams without stirrups, Collins & Mitchell [11] suggested a value for the effective concrete strength of the strut related to the strain in the longitudinal reinforcement. This alternative model was also investigated and compared with EC2 recommended value; results are discussed in detail in section 3.4.

In general, good predictions were obtained for the ultimate load if the width of the strut (w_{strut}) was estimated from the geometry of the bottom node, see equation (7.20).

$$w_{strut} = \lambda l_b \sin\theta + 2c\beta\cos\theta \qquad \ldots (7.20)$$

Limiting the stress in the strut to $0.6\nu f_{cd}$ and imposing vertical equilibrium at the bottom node leads to equation (7.21).

$$\frac{\lambda}{1-\lambda}\cdot\sum_{1}^{n} T_{Si} = \left(\lambda l_b \sin^2\theta + c\beta\sin 2\theta\right) b.0.6\nu f_{cd} \qquad \ldots (7.21)$$

The system of non-linear equations (7.14 to 7.19 and 7.21) presented can be used to solve for P or A_{sw} in design or analysis of short span beams respectively. However, as in most of strut-and-tie models, in order to find a converged solution an iterative process is required. In the following section an iterative algorithm is presented to solve this system of equations in a simple manner, which could be easily implemented in a subroutine or spreadsheet.

7.3.3 Simplified strut-and-tie model: design and analysis equations

The strut-and-tie model for short span beams is defined in its most general form by the system of equations given in previous section, which takes into account the spacing of the vertical reinforcement. In practice, stirrups are distributed uniformly and centred with respect the clear shear span. The system of equations (7.14 to 7.19 and 7.21) can be simplified for this particular case where the resultant of the stirrups is located at the centre of the clear shear span. Failure is assumed to occur due to crushing of the direct strut assuming the strut width from the geometry of the bottom node. The stresses under the loading and supporting plates must be limited to νf_{cd} and $0.85\,\nu f_{cd}$ respectively.

Firstly, equation (7.16) can be written in terms of the inclination of the direct and indirect struts reaching the bottom node to assure uniform stresses at the rear face of the bottom node. The previous relationship can be written as shown in equation (7.22).

$$\frac{\lambda}{(1-\lambda)} = \frac{\beta}{(1-\beta)} \cdot \frac{\cot\phi'}{\cot\theta} \qquad \ldots (7.22)$$

In the simplified strut-and-tie model, the resultant of the stirrup forces is placed at a distance S_1 equal to ($l_t.n_{lp}/2+a_v/2$) and $C_1' = T_i'/2bf_{cnt}$, refer to Figure 7.7. Equation (7.18) can be simplified into equation (7.23)

$$\cot\phi' = \frac{1}{2} \cdot \frac{a_v + (1+\lambda)l_b}{h - (1+\beta)c - \dfrac{T_i'}{2bf_{cnt}}} \qquad \ldots (7.23)$$

Lastly, the value of β can be obtained from the failure mode assumed given by equation (7.21), which results in equation (7.24).

$$\beta = \frac{C_1\left(1+\cot^2\theta\right) - \lambda.l_b}{2c.\cot\theta} \qquad \ldots (7.24)$$

where $C_1 = \dfrac{\lambda.\sum T_{si}}{(1-\lambda).0.6.\nu f_{cd} b}$

Equations (7.22 to 7.24) above can be used along with equations (7.14, 7.15, 7.17), in the following iterative algorithm where λ_i and $cot\theta_i$ are solved. In order to ease the iterative process, it is recommended to take initial guess values ($0<\lambda_0<1$ and $cot\theta_0 \sim a_v/d$) so that β_i estimated in the first step is positive.

- **Step 1:** Estimate λ_i and $cot\theta_i$

- **Step 2:** Calculate β_i

$$\beta_i = \frac{C_1\left(1+\cot^2\theta_i\right)-\lambda_i l_b}{2c.\cot\theta_i} > 0 \qquad \text{where} \quad C_1 = \frac{\lambda_i.\sum_1^n T_{Si}}{\left(1-\lambda_i\right).0.6.vf_{cd}b}$$

- **Step 3:** Calculate tensile forces $T_i^{'}$ and T_d

$$\cot\phi_i' = \frac{\lambda_i\left(1-\beta_i\right)}{\beta_i\left(1-\lambda_i\right)}.\cot\theta_i$$

$$T_i^{'} = \cot\phi_i'.\sum_1^n T_{Si}. \qquad \text{and} \qquad T_d = \frac{\lambda}{1-\lambda}.\cot\theta.\sum_1^n T_{Si}$$

- **Step 4:** Calculate values for step i+1

$$\lambda_{i+1} = \frac{\cot\theta_i.\left(h-c\beta_i-C_3\right)-a_v}{\frac{l_b}{2}+\frac{l_t.n_{lp}}{4}} \qquad \text{where } C_3 = \frac{T_i^{'}+T_d/2}{bf_{cnt}}$$

$$\cot\phi_{i+1}' = \frac{1}{2}.\frac{a_v+\left(1+\lambda_{i+1}\right)l_b}{h-\left(1+\beta_i\right)c-\frac{T_i^{'}}{2bf_{cnt}}}$$

$$\cot\theta_{i+1} = \cot\phi_{i+1}^{'}.\frac{\beta_i\left(1-\lambda_{i+1}\right)}{\lambda_{i+1}\left(1-\beta_i\right)}$$

- **Step 5:** Check for convergence

  if $\left|\lambda_{i+1}-\lambda_i\right| > tolerance$ and $\left|\cot\theta_{i+1}-\cot\theta_i\right| > tolerance$ go back to **Step 1**

  otherwise go to **Step 6**

- **Step 6:** Calculate solution

$$Analysis:\ P = \frac{2.\sum_1^n T_{Si}}{1-\lambda_{i+1}} \quad \text{for } Design:\ A_{sw} = \frac{P\left(1-\lambda_{i+1}\right)}{2f_y} \text{ with } \sum_1^n T_{Si} = \frac{P\left(1-\lambda_{i+1}\right)}{2}$$

if λ_{i+1}<0 Change section size, f_{cd}, l_t or l_b (stirrups might not yield)

if λ_{i+1}>1 No stirrups required (provide minimum quantity of shear reinforcement)

In the analysis of experimental data shown in sections 3.4 and 3.5 the use of either the most general STM formulation for short span beams with stirrups or the simplified version described above, give very similar answers. The simplified STM model provides good predictions of the ultimate strength although it is not valid for high stirrup indexes, where λ becomes almost zero. As described in next section, this is due to the fact that for high *SI* the direct strut disappears and the strut-and-tie model do no longer applies. In addition, the assumption of yielding of the stirrups can be questionable for such large values of *SI*.

Stirrup index at the limit case in the STM, where the direct strut vanishes (λ=0)

In order to calculate limit case λ=0 in the STM, in which the direct strut vanishes completely, the infinitesimal strut width can be written as shown in equation (7.25). Ratio $\delta\beta/\delta\lambda$ is obtained from differentiating equation (7.22) and substituting λ=0 and β=0, see equation (7.26).

$$\delta w = \delta\lambda . l_b \sin\theta + 2c\delta\beta . \cos\theta \qquad \ldots (7.25)$$

$$\frac{\delta\beta}{\delta\lambda} = \frac{1-\beta^2}{1-\lambda^2} . \frac{\cot\theta}{\cot\phi} = \frac{\cot\theta}{\cot\phi} \qquad \ldots (7.26)$$

Similarly as in equation (7.21), if the stress in the strut is limited to $0.6\nu f_{cd}$ and vertical equilibrium is stated, this results in equation (7.27).

$$P_{\max} = 2\left(\frac{l_b + 2c\dfrac{\cot^2\theta}{\cot\phi'}}{1+\cot^2\theta} \right) 0.6 b \nu f_{cd} \qquad \ldots (7.27)$$

If λ=0 and β=0 subsequently T_d =0 and so expressions for $cot\phi'$, $cot\theta$ and T_i' can be simplified as shown in equations (7.28).

$$\cot\phi' = \frac{1}{2} . \frac{a_v + l_b}{h - c - \Delta/2}; \quad \cot\theta = \frac{a_v}{h-\Delta}; \quad T_i' = \frac{P}{2} . \cot\phi' \qquad \ldots (7.28)$$

where $\Delta = \dfrac{T_i'}{b f_{cnt}}$

A simple approach to solve for P_{max} would be iterating for Δ in equations (7.27) and (7.28) until $T_i'=P_{max}/2.cot\phi'$. The entire shear force is taken by the stirrups (λ = 0), so SI_{max} can be defined as $P_{max}/(2bhf_{cd})$. By solving equation (7.27) and (7.28) it can be seen

that the results obtained for SI_{max} are independent of b. This would also be the case for the concrete strength f_{cd}, if parameter SI_{max} was defined in terms of νf_{cd}. However, this is not usually the case and so values of SI_{max} defined in this manner have to be corrected by a factor of ν to account for different concrete strengths (see Figure 7.8).

According to equations (7.27) and (7.28) the main parameters influencing the magnitude of SI_{max} at which the direct strut vanishes, are purely geometrical (a_v, l_b, h, c). A parametric analysis was performed for beams AG (a_v/d=1.13, f_{cd}=80.2MPa, SI_{max}=1.20), in order to investigate the relevance of each of these parameters separately. As shown in Figure 7.8, SI_{max} reduces as a_v/d increases, although the rate varied depending on which parameter was modified. For example, changes in the length of the bearing plates were found to have a significantly larger effect on SI_{max} than increasing the clear shear span while keeping d constant. Increasing the total height of the specimen, while keeping the d/c ratio constant, had a similar effect as decreasing a_v, as shown in Figure 7.8

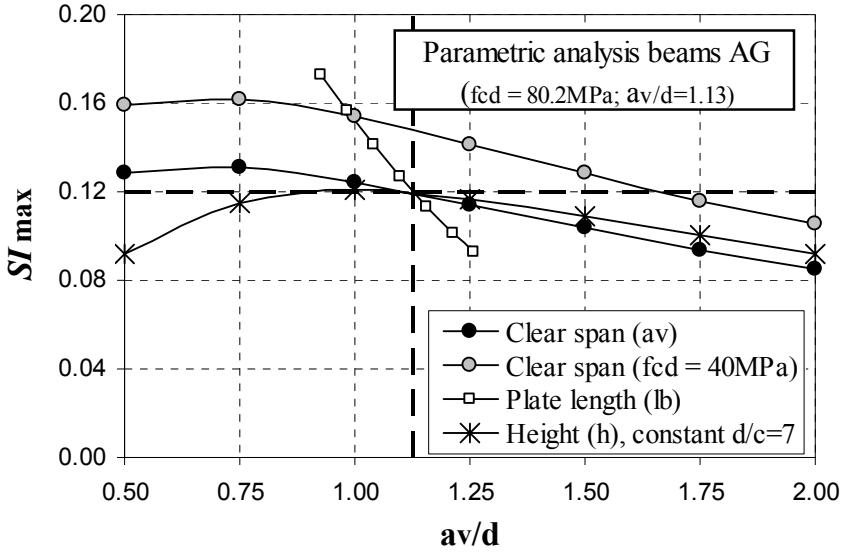

Note: Additional parameter in AG: a_v=660mm, h=500mm, l_b=125mm

Figure 7.8: Parametric analysis of SI_{max} (λ=0) for different values of a_v/d in beams AG, by changing clear shear span (a_v), length of the bearing plate (l_b) and height of the beam (h)

Although the proposed STM is only applicable for beams with $SI<SI_{max}$, normal values of the stirrup index (see section 7.3.5) are in most of the cases bellow this threshold value. Only specimens with either a_v/d ratios close to 2, low concrete strengths, small bearing plates and large number of stirrups can produce values of the stirrup index large enough to have λ=0. In such instances, it is also questionable whether all stirrups would yield at failure.

7.3.4 Experimental evidence

A database was gathered from previous experimental work [129, 130, 134, 137, 140, 150-154] in order to validate the strut-and-tie model and compare its performance with existing design methods for short span beams. Only beams failing in shear were included in the database, neglecting specimens with a flexural failure or local failure at the supports. The type of failure mode generally reported was shear-compression and shear-proper (diagonal tension). However in many instances it was not specified which type of shear failure prevailed and only a "shear" failure was reported. Several difficulties were observed in developing a reliable database since in many cases important information was not reported.

Bearing plates

Firstly, the importance of the bearing plates has often been neglected. Many researchers omitted to give the size of the bearing plates, which is required in the STM. Furthermore some beam tests have been carried out using rollers for the supports, see section 7.3.6. These tests were excluded from the main database to avoid possible deviations due to bearing failure under the rollers. According to these considerations it seems questionable whether the widely used a/d ratio, where a is the distance measured between the centrelines of the load and support, should be applied to classify beam test results. In slender beams the size of the bearing plates becomes less relevant since the failure mechanism is located away from the supports. In addition, the difference between a/d and a_v/d is smaller in slender beam than in short span beams.

Shear reinforcement ratio

The second difficulty in developing the database was that the shear reinforcement ratio (ρ_w) was given in some references in terms of the distance between stirrups (s) without giving the exact position of the reinforcement bars. This can lead to errors when calculating the ultimate strength since the value of ρ_w defined in terms of s does not consider whether the stirrups are effective or not, i.e. the stirrups crosses the main diagonal crack. In order to avoid misinterpretation of the data of short span beams, it is recommended that ρ_w is given in terms of the area of stirrups located within the clear shear span (a_v).

Lateral stability

An additional aspect which must be considered when gathering experimental data on short span beams is the slenderness in the out-of-plane direction (h/b~4, l/b~20) of the specimens tested. The question arises of whether lateral stability could have had an influence on the results. Kotsovos & Pavlovic [155] have argued that for very slim cross-sections the stresses induced by unintended out-of-plane action may have a significant effect on the beam strength, being out-of-plane actions the primary cause of size effects. The most slender beams included in the database were near the boundary limit recommended by EC2, which separates cases where second order effects should be considered. However, the nominal shear strengths of the most critical beams according to EC2 recommendations on lateral stability were no lower than the average values, which suggest that lateral effects were unimportant in the beams analysed.

Further evidence is provided by recent work carried by Zhang & Tan [140] who investigated out-of-plane deflections (δ) as a possible source for size effect in deep beams (a_v/d=0.95). Their most slender specimens were 1000mm high with a slenderness ratio of (h/b=12.5, l/b=37.5), which is considerably more slender than the remaining specimens implemented in the database. Measurements of the out-of-plane deflections showed relatively small values (δ/h around 2:10000), which are similar to the lateral deflections measured in beams A with (h/b=3.7, l/b=9.8). Zhang & Tan [140] concluded from their experimental work that unintended out-of-plane actions have an insignificant effect on shear strengths "under a properly-controlled testing environment". In the author's opinion, a clearer line should be established to distinguish cases where out-of-bound deflections can become critical. As pointed out by Zhang & Tan [140], the h/b ratios observed in tests could range from 0.5 (Kani [156]) to around 10 in most general cases and up to 67 (Kong et al. [157]).

Type of aggregate

Lastly, information is seldom if ever given on either the type of aggregate or whether it had fracture. These uncertainties, which can have an influence on the roughness of the crack surface, motivated the experimental work carried for beams A and are further discussed in section 7.5.

7.3.5 Performance of existing design methods compared with proposed STM model (Experimental validation)

Ultimately, the experimental database used to validate the strut-and-tie model proposed for short span beams with stirrups consisted of 143 beams of which 47 had an a_v/d ratio between 1 and 2. The performance of the methods suggested in MC90, BS8110 and EC2 was also examined. The results of the 143 beams analysed from [129, 130, 134, 137, 140, 150-154] are summarised in Tables 7.7(a)-(b)-(c), for which material factors of safety has been taken as 1.

The clear shear span to effective depth ratio (a_v/d) of interest was between 1 and 2, although some beams with a_v/d out of this range were also included in order to assess the accuracy of the methods for boundary cases, refer to Tables 7.7(b) and (c). The majority of the beams included in the database had bearing plates at top and bottom of equal lengths ($l_t.n_{lp}/2l_b = 1$). A few cases were investigated with $l_t.n_{lp}/2l_b$ ratios around 0.5 and 1.5. For either cases the STM predictions did not differ much from beams with $l_t.n_{lp}/2l_b = 1$. The influence of the $2l_b/(l_t.n_{lp})$ ratio was only noticeable in beams with $l_t.n_{lp}/2l_b > 1.5$, especially for beams without stirrups, where the predictions were slightly conservative since the width of the strut was estimated from the geometry of the bottom node.

According to Table 7.7(a) the simple strut-and-tie model provided more accurate predictions of the ultimate strength of short span beams with stirrups than the other design methods considered. The performance of the strut-and-tie model was very similar using both the simplified and more general formulation, which takes into account the actual position of the stirrups. The actual position of the stirrups relative to the clear shear span was only known in 119 beams out of the 143 beams shown in Tables 7.7. An average value of P_{calc}/P_{test} of 0.91 and coefficient of variation of 10.9% for a_v/d between 1 and 2 was obtained using the general formulation for the STM. Equally, the values for P_{calc}/P_{test} and their coefficient of variations were 0.83 (26.5%) for $a_v/d < 1$ and 1.37 (27.3%) for $a_v/d > 2$.

As shown in Table 7.7(a) for beams with $2 > a_v/d > 1$, the predictions of the strut-and-tie model using either Collins & Mitchell's [11] formula or EC2 effective concrete strength of the direct strut, were very similar. However for values of a_v/d outside this range, the predictions of the two models were somewhat different, as shown in Tables 7.7(b) and (c).

2 >av/d >1								Pcalc/Ptest				Pcalc/Ptest ¦ F.M			
Author	**Beam**	**av/d**	**d [mm]**	**b [mm]**	**fc' [MPa]**	***SI***	**Ptest [kN]**	**MC90**	**Vc+Vs**	**Vc-STM +Vs**	**EC2**	**STM-EC2**		**STM-Collins**	
Lehwalter	V3511/3	1.25	560	250	17	0.154	970	0.73	1.19	1.17	1.30	-	-	-	-
Regan	J6	1.57	272	152	32	0.046	292	0.32	0.89	1.13	0.58	0.87	M2	0.71	M2
	J10	1.10	272	152	32	0.031	272	0.30	0.99	1.25	0.66	1.05	M2	0.99	M2
	J17	1.10	272	152	40	0.054	530	0.34	0.74	0.94	0.68	0.72	M2	0.70	M2
	J19	1.10	272	152	35	0.028	366	0.22	0.75	0.98	0.51	0.84	M2	0.78	M2
	J20	1.10	272	152	35	0.028	320	0.25	0.86	1.14	0.58	0.97	M2	0.91	M2
	J8	1.68	254	152	34	0.029	370	0.16	0.59	0.94	0.34	0.81	M2	0.64	M2
Tan	E-1.62-3.23	1.30	463	110	51	0.042	440	0.45	0.96	1.30	0.83	1.06	M2	0.92	M2
Tan et al	III-2N/1.50	1.41	443	110	78	0.052	670	0.53	1.00	1.40	0.94	1.10	M2	1.08	M2
	III-2S/1.50	1.41	443	110	78	0.066	800	0.56	0.98	1.32	0.99	0.99	M2	1.00	M2
Vollum	5	1.14	180	100	44	0.058	220	0.40	0.92	1.11	0.81	0.83	M2	0.84	M2
& Tay	6	1.14	180	100	44	0.115	250	0.70	1.21	1.38	1.42	0.87	M2	0.93	M2
Clark	B1-1	1.72	390	203	23	0.065	558	0.35	0.87	1.11	0.59	0.83	M2	0.71	M2
	B1-2	1.72	390	203	25	0.060	513	0.38	0.96	1.26	0.64	0.95	M2	0.81	M2
	B1-3	1.72	390	203	24	0.064	570	0.34	0.86	1.10	0.57	0.82	M2	0.70	M2
	B1-4	1.72	390	203	23	0.065	536	0.36	0.91	1.16	0.61	0.86	M2	0.74	M2
	B1-5	1.72	390	203	25	0.062	483	0.40	1.02	1.32	0.68	0.99	M2	0.84	M2
	B2-1	1.72	390	203	23	0.109	602	0.54	1.12	1.34	0.91	0.90	M2	0.81	M2
	B2-2	1.72	390	203	26	0.096	644	0.50	1.06	1.31	0.85	0.90	M2	0.81	M2
	B2-3	1.72	390	203	25	0.101	670	0.49	1.01	1.24	0.81	0.84	M2	0.76	M2
	B6-1	1.72	390	203	42	0.036	759	0.26	0.70	1.11	0.43	0.91	M2	0.72	M2
	C1-1	1.33	390	203	26	0.039	555	0.29	0.83	1.14	0.51	0.95	M2	0.84	M2
	C1-2	1.33	390	203	26	0.038	622	0.26	0.74	1.04	0.45	0.86	M2	0.76	M2
	C1-3	1.33	390	203	24	0.042	492	0.33	0.92	1.24	0.57	1.02	M2	0.90	M2
	C1-4	1.33	390	203	29	0.035	572	0.28	0.83	1.20	0.50	1.01	M2	0.88	M2
	C2-1	1.33	390	203	24	0.064	580	0.42	0.94	1.20	0.73	0.92	M2	0.85	M2
	C2-2	1.33	390	203	25	0.061	602	0.40	0.92	1.19	0.70	0.92	M2	0.84	M2
	C2-4	1.33	390	203	27	0.056	576	0.42	0.97	1.30	0.73	1.01	M2	0.92	M2
	C3-1	1.33	390	203	14	0.072	447	0.36	0.92	1.00	0.63	0.75	M2	0.72	M2
	C3-2	1.33	390	203	14	0.073	401	0.41	1.02	1.10	0.70	0.83	M2	0.79	M2
	C3-3	1.33	390	203	14	0.073	376	0.43	1.09	1.18	0.75	0.89	M2	0.85	M2
	C4-1	1.33	390	203	24	0.041	619	0.26	0.74	1.00	0.46	0.82	M4	0.76	M2
	C6-2	1.33	390	203	45	0.022	848	0.19	0.61	0.94	0.39	0.94	M2	0.84	M2
	C6-3	1.33	390	203	45	0.023	870	0.19	0.59	0.92	0.38	0.91	M2	0.81	M2
	C6-4	1.33	390	203	48	0.021	857	0.19	0.61	0.94	0.39	0.97	M2	0.86	M2
	D1-6	1.66	314	152	28	0.029	349	0.19	0.68	1.10	0.41	0.95	M2	0.73	M2
	D1-7	1.66	314	152	28	0.029	358	0.18	0.66	1.08	0.40	0.94	M2	0.72	M2
	D1-8	1.66	314	152	28	0.029	372	0.18	0.64	1.03	0.38	0.90	M2	0.69	M2
	E1-2	1.74	314	152	30	0.080	444	0.42	0.95	1.31	0.73	0.96	M2	0.82	M2
Kong	S5-4	1.64	292	250	89	0.011	953	0.12	0.53	1.05	0.35	1.14	M2	0.83	M2
& Rangan	S5-5	1.40	292	250	89	0.008	1147	0.09	0.45	0.94	0.34	1.04	M2	0.81	M2
Sagaseta	AG2	1.13	438	135	80	0.020	1126	0.18	0.50	0.94	0.35	0.82	M2	0.84	M2
& Vollum	AG3	1.13	438	135	80	0.031	1309	0.23	0.52	0.89	0.45	0.73	M2	0.77	M2
	AG4	1.13	438	135	80	0.041	1414	0.28	0.56	0.90	0.56	0.71	M2	0.75	M2
	AL2	1.13	438	135	68	0.024	1064	0.19	0.51	0.92	0.37	0.79	M2	0.80	M2
	AL3	1.13	438	135	68	0.036	961	0.31	0.68	1.14	0.61	0.92	M2	0.95	M2
	AL4	1.13	438	135	68	0.048	1204	0.33	0.64	1.00	0.65	0.77	M2	0.81	M2
Total =	**47**							**MC90**	**Vc+Vs**	**Vc-STM +Vs**	**EC2**	**STM-EC2**		**STM-Collins**	
	max value =	1.74	560	250	89	0.154	**Mean**	**0.33**	**0.82**	**1.12**	**0.62**	**0.90**		**0.82**	
	min value =	1.10	180	100	14	0.008	**SD**	**0.14**	**0.20**	**0.15**	**0.23**	**0.10**		**0.09**	
							COV %	**42.16**	**24.12**	**12.96**	**37.66**	**11.03**		**11.05**	

Note: STM-EC2 – using simplified formulas (section 3.3)
FM – Critical failure mode (M1- flexure, M2- crushing in strut at bottom node, M4- bearing failure at bottom node, M6- bearing failure at top node)
$SI=nA_{sw}f_y/(bh f_c')$
"-" STM not applicable (λ<0)

Table 7.7(a): Summary of experimental database of short span beams with stirrups (2>a_v/d>1)

av/d<1								Pcalc/Ptest				Pcalc/Ptest ¦ F.M			
Author	**Beam**	**av/d**	**d [mm]**	**b [mm]**	**fc' [MPa]**	***SI***	**Ptest [kN]**	**MC90**	**Vc+Vs**	**Vc-STM +Vs**	**EC2**	**STM-EC2**		**STM-Collins**	
Lehwalter	V411/3	0.75	740	250	19	0.083	1330	0.63	1.02	1.06	1.23	0.60	M6	0.60	M6
	V411/4	0.75	740	250	16	0.049	934	0.45	1.09	1.07	0.90	0.74	M6	0.74	M6
	S511/3	0.75	560	250	18	0.087	1064	0.60	0.99	0.96	1.18	0.55	M6	0.55	M6
	V511/4	0.75	560	250	18	0.038	930	0.29	0.84	0.80	0.58	0.62	M6	0.62	M6
	V022/3	0.75	360	250	18	0.085	760	0.56	0.96	0.92	1.10	0.50	M6	0.50	M6
	V022/4	0.75	360	250	17	0.033	634	0.24	0.82	0.74	0.64	0.57	M6	0.57	M6
	V711/3	0.75	160	250	17	0.066	414	0.37	0.82	0.66	0.73	0.39	M6	0.39	M6
	V711/4	0.75	160	250	18	0.027	414	0.16	0.68	0.53	0.56	0.41	M6	0.41	M6
	W511/3	0.75	560	250	20	0.079	1160	0.55	0.93	0.93	1.08	0.56	M6	0.56	M6
	V511/3	0.75	560	250	17	0.092	1004	0.63	1.04	0.99	1.25	0.55	M6	0.55	M6
	V2511/3	0.25	560	250	16	0.034	1050	0.40	0.89	0.64	0.74	0.49	M6	0.49	M6
	W2511/3	0.25	560	250	21	0.025	1196	0.35	0.84	0.68	0.71	0.55	M6	0.55	M6
Regan	J15	0.64	272	152	33	0.015	412	0.15	0.87	0.93	0.76	0.85	M2	1.01	M2
Tan	D-1.08-2.15	0.76	463	110	48	0.022	540	0.27	0.80	1.15	0.58	1.07	M2	1.12	M2
	C-0.81-2.15	0.49	463	110	51	0.021	806	0.24	0.75	0.95	0.60	0.86	M2	1.01	M2
	C-0.81-3.23	0.49	463	110	44	0.024	800	0.25	0.72	0.87	0.59	0.78	M2	0.92	M2
	B-0.54-2.15	0.22	463	110	56	0.019	936	0.31	0.66	1.01	0.53	0.91	M2	1.30	M4
	B-0.54-3.23	0.22	463	110	46	0.023	890	0.33	0.66	0.94	0.53	0.83	M2	1.18	M4
	B-0.54-4.30	0.22	463	110	54	0.020	1000	0.29	0.61	0.93	0.49	0.83	M2	1.19	M4
Tan et al.	II-2N/1.00	0.85	443	110	78	0.039	1040	0.38	0.68	0.97	0.76	0.78	M2	0.93	M2
	I-2N/0.75	0.56	443	110	56	0.072	1520	0.47	0.62	0.72	0.84	0.50	M2	0.54	M4
Kong	1-10	0.82	216	76	22	0.194	180	1.03	1.42	1.54	1.08	0.92	M2	1.07	M2
et al.	2-10	0.82	216	76	20	0.078	200	0.35	0.76	0.84	0.74	0.66	M2	0.69	M2
	1-15	0.52	343	76	21	0.131	328	0.90	1.05	0.95	0.93	0.54	M2	0.58	M4
	2-15	0.52	343	76	23	0.046	280	0.39	0.88	0.78	0.83	0.61	M2	0.73	M4
	1-20	0.38	470	76	21	0.099	380	1.06	1.00	0.85	1.10	0.46	M2	-	-
	2-20	0.38	470	76	20	0.040	432	0.35	0.64	0.49	0.56	0.37	M2	0.42	M4
	1-25	0.30	597	76	25	0.068	448	1.14	0.93	0.77	1.35	0.44	M2	-	-
	2-25	0.30	597	76	19	0.034	448	0.43	0.66	0.46	0.54	0.33	M2	-	-
	1-30	0.25	724	76	22	0.065	478	1.30	0.90	0.68	1.35	0.36	M2	-	-
	2-30	0.25	724	76	19	0.027	498	0.47	0.64	0.42	0.52	0.30	M2	-	-
De Pavia	G33S-12	0.50	203	76	20	0.061	169	0.34	1.09	0.89	0.99	0.80	M2	0.89	M2
et al.	G33S-32	0.50	203	76	20	0.060	203	0.28	0.96	0.74	0.83	0.67	M2	0.79	M2
Clark	D1-1	0.94	390	203	26	0.039	602	0.36	0.91	1.24	0.66	1.05	M2	1.06	M2
	D1-3	0.94	390	203	25	0.041	513	0.42	1.06	1.39	0.78	1.16	M2	1.19	M2
	D2-1	0.94	390	203	24	0.063	580	0.56	1.09	1.38	1.03	1.07	M2	1.12	M2
	D2-2	0.94	390	203	26	0.059	624	0.52	1.03	1.34	0.96	1.05	M2	1.09	M4
	D3-1	0.94	390	203	28	0.072	790	0.55	0.98	1.23	1.01	0.93	M2	0.97	M4
	D4-1	0.94	390	203	23	0.110	624	0.87	1.31	1.55	1.60	1.03	M2	1.03	M2
Zhang	1DB35bw	0.95	313	80	26	0.066	199	0.58	1.03	1.13	1.02	0.81	M2	0.83	M4
& Tan	1DB50bw	0.94	454	115	27	0.061	373	0.63	1.10	1.21	1.10	0.96	M4	0.96	M4
	1DB70bw	0.93	642	160	28	0.059	854	0.54	0.91	1.01	0.94	0.74	M2	0.84	M4
	1DB100bw	0.94	904	230	29	0.065	1550	0.68	1.05	1.27	1.18	0.75	M2	0.90	M2
Total =	**43**							**MC90**	**Vc+Vs**	**Vc-STM +Vs**	**EC2**	**STM-EC2**		**STM-Collins**	
	max value =	0.95	904	250	78	0.194	**Mean**	**0.50**	**0.90**	**0.94**	**0.87**	**0.70**		**0.81**	
	min value =	0.22	160	76	16	0.015	**SD**	**0.26**	**0.19**	**0.27**	**0.27**	**0.23**		**0.26**	
							COV %	**52.31**	**20.57**	**29.11**	**31.34**	**33.51**		**32.22**	

Note: STM-EC2 – using simplified formulas (section 3.3)
FM – Critical failure mode (M1- flexure, M2- crushing in strut at bottom node, M4- bearing failure at bottom node, M6- bearing failure at top node)
$SI=nA_{sw}f_y/(bh f_c')$
"-" STM not applicable (λ<0)

Table 7.7(b): Summary of experimental database of deep beams with stirrups (a_v/d <1)

av/d >2								Pcalc/Ptest				Pcalc/Ptest ¦ F.M			
Author	**Beam**	**av/d**	**d [mm]**	**b [mm]**	**fc' [MPa]**	***SI***	**Ptest [kN]**	**MC90**	**Vc+Vs**	**Vc-STM +Vs**	**EC2**	**STM-EC2**		**STM-Collins**	
Clark	A1-1	2.11	390	203	25	0.082	445	0.49	1.25	1.54	0.84	0.90	M6	0.86	M2
	A1-2	2.11	390	203	24	0.086	418	0.52	1.32	1.61	0.90	0.92	M6	-	-
	A1-3	2.11	390	203	23	0.086	445	0.49	1.24	1.50	0.84	0.86	M6	-	-
	A1-4	2.11	390	203	25	0.082	489	0.44	1.14	1.40	0.77	0.82	M6	-	-
	D2-6	2.14	314	152	30	0.110	337	0.62	1.47	1.85	1.12	1.25	M2	-	-
	D2-7	2.14	314	152	28	0.114	315	0.67	1.57	1.96	1.20	1.31	M2	-	-
	D2-8	2.14	314	152	26	0.124	337	0.62	1.46	1.78	1.12	1.17	M2	-	-
	D4-1	2.14	314	152	27	0.089	337	0.47	1.19	1.53	0.84	1.07	M2	0.86	M2
	D4-2	2.14	314	152	26	0.095	337	0.47	1.18	1.49	0.84	1.04	M2	-	-
	D4-3	2.14	314	152	22	0.110	330	0.48	1.19	1.43	0.85	0.97	M2	-	-
	D5-1	2.14	314	152	28	0.058	292	0.36	1.05	1.44	0.64	1.10	M2	0.82	M2
	D5-2	2.14	314	152	29	0.056	315	0.33	0.98	1.37	0.60	1.06	M2	0.78	M2
	D5-3	2.14	314	152	27	0.060	315	0.33	0.97	1.33	0.60	1.01	M2	0.76	M2
Sarsam et al.	AS2-N	2.07	235	180	39	0.022	379	0.12	0.55	0.84	0.33	0.72	M2	0.45	M2
	AS2-H	2.07	232	180	76	0.011	402	0.11	0.59	1.18	0.38	1.08	M2	0.64	M2
	AS3-N	2.07	235	180	40	0.032	398	0.17	0.63	0.91	0.32	0.75	M2	0.50	M2
	AS3-H	2.07	235	180	72	0.018	398	0.17	0.70	1.23	0.39	1.06	M2	0.67	M2
	BS2-H	2.07	233	180	74	0.011	447	0.10	0.53	1.04	0.34	0.94	M2	0.59	M2
	BS3-H	2.07	233	180	73	0.017	456	0.15	0.61	1.11	0.34	0.96	M2	0.63	M2
	BS4-H	2.07	233	180	80	0.021	414	0.22	0.78	1.36	0.40	1.16	M2	0.79	M2
	CS2-H	2.07	233	180	70	0.012	494	0.09	0.47	0.92	0.31	0.83	M2	0.53	M2
	CS3-H	2.07	233	180	74	0.017	494	0.14	0.56	1.02	0.31	0.90	M2	0.60	M2
	CS4-H	2.07	233	180	76	0.022	441	0.20	0.72	1.25	0.37	1.06	M2	0.74	M2
Kong	S1-1	2.16	292	250	64	0.020	457	0.26	1.01	1.88	0.53	1.68	M2	1.06	M2
& Rangan	S1-2	2.16	292	250	64	0.020	417	0.28	1.10	2.06	0.58	1.84	M2	1.16	M2
	S1-3	2.16	292	250	64	0.020	412	0.29	1.12	2.08	0.59	1.86	M2	1.17	M2
	S1-4	2.16	292	250	64	0.020	556	0.21	0.83	1.55	0.43	1.38	M2	0.87	M2
	S1-5	2.16	292	250	64	0.020	507	0.23	0.91	1.70	0.48	1.51	M2	0.95	M2
	S1-6	2.16	292	250	64	0.020	448	0.26	1.03	1.92	0.54	1.71	M2	1.08	M2
	S2-1	2.16	292	250	73	0.010	521	0.14	0.74	1.50	0.48	1.50	M2	0.89	M2
	S2-2	2.16	292	250	73	0.010	465	0.15	0.82	1.68	0.54	1.68	M2	0.99	M2
	S2-3	2.16	292	250	73	0.017	507	0.23	0.93	1.71	0.50	1.62	M2	1.02	M2
	S2-4	2.16	292	250	73	0.017	439	0.27	1.07	1.98	0.58	1.87	M2	1.18	M2
	S2-5	2.16	292	250	73	0.021	564	0.25	0.91	1.61	0.46	1.49	M2	0.97	M2
	S3-1	2.15	297	250	67	0.013	418	0.21	0.94	1.36	0.56	1.74	M2	0.97	M2
	S3-2	2.15	297	250	67	0.013	356	0.24	1.10	1.60	0.66	2.04	M2	1.15	M2
	S3-3	2.15	293	250	67	0.013	457	0.19	0.89	1.76	0.54	1.66	M2	1.01	M2
	S3-4	2.15	293	250	67	0.013	350	0.25	1.16	2.30	0.71	2.16	M2	1.31	M2
	S3-5	2.16	287	250	67	0.013	593	0.14	0.68	1.48	0.41	1.34	M2	0.84	M2
	S3-6	2.16	287	250	67	0.013	566	0.15	0.71	1.55	0.43	1.41	M2	0.88	M2
	S4-1	2.29	524	250	87	0.015	708	0.30	1.16	2.01	0.60	1.71	M2	1.20	M2
	S4-2	2.27	428	250	87	0.014	1146	0.14	0.58	1.11	0.32	0.97	M2	0.65	M2
	S4-3	2.20	332	250	87	0.015	487	0.29	1.15	2.15	0.61	2.10	M2	1.35	M2
	S4-4	2.16	292	250	87	0.014	516	0.23	0.94	1.70	0.52	1.74	M2	1.10	M2
	S4-6	2.02	198	250	87	0.012	406	0.17	0.81	1.38	0.49	1.84	M2	1.09	M2
	S5-2	2.40	292	250	89	0.017	520	0.25	1.02	1.66	0.52	1.64	M2	1.02	M2
	S5-3	2.16	292	250	89	0.014	488	0.24	1.00	1.80	0.55	1.86	M2	1.18	M2
	S8-1	2.16	292	250	75	0.010	544	0.13	0.71	1.48	0.47	1.49	M2	0.90	M2
	S8-2	2.16	292	250	75	0.013	502	0.19	0.86	1.69	0.51	1.66	M2	1.03	M2
	S8-3	2.16	292	250	75	0.017	619	0.19	0.76	1.44	0.41	1.37	M2	0.87	M2
	S8-4	2.16	292	250	75	0.017	532	0.22	0.89	1.68	0.48	1.60	M2	1.02	M2
	S8-5	2.16	292	250	75	0.020	578	0.24	0.89	1.62	0.45	1.50	M2	0.98	M2
	S8-6	2.16	292	250	75	0.023	568	0.29	0.99	1.72	0.54	1.57	M2	1.04	M2
Total =	**53**							**MC90**	**Vc+Vs**	**Vc-STM +Vs**	**EC2**	**STM-EC2**		**STM-Collins**	
	max value =	2.40	524	250	89	0.124	**Mean**	**0.27**	**0.94**	**1.55**	**0.57**	**1.37**		**0.91**	
	min value =	2.02	198	152	22	0.010	**SD**	**0.14**	**0.25**	**0.33**	**0.21**	**0.39**		**0.22**	
							COV %	**52.25**	**27.06**	**21.03**	**36.88**	**28.30**		**23.86**	

Notes: *STM-EC2 – using simplified formulas (section 3.3)
FM – Critical failure mode (M1- flexure, M2- crushing in strut at bottom node, M4- bearing failure at bottom node, M6- bearing failure at top node)
$SI=nA_{sw}f_y/(bh f_c')$
"-" STM not applicable (λ<0)

Table 7.7(c): Summary of experimental database of beams with stirrups (a_v/d >2)

It is noteworthy that EC2 and standard truss (V_c+V_s) predictions for beams with $1<a_v/d<2$, had a considerable scatter with a coefficient of variance of 37.7% and 24.1% respectively. These values are significantly larger than those obtained using the strut-and-tie models proposed (*COV*=11%). The reason behind this large scatter is related to the stirrup index *SI*. The predictions of the standard truss and EC2 methods were highly dependent to the stirrup index, as shown in Figure 7.9. The results obtained using MC90 formula and alternative method $V_c(STM)+V_s$ showed a similar trend to the standard truss and EC2 methods. However, the shear strength was clearly underestimated using MC90 formula as opposed to the alternative method $V_c(STM)+V_s$ where the strength was clearly overestimated.

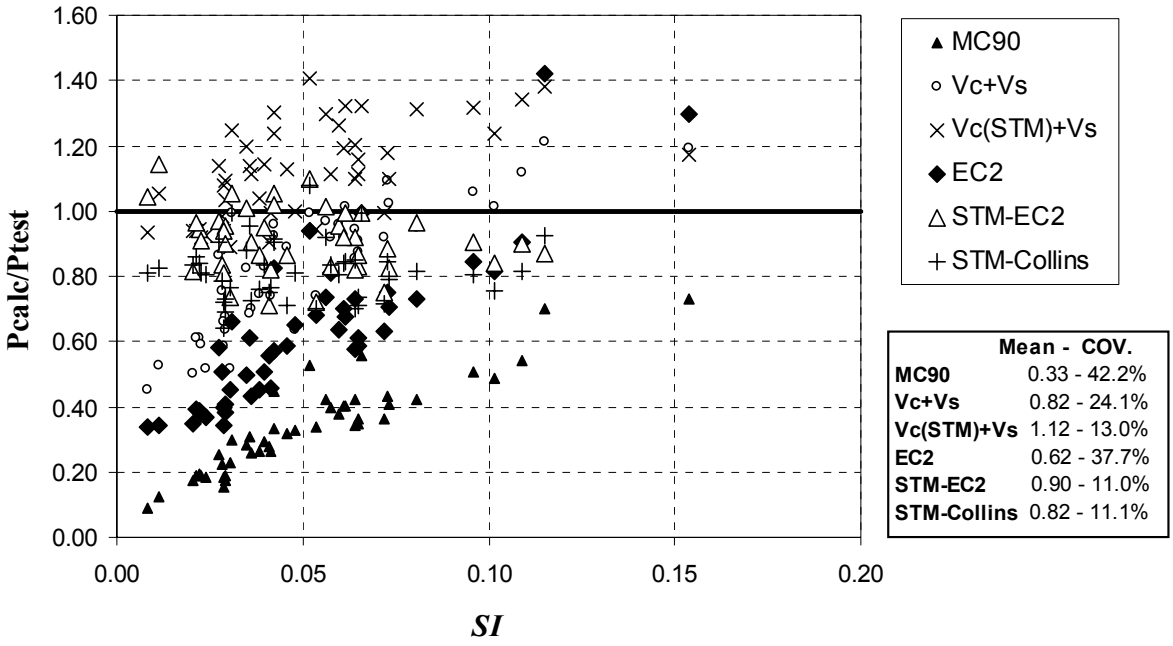

Note: refer to data in Table 7.7(a)

Figure 7.9: Performance of design methods of short span beams ($1<a_v/d<2$) with stirrups; namely MC90 formula, standard truss (V_c+V_s) method, alternative standard truss ($V_c(STM)+V_s$) method and strut-and-tie method (STM)

The performance of the suggested strut-and-tie model was independent of *SI* due to the fact that the fraction of load taken by the direct strut (λ) decreases as *SI* increases. The reduction of the contribution of the direct strut as *SI* increases predicted by the strut-and-tie model was in agreement with experimental evidence (see Figure 7.10). Softening models, which are commonly used in strut-and-tie modelling, have a similar philosophy since the effective concrete strength of the struts is reduced by transverse forces introduced by stirrups. The direct strut in the STM model developed by the author shown in Figure 7.7 becomes steeper as the stirrup index increases resulting in an increase of

strength. The increase in strength due to this reorientation of the direct strut is possible in the STM model up to a certain value of $SI=SI_{max}$ where λ becomes 0 and the direct strut vanishes. As described in section 7.3.3, this limit case is dependent on the geometry of the specimen (mainly l_b and a_v/d). As shown in Figure 7.10, only one beam out of 143 investigated, had a stirrup index greater than SI_{max}, so this shows that vanishing of the direct strut is not generally a problem and so the proposed STM is applicable to the majority of the cases. Usual values of SI_{max} ranges from 0.1 to 0.2 depending on the concrete strength (factor ν) and main dimensions of the beam.

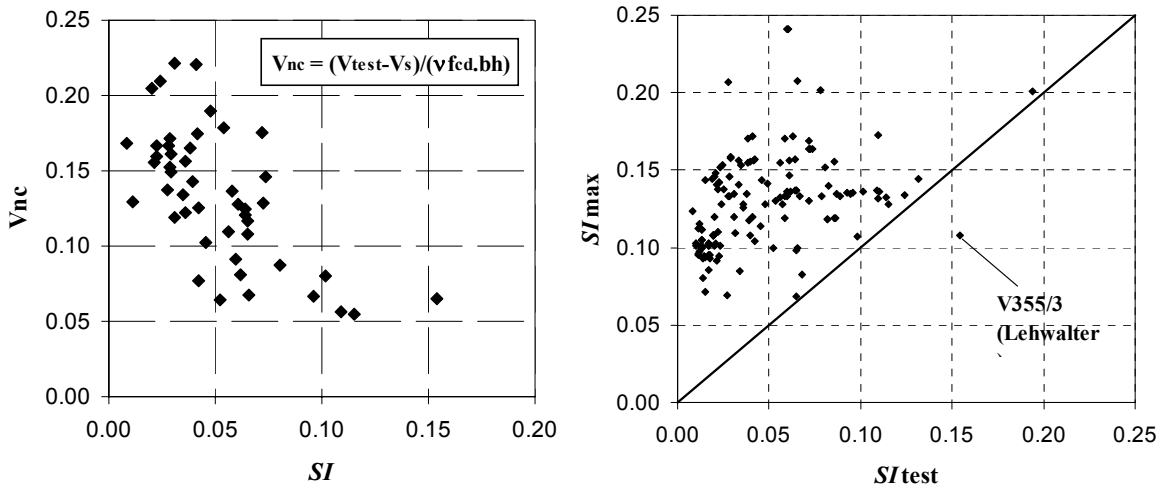

Figure 7.10: Influence of stirrup index in: a) Nominal shear carried by the direct strut (V_{nc}), beams with $1<a_v/d<2$; b) Beams where $\lambda=0$ due to $SI>SI_{max}$

Although not much experimental data is available of short beams with *SI* higher than 0.10, the results shown in Figure 7.9 suggest that EC2 and standard truss approaches can produce predictions on the unsafe side for large values of *SI*. However, the two beams shown in Figure 7.9, which have the highest P_{calc}/P_{test} ratio using the EC2 method, were only 6 and 10% below the maximum applied shear force allowed in EC2 ($0.5bd0.6\nu f_c'$). Hence, the worse P_{calc}/P_{test} could be extrapolated to be somewhere around 1.5, while for the lowest *SI* analysed P_{calc}/P_{test} was as low as 0.4. As described in section 7.2.3, EC2 allows for an overall factor of safety (*FOS*) of 2.14, assuming *DL=LL* and a material factor of safety for concrete of 1.5. This implies that the *FOS* can vary from 5.35 for beams with low *SI* to 1.43 for beams with *SI* up to 0.15. This large variation of the *FOS* seems rather inconsistent, although the predictions are on the safe side. On the other hand, the strut-and-tie model proposed, which is consistent with EC2 specifications, the *FOS* is fairly constant; FOS_{min}=1.88 for *SI*=0.01 and $FOS_{avg.}$=2.38.

The influence of the clear shear span to effective depth ratio (a_v/d) on the performance of the design methods is shown in Figure 7.11. All design methods captured the increase in shear strength as a_v/d decreases. However, the STM using EC2 was more sensitive to variations of the inclination of the direct strut, which resulted from changes in a_v/d, than the rest of the methods. As shown in Figure 7.11, for a_v/d ratios lower than 1, with a very steep direct strut, the STM models tended to underestimate the strength.

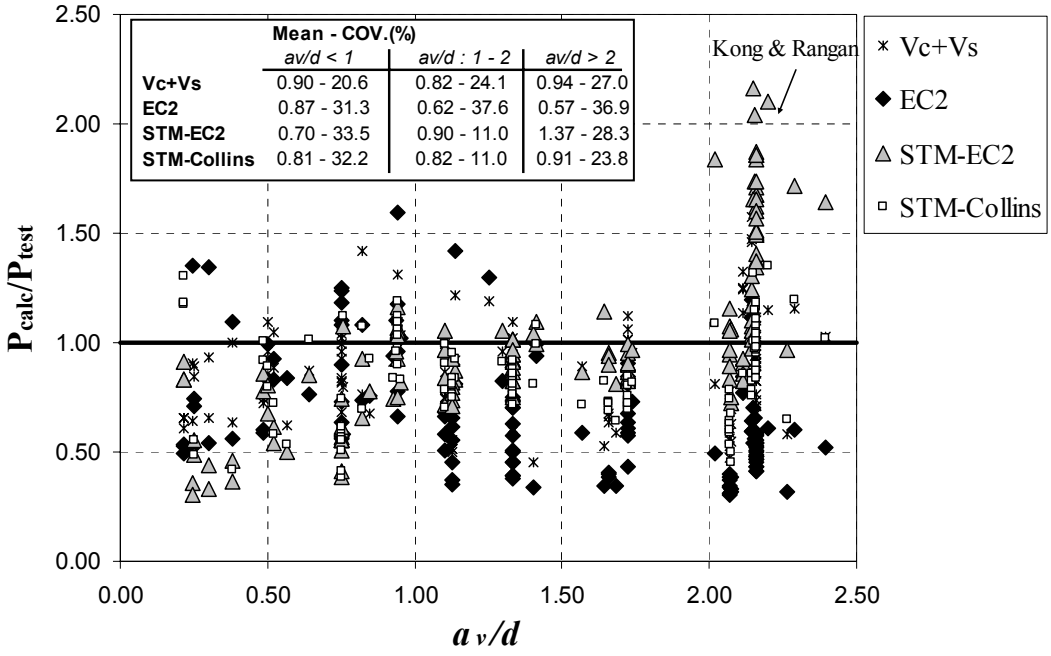

Figure 7.11: P_{calc}/P_{test} variation with a_v/d for (V_c+V_s), EC2, STM-EC2 and STM-Collins methods

Again, the large scatter shown in Figure 7.11 for EC2 method is due to variations in *SI*, which extends to beams with a_v/d up to 2.5. The coefficient of variation remained constant with a_v/d for EC2 and (V_c+V_s) methods, while for the strut-and-tie models *COV* was significantly lower for beams with a_v/d between 1 and 2. Standard truss (V_c+V_s) predictions had a fairly constant performance with a_v/d, and the scatter in the data was primarily due to changes in *SI*. EC2 method became less conservative with decreasing a_v/d.

According to Figure 7.11 the strength of the beams seemed to be overestimated using the STM-EC2 approach for a_v/d larger than 2, which might be due to the reduced angle between the direct strut and the tie. It is widely accepted that strut-and-tie models are not suitable for such configurations since the transverse strains induced in the strut would be excessive. However, there is a large number of beams with a_v/d slightly larger than 2 for which the STM model still provided reasonable answers, see beams from Clark [130]

(a_v/d =2.14; a/d=2.43) or Sarsam & Al-Musawi [154] (a_v/d=2.07; a/d=2.5) in Table 7.7(c). On the other hand, the strength of beams tested by Kong & Rangan [152] with a_v/d equal to 2.2 (a/d=2.5) were clearly overestimated using the strut-and-tie model. It is questionable whether the low strengths obtained in Kong & Rangan's tests were simply related to their a_v/d ratio. Unless further experimental data of beams with a_v/d close to 2.5-3.0 is provided, it seems reasonable and consistent with design codes to recommend the limit of a_v/d of 2 for the STM using EC2 effective strength. The rather unsafe predictions using STM-EC2 method for beams with a_v/d larger than 2, could be mitigated by using Collins & Mitchell's [11] formula, which seems to provide more accurate predictions for beams with a_v/d between 2.0 and 2.5. However, Collins & Mitchell's [11] formula can become rather conservative for larger ratios of a_v/d, which worsens for beams without stirrups (see section 7.2.3) since the direct strut in the STM become even flatter. This is not problematic, since for such instances sectional models govern over STM predictions.

Demerit Point Classification

In order to compare the performance of the different shear design methods for the three ranges of a_v/d investigated (see Figure 7.12), Collins [148] "Demerit Points (*DP*) Classification" approach was applied, in a similar manner as in section 7.2.3. Results are shown in Figure 7.12 and Table 7.8.

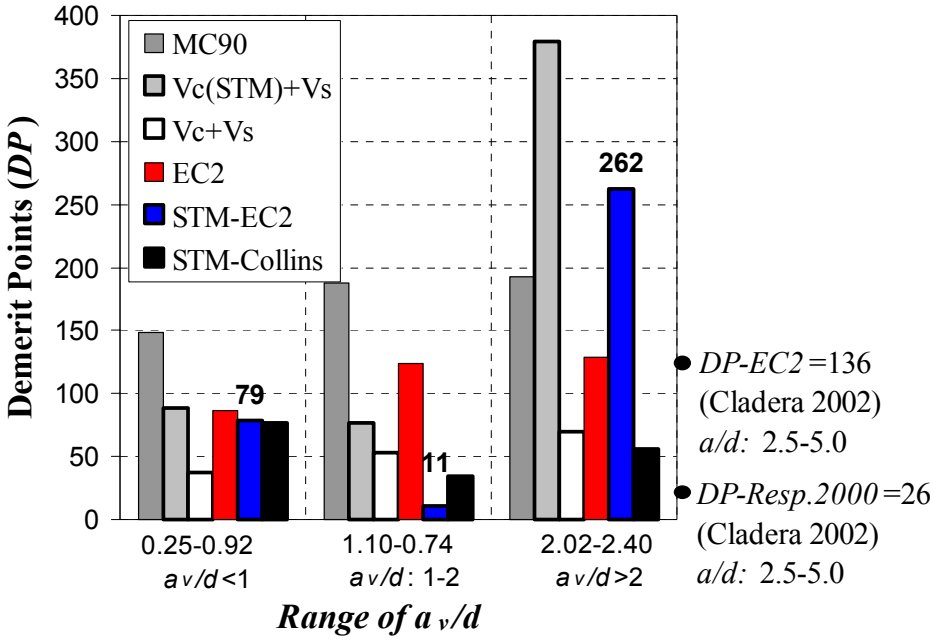

Figure 7.12: Demerit Points classification of shear methods according to Collins [148] for different ranges of a_v/d (beams with stirrups)

Ptest/Pcalc	$a_v/d<1$	DP	MC90	Vc+Vs	Vc(STM) +Vs	EC2	STM-EC2	STM-Collins
<0.5	Extremely dangerous	10	0	0	0	0	0	0
0.5-0.65	Dangerous	5	0	0	5	2	0	0
0.65-0.85	Low safety	2	2	5	16	14	0	11
0.85-1.30	Appropiate safety	0	12	67	53	40	42	45
1.30-2.00	Conservative	1	28	28	19	42	37	34
>2.00	Extremely conservative	2	58	0	7	2	21	11
		TOTAL DP	149	37	88	86	79	76

Ptest/Pcalc	a_v/d: 1 - 2	DP	MC90	Vc+Vs	Vc(STM) +Vs	EC2	STM-EC2	STM-Collins
<0.5	Extremely dangerous	10	0	0	0	0	0	0
0.5-0.65	Dangerous	5	0	0	0	0	0	0
0.65-0.85	Low safety	2	0	4	38	4	0	0
0.85-1.30	Appropiate safety	0	0	53	62	15	89	65
1.30-2.00	Conservative	1	13	40	0	47	11	35
>2.00	Extremely conservative	2	87	2	0	34	0	0
		TOTAL DP	187	53	77	123	11	35

Ptest/Pcalc	$a_v/d>2$	DP	MC90	Vc+Vs	Vc(STM) +Vs	EC2	STM-EC2	STM-Collins
<0.5	Extremely dangerous	10	0	0	9	0	6	0
0.5-0.65	Dangerous	5	0	2	43	0	32	0
0.65-0.85	Low safety	2	0	15	34	2	21	13
0.85-1.30	Appropiate safety	0	0	55	13	17	38	62
1.30-2.00	Conservative	1	8	26	0	38	4	20
>2.00	Extremely conservative	2	92	2	0	43	0	4
		TOTAL DP	192	70	379	128	262	56

Table 7.8: Demerit point classification for beams with stirrups; refer to Tables 7.7(a)-(b)-(c)

The demerit point classification confirmed the strut-and-tie models to be the most suitable approach for beams with an a_v/d range between 1 and 2. However for the STM-EC2 approach, the value of *DP* increased considerably for $a_v/d>2$, while STM-Collins model provided a more uniform performance. The demerit point classification also showed that MC90 and $V_c(STM)+V_s$ approaches were not acceptable for being extremely conservative for the former method or with low safety for the latter method.

Cladera [24] carried out a similar analysis for an experimental database of 124 beams with stirrups and *a/d* ratio from 2.5 to 5.0, to study the performance of several design standards (EHE, EC2, AASHTO, ACI11-5, ACI11-3 and Response 2000). In his analysis using EC2, the sectional approach was applied as opposed to the simple method related for short span beams applied here (see section 7.3.1), which takes into account the actual amount of stirrups within the shear span. These two approaches provide very similar answers for beams with *a/d* between 2 and 2.5 and low amount of shear reinforcement ($cot\theta$=2.5). The total demerit score for EC2 (*DP-EC2*=136) obtained by Cladera [24] is

similar to the one obtained in this work for beams with a_v/d between 2 and 2.5, as shown in Figure 7.12. The value of *DP-EC2* obtained by Cladera [24] was the highest from all the methods reviewed while the lowest demerit score was obtained using Response 2000 (*DP-Resp.200*=26). Cladera's conclusions are further discussed with regards the analysis of slender beams in chapter 8.

As discussed in section 7.2.3, the Demerit Point system does not reflect the influence of the different material and load factors of safety used in design codes. Hence, it could be argued that values shown in Table 7.8 are not representative in order to establish a comparison in terms of safety by the different design methods. The modified Demerit Point system classification proposed in section 7.2.3 was performed in which material and load factors of safety were applied (see Table 7.9). Again, only approaches based on one single design code were examined to apply consistent material and load factors of safety. As shown in Table 7.9, both STM and V_c+V_s methods, which are based on EC2 and BS8110 codes respectively, had a fairly similar DP mark as in the original Demerit Point method proposed by Collins [148] (Table 7.8). However, the mark obtained using EC2 was considerably lower. The improvement in the overall factors of safety in EC2 simple formula was due to lower material factors used, since the design shear force is factored by γ_s only.

			Sectional		STM
Ptest/Pd	**av/d: 1 - 2**	*DP*	**Vc+Vs**	**EC2**	**STM-EC2**
<1.0	*Extremely dangerous*	*10*	0	0	0
1.0-1.15	*Dangerous*	*5*	0	0	0
1.15-1.5	*Low safety*	*2*	4	2	0
1.5-2.3	*Appropiate safety*	*0*	53	32	78
2.3-3.5	*Conservative*	*1*	36	38	22
>3.5	*Extremely conservative*	*2*	6	28	0
		TOTAL DP	**57**	**98**	**22**

Note: P_d design load using material and load factors (*DL=LL*; γ_{load}=1.42/1.5, γ_c =1.5/1.25 and γ_s =1.15/1.15 for EC2/BS8110 design codes)

Table 7.9: Modified demerit point classification for short span beams with stirrups

7.3.6 Other applications: CFRP reinforced beams

Fibre Reinforced Polymer (FRP) composites are commonly used to strengthen concrete structures which have been subjected to structural damage, deterioration or changes in their design loads. An example of such applications is the use of externally bonded Carbon Fibre Reinforced Polymer CFRP sheets as shear reinforcement. Recent *fib* publication [158] describes some of the research that has been carried out in the past on CFRP used as externally bonded reinforcement. The strut-and-tie model described in section 7.3.2 was adapted to estimate the ultimate strength of short span beams which had been strengthened in shear using CFRP sheets to the full depth of the beam. In order to validate the STM model, experimental data provided by Imran Bukhari was used. The author is grateful to Bukhari for letting him include some of the experimental data in this section, which has not been published.

According to researchers such as Bukhari et al. [159], Berset [160] or Uji [161] amongst others, CFRP sheets have been shown to be efficient to increase the shear capacity of a section providing an alternative solution to traditional steel shear reinforcement. Two main challenges were faced in modelling Bukhari's beams; namely idealized the CFRP into equivalent ties and modelling the roller support in the STM. In addition, the *a/d* ratio in the beams was close to 2, which is near the limit of range of validity of the STM model for short span beams.

Idealization of CFRP sheets in the strut-and-tie model

The tensile stress assumed in the CFRP sheets at failure in the STM can be estimated on the basis of the "effective strain" concept (ε_{fe}). According to Taljsten [162], Triantafillou [163] or Triantafillou & Antonopoulos [164] the tensile stress reached in the external FRP at shear failure is lower than the tensile fracture strain (ε_{fu}=0.0015). The fraction $R= \varepsilon_{fe}/\varepsilon_{fu}$ is difficult to assess accurately and experimental formulas are commonly applied, which are generally given in terms of the axial rigidity of the FRP ($\rho_f E_f$) and the shear strength of the concrete ($f_{cm}^{2/3}$). However, there are design aids in which the axial rigidity of the FRP is not taken into account, see Concrete Society Technical Report TR55 [165]. Current research is focused towards the development of improved design formulas to estimate parameter *R*, although this is not the main concern of this work. In order to illustrate the performance of the STM model developed, *R* was estimated taking the least value given by TR55 approach and empirical formula suggested by Bukhari et al. [159].

The CFRP sheets were taken into account in the STM model as four "equivalent stirrups", which were located at quarter points along the length of shear span reinforced with CFRP sheet, as shown in Figure 7.13. The shear contribution of each equivalent stirrup was calculated as the effective area of each strip (see Figure 7.13) times the tensile stress assumed for the CFRP. Only the CFRP sheet within the central three quarters of the clear shear span was considered effective as assumed in beams with steel stirrups. This assumption, which is consistent with EC2 design recommendations, seemed reasonable since the strength of specimens C5, C8 and C9, which had a small amount of CFRP sheet outside the central three quarters of the clear shear span, was not significantly underestimated.

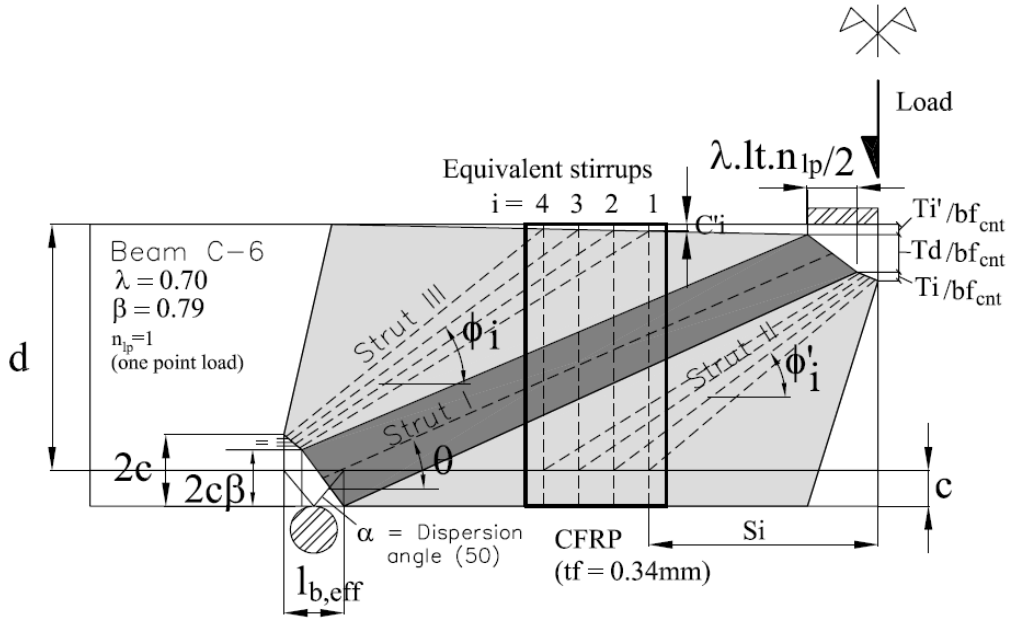

Figure 7.13: STM model for CFRP strengthened short span beam

Modelling of the roller support

Several assumptions had to be made regarding the geometry of the bottom node since the specimens were supported on rollers (see Figure 7.13). In order to assess the accuracy of these geometrical assumptions similar beam tests with vertical steel stirrups carried by Shin et al. [166] were examined. The beams tested by Shin et al. [166] were also supported on rollers and had an a_v/d ratio of 1.5 and 2.0, which were similar to beams tested by Buckhari. Beams which failed due to local crushing of the concrete at the support were not considered in the analysis. The bottom node was modelled assuming an equivalent bearing plate length $l_{b,eff} = 2c.\cot\alpha$ (see Figure 7.13), where α is the dispersion angle measured from roller centreline to the flexural reinforcement relative to the horizontal.

An optimal value for the dispersion angle α equal to 48.9˚ was obtained from the analysis of Shin's 16 test results. In the STM a value of 50˚ was assumed, which was on the conservative side. The average P_{calc}/P_{test} ratio obtained for the 16 beams tested by Shin et al. [166] using the STM was 0.98 with a standard deviation of 0.10.

Predictions of ultimate strength

The strut-and-tie model developed by the author provided reasonable predictions of the shear strength of the six beams tested by Bukhari (Figure 7.14), which were strengthened with externally-bonded CFRP to the full depth. The concrete strength was around 50MPa and d was equal to 305mm. The average P_{calc}/P_{test} ratio for the six beams analysed was 1.03 with a standard deviation of 0.10. The STM predictions were accurate despite specimens had a clear shear span to effective depth of 2, which is in the limit of validity of the STM model. The ultimate strength was slightly overestimated for beams C6 and C11, which was probably due to premature failure caused by debonding of the CFRP sheets. Nevertheless, the STM provided safe estimations of the ultimate strength of all the beams once standard material factors of safety were applied (γ_c=1.5 and γ_f=1.35).

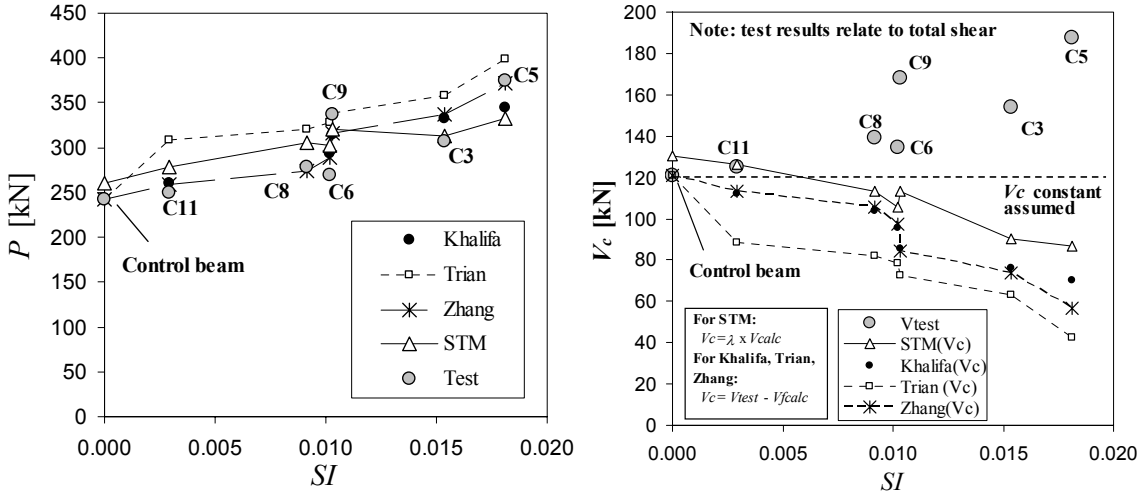

Note: (Left) The ultimate load was estimated using Khalifa, Triantafillou and Zhang's empirical equations for V_f, while V_c was taken from the control beam without shear reinforcement

Figure 7.14: *Left* – Predictions of beams tested by Bukhari; *Right* – V_c component estimated for each method ($V_c=V_{test}-V_f$ using empirical approaches; $V_c=\lambda V_{calc}$ for STM)

Alternatively, the ultimate strength of concrete beams that have been strengthened using externally bonded CFRP sheets can be estimated using the more traditional superposition method V_c+V_f. This approach, which is based on the classical truss model, requires the contribution of the CFRP (V_f) to be estimated from statistical regression of empirical data, see Khalifa [167], Triantafillou [163] or Zhang & Hsu [168] models. In addition, V_c

is assumed to be constant in the classical truss model, which is obtained generally from the control beam without web reinforcement. As discussed earlier, the shear component of the direct strut ($V_c=\lambda V$) in the strut-and-tie model presented here, reduces as the stirrup index increases.

In order to compare these assumptions the concrete component V_c was obtained for each method, as shown in Figure 7.14 (right). For design methods based on the superposition concept, V_c was estimated by subtracting the calculated V_f from the ultimate shear strength obtained in the experiments. The results obtained from this analysis showed that the V_c component decreased with increasing *SI*, as predicted in the STM (see Figure 7.14). Although the concrete component seemed to be overestimated in the superimposition methods, the ultimate loads obtained were similar to the STM predictions. This suggested that the reduction factor *R* derived empirically in the superposition methods must compensate to some extent for this overestimation of the concrete component. Moreover, in design cases V_c has to be estimated using empirical formulae such as the one described in section 7.2.1, which usually provide conservative predictions as shown in Figure 7.4 using EC2 formula.

7.4 NLFEA of short span beams

A Non-Linear Finite Element Analysis of beams A using different smeared cracking elements was performed in order to validate the strut-and-tie model suggested for short span beams. Once the smeared cracking models have been shown to be consistent with the empirical data, interface elements were implemented into the mesh (see section 7.5.3) in order to study the influence of aggregate interlock action at the main diagonal shear crack.

The fundamentals of the NLFEA models applied in this section are described in more detailed in chapter 3. For the preliminary analysis using only smeared cracking elements the following three cracking models were examined:

1. Total Strain Fixed angle (Tot. Str. Fix)
2. Total Strain Rotating angle (Tot. Str. Rot)
3. Multi-directional fixed angle (Mult. Fix)

7.4.1 Description of NLFE models

Beams AG and AL were modelled with an orthogonal grid of 8-node quadrilateral plane stress elements, as shown in Figure 7.15. The load was applied through a bearing plate with displacement control equal in all the nodes at the top. Similar results were obtained with a load control applying a pressure load on top of the plate. The beam was supported on pin rollers which allowed for horizontal and pin rotation as shown in Figure 7.15.

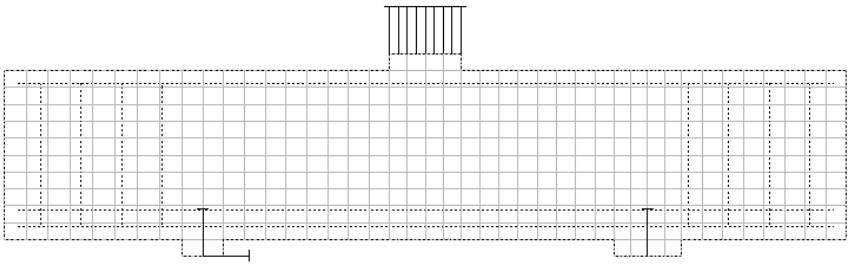

Figure 7.15: Finite element mesh and boundary conditions of short span beam (beam A0)

The material properties used in the finite element model are summarized in Table 7.10. The Young's modulus (E_c) used in the model, along with the concrete compressive (f_c) and tensile (f_{ct}) strengths were obtained experimentally whilst the remaining parameters had to be estimated. The reinforcement was modelled as discrete embedded elements, shown as dashed lines in Figure 7.15, with a perfect plasticity (Von Misses) constitutive

model. In order to avoid stress concentrations at the loading points, the loading plates were included in the model, which were assigned with a steel perfect plasticity material.

Concrete	***AG***	***AL***	**Steel**	***Plates***	***Long reinf.***	***Shear Reinf.***
E_c [MPa]	42608	34969	E_s [GPa]	200	200	200
ν	0.2*	0.2*	ν	0.3	0.3	0.3
f_{ct} [MPa]	5.7	4.9	f_y [MPa]	500	580	550
G_f [N/mm]	0.113	0.101				
f_c [MPa]	80.2	68.4				

Notes: * For the Total Strain models $\nu = 0$
$^{+}$ An estimated value of $G_c = 100G_f$ was assumed, where $G_f(\text{MC90})=G_{fo}.(f_{cm}/f_{cmo})^{0.7}$
Values of E_c, f_c, f_{ct} and f_y were obtained experimentally

Table 7.10: Material properties in the NLFEA of beams AG and AL

In all the models a Hordijk [79] softening curve, which is defined by G_f, was adopted for tension and a parabolic relationship for compression, see chapter 3. In addition, the compression softening algorithm from Vecchio and Collins (VC1993) was implemented in the Total Strain models, while for the multi-fix model the concrete strength was not reduced. Surprisingly, the strength of short span beams analysed using the multi-fix model was not overestimated. As shown in section 5.4, the same did not apply for shear panel tests. In the multi-fixed angle model a threshold angle value (α) was taken as 60º, although in some of the gravel beams (AG3) with higher concrete strength α was increased to 75 º to avoid numerical instabilities. For the fixed angle model a constant shear retention factor (β) of 0.1 was adopted.

The solver used in the increment-iterative procedure was a standard Newton-Raphson with an energy based converged norm criteria, see chapter 3. The size of each displacement increment was kept fixed to 0.1mm which provided a converged solution within a few iterations. Only the multi-fixed crack model showed numerical difficulties near failure which could not be overcome by using other types of solvers such a Quasi-Newton (secant) procedure or the Constant method, described in chapter 3.

The size of the load/displacement increment had a minor influence on the ultimate load predicted by the model. Increments in the ultimate load up to 10% were detected for cases were an excessive step size was adopted. Adaptive loading algorithms in combination with arc-length method, described in chapter 3 were also investigated. In order to obtained optimal solutions the parameters required by these algorithms had to be

modified for each beam and constitutive model. For simplicity fixed increment steps were finally adopted, which provided reliable solutions.

7.4.2 NLFEA results and comparison with other design methods

In general the ultimate loads were predicted satisfactory by the NLFEA although several assumptions were required regarding the tensile strength of the elements. The results of the NLFEA are compared in Table 7.11 with the predictions from EC2 and proposed STM design methods for short span beams with and without stirrups.

		V_{calc}/V_{test}				
Beam	V_{test} [kN]	EC2	STM	NLFEA Tot. Fix	NLFEA Tot. Rot	NLFEA Mult-Fix
AG0	325.76	0.53	1.28	0.97	0.97	0.95
AG2	563.02	0.35	0.79	0.79	0.65	0.90
AG3	654.60	0.45	0.69	0.71	0.59^{+}	0.82
AG4	707.10	0.56	0.66	0.70	0.67	0.53^{+}
AL0	365.50	0.45	1.04	0.80	0.97	0.80
AL2	531.89	0.37	0.76	0.75	0.65	0.98
AL3	480.73	0.61	0.87	0.89	0.76	0.97
AL4	602.19	0.65	0.71	0.71	0.74	0.83
	Mean	0.50	0.85	0.79	0.75	0.84
	SD	0.11	0.21	0.10	0.15	0.14
	COV %	22.00	24.70	12.65	20.00	17.27

Note: +Analysis stopped prematurely
NLFE results are shown for reduced values of f_{ct} = 2.95MPa (AG) and 2.70MPa (AL)

Table 7.11: NLFEA prediction for beams A compared with EC2 and STM methods

The accuracy of the predicted failure load of the short span beams was improved if the concrete tensile strength f_{ct} was reduced in the NLFEA, unlike the slender beams without stirrups where the converse was not always true. Reducing f_{ct} to 2.95 and 2.70MPa for the AG and AL series of beams respectively in accordance with the Bresler & Scordelis [169] formula $0.33(f_c')^{0.5}$ was found to significantly improve the predictions of crack development and ultimate load. These improvements were more noticeable in beams without stirrups (A0). The load-deflection response became excessively stiff when the measured values of f_{ct} given in Table 7.10 were used in the analysis. This over-stiff behaviour arose since the principle shear crack in the NLFEA formed below the actual position of the crack in the tests and had a break point in the middle where the slope changed suddenly, as shown in Figure 7.16.

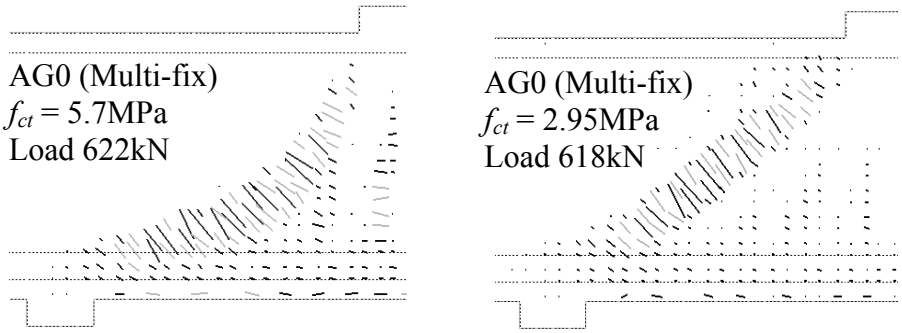

Figure 7.16: Influence of tensile strength on crack pattern predicted in NLFEA

Variations in the shear retention factor β assumed in the total fixed and multi-fixed models were also investigated. As shown in Figure 7.17, the initial value assumed of 0.1 for the shear retention factor seemed to give best predictions. Higher values of β of 0.2 or 0.4 incorrectly predicted a diagonal shear crack that was clearly above the one observed experimentally, as shown in Figure 7.17. In addition the predicted shear crack was flatter and the ultimate load was clearly over predicted.

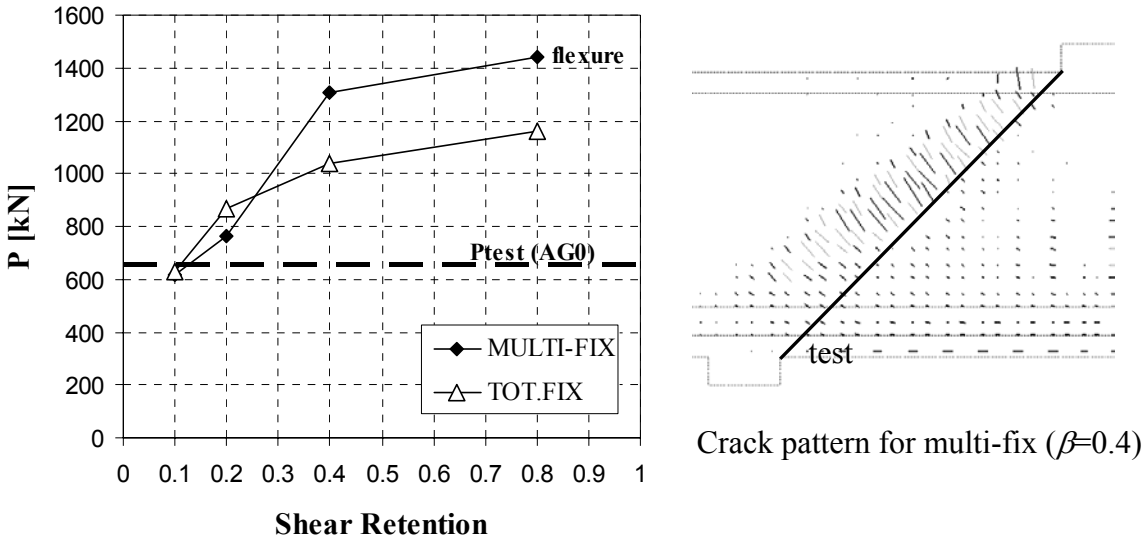

Crack pattern for multi-fix (β=0.4)

Figure 7.17: Influence of shear retention factor in NLFE predictions (beam AG0)

From the numerical analysis using the three smeared cracking models, the multi-fixed model gave the best predictions, although the total strain models were more robust numerically. The total strain fixed and rotating models provided very similar results to each other due to the limited crack rotation within the shear span of short span beams. The total strain models exhibited a spurious post-failure response due to the formation of new cracks on top of the main diagonal crack near the loading plate, see Figure 7.18. The latter cracks were similar to the ones observed in the experiments after the peak load had

been reached. Good predictions of the load-deflection curves were obtained up to failure for most of the beams. However in some specimens the ultimate load was underestimated due to local failure of the elements near the loading plate. No attempt was made to improve the predictions of the ultimate load since the primary aim of the analysis was to investigate which of the smeared crack models was most suitable for implementation into the combined smeared/discrete crack models described in section 7.5.3. To overcome this premature failure, a possible approach is to strengthen the elements adjacent to the loading plate, as shown in section 7.5.3. This could be justified by the confinement introduced by the loading plate, which enhances the concrete strength in this region.

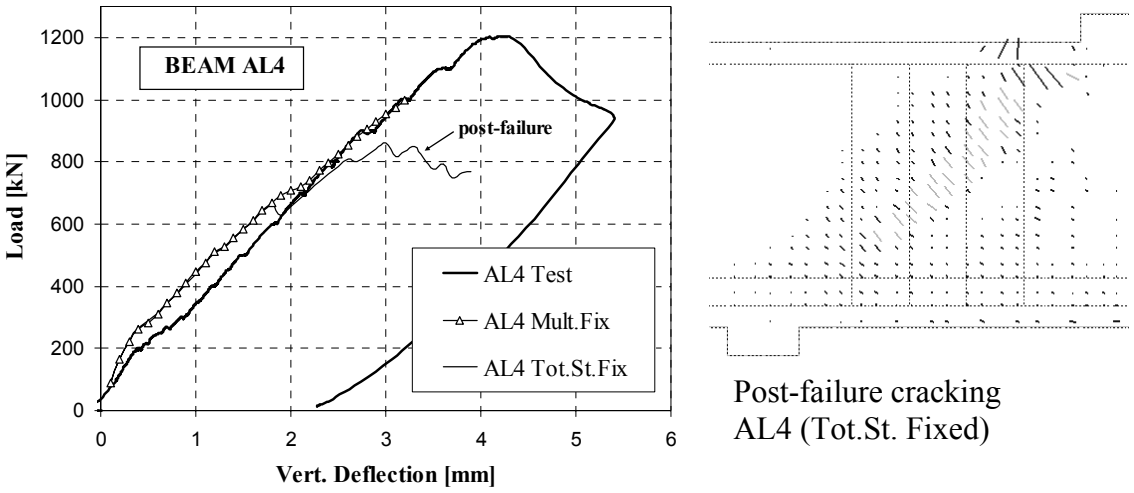

Figure 7.18: Load-deflection response predicted by NLFE model in beam AL4 and post-failure behaviour predicted in Total Strain Fixed model

Comparison between NLFE and STM predictions

An important aspect that needs to be mentioned is the difference in stress distribution under the loading plates assumed in STM and NLFE models. The stresses under the load plate were assumed constant in the strut-and-tie model. However, the non-linear-finite element analysis suggested that there is a concentration of stresses at the edge of the loading plate, as shown in Figure 7.19. The cracks which formed in the tests near the edge of the loading platens at failure could indicate a certain degree of stress concentration in that area, although additional experimental evidence is not available. The concentration of stresses predicted in the FE model depended on the stiffness assumed for the loading platen and smeared cracking model applied for the concrete. Considerations on modelling of loading plates in FE are described in section 3.5.3.

As a consequence of the concentration of stresses near the edge of the loading plate in the NLFEA, a slightly steeper strut than the one predicted in the strut-and-tie model was obtained, as shown in Figure 7.19. Even so, in particular cases such as in beam AL4 the numerical predictions were in excellent agreement with the strut-and-tie model, where the direct strut in both cases almost matched.

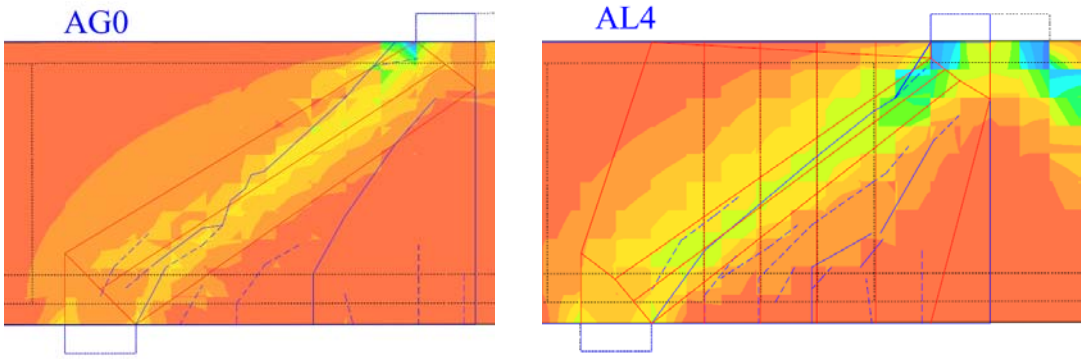

Figure 7.19: Principal compressive stresses predicted in the NLFEA (Mult. Fix) and superimposition of experimental crack pattern and STM (beams AG0 and AL4)

The width of the direct strut is assumed to be almost constant in the strut-and-tie model. This assumption was examined in the light of the numerical results from the NLFEA and strain readings obtained from demec gauge reading in beams A (see Figure 6.8). Figure 7.20 shows the transverse profile of compressive strains at the middle cross section of the direct strut, which was measured by the Demec gauge. The empirical results of the compressive strains are compared with NLFE and STM predictions. The compressive strains obtained in the NLFEA had a reasonable correlation with the experimental data, although the ultimate loads predicted by the STM and NLFE were generally lower than the experimental values. As expected, peak values for the compressive strains were observed near the centreline of the direct strut. The gradient of strains along the transverse section of the strut was slightly exaggerated in the NLFEA. In general, the widths predicted for the direct struts in the STM of beams A varied from 170mm (A0) to around 90mm (A4). The maximum variation of the compression strains obtained experimentally for the largest strut width obtained in the STM was around 35% of the peak strain. Hence the strains along the idealized strut can be considered constant. The variation in the strut width along the direction of the strut predicted by the NLFEA was negligible.

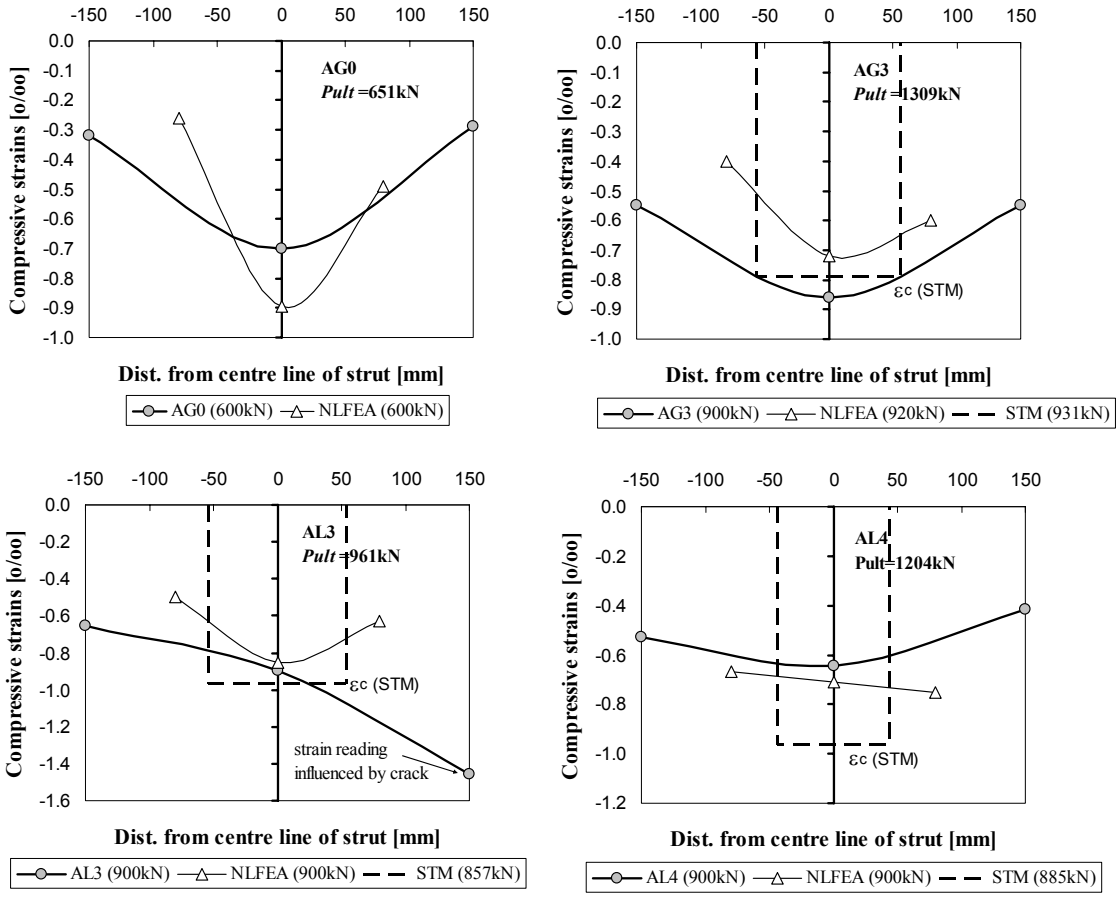

Note: ε_c (STM) = 0.6 $\nu f_{cd}/E_c$ = 0.00079 (Gravel), = 0.00096 (Limestone)
STM overestimated the strength of beam AG0 to 834kN, hence STM results are not shown
Test values were obtained with a Demec gauge at three points (see Figure 6.8)
NLFEA (Multi-fixed model); results are mean values obtained for three elements crossing the strut

Figure 7.20: Comparison of numerical and experimental strains at the main strut, variation along transverse section

Tensile strains in shear reinforcement

The NLFEA predicted yielding of the shear reinforcement prior to failure, which was in agreement with Demec and strain gauge readings, shown in chapter 6. The highest stresses in the stirrups were predicted in the NLFEA at the level where the diagonal crack originated, which is also in agreement with experimental evidence. Figure 7.21 shows the strains measured by strain gauges 13 (at the crack) and 14 (90mm above the crack) at the central stirrup of beam AG3 in comparison with numerical predictions. In the light of these numerical and experimental results, the assumption made in the strut-and-tie model regarding the force transmitted by the stirrups, which is determined by their yielding strength, could be confirmed for beams A.

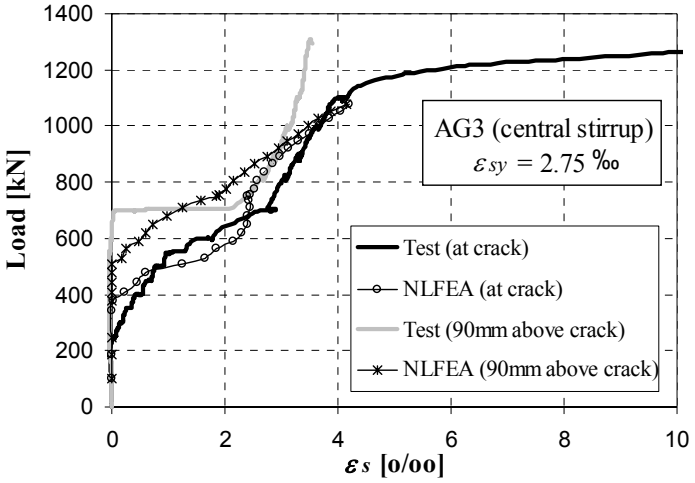

Note: Test readings relate to SG13 (crack) and SG14 (above the crack), at central stirrup
NLFEA (Multi-fixed model)

Figure 7.21: Comparison of experimental and numerical predictions of strain developments of the central stirrup at two different heights

A good agreement between experimental data and NLFE predictions of strains in stirrups was also obtained at different heights of the stirrups. Figure 7.22 shows the strain distribution along the stirrups measured in beams A3 using both demec and strain gauges at the load step in which the last demec reading could be taken. The strain distribution had maximum values where the main shear crack crossed the stirrup. Demec reading were greater at this sector of the stirrup than NLFE and experimental values, which could be due to bond-slip. As described in section 3.4.1, perfect bond between the concrete and steel is assumed in the embedded reinforcement elements adopted in the NLFEA. In addition, tension stiffening is modelled with residual tension in the concrete after cracking, by means of the Hordijk [79] softening model. Although both of these assumptions are not entirely accurate, predictions were sensible without having to introduce interface elements to model bond more realistically

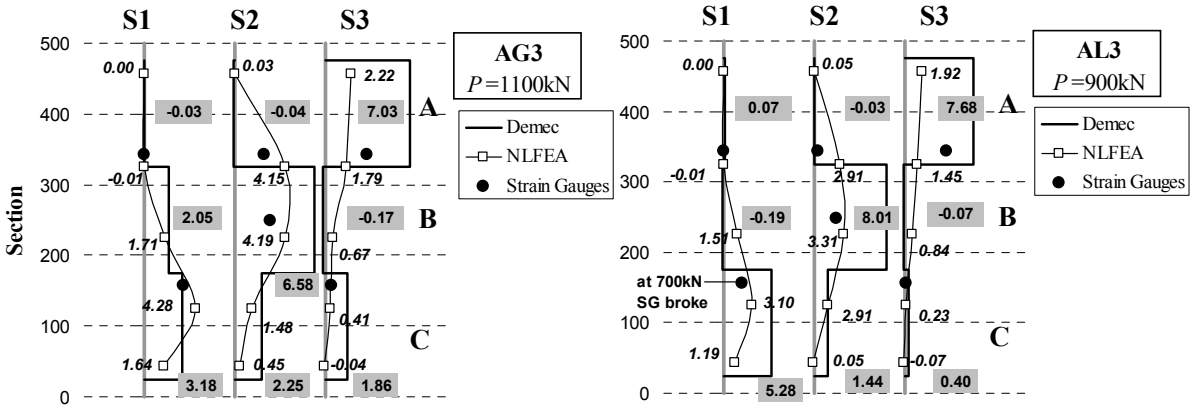

Note: failure loads for beams AG3 and AL3 are 1309kN and 961kN respectively

Figure 7.22: Variation of strains at different heights of the stirrups (beams AG3 and AL3)

Tensile strains along the flexural reinforcement

The tensile strain in the flexural reinforcement (ε_s) predicted by the NLFEA was slightly smaller than the experimental values obtained from the strain gauges located in beams A0 and A3, as show in Figure 7.23. The strains predicted in the NLFEA remained in the elastic domain in all the beams. However, in beams AG3 and AG4 the strain gauge and Demec readings showed that the flexural reinforcement had started to yield near failure.

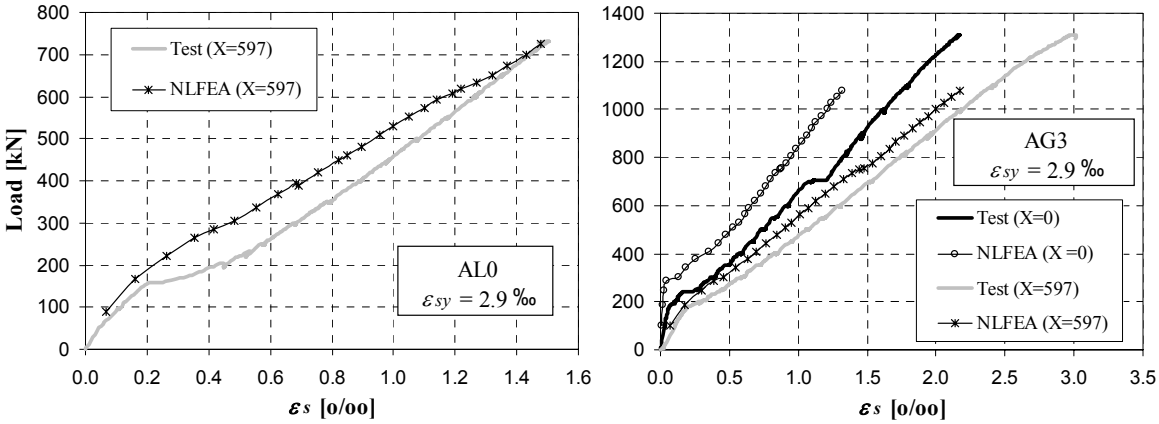

Note: NLFEA (Multi-fixed model)
X = distance along flexural reinforcement measured from the inner edge of the support

Figure 7.23: Comparison of numerical and experimental tensile strains at centre (X=597mm) and inner edge of support (X=0) for beams AL0 and AG3

It is generally believed that the tensile strain along the flexural reinforcement of short span beams is reasonably constant. A small gradient in the tensile strains was observed from the strain gauge reading located along the flexural reinforcement, see Figure 7.24. In the strut-and-tie model proposed by the author, the strains along the tie are constant only in short beams without stirrups. According to the STM model, a reduced gradient in the tensile strains is expected in short span beams with stirrups. In particular, in the STM model suggested, where the position of each stirrup is considered, ε_s is assumed constant between each stirrup, as shown in Figure 7.24. The gradient in the tensile strains along the flexural reinforcement predicted by the STM model was in good agreement with NLFEA and empirical values for beams with stirrups.

In beams without stirrups the gradient could only be obtained empirically for beam AG0 due to a faulty strain gauge in beam AL0. Although the STM assumes a constant value of ε_s, the gradient observed in AG0 was insignificant compared to the remaining beams. The NLFEA predicted a gradient of ε_s in beams without stirrups, which would develop only in the third of the clear shear span nearest the support, as shown in Figure 7.24.

This prediction is not consistent with the STM model, and it does not seem to agree with the empirical results, although more information from additional data points along the reinforcement would be desirable.

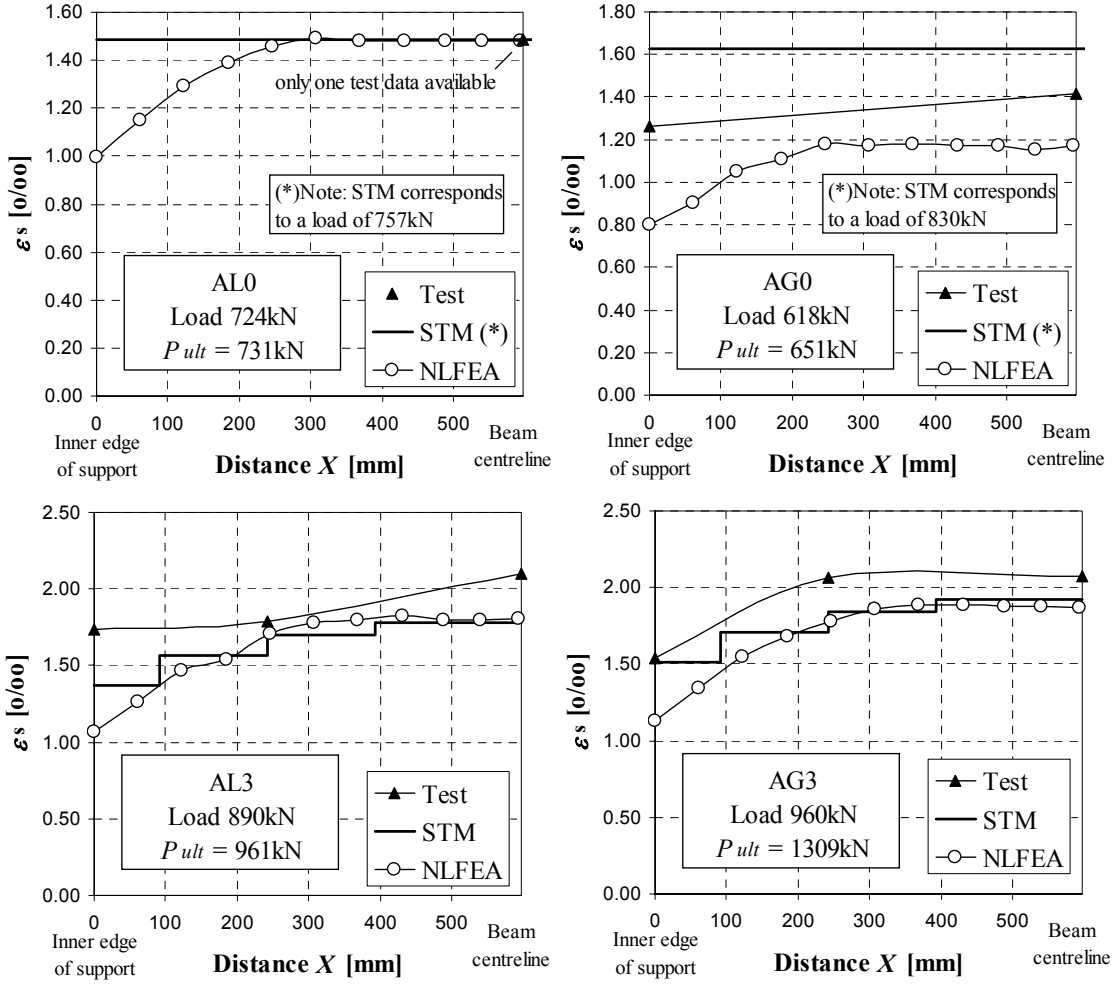

Note: Results are shown for the same load step except for beams A0 where the STM overestimated the ultimate strength. X = distance along flexural reinforcement measured from the inner edge of the support. NLFEA (Multi-fixed model)

Figure 7.24: Comparison of predicted and experimental gradient of tensile strains along the flexural reinforcement from the inner edge of the support to the centre of the beam (beams A0 and A3)

7.5 Considerations of shear stresses transmitted at the main shear crack

7.5.1 Experimental evidence

The early formation of the diagonal shear crack observed in short span beams, raises the question of whether the shear that develops along the crack surface by means of aggregate interlock can become critical. The limitation of shear carrying capacity of the shear crack appears to be more critical in beams without stirrups since the additional truss load path provided by the stirrups is not present. According to the experimental evidence provided by beams A, the location of the critical shear crack with respect the direct strut can be critical such as in beams AG0 and AL3. Beam AG0 failed at a lower load than beam AL0, which had lower concrete strength and smoother crack surface. Furthermore, the ultimate load of beam AL3 was lower than beam AL2, which had fewer stirrups. These apparent contradictions could only be explained by the relative position of the diagonal shear crack with respect the direct strut and could justify the large scatter detected in experimental data of short span beams, especially for beams without stirrups.

The relatively large crack openings recorded compared with the sliding suggested that the shear carrying capacity of the diagonal crack was limited. However, results from the push-off test revealed that considerable shear stresses could still be transmitted, even for cases where the aggregate fractured at the crack. In order to provide further evidence about the shear developed at the diagonal crack, analytical and numerical methods were performed, see sections 7.5.2 and 7.5.3.

The shear stresses at the diagonal crack (τ_{cr}) were interpolated from the push-off tests using the crack opening and sliding recorded at failure. Unfortunately, only limestone short span beams and push-off specimens could be correlated (see Table 7.12) due to their similar concrete strengths. On the contrary, gravel concrete short span beams had a considerably larger concrete strength compared to equivalent push-off specimens (f_c'=80.2MPa as opposed to 31.7MPa) and so the correlation was dubious. The interpolation surfaces (w-s-τ_{cr}) obtained in section 4.3, were applied to both short span and slender beams; beams A and B respectively. However, this approach seemed more appropriate for beams B (see Chapter 8), which had a more similar $\delta w/\delta s$ ratio to push-off tests than beams A. In addition, the concrete used was the same for push-off tests and beams B.

Table 7.12 summarizes the results obtained for beams AL. The interpolated surfaces and main drawbacks of this approach are described in section 4.3.

	Test			*Interp.*	
Beam	$v=V/b_w d$ [MPa]	w [mm]	s [mm]	τ_{cr}^{*} [MPa]	τ_{cr}^{*}/v
AL0	6.19	1.15	0.41	3.70	0.60
AL2	9.01	1.35	0.28	3.70	0.41
AL3	8.14	1.30	0.45	3.64	0.45
AL4	10.20	0.94	0.31	3.75	0.37

Note: * results interpolated from push-off tests (specimens PL); refer to section 4.3
- Relative crack displacements (refer to Table 6.5); readings shown for AL2 and AL4 were taken at mid-depth by LVTD crosses, while for AL0 and AL3 the readings relate to Demec cross at 340mm from the bottom
- Results for beams AG are not shown due to the large difference in f_c' compared to push-off test data

Table 7.12: Interpolated shear stresses at the diagonal crack of beams AL

The shear transferred by the main diagonal crack is highly sensitive to the angle β between the crack plane and the direct strut, as shown in Figure 7.25. As an order of magnitude, the shear stresses estimated in beams A, which are shown in Table 7.12, corresponded to values of β between 5° and 10°. Due to the irregularities in the profile of the diagonal crack it seemed unreasonable to try to estimate the actual shear stresses at each point at the crack. Although, average values of the crack inclination could be assumed in order to obtain a mean value for τ_{cr}.

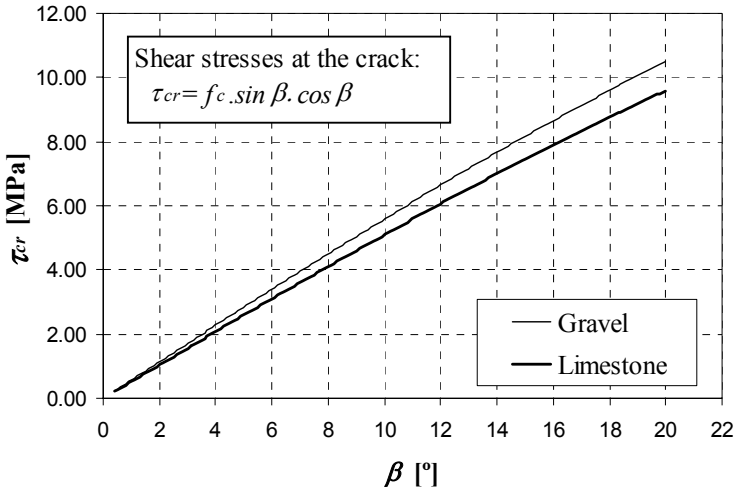

Note: $f_c = 0.6\nu f_{cd} = 32.68$MPa (Gravel), = 29.82MPa (Limestone)

Figure 7.25: Sensitivity of shear stresses at the crack (τ_{cr}) to the angle β between centreline of direct strut and crack plane

As shown in Figure 7.26, the inclination of the main crack was fairly parallel to the direct strut for low-middle load stages in all beams A, except AG0 and AL3. Near failure, a crushing type of crack, which was steeper than the shear crack, originated under the loading point. This shear-compression type of failure, which was common in all beams A except AG0 and AL3, allowed most of the load carried by the direct strut to be transmitted above the main diagonal crack. However in beams AG0 and AL3 load was forced to be transferred through the main diagonal crack since the direct strut was crossed completely by the crack, which is usually referred to as shear proper failure, from early load stages as shown in Figure 7.26. This restriction in the load path in beams AG0 and AL3 explained the lower strengths obtained experimentally, especially in AG0. The lower strengths in beams AG0 and AL3 are discussed in next section in the light of a modified strut-and-tie model which incorporates a shear friction constraint at the critical crack.

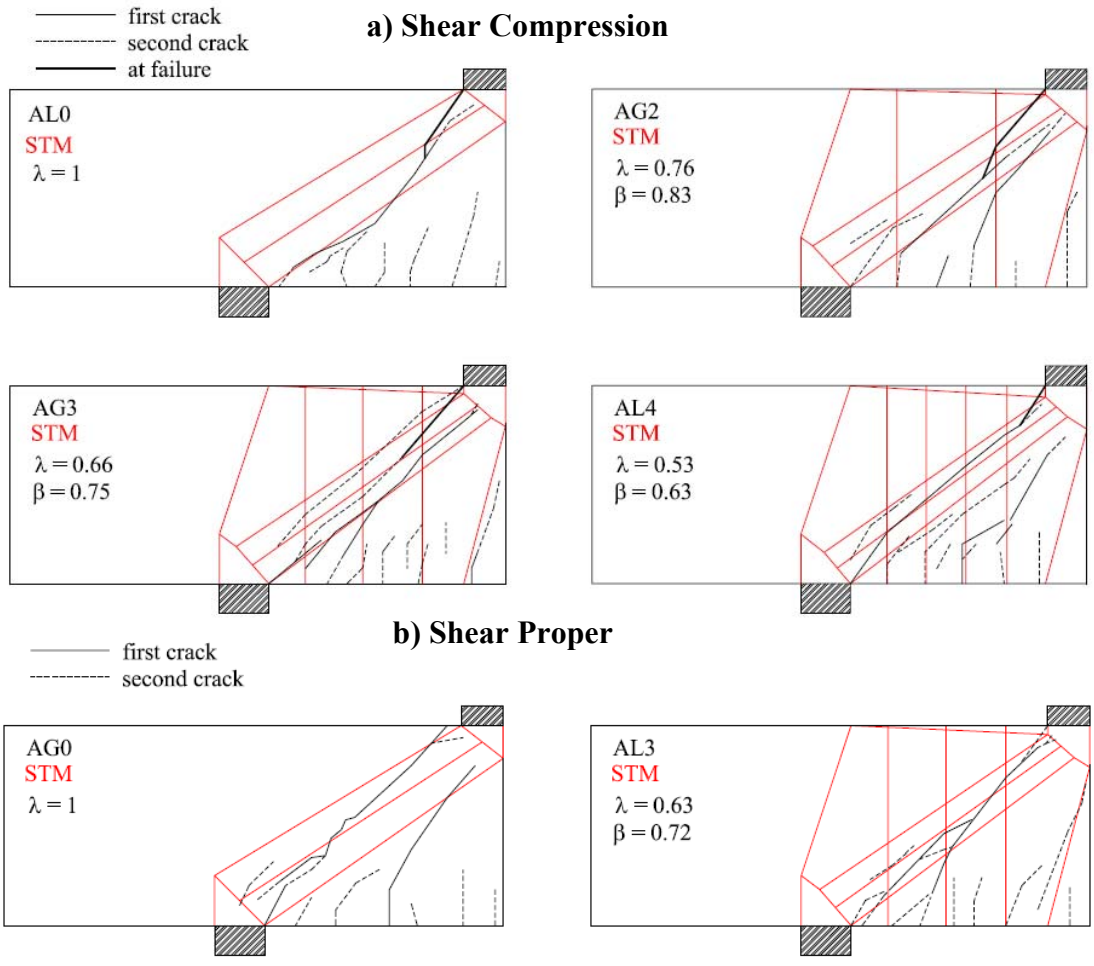

Figure 7.26: Crack pattern in relation with direct strut in STM model (beams A)

Considerations regarding the crack opening-sliding ratio (suggested relationship)

As mentioned earlier the crack opening-sliding ratio obtained experimentally was relatively large ($\delta w/\delta s$~3) compared with in general the slender beams tested, as shown in Figure 7.27. The difference is even larger with respect push-off tests, in which $\delta w/\delta s$ is well described by MC90 formula ($w = 0.6s^{2/3}$), as discussed in section 4.2.4.

The crack dilatancy observed in short span beams was consistent with NLFE predictions obtained in section 7.5.3, which are also shown in Figure 7.27. According to most crack dilatancy models, such large values of $\delta w/\delta s$ result in very small shear stresses at the crack, which could be considerably lower than those obtained from interpolating push-off test data shown in Table 7.12. In order to illustrate this, Walraven and Reinhardt's [46] linear aggregate interlock model was used to estimate the minimum sliding (S_o) required to activate the shear stresses in the crack. This limit in crack slip S_o was calculated for each load taking the crack opening obtained in the experiment. The values obtained in the experiments for sliding were lower than S_o as shown in Figure 7.27, which indicated that shear stresses at the crack according to this model were negligible.

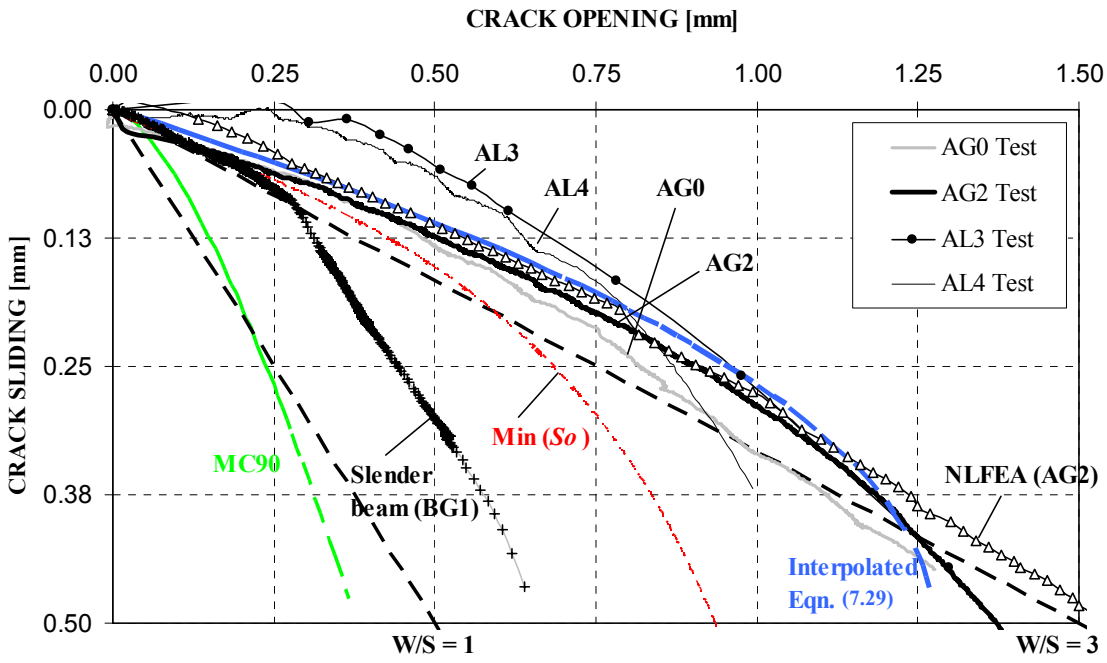

Figure 7.27: Crack opening-sliding relationship for beams A compared with analytical models and representative test results from slender beams and push-off tests (MC90)

The $\delta w/\delta s$ ratio in beams A could be estimated as 3 as shown in Figure 7.27. An analytical expression was obtained for the crack dilatancy of beams A, from fitting experimental data, as shown in Figure 7.28. A linear and parabolic fit were applied for crack opening and sliding respectively. The formulas are valid up to a maximum opening and sliding of 1.27mm and 0.5mm respectively. As shown in Figure 7.28, the fit overestimated slightly the crack displacements for beam AL4. However this overestimation was consistent for both w and s and so the overall crack dilatancy $\delta w/\delta s$ was not significantly different to the remaining beams considered for the curve fitting.

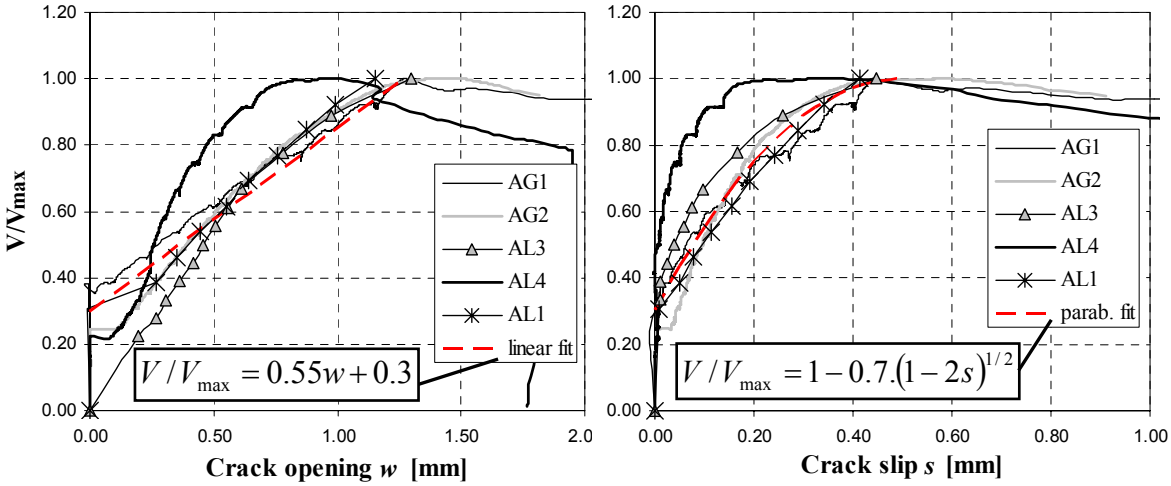

Note: Only beams A considered which failed in same shear span (a_v/d=1.12); refer to section 6.3.4
V/V_{max} ratio between shear and ultimate shear load measured in the test

Figure 7.28: Curve fitting of crack displacements in beams A; estimation of crack dilatancy

Equating V/V_{max} in both equations obtained in Figure 7.28 leads to a simple relationship between w and s given by equation (7.29).

$$s = 0.5.\left(1 - \sqrt{1 - 0.785.w}\right) \qquad \ldots(7.29)$$

Equation (7.29) fitted experimental data from beams A reasonably well, which also seemed consistent with predictions from the NLFEA obtained in section 7.5.3 (see Figure 7.27). Nevertheless, equation (7.29) should only be considered as a reference, since it has been derived for a particular beam geometry and concrete strength. Additional experimental data would be required to obtain a more general relationship.

Observations regarding the type of aggregate

One important aspect observed in short beams A was that the influence of aggregate fracture seemed to be insignificant and design methods provided similar performances for both limestone and gravel specimens. An interesting example is provided by the already mentioned performance of beam AG0 compared with AL0, where the former had higher concrete strength and rougher crack surface and still failed at lower failure load than AL0. In addition, it seemed clear that higher shear stresses must have developed along the main crack in beam AG0 than in AL0, since identical crack opening and sliding were measured in both beams.

This example clearly showed that the position of the diagonal crack in beams A0 had a more important role in this case than the reduction in the roughness of crack surface due to fracture of the aggregate. Unfortunately, additional experimental evidence is not available for beams with larger member depths in which the crack at failure would probably be wider. For the beam heights tested (h=500mm), the crack widths at the main shear crack of the short span beam were around 1 to 1.25mm near failure, as shown in Figure 7.27.

7.5.2 Analytical predictions: STM with shear friction

In order to quantify the possible reduction in strength due to the influence of the diagonal crack, the direct strut in the STM model can be idealized as a compression member similar to a slant test specimen shown in Figure 7.29. It is widely accepted that a "shear friction" relationship $\tau = C+\mu\sigma$ (Coulomb failure criteria) can be applied to predict the failure of slant tests with a preformed crack, see Climaco & Regan [113].

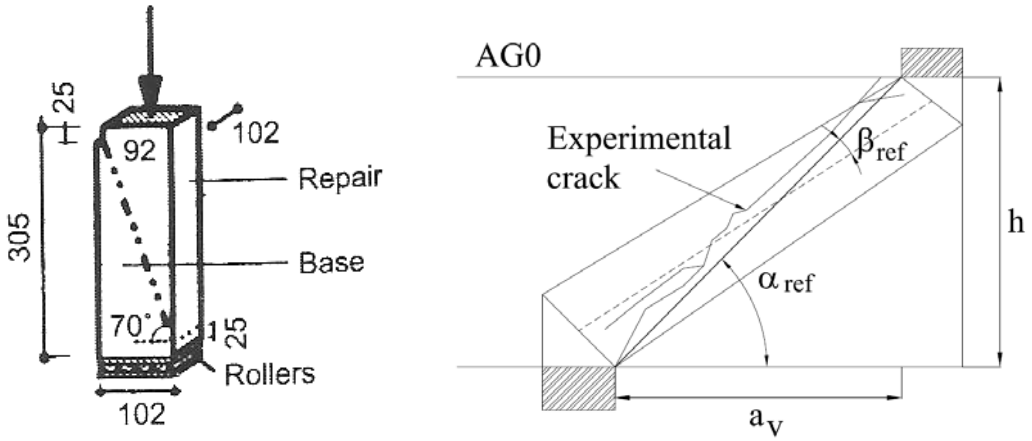

Figure 7.29: Idealization of direct strut to slant tests; example of slant test for β =30º (adapted from Climaco and Regan [113])

In the strut-and-tie model described in sections 7.2.2 and 7.3.2 the effective concrete strength of the strut ($f_{c,eff}$) was taken from plasticity as recommended in EC2, which assumes a constant value of $0.6\nu f_{cd}$. It has been shown that this effectiveness parameter for the concrete provides in general good correlation with experimental data and only in a few specimens such as beam AG0 the strength could be overestimated.

An alternative approach to assuming a constant value of $f_{c,eff}$ would be limiting the effective strength of the direct strut according to a shear friction relationship such as equation (7.30).

$$f_{c,eff}\,(shear-friction) = c.\frac{1+\cot^2\beta}{\cot\beta-\mu} \qquad \ldots(7.30)$$

where β is the angle between the strut and the crack plane $\beta=\alpha-\theta$.

In this alternative approach, which is denoted as STM-(eqn.7.30), the inclination of the diagonal crack (α) would have to be assumed. For beams A the angle of the crack α could be taken directly from the tests (α_{test}), as shown in Figure 7.30. Alternatively a reference value for the inclination of the crack (α_{ref}) can be estimated from the geometry of the

beam $\alpha_{ref} = a.tan(h/a_v)$, refer to Figure 7.29. The value of α_{ref} was very similar to the experimental one for beams AG0 and AL3. Even though the reference value α_{ref}=45.5º provided a safe low boundary of the ultimate strength of the strut, the inclination of the main diagonal crack was in some cases significantly flatter. As shown in Figure 7.30, beam AL0 presented two different crack inclinations and so it was dubious which angle should be adopted in the analysis. The remaining beams had a more uniform profile and so the value of was more certain than for beam AL0.

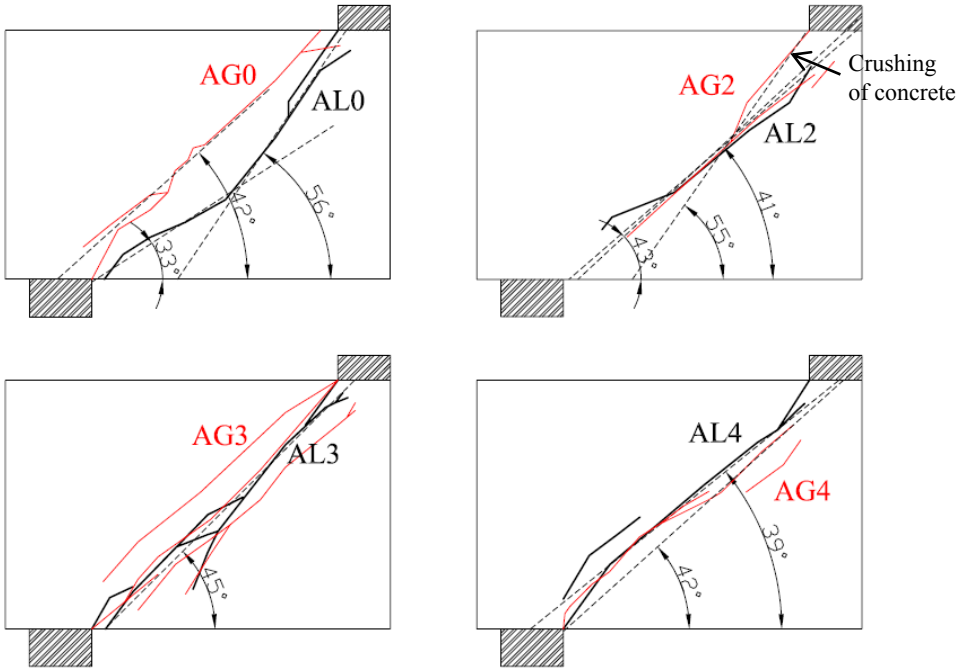

Figure 7.30: Measurements of inclination of the main shear crack in beams A

The value applied in equation (7.30) for the cohesion (c) was taken as $0.625f_{ct}$, as recommended in EC2. This estimated value for c was similar to the one applied in the shear friction approach for slender beams described in chapter 8. Similarly, the friction used in equation (7.30) was taken as 1.06 and 0.95 for gravel and limestone beams respectively. It must be highlighted that both c and μ assumed are approximated values since the concrete strength of the push-off specimens used to obtain μ (see section 4.4) was different than in the beams A, especially for the gravel specimens. However, the values assumed ultimately for equation (7.30) are in agreement with most design codes and can be used to assess a reasonable boundary of the effective concrete strength of the strut. The variation of the effective concrete strength given by equation (7.30) is shown in relation to angle β in Figure 7.31. For low values of β the concrete strength should be limited to the uniaxial strength of the concrete f_{cd}.

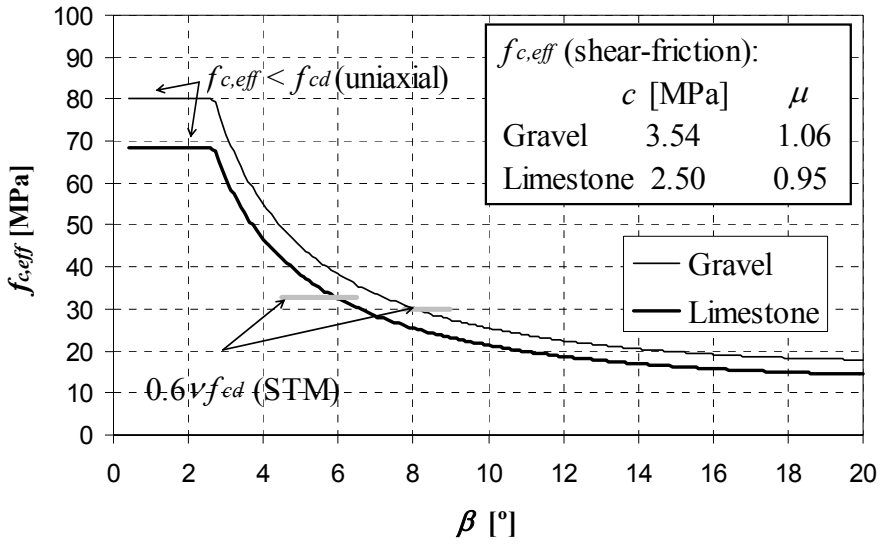

Figure 7.31: Effective concrete strength ($f_{c,eff}$) according to shear friction model

As shown in Figure 7.32, the prediction of the ultimate strength of beam AG0 was improved by introducing equation (7.30), whilst a similar strength was obtained for beam AL3 with larger *SI*. The shear friction constraint given by equation (7.30) becomes less restrictive in the STM as the stirrup index increases, since the direct strut becomes steeper and more parallel to the crack plane. Figure 7.32 illustrates the range where the shear friction restriction can be critical in beams A. The prediction obtained from the STM with friction model was variable depending on the inclination of the crack assumed. In general the results were similar using either α_{test} or α_{ref}.

The lower bound of the crack inclination of around 35º, which is shown in Figure 7.32, corresponds to cases where the diagonal crack was almost parallel to the direct strut. In such instances with high values of *SI*, equation (7.30) had to be limited by the uniaxial strength f_{cd}. The higher bound of the crack inclination shown in Figure 7.32 was taken as 55º, which relates to the steepest segment of the diagonal crack observed at the top, see beam AG2 in Figure 7.30. Using this rather large value of α in the shear friction model provided excessively low predictions, as shown in Figure 7.32. It seems unrealistic to assume such a large value of α in the model since the crack at the top, which formed near failure, is caused by crushing of the concrete rather than shearing.

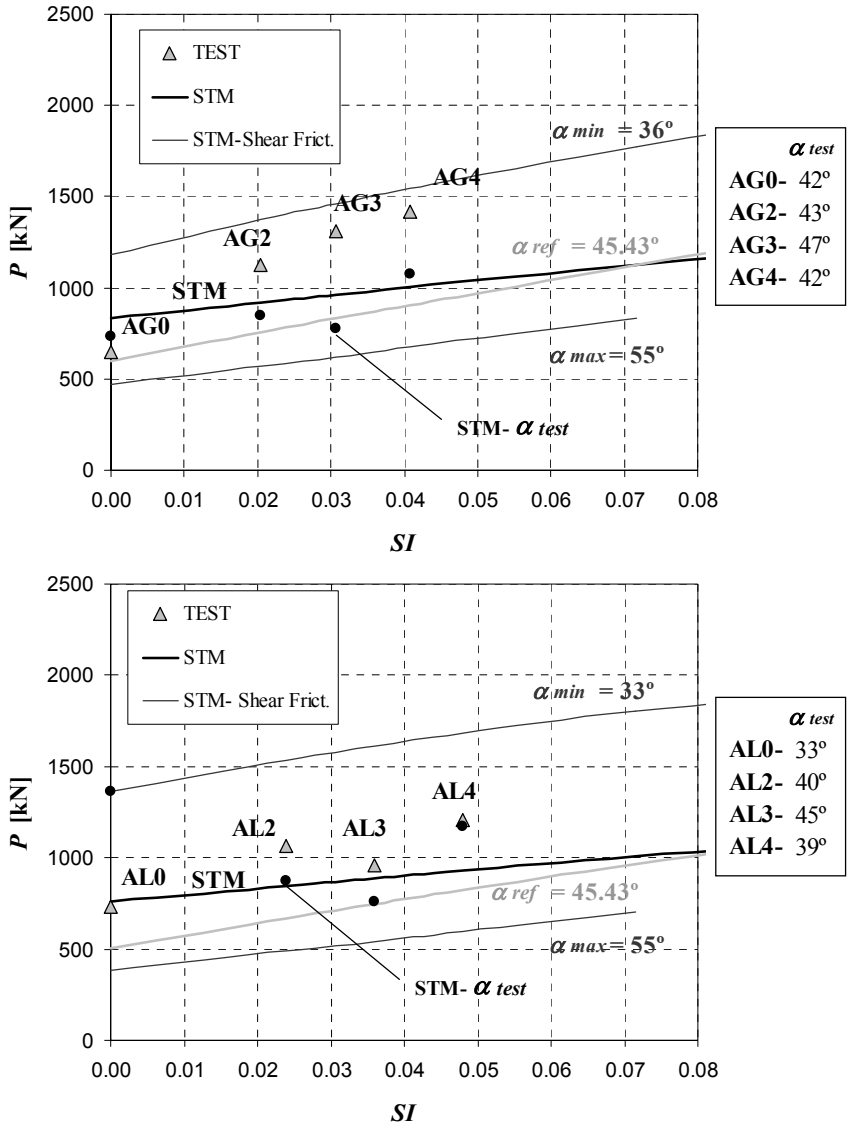

Figure 7.32: Predictions of STM with shear friction constraint at diagonal crack

In beam AL0, the strength predicted by STM-(eqn.7.30) using α_{test} was clearly overestimated since the inclination of the crack was essentially parallel to the strut. On the other hand for the remaining beams the predictions did not differ much from the original strut-and-tie model suggested, as shown in Figure 7.32. The shear stresses predicted at the crack by the STM-(eqn.7.30) approach varied between 3 and 4MPa, see Table 7.13, which are in agreement with interpolated values from the push-off tests (Table 7.12). The critical shear stresses predicted were slightly higher for beams AG than for beams AL, which resulted from being the concrete strength of beams AG higher than in beams AL.

		STM-(eq. 7.30) α_{ref}		STM-(eq. 7.30) α_{test}		STM ($0.6\nu f_c'$)	
Beam	α_{test} [°]	P_{calc}/P_{test}	τ_{cr} [MPa]	P_{calc}/P_{test}	τ_{cr} [MPa]	P_{calc}/P_{test}	τ_{cr}^{+} [MPa]
AL0	56.00*	0.69	3.76	0.52	4.86*	1.04	6.08
AL2	40.82	0.63	3.60	0.82	3.39	0.79	5.72
AL3	45.00	0.78	3.55	0.79	3.53	0.92	5.80
AL4	39.00	0.68	3.51	0.97	3.29	0.77	5.89
AG0	42.00	0.92	4.53	1.12	4.23	1.27	5.07
AG2	43.15	0.67	4.34	0.76	4.18	0.82	4.74
AG3	47.00	0.64	4.27	0.59	4.38	0.73	4.87
AG4	42.00	0.64	4.21	0.76	4.03	0.71	5.24

Note: $\alpha_{ref} = 45.43°$

*High value of α assumed in the analysis. The crack was inclined 33° in most of its length see Figure 7.32, which results on a τ_{cr} of 3.20 MPa with a P_{calc}/P_{test} of 1.86

+$\tau_{cr} = \sigma.cot\beta/(1+cot^2\beta)$ where $\sigma=0.6\nu f_{cd}$ and $\beta=\alpha_{test}-\theta$

Table 7.13: Shear stresses estimated at the shear crack

It is significant to highlight that neither plastic nor shear friction solutions adopted in the STM model so far take into account for size effects. Although there is not a general agreement on size effects for short span beams, as discussed in section 7.6, the question could be raised of whether it is reasonable to ignore the influence of larger crack widths in STM predictions of large members. A possible solution would be to apply a different shear friction formula in the STM, in which the crack width would be considered such as the one used in the MCFT or Swiss design formulas for shear, which are based on the Critical Shear Crack Theory. These formulas relate the critical shear to $(f_c)^{0.5}$, crack width and aggregate size. Moreover, this would also allow to take into account aggregate fracture, by taking a=0 as proposed by Collins et al. [31, 32]. An example of this alternative approach to equation (7.30) is shown in Figure 7.33, in which formula proposed by Muttoni [170] was adopted.

As shown in Figure 7.33, the predictions using sensible values of w and a were not dissimilar to those obtained using the shear friction approach. The strengths obtained assuming that the aggregate had fractured (a=0) were around 40% lower than predicted using a=10mm, as shown in Figure 7.33.

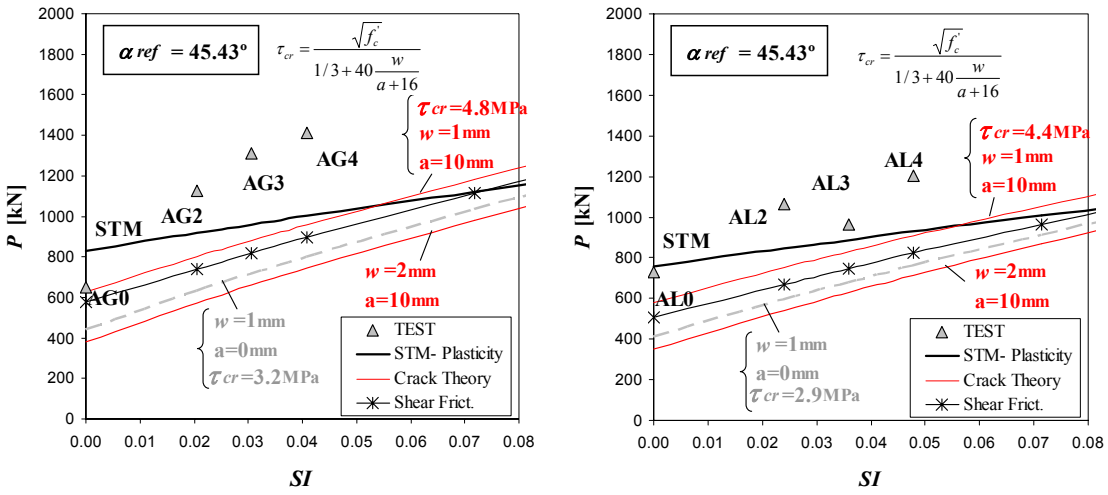

Figure 7.33: STM with shear constraint at the crack using Critical Shear Crack Theory formulas

The shear friction approaches described in this section are transparent and can be practical to demonstrate the relative low strengths obtained for some of the specimens tested (beams AG0 and AL3). However, two main difficulties would arise if the STM-(eqn.7.30) approach was to be used in a design basis. Firstly, the predictions are highly influenced by the cohesion and friction parameters applied, which are in general difficult to estimate in case experimental data is not available. Secondly, the position of the main diagonal crack would have to be assumed. Although the reference angle α_{ref} could give a good lower bound estimate for $f_{c,eff}$, it has been shown that the actual position of the crack can varied significantly and so the strength could be clearly underestimated. The parameters that can influence the position of the crack such as load history of initial stress states are difficult to take into consideration. Lastly, size effects and crack widths are neglected. As it has been shown, more elaborate shear friction relationships can be implemented, which could account for additional aspects such as aggregate fracture. However, crack widths would have to be estimated analytically increasing the level of complexity of the model.

In conclusion, the STM suggested, which limits the concrete strength of the strut to $0.6\nu f_{cd}$, seems to be a more reasonable approach for design purposes than alternative methods described in this section using shear friction formulas. As shown in section 8.3.3, similar approaches can be adopted for more slender beams, in this case using a truss with crack friction method.

7.5.3 NLFEA predictions using combined discrete/smeared cracking elements

In order to provide further evidence regarding the crack opening/sliding and shear stresses of the main diagonal crack, a NLFEA, which combined smeared and discrete cracking, was performed. Linear interface elements were introduced in the finite element mesh to model aggregate interlock behaviour more accurately. For the remaining elements of the mesh, smeared cracking models were applied, which had been previously validated in section 7.4. For the interface elements several discrete cracking formulations, described in chapter 3, were investigated, although a simple discrete crack model was finally adopted. As shown in this section, the crack opening and sliding were satisfactorily reproduced by the FE models, although several assumptions were necessary to find a balance between realistic behaviour and numerical stability.

Definition of combined smeared/discrete NLFE models

Figure 7.34 shows the FE mesh used, which combined line interface elements with a discrete crack model (line A–B) and smeared cracking model for the remaining elements. As reported by Feenstra et al. [53] numerical oscillations can occur in interface elements with small thicknesses that can be solved by applying Newton-Cotes quadrature elements. Hence a 6-node and 5-point Newton-Cotes integration scheme interface elements were applied. After the validation process of the smeared cracking models shown in section 7.4, the multidirectional-fixed smeared crack model was finally chosen for the concrete elements. The reinforcement was modelled with embedded elements assuming perfect bonding between the steel and the concrete. Especial considerations, which are discussed below, had to be made regarding the normal and transverse stiffness of the reinforcement elements crossing the interface plane. For the remaining elements, all material properties for steel and concrete were identical to the NLFE models shown in section 7.4, see Table 7.10. Only few additional considerations on the smeared cracking models, which are described below, were necessary in order to obtain a satisfactory combined performance of the smeared and discrete cracking elements.

An initial analysis was made to investigate the effect of refining the meshes shown in Figures 7.15 and 7.34, on the predicted response of the beams. In this analysis, the interface elements were given a large value of f_{ct} to ensure that the discrete crack remained closed. The other material properties were kept the same as in the previous

analyses with only smeared cracking. The ultimate loads and stiffness of the specimens were found to be similar for both the smeared/discrete and smeared crack models.

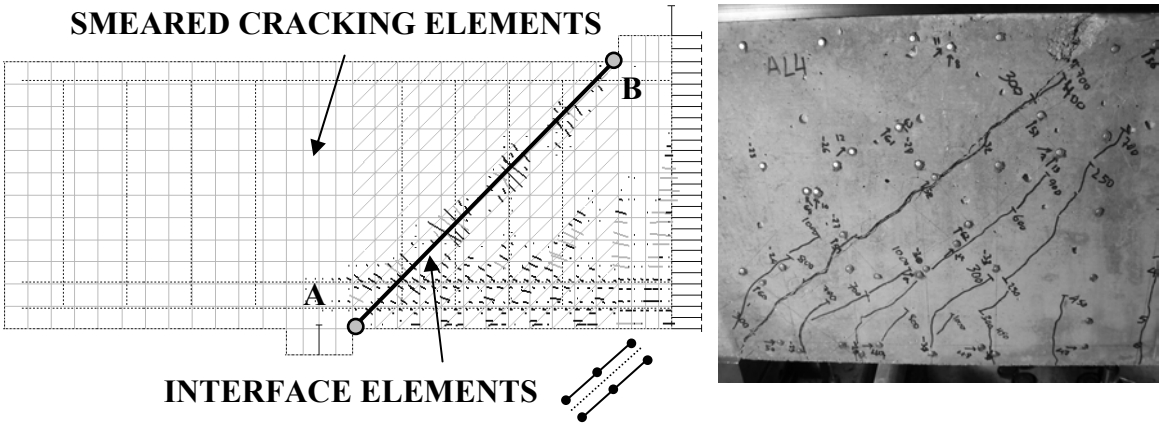

Figure 7.34: FE mesh of combined smeared/discrete model for beam AL4

Considerations for the discrete crack model in the interface elements

In order to keep the model numerically stable, a simple discrete crack constitutive model was initially adopted for the interface elements in which cracking was initiated when the concrete tensile strength was reached. In this model, which is designated as "Discrete Crack model" in chapter 3 (see section 3.2.2), the tensile and shear stresses were assumed to be uncoupled in the open crack. A linear softening curve was used for cracked concrete in tension once cracking had initiated.

In a preliminary analysis a constant shear retention factor of zero was assumed, which provided reasonable estimations of the crack opening and sliding. However, as it is shown in next section, this can result in high concentration of stresses at the ends of the discrete crack (points A and B in Figure 7.34). Hence, a more realistic value of the aggregate interlock stiffness after cracking (D_T) was applied in further analysis, which was estimated using simple formula suggested by Hamadi & Regan [19] ($D_T=k/w$). As shown in section 4.5, this formula provided reasonable predictions of push-off tests carried in this work; recommended value of k =5.4MPa for gravel specimens given by Hamadi & Regan [19] seemed also valid for limestone specimens tested by the author. For simplicity, a constant value of D_T was adopted in the NLFEA, which was estimated for a crack opening of 1.25mm. This value corresponds to average crack widths observed in beams A near failure. According to these assumptions, the final parameters used in the NLFEA are summarized in Table 7.14.

Discrete Crack Model	*AG*	*AL*		D_{dw} [N/mm^3]	D_{ai} [N/mm^3]
D_I [N/mm^3]	213040	174840	***A0***	0.00	4.32
D_{II} [N/mm^3]	88767	72850	***A2***	1.80*	2.50*
f_{ct} [MPa]	2.95	2.00	***A3***	2.33	2.00
G_f [N/mm]	0.113	0.101	***A4***	3.50	0.82
D_T [N/mm^3]	4.32	4.32			

Note: D = elastic stiffness (I- normal; II- shear); estimated as $D_I = E_c/h$ and $D_{II} = G/h$ where h = 0.2mm. D_T =overhall shear stiffness; D_{dw} =dowel action contribution estimated by DIANA for given l_{fr}=150mm, crack angle 45.43º and stirrup spacing; $D_{ai} = D_T - D_{dw}$
*In A2, D_{dw} was taken as 0 for all interface elements except for adjacent elements to stirrups, for which the values shown were applied

Table 7.14: Material properties of interface elements in NLFEA

Considerations for reinforced elements crossing the crack interface

The normal and shear stiffness of the reinforcement elements crossing the crack interface were taken into account through the free-length parameter (l_{fr}), described in more detail in section 3.4.2. The value of l_{fr} applied to the longitudinal reinforcement was taken equal to 0.2mm, which restrained the crack from opening and sliding at those local points. This assumption was necessary for numerical stability reasons. However, the assumption seemed realistic, since the shear crack observed in the experiments did not reach both top and bottom ends until near failure. As discussed in next sections, the diagonal crack propagation to top and bottom ends near failure was assigned to the smeared cracking elements surrounding the interface elements.

A value of l_{fr} of 150mm was assumed for the shear reinforcement crossing the interface elements. This value of l_{fr} was estimated from the crack widths obtained experimentally at which the stirrups began to yield (w~0.4mm). This preliminary guess allowed for a constant slip to be obtained along the crack in most of the beams. As described in section 3.4.2, DIANA assumes that the tangential stiffness introduced by embedded reinforcement crossing interface elements (D_{dw}), which is attributed to dowel action, is half the normal stiffness. The contribution of D_{dw} estimated in this manner is considerably larger compared to analytical models developed from empirical data. Alternative solutions are using truss or spring elements, as discussed in section 3.4.2, although they can introduce several difficulties into the model. Hence, a simpler approach was finally adopted, which consisted in reducing the value of the shear stiffness of the interface elements after cracking ($D_{ai}=D_T–D_{dw}$) to account for the stiffness already provided by embedded reinforcement elements, see Table 7.14.

Beams with stirrups evenly distributed along the crack (A3 and A4) D_{ai} was taken equal for all elements, while for beam A2 D_{ai} was only reduced in interface elements adjacent to the stirrups. This was necessary in order to obtain an uniform shear stiffness along the discrete crack. The values shown in Table 7.14 for the shear stiffness component D_{dw} were estimated using DIANA's formula (see section 3.4.2), which can be expressed in terms of the free length parameter and shear reinforcement ratio defined along the crack surface $D_{dw}=E_s/(2l_{fr})\rho_{ck}$. The shear reinforcement ratio ρ_{ck} was estimated using the stirrup spacing and crack angle for beams A3 and A4, where stirrups were evenly distributed. As mentioned earlier, for beam A2 stiffness $E_s/(2l_{fr})$ was smeared out to the interface elements adjacent to the stirrup.

Additional considerations for the smeared cracking models

The tensile strength of the interface elements had an important role in activating the discrete crack. In order to ensure that the discrete crack would open in preference to cracking in the smeared crack elements nearby, the tensile strength of the interface elements was taken as around half that of the smeared crack elements. The reduced value of f_{ct}, which is suggested in section 7.4 for the smeared cracking elements, was not necessary since the formation of the discrete crack had already been encouraged by reducing the tensile strength of the interface elements. Therefore the tensile strengths from the cylinder splitting tests were adopted in the smeared cracking elements.

A Hordijk [79] tension softening model was used for the smeared cracking elements in beams with little shear reinforcement (beams A0-A2). As mentioned earlier numerical difficulties were found in the beams with large number of stirrups crossing the crack interface due to excessive local cracking of the smeared crack elements near the stirrups at the level of the discrete crack (see Figure 7.34). This problem was overcome partially by using a linear softening for tension in the smeared elements instead of the Hordijk relationship [79]. In addition, the fracture energy was increased to 0.15 N/mm in the smeared elements of beams with large amounts of stirrups to account for tension stiffening effects. These modifications to the tensile behaviour of the smeared cracking elements influenced the load at the initiation of the discrete crack and the numerical stability of the analysis but not the ultimate load.

NLFEA results for beams without stirrups

The numerical predictions of the crack opening *w* and sliding *s* (Figure 7.35) were in excellent agreement with experimental results. In addition, the vertical deflections were better predicted using the discrete/smeared model than the pure smeared crack model, as shown in Figure 7.35. However, the ultimate strength of beam AG0 was over predicted. The numerical load-deflection curve indicated a change in stiffness at the load where failure occurred (point A in Figure 7.35), which was due to the propagation of the diagonal crack to the supports. The propagation of the main crack occurred though the smeared cracking elements right next to the interface plane due to considerations of the reinforced elements crossing the interface plane, which have been discussed previously.

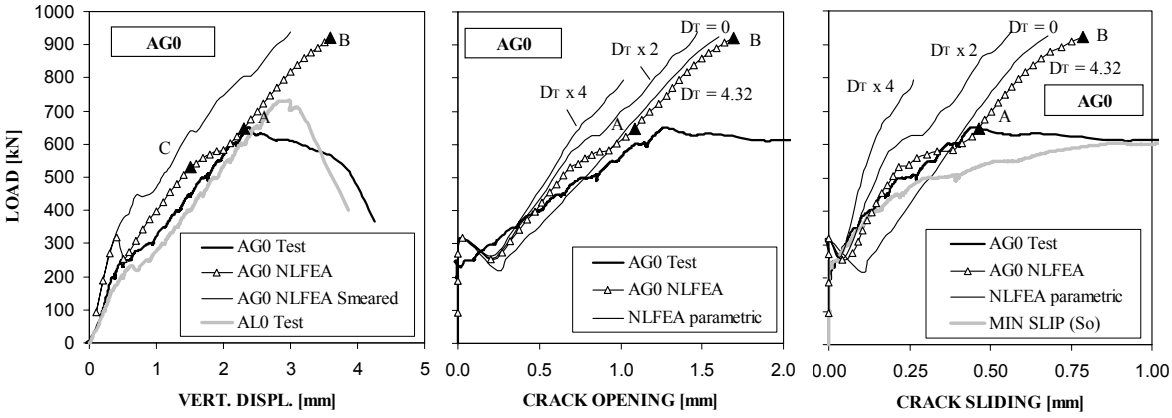

Figure 7.35: Comparison of numerical and experimental load-deflection curves and crack opening/sliding of beam AG0

The predicted crack opening and sliding shown in Figure 7.35 relate to the interface element nearest to the cross LVTD, which was located at mid-height of the beam. The crack opening and sliding obtained experimentally from beam AL0, which are not shown in order to simplify the figures, were very similar to those obtained from beam AG0. Figure 7.36 shows that the crack opening and sliding predicted was reasonably constant along the discrete crack that became active. Interface elements crossed by longitudinal reinforcement remained inactive thus both crack opening and sliding were negligible.

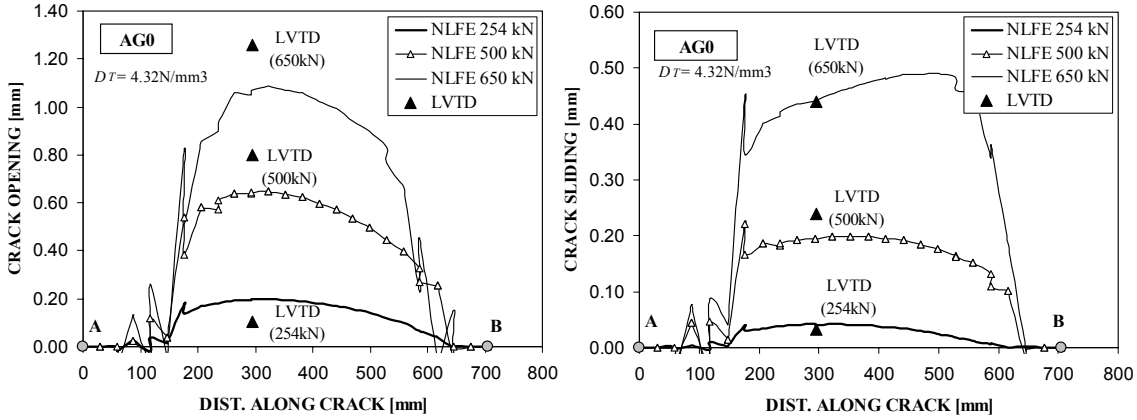

Figure 7.36: NLFE predictions of crack opening and sliding along interface plane

Close examination of the shear stresses predicted along the discrete crack that became active in beam AG0 (Figure 7.37), showed that the maximum values of τ_{cr} occurred at the top of the crack. This maximum value of τ_{cr} at load point A was equal to 4.33MPa at loads near failure, which agreed with the shear threshold value predicted by the STM-shear friction model described in section 7.5.2. In order to establish a reasonable comparison between the STM-shear friction model and the NLFEA, the reference crack inclination angle (α_{ref}) was adopted in the STM (see Figure 7.29). The shear stress at the crack predicted by the NLFEA at a load of 579kN, which corresponded to the ultimate load according to the STM, was 3.85MPa as opposed to 4.34MPa obtained in the STM (see Table 7.13).

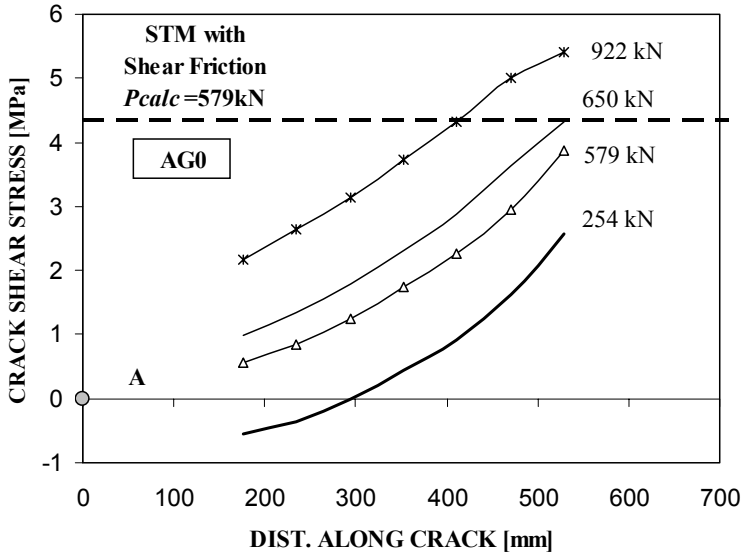

Figure 7.37: NLFE predictions shear stresses along active discrete crack compared with shear friction threshold value

In view of these results it seems clear that since no shear limit was imposed at the diagonal crack in the NLFEA, failure was governed by crushing of the strut rather than

failure at the shear crack itself. Furthermore, the ultimate load predicted in the NLFEA (922kN) was more consistent with the standard strut-and-tie prediction (830kN) than with the experimental value (651kN) or the STM with shear friction approach. In addition, the predicted load-deflection path between points A and B shown in Figure 7.35, had similar stiffness as the one observed in AG0 before failure. This stiffness also agreed with beam AL0, which had weaker concrete but failed at higher load due to crushing of the strut.

The effect of changing the shear retention factor β in the interface elements was examined. The objective of this analysis was to verify the sensitivity of the numerical predictions to the assumed parameter D_T (Table 7.14). Assuming values of the aggregate interlock stiffness (D_{ai}) equal to zero resulted in a premature failure at load point C (Figure 7.35), which was due to excessive concentration of compressive stresses at the element near the edge of the loading plate. Figure 7.38 shows the change in inclination of the principal compressive stress trajectories for different values of D_{ai}. It can be seen in Figure 7.38 (left) that assuming D_{ai}=0 lead to the entire load being transferred near the edges of the loading plates, where the discrete crack remained closed.

In order to avoid premature failure for such cases, the strength of the concrete at the elements near the loading plate was enhanced. For simplicity the concrete strength was factored by three for these elements.

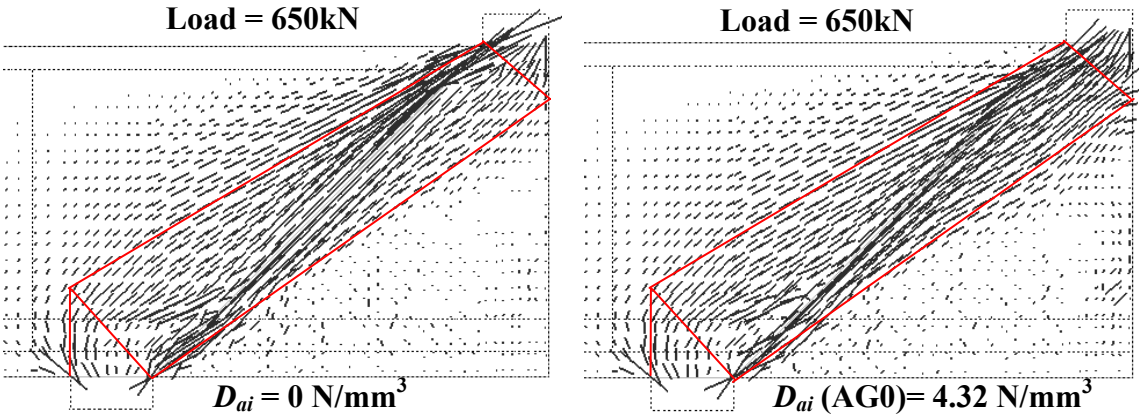

Figure 7.38: Principal compressive stress trajectories in the NLFEA for cases of zero and normal aggregate interlock stiffness assumptions

The predictions of crack opening and sliding using D_{ai} = 0, which are shown in Figure 7.35, were slightly higher than in the previous analysis, although the results were still acceptable. On the contrary, high values of the aggregate interlock stiffness resulted in a clear underestimation of w and s, especially on the crack slip. The results of the

parametric analysis are shown in Figure 7.35 for D_{ai} equal to two and four times the stiffness assumed in the first analysis (Table 7.14). The parametric analysis concluded that the values assumed initially for D_{ai} provided optimal predictions of w and s for beams A0. In addition, the principal stress trajectories had a better agreement with the STM than when low values of D_{ai} were used, which resulted in high concentration of stresses. The strut width predicted in the NLFEA and principal compressive stress trajectories were consistent with the STM, as shown in Figure 7.38.

NLFEA results for beams with stirrups

Good numerical estimations of crack opening and slip were also obtained for beams with stirrups as shown in Figure 7.39, although the slip was slightly overestimated for beams with large number of stirrups, such as beam AL4. A better performance of the NLFE model was achieved if the concrete strength of the elements adjacent to the loading platen was factored, results denoted as "high fc". An enhancement factor of three was adopted in order to assess the crack opening and sliding at loads near failure. As shown in Figure 7.39 the slip was clearly over predicted if the strength of these elements was not enhanced. This overestimation of the slip resulted from excessive cracking of the smeared cracking elements surrounding the interface plane at the top of the beam.

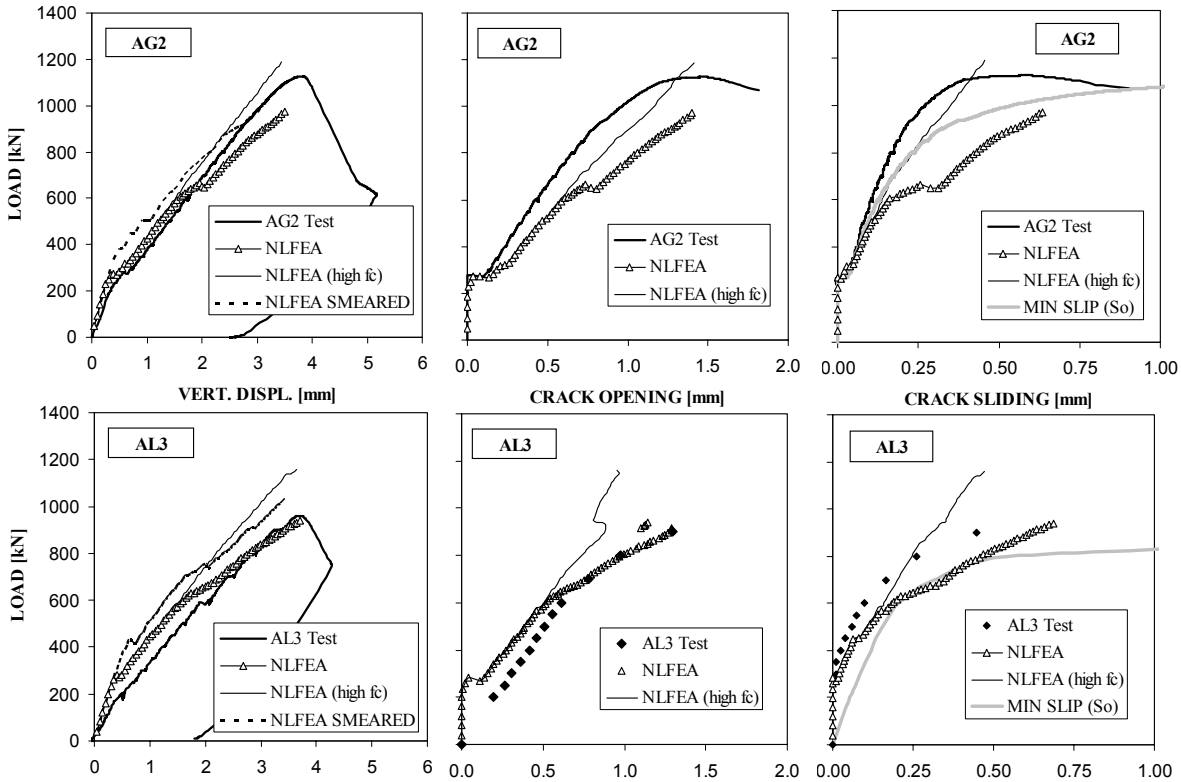

Figure 7.39: Comparison of numerical and experimental load-deflection curves and crack opening/sliding of beams AG2, AL3 and AL4

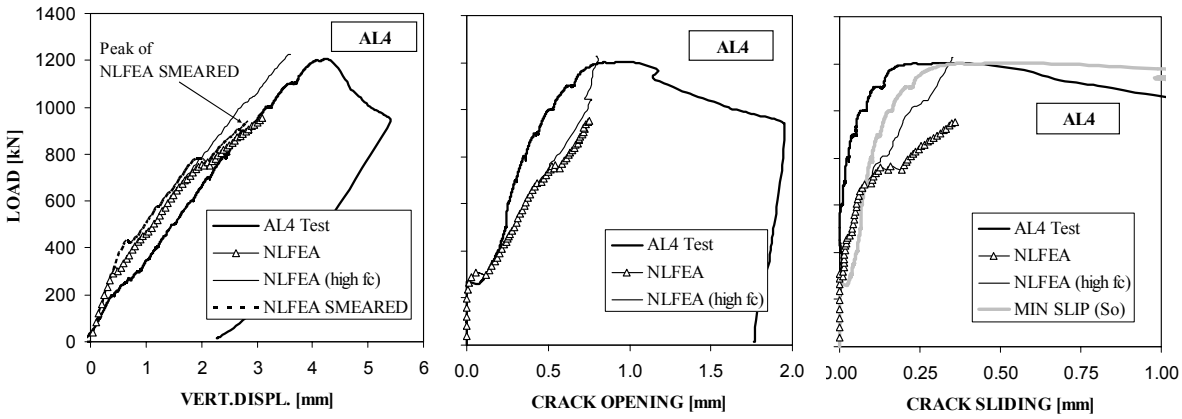

Figure 7.39 (Cont.): Comparison of numerical and experimental load-deflection curves and crack opening/sliding of beams AG2, AL3 and AL4

The large concentration of stresses at the edge of the loading plate predicted in the NLFEA of short beams with stirrups seemed to be related to the geometry of the top node as opposed to values of D_{ai} assumed in the model. In view of the results obtained for short beam without stirrups, low values of D_{ai} were avoided and average values shown in Table 7.14 were used in the NLFEA.

Figure 7.40 shows the principle compressive stress trajectories of beams AG3 compared with AG0 predicted by the NLFEA; the strut-and-tie model proposed has been superimposed. The slightly steeper direct strut, assumed in the STM for beam AG3, was consistent with NLFE predictions (Figure 7.40). In addition, the geometry of top and bottom nodes was similar in both models.

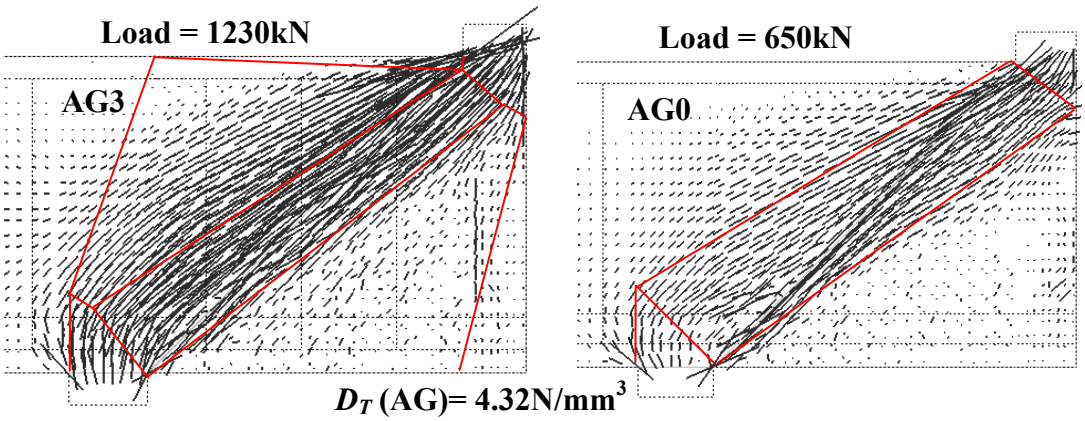

Figure 7.40: Principle compressive stress trajectories predicted in the NLFEA compared with STM for beams with and without stirrups (beams AG3 and AG0)

The crack opening obtained was constant along the discrete crack for early load stages, while for higher loads *w* was considerably smaller at points where the stirrups crossed the discrete crack, as shown in Figure 7.41. As mentioned earlier, these local variations in the crack width were expected since no bond-slip was taken into account in the NLFE model. The sliding was constant along the crack throughout the loading, as shown in Figure 7.41 for beams AL3 and AL4. However, the crack slip predicted in beam AL4 was only mobilized until a distance of 500mm from the bottom, which corresponded to the stirrup closer to the loading point.

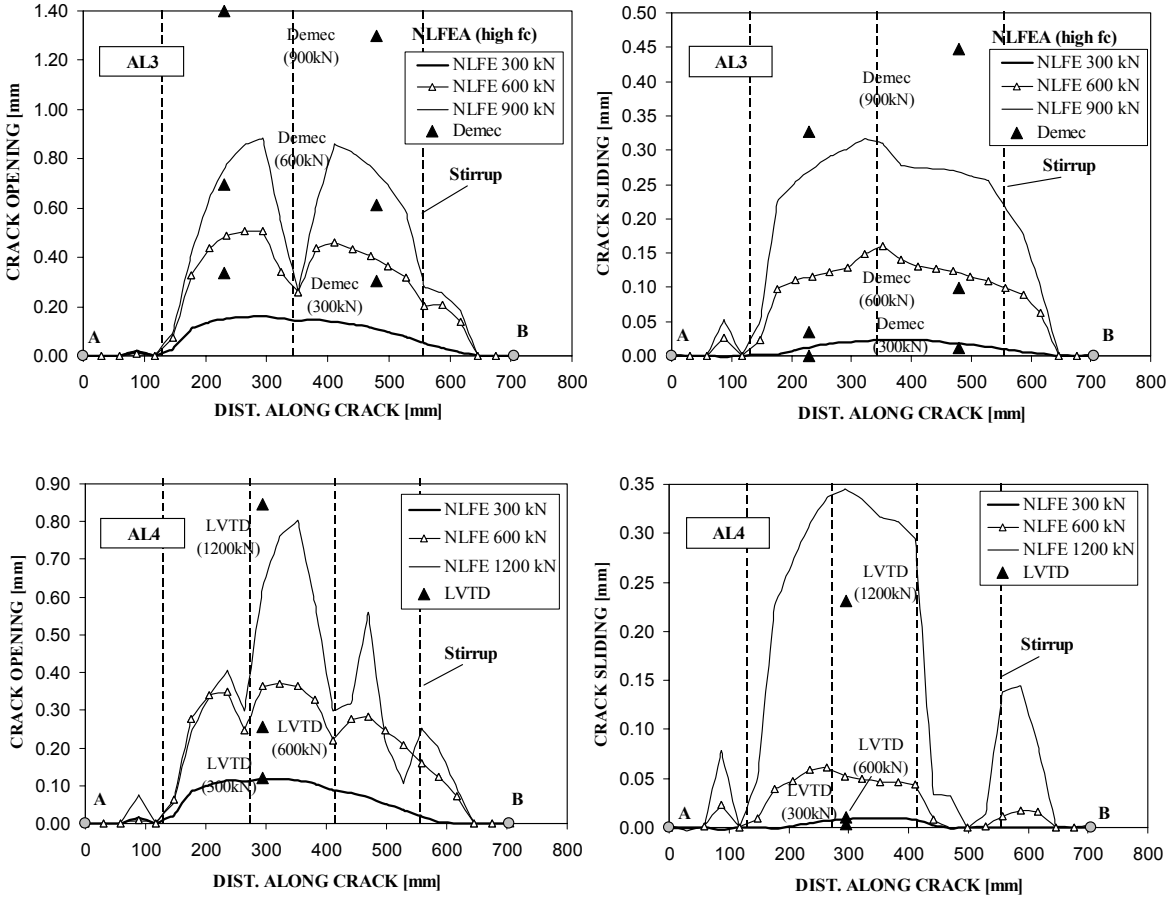

Note: P_{ult} (AL3) =961kN and P_{ult} (AL4) =1204kN

Figure 7.41: NLFE predictions of crack opening and sliding along interface plane (beams AL3 and AL4)

As discussed in previous section, beam AL3 had an unusually low strength in comparison the rest of beams AL. The shear stresses at the main diagonal crack predicted in the NLFEA are shown in Figure 7.42 for the interface elements that became active. The magnitude of the shear stresses obtained was similar to those for beam AG0, see Figure 7.37. Moreover, the shear stress predicted at the crack in beam AL3 was in good agreement with those obtained from the STM–shear friction model. Figure 7.42 shows a similar distribution of shear stresses along the discrete crack in beam AL3 as in beam AG0. The value assumed in the NLFE model for D_{ai} did not have a significant effect on the predictions of τ_{cr}, as shown in Figure 7.42. The results are shown for a load of 750kN, which corresponds to the ultimate load according to the STM. The NLFE prediction for the max τ_{cr} at failure load of 960kN was only 5% higher than the ones shown in Figure 7.42. The shear stress interpolated from the push-off tests for beam AL3 was 3.64MPa, which is slightly higher than the values predicted in the NLFEA and STM model (see Figure 7.42).

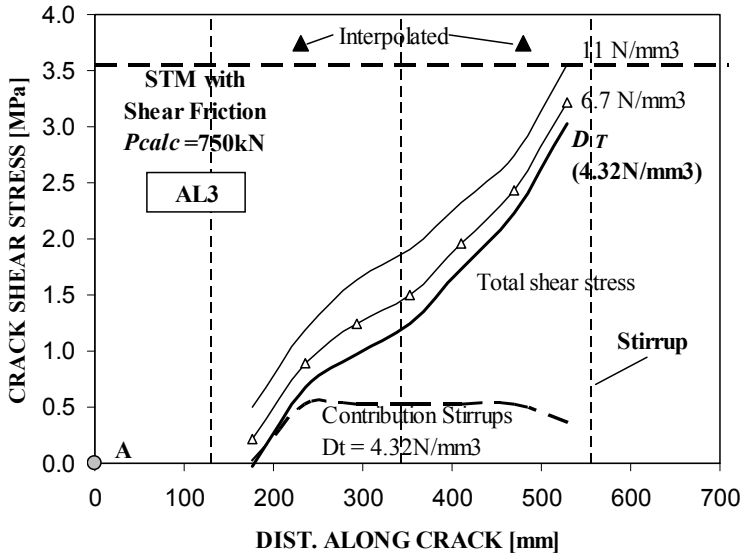

Note: results shown for load of 750kN (P_{ult}=961kN)
Interpolated results for shear stress at the crack were obtained from (*w, s*) data from Demec crosses

Figure 7.42: NLFE predictions shear stresses along active discrete crack compared with shear friction threshold value

The shear stresses obtained in the NLFEA were in reasonable agreement with previous estimations, although clear values of τ_{cr} could not be obtained for all specimens tested due to numerical oscillations in beams with large number of stirrups. These numerical difficulties were due to discontinuities in the crack slip along the interface plane, which were similar to the one shown in Figure 7.41 at the top of beam AL4. These local effects were aggravated for beams AG with a higher concrete strength.

Final remarks about NLFE predictions

Several simplifications were assumed regarding bond-slip, dowel action and aggregate interlock behaviour in the NLFEA. However reasonable predictions were obtained for crack opening and slip at the shear diagonal crack of short span beams. In addition, even though the inclination of the main crack in the NLFEA was assumed constant, the numerical predictions of *w* and *s* were still acceptable for beams such as AL0, where this assumption could be more dubious (Figure 7.30).

The numerical predictions supported the low values obtained experimentally for crack slip compared with crack opening, discussed in section 7.5.1 (see Figure 7.27). These reduced values of *s* compared to *w* justified the use of simple discrete crack model as opposed to a more realistic crack dilatancy model, in which shear stiffness is a function of the crack displacements. In addition, although a constant shear retention factor was applied at the discrete crack, the shear stresses predicted in the NLFE model were in a similar range to those given in the STM-shear friction model.

7.6 Additional considerations on short span beams

As shown in previous sections the sensitivity of the ultimate strength predictions of short span beams to different geometrical and material parameters varies significantly depending on the design method applied. In this chapter, the influence of parameters such as the clear shear span to effective depth ratio (a_v/d) or stirrup index on shear strength predictions has been shown. In this section additional considerations are made regarding bearing plates, size effects and relative position of stirrups.

Bearing plates

As discussed in section 7.3.4, the influence of the bearing plates on the ultimate strength of short span beams is ignored in many cases. The influence of using roller supports in beam tests was also discussed and an approximated approach was suggested by the author to include them in the STM (see section 7.3.6). However, the existing design methods for short span beams, which are described in sections 7.2.1 and 7.3.1, are inconsistent with each other with regards the influence of the size of bearing plates.

The strut-and-tie models are very sensitive to changes in the length of the plates since the inclination and width of the direct strut are highly dependent on these geometrical constraints. On the other hand, equation (7.11) in MC90 ignores completely the size of the bearing plates. The remaining methods reviewed consider the size of the bearing plates indirectly through the enhancement factor β, which increases linearly with the length of the plates. Furthermore, the standard truss method applies factor β to the concrete component only and so the influence of the size of the bearing plates is independent of the stirrup index, which is not the case for the rest of the design methods.

Unfortunately there is a lack of experimental data which provides clear evidence regarding the consequences of changing the size of the plates in short span beams since the bearing plates were generally kept constant within each set of beam tests. A group of eight beams was selected from the database with similar *a/d* (1.49-1.56) and *SI* (0.04-0.06) in order to avoid dispersions in the predictions (see Figure 7.43). The beams had different relative bearing lengths with respect the shear span (a/a_v = 1.17-1.35-1.45). A parametric analysis was performed for each design method, changing the size of both support and load plates simultaneously for beams C2-4 (Clark [130]), which had average values of the *SI*. The results from the author's parametric analysis showed an increase in strength due to reducing a_v whilst keeping *a/d* constant, which was in good agreement

with the strut-and-tie model predictions. Values of a/a_v below 1.1 corresponded to failure of the bearing plates, which is taken into account in the strut-and-tie based methods as shown in Figure 7.43.

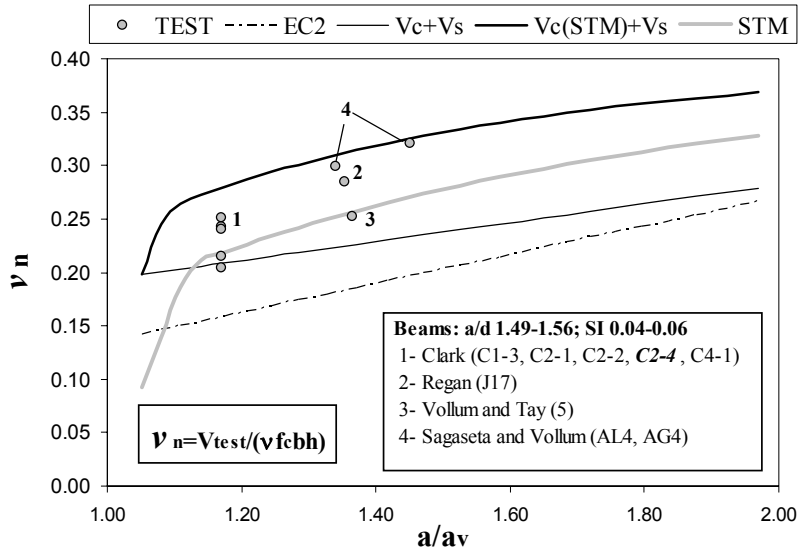

Note: parametric analysis carried out by changing bearing plates in beam C2-4 (Clark [130]);
Experimental results from data base shown in Table 7.7(a)
l_b/d ratio is 0.22 for all beams except for AL4 and AG4 where l_b/d is 0.28 and 0.45 respectively
c/d ratio was similar in all beams (0.17-0.12)

Figure 7.43: Influence of size of bearing plates (a/a_v) for beams with similar *SI* and *a/d* ratios

Short span beam tests carried in this work showed that failure could be encourage in one of the shear spans by increasing the bearing plate of the other span by 37.5% ($l_{b,left}$=125mm, $l_{b,right}$=200mm). This difference in the size of the bearing plates results in a 20% increase in strength according to the STM as opposed to 8% if the simplified EC2 method is applied. Of the 8 beams tested, 6 failed in the shear span with smaller bearing plate and only two on the span with $l_{b,right}$ =200mm.

Walraven and Lehwalter [171] derived interpolated surfaces from the basis of test results of short span beams without stirrups, in which various sizes, *a/d* ratios and support widths were tested (see Figure 7.44). The maximum stresses in the concrete struts were calculated using a STM model with hydrostatic nodes, as shown in Figure 7.44. The interpolated surfaces provided showed that the stresses in the strut decrease with increasing *a/d* and l_b/d, although they were in general higher than the constant νf_c limit used in practice. As reported by Walraven [23], this limit seemed valid for members with a/d<2, depths up to 1m and l_b up to around 0.25d.

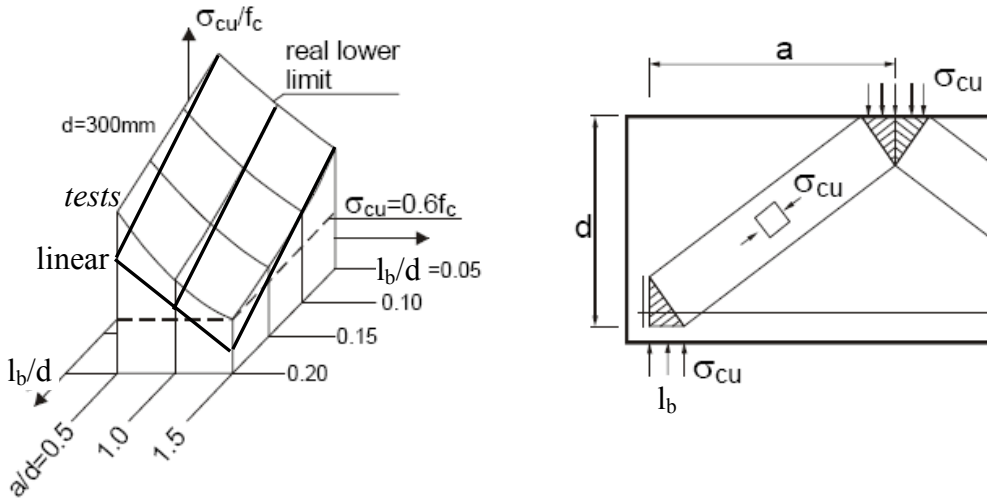

Figure 7.44: Maximum stresses in concrete struts according to experimental data (adapted from Walraven & Lehwalter [171])

It is interesting to highlight in Figure 7.44 that the rate at which stresses decreased with increasing l_b/d was not linear. Hence ultimate failure load must have increased slightly by increasing l_b, which is consistent with the results obtained in the parametric analysis shown in Figure 7.43.

Size effect

The reduction of shear strength of reinforced concrete beams with increasing the size of the member, also know as "size effect", was first raised by Kani [127] in the mid-1960s. Currently, design provisions are being revised with regards size effects since as reported by Collins et al. [12], old design codes have been shown to be inadequate in this matter.

Researchers have justified size effect by means of different factors influencing the shear behaviour of reinforced concrete beams. Taylor [172] suggested that keeping the aggregate size while increasing the beam size would decrease the aggregate interlock contribution hence size effect would occur. However, tests carried out by Walraven [173] using lightweight aggregate, which fractured at cracks, was also subjected to size effects. In view of these results and further experiments, Walraven & Lehwalter [132] suggested that size effect was primary due to the rate of crack formation rather than aggregate interlock. According to Walraven & Lehwalter [132], the energy-release of larger members is greater compared with smaller beams hence the crack pattern developed much faster in larger beams. In addition, the capacity of cracks to transmit tensile forces is significantly lower for larger specimens since cracks are considerably wider. Several size effects factors have been proposed by different researchers, such as Bazant & Kim

[174] or Fujita et al. [175]. Tests carried by Fujita et al. [175] for high-strength concrete showed size effect to be related directly with the concrete strength f_c.

On the other hand, the modified compression field theory (MCFT) developed by Collins & Vecchio [8], size effect is assumed to be caused by the loss of shear stress transmitting capacity of wide crack for deeper members, due to larger crack spacing. This brings back to Taylor's premise of aggregate interlock as main reason for size effect. On the basis of the MCFT authors such as Sherwood et al. [176], Lubell et al. [30], Bentz & Collins [177] support the idea of aggregate interlock capacity as the main parameter for size effect. Lastly, another possible cause for size effect, which was reported by Kotsovos & Pavlovic [155] (see section 7.3.4), is related to unintended out-of-plane actions induced in very slender members.

Although there is not a general agreement for explaining size effect in RC beams, it is widely accepted that it can be significant, especially for cases such as slender beams (a/d>3.0) without stirrups. Furthermore, size effect is believed to be mitigated in beams with stirrups due to closely spaced cracks with lower crack widths (Collins & Kuchma [178]). As reported by Tan & Lu [139], less experimental data is available regarding size effects on short span beams compared with slender beams. As described in previous section, especial attention must be paid into the size of the bearing plates since in many instances the length of the bearing plates were kept constant while changing the member depth. In such instances, it can be questionable whether the decrease in shear strength is a measure of size effect or a consequence of variations in the a_v/d ratio. According to Zhang & Tan [140], this might have been the problem in several sets of experimental data (Collins & Kuchma [178], Tan & Lu [139], Yang et al. [179]).

Early experimental work carried out by Walraven & Lehwalter [132] suggested that short span beams are subjected to size effects equally as slender beams. According to their work, size effect in short span beams is related to the direct strut component only and not to the load path provided by stirrups. As shown in Figure 7.45, the interpolated surface of maximum stresses in the strut for different a/d and l_b/d ratios, was considerably lower for members with d=1m compared to 300mm, which is shown in Figure 7.44. In view of these results, empirical equations with the enhancement factor $\beta=2d/a_v$ were introduced in EC2 as an alternative method to STM. Attempts have been made to include size effect factors into STM models (see example in STM model proposed by Zhang & Tan [140]), although these types of approaches have yet not been implemented in design codes.

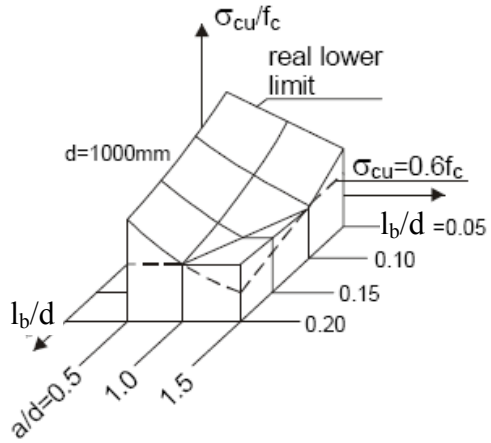

Note: refer to Figure 7.44 for members with d=300mm

Figure 7.45: Maximum stresses in concrete struts according to experimental data of members with depths of 1m (taken from Walraven & Lehwalter [171])

The performance of the predictions from the strut-and-tie models described in sections 7.2.3 and 7.3.5 for cases with and without stirrups were investigated for different effective depths. The predictions of the proposed strut-and-tie model for short span beams with stirrups did not seem to be influenced by the effective depth, as shown in Figure 7.46 (left). This supports Walraven & Lehwalter's [132] findings for short span beams with stirrups.

On the other hand, the STM strength predictions of beams without stirrups tested by Walraven & Lehwalter [132] (see Table 7.2) became less conservative for larger values of *d*. According to the authors these beam tests showed a significant size effect. However, the STM applied to more recent results provided by Zhan & Tan [140] (a_v/d=0.94) with similar beam heights, did not show such a pronounced size effect (see Figure 7.46).

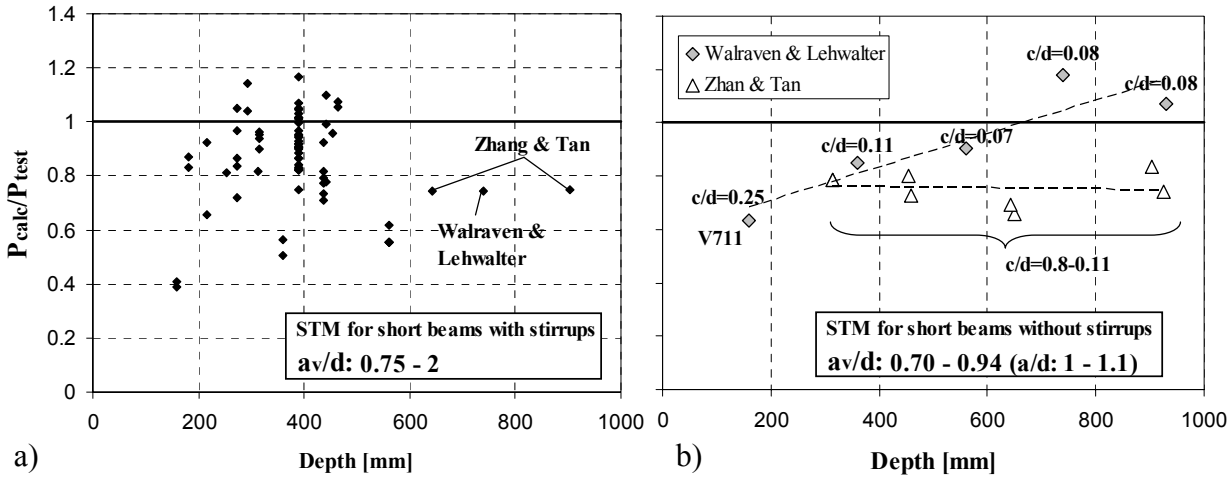

Figure 7.46: Size effect on short span beams; a) beams with stirrups ($0.75<a_v/d<2$; Table 7.7); b) beams without stirrups (tests by Walraven & Lehwalter [132] and Zhang & Tan [140])

The difference between predictions of Walraven & Lehwalter's and Zhan & Tan's test (Figure 7.46.b) might seem contradictory regarding the relevance of size effect, since both sets of experiments had similar f_c (20-30MPa), longitudinal reinforcement ratios (~1.2%) and a/d (1-1.1%). In addition, the bearing plates were scaled appropriately in both sets of beams so that l_b/d was maintain constant; l_b/d were around 0.30 and 0.15 in beams tested by Walraven & Lehwalter [132] and Zhang & Tan [140] respectively. These variations in relative size of the bearing plates could justify that the P_{calc}/P_{test} ratio was generally higher for Walraven & Lehwalter's beams using the STM (Figure 7.46.b). Moreover, according to Figure 7.44(left) stresses in the strut could be overestimated using the constant value of νf_c for a/d=1 and l_b/d=0.30, as in beams tested by Walraven & Lehwalter [132].

Most importantly, beam with lowest value of d (V711, see Figure 7.46.b), which had the lowest P_{calc}/P_{test} ratio, had a considerably large value of the concrete cover (c/d=0.25). The c/d ratio of beam V7110 was three times larger than for the deeper beams, which explains the conservative prediction of this beam using the STM model. This raises the question of whether the data shown in Figure 7.46.b is reflecting a size effect problem or not.

Recent experimental and analytical work carried in Toronto by Uzel et al. [180] on large footing with no stirrups and a/d between 1 and 3, seem to suggested that size effect is much less critical in beams with a direct strut action than slender beams. Authors such as Collins [181] believe that size effect is unimportant for short span beams, since failure is generally governed by crushing of the direct strut and not by the lost of shear stress capacity along the main diagonal crack. Although this assumption might be true for a large number of cases, it seems questionable for others, such as beams AG0 and AL3 tested in this work, in which a shear proper type of failure was obtained (see section 7.5). In the author's opinion, the relative position of the main diagonal crack respect the direct strut, which seems difficult to predict a priori, could have an effect not only on the ultimate strength but also on size effect considerations. According to the author, additional experimental data from short beams failing in a shear proper type of failure and different beam depths is required in order to verify this hypothesis.

Relative position of stirrups

One aspect that is generally ignored in the design of short span beams is the relative position of the stirrups within the effective shear span. The only restriction regarding the location of the stirrups is that they must lie within the effective shear span in order to be mobilized when crossed by the main diagonal crack. Design codes usually recommend a uniform distribution of the transverse reinforcement, which also enhances ductility and control over the crack width.

From the design methods discussed in this chapter only the proposed strut-and-tie model makes allowance for changing the actual position of the stirrups. Parametrical analysis of the strut-and-tie model showed that changes in the position of the stirrups within the effective shear span had a small effect, less than 1%, on the predictions of the ultimate load. The highest strength scenario was obtained by placing the stirrups towards the support, with a small spacing between the stirrups. Even for this extremely odd scenario, the strut-and-tie model predicted only a 0.78% increase in strength from the normal case with uniform stirrup distribution along the clear shear span.

No experimental evidence could be found regarding the influence of changing the position of the stirrups in short span beams, although the parametric study supported the idea that a non-uniform distribution of the stirrups did not offer any particular advantage in terms of strength compared to the conventional uniform layout.

7.7 Conclusions

Design codes make the allowance of applying alternative design methods for short span beams in order to take into consideration the enhancement in shear strength due to arching action. According to the analysis of the experimental database gathered of short span beams it was concluded that existing design equations for short span beams with and without stirrups were in general over conservative. The strut-and-tie model proposed provided better predictions of the ultimate shear strength, although a large scatter was found for short span beams without stirrups. This scatter was most likely due to the influence of the position of the main diagonal crack with respect the direct strut. A modified STM was examined, in which a shear friction relationship was implemented in the model. This approach provided a formal explanation for the low strength of beams AG0 and AL3. Furthermore, if a more elaborate crack friction relationship was applied, aspects such as crack width and aggregate size could also be taken into account. However, up-to-date these alternative techniques implemented in STM, seem not suitable for design purposes due to excessive uncertainties in the material and geometrical parameters involved.

The sensitivity of different design parameters such as the clear span to effective depth ratio or the stirrup index were examined for the proposed STM model and compared with existing design methods. The performance of EC2 simple approach for short span beams with stirrups was highly dependent on the stirrup index. Similar problem was observed in MC90 simplified formula, which provided rather conservative results. The STM overcame this dependency between the predictions and *SI* due to the fact that the contribution of the direct strut reduces as *SI* increases. On the contrary, the STM was sensitive to variation on a_v/d. According to experimental data, the range of validity of a_v/d in the STM was confirmed between 1 and 2. In addition, yielding of the stirrups was assumed in the STM. The proposed STM for short span beams with stirrups is not applicable for large values of *SI*, in which the direct strut vanishes (λ=0). However, the critical value of SI_{max} at which λ=0 is significantly larger than general stirrup indeces provided in practice; only one beam out of 143 investigated had a stirrup index greater than SI_{max}. The strut-and-tie model for short span beams developed by the author was also applicable to short span beams strengthened in shear with externally bonded CFRP sheets to the full depth of the beam.

The NLFEA performed for short span beams A, showed that ultimate loads and crack patterns could be estimated accurately. However, the sensitivity of the numerical predictions to material parameters such as tensile strength was considerable. The multi-directional fixed smeared crack model was finally chosen between all the smeared cracking models examined, although the model faced numerical difficulties near failure. The implementation of interface elements with discrete crack formulation was required in order to assess the relative crack displacements and shear stresses along the crack. Although the predictions of w and s were reasonable, several assumptions had to be made regarding aggregate interlock behaviour, dowel action and bond-slip in order to avoid numerical instabilities.

In view of the experimental and analytical results, the influence of the fracture of the aggregate was insignificant for beams A. Design methods examined, including the proposed STM, had similar performance for limestone and gravel beams. Other aspects such as the location of the shear crack in relation to the direct strut seemed to have a more important role on the ultimate strength than the roughness of the main crack in beams A. The crack opening-sliding ratio obtained at the main diagonal crack was around 3, which is considerably larger than in slender beams or push-off tests ($\delta w/\delta s \sim 1$). This large value of $\delta w/\delta s$, which was in agreement with predictions from the NLFEA, suggested that the shear stresses developed at the crack by means of aggregate interlock were small.

CHAPTER 8 - Analysis of Slender Beams

8.1 Introduction

Extensive experimental and numerical research has been carried out in the past into shear behaviour of RC slender beams, especially for beams without stirrups. According to experimental work of slender beams without stirrups, three main shear-carrying mechanisms have been reported; namely shear carried at the compression head, aggregate interlock action and dowel action. The contribution of each mechanism is not clearly understood, although it is generally accepted that aggregate interlock action along the crack surface is critical at failure due to the formation of the diagonal shear crack from a previous flexural crack. According to experimental evidence from Taylor [1] or Regan et al. [4], there seems little doubt that shear strength is reduced in beams without stirrups due to aggregate fracture at the crack. However, the influence of aggregate fracture is less clear in beams with stirrups due to lack of appropriate test data.

In addition, most of experimental data available of slender beams with stirrups consists of simply supported beams where there is a clear interaction between bending and shear. Moreover, the shear strength of beams loaded at mid-span has the unavoidable contribution of shear at the compression head, which is generally difficult to estimate. Empirical data of continuous beams with stirrups, which were critical in shear, are rarely found in the literature. Design methods, such as the variable strut inclination method suggested in EC2, have been validated using simply supported beams but few using beams with a point of contra-flexure. To the best of the author's knowledge the influence of aggregate fracture into the shear strength of continuous beams with stirrups has not yet been investigated.

In this chapter the experimental results of beams B0, B, C and D (see chapter 6) are analysed using proposed design methods in EC2, BS8110 and CSA, as well as numerical predictions from non-linear finite element models developed by the author. An experimental database of continuous beams tested by other authors was gathered to verify the results obtained from beams B and C. The results were also compared with traditional simply supported beam tests found in the literature, similar to beams D tested in this work.

The crack pattern and crack dilatancy at the main shear cracks were modelled numerically using NLFEA and analytically using discrete crack truss models. Results are compared with those obtained for short span beams, which are discussed in previous chapter. In order to estimate the shear stresses at the crack in beams B, the test data from the push-off tests shown in chapter 4 was interpolated. These empirical interpolated values were used to validate analytical discrete approaches developed. The discrete crack-slip model presented for shear panels (see section 5.5) was adapted in order to predict the relative crack displacements and stresses along shear cracks in continuous beams. On the other hand, predictions of shear stresses at the crack from truss models with crack friction are also discussed.

8.2 Analysis of slender beams without shear reinforcement (Beams B0)

8.2.1 Comparison between test results, EC2 empirical formula and MCFT; influence of aggregate fracture

The experimental results from slender beam without shear reinforcement (beams B0) showed a good correlation with previous tests from Regan et al. [4] with similar type of aggregate. As described in chapter 6, the type of failure observed for limestone and normal gravel beams were identical to each other. Failure occurred suddenly after the formation of the critical diagonal crack, which extended horizontally into the compression zone and along the flexural reinforcement towards the support. The failure crack surface was smoother for BL0 than for BG0 due to aggregate splitting at the crack of the limestone aggregate. The crack patterns were similar between limestone and gravel specimens with the only exception that the angle at which the diagonal crack met the horizontal dowel crack was slightly steeper for the limestone beams than for the gravel beams, as described in chapter 6.

The influence of aggregate fracture on shear strength prediction of slender beams without stirrups was examined at first using the EC2 empirical formula (8.1), applying no partial material safety factors:

$$V_{Rd,c}(EC2) = 0.18.\left(100.\rho_l f_c^{'}\right)^{1/3}.\left(1+\sqrt{200/d}\right)bd \qquad \ldots (8.1)$$

where ρ_l = longitudinal reinforcement ratio; $f_c^{'}$ = cylinder compressive strength; d = effective depth; and b = width.

Table 8.1 summarizes the predictions of the ultimate strength of beams B0 using characteristic strengths (γ_f=1). Predictions are shown in Table 8.1 for both cases of ignoring and considering the limitation on the concrete strength of 60MPa, as recommended in the UK National Annex. As expected from Regan's experiments, the V_{test}/V_{calc} ratio was lower than 1 for all beams B0 tested. The limitation on the concrete strength to 60MPa had a noticeable improvement on the predictions of the gravel beams, which had a concrete strength of 80.2MPa. However the limitation of concrete strength showed to be inefficient for the limestone beams since $f_c^{'}$ was only 68.4MPa. Whilst safe, the limit on the concrete strength seems inconsistent with experimental evidence, since this constraint was only effective for the gravel beams, where only a small portion of the

course aggregate fractured at the crack (~30%), and not in limestone specimens where all aggregate particles fractured. Hence, this supports Regan's [4] conclusion in which the f_c'≤60MPa limitation should be considered as a compromise solution before a more rational approach is developed.

Beam	V_{test} [kN]	V_{flex} [kN]	*EC2 empirical formula* V_{test}/V_{calc}	*EC2 empirical formula* V_{test}/V_{calc} [f_c'≤60MPa]	*Response 2000* V_{test}/V_{calc} [a_{eff}=10mm]	*Response 2000* V_{test}/V_{calc} [a_{eff}=0]
BG0-1	61.31	100	0.76 (1.14)	0.84 (1.26)	0.88 (1.34)	0.94 (1.44)
BG0-2	63.11	100	0.78 (1.17)	0.86 (1.29)	0.91 (1.38)	0.97 (1.48)
BL0-1	46.86	98.5	0.61 (0.91)	0.64 (0.96)	0.71 (1.08)	0.76 (1.16)
BL0-2	54.07	98.5	0.71 (1.06)	0.74 (1.11)	0.82 (1.25)	0.88 (1.34)
	Avg.	***BG0***	0.77 (1.15)	0.85 (1.27)	0.89 (1.36)	0.95 (1.46)
		BL0	0.66 (0.98)	0.69 (1.03)	0.76 (1.16)	0.82 (1.25)

Note: values in parenthesis correspond to design values (EC2: γ_c =1.5; CSA: γ_c =1.53)
Parameters adopted in Response 2000: base curve (Popovic/Thorenfeld/Collins), Comp. Softening (Vecchio & Collins 1986), Tension Stiffening (Bentz 1999), crack spacing (auto), f_{ct} and ε_c' (auto)

Table 8.1: Predictions of ultimate strength using EC2 empirical formula

As shown in Table 8.1, the V_{calc}/V_{test} ratio using equation (8.1) was 16% larger for the limestone beams than for the normal gravel beams due to fracture of the aggregate. These results were consistent with Regan's [4] findings for beams with similar f_c' and d, as shown in Figure 8.1. The interpolated surfaces proposed by Regan clearly illustrate that the predictions worsens for higher beam depths and concrete strengths.

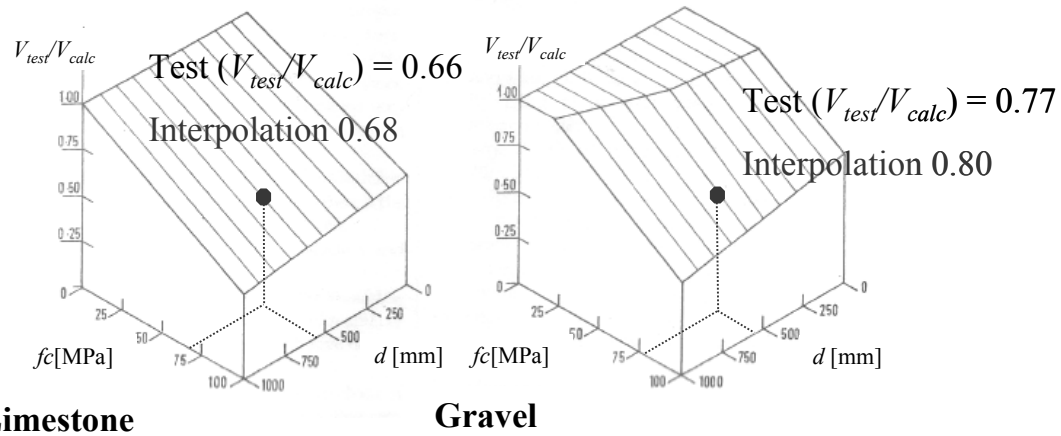

Figure 8.1: Correlation of experimental results of beams B0 with interpolated surfaces (V_{test}/V_{calc}-f_c-d) proposed by Regan [4] for limestone and gravel aggregate concrete beams without stirrups using EC2 empirical formula

Predictions from sectional approach using Response 2000 (Table 8.1), which is based on MCFT, are more accurate than EC2 empirical formula, although the V_{test}/V_{calc} ratio was still lower than 1 for all beams (no material factors of safety applied). The crack spacing predicted using CEB-FIB [6] formulas implemented in MCFT, were in agreement with experimental values. Moreover, the maximum vertical deflections predicted were between 4 and 5mm, as observed in the tests.

Again, predictions using Response 2000 are shown for two distinctive cases; firstly with an effective aggregate size (a_{eff}) equal to 10mm and secondly with a_{eff} equal to zero. The second case corresponds to the CSA recommendations for the given concrete strengths, while the former (a_{eff} =10mm) would be assuming that the aggregate did not fracture at the crack independently of $f_c^{'}$, which was the case for beams BG0. As shown by figures in Table 8.1, reducing a_{eff} provided a similar improvement of the V_{test}/V_{calc} ratio for all beams, which seemed to be more rational than the simpler approach suggested for EC2. The V_{test}/V_{calc} ratio is very similar for BG0 and BL0 if a_{eff} is taken as 10mm for the gravel and zero for the limestone beam, as suggested by observed behaviour.

In view of these results it can be concluded that both EC2 and MCFT constraints applied to deal with aggregate fracture, which are based on concrete strength rather than type of aggregate, can be used to obtain safer design strengths. However, these approaches are not necessarily consistent with experimental data, as shown for beam BG0. Although to be fair, MCFT approach seems more rational from a theoretical perspective. In addition, this approach was more effective than EC2 method for beam BL0 in which the aggregate fractured completely.

8.2.2 Predictions of NLFEA using smeared cracking models

Numerical simulations using a non-linear finite element analysis of beams B0 were carried by the author using the three smeared cracking approaches described in chapter 3: total strain fixed crack model, total strain rotating crack model, multi-fixed crack model. A shear retention factor β of 0.1 was used in both totally fixed and multi-fixed models. The threshold angle (α) was selected as 30° in the multi-fixed model, according considerations made for multi-directional fixed models in section 3.2.1. The remaining material properties considered in the models are summarized on Table 8.2. The concrete elastic modulus (E_c), tensile strength (f_{ct}), compressive strength (f_c') and the steel yield strength (f_y) were obtained experimentally whilst the remaining parameters had to be estimated. The stress-strain models used were the Hordijk softening curve for tension and the parabolic curve proposed by Feenstra [82], which are defined by respective tension and compression fracture energy, see section 3.3.

Concrete	***BG0***	***BL0***	**Steel**	***Plates***	***Long reinf.***
E_c [MPa]	42608	34969	E_s [GPa]	200	200
ν	0.2*	0.2*	ν	0.3	0.3
f_{ct} [MPa]	5.7	4.9	f_y [MPa]	500	580
G_f [N/mm]	0.113	0.101			
f_c [MPa]	80.2	68.4			

Notes: * For the Total Strain models $\nu = 0$
+ An estimated value of $G_c = 100 G_f$ was assumed, where $G_f(\text{MC90}) = G_{fo}.(f_{cm}/f_{cmo})^{0.7}$

Table 8.2: Material properties in NLFEA

The total strain fixed crack model incorrectly predicted flexural failure and consequently overestimated the failure load (Figure 8.2). The use of totally fixed crack models within a total strain formulation can give inconsistent results in cases where cracks cross previous cracks with different inclinations. On the other hand, the total strain rotating and multi-fixed models predicted the ultimate load and mode of failure satisfactory as shown in Figure 8.2. However, numerical difficulties were faced at loads near experimental failure, which needs further discussion.

The iterative procedure in the multi-fixed model diverged on the last load step, although the ultimate load corresponding to the last converged load step was very similar to the experimental value, as shown in Table 8.2. Divergence of the iterative process in a NLFEA is not always related to failure (Borst & Nauta [67]), although in this case it appears to be related to the sudden formation of the diagonal crack.

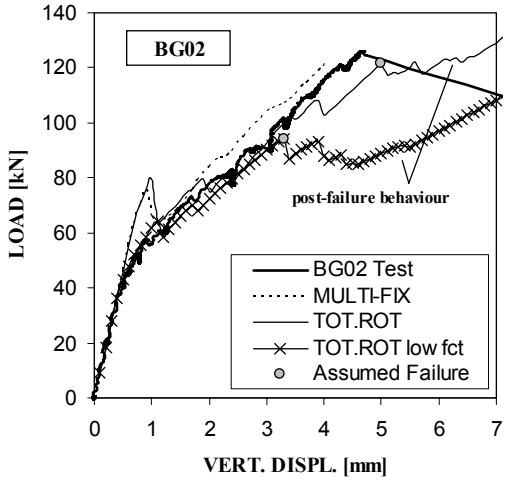

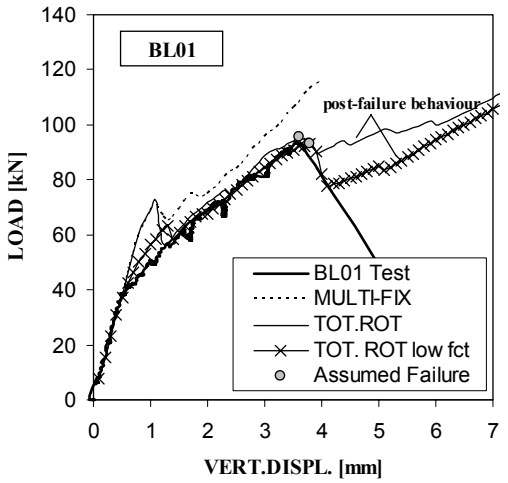

Beam	P_{test}* [kN]	P_{flex} [kN]	V_{test}/V_{calc} NLFEA Tot. Fix	NLFEA Tot. Rot	NLFEA Mult-fix
BG0	124.42	200	0.57	1.02	1.01
BL0	100.92	197	0.45	1.06	0.87
	Mean/Std.Dev.		0.51/0.08	1.04/0.02	0.94/0.10

Note: P_{test}* is the average value of beams B01 and B02
In the total strain rotating model the failure load is taken at load step where the diagonal crack was predicted (see circle mark); load branch above this load is denoted as "post-failure behaviour"

Figure 8.2: Performance of smeared cracking models for slender beams without shear reinforcement

The total strain rotating model provided sensible predictions for the failure load and crack pattern but the predicted post-failure response was unrealistic as shown in Figure 8.2. It is important to note that failure in the total strain rotating model was assumed at load step in which the diagonal crack was predicted to form. This critical step also corresponded to a considerable increase in vertical deflection; refer to circle mark in Figure 8.2. A considerable amount of load was predicted to be carried after this point, which was not consistent with experimental evidence. This spurious load branch, which is partially shown in Figure 8.2, is denoted as "post-failure behaviour".

The increment in load obtained in the post-failure branch was accompanied with the development of a horizontal smeared crack along the longitudinal reinforcement as shown in Figure 8.3. This suggests that the spurious load mechanism obtained seems to be related to the complete debonding of the concrete from the longitudinal reinforcement at failure not being reflected in the NLFE model. This is further supported by NLFEA of small scale beams carried by Ueda [182], which showed that a discrete horizontal crack

along the reinforcement had to be introduced in the model in order to obtain reasonable failure loads.

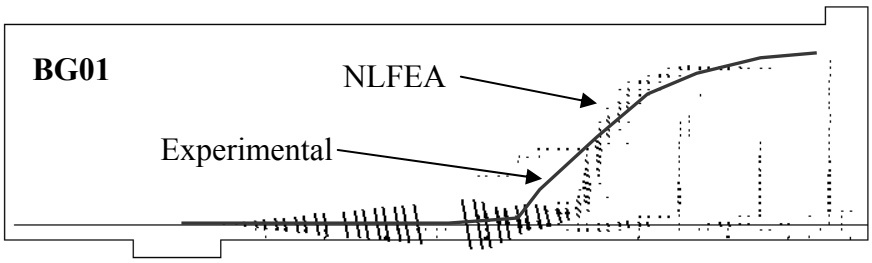

Figure 8.3: NLFEA (total strain rotating) crack pattern predictions, post-failure behaviour

Experimental data from the post-peak branch is rarely available for slender beams without stirrups. Experimental work from Chana [183], which included high-speed recording of crack widths at the dowel and diagonal cracks, showed that after the peak load was reached the dowel crack opened up at approximately twice the rate as the diagonal crack. At loads lower the peak value, the dowel crack started to open right before the diagonal crack and both continued opening at a similar rate until failure.

Regarding the influence of parameters assumed on numerical predictions, the concrete tensile strength (f_{ct}) had a significant effect, as shown in Figure 8.2. This observation agreed with Vecchio & Shim [98] conclusions. In the previous analyses, f_{ct} shown in Table 8.2 was obtained from the split cylinder test. Adopting this value for f_{ct} provided a sensible estimate of the ultimate load but the first flexural cracks formed later in the analysis than in the tests. The prediction of the initial crack development was improved if the tensile strength was reduced to $f_{ct}=0.33(f_c')^{1/2}$ as recommended by Bresler & Scordelis [169] but the ultimate load was underestimated in some cases such as beam BG02 (see "Tot. Rot low f_{ct}" in Figure 8.2).

It can be concluded that despite the numerical difficulties faced and assumptions made by the smeared cracking models applied, the NLFE estimations of the ultimate strength (Figure 8.2) were reasonable. The NLFEA presented here did not model the effect of aggregate fracture. Hence, it could be expected that predictions for BL0 to be less conservative than those obtained for BG0. However, this was only true using the multi-fix model. This was probably due to the difference in concrete properties between both set of beams assigned in the numerical models such as f_c or f_{ct}, which had a significant effect on the numerical predictions.

8.3 Analysis of slender beams with shear reinforcement (Beams B, C and D)

8.3.1 Influence of the load arrangement: continuous beams

Experimental evidence

Most of the available experimental data on beam tests with shear reinforcement correspond to simply supported beams with a high flexural capacity in order to ensure a shear type of failure. "T" or "I" cross sections with thin webs were generally applied in order to avoid flexural failure due to their high efficiency. Rectangular sections can also be adopted, such as beams D tested in this work, although flexural reinforcement had to be distributed in three layers. Beam tests designed using either type of cross sections have been widely used to validate analytical models such as the standard truss method or the more recent variable strut inclination method (EC2), as shown in Figure 8.4, which was taken from Walraven [23].

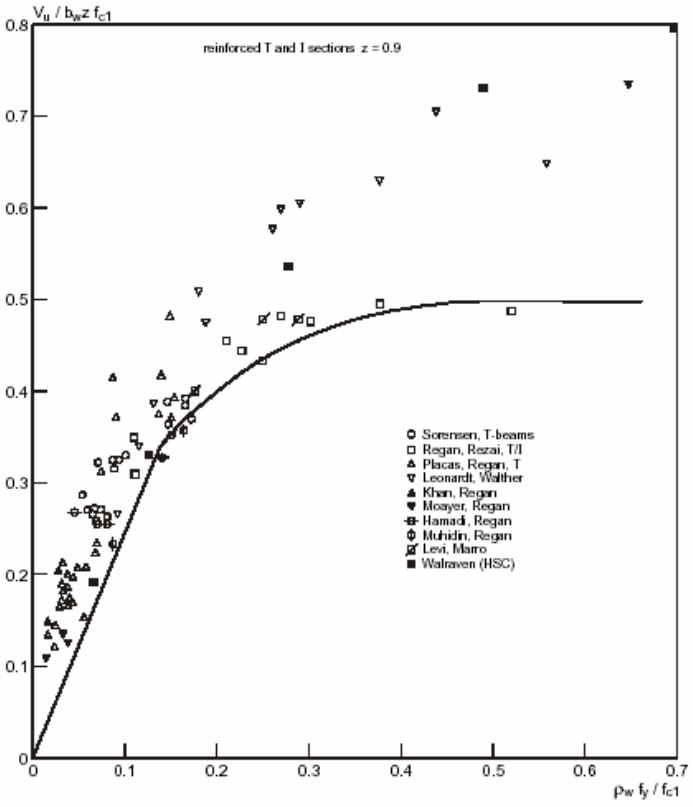

Note: $\rho_w = \rho_v = A_{sw}/(s.b_w)$
$f_{c1} = \nu f_c'$
$z = 0.9d$, No material factors of safety applied

Figure 8.4: Validation of variable inclination strut method (adapted from Walraven [23])

Beams B & C, described in chapter 6, were loaded at two points, one of them at a cantilever end, in order to have a point of contra-flexure at the shear critical span (see Figure 6.33). This load arrangement reduces considerably the shear contribution at the compression head and relates to structural cases with pure shear action rather than combined shear-flexure behaviour of a simply supported beam. Experimental data of beam tests critical in shear with a point of contra-flexure are less common than simply supported beam tests. Tests carried by Ramirez et al. [184] or Regan [149] (Table 8.3) had a similar load arrangement to beams B & C, although the shear reinforcement ratios were lower. As shown in Tables 8.3 and 8.4, all beams considered had stirrup ratios greater than minimum requirements by EC2 and BS8110 (see section 7.3); beams with lower amounts of stirrups had at least twice these minimum values.

Watanabe & Lee [185] referred to a series of 95 beam tests similar to beams B & C carried in Japan in the early 90s by several researchers. Unfortunately only data of 56 specimens (Table 8.4) could be retrieved from this source, refer to [186-190]. Useful information was obtained about ultimate strength and crack patterns from these tests, although the references were in Japanese and so the interpretation of the results was very limited. The cross section and reinforcement arrangement in the Japanese beams were very similar to beams B & C, although the type of aggregate used is unknown. The cracks in these tests might have been wider than in beams tested in this work since very high yield strength steel was generally used for the stirrups as shown in Table 8.4.

Cont. Beams											Vcalc/Vtest		
Author	Beam	a/d	d [mm]	b [mm]	fc' [MPa]	fy [MPa]	ρl [MPa]	ρfy/vfc	ρ/ρmin [EC2]	Vtest [kN]	EC2	BS8810	CSA
Ramirez	1-NWLA	4.95	308	356	46.2	520	2.33	0.090	6.7	1308.0	1.16	0.84	0.86
et al.	2-NWLB	4.95	308	356	46.2	520	2.33	0.090	6.7	1455.0	1.04	0.76	0.77
	3-NWLC	4.98	306	356	46.6	472	2.37	0.082	6.0	1263.0	1.08	0.82	0.84
	4-NWLD	4.98	306	356	45.8	472	2.37	0.055	4.1	1044.0	0.87	0.80	0.84
	5-LWLA	4.95	308	356	43.4	520	2.33	0.095	6.9	984.0	1.54	1.12	1.13
	6-LWLB	4.95	308	356	43.0	520	2.33	0.096	6.9	1116.0	1.35	0.99	1.00
	7-LWLC	4.98	306	356	43.4	472	2.37	0.086	6.3	1071.0	1.27	0.97	0.99
	8-LWLD	4.98	306	356	44.3	472	2.37	0.057	4.1	840.0	1.08	0.99	1.04
	9-NWLD	4.98	306	356	40.0	472	2.37	0.061	4.3	930.0	0.98	0.90	0.92
	10-NWHD	4.98	306	356	60.1	472	2.37	0.045	3.5	1077.0	0.84	0.77	0.85
	11-LWHD	4.98	306	356	72.3	472	2.37	0.040	3.2	1188.0	0.76	0.70	0.77
	12-NWHD	4.98	306	356	75.2	472	2.37	0.039	3.2	1191.0	0.76	0.70	0.77
Regan	J-18	3.75	271	152	31.3(+)	-	1.46	0.070	2.6	163.0	0.65	0.58	-

Note: for slender beams the stirrup ratio ρ is defined as $A_{sw}f_y/(bs)$
(+) estimated from cube strength (assuming $f_c' = 0.8f_{cc}$)
Beams LW tested by Ramirez et al. refer to light-weight aggregate concrete

Table 8.3: Continuous beams with stirrups tested by Ramirez et al. [184] and Regan [149]

Cont. Beams											Vcalc/Vtest		
Author	Beam	a/d	d [mm]	b [mm]	fc' [MPa]	fy [MPa]	ρl [MPa]	ρfy/vfc	ρ/ρmin [EC2]	Vtest [kN]	EC2	BS8810	CSA
Kagami	F-90-041*	4.44	360	200	38.3	922	1.73	0.207	8.1	268.21	1.92*	1.39*	1.25*
et al.	E-90-041*	4.64	345	200	38.3	922	2.41	0.207	8.1	325.59	1.52*	1.13*	1.08*
	B-90-041	4.76	336	200	38.3	922	3.09	0.207	8.1	374.25	1.27	0.97	0.98
	G-90-041	4.85	330	200	38.3	922	3.78	0.207	8.1	374.25	1.25	0.96	1.01
	H-90-041	4.80	333	200	38.3	922	3.15	0.207	8.1	350.22	1.35	1.03	1.04
	E-30-041	4.64	345	200	38.3	225	2.41	0.051	2.0	223.08	0.68	0.70	0.74
	G-30-041	4.85	330	200	38.3	225	3.78	0.051	2.0	216.02	0.68	0.73	0.81
Kokusho	B-210-6.0	3.53	340	180	21.2	1386	3.11	0.374	11.8	241.33	1.29	1.31	1.21
et al.	B-210-7.4	3.53	340	180	21.2	1478	3.11	0.564	17.8	279.59	1.15	1.13	1.04
	B-210-9.2	3.53	340	180	21.2	1458	3.11	0.890	28.1	321.77	1.00	0.98	0.91
	B-210-11.0	3.53	340	180	21.2	1488	3.11	1.278	40.4	356.10	0.90	0.88	0.82
	B-360-4.1	3.53	340	180	39.0	1448	3.11	0.108	4.3	625.88	0.97	0.71	0.78
	B-360-5.1	3.53	340	180	39.0	1478	3.11	0.170	6.7	721.39	1.17	0.83	0.89
	B-360-6.0	3.53	340	180	39.0	1386	3.11	0.220	8.7	757.96	1.23	0.96	1.00
	B-360-7.4	3.53	340	180	39.0	1478	3.11	0.332	13.1	762.03	1.39	1.04	1.29
	B-360-9.2	3.53	340	180	39.0	1458	3.11	0.524	20.7	953.04	1.18	0.83	1.17
	B-360-11.0	3.53	340	180	39.0	1488	3.11	0.753	29.8	1056.68	1.07	0.75	1.05
	B-570-4.1	3.53	340	180	56.0	1448	3.11	0.082	3.6	300.19	0.98	0.72	0.82
	B-570-6.0	3.53	340	180	56.0	1386	3.11	0.167	7.3	416.93	1.28	0.84	0.89
	B-570-7.4	3.53	340	180	56.0	1478	3.11	0.252	11.0	485.60	1.28	0.79	0.99
	B-570-9.2	3.53	340	180	56.0	1458	3.11	0.398	17.3	549.36	1.28	0.70	1.17
	B-570-11.0	3.53	340	180	56.0	1488	3.11	0.571	24.9	593.51	1.21	0.64	1.30
Matsuzaki	C-210-0.19	3.57	336	200	23.9	710	2.83	0.104	3.5	254.08	0.80	0.68	0.76
et al.	C-210-0.40	3.57	336	200	23.9	710	2.83	0.220	7.3	320.79	1.01	0.85	0.93
	C-210-0.59	3.57	336	200	23.9	751	2.83	0.342	11.3	329.62	1.13	1.11	1.09
	C-210-0.89	3.57	336	200	23.9	751	2.83	0.516	17.1	377.69	1.04	0.97	0.95
	C-210-1.18	3.57	336	200	23.9	751	2.83	0.685	22.7	423.79	0.92	0.87	0.85
	C-360-0.19	3.57	336	200	38.4	706	2.83	0.069	2.7	259.18	0.78	0.70	0.79
	C-360-0.89	3.57	336	200	38.4	756	2.83	0.345	13.6	462.05	1.21	0.91	1.16
	C-360-1.18	3.57	336	200	38.4	756	2.83	0.457	18.0	525.82	1.12	0.80	1.11
	C-570-0.40	3.57	336	200	68.5	710	2.83	0.095	4.3	441.45	0.97	0.64	0.73
	C-570-0.59	3.57	336	200	68.5	751	2.83	0.149	6.7	588.60	1.09	0.66	0.72
	C-570-0.89	3.57	336	200	68.5	751	2.83	0.224	10.1	652.37	1.15	0.64	0.83
	H-210-1.18	3.57	336	200	23.9	751	2.83	0.685	22.7	437.53	0.89	0.84	0.82
	U-210-1.18	3.57	336	200	23.9	751	2.83	0.685	22.7	412.02	0.95	0.89	0.88
Takagi et al.	B-30-046	4.76	336	200	34.1	363	3.09	0.094	3.5	268.70	0.93	0.76	0.80
	B-30-121	4.76	336	200	33.5	297	3.09	0.206	7.7	403.19	1.06	0.83	0.84
	B-60-030	4.76	336	200	33.9	512	3.09	0.087	3.3	249.37	0.92	0.79	0.83
	B-60-059	4.76	336	200	34.3	576	3.09	0.192	7.3	410.55	1.03	0.79	0.80
	B-80-019	4.76	336	200	34.7	900	3.09	0.098	3.7	277.52	0.96	0.76	0.80
	B-80-022S	4.76	336	200	35.0	856	3.09	0.093	3.5	274.48	0.92	0.75	0.79
	B-80-046	4.76	336	200	35.0	937	3.09	0.237	9.0	377.69	1.23	1.01	1.01
	B-80-058S	4.76	336	200	35.1	875	3.09	0.286	10.9	418.49	1.18	1.00	1.03
	B-80-059	4.76	336	200	35.1	937	3.09	0.306	11.7	462.35	1.09	0.91	0.97
	B-80-110S	4.76	336	200	35.2	835	3.09	0.556	21.3	527.88	1.04	0.80	1.01
	B-80-121	4.76	336	200	35.2	934	3.09	0.622	23.8	507.47	1.08	0.83	1.05
	B-120-019	4.76	336	200	35.9	1104	3.09	0.117	4.5	324.22	1.00	0.73	0.77
	B-120-030	4.76	336	200	36.2	1104	3.09	0.177	6.8	386.81	1.11	0.81	0.83
	B-120-059	4.76	336	200	36.1	1103	3.09	0.352	13.6	474.90	1.13	0.88	1.05
	B-120-121	4.76	336	200	36.2	1108	3.09	0.721	27.8	540.83	1.04	0.78	1.01
	B-150-019	4.76	336	200	36.3	1284	3.09	0.135	5.2	311.66	1.22	0.84	0.88
	B-1.5-022	3.57	336	200	36.7	856	3.09	0.089	3.4	281.55	0.90	0.73	0.78
	B-1.5-058	3.57	336	200	36.8	875	3.09	0.275	10.7	439.19	1.16	0.96	0.98
	B-1.5-110	3.57	336	200	36.9	835	3.09	0.535	20.8	531.60	1.07	0.79	1.05
Simokaichi	B1	3.46	260	150	63.8	376	3.06	0.041	1.8	158.16	0.65	0.65	0.77
et al.	B2	3.46	260	150	63.8	929	3.06	0.274	12.2	444.82	1.00	0.55	0.78
Total =	**69**	**including beams in Table 8.3**								**Summary of results***	**EC2**	**BS8810**	**CSA**
	max value =	4.85	360	200	68.5	1488	3.78	1.278	40.4	**Mean**	**1.06**	**0.84**	**0.93**
	min value =	3.46	260	150	21.2	225	1.73	0.041	1.8	**SD**	**0.19**	**0.14**	**0.14**
										COV %	**17.68**	**17.09**	**15.42**

Note: *Bond failure (results are neglected); summary table refers to the remaining 67 beams

Table 8.4: Continuous beams with stirrups (test carried by Japanese researchers)

Differences in ultimate strength and crack pattern

The experimental data from the 69 beams shown in Tables 8.3 and 8.4, was consistent with results from beams B & C. Several differences were observed between the shear behaviour of simply supported beam tests and beams with a point of contra-flexure. The ultimate strength and crack pattern seemed to be influenced by the type of loading.

Ultimate load

The ultimate shear strength of beams B & C was significantly lower than those shown in Figure 8.4, which were simply supported and had a flanged compression head. This reduction in strength in beams B & C was in agreement with experimental data shown in Tables 8.3 and 8.4. This is clearly shown in Figure 8.5, where the strength of continuous beams was generally under the predicted strength curve suggested in EC2, as opposed to simply supported beams shown in Figure 8.4, where points were clearly above it. This disagreement between both sets of experimental data, seems to worsen for higher values of shear stresses. The shear strength of simply supported beam with a rectangular section, which was tested in this work (see beam D in section 6.6), was similar to equivalent continuous beam. This suggests that the difference between Figure 8.4 and 8.5 results might be mainly due to the compression flange.

The shear force resisted by the compression flange at failure can be estimated using equation (8.2), suggested by Placas & Regan [143]. Equation (8.2) takes into account the rigidity of the flange, although the formula had not been validated for neither lightweight nor high-strength concrete. Despite this limitation, equation (8.2) was applied in order to obtain an order of magnitude of the shear carried by the flange.

$$V_{cu} = 0.1 f_{cu}^{2/3} \left(b_w + 1.5\lambda . h_f\right) h_f \qquad \ldots (8.2)$$

where $\lambda = 1.0$ if $[(b_f - b_w) > 3h_f]$ and $\lambda = (b_f - b_w)/3h_f$ if $[(b_f - b_w) < 3h_f]$

Figure 8.5 compares the results of beams tested with a point of contra-flexure (black squares) with simply supported beams (white circles). The simply supported beams shown in Figure 8.5 correspond to tests by Hamadi & Regan [19] and Walraven [10], which had a "T" and "I" section respectively. The estimated shear contribution carried at the flanged V_{cu} has been subtracted from the total shear force, which is represented by triangle markers in Figure 8.5. The results obtained showed a reasonable correlation, especially for values of $\rho_l f_y / v f_c' < 0.4$, which seems to suggest that flanged sections can provide a significant contribution to shear strength. According to this analysis the shear

carried by the flange V_{cu} had a contribution to the total strength that varied from 10 to 20% for the 14 simply supported beams considered.

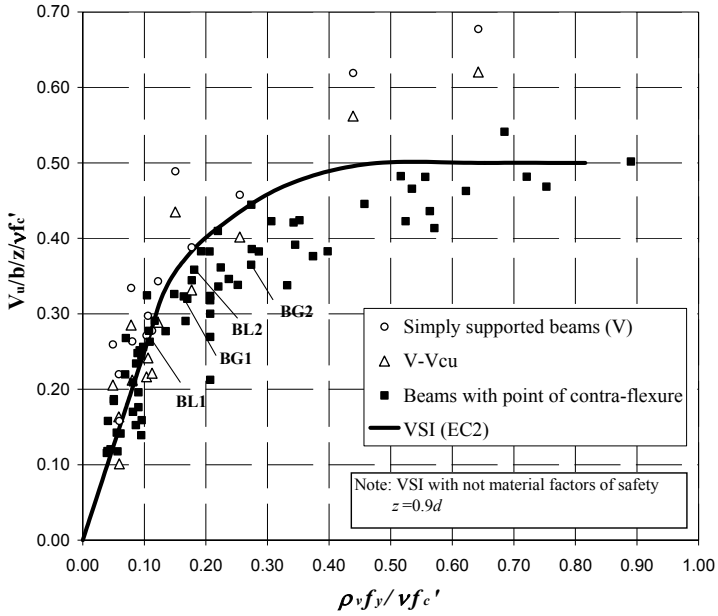

Note: Refer to Tables 8.3 and 8.4 for data of beams with point of contra-flexure

Figure 8.5: Ultimate shear strength with $\rho_v f_y / \nu f_c'$ for simply supported and continuous beams; contribution of shear carried at the flanges (V_{cu}) in simply supported beams

In order to investigate the influence of compression flanges on shear behaviour of reinforced concrete beams, two beam test series were carried out by Regan [149], which consisted of simply supported beams with similar dimensions, concrete strengths and amount of stirrups. The results shown in Figure 8.6 correspond to beams with vertical stirrups and *a/d* ratios between 3.4 and 3.6.

Again the contribution of the compression flange is observed (Figure 8.6), although in two of the beam tests, which had low transverse flange reinforcement, premature failure occurred at the flange. For the remaining beams, the strength was generally greater compared with equivalent beams with a rectangular section, the figure of 10-20% estimated previously was in good agreement with the experimental data. These results further support the relevance of flanged sections, although more experimental data of beams with higher stirrups indexes would be desirable.

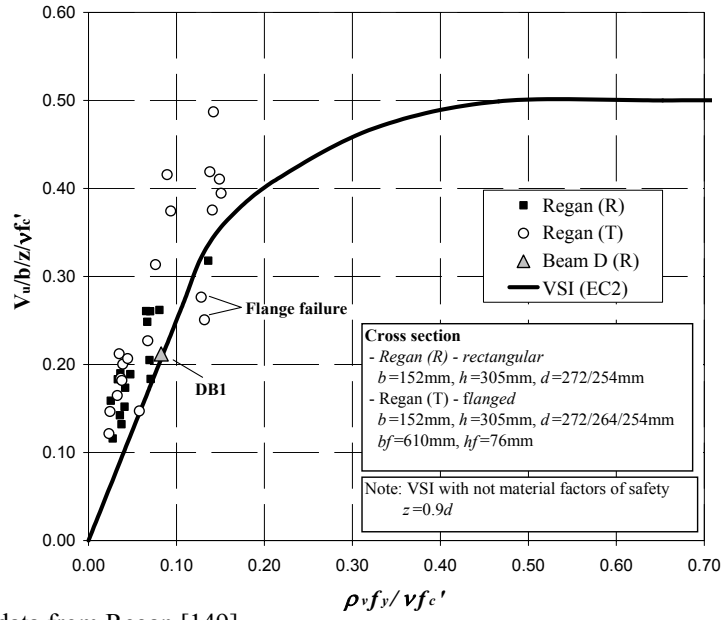

Note: experimental data from Regan [149]

Figure 8.6: Ultimate shear strength for simply supported beams with rectangular and T sections

Differences in crack pattern

The crack pattern was also influenced by the type of loading. Experimental evidence shows that in simply supported beams failing in shear, initial 45° shear cracks form at early load stages at the mid-height of the web along the shear span (Figure 8.7). However, in beams B & C, these cracks formed at a distance equal to the effective depth *d* from the loading points as part of the fanned shape strut (Figure 8.8), while the central span remained uncracked. The difference in the stress fields between simply supported and continuous beams before cracking is clearly shown in Figure 8.9 adapted from Calavera [191].

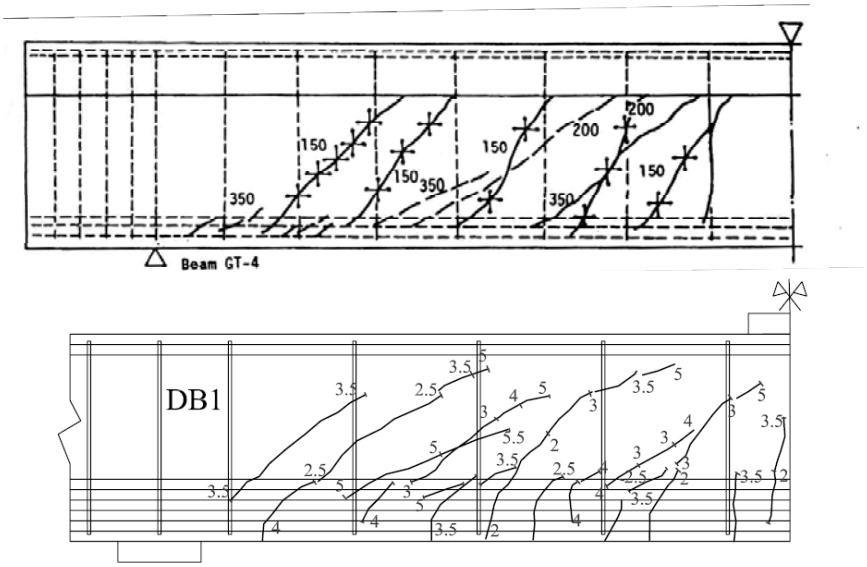

Figure 8.7: Crack pattern of simply supported beam; *Top* – T section (GT4, Hamadi & Regan [19]); *Bottom* – Rectangular section (beam DB1 tested in this work)

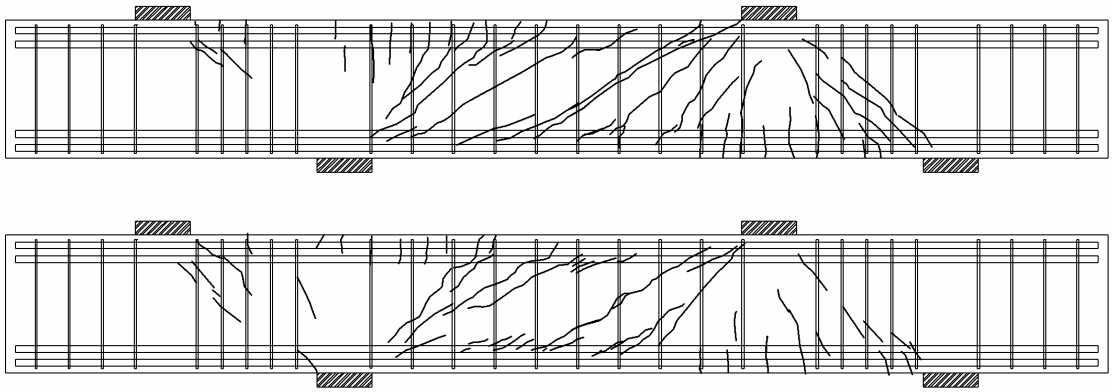

Figure 8.8: Typical crack pattern of continuous beam. *Top* – (BL1); *Bottom* – Bond split crack along flexural reinforcement (BG1)

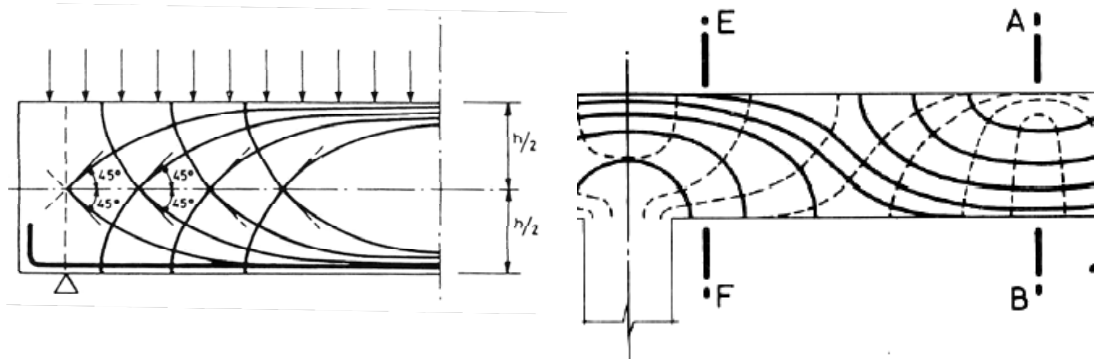

Figure 8.9: Compression and traction lines in simply supported and continuous beams before cracking (adapted from Calavera [191])

Once the preliminary shear cracks had developed, redistribution of stresses is required to stabilize the system. As the load increases and the stirrups begin to yield the strut changes its orientation in order to activate a larger number of stirrups and flatter cracks (35˚) may form. In the case of simply supported beams, these later cracks crossed the previous 45˚ ones as shown in Figure 8.7. On the other hand, in beams B & C, these newer cracks formed at the centre of the shear span, where the concrete was uncracked. Most likely these differences in the crack development resulted in a different contribution of aggregate interlock to the shear strength of the specimen. At failure, the behaviour of the main shear crack depended on the stirrup index (*SI*). Beams with lower *SI*, such as BL1, the crack got wider and failure was due to the complete lost of aggregate interlock while for the remaining beams crack slip was also mobilized.

In some of the continuous beams examined (see Kagami et al. [186], Regan [19], or beams tested BG1-BG2), near failure the main diagonal shear crack extended to the ends along the main flexural steel in a bond splitting horizontal crack (see Figure 8.8 top). This type of bond failure does not appear to be related with the type of loading since similar

crack propagation was reported in simply supported beams such beams GT4-5 and LT4-5 tested by Hamadi & Regan [19] (Figure 8.7 top). The ultimate load of the beams, which exhibited a bond split crack at failure, was not significantly lower than the rest of the beams, except for tests by Kagami et al. [186] which had considerably low flexural reinforcement ratios (ρ_l =1.73-2.4%). The beams by Kagami et al. [186] in which the ultimate strength appeared to be influenced by the low longitudinal reinforcement ratio corresponded to the lowest two data points in Figure 8.5 with $\rho_v f_y / \nu f_c' = 0.2$. Even though in some beams bond failure was predominant, in other cases such as beams BG1 and BG2, failure seemed to occur as a combination of both shear and bond failures.

NLFEA of simply supported and continuous beams

In order to assess clearly the differences described above between simply supported and continuous beams, a simple comparative scenario with identical beams was established using a non-linear finite element analysis. Numerical predictions of crack pattern and stress redistributions of tested beams B were compared with identical beams without the load point applied at the cantilever end. These beams, for which no experimental data was available, are denoted as beams Bs.

Two major changes were required in order to model beams Bs. Firstly, the width of the elements in the right short shear span had to be factored by three, in order to avoid failure in that span, which had twice the shear force in beams B. Secondly, the yield strength of the flexural reinforcement was increased to 980MPa and a compression flange was included (h_f =125mm, b_f =405mm) to avoid flexural failure. These changes in the cross section were required since the maximum bending moments in the simply supported beam Bs were twice as in continuous beam B. As a result from these changes in the cross section, the lever arm was around 5% larger in beams Bs than in beams B.

In the NLFEA, the multi-fixed smeared crack model was adopted. Similar material properties as in beams A were applied see section 7.4. As shown in Figure 8.10, the different crack development obtained for simply supported beams Bs and continuous beams B was satisfactory reproduced by the NLFE models.

As shown in Figure 8.10 the crack development predicted at a shear force of 360kN, which was near the experimental failure load in beam BL1, was much lower in beam BsL1. The predicted critical shear crack at the centre of the span clearly crossed the preliminary 45º shear crack (Figure 8.8), as observed in tests.

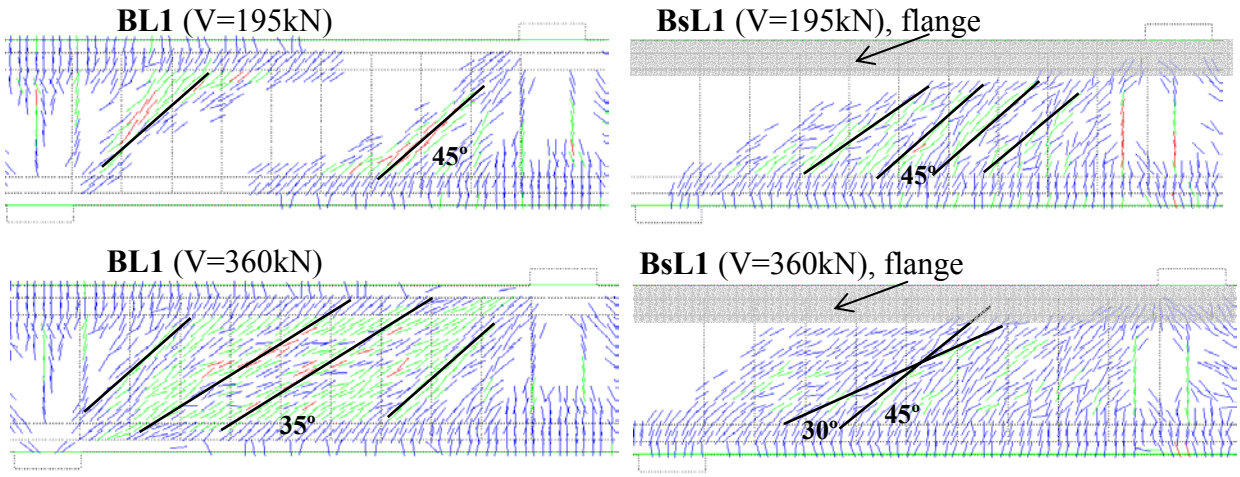

Figure 8.10: NLFE prediction of crack development in beams B and Bs

The directions of the principle compressive stresses before cracking were similar to those shown in Figure 8.9. However, the struts in the continuous beams seemed considerably flatter than those in beams Bs, as shown in Figure 8.11. The truss system generally described for simply supported beams was clearly reproduced in the NLFEA, see Figure 8.11 top. The vectors of the principle compressive stresses were orientated at 45º around preliminary shear cracks and were flatter between these cracks. In addition, arching action near the support was also captured in the NLFEA.

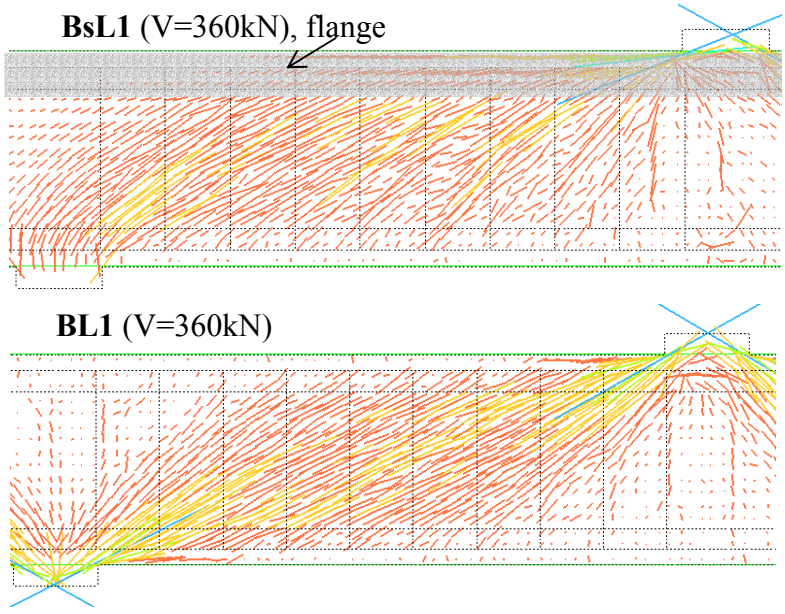

Figure 8.11: Principle compressive stresses at ultimate loads for beams BL1 and BLs1

8.3.2 Comparison between predictions from variable strut inclination method (EC2), simple truss (BS8110) and MCFT

Variable strut inclination method (EC2)

As discussed in section 8.3.1, the variable inclination strut method (VSI) was applied to predict the ultimate strength of beams presented in Tables 8.3 and 8.4, along with continuous beams tested in this work (beams B & C). The VSI method produced satisfactory predictions of the ultimate strength of beams with $\rho f_y/\nu f_c'$ ratios up to around 0.15 (see Figure 8.12). Above this value, where the predicted $\cot\theta$ becomes lower than 2.5, the strength was generally overestimated. The V_{calc}/V_{test} ratio obtained for beams B, C & D are summarised in Table 8.5, in which no material factors of safety have been applied; for the remaining beams refer to Tables 8.3 and 8.4.

As discussed in previous section, the overestimation of the ultimate strength seemed related with the type of loading in the test, in particular with the type of cross section used. However, parameters assumed in the VSI method such as the lever arm (z) or the effectiveness factor of the concrete (ν) had a significant influence on the shear strength predictions.

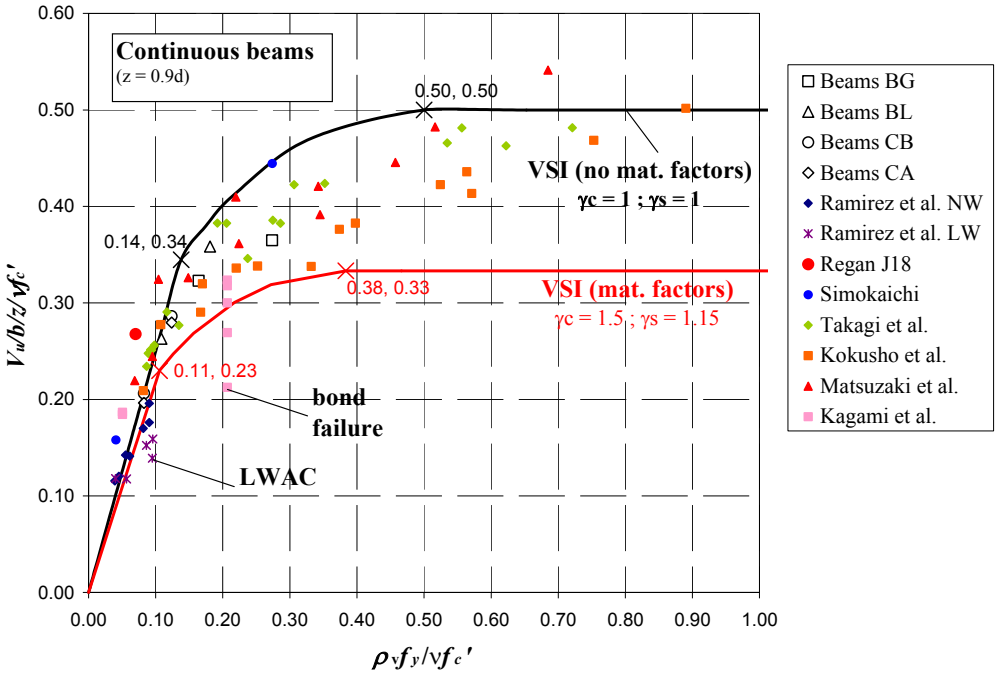

Note: refer to Tables 8.3, 8.4 and 8.5

Figure 8.12: Variable strut inclination method predictions for continuous beams

In Figure 8.12, both design and characteristic strength curves using VSI are presented. As shown in Figure 8.12, the application of material factors of safety (1.5 and 1.15 for the

concrete and steel, EC2) still allows for a certain margin of safety, which seems to decrease quite considerably for beams with $cot\theta$ equal to 2.5. The ultimate strength of these beams is governed by yielding of the stirrups and so only steel material factor of safety is applied (1.15). In this range, only light-weight aggregate continuous beams tested by Ramirez et al. [184] were below the design curve. In addition, two beams from Kagami were below the design VSI curve in the plastic range, which could be explained to local bond failure. The accuracy of the predictions is discussed in further detailed in the next sections; the performance of other design codes such as BS8110 and CSA are also shown in Tables 8.3, 8.4 and 8.5.

			VSI (EC2)		**BS8810**	**Respons. 2000**	**MCFT (CSA)**	
Beam	$SI=\rho f_y/\nu f_c'$	V_{test} *[kN]*	V_{calc}/V_{test}	$cot\theta$	V_{calc}/V_{test}	V_{calc}/V_{test}	V_{calc}/V_{test}	$cot\theta$
BG1	0.16	285.19	1.15	2.26	0.84	1.02	0.96	1.49
BG2	0.27	322.24	1.22	1.63	1.08	1.23	1.19	1.38
BL1	0.11	350.73	1.03	**2.50**	0.68	0.94	0.82	1.48
BL2	0.18	478.18	1.07	2.13	0.73	0.96	0.82	1.38
CB1	0.08	308.80	1.00	**2.50**	0.74	0.98	0.88	1.49
CA1	0.08	293.96	1.05	**2.50**	0.78	1.03	0.92	1.49
CB2	0.12	428.71	1.08	**2.50**	0.69	0.92	0.80	1.42
CA2	0.12	418.66	1.11	**2.50**	0.71	0.94	0.81	1.42
DB1*	0.08	311.37	0.94	**2.50**	0.70	0.98	0.81	1.43
DA1*	0.08	299.22	0.97	**2.50**	0.63	0.94	0.77	1.43
		Avg.	1.06		0.76	0.99	0.88	
		SD	0.08		0.13	0.09	0.12	
		COV (%)	7.93		16.73	9.26	14.18	

Note: no material factors of safety have been applied; *all specimens were continuous beams except for DB1/DA1.

Additional assumptions are:
- In EC2 (VSI), z=0.9d
- In BS8110 cube strengths have been assumed as $0.8f_c'$ and $f_{cu}\leq$40MPa
- In Response 2000: base curve (Popovics/Thorenfeldt/Collins), Comp. Softening (Vecchio & Collins 86), Tens. Stiffening (Bentz 99); aggregate size 10mm; no strain hardening considered for steel
- MCFT (CSA), design equations (2.18) & (2.19) with s_{ze}=300mm; M_f was taken not lower than Vd_v

Table 8.5: Summary of predictions of the ultimate strength of beams B, C & D using the variable strut inclination method (EC2), classical truss (BS8110) and MCFT (Response 2000 and general design equations CSA)

The value assumed for the lever arm $z=kd$, had a significant influence on the prediction of the ultimate strength using the VSI. In design codes k is suggested to be taken as 0.9, although allowance is made to estimate this parameter more accurately. However, no general guidance is provided in order to assess z. A preliminary estimate of the lever arm could be obtained from the maximum flexural capacity of the section, but this approach would be problematic since it is dependent on the longitudinal reinforcement ratio.

The lever arm estimated from the maximum flexural capacity of the section can differ from the actual value at failure especially in shear tests where beams are designed with a considerable safety margin from flexural failure. Hence, the lever arm was estimated at the section of maximum bending moments for the beams described in Tables 8.3 to 8.5, from first principles using the bending moment obtained experimentally. Reasonable predictions of the strains in the longitudinal reinforcement were obtained for beams BG2 and BL2 in which a parabolic-rectangle relationship was assumed between strain and stresses at the concrete as suggested in EC2. The strains in the tensile reinforcement were 60% and 86% of the yield strain for beams BG2 and BL2.

The experimental values obtained for k from this analysis are shown in Figure 8.13, with an average value of 0.84. In particular k was equal to 0.86 for beams BL and BG. When analysing beams with a point of contra-flexure, Regan [3] suggested a lower value of k = 0.8 in order to fit experimental data from Watanabe [192].

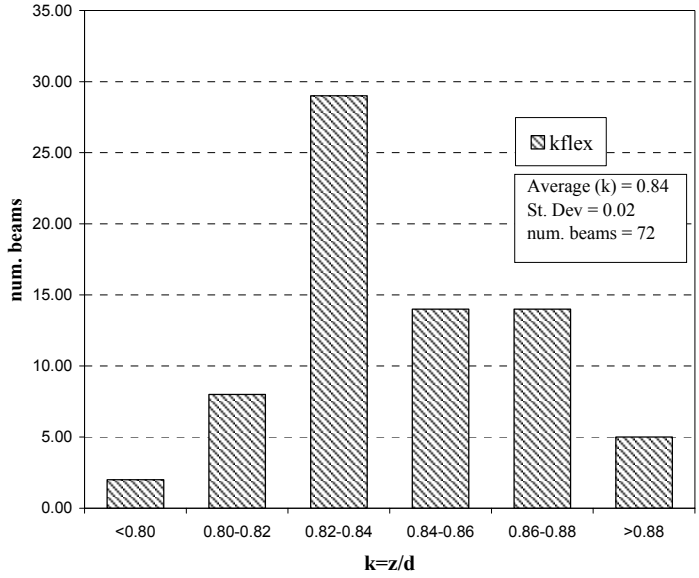

Figure 8.13: Average values for factor k for beams with a point of contra-flexure

This conservative value of k=0.8 seems more consistent with experimental data shown in Figure 8.13 and provides a better estimate of the ultimate load of continuous beams when using the VSI (see Figure 8.14). For simply supported beams with and "I" or "T" section, such as beams Bs, described in section 8.3.1, the value of k=0.9 seems more suitable.

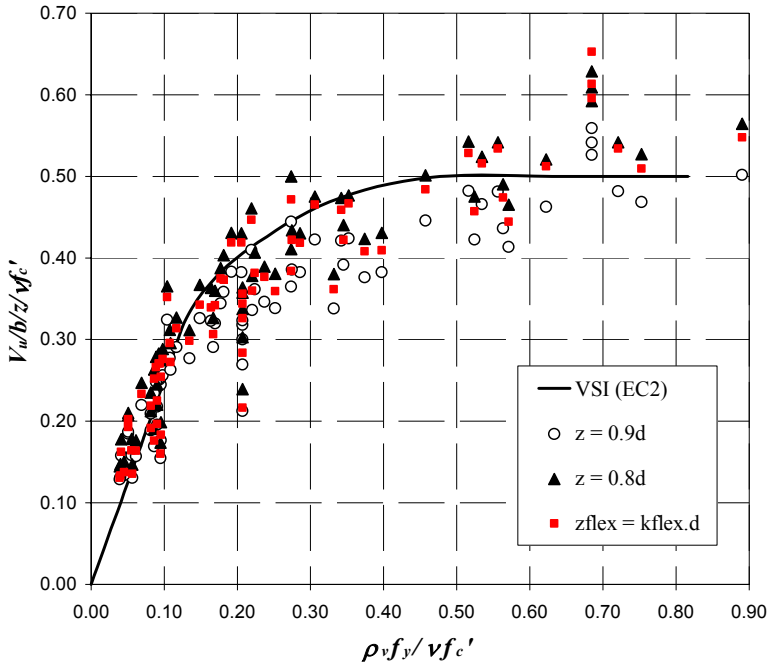

Figure 8.14: Predictions of variable strut inclination method for different lever arm assumptions (z_{flex}=k_{flex}.d, see Figure 8.13)

A large group of the beams included in the experimental database had a stirrup index (SI=$\rho_v f_y/\nu f_c'$) lower than 0.138 hence $cot\theta$ was limited to 2.5 in the VSI. This range of SI corresponds to a linear cut-off in the prediction curve. According to the VSI method, in such instances where the angle of the strut is restricted to 21.8º as in beam BL1, the shear strength is only governed by the yielding capacity of the stirrups within a length of 2.5z. Hence the influence of the concrete strength is ignored. On the other hand, shear design methods based on the standard truss model (V_c+V_s), such as in BS8110, f_c' is taken into account to estimate the ultimate strength.

The suggested VSI cut-off seemed to fit experimental data of continuous beams with low values of SI as shown in Figure 8.14. In addition, Figure 8.15 showed that the predictions for the continuous beams with low SI were not very sensitive to variations in f_c' for concrete strengths up to 70MPa. Additional data of simply supported beams, which is also shown in Figure 8.15, seemed to suggest a reduction in the P_{test}/P_{calc} ratio as f_c' increased. However, beam tests provided by Walraven & Stroband [10] still showed accurate predictions for concrete strengths as high as 115MPa using the $cot\theta$=2.5 cut-off. As

described in next section, predictions of the ultimate strength using BS8110 and CSA were more conservative (Figure 8.15). This is particularly interesting since both of these codes apply both material factors of safety, one for concrete and one for steel, unlike EC2 where only 1.15 for steel is applied. The question may arise of whether is sensible to have such a low material factor using EC2 for such cases, considering that the predictions are close to experimental values.

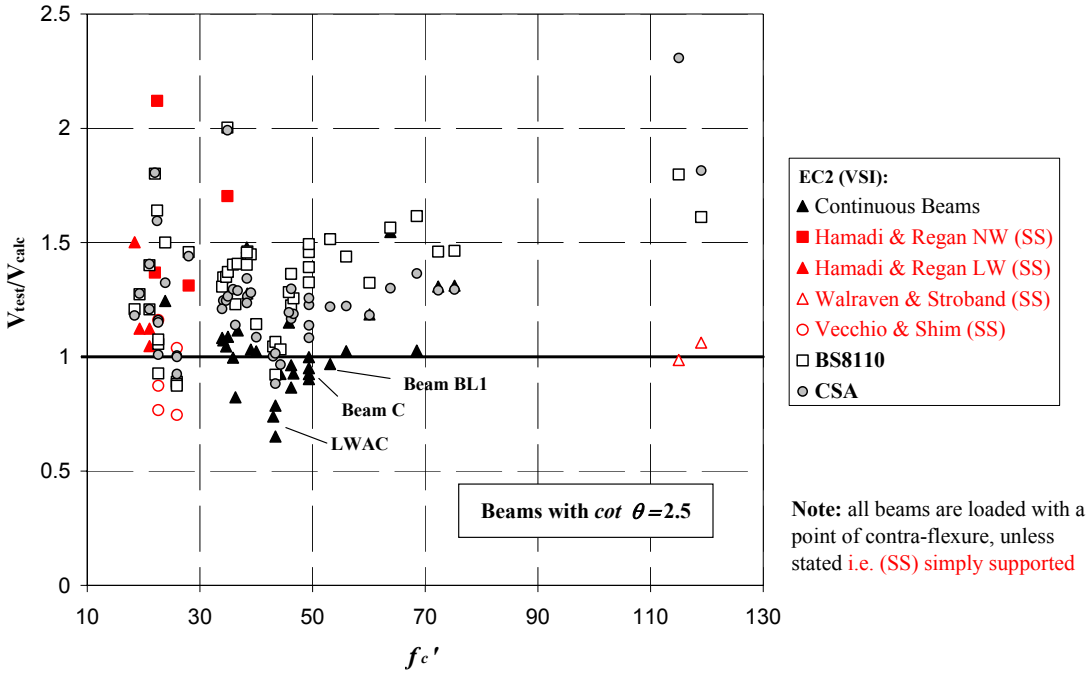

Note: Continuous beams (data from Tables 8.3 and 8.4 for SI<0.138)
Simply supported beams: Hamadi & Regan [19], Walraven & Stroband [10], Vecchio & Shim [98]

Figure 8.15: Influence of concrete strength in shear strength predictions using EC2, BS8110 and CSA methods for beams with $cot\theta$=2.5

Comparison with standard truss (BS8110) and MCFT predictions

The ultimate strength of beams tested in this work was also estimated using standard truss method (BS8110) and MCFT (Response 2000 and CSA design equations), see results in Table 8.5. Average values of the V_{calc}/V_{test} ratio obtained for the 10 beams tested showed that the accuracy was highest using Response 2000, while the most conservative predictions were obtained using the BS8110 approach.

The design equations proposed in CSA code provided a similar performance to more elaborate analysis using Response 2000. Hence, the CSA approach was adopted for estimating the shear strength of the remaining 69 beams shown in Tables 8.3 and 8.4. The performance of the different design methods varied for different ranges of $\rho f_y/vf_c'$. In order to compare the results with EC2 predictions three cases were investigated. Firstly,

beams with $\rho f_y/\nu f_c' \leq 0.11$, which refers to $cot\theta = 2.5$ using material factors of safety according to EC2 (see Figure 8.12). Secondly, beams with $\rho f_y/\nu f_c' > 0.11$, which relates to cases where $cot\theta < 2.5$. Thirdly, the overall performance was studied for all 75 continuous beams described in Tables 8.3, 8.4 and 8.5.

Similarly as in the study of short span beams (see section 7.2.3 and 7.3.5), a Demerit Point Classification (Collins [148]) was carried out, using test data from 75 continuous beams shown in Tables 8.3 to 8.5. This classification system assumes that an appropriate level of safety is found for P_{test}/P_{calc} values between 0.85 and 1.30. A Demerit Point mark is assigned, as described in section 7.2.3, according to the percentage of specimens found at the different ranges of P_{test}/P_{calc}. Lowest values of *DP* indicate a better performance of the design method. The results obtained for the three design methods examined are summarized in Table 8.6 and Figure 8.16.

Ptest/Pcalc	**ρfy/νfc'≤0.11**	*DP*	**VSI-EC2**	**BS8110**	**CSA**	**VSI-z=0.8d**
<0.5	*Extremely dangerous*	*10*	0	0	0	0
0.5-0.65	*Dangerous*	*5*	0	0	0	0
0.65-0.85	*Low safety*	*2*	10	0	0	7
0.85-1.30	*Appropiate safety*	*0*	69	38	86	62
1.30-2.00	*Conservative*	*1*	21	62	14	31
>2.00	*Extremely conservative*	*2*	0	0	0	0
		TOTAL DP	**41**	**62**	**14**	**45**

Ptest/Pcalc	**ρfy/νfc'>0.11**	*DP*	**VSI-EC2**	**BS8110**	**CSA**	**VSI-z=0.8d**
<0.5	*Extremely dangerous*	*10*	0	0	0	0
0.5-0.65	*Dangerous*	*5*	0	0	0	0
0.65-0.85	*Low safety*	*2*	35	2	9	4
0.85-1.30	*Appropiate safety*	*0*	65	76	89	96
1.30-2.00	*Conservative*	*1*	0	22	2	0
>2.00	*Extremely conservative*	*2*	0	0	0	0
		TOTAL DP	**70**	**26**	**20**	**9**

Ptest/Pcalc	**ALL**	*DP*	**VSI-EC2**	**BS8110**	**CSA**	**VSI-z=0.8d**
<0.5	*Extremely dangerous*	*10*	0	0	0	0
0.5-0.65	*Dangerous*	*5*	0	0	0	0
0.65-0.85	*Low safety*	*2*	25	1	5	5
0.85-1.30	*Appropiate safety*	*0*	67	61	88	83
1.30-2.00	*Conservative*	*1*	8	37	7	12
>2.00	*Extremely conservative*	*2*	0	0	0	0
		TOTAL DP	**59**	**40**	**18**	**23**

Note: Total number of beam 75: $\rho f_y/\nu f_c' \leq 0.11$ (29 beams), $\rho f_y/\nu f_c' > 0.11$ (46 beams)

Table 8.6: Demerit point classification for continuous beams

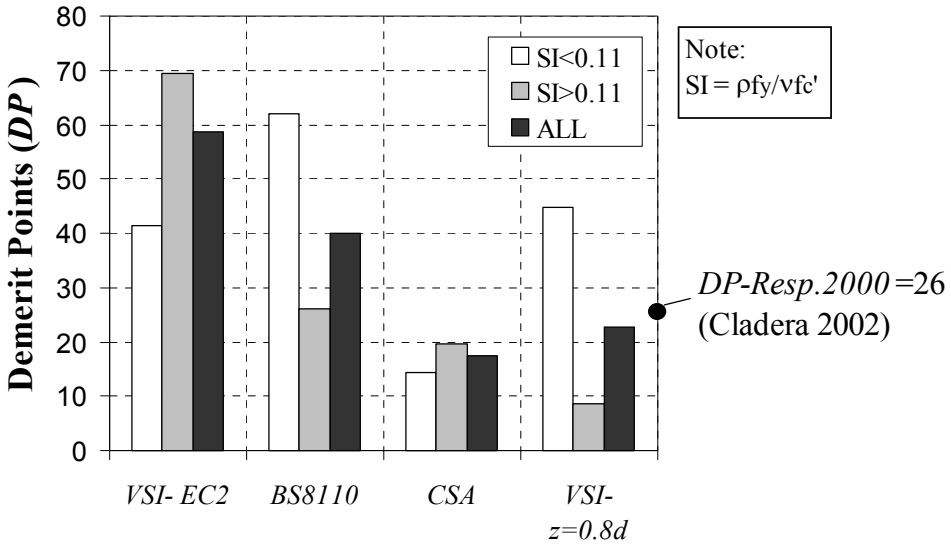

Figure 8.16: Demerit point classification proposed by Collins [148]; results for continuous beams

Table 8.6 shows that the Canadian approach provides the lowest demerit point mark, with a noticeable constant performance for different values of the stirrup index. It is noteworthy that the critical section was assumed at a distance of 0.9*d* from the support, in which most of continuous beams examined had a *M/V* ratio lower than *d*. According to CSA approach *M/V* should not be taken less than *d* since the strain at the top chord might become tensile, which in turn would lead to an unconservative estimate of the strain at the mid-depth taken as $\varepsilon_x=\varepsilon_t/2$.

EC2 and BS8110 perform very differently depending on the stirrup index. Classical truss approach (V_c+V_s), which is suggested in BS8110, provides rather conservative results for *SI*<0.11 compared to EC2 and CSA methods, which results in a *DP* mark equal to 70. A similar mark is obtained for EC2 method with *SI*>0.11, although in this case this is due to the fact that 35% of the specimens lay on the "low safety range" and not due to an excessive level of conservatism as in BS8110. This percentage is significantly large, in fact it is one of the largest observed in this work, see sections 7.2.3 and 7.3.5 for short span beams (a_v/d=1-2) with and without stirrups.

As discussed earlier, assuming a lower value of the level arm equal to 0.8*d* improved the predictions considerably. This is clearly reflected on the demerit point classification shown in Table 8.6 and Figure 8.16 for beams with *SI*>0.11, where the performance of EC2(*z*=0.8*d*) is remarkable. In addition, for beams with *SI*<0.11 using EC2(*z*=0.8*d*), the DP mark is similar to EC2(*z*=0.9d), although the predictions become slightly more conservative. It can be argued that this is desirable, since as discussed earlier EC2 applies a lower material factor of safety for such cases compared to CSA and BS8110.

It is of interest to compare these values of demerit marks with those obtained by other authors. Cladera [24] gathered an experimental database of 123 simply supported beams with stirrups, in which the *DP* mark obtained using Response 2000 was 26. This is consistent with the one obtained here using CSA design equations, see Figure 8.16. On the other hand, Cladera obtained a considerably large value of *DP* (136) using EC2 method, which was due to an excessive level of conservatism in the results. The beams studied by Cladera [24] were high strength concrete beams. Cladera [24] also observed that predictions became in general less conservative as the shear stresses increased, which is also in agreement with results shown in Table 8.6.

As shown in sections 7.2.3 and 7.3.5 the Demerit Point system proposed by Collins [148] can be misleading, since the approach neglects the differences in material and load factors of safety applied in design codes. Hence, overall factors of safety need to be considered in order to obtain a more realistic comparison between the different design methods. Similarly as in sections 7.2.3 and 7.3.5, the design strength (P_d) of the beams investigated was obtained considering material and load factors of safety, assuming *DL=LL* (see Figure 8.17). The overall *FOS* (P_{test}/P_d) for the 75 beams studied is shown in Figure 8.17. A modified Demerit Point Classification system suggested by the author is shown in Table 8.7, which is based on the P_{test}/P_d ratio, as described in sections 7.2.3 and 7.3.5.

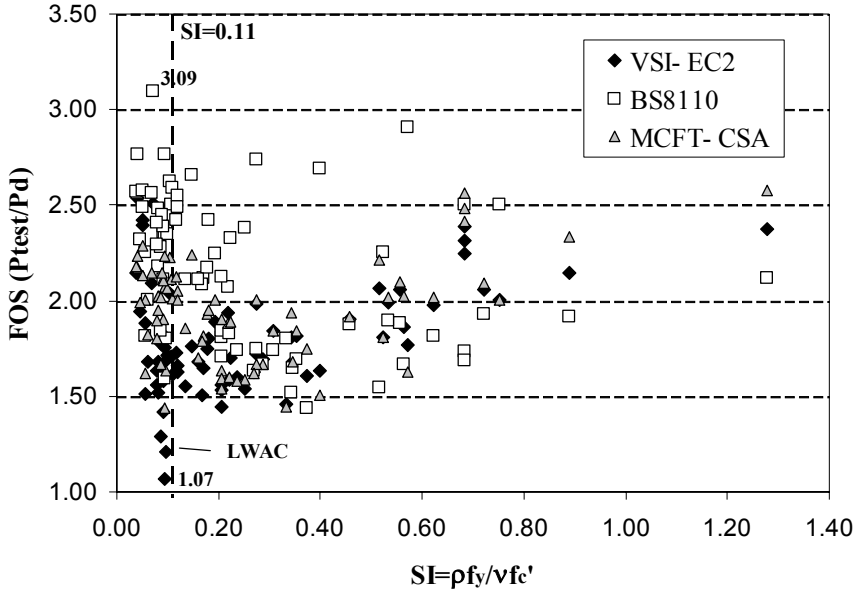

Note: Dead Load=Live Load; EC2 (1.35+1.5)/2; BS8110 (1.4+1.6)/2; CSA (1.25+1.5)/2
Material factors of safety (γ_c/γ_s): EC2 (1.5/1.15); BS8110 (1.25/1.15); CSA (1.54/1.18)

Figure 8.17: Summary of factors of safety of continuous beams using EC2, BS8110 and CSA

Although the VSI (z=0.9d) predictions of continuous beams studied were not accurate for values of *SI* larger than around 0.11, the factors of safety shown in Figure 8.17 were still

acceptable, except for some of the LWAC beams tested by Ramirez et al. [184]. This is highly inconsistent with the results obtained in the original Demerit Point Classification proposed by Collins [148] (see Table 8.6). The modified Demerit Point Classification approach presented here, reflects this improvement in *FOS* using the VSI method for stirrup indexes higher than 0.11; see reduction in *DP* mark in Table 8.7. On the other hand, the marks shown for both demerit point classifications (Table 8.7) were similar for the remaining design methods investigated. Lastly, it is noteworthy that both demerit point approaches showed that the *FOS* obtained using the VSI method were significantly lower for *SI*<0.11. From the beams tested in this work, the lowest *FOS* obtained was 1.56, which corresponded to beam CA1 using the VSI method. The average *FOS* obtained for the 8 continuous beams tested were 1.65/2.31/1.88 using EC2/BS8110/CSA design codes respectively; the COV were 4.4/13.6/8.3% using EC2/BS8110/CSA respectively.

ρfy/νfc'≤0.11	*Ptest/Pd*	WITH FOS			*Ptest/Pcalc*	NO FOS		
		VSI-EC2	**BS8110**	**CSA**		**VSI-EC2**	**BS8110**	**CSA**
Extremely dangerous	*<1.0*	0	0	0	*<0.5*	0	0	0
Dangerous	*1.0-1.15*	3	0	0	*0.5-0.65*	0	0	0
Low safety	*1.15-1.5*	10	0	4	*0.65-0.85*	10	0	0
Appropiate safety	*1.5-2.3*	72	34	96	*0.85-1.30*	69	38	86
Conservative	*2.3-3.5*	14	66	0	*1.30-2.00*	21	62	14
Extremely conservative	*>3.5*	0	0	0	*>2.00*	0	0	0
	TOTAL DP	**52**	**66**	**7**		**41**	**62**	**14**

ρfy/νfc'>0.11	*Ptest/Pd*	WITH FOS			*Ptest/Pcalc*	NO FOS		
		VSI-EC2	**BS8110**	**CSA**		**VSI-EC2**	**BS8110**	**CSA**
Extremely dangerous	*<1.0*	0	0	0	*<0.5*	0	0	0
Dangerous	*1.0-1.15*	0	0	0	*0.5-0.65*	0	0	0
Low safety	*1.15-1.5*	4	2	2	*0.65-0.85*	35	2	9
Appropiate safety	*1.5-2.3*	89	72	87	*0.85-1.30*	65	76	89
Conservative	*2.3-3.5*	7	26	11	*1.30-2.00*	0	22	2
Extremely conservative	*>3.5*	0	0	0	*>2.00*	0	0	0
	TOTAL DP	**15**	**30**	**15**		**70**	**26**	**20**

ALL	*Ptest/Pd*	WITH FOS			*Ptest/Pcalc*	NO FOS		
		VSI-EC2	**BS8110**	**CSA**		**VSI-EC2**	**BS8110**	**CSA**
Extremely dangerous	*<1.0*	0	0	0	*<0.5*	0	0	0
Dangerous	*1.0-1.15*	1	0	0	*0.5-0.65*	0	0	0
Low safety	*1.15-1.5*	7	1	3	*0.65-0.85*	25	1	5
Appropiate safety	*1.5-2.3*	83	57	91	*0.85-1.30*	67	61	88
Conservative	*2.3-3.5*	9	41	7	*1.30-2.00*	8	37	7
Extremely conservative	*>3.5*	0	0	0	*>2.00*	0	0	0
	TOTAL DP	**29**	**44**	**12**		**59**	**40**	**18**

Note: Dead Load=Live Load; EC2 (1.35+1.5)/2; BS8110 (1.4+1.6)/2; CSA (1.25+1.5)/2
Material factors of safety (γ_c/γ_s): EC2 (1.5/1.15); BS8110 (1.25/1.15); CSA (1.54/1.18)

Table 8.7: Modified Demerit Point Classification proposed by the author

Parametric analysis of aggregate size using MCFT (Response 2000)

In the shear strength predictions shown in previous section using CSA formulas, the effective crack spacing (s_{ze}) was assumed to be 300mm, which is the value recommended for members with shear reinforcement. On the other hand, members without shear reinforcement, allowance is made for estimating s_{ze} as a function of the crack spacing parameter and aggregate size (a). As discussed in section 8.2.1, this allows to take into account for aggregate fracture at cracks by reducing a.

In order to investigate the effect of reducing the aggregate size in members with shear reinforcement, a parametric analysis was carried out for beams BL, using Response 2000. The aim was to assess the stirrup index at which aggregate fracture would be more critical according to MCFT. According to shear panels investigated in section 5.3.3, the influence of reducing the aggregate size using MCFT in members with shear reinforcement was insignificant. The results obtained from the parametric analysis for beams BL showed a similar conclusion as for shear panels (see Figure 8.18). The largest differences in shear strength between predictions using a=10mm and a=0 were 2.75% for beams without stirrups and 2.17% for SI about 0.16.

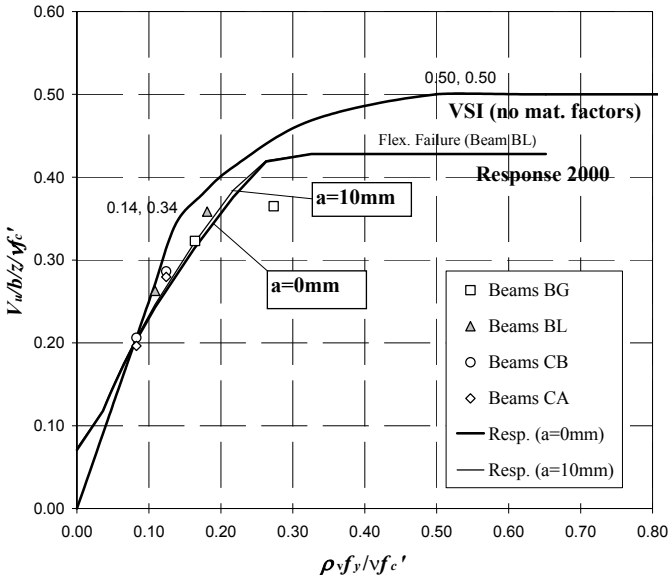

Figure 8.18: Influence of aggregate size in MCFT predictions of continuous beams

In the parametric analysis carried for beams BL, flexural failure was obtained at SI=0.26. However, the differences between a=10mm and a=0 curves were similar to that shown in Figure 8.18, if a higher yield strength of the longitudinal reinforcement was adopted in order to increase the load at which flexural failure occur.

8.3.3 Estimation of shear stresses at cracks

In this section, the shear stresses carried along critical cracks in beams B were estimated initially from interpolating crack displacement and stress data from push-off tests. These experimental results are compared with predictions from different analytical models, which are further discussed in the following sections. These are:

1. Equilibrium at the crack assuming angle of the strut from VSI and MCFT
2. Variable strut inclination method with "shear friction" constraint
3. Discrete crack-slip model
4. NLFEA with smeared and discrete cracking elements

The methods mentioned above, which are used to assess the shear at the crack (τ_{cr}) were based on analytical models, in which several parameters needed to be estimated and therefore variations in the solutions were expected.

Experimental values of shear stresses according to push-off test data

In order to estimate the shear stresses at the critical cracks in the beams from push-off test data, interpolated curves were obtained in section 4.3, which provided values of τ_{cr} for different crack opening (w) and slip (s) displacements. These curves were generated for the same concretes used for beams BL and BG, as well as for different shear reinforcement ratios. Interpolating the shear stresses at crack in beams from push-off test data can offer several advantages, although it can also bring several uncertainties, as described in section 4.3. Monitoring crack displacements was possible in beams with stirrups due to their more ductile behaviour compared to beams without stirrups, for which measuring w and s is complicated as pointed by Taylor [2].

One of the main differences between cracks measured in push-off tests and those obtained in beam tests is that the crack dilatancy ($\delta w/\delta s$) is considerably lower for the first type of tests (Figure 8.19). In addition, as shown in chapter 6 (sections 6.3.4 and 6.5.4), the crack widths were generally greater in short span beams, which resulted in $\delta w/\delta s$ ratios of around 3. These values were considerably larger than slender beams with stirrups ($\delta w/\delta s$~1.5), which could result in a lower contribution of aggregate interlock action. These variations in the crack dilatancy are shown in Figure 8.19. In addition, the crack opening-slip relationships obtained experimentally were satisfactory reproduced by either non-linear finite element models and discrete crack slip model described in the next sections. The interpolated curve, which was obtained to fit the crack dilatancy observed in

short span beams tested in this work (section 7.5), is also shown in Figure 8.19 in order to illustrate the difference between cracks in slender beams, short span beams and push-off tests.

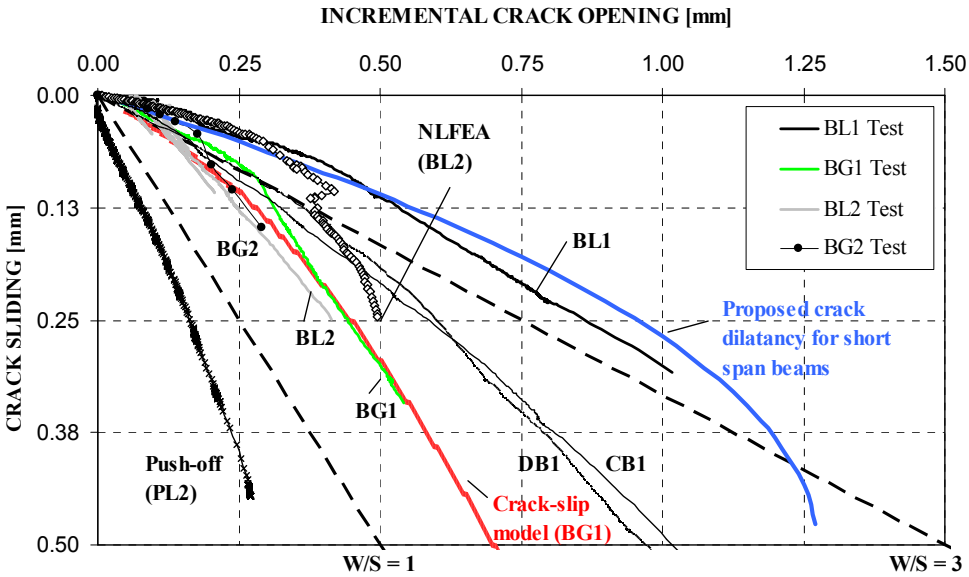

Note: relative crack displacements are shown up to peak load
Refer to section 7.5 for crack dilatancy relationship obtained for short span beams A

Figure 8.19: Comparison between crack dilatancy of slender beams with stirrups (beams B, C and D), short span beams and push-off tests

As shown in Figure 8.19, beam BL1 had a slightly different crack dilatancy compared to the remaining slender beams tested. Initially this was believed to be due to wider cracks related to the lower reinforcement ratio of BL1. However later experimental evidence from beams with similar stirrup indexes (beams CB1 and DB1) did not support this idea, as shown in Figure 8.19. The crack widths at failure observed in both beams C and D were of similar magnitude as those measured in beam BL1 (Figure 8.19), which might indicate that the problem is related perhaps to the crack slip measurements in BL1.

The crack shear stresses obtained at failure load in beams B are summarised in Table 8.8. These figures were obtained from curves given in section 4.3 (see Figure 4.12), using crack displacements at failure shown in Table 8.8. The shear stresses at the crack shown in Table 8.8 were higher in beams BL than in beams BG, which was probably due to the significant difference in the concrete strength. It is interesting to note that the ratio between the shear estimated at the crack and the total shear (τ_{cr}/v), assuming a constant distribution along the section, was larger than the one obtained for short span beams (see Table 7.12). This further supports the idea that aggregate interlock had a lower contribution in short span beams tested compared to beams B.

Beam	*Test*			*Interp.*	
	$v=V/b_w d$ [MPa]	w [mm]	s [mm]	τ_{cr} [MPa]	τ_{cr}/v
BG1	4.83	0.55	0.35	3.15	0.65
BG2	5.46	0.33	0.09	4.10	0.71
BL1	5.94	1.02	0.31	3.75	0.63
BL2	8.10	0.39	0.23	5.10*	0.63

Note: *This value corresponds to push-off tests PL3, which provides a higher bound since had a slightly larger reinforcement ratio; the actual crack had a reinforcement ratio between that provided to PL2 and PL3. A lower bound would correspond to PL2 (τ_{cr}=4.6MPa)

Table 8.8: Interpolated shear at the crack (τ_{cr}) at failure in beams B from push-off test data

In the following sections τ_{cr} is estimated using different analytical approaches. Firstly, results from smeared crack approaches are presented using the variable inclination strut truss and MCFT. Secondly, discrete approaches are adopted (Discrete crack-slip model and NLFEA).

1- Equilibrium at the crack assuming angle of the strut from VSI and MCFT

The shear and normal stresses at the crack can be estimated once the inclination of the crack (α) and the strut are known, as shown in Figure 8.20. The shear stresses at the crack can be estimated from the equilibrium conditions of a differential element at the crack, which leads to equation (8.3), see Hamadi & Regan [19]. The results for τ_{cr} are highly dependent on the difference in angle β assumed between the crack and the stress field. The inclination of the crack (α) was taken from the observed shear crack at mid-height of the beam, as shown in Figures 8.20 and 8.21.

$$\tau_{cr} = \sigma . \frac{\cot \beta}{1 + \cot^2 \beta} \qquad \ldots (8.3)$$

where β=($\alpha - \theta$).

The angle of the strut (θ) was estimated with both the variable inclination strut method and the MCFT, see Table 8.5. In the VSI the inclination of the strut was given by the plastic solution in beams BG and BL2, while for the remaining beams $cot\theta$ was limited to 2.5. An alternative approach for assessing θ is to assume that failure was governed by yielding of the stirrups without crushing of the struts. In this latter method, the experimental ultimate load was used to determine the inclination of the strut required to mobilize the sufficient stirrups to resist the entire shear force. The stirrups were assumed to be smeared out uniformly along the beam.

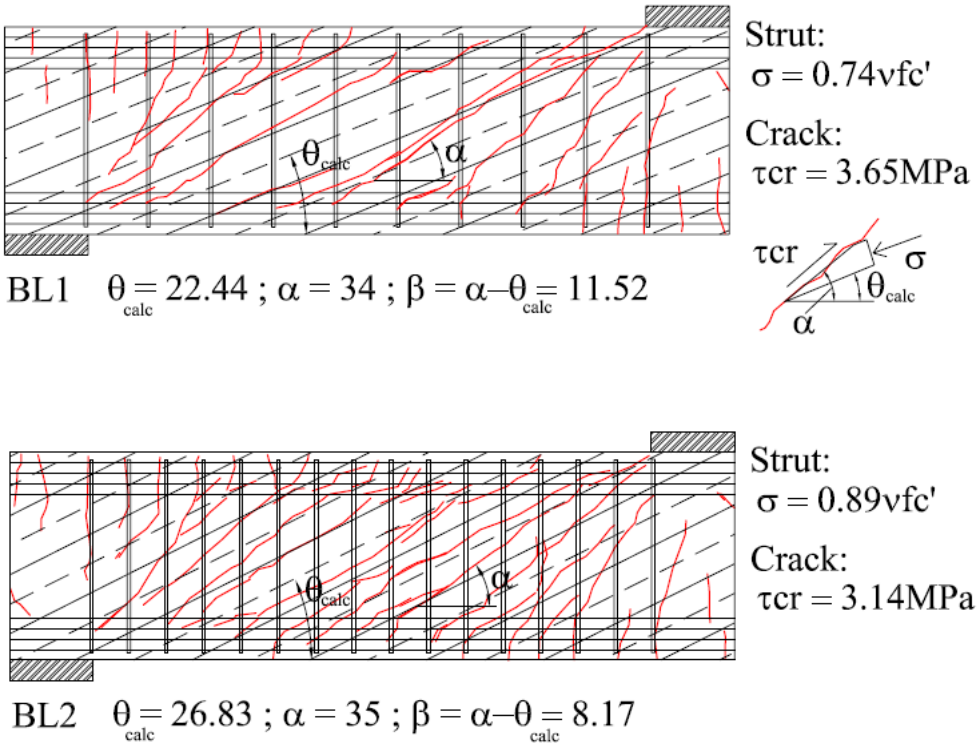

Figure 8.20: Crack pattern in relation with the inclination of the strut (θ) obtained from V_{test} (Limestone beams)

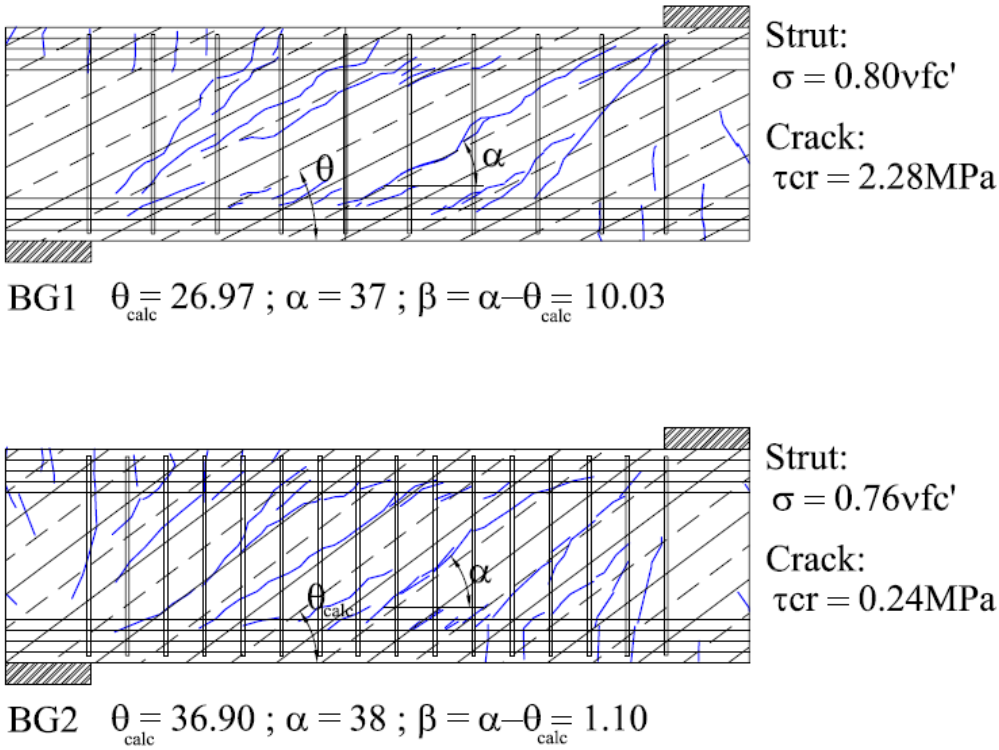

Figure 8.21: Crack pattern in relation with the inclination of the strut (θ) obtained from V_{test} (Gravel beams)

According to this analysis, the struts would only reached around 80% of their plastic capacity ($\nu f_c'$) in beams B, see Figures 8.19 and 8.20. Both this approach and the VSI gave similar predictions of θ since shear strength predicted by the VSI method was close to the actual failure load. The largest difference in strut inclination was (5º) in BG2, with the lowest V_{test}/V_{calc} ratio. The inclination of the strut (θ) and crack (α) are summarized in Figures 8.20 and 8.21, which also show the crack pattern in relation with the orientation of the struts. As expected, the angle between the crack plane and strut direction decreased as the stirrup index increased, resulting in lower shear stresses at the crack.

The MCFT was also used to estimate θ. The inclination of the struts predicted using CSA approach is considerably steeper than those obtained with EC2, as shown in Table 8.5. This is due to the fact that a concrete contribution is taken into account. As described by Bentz & Collins [177], CSA design equations provide similar predictions to MCFT, although a larger value of V_c is needed in the CSA approach to compensate for neglecting the limit of shear transfer capacity of the crack. Hence, it seems more sensible to estimate θ by solving the full set of equations in the MCFT (Response 2000) rather than using CSA design equations. The results obtained for θ and τ_{cr} at failure are summarized in Table 8.9 for both EC2 and MCFT approaches.

	VSI (at V_{test})		*MCFT (Response 2000)* (at V_{calc} except #, see Table 8.5)				*Tests* (section 4.3)		*Eqn.* (2.14)
Beam	θ [º]	τ_{cr}^{+} [MPa]	θ [º]	σ [MPa]	τ_{cr}^{+} [MPa]	w_{MCFT} [mm]	w [mm]	τ_{cr}^{*} [MPa]	v_{ci}^{**} [MPa]
BG1	26.97	2.28	27.34	13.70	2.27	0.82	0.55	3.15	4.56
BG2	36.90	0.24	33.31#	12.62#	1.02#	0.36	0.33	4.10	6.14
BL1	22.40	3.65	23.62	17.94	3.18	1.45	1.02	3.75	4.09
BL2	26.83	3.14	29.22	20.60	2.06	0.72	0.39	5.10	6.49

Note: +Shear stress obtained according to equation (8.3)
*Test values correspond to Table 8.8 which are estimated from push-off test data
MCFT (Response 2000): results shown for a section at a distance 0.9d from load point; w (average values); σ, θ obtained at mid-depth of section
#Values are given at load similar to experimental failure load, since V_{calc}/V_{test}=1.23 (Table 8.5)
**Equation (2.15) used in MCFT, taking experimental values of w. Normal crack stresses have been estimated assuming yielding of stirrups crossed by the crack (f_{ci}=2.47/3.36/2.31/3.25MPa for beams BG1/BG2/BL1/BL2 respectively)

Table 8.9: Summary of predictions of using approaches based on inclination of strut

Table 8.9 shows that the inclinations of the strut were similar using VSI and MCFT. Hence, the shear stresses obtained along the crack were comparable using either approach. However, both predictions were lower than those obtained experimentally, especially for beams with larger number of stirrups (see Table 8.9). In particular, the inclination of the strut predicted for BG2 was almost parallel to the crack plane, which resulted in very low values of the shear stresses at the crack.

Crack widths predicted by MCFT were around 50% greater than those obtained experimentally. As a result, the maximum shear stress capacity that can be transmitted along the crack according to MCFT equation (2.14) is underestimated. The last column in Table 8.9 shows the shear stresses estimated at the crack using MCFT equation (2.14) and (2.15). In order to get a more realistic estimate, the crack openings adopted in these equations were taken from the experimental values. In addition, the normal stresses at the crack were estimated assuming yielding of the stirrups, which were crossed by the crack; refer to Table 8.9. The shear stresses at the crack assessed in this manner, which are shown in Table 8.9, were closer to the values derived from the curves in section 4.3.

It can be concluded that the approaches followed here to estimate the shear stresses at the crack must be considered as rought approximations primarily because the inclination of the strut had to be estimated analytically. In this work, the value of θ has not been measured experimentally, although several techniques are available. Firstly, principal strains could be measured experimentally by means of a rosette of transducers, which provide strains readings in three directions. The inclination of the principal stresses could be assumed to be equal to strains, which seems to be the basis of Walraven & Stroband [10] results for θ. Another approach was used by Hamadi & Regan [19], who calculated θ from equilibrium at the bottom chord of the truss using strains measured in longitudinal and shear reinforcement respectively. These approaches can provide reasonable values of the inclination of the strut, although they are approximate solutions.

The second uncertainty in the values of τ_{cr} presented in Table 8.9 is that the inclination of the crack is not constant as assumed, which can produce high variations in the predictions. Even so, the crack patterns were in good agreement with the predictions from the variable strut inclination truss model, as shown in Figures 8.20 and 8.21.

2- Variable strut inclination angle truss with "shear friction" constraint

In many design codes such as EC2 or ACI-318 a "shear friction" relationship in the form of $\tau = C+\mu\sigma$ (Coulomb failure criteria) is suggested to design contact interfaces between two concrete surfaces. As discussed in section 4.4, the cohesion factor (C) is generally given as a function of the tensile strength of the concrete and the friction μ depends exclusively on the roughness of the interface. However, design codes can be inconsistent regarding recommended values for C and μ, which can complicate the use of this formula in more general shear design method since results are highly dependent on these parameters. For the particular case of beams B, the cohesion and friction were calibrated using push-off test data available (see Table 4.3); C(BG/BL1)=1.20/2.50MPa and μ(BG/BL)=1.06/0.95, these values are discussed in further detailed in section 4.4.

As reported by Regan [3], recent German revisions to EC2 implemented in DIN1045:2000, seem to introduce this shear friction equation into the variable inclination strut model, being the limiting factor for intermediate shear reinforcement ratios. In this manner web failures due to crushing and sliding at the cracks are treated separately, as shown in Figure 8.22. A similar approach can be adopted in a strut-and-tie model, as shown in section 7.5.2, for short span beams. These types of approaches seem transparent and consistent with code guidelines, although as mentioned earlier the results are highly dependent on parameters C and μ assumed.

The formulas derived by Regan [3] in which a shear friction equation was implemented into the VSI truss, could not be applied directly to beams B since they assumed a crack inclination of α = 45º and a friction μ equal to 1. The previous assumptions led to the exact linear solution $v=V/bz=C+\rho_v f_y$. In a more general case shown in Figure 8.22, the system of equations (8.4 to 8.6) must be solved iteratively. Equations (8.4) and (8.5) relate to the variable strut inclination truss, with the stress in the strut (σ) limited to $\nu f_c'$.

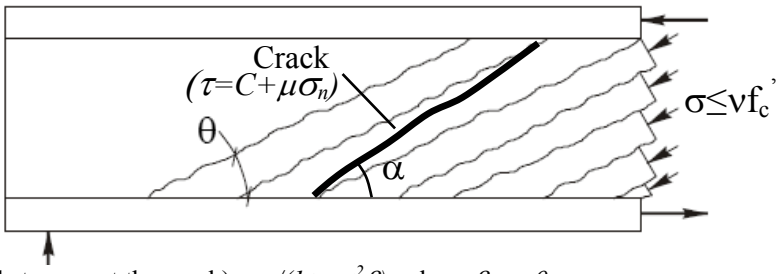

Note: σ_n (normal stresses at the crack) $=\sigma/(1+\cot^2\beta)$, where $\beta=\alpha-\theta$

Figure 8.22: Variable inclination strut method with shear friction condition at cracks

$$v = \frac{V}{bz} = \sigma . \frac{\cot\theta}{1+\cot^2\theta} \quad \ldots (8.4)$$

$$v = \rho_v . f_y . \cot\theta \quad \ldots (8.5)$$

$$\sigma = c . \frac{1+\cot^2\beta}{\cot\beta - \mu} (shear - friction) \le \nu f_c' \quad \ldots (8.6)$$

where $\beta = \alpha - \theta$

The shear friction condition, given by equation (8.6), is considerably less restrictive for 35º inclined cracks such as those in beams B than for the 45º cracks studied by Regan or short span beams investigated in chapter 7. Figure 8.23 shows the results obtained for beams BG and BL with average crack inclinations of 37.5º and 34.5º respectively. The numerical results shown in Figure 8.23 seemed consistent with the experimental data except for beam BG2, which had the largest $\rho_v f_y / \nu f_c'$. The shear estimated at the crack (τ_{cr}) and the strut inclination (θ) are also shown in Figure 8.23.

The predictions of the ultimate strength were reasonable for most of beams B, although they did not differ much from the standard VSI predictions. Therefore, the benefit of imposing a simplistic shear friction restriction into the VSI in this case was not significant. It is also noteworthy that simplified estimate of τ_{cr} provided by FIP [21], which is adopted in the truss with crack friction model (see section 2.4), were in good agreement with predictions from the VSI with shear friction approach (see Figure 8.23).

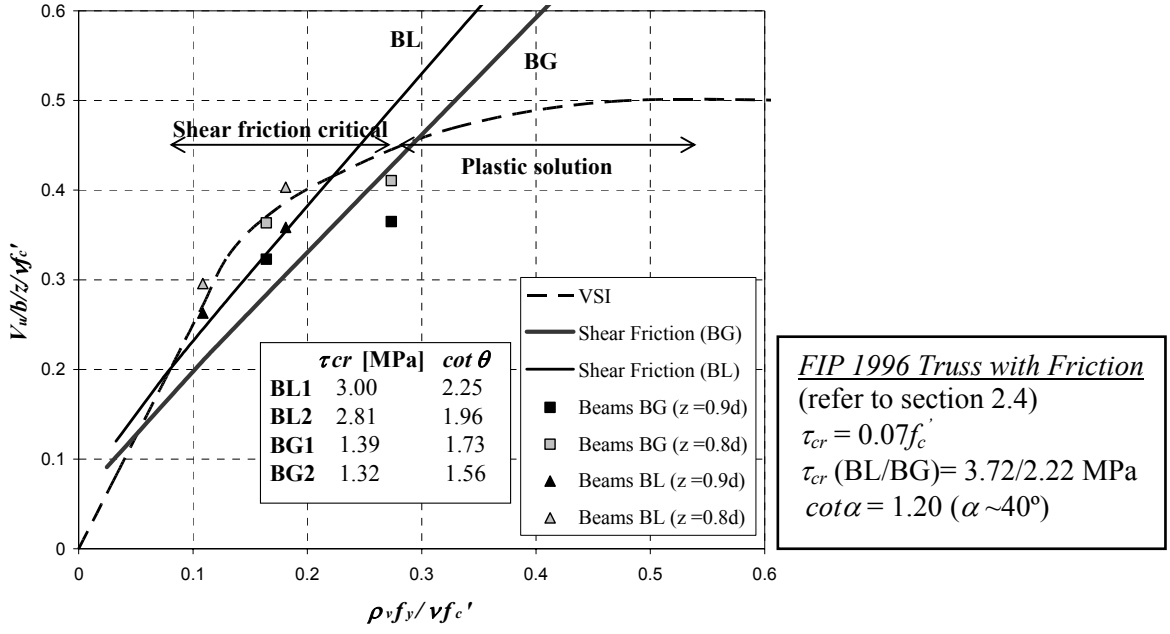

Figure 8.23: VSI with shear friction constraint at the cracks in beams B

3- Discrete crack-slip model

An alternative method to a shear friction formulation for limiting the shear strength in the beam by means of shear transfer across shear cracks is to apply a discrete approach using a crack slip model. The previous technique was developed by the author for shear panels with 45º inclined cracks and a pure shear stress state, see section 5.5. Strain compatibility and equilibrium of an element at the discrete crack is formulated in terms of the crack slip and opening. The main advantage of the crack-slip approach is that the shear stresses at the crack can be estimated in combination with the crack opening and sliding, which were obtained empirically. This seemed to be a more realistic approach than the shear friction model since relative crack displacements are taken into account. However, several difficulties arose from including realistically complex aspects such as aggregate interlock behaviour or tension stiffening into the model. Hence, several simplifications were necessary in the crack-slip model, which are discussed here and section 5.5.

The crack-slip model was initially conceived for pure shear panels, although the crack pattern and stress fields at the centre of the critical span of beams B are in some extent similar to the panels, see Figure 8.24. This assumption does not apply for neither simply supported beams nor for regions closer to the loading points, where the compression stress fields are fanned shaped. The main difference between panels and beam tests is that panels are usually reinforced in two orthogonal directions whilst the webs of the beams have vertical reinforcement only. In addition, the cracks at the beams were flatter than the typical 45º cracks observed in a pure shear panel.

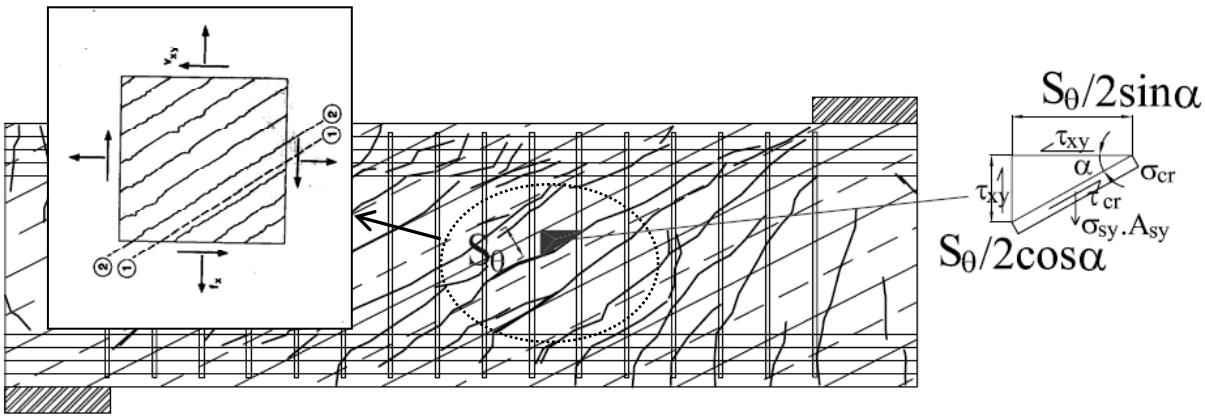

Figure 8.24: Differential element used in the crack-slip model for continuous beams

The values for crack inclination (α) and diagonal spacing (S_θ) used in the crack-slip model were taken directly from the experiments of beams B. In a general case, these parameters can be estimated using approximate formulas available, which are function of the stirrup spacing, refer to CEB-FIB[6] formulas. In addition, the linear aggregate interlock model proposed by Walraven & Reinhardt [46] was adopted to relate normal/shear displacements and stresses at the crack. This aggregate interlock model, which had been validated in this work against push-off experimental data, provided sensible predictions of shear panel tests, as shown in section 5.5.3.

The equilibrium and compatibility conditions shown in section 5.5.2 for the particular case of shear panels with 45º cracks can be generalized as shown by equations (8.7) to (8.13). The horizontal and vertical faces of the differential element shown in Figure 8.24 have lengths equal to $L_x=S_\theta/(2sin\alpha)$ and $L_y=S_\theta/(2cos\alpha)$ respectively. The strains generated in both global *x-y* directions and local *r-d* axis, due to crack opening in the *r* direction are given by equations (8.7), (8.8) and (8.9).

$$\varepsilon_{rcr} = \frac{w}{S_\theta} \quad \text{and} \quad \varepsilon_{dcr} = 0 \qquad \ldots (8.7)$$

$$\gamma_{cr} = \varepsilon_{rcr} - \varepsilon_{dcr} = \varepsilon_{rcr} \qquad \ldots (8.8)$$

$$\varepsilon_{xcr} = \frac{2w}{S_\theta}.\sin^2\alpha \quad \text{and} \quad \varepsilon_{ycr} = \frac{2w}{S_\theta}.\cos^2\alpha \qquad \ldots (8.9)$$

Similarly, the strains generated due to crack sliding *s* are given by equations (8.10) and (8.11).

$$\varepsilon_{rcr} = \varepsilon_{dcr} = \gamma_{cr} = 0 \qquad \ldots (8.10)$$

$$\varepsilon_{xcr} = \frac{2s}{S_\theta}.\sin\alpha\cos\alpha \quad \text{and} \quad \varepsilon_{ycr} = \frac{-2s}{S_\theta}.\sin\alpha\cos\alpha \qquad \ldots (8.11)$$

Equilibrium conditions at the differential element shown in Figure 8.24 yield to the following expressions:

$$\tau_{xy} + \sigma_{ncr}.\tan\alpha = \tau_{cr} \qquad \ldots (8.12)$$

$$\tau_{xy} + \sigma_{ncr}.\cot\alpha = \sigma_{sy}\rho_{sy}\cot\alpha - \tau_{cr} \qquad \ldots (8.13)$$

where σ_{sy}=min[f_y, $E_{sm}.\varepsilon_{xcr}$] and E_{sm} =enhanced value of the Young's modulus

As discussed in section 5.5.3, the enhanced value of the Young's modulus E_{sm} due to tension stiffening can be estimated using approximate formulae such as proposed by Hsu [114]. For simplicity, E_{sm} was taken as 1.5 times E_s (200000MPa). In addition elastic strains in the concrete and bond-slip between the concrete and reinforcement were neglected. It is also important to note that the pre-cracked state is not taken into account. As already mentioned, the Walraven & Reinhardt [46] linear aggregate interlock relationship, see equations (2.28) and (2.29), were adopted to relate τ_{cr} and σ_{ncr} in equations (8.12) and (8.13) to relative crack displacements w and s.

The crack opening and slip can be solved numerically implementing equations (8.7) to (8.13) into a spreadsheet. The results obtained using the crack-slip model are summarised in Table 8.10. Surprisingly, the maximum shear stresses at the crack were similar to the ones obtained from the shear friction approach shown in Figure 8.23. These values are lower than those interpolated experimentally (Table 8.9).

		Crack-slip model				*VSI*	*Test*		
	SI $\rho_v f_y / v f_c$	τ_{cr} [MPa]	w [mm]	s [mm]	θ [º]	θ [º]	w [mm]	s [mm]	τ_{cr} [MPa]
BG1	0.16	1.77	0.55	0.34	23.98	26.97	0.55	0.35	3.15
BG2	0.27	2.39	0.55	0.43	21.32	36.90	0.29	0.15	4.10
BL1	0.11	2.36	0.45	0.27	28.00	22.44	1.02	0.31	3.75
BL2	0.18	3.57	0.25	0.18	26.19	26.83	0.39	0.23	5.10

Note: Diagonal spacing S_θ adopted from tests observation (230/177/206/65mm) for beams BG1/BG2/BL1/BL2 respectively

Table 8.10: Crack-slip model predictions

Similarly as in shear panels, the inclination of the strut θ was calculated from Mohr's circle knowing points A($\sigma_{sx}\rho_x$, τ_{xy}) and B($\sigma_{sy}\rho_y$, $-\tau_{xy}$), as shown in equation (5.22). In Beams B, σ_{sx} was zero since only vertical reinforcement was provided at the web. It is interesting to note that the inclination of the principle compression stresses predicted by the crack-slip model was consistent with the plasticity estimations for all beams B, except for BG2, which was considerably flatter (see Table 8.10). Figure 8.25 shows the predicted and experimental development of the crack opening and sliding through the loading (V/V_{max}).

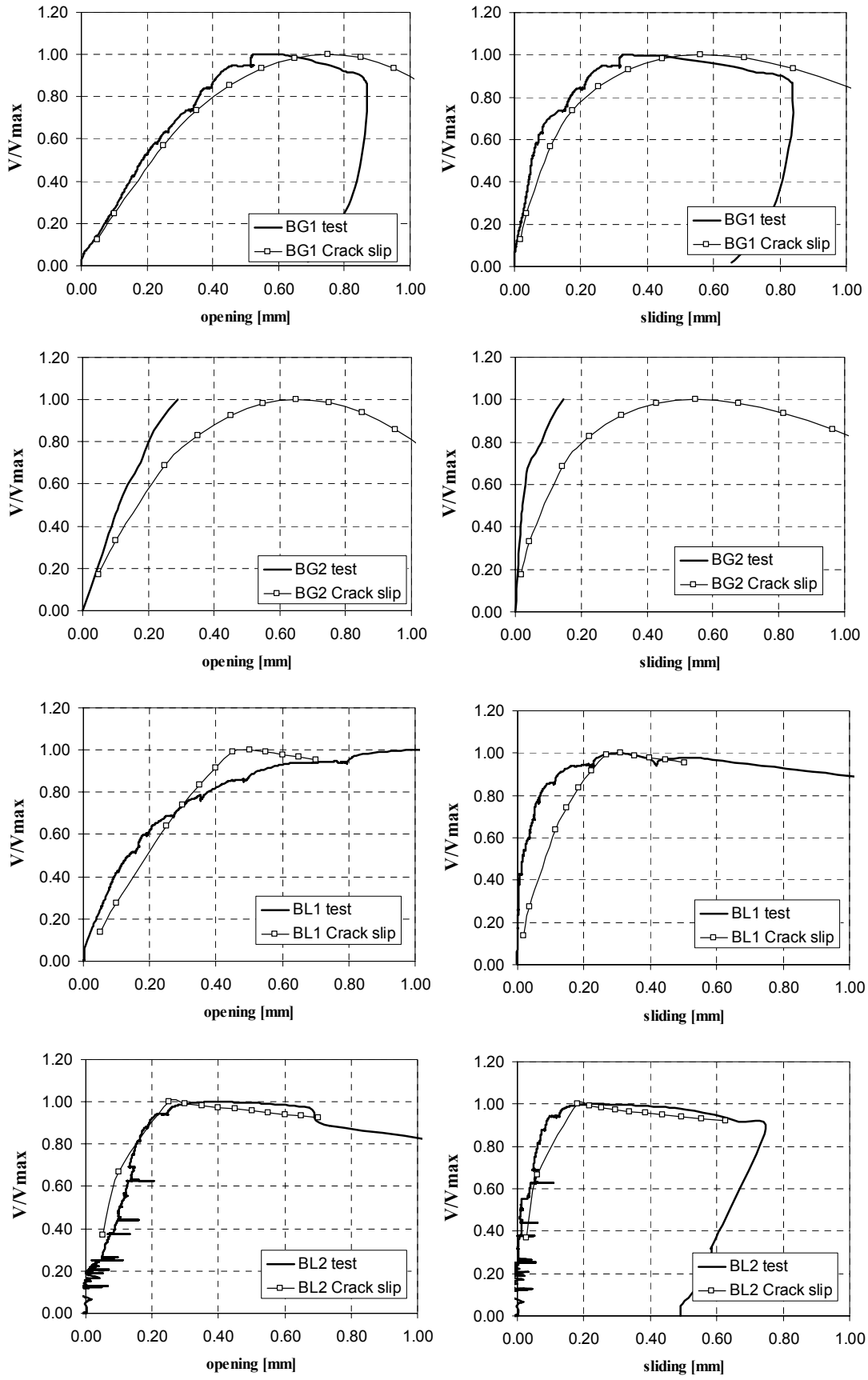

Note: V/Vmax for "test" refers to the shear ratio applied in the span
V/Vmax for the "Crack slip" refers to the shear ratio at the crack

Figure 8.25: Comparison between experimental and predicted crack opening and sliding

The crack opening and sliding predicted by the crack-slip method were reasonable in general as shown in Figure 8.25 and Table 8.10. The $\delta w/\delta s$ ratio predicted was around 1.5, as discussed at the beginning of this section (refer to Figure 8.19). The worse predictions were obtained for BG2 where w and s were overestimated. In addition, the relatively large crack opening in beam BL1 was not well captured by the crack-slip model. It must be highlighted that curves shown in Figure 8.25 refer to the tests of the pre-cracked beams and so the change in stiffness at early load stages is not reflected. This is consistent with the crack-slip model assumption, which does not take into account the pre-crack state, and so results were similar for early load stages. Yielding of the shear reinforcement was predicted in all the beams by the crack slip model, except for beam BG2. This did not agree with experimental evidence since according to Demec gauge readings stirrups yielded at failure in all beams B

In view of these results it can be concluded that the crack-slip model provided better predictions for beams B with intermediate $SI=\rho_v f_y/\nu f_c'$ (BG1, BL2). In extreme cases with high SI (BG2), where the w and s were small, the crack-slip model did not provide accurate results. This performance was expected since the crack-slip model suggested assumed that the shear strength is only limited by the shear transfer across the cracks. However, experimental evidence shows that the aggregate interlock action is mobilized only for intermediate ranges of SI.

4- NLFEA with smeared and discrete cracking elements

The crack opening and sliding at the main shear crack were assessed using a non-linear finite element model, which combined discrete and smeared cracking elements, in a similar fashion as for short span beams A. The mesh applied for beams B, shown in Figure 8.26, was assembled after the position of the main shear cracks was obtained experimentally. As in the NLFEA of short span beams described in section 7.5.3, a preliminary analysis using smeared cracking elements only was performed. This analysis was required firstly to validate the smeared crack models and secondly to verify that the main shear cracks formed at a similar position as the discrete interface plane assumed.

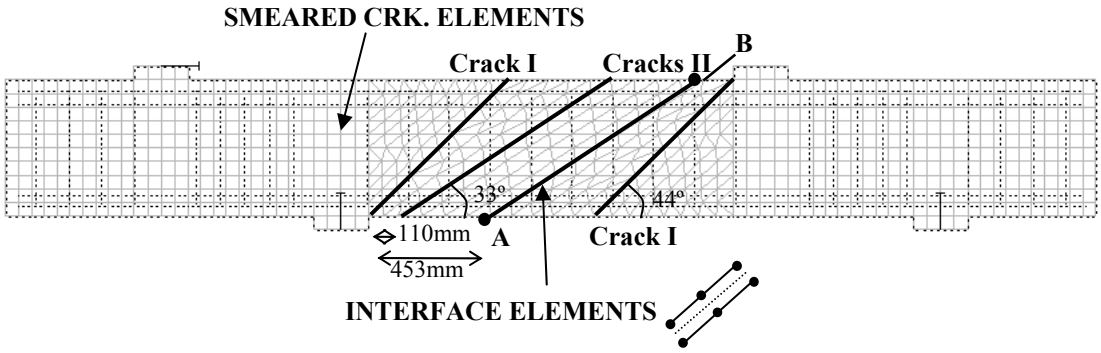

Figure 8.26: Finite element mesh of beams B, using discrete and smeared cracking elements

Same types of elements were applied for beams B as in the short span beams models (refer to section 7.5.3). Analogously, the multi-fixed smeared crack model was chosen for the concrete and a perfect Von Misses plastic material was assumed for the embedded reinforcement elements. In addition, no bond-slip considerations were made and identical free-length values (l_{fr}) were assigned to the reinforcement crossing the interface elements (refer to section 7.5.3).

The splitting tensile strength was adopted for the smeared cracking elements. On the other hand, the interface elements were assumed to be pre-cracked (f_{ct} =0.1MPa), to be consistent with experimental data, which corresponded to a pre-cracked specimen. The interface elements crossed by longitudinal reinforcement remained inactive due to the low l_{fr} assigned to the reinforcement. The material properties applied to steel and concrete are summarized in Table 8.11. Similarly as in the NLFEA of short span beams, the concrete strength of the elements near the bearing plates was enhanced in order to avoid local failure of these elements and allowing to obtain crack displacements at loads near failure load.

Concrete	*BG*	*BL*	Steel	*Plates*	*Long Reinf.*	*Shear Reinf.*
E_c [MPa]	27215	36306	E_s [GPa]	200	200	200
ν	0.2	0.2	ν	0.3	0.3	0.3
f_{ct} [MPa]	2.8	3.8	f_y [MPa]	500	580	550
G_f [N/mm]*	0.15	0.15	l_{fr} [mm]	-	0.2	150
f_c [MPa]	31.7	53.1				

Notes: + An estimated value of $G_c = 100G_f$ was assumed, where $G_f(\text{MC90})=G_{fo}.(f_{cm}/f_{cmo})^{0.7}$
* A Hordijk tension softening was applied

Table 8.11: Material properties in NLFEA of beams BG and BL

Considerations of constitutive model for interface elements

As discussed in section 7.5.3, the use of a simple discrete crack model where the shear and normal stresses were uncoupled, was justified for short span beams due to the relatively large crack opening compared with slip obtained. This assumption seemed more dubious for most of beams B, where the crack opening/slip relationship was lower. However, the performance obtained using the simpler discrete crack model was acceptable even for beams B, as it is shown in this section. Severe numerical difficulties were faced if a more complex crack dilatancy model was implemented in the NLFEA. For simplicity the discrete crack model was finally adopted, hence the shear stresses predicted in the NLFEA were only considered as a guidance value.

The overall shear stiffness of the interface elements after cracking (D_T) was initially estimated using Hamadi & Regan's [19] expression for aggregate interlock stiffness $D_T = k/w$. For simplicity a constant value of D_T (Table 8.12) was adopted assuming an average crack width near failure of around 0.5mm. Unlike short span beams, experimental data regarding the shear stiffness at the crack was available from push-off tests given in chapter 4. As described in section 4.5, Hamadi & Regan's [19] formula provided sensible predictions using a value of k equal to 5.4MPa for all specimens except for specimen PG2. Although the shear stiffness is generally assumed to be independent of the normal stresses at the crack, the value in this case seemed to be lower, as shown in Figure 8.27. Subsequently, k was assumed as 2.7MPa for BG2 and 5.4MPa for the remaining beams as shown in Table 8.12. The influence of changing D_T in the predictions was examined in the NLFEA.

As explained in section 3.4.2, modelling of reinforcement crossing discrete cracks is complicated. Simple approach adopted in DIANA, which is described in section 3.4.2, seems to overestimate the contribution of dowel action to the overall shear stiffness at the

interface. This can be compensated by reducing the shear stiffness assigned to interface elements (D_{ai}) in order to have an equivalent overall stiffness (D_T), which is measured in push-off tests. The dowel action stiffness (D_{dw}) assumed in the model can be calculated in terms of the free length parameter and shear reinforcement ratio defined along the crack surface $D_{dw}=E_s/(2l_{fr})\rho_{ck}$. The decomposition of D_T into D_{dw} and D_{ai} components finally adopted in the models is shown in Table 8.12.

Parameters	***BG1***	***BG2***	***BL1***	***BL2***
D_I [N/mm^3]	136070	136070	181530	181530
D_{II} [N/mm^3]	56698	56698	75637	75637
f_{ct} [MPa]	0.1	0.1	0.1	0.1
G_f [N/mm]	0.054	0.054	0.084	0.084
D_T *[N/mm^3]	5.4	10.8	10.8	10.8
D_{dw} [N/mm^3]	2.78	4.64	2.78	4.64
D_{ai} [N/mm^3]	2.6	6.2	8.0	6.2

Note: D = elastic stiffness (I- normal; II- shear); estimated as $D_I = E_c/h$ and $D_{II} = G/h$ where h = 0.2mm.
D_T^* = overall shear stiffness at the discrete crack assuming $D_T=k/w$ where w=0.5mm and k=2.7(BG1)/5.4MPa for remaining beams
D_{dw} = dowel action contribution estimated by DIANA for given l_{fr}=150mm, crack angle (33º) and stirrup spacing (E_s=200000MPa)
D_{ai} = shear stiffness assigned to interface elements ($D_{ai} = D_T - D_{dw}$)

Table 8.12: Material properties in the NLFEA of beams BG and BL

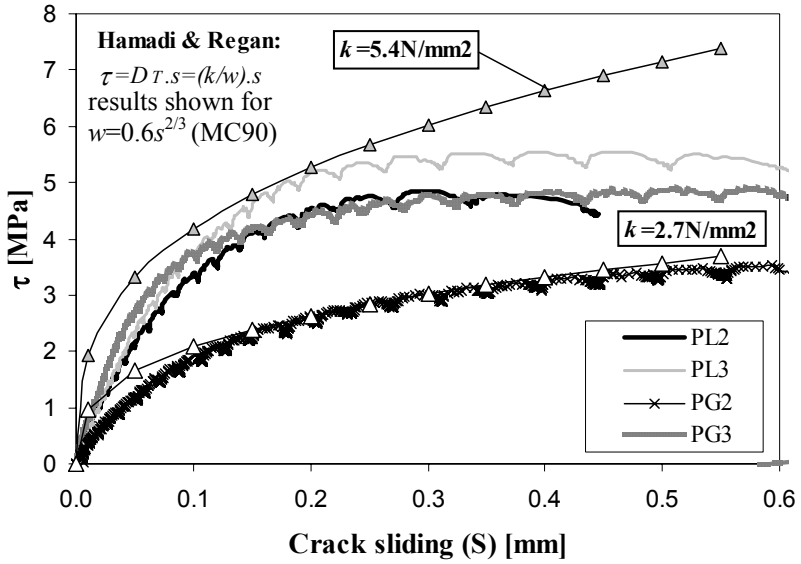

Note: Specimens P2-P3 had similar reinforcement ratio crossing the crack to beams B1-B2 respectively
Test data corresponds to first load cycle (see section 4.2.4)

Figure 8.27: Estimation of overall shear stiffness of cracks from push-off test data

NLFEA predictions for beams B

The numerical predictions of the crack opening and sliding at the central shear cracks (Cracks II in Figure 8.26) had a good correlation with experimental data, as shown in Figures 8.28, 8.29 and 8.30. The estimated crack slip was constant through the discrete plane in all beams as shown in Figure 8.28 for beam BL1, which is consistent with experimental data from either cross LVTDs, photogrammetric targets and Demec crosses placed at the crack. Similarly as in beams A, the crack opening predicted in the NLFEA was uniform along the interface plane for early load stages while for loads near failure w was considerably lower at interface elements crossed by shear links. As shown in Figure 8.28, interface elements crossed by longitudinal reinforcement were not active. This was intentional (refer to value of l_{fr} in Table 8.11) and the crack propagation in this region was relied upon the smeared cracking elements. As discussed in section 7.5.3, this approach was required in order to keep the model numerically stable.

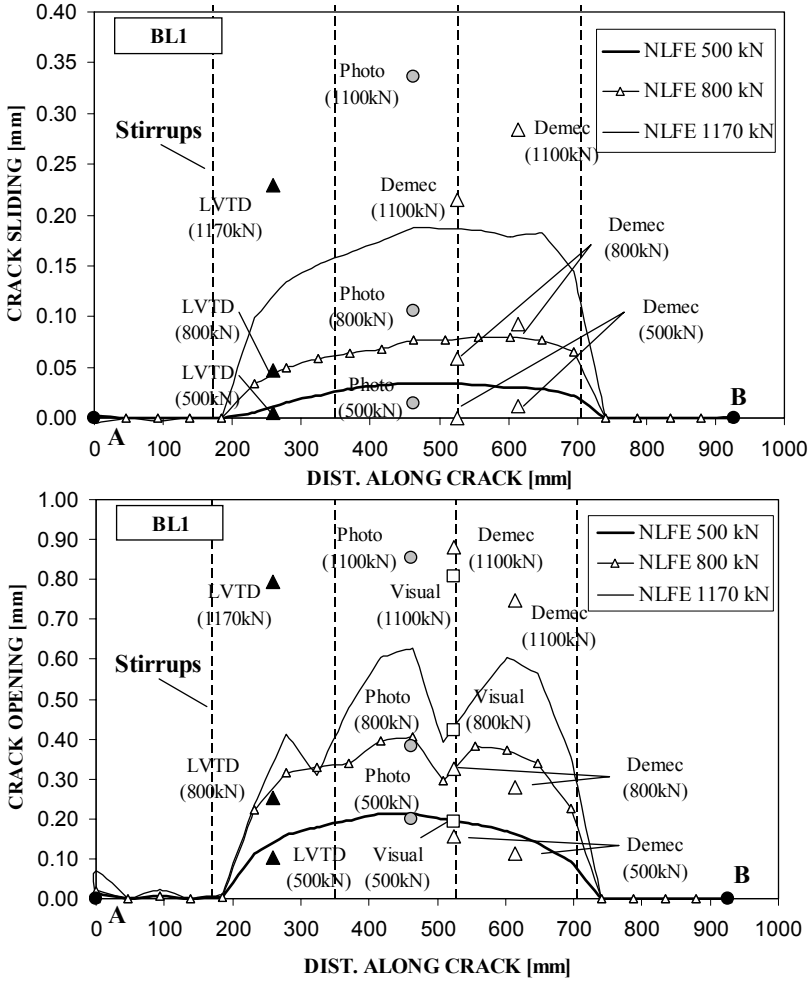

Note: Plane A-B is defined in Figure 8.26

Figure 8.28: Numerical and experimental crack displacements along discrete crack plane A-B of beam BL1 (results shown for D_T=10.8N/mm^3)

In addition, the load-deflection response was satisfactorily reproduced by the FE models, although the solution was very similar to the model using smeared cracking elements only (Figure 8.29 and 8.30). In general the crack opening w was slightly overestimated, especially for beams with higher stirrup indexes. The predicted crack openings were independent from changes in the shear stiffness at the discrete crack. However, the same was not true for the crack slip.

The crack sliding was slightly under-predicted in beams BG, especially for high values of D_T, see Figure 8.29. Better predictions of s were obtained in beams BG by reducing D_T. On the contrary, in beams BL the opposite was true, especially for beam BL2. The good predictions obtained for beams BG using low values of D_T suggested that the struts must had been almost parallel to the crack in those beams. This implied that a lower shear forces was transferred along the crack in beams BG compared to BL. This conclusion seems consistent with both interpolated shear stresses from push-off tests and analytical predictions given in this section.

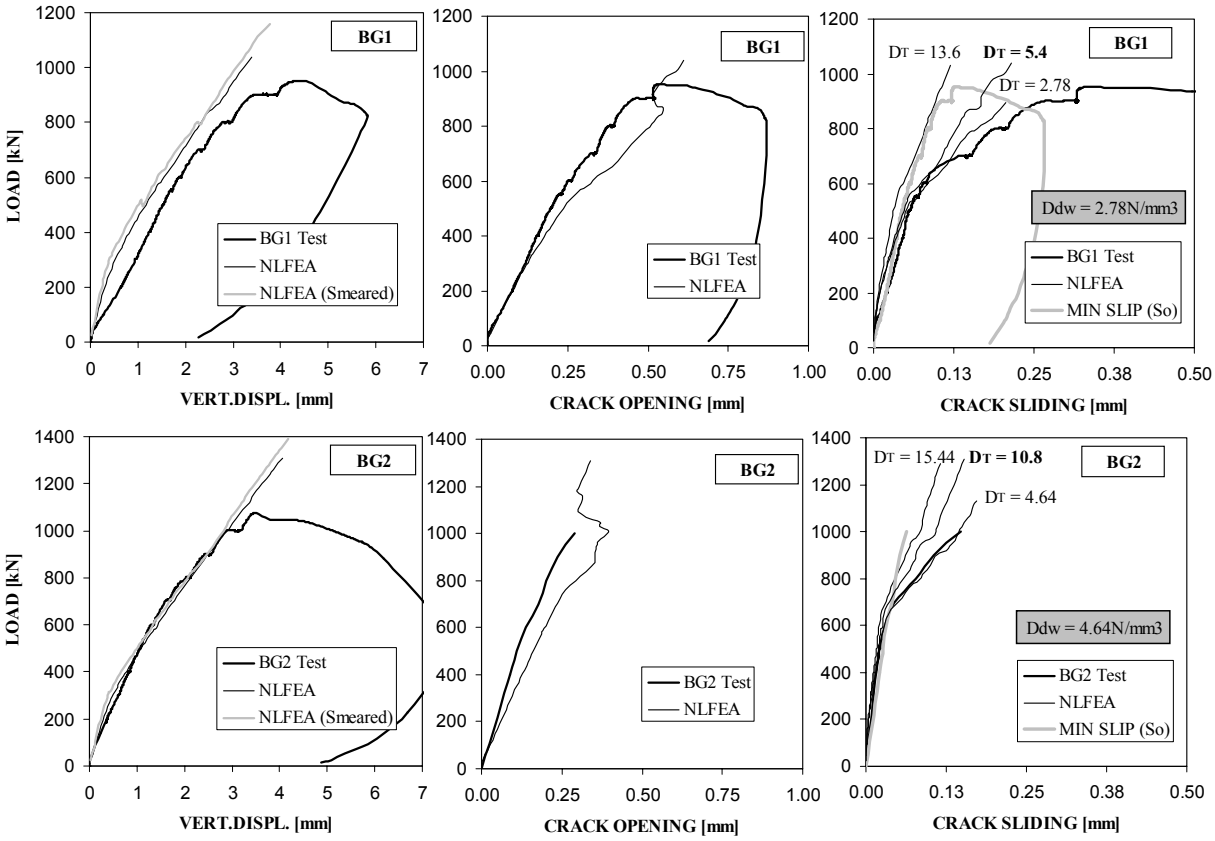

Note: NLFEA results relate to values of D_T shown in Table 8.12 unless stated

Figure 8.29: Comparison of numerical and experimental load-deflection curves and crack opening/sliding of beams BG

Despite the small discrepancies in w and s shown in Figures 8.29 and 8.30, the NLFEA reflected two important aspects observed in the experiments regarding the $\delta w/\delta s$ ratio. Firstly, the relatively large opening measured in beam BL1 ($\delta w/\delta s$=3), which had the lowest SI, was confirmed by the numerical analysis. Moreover, the predicted and experimental values of w and s for beam BG2, which had the highest SI, were considerably small (Figure 8.29). Secondly, for higher SI a change in the slope was also predicted (see Figure 8.19) in the w-s curve from early load stages, where the crack re-opened ($\delta w/\delta s$=3), to near failure, where crack slip was mobilized ($\delta w/\delta s$=1). These results were consistent with the predictions from the crack-slip model presented in previous section.

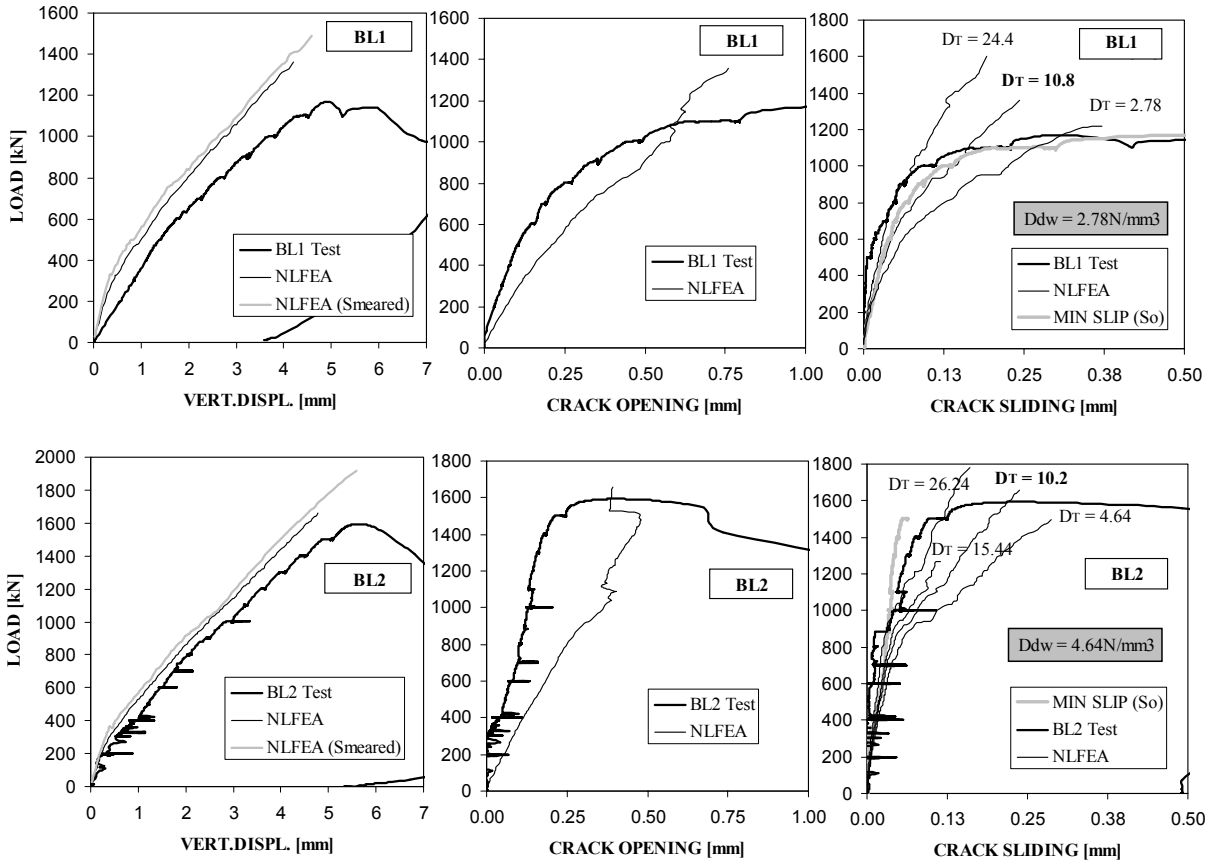

Note: NLFEA results relate to values of D_T shown in Table 8.12 unless stated

Figure 8.30: Comparison of numerical and experimental load-deflection curves and crack opening/sliding of beams BL

NLFEA predictions of crack shear stresses

The crack shear stresses predicted along the discrete plane (Crack II) were uniform throughout the loading, as shown in Figure 8.31 for the interface elements that became active. The values obtained for τ_{cr} were highly dependent on the shear stiffness assumed in the analysis (D_T). The stresses shown in Figure 8.31, include the contribution of stirrups crossing the interface, which for the case of BL2 (D_T =26.3N/mm3) was around 20% of the total shear stress τ_{cr}. It could be debatable whether the shear stresses obtained from the NLFEA are realistic, since the D_T was assumed constant. A consequence of this assumption is that increase of crack slip observed at failure due to crack widening could not be reproduced accurately; instead a linear response is predicted as shown in Figures 8.29 and 8.30. Nevertheless, useful information regarding crack displacements and stresses was still obtained by providing different values of D_T.

As mentioned earlier, the crack slip of beams BG was predicted more accurately assuming relatively low values of D_T, which results on minor shear stresses τ_{cr} at the crack. On the contrary, the prediction of the crack slip in beams BL was improved considerably assuming higher values of the aggregate interlock stiffness (D_T~25N/mm^3), as shown in Figure 8.31. The shear stresses predicted in the NLFEA for beam BL2 at loads near the experimental failure load, using optimal values of D_T, were around 3.5MPa (see Figure 8.28), which has a good agreement with crack-slip model predictions shown in previous section (see Table 8.10).

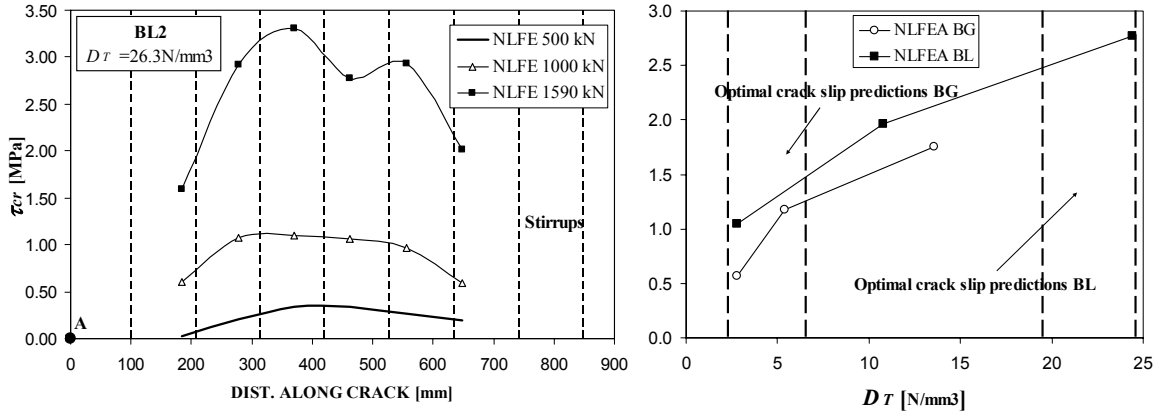

Note: Results of shear stresses at the crack shown for beam BL2 (left), using optimal values of D_T according to Figure 8.30; Shear stresses include contribution from stirrups crossing the crack

Figure 8.31: Shear stresses along discrete crack. *Left* – τ_{cr} distribution along interface elements that became active (BL2); *Right* – τ_{cr} at experimental failure load for different values of aggregate interlock stiffness

The shear stresses were estimated using a more realistic crack dilatancy model such as the linear aggregate interlock relationship (Walraven & Reinhardt [46]). The experimental values of the crack opening and sliding were assumed in order to obtain the aggregate interlock shear stiffness and the corresponding shear stress for each load, see Figure 8.32. According to the linear aggregate interlock relationship, τ_{cr} was zero for beams with large crack opening compared with sliding i.e. beams A and beam BL1.

The results shown in Figure 8.32 were comparable to those obtained from the NLFEA assuming a constant value of D_T. Furthermore, the shear stiffness near failure was similar to the optimal values shown in Figure 8.31. It can be concluded that the benefit of using crack dilatancy models instead of the simpler approach (D_T constant), is dubious in this case, since the increase in accuracy does not seem to compensate for numerical difficulties faced by the crack dilatancy models.

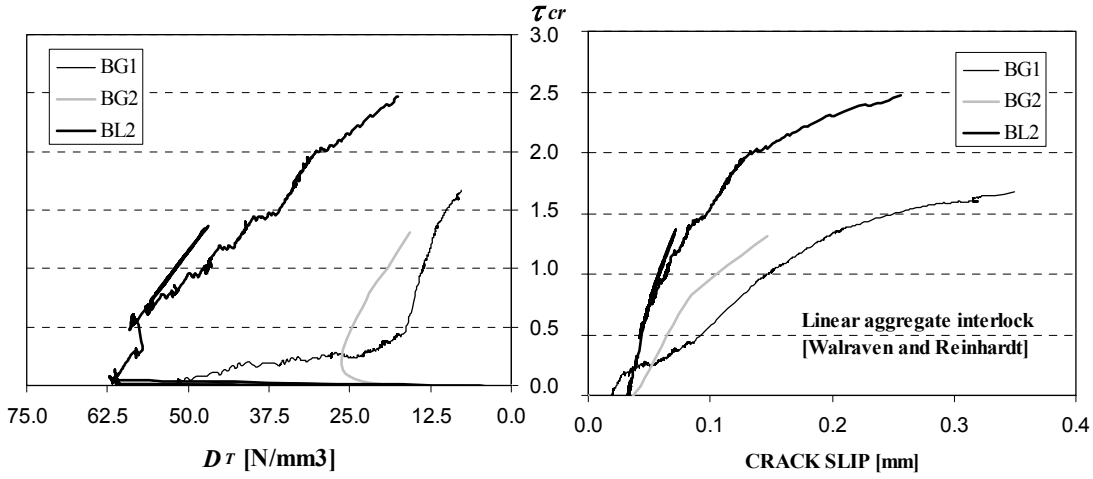

Note: $D_T = D_{22}$ in the crack dilatancy model

Figure 8.32: Shear stresses and stiffness assumed by linear aggregate interlock relationship (Walraven & Reinhardt [46])

Strain predictions in the shear reinforcement

The strain predicted by the NLFEA supported that stirrups had yielded at failure. The NLFEA showed lower strains in the shear links in beam BG2, which also agreed with experimental evidence. Figure 8.33 shows the average strain readings from the Demec gauge compared to numerical results at gauss points immediately next to the discrete cracks. In general the Demec readings were slightly larger than those predicted in the NLFEA as shown in Figures 8.33 and 8.34. The experimental values shown in Figure 8.33 relate to the sector of the stirrup with highest strains, which is highlighted.

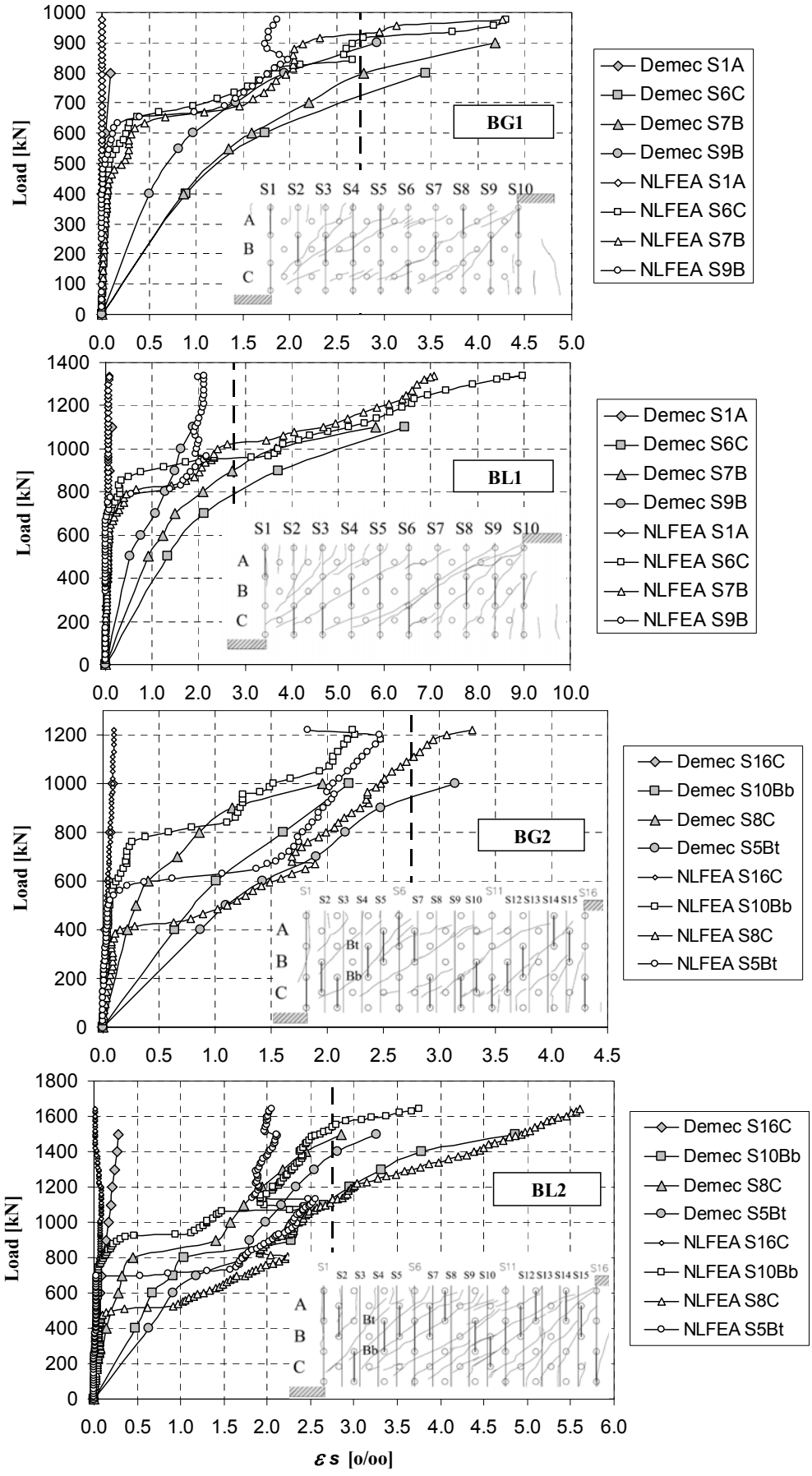

Figure 8.33: Experimental and numerical predictions of strains in stirrups

As described in section 6.5.4, the maximum strains were obtained at sectors of the stirrup which were crossed by the main shear crack (see Figure 8.33). The distribution of strains along stirrups predicted in the NLFEA was in good agreement with test data. This is clearly shown in Figure 8.34 for the last load step in which Demec readings were taken before failure; results refer to stirrups S6/S7/S8 (beams B1) and S9/S11/S13 (beams B2) see Figure 8.33. These stirrups were at similar distance with respect the loading point at the central span (around *d*), and were crossed by the main shear crack, as shown in Figure 8.33.

The strains measured using the Demec gauge were fairly similar for symmetrical stirrups, which was satisfactory reproduced in the NLFEA. In addition, the predicted strains of the first two stirrups closer to the loading points were negligible, as observed experimentally (see Figure 8.33).

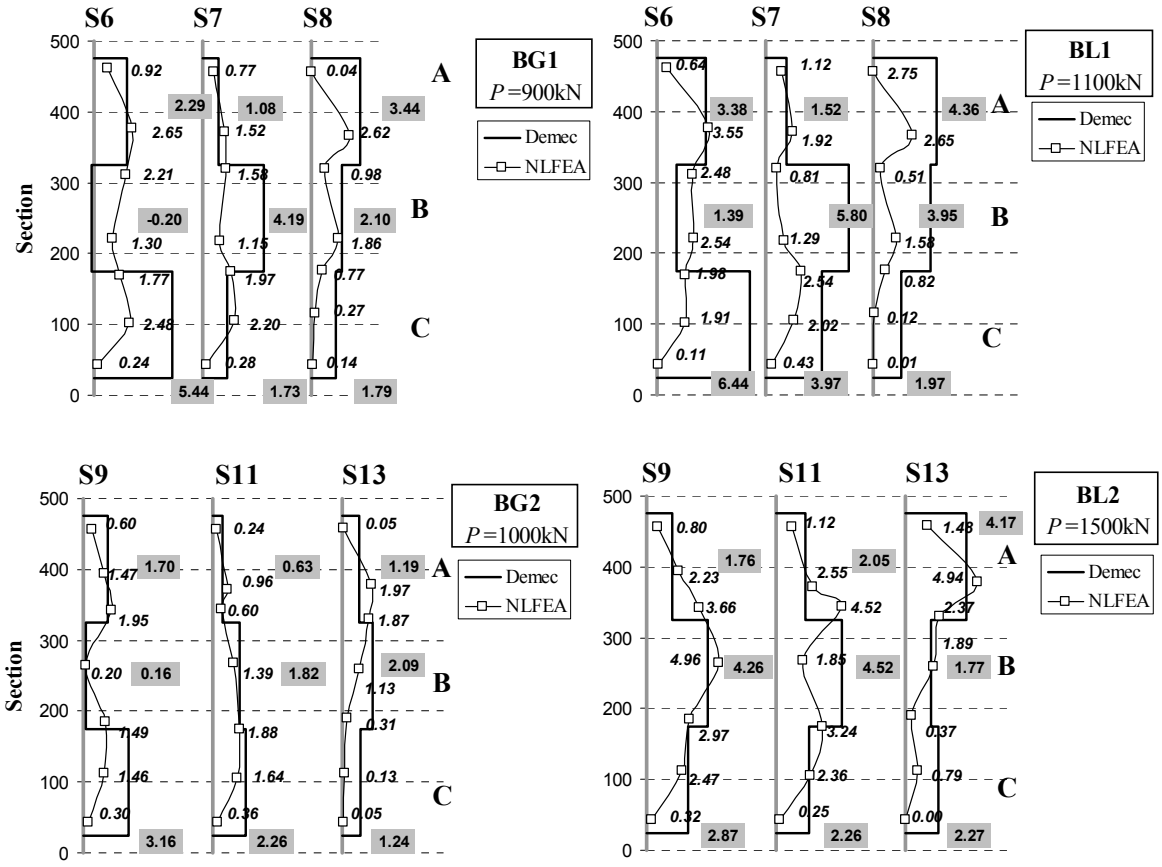

Figure 8.34: Distribution of strains over height of stirrups for beams B1 and B2

Strain predictions in the longitudinal reinforcement

The strains in the flexural reinforcement obtained in the NLFEA were in good agreement with experimental data from strain gauges located at points of maximum and minimum bending moments, as shown in Figure 8.35. Moreover, the strain predictions using bending theory for a cracked section at the location of maximum bending moments (loading points) were satisfactory. The longitudinal strains at the centre of the shear span (*M=0*) were around half those at M_{max}, which was accurately predicted by both the NLFEA and the curtailment rule ($T=V\cot\theta/2$) used in EC2. In order to estimate ε_s using the curtailment rule z was taken as $0.8d$, according to section 8.3.2.

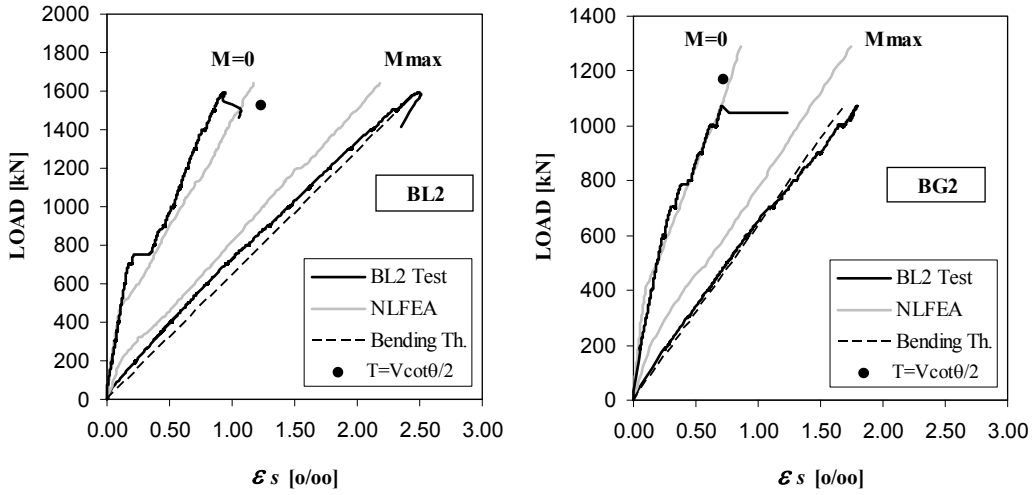

Figure 8.35: Experimental and numerical predictions of the strains in the flexural reinforcement at points of maximum and minimum bending moments

8.4 Conclusions

The influence of aggregate fracture on the shear strength of slender beams was found to be more critical in beams without stirrups (B0), where aggregate interlock action seemed predominant, compared to continuous beams B with stirrups. The experimental results of beams B0 were in good agreement with previous experimental data from Regan et al. [4] with similar concrete strengths and effective depths. The V_{calc}/V_{test} ratio was 16% higher in limestone beams than in gravel beams due to cracking of the coarse aggregate.

Imposing a limit to the concrete strength of 60MPa in the shear design equations, as recommended in the UK National Annex, slightly improved the predicted strength for beams BG, which had a concrete strength of 80.2MPa. However, the same was not true for beams BL, which had a lower concrete strength (68.4MPa). For this case MCFT approach, in which the aggregate size is reduced linearly according to f_c', was more effective. Although both EC2 and MCFT approaches for dealing with aggregate fracture provided safer design strengths, they were not necessarily consistent with experimental evidence such as beam BG, in which the crack went round the aggregate.

The NLFEA of beams B0 using smeared cracking elements provided sensible estimations of the crack pattern, deflections and ultimate loads. However the influence of the aggregate fracture or the post-failure behaviour of beams B0 could not be assessed by the NLFEA using smeared cracking elements only. In order to model these aspects accurately, a discrete crack approach seems necessary.

The main shear cracks of continuous beams tested with a point of contra-flexure were significantly flatter (~33º) compared with simply supported beams. The difference in the crack pattern could have had an influence of the contribution of the aggregate interlock action to the shear strength of the beam. Additional experimental evidence from other researchers showed that the shear strength of beams with a point of contra-flexure was considerably lower than traditional simply supported beams. The higher strength observed in simply supported beams, which usually had a flanged section, was probably due to the shear strength resisted at the compression head. The variable strut inclination method, suggested in EC2, seems to provide safe predictions for simply supported beams assuming values of z equal to $0.9d$, as recommended in EC2. However, the shear strength was clearly overestimated in continuous beams and a value of $z = 0.8d$ provided a significant improvement in the predictions. This suggested lower estimate for the lever

arm of continuous beams with symmetrical reinforcement was more consistent with experimental evidence of the 72 beams studied, in which the average lever arm at failure was *0.84d*.

The comparative study between EC2, BS8110 and CSA design methods for the continuous beams investigated, showed that the first two approaches had a significantly different performance depending on the stirrup index ($SI=\rho f_y/\nu f_c'$). The predictions using CSA design formulas were accurate for all ranges of *SI*. On the contrary, for low values of the stirrup index ($cot\theta$=2.5), EC2 provided more accurate predictions than BS8110. The analysis showed that EC2 provides lower factors of safety than CSA and BS8110 for continuous beams with stirrups indices lower than 0.11. In addition, the study of the performance of different design method by means of the Demerit Point Classification system proposed by Collins [148] showed that the results can be misleading. This is due to neglecting the effect of different material and load factors used in the design codes. According to the author, in order to compare the different design methods the influence of material and load factors should be taken into account. Hence, the modified Demerit Point Classification system proposed by the author seems a rational approach, although the marking scheme proposed is opened to discussion.

The aggregate interlock shear stresses at the main shear crack in the continuous beams B were interpolated from crack displacements and stress data obtained from push-off test using identical concrete and similar reinforcement ratios. These values were compared to four different techniques based on smeared and discrete crack approaches; these were equilibrium at the crack estimating the strut inclination, VSI with shear friction, discrete crack-slip model and NLFEA. As expected, the estimations of τ_{cr} varied for each method, since different simplifications were assumed in each approach. However, the predictions of τ_{cr} were in a similar range of magnitude. In addition, the crack opening and sliding at the main shear crack could be reproduced accurately by both proposed discrete crack-slip method and NLFEA (discrete/smeared cracking). In general, predicted values of crack width, at which shear at the crack started to reduce were around 0.3-0.5mm for both gravel and limestone specimens. These values were in good agreement with experimental data. In addition, the crack opening/sliding ratio obtained was in general much lower ($\delta w/\delta s$~1.5) than the one obtained for short span beams A ($\delta w/\delta s$~3) due to smaller values of *w*. The relatively low values of $\delta w/\delta s$ obtained in slender beams with stirrups, implied a higher contribution of aggregate interlock action compared to short span beams.

CHAPTER 9 – Conclusions

9.1 Summary

The thesis presents the details of experimental and analytical studies into the influence of crack roughness and aggregate fracture on the behaviour of RC beams failing in shear. Various commonly used design methods for shear are reviewed and assessed against a large database of experimental results, including the author's tests in which gravel and limestone aggregates were used. The effect of the reduction in aggregate interlock due to aggregate fracture has been investigated experimentally and numerically in short span and slender beams failing in shear.

The study focused firstly on isolated cracks, which were analysed by means of push-off tests carried by the author. Subsequently, in-plane pure shear stress states were investigated using shear panel test data available in the literature. Analytical smeared and discrete crack models were validated against these simple test arrangements. However, information regarding the type of aggregate or whether it had fractured was not available to the author for these panels. Lastly, the experimental results obtained from a total of 22 beam tests carried in this work were analysed and compared with previous experimental data from other researchers. The shear stresses transmitted along critical shear cracks were estimated from interpolating the data obtained from push-off tests. These results were compared with analytical predictions using several approaches that had been previously validated using push-off and shear panel test data. In addition, the performance of different design methods for shear was compared for both slender and short span beams. The conclusions and main contributions of this work are summarised in the following sections.

9.1.1 Transfer of stresses at cracks by means of aggregate interlock

Aggregate type

Tests showed that the aggregate type had a larger impact on the crack roughness than the concrete strength. Aggregate fractured at the crack in specimens with limestone aggregate for concrete strengths of around 50MPa. On the other hand, in gravel specimens, the crack went round the aggregate. This was true even for beams with concrete strengths up to 80MPa, in which only a small portion of the aggregate fractured at the crack (30%). This seems inconsistent with assumptions made in design codes where aggregate fracture is dealt only in terms of the concrete strength.

Push-off tests

Crack stresses and relative displacements can be studied with standard push-off tests. This test arrangement is practical since the entire shear force is transferred through a pre-crack surface of which both geometry and normal stresses are known. For normal size stirrups and concrete strengths used, the contribution of dowel action to the shear strength was negligible.

The push-off tests carried out by the author using gravel and limestone aggregates showed that considerable shear stresses could be transmitted through cracks even in the limestone specimens in which the aggregate particles had fractured at the crack surface.

Shear friction formulae can be used to estimate the ultimate shear strength of crack interfaces, although the influence of crack width is ignored. The cohesion factor obtained from linear regression of the test data agreed well with the EC2 recommendations. However, the value of the friction parameter obtained for the limestone specimens were surprisingly high and comparable to the gravel tests. This could be due to a certain level of roughness at a macro-level.

In general, the shear stress predictions from the crack dilatancy models investigated tended to overestimate the shear stress for crack displacements near the peak load. On the other hand, for low crack slips (s<0.2mm) the stresses were underestimated. The predictions of normal and shear stresses were sensible up to slips of around 1mm using the linear aggregate interlock relationship proposed by Walraven & Reinhardt [46], similarly as the rough crack model (Gambarova & Karakoç [48]). For simplicity the former model was adopted in subsequent calculations, although other models such as the one suggested in MC90 also provided sensible predictions.

Estimation of stresses at critical shear cracks in beam tests

Shear stresses were estimated at critical shear cracks in both short span beams with and without stirrups and slender beams with stirrups by interpolating stresses and relative crack displacement data from the push-off tests. This extrapolation was possible due to the similar geometry of the crack surface, shear reinforcement crossing the crack and concrete strength. Uncertainties arise in the interpolation of stresses due to the differences in the inclination of the stirrups with respect the crack plane and differences in crack paths between the push-off and beam tests. Nevertheless, the empirically derived crack stresses were similar in magnitude to those predicted analytically using different discrete crack approaches such as NLFEA with discrete cracking, crack slip model, variable inclination truss or strut-and-tie models with shear friction constraints. Moreover, the crack opening and slip were reasonably predicted using either crack slip model developed by the author for slender continuous beams or NLFE models applicable to both short span and slender beams.

The relative crack displacements were in general very similar for otherwise identical gravel and limestone beams, which resulted in similar shear stresses being developed along the critical shear cracks. The crack opening and sliding measurements at different levels of the crack were fairly constant, which agreed with the NLFE predictions. This might be different for larger member depths and lower longitudinal reinforcement ratios.

The crack paths obtained experimentally, i.e. w-s relationship, varied considerably depending on the type of test. Crack sliding was predominant in push-off tests ($\delta w/\delta s$~0.5), which was in agreement with the MC90 simple formula $w=0.6s^{2/3}$ for normal values of crack slip. Crack opening was predominant along the critical shear crack in short span beams, where the $\delta w/\delta s$ ratio was around 3. In general, slender beams with stirrups had an intermediate value of $\delta w/\delta s$ of around 1.5 near failure. These variations in crack dilatancy could result in different contributions of aggregate interlock action, which seems to be less critical in short span beams.

9.1.2 Modelling of in-plane pure shear stress states by means of smeared and discrete crack approaches

Shear panel tests

Shear panel tests can be relevant to the prediction of the strength of beams since a pure shear stress state is attained, which can be helpful to obtain a better understanding in the contribution to shear behaviour of aggregate interlock and compression softening. Chapter 5 shows that the MCFT can predict accurately the shear strain-stress response of shear panel tests, although shear stresses at previous cracks are ignored since the model follows a rotating crack approach. Alternatively, the discrete crack slip model derived by the author is a simple whilst rational approach to assess the limit case where the behaviour is governed by shear stresses along cracks. Despite the large number of simplifications adopted in the model, comparable predictions of the shear stress-strain response and ultimate strength to MCFT were obtained. Subsequently, the crack slip model was applied to estimate relative displacements and stresses at the crack in continuous beams.

As shown in chapter 5, simple plasticity rotating truss formulas can provide accurate predictions of the ultimate strength of shear panel tests. Similar predictions could be obtained performing a simple NLFEA using total strain and multi-directional fixed smeared cracking models. This analysis showed that compression softening due to transverse tensile strains must be taken into account in order to obtain reasonable predictions. However, several uncertainties are still found about parameters assumed in these models for the softening behaviour of concrete in compression or the yield strength assumed for the reinforcement depending on the governing failure mode.

Non-Linear finite element analysis of beams

The NLFE models developed in this work, in which only smeared cracking elements were applied, showed that sensible predictions of the crack pattern, deflections and ultimate loads could be obtained. However, these predictions were highly sensitive to parameters assumed in the models such as tensile strength or local values of the compression strength assumed for elements near the loading plates. In addition, the brittle nature of some of the shear failures studied resulted on several numerical instabilities that were difficult to overcome with simple smeared crack elements only. Aspects such as lateral confinement near loading plates or debonding and dowel action failure cracks cannot be modelled realistically using these simple smeared crack approaches.

The multi-directional fixed approach provided accurate predictions, although the model faced numerical difficulties near failure and in some instances divergence occurred in the last incremental step. The total strain models, which showed a good performance for shear panel tests, were robust numerically for beam models, although for slender beams without stirrups a spurious post-failure behaviour was obtained.

In order to assess crack opening-slip and normal-shear stresses using NLFE models, it has been shown that combining smeared and discrete cracking elements in the same mesh with relatively simple discrete crack models for the interface elements can provide sensible predictions. However, estimating parameters used in the models is not straightforward. Shear retention factors applied in the interface elements can be estimated from push-off test data or simple analytical equations, for which the expected crack width at failure is needed. In addition, several assumptions had to be made regarding the normal and transverse stiffness transferred into the interface elements by embedded reinforcement crossing the discrete crack. Introducing interface elements with complex crack dilatancy models and bond slip considerations is not recommended since the FE models can become highly unstable.

9.1.3 Additional experimental evidence provided by beam tests

Relative crack displacements monitored in beam tests were valuable to obtain a better understanding of the aggregate interlock contribution as explained in section 9.1.1. The following conclusions can be drawn from the beam test data obtained in this work.

Crack patterns

The relative position of the diagonal shear crack had an important role on the shear strength of short span beams, especially on members without shear reinforcement. Beams in which the diagonal crack formed at early load stages crossing completely the direct strut (shear proper failure) showed a relatively low strength compared with others in which the diagonal crack formed slightly below and where failure seemed to be more related to crushing of the strut. This is relevant since this type of failure might have an effect on size effect considerations.

For the remaining beams the crack patterns varied significantly depending on the load arrangement. The critical shear cracks remained independent of flexural cracks in the short span beams and continuous beams, but not in the simply supported beams. Shear cracks that formed near failure crossed previous 45º shear cracks in the simply supported

slender beams with stirrups. However, this was not observed in identical beams loaded with a point of contra-flexure. Critical shear cracks formed at service loads and remained stable until failure, except in slender beams (a/d=3.5) without shear reinforcement, where failure occurred immediately after the diagonal crack had formed.

Additional conclusions from short span beam tests

Short span beam tests presented here showed the relevance of size of bearing plates. An increase of the bearing length of one of the supports from 125 to 200mmm resulted in failure of the opposite shear span in 6 specimens out of 8 beams tested. In general failure was due to crushing of the concrete near the load plate, which is not consistent with STM assumptions in which the bottom node is assumed to be critical.

Additional conclusions from slender beam tests

The shear cracks that formed at early load stages in the continuous beams were considerably flatter than in simply supported beams. This could have resulted in a different contribution of aggregate interlock action between both types of loading arrangements. However, the ultimate shear stress for simply supported and continuous beams with rectangular sections and equal shear reinforcement ratios was very similar.

General conclusions from measuring techniques in lab testing

In general, the different types of measuring crosses used for recording opening and slip displacements at the crak (LVTDs and Demec discs) provided values that were in agreement with each other and with visual reading. The more innovative technique used for measuring global deflections, which was based on digital photogrammetry, provided accurate readings at several points. Although these readings were in good agreement with LVTDs measurements, they were not accurate enough to obtain strain values. Furthermore, only in few tests where the working distance was small, reasonable measurements of crack opening and sliding could be obtained. Although, digital photogrammetry is a fairly recent technique and current work is taking place to improve its performance, the results shown in this work look quite promising for future applications.

9.1.4 Shear design of short span beams

According to the experimental database gathered in this work, which includes beams tested by the author, it was concluded that existing design equations for short span beams with and without shear reinforcement were in general over conservative. The performance of the predictions using the simplified approaches assumed in EC2 and BS8110 for short span beams were highly dependent on the stirrup index.

A strut-and-tie model was developed by the author, which was consistent with EC2 recommendations for STM, for both short span beams with and without stirrups. These models provide more accurate predictions of the ultimate strength than simplified formulas in EC2 and BS8110. In addition, the strut-and-tie model provided reasonable predictions of the shear strength of short span beams strengthened with externally-bonded CFRP sheets to the full depth.

The factors of safety provided using the strut-and-tie model proposed for specimens with steel stirrups was appropriate for concrete strengths up to 80MPa, although a large scatter was found for short span beams without stirrups. This scatter was most likely due to influence of the position of the diagonal crack relative to the direct strut, as mentioned in section 9.1.3. The implementation of a shear friction constraint into the STM as presented in this work can be used to relate the effective strength of the direct strut to shear strength capacity along the critical crack. More advanced relationships for the ultimate shear capacity of the crack can be used in which the crack width or aggregate size are considered. Although this type of approach can be used to provide a formal explanation for the lower strength obtained for those beams failing in a shear proper type of failure, the method is not practical from a design perspective due to the uncertainties in the parameters involved.

The performance of the predictions of the short beams tested in this work using the different methods studied, were identical for gravel and limestone specimens. This suggests that aggregate fracture was not critical for these beams, which seems to be supported by the large crack dilatancy $\delta w/\delta s$ ratio obtained experimentally. As suggested in next section regarding future work, it would be interesting to verify this conclusion for members with different member depths and longitudinal reinforcement ratios.

9.1.5 Shear design of slender beams

Unlike short span beams, aggregate fracture was found to be more critical for slender beams without shear reinforcement. The V_{calc}/V_{test} ratio using EC2 empirical formula for beams without shear reinforcement was 16% greater in the limestone beams than in the gravel ones due to cracking of the course aggregate at the crack. The performance of this equation suggested in EC2 can be questionable since the V_{calc}/V_{test} ratio was greater than 1 for both beams tested; the ratio was as high as 1.5 for the limestone beams. These results were expected in light of Regan et al. [4] findings for similar beams in which limestone and gravel aggregates were used; the V_{calc}/V_{test} ratios obtained were in excellent agreement with interpolated surfaces proposed by Regan et al. [4] in which EC2 predictions worsen with increasing d and f_c'.

Imposing the limit of 60MPa for the concrete strength, as recommended in the UK National Annex to EC2 provided a slight improvement in the predictions of gravel beams, in which the crack went round to a large portion of the aggregate (~70%) and the concrete strength was around 80MPa. Interestingly, the prediction of the shear strength in the limestone beam, in which the aggregate fractured completely, the limit of 60MPa was inefficient, since the concrete strength was only 68MPa. This supports Regan's [4] conclusion that this limit on the concrete strength should be considered only as a temporary compromise before a more rational approach is developed.

A good attempt towards this aim can be seen in MCFT method for dealing with aggregate fracture, which consists in reducing the aggregate size in the calculation according to f_c'. Although this approach provided a better performance for beams BL0 and BG0 than EC2 method, the type of aggregate is also ignored. Hence, the approach was inconsistent with beam BG0, similarly as EC2, since aggregate was assumed to fracture at the crack according to its high value of f_c'.

The predictions of the slender beams with stirrups tested in this work did not seem to be highly influenced by whether limestone or gravel aggregate was used. However, the strength of the continuous beams tested, especially those with theoretical values of $cot\theta$ lower than 2.5, were generally lower than predicted using the variable strut inclination method with a conventional value of z equal to $0.9d$. These results were verified by additional test data of continuous beams carried out in Japan in the late 80's. According to the database gathered of continuous beams, a better fit was obtained using an estimated value of the lever arm close to $0.8d$.

The relatively low strength of the continuous beams studied was unexpected in view of experimental data of simply supported beams, which have been widely used to validate the variable strut inclination method. The set of experimental data of simply supported beams lays considerably above the variable inclination strut predicted strength, especially for cases where the predicted $cot\theta$ is lower than 2.5. This difference seems to be due to the contribution of shear taken by the compression head since many of these simply supported beams had large compression flanges. The simply supported beams with stirrups tested in this work had similar shear strength to equivalent continuous beams, both of which had rectangular sections. However, there is experimental evidence available that shows that simply supported beams with flanges have higher strength than identical beams with rectangular sections. This seems to support the idea that the difference between both sets of data from simply supported and continuous beams was mainly due to shear at the compression head.

Lastly, the VSI method was compared with the design equations given in BS8110 and CSA. This comparative analysis showed that the CSA method gave a reasonably consistent safety factor for the continuous beams investigated which was independent of the stirrup index. The BS8110 predictions were acceptable for stirrup indices $\rho f_y / v f_c'$ higher than around 0.11, but the method was extremely conservative for lower values of the stirrup index. Direct comparison between EC2, CSA and BS8110 predictions is difficult since different partial material and load factors are used in each code. Hence, the study of the performance of different design codes by using P_{test}/P_{calc} ratio only, such as in the Demerit Point Classification (Collins [148]) can be questionable. The analysis of the performance of design methods for short span beams (chapter 7), showed a similar conclusion with regards the Demerit Point Classification system.

The Modified Demerit Classification system proposed by the author seems to be a more reasonable method since the design strength is used in the approach, to account for variations in material and load factors of safety. The author's analysis shows that EC2 gives significantly lower factors of safety than CSA or BS8110 for continuous beams with stirrup indices lower than 0.11. However, the lowest *FOS* (P_{test}/P_d) obtained with EC2 for the author's beams was 1.56, which is similar to that used in flexural members. It could be argued that a higher *FOS* should be used for members failing in shear since the failure mode is potentially catastrophic. Flexural strength is also potentially increased by membrane action.

9.2 Suggestions for future work

The thesis includes new experimental results and develops analytical methods that can be used to assess the influence of crack roughness on the shear strength of reinforced concrete beams.

However, the number of tests performed was restricted due to limited resources in the project. Future experimental work could include similar tests using other types of aggregate such as granite or lightweight aggregates to further validate these results. In addition, it could be of interest to carry out these tests using different depths and longitudinal reinforcement ratios, in order to assess the influence of potential size effects or larger values of crack widths at failure.

The analytical work carried out in this thesis was largely focused on the development of a rational strut-and-tie model for short span beams, which could provide more accurate predictions of the shear strength than current simplified design equations given in EC2 and BS8110. Although the strut-and-tie model was formulated according to the EC2 recommendations for STM, research on size effects seems timely since large discrepancies are found among researches regarding this particular point. Moreover, further experimental and analytical work is required to investigate the influence of node regions which are frequently critical in STM and non-linear finite element analysis. This work would show whether existing strut-and-tie provisions for node regions are realistic.

Finally, further work is required to develop rational methods for assessing the influence of crack roughness on the shear strength of reinforced concrete members.

Bibliography

1. Taylor H.P.J., *Investigation of the forces carried across cracks in reinforced concrete beams in shear by interlock of aggregate*, Technical report *42.447*, CCA, 1970, London.

2. Taylor H.P.J., *Further tests to determine shear stresses in reinforced concrete beams*, Technical report *TRA 438*, CCA, 1970, London.

3. Regan P.E., *EC2 and shear in lightweight aggregate and high-strength concretes*, Technical report for W.S. Atkins Transportation Engineering, Nov. 2001, London.

4. Regan P.E, Kennedy-Reid I.L., Pullen A.D., and Smith D.A., *The influence of aggregate type on the shear resistance of reinforced concrete,* The Structural Engineer, 2005: pp. 27-32.

5. BS8110, *Part 1: Structural use of concrete: Code of practice for design and construction*, British Standards Institution, 1997, London.

6. Comité Euro-Interational Du Béton and Federation International De La Precontrainte, *Model Code for Concrete Structures*, CEB-FIP International Recommendations, 1990, ed. Thomas Telford, 1993.

7. British Standards Institution, *Eurocode 2: Design of Concrete Structures. Part 1, General Rules and Rules for Buildings*, DD ENV 1992-1-1, ed. M.K. BSI, 1992.

8. Vecchio F.J. and Collins M.P., *The Modified Compression-Field Theory for Reinforced Concrete Elements Subjected to Shear*, ACI Journal, No.83(2), 1986: pp. 219-231.

9. Walraven J.C. and Al-Zubi N., *Shear capacity of lightweight concrete beams with shear reinforcement*, in *Proceedings Symposium on Lightweight Aggregate Concrete,* 1995, Sandefjord, Norway.

10. Walraven J.C. and Stroband J., *Shear capacity of high strength concrete beams with shear reinforcement*, in *Symposium on High Strenth Concrete*, 1999, Sandefjord, Norway.

11. Collins M.P. and Mitchell D., *Prestressed Concrete Structures*, 1st edn. Prentice-Hall, 1991, Englewoods Cliffs, New Jersey.

12. Collins M.P., Mitchell A.D., and Bentz E.C., *Shear Design of Concrete Structures,* The Structural Engineer, 20th May, 2008.

13. Johnson P.M., Couture A.C., and Nicolete R., *Commission of inquiry into the collapse of a portion of de la Concorde overpass*, Gouvernement du Quebec, 2007.

14. Ritter W., *Die Bauweise hennebique*, Schweizerische Bauzeriturg, 1899.

15. Mörsch E., *Der Eisenbeton. Seine Theorie und Auwendung*, 1908, Stuttgart.

16. Muttoni A., Schwartz J., and Thürlimann B., *Design and Detailing of Reinforced Concrete Structures Using Stress Fields*, Swiss Federal Institute of Technology, 1989, Zürich.

17. Nielsen M.P., *Limit State Analysis and Concrete Plasticity*, Prentice-Hall, 1984, Englewood Cliffs, New Jersey.

18. Nielsen M.P. and Braestrup M.W., *Plastic shear strength of reinforced concrete beams*, 1976, University of Denmark.

19. Hamadi Y.D. and Regan P.E., *Behaviour of normal and lightweight aggregate beams with shear cracks,* The Structural Engineer, 58B(4), 1980: pp. 71-79.

20. Regan P.E., *Research on shear: A benefit to humanity or a waste of time?,* The Structural Engineer, 71(19), 1993: pp. 337-347.

21. Reineck K.H., *Shear design in a consistent design concept for structural concrete based on strut-and-tie models*, in *fib Bulletin 16: Design Examples for the 1996 FIP Recommendations 'Practical design of structural concrete'*, FIB, 1996: pp. 165-186.

22. Comisión Permanente del Hormigón, *Instrucción de Hormigón Estructural. EHE*, Centro de Publicaciones del Ministerio de Fomento, 1999, Spain.

23. Walraven J.C., *Background document for EC-2, Chapter 6.2 Shear*, 2002, Delft University of Technology.

24. Cladera A., *Shear design of reinforced high-strength concrete beams*, in *Departament d'Enginyeria de la Construcció*, Ph.D Thesis, 2002, Universitat Politécnica de Catalunya: Barcelona.

25. Vecchio F.J. and Collins M.P., *Compression Response of Cracked Reinforced Concrete,* Journal of Structural Engineering, 119(12), 1993: pp. 3590-3610.

26. Kollegger J. and Mehlhorn G., *Experimentelle Untersuchungen zur Bestimmung der Druckfestigkeit des gerissenen Stahlbetons bei einer Querzugbeanspruchung*, in *Report 413*, D.A.F. Stahlbeton, 1990, Berlin.

27. Miyahara T., Kawakami T., and Maekawa K., *Nonlinear behavior of cracked reinforced concrete plate element under uniaxial compression,* Concrete Library International, Japan Society of Civil Engineers, 11, 1988: pp. 306-319.

28. Belarbi A. and Hsu T.C., *Constitutive laws of reinforced concrete in biaxial tension-compression*, in *Research Report UHCEE 91-2*, 1991, Univ. of Houston: Texas.

29. Vecchio F.J., *Disturbed Stress Field Model for Reinforced Concrete: Formulation,* Journal of Structural Engineering, 126(9), 2000: pp. 1070-1077.

30. Lubell A., Sherwood E.G., Bentz E.C., Collins M.P., *Safe shear design of large wide beams,* Concrete International, 26(1), 2004: pp. 66-78.

31. Angelakos D., Bentz E.C., and Collins M.P., *Effect of concrete strength and minimum stirrups on shear strength of large members,* ACI Structural Journal, 98(3), 2001: pp. 290-300.

32. Bentz E.C., Vecchio F.J, and Collins M.P, *Simplified Modified Compression Field Theory for Calculating Shear Strength of Reinforced Concrete Elements,* ACI Journal, 2006(no.103-S65): p. 614-624.

33. CSA, *A23.3-04 Design of Concrete Structures*, Canadian Standards Association, 2004.

34. Collins M.P., Bentz E.C., and Mitchell A.D., *Concrete Design Handbook*, Edited by Cement Association of Canada, 2006.

35. Schlaich J., Jennewein M., and Schafer K., *Towards a consistent design of structural concrete,* PCI Journal, 32(3), 1987: pp. 74-150.

36. Poli D., Gambarova P.G., and Karakoç C., *Aggregate interlock role in r.c. thin-webbed beams in shear,* ASCE-Journal of Structural Engineering, 113(1), 1987: pp. 1-19.

37. Poli D., Prisco M.D., and Gambarova P.G., *Stress Field in Web of RC Thin-Webbed Beams Failing in Shear,* ASCE-Journal of Structural Engineering, 116(9), 1990: pp. 2496-2515.

38. Kirmair M., *Das Schubtragverhalten schlanker Stahlbetonbalken - theoretische und experimentelle Untersuchungen fur Leicht - und Normalbeton*, 1985/87, TU Munchen; DAfStb: Munchen, Berlin.

39. Kupfer H.B. and Moosecker W., *Beanspruchung und Verformung der Schubzone des schlanken profilierten Stahlbetonbalkens,* Forschungsbeitrage fur die Baupraxis, 1979: pp. 225-236.

40. Reineck K.H., *Modelling of members with transverse reinforcement,* in *IABSE Colloquim- Structural Concrete*, 1991. Stuttgart.

41. Schlaich J. and Schafer K., *Zur Druck-Querzug-Festigkeit des Stahlbetons,* BuStb, 78(H.3), 1983: pp. 73-78.

42. Schafer K., Schelling G., and Kuchler T., *Druck-und Querzug in bewehrten Betonelementen*, D.A.F. Stahlbeton, 1990, Berlin.

43. Eibl J. and Neuroth U., *Untersuchungen zur Druckfestigkeit von bewehrtem Beton bei gleichzeitig wirkendem Querzug*, Institute fur Massivbau und Baustofftechnologie, 1988, Univ. Karlsruhe.

44. Prisco M.D., Pietro G., and Gambarova P.G., *Comprehensive model for study of shear in thin-webbed RC and PC beams,* Journal of Structural Engineering, 121(12), 1995: pp. 1822-1831.

45. Walraven J.C., *Aggregate Interlock: a Theoretical and Experimental Analysis*, Ph.D Thesis, 1980, Delft University of Technology.

46. Walraven J.C. and Reinhardt H.W., *Theory and experiments on the mechanical behaviour of cracks in plain and reinforced concrete subjected to shear loading*, in *Concrete Mechanichs, part A*, Heron, 1981, Dept. of Civil Engineering, Delft University of Technology.

47. Bazant Z.P. and Gambarova P.G., *Rough crack models in reinforced concrete,* ASCE-Journal of Structural Engineering, 106(4), 1980: pp. 819-842.

48. Gambarova P.G. and Karakoç C., *A new approach to the analysis of the confinement role in regularly cracking concrete elements,* Trans. 7th Struct. Mech. in Reactor Tech., Vol.H, 1983: pp. 251-261.

49. Li N., Maekawa L., and Okamura H., *Contact density model for stress transfer across cracks in concrete,* Journal of the Faculty of Engineering, University of Tokyo, XL, 1989: pp. 9-52.

50. Paulay T. and Loeber P.J., *Shear transfer by aggregate interlock,* ACI - Special Publication SP42, 1974: pp. 1-15.

51. Daschner F. and Kupfer H., *Versuche zur Schubkraftubertragung in Ribe von Normal - und Leichtbeton,* Bauingenieur, 57, 1982: pp. 57-60.

52. Maekawa K., Pimanmas A., and Okamura H., *NonLinear Mechanics of Reinforced Concrete*, Spon Press, 2003.

53. Feenstra P.H., De Borst R., and Rots J.G., *Numerical Study on Crack Dilatancy I: Models and Stability Analysis,* Journal of Engineering Mechanics, 117(4), 1991: pp. 733-753.

54. Soltani M., *Micro computational approach to post cracking constitutive laws of reinforced concrete and applications to nonlinear finite element analysis*, in *Department of Civil Engineering*. Ph.D Thesis, 2002, University of Tokyo.

55. Fenwick R.C. and Paulay T., *Mechanisms of shear resistance of concrete beams,* Journal of the Structural Division, ASCE, 94(ST10), 1968: pp. 2235-2350.

56. Collins M.P., *Shear design of concrete structures*, evening meeting organized by IStructE, June 11th, 2008: London.

57. Motamed J., *Shear in normal strength and high strength reinforced concrete beams with stirrups and horizontal web bars*, MSc Thesis, 1997, University of Westminster: London.

58. Schlaich J. and Schafer K., *The Design of Structural Concrete,* in *IABSE Workshop New Delhi 1993*: New Delhi.

59. Brown M.D., Sankovich C.L., Bayrak O., Jirsa J.O., Breen J.E., Wood S.L., *Design for Shear in Reinforced Concrete Using Strut-and-Tie Models*, in *Examination of the AASHTO LRFD Strut and Tie Specification*, Texas Dept. of

Transportation and U.S Dept. of Transportation, 2005, The University of Texas: Austin.

60. fib, *fib bulletin 2: Structural Concrete - Textbook on behaviour, design and performance. Updated knowledge of the CEB/FIP MC90*, in *Volume 2*, fib, 1999: Lausanne.

61. Schlaich J. and Schafer K., *Design and Detaling of Structural Concrete Using Strut-and-Tie Models.* The Structural Engineer, 69(6), 1991: pp.113-125.

62. Almeida J.F. and Lourenco M.S., *Stress Field Models For Structural Concrete*. in *fib Symposium "Keep Concrete Attractive", Budapest 2005*, fib.

63. Vollum R.L. and Newman J.B., *Strut and tie models for analysis/design of external beam-column joints,* Magazine of Concrete Research, 51(6), 1999: pp. 415-425.

64. Qing Quang Liang, Yi Min Xie, and Steven G.P., *Topology Optimization of Strut-and-Tie Models in Reinforced Concrete Structures Using an Evolutionary Procedure,* ACI Structural Journal, 97(2), 2000: pp. 322-330.

65. Tjhin T.N. and Kuchma D.A., *Computer-Based Tools for Design by Strut-and-Tie Method: Advances and Challenges,* ACI Structural Journal, 99(5), 2002: pp. 586-594.

66. Rots J.G. and Blaauwendraad J., *Crack models for concrete: Discrete or smeared? Fixed, multi-directional or rotating?*, Heron, 1989, Delft University of Technology, Faculty of Civil Engineering/TNO Institute for Building Materials and Structures, Department of Computational Mechanics: Delft.

67. De Borst R. and Nauta P., *Non-orthogonal cracks in a smeared finite element model,* Engineering Computations, 2, 1985: pp. 35-46.

68. Rots J.G., Nauta P., and Kusters G.M.A., *Smeared crack approach and fracture localization in concrete*, Heron, *30(1)*, 1985: pp. 1-48.

69. Riggs H.R. and Powel G.H., *Rough crack model for analysis of concrete.* Journal of Engineering Mechanics ASCE, 112(5), 1986: pp. 448-464.

70. Suidan M. and Schnobrich W.C., *Finite element analysis of reinforced concrete.* Journal of Structural Division ASCE, 99(10), 1973: pp. 2109-2122.

71. TNO DIANA BV., *User's Manual Release Notes*, Frits C. de Witte and Gerd-Jan Schreppes, 2005: Delft.

72. Kotsovos M.D. and Pavlovic M.N., *Structural Concrete. Finite-element analysis for limit-state design*, Thomas Telford, 1995.

73. Pimentel M., *Modelaçao e análise de estructuras laminares de betao: Possibilidades e desafios*, Master Thesis, *Faculdade de Engenharia*, Universidade do Porto, 2004: Porto.

74. Cervenka V., Jendele L., and Cervenka J., *ATENA Program Documentation Part 1- Theory*, Cervenka Consulting, 2002: Prague.

75. Figueiras J.A., *Ultimate Load Analysis of Anisotropic and reinforced Concrete Plates and Shells*. 1983, University of Swansea: Swansea.

76. Bazant Z.P., *Comment on orthotropic models for concrete and geomaterials.* Journal of Engineering Mechanics, ASCE, 109(3), 1983: pp. 849-865.

77. William K., Pramono E., and Sture S., *Fundamental issues of smeared cracking models*, in *Proceedings SEM-RILEM International Conference on Fracture of Concrete and Rock*, 1987: Bethel.

78. Vecchio F.J., *Reinforced Concrete Membrane Element Formulations,* Journal of Structural Engineering, 116(3), 1990: pp. 730-750.

79. Hordijk D.A., *Local Approach to Fatigue of Concrete*, Ph.D Thesis, 1991, Delft University of Technology: Delft.

80. Bazant Z.P. and Oh B.H., *Crack band theory for fracture of concrete,* Materials and Structures, 16(1), 1983: pp. 155-177.

81. fib, *fib bulletin 1: Structural Concrete - Textbook on behaviour, design and performance*, fib, 1999: Lausanne.

82. Feenstra P.H., *Computational aspects of biaxial stress in plain and reinforced concrete*, Ph.D Thesis, 1993, Delft University of Technology: Delft.

83. Wong P.S. and Vecchio F.J., *VecTor2 & FormWorks User's Manual*, 2002, VecTor2: Toronto.

84. Ozbolt J. and Reinhardt H.W., *Numerical study of mixed-mode fracture in concrete*, in *International journal of fracture*, 2002: pp. 145-162.

85. Majewski T., Korzeniowski P., and Tejchman J. *Theoretical analysis of failure behaviour of reinforced concrete columns under biaxial bending*, in *6th International Conference AMCM' 2008*, Lodz, Poland.

86. Markeset G. and Hillerborg A., *Softening of concrete in compression- localization and size effects,* Cement and Concrete Research, 25(4), 1995: pp. 702-708.

87. Vonk R.A., *A micromechanical investigation of concrete loaded in compression*, Heron, *38(3)*, 1993.

88. Kupfer H.B. and Gerstle K.H., *Behaviour of concrete under biaxial stress,* Journal of Engineering Mechanics Division, 99(EM4), 1973: pp. 853-866.

89. Pimentel M., Cachim P., and Figueiras J.A., *Deep-beams with indirect supports: numerical modelling and experimental assessment,* Computers and Concrete, 5(2), 2008.

90. Soltani M., An X., and Maekawa K., *Computational model for post cracking analysis of RC membrane elements based on local stress-strain characteristics,* Engineering Structures, 25, 2003: pp. 993-1007.

91. Millard S.G. and Johnson R.P., *Shear transfer across cracks in reinforced concrete due to aggregate interlock and to dowel action,* Magazine of Concrete Research, 36(126), 1984: pp. 9-21.

92. He X.G. and Kwan A.K.H., *Modelling of dowel action of reinforcement bars for finite element analysis of concrete structures,* Computers and Structures, 79, 2001: pp. 595-604.

93. Poli D., Prisco M.D., and Gambarova P.G., *Shear response, deformations, and subgrade stiffness of a dowel bar embedded in concrete,* ACI Structural Journal, 89(6), 1992: pp. 665-75.

94. Dulacska H., *Dowel action of reinforcement crossing cracks in concrete,* ACI Journal, 69(12), 1972.

95. Vintzeleou E.N. and Tassios T.P., *Behavior of dowels under cyclic deformations.* ACI Structural Journal, 84(1), 1987: pp. 18-30.

96. Eleiott A.F., *An experimental investigation of shear transfer across crack in reinforced concrete*. M.S. Thesis, 1974, Cornell University: Ithaca.

97. Eierle B. and Schikora K., *Computational modelling of concrete at early ages using DIANA*, in *DIANA World 2/99*. 1999: Technische Universitat Munchen.

98. Vecchio F.J. and Shim W., *Experimental and analytical reexamination of classic concrete beam tests,* Journal of Structural Engineering, 130(3), 2004: pp. 460-469.

99. Feenstra P.H., De Borst R., and Rots J.G., *Numerical Study on Crack Dilatancy II: Applications,* Journal of Engineering Mechanics, 117(4), 1991: pp. 754-769.

100. Rots J.G., *Comparative study of crack models,* Finite Elements in Civil Engineering Applications, 2002: pp. 17-29.

101. Rots J.G. and De Borst R., *Analysis of mixed-mode fracture in concrete,* Journal of Engineering Mechanics, 113(11), 1987: pp. 1739-1758.

102. Li Y.-J. and Zimmerman T., *Numerical evaluation of the rotating crack model,* Computers and Structures, 68, 1998: pp. 487-497.

103. Khwaounjoo Y.R., Foster S.J., and Gilbert R.I., *3D Finite element modelling of punching type problems using DIANA*, in *UNICIV Report No.R-393*. 2000, The University of New South Wales: Sydney.

104. Collins M.P., Vecchio F.J., and Mehlhorn G., *An international competition to predict the response of reinforced concrete panels,* Canadian Journal of Civil Engineering, 12, 1985: pp. 624-644.

105. Walraven J.C., *Personal communication from Cervenka V. to author regarding NLFE modelling of shear panel test for international contest (Collins et al. 1985)*, Taylor Made Concrete Structures, International *fib* Symposium 2008: Amsterdam.

106. Mattock J.A., Johal L., and Chow H.C., *Shear Transfer in Reinforced Concrete with Moment or Tension Acting Across the Shear Plane,* PCI Journal, 20(4), 1975: pp.76-93.

107. Hamadi Y.D., *Force transfer across cracks in concrete structures*, Ph.D Thesis, 1976, Polytechnic of Central London.

108. McCarthy C., *Measurement of deflections in timber beams by digital photogrammetry*, MSc Thesis, in *Department of Civil & Environmental Engineering*, 2007, Imperial College London.

109. Jauregui D.V., White K.R., Woodward C.B., Leitch K.R., *Static measurement of beam deformations via close-range photogrammetry*, in *Design of structures. Transportation Research Record*. 2002: pp. 3-8.

110. Ortlepp R., Hampel U., and Curbach M., *A new approach for evaluating bond capacity of TRC strengthening,* Cement and concrete composites, 28(7), 2006: pp. 589-597.

111. Lee T.K. and Al-Mahaidi R., *An experimental investigation on shear behaviour of RC T-beams strengthened with CFRP using photogrammetry*, in *Composite structures*. 2008: pp. 185.

112. Barber C.B., Dobkin D.P., and Huhdanpaa H., *The Quickhull algorithm for convex hulls,* ACM Transactions on Mathematical Software, 1996.

113. Climaco J.C.T.S. and Regan P.E., *Evaluation of bond strength between old and new concrete in structural repairs,* Magazine of concrete research, 53(6), 2001: pp. 377-390.

114. Hsu T.C., *Unified Theory of Reinforced Concrete*, ed. W.F.Chen Purdue University, CRC Press, 1993: Houston.

115. Vecchio F.J. and Collins M.P., *Stress-strain characteristics of reinforced concrete in pure shear*, in *IABSE Colloquium*, 1981: Delft.

116. Yamaguchi T., Koike K., Naganuma K., Takeda T., *Pure shear loading tests on reinforced concrete panels part I: Outlines of tests,* Proceedings, Japonesse Architectural Association, 1988.

117. Andre H., *Toronto/Kajima study on scale effects in reinforced concrete elements*, in *Departement of Civil Engineering*, 1987, University of Toronto, Ontario.

118. Kirschner U. and Collins M.P., *Investigating the behaviour of reinforced concrete shell elements*, in *Publication No. 86-09,* 1986, Department of Civil Engineering, University of Toronto, Ontario.

119. Porasz A. and Beidermann J., *An investigation of the stress-strain characterisitics of high strength concrete in shear*, in *Department of Civil Engineering*, 1989, University of Toronto, Ontario.

120. Vecchio F.J., Collins M.P., and Aspiotis J., *High-strength concrete elements subjected to shear,* ACI Structural Journal, 91(4), 1994: pp. 423-433.

121. Pang X. and Hsu T.C., *Behavior of reinforced concrete membranes in shear,* ACI Structural Journal, 92(6), 1995: pp. 665-679.

122. Zhang L. and Hsu T.C., *Behavior and analysis of 100MPa concrete membrane elements,* Journal of Structural Engineering, 124(1), 1998: pp. 24-34.

123. Vecchio F.J., *Nonlinear Finite Element Analysis of Reinforced Concrete Membranes,* ACI Structural Journal, 86, 1989: pp. 26-35.

124. Broo H., Plos M., Lundgren K., Engström B., *Simulation of shear-type cracking and failure with non-linear finite-element method,* Magazine of Concrete Research, 59(9), 2007: pp. 673-687.

125. Hsu T.C. and Zhang L., *Tension Stiffening in Reinforced Concrete Membrane Elements,* ACI Structural Journal, 93(1), 1996: pp. 108-115.

126. De Larrard F., Belloc A., Renwez S., Boulay C., *Is the cube test suitable for high performance concrete?* Materiaux et constructions, 27(174), 1994: pp. 580-583.

127. Kani G.N, *Basic Facts Concerning Shear Failure.* Journal of the American Concrete Institute, No.63 32, 1966: pp. 675-691.

128. Zsutty T.C., *Beam Shear Strength Prediction by Analysis of Existing Data,* ACI Journal, 65, 1968: pp. 943-951.

129. Regan P.E., *Shear in Reinforced Concrete - An Analytical Study*, Report to the Construction Industry and Information Association (CIRIA), 1971.

130. Clark A.P., *Diagonal Tension in Reinforced Concrete Beams,* Journal of the American Concrete Institute, 23(2), 1951: pp. 145-156.

131. Kong F.K., Robins P.J., and Cole D.F., *Web Reinforcement Effects on Deep Beams,* ACI Journal, No.67-73, 1970: pp. 1010-1017.

132. Walraven J.C. and Lehwalter N., *Size Effects in Short Beams Loaded in Shear,* ACI Structural Journal, 91(5), 1994: pp. 585-593.

133. Marti P., *Basic Tools of Reinforced Concrete Beam Design,* ACI Journal, 82, 1985: pp. 46-56.

134. Vollum R.L. and Tay U.L., *Strut and tie modelling of shear failure in short-span beams*, in *Concrete Communication Conference* 2001, United Kingdom, pp 193-199.

135. Mathey R.G. and Watsein D., *Shear Strength of Beams without web Reinforcement Containing Deformed Bars of Different Yield Strengths,* ACI Journal, 60(2), 1963: pp. 183-207.

136. Smith K.N. and Vantsiotis A.S., *Shear strength of deep beams,* ACI Journal, 79(22), 1982: pp. 201-213.

137. Tan K.H., Kong F.K., Teng S., Weng L.W., *Effect of Web Reinforcement of High-Strength Concrete Deep Beams,* ACI Structural Journal, 94(5), 1997: pp. 572-582.

138. Oh J.K. and Shin S.W., *Shear Strength of Reinforced High-Strength Concrete Deep Beams,* ACI Structural Journal, 98(2), 2001: pp. 164-173.

139. Tan K.H. and Lu H.Y., *Shear Behavior of Large Reinforced Concrete Deep Beams and Code Comparisons,* ACI Structural Journal, 96(5), 1999: pp. 836-845.

140. Zhang N. and Tan K.H., *Size effect in RC deep beams: Experimental investigation and STM verification,* Engineering Structures, 29, 2007: pp. 3241-3254.

141. Moody K.G., Viest I.M., Ester R.C., Hognestad E., *Shear Strength of Reinforcement Concrete Beams Part 1- Test Simple Beams,* ACI Journal, 26(4), 1954: pp. 317-332.

142. Leonhardt F. and Walter R., *The Stuttgart Shear Test, 1961/1962- Contributions to the treatment of the problems of shear in reinforced concrete construction.* 1961.

143. Placas A., *Shear Strength of Reinforced Concrete Beams*, in *Civil Engineering Department*. Ph.D Thesis, 1969, Imperial College of Science and Technology, London.

144. Reys de Ortiz I., *Strut and Tie Modelling of Reinforced Concrete Short Beams and Beam-Column Joints*, Ph.D Thesis, 1993, University of Westminster: London.

145. Cheng G., Tan K.H., and Cheong H.K., *Shear behaviour of large reinforced concrete deep beams*, in EASEC8.

146. De Cossio R.D. and Siess C.P., *Behavior and strength in shear of beams and frames without web reinforcement,* ACI Journal, 56(2), 1960: pp. 695-735.

147. Muttoni A. and Schwartz J., *Behaviour of Beams and Punching in Slabs without Shear Reinforcemen,* in IABSE Colloquium Vol. 62, Stuttgart, 1991: pp. 703-708.

148. Collins M.P., *Evaluation of shear design procedures for concrete structures*, in *A report prepared for the CSA Technical Committee on Reinforced Concrete Design*. 2001: Canada.

149. Regan P.E., *Shear in Reinforced Concrete - An Experimental Study*, Report to the Construction Industry and Information Association (CIRIA), 1971.

150. Lehwalter N., *The bearing capacity of concrete compression struts in strut and tie models with examples of deep beams*, Ph.D Thesis, 1988, Technical University of Darmstadt: Germany.

151. Tan K.H, Kong F.K., Teng S., Guan S., *High-Strength Concrete Deep Beams with Effective Span and Shear Span Variations,* ACI Structural Journal, 92(4), 1995: pp. 395-405.

152. Kong Y.L. and Rangan B.V., *Shear Strength of High-Performance Concrete Beams,* ACI Structural Journal, 94(6), 1998: p. 677-688.

153. Rawdon de Paiva H.A. and Siess C.P., *Strength and Behavior of Deep Beams in Shear,* Journal of the Structural Division, Proceeding of the American Society of Civil Engineers, 91(ST5), 1965: pp. 19-41.

154. Sarsam K.F. and Al-Musawi J.M., *Shear Design of High-and Normal Strength Concrete Beams with Web Reinforcement,* ACI Structural Journal, 89(6), 1992: pp. 658-664.

155. Kotsovos M.D. and Pavlovic M.N., *A possible explanation for size effects in structural concrete,* Archives of Civil Engineering, 40(2), 1994: pp. 243-261.

156. Kani G.N., *How safe our large reinforced concrete beams,* ACI Journal, 64(3), 1967: pp. 128-141.

157. Kong F.K., Garcia R.C., Paine J.N., Wong H.H.A., Tang C.W.J., *Strength and stability of slender concrete deep beams,* The Structural Engineer, 64(15), 1986: pp. 49-56.

158. fib (Task Group 9.3), *Externally bonded FRP reinforcement for RC structures*, in *Technical report, bulletin 14*, *fib*, 2001.

159. Bukhari I.A., Vollum R.L., Sagaseta J., *Shear strengthening of reinforced concrete beams with CFRP,* Magazine of Concrete Research, (in review).

160. Berset J., *Strengthening of reinforced concrete beams for shear using FRP composites*, MSC Thesis, in *Department of Civil and Environmental Engineering*. 1992, MIT: Boston.

161. Uji K., *Improving shear capacity of existing reinforced concrete members by applying carbon fiber sheets*, in *Vol. 14*, Transactions of the Japan Concrete Institute, 1992: pp. 253-266.

162. Taljsten B., *Strengthening concrete beams for shear with CFRP sheets,* Construction and Building materials, 17, 2003: pp. 15-26.

163. Triantafillou T.C., *Shear strengthening of reinforced concrete beams using epoxy -bonded FRP composites,* ACI Structural Journal, 1998: pp. 107-115.

164. Triantafillou T.C. and Antonopoulos C.P., *Design of concrete flexural members strenghened in shear with FRP,* Journal of Composites for Construction, 4(4), 2000: pp. 198-205.

165. Concrete Society, *Design Guidance for strengthening concrete structures using fibre composite materials*, in *Technical report 55*, 2003: United Kingdom.

166. Shin S.W, Lee K.S., Moon J.I., Ghosh S.K., *Shear Strength of Reinforced High-Strength Concrete Beams with Shear Span-to-Depth Ratios between 1.5 and 2.5,* ACI Structural Journal, 96(4), 1999: pp. 549-556.

167. Khalifa A., Gold W., Nanni A., Abbel-Aziz M.I.., *Contribution of externally bonded FRP to the shear capacity of RC flexural members,* Journal of Composites for Construction, 2(4), 1998: pp. 195-202.

168. Zhang Z. and Hsu T.C., *Shear strengthening of reinforced concrete beams using carbon-fibre-reinforced polymer laminates,* Journal of Composites for Construction, 9(2), 2005: pp. 158-169.

169. Bresler B. and Scordelis A.C., *Shear strength of reinforced concrete beams,* Journal of Americal Concrete Institute, 60(1), 1963: pp. 51-72.

170. Muttoni A., *Shear and punching strength of slabs without shear reinforcement.* Beton-und Stahlbetonbau, 98, 2003: pp. 74-84.

171. Walraven J.C. and Lehwalter N., *The bearing capacity of concrete struts in strut and tie models exemplified for the case of short beams,* Beton-und Stahlbetonbau, 1989, Helf 4, April '89 (In German).

172. Taylor H.P.J., *Shear strength of large beams,* Journal of Structural Division ASCE, 1972: pp. 2473-2490.

173. Walraven J.C., *Influence of member depth on the shear strength of lightweigth concrete beams without shear reinforcement*, in *Steven Report 5-78-4,* 1978, Delft University of Technology: Delft.

174. Bazant Z.P. and Kim J.K., *Size effect in shear failure of longitudinally reinforced beams,* ACI Journal, 81(5), 1984: pp. 456-468.

175. Fujita M., Sato R., Matsumoto K., Takagi I., *Size effect on shear capacity of RC beams using HSC without shear reinforcement*, in *Proceedings of the 6th International Symposium on Utilization of High Strength/High Performance Concrete*, 2002: Leipzig.

176. Sherwood E.G., Bentz E.C., and Collins M.P., *Effect of Aggregate Size on Beam-Shear Strength of Thick Slabs,* ACI Structural Journal, 104(2), 2007: pp. 180-190.

177. Bentz E.C. and Collins M.P., *Development of the 2004 Canadian Standards Association (CSA) A23.3 shear provisions for reinforced concrete,* Canadian Journal of Civil Engineering, 33, 2006: pp. 521-534.

178. Collins M.P. and Kuchma D., *How safe are our large, lightly reinforced concrete beams, slabs and footings,* ACI Structural Journal, 96(4), 1999: pp. 482-490.

179. Yang K.H., Chung H.S., Lee E.T., Eun H.C., *Shear characteristics of high-strength concrete deep beams without shear reinforcement,* Engineering Structures, 25(10), 2003: pp. 1343-1352.

180. Uzel A., Podgorniak B., Bentz E.C., Collins M.P., *Design of large footings for one-way shear,* ACI Structural Journal, paper submitted Oct 24th 2007.

181. Collins M.P., *Personal communication in one-day course "Shear strength evaluation of concrete structures",* Univ. Cambridge, 2008: Cambridge.

182. Ueda T., *Numerical modelling for concrete and masonry as heterogeneous and discontinuum material*, in *6th International Conference AMCM'2008*, 2008, Lodz, Poland.

183. Chana P.S., *Investigation of the mechanism of shear failure of reinforced concrete beams,* Magazine of Concrete Research, 39(141), 1987: pp. 196-204.

184. Ramirez J.A, Olek J., and Malone B.J., *Shear Strength of Lightweight Reinforced Concrete Beams,* ACI - Special Publication, SP218-5, 2004.

185. Watanabe F. and Lee J.Y., *Theoretical prediction of shear strength and failure mode of reinforced concrete beams,* ACI Structural Journal, 95(6), 1998: pp. 749-757.

186. Kagami Y., Mazuhara H., Takagi H., Karino Y., *Splitting-bond failure of a dabble reinforced concrete beam, Part 1*, in *Summaries of Technical Papers of Annual Meeting,* AIJ, 1991.

187. Kokusho S., Kobayashi K., Mitsugi S., Kumagai H., *Ultimate shear strength of RC beams with high tension shear reinforcement and high strength concrete,* Journal of Structural Construction Engineering, AIJ, 373, 1987: pp. 83-91.

188. Matsuzaki Y., Nakano K., Iso M., Watanabe H., *Experimental study on shear characteristics of RC beams with high tension shear reinforcement,* JCI Proceedings, 12(2), 1990: pp. 325-328.

189. Takagi H., Okude H., and Nitta T., *Shear strength of beam depending on the strength of web reinforcements,* JCI Proceedings, 17(2), 1989: pp. 75-80.

190. Simokaichi T., *Research on shear transfer mechanism of reinforced concrete members*, MSc Thesis, in *Department of Architectural Engineering*, 1994, Kyoto University, Japan.

191. Calavera J., *Proyecto y Cálculo de Estructuras de Hormigón*. INTEMAC, Vol. 1. 1991.

192. Watanabe F., Nishiyama M., and Mugurama H., *Strength and ductility of high strength concrete beams subjected to combined bending and shear*, in *Symposium on the Utilization of High Strength Concrete*, 1993, Lillehammer, Norway.